

GLO1340

UNIVERSITY OF UTAH
RESEARCH INSTITUTE
EARTH SCIENCE LAB.

SUBJ
GCHM
ACH

ACTIVITY COEFFICIENTS IN HYDROMETALLURGY

by

C. L. KUSIK
Arthur D. Little, Inc.
Cambridge, Massachusetts 02140

and

H. P. MEISSNER
Department of Chemical Engineering
Massachusetts Institute of Technology
Cambridge, Massachusetts 02139

Presented at
The 106th AIME Annual Meeting
Atlanta, Georgia

March 8, 1977

Arthur D Little Inc

ACTIVITY COEFFICIENTS IN HYDROMETALLURGY

Aqueous systems dealt with in hydrometallurgy usually involve solutions of strong electrolytes. Equilibrium calculations in such systems require information on the thermodynamic activity coefficients of the dissolved species. Unfortunately, relatively little experimental information on these activity coefficients has been available, especially in the more concentrated multi-ion solutions commonly encountered in hydrometallurgy. Within recent years, however, empirical methods for prediction of these activity coefficients have appeared. The object here is to review these methods, with particular reference to typical hydrometallurgical systems.

Activity Coefficients Versus Concentration. The generalized formula for a strong electrolyte is $A_{v_1} B_{v_2}$. A solution of this electrolyte is called "pure" when alone, and "mixed" when other ions are present. Dissociation is as follows:



where z_1 and z_2 are respectively the absolute value of the charges on the cations and anions present, v_1 and v_2 are the stoichiometric coefficients, with the subscripts identify the ions involved.

The mean ionic activity of an electrolyte in a pure solution is γ_{12}° indicated by a superscript \circ , while the mean ionic activity coefficient of this same ion pair in a mixed solution is γ_{12} . The corresponding "reduced" activity coefficients Γ_{12}° and Γ_{12} are defined as follows:

$$\Gamma_{12}^\circ = (\gamma_{12}^\circ)^{1/z_1 z_2} \quad (2a)$$

$$\Gamma_{12} = (\gamma_{12})^{1/z_1 z_2} \quad (2b)$$

Concentrations of electrolytes and of individual ions are often expressed in molalities, namely gram moles per 1,000 grams water or ionic strength I (see nomenclature).

It has been found (9.) that at 25°C in pure aqueous solutions of most strong electrolytes, the reduced activity coefficient Γ° varies with the ionic strength in accordance with some one of the isotherms of Figure 1. To illustrate, experimental points for a selected number of salts of interest in hydrometallurgy are plotted on this figure. Inspection shows reasonable agreement of these data points with one or another of these isotherms. Thus, each isotherm on Figure 1 may be viewed as representing an electrolyte, and is identified by a numerical value of the parameter "q" as further discussed below. Values of q for a number of metal sulfates, chlorides, and other electrolytes of interest are listed in Table 1. Inspection of these isotherms shows that they all start at a Γ° value of unity at low concentrations, and then diverge markedly as concentrations increase. This behavior is independent of the fact that some of these electrolytes may be hydrated (5) like $\text{CuSO}_4 \cdot 5\text{H}_2\text{O}$, may be double salts (6) like $\text{KMgCl}_3 \cdot 6\text{H}_2\text{O}$, or may be acid salts (8) like NH_4HSO_4 .

Further inspection of Figure 1 shows little or no cross-over of the isothermal data points and curves. Location of a single known point of the reduced activity coefficient Γ° at some (higher) value of I makes it possible to locate the entire isotherm over its whole concentration range. Interpolation between experimental points, or extrapolation to concentrations often far beyond saturation for a pure solution, can thus be made directly.

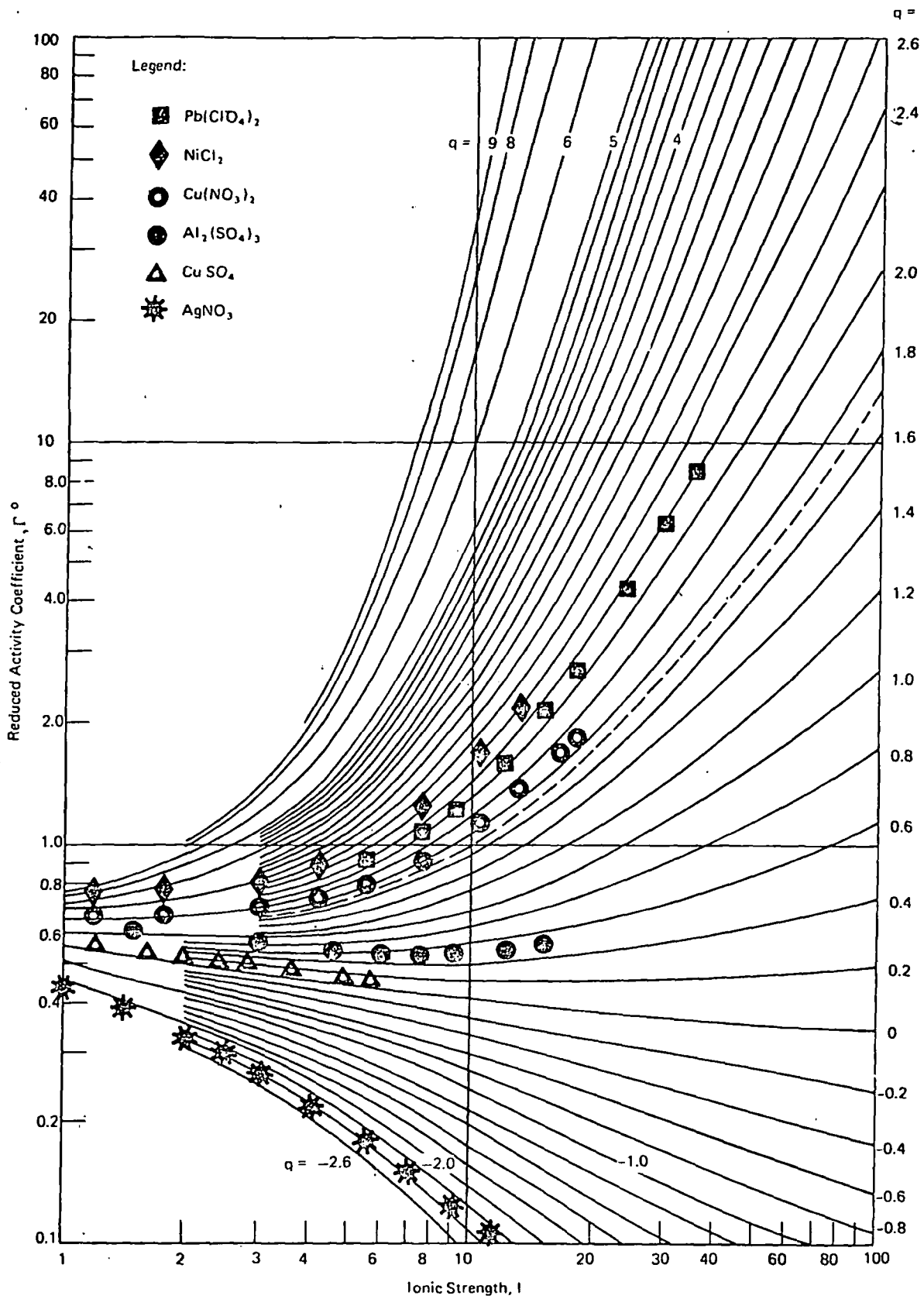


FIGURE 1 ACTIVITY COEFFICIENTS FOR SELECTED METALLIC ELECTROLYTES COMPARED WITH CURVES DERIVED FROM EQUATION 3 Activity Coefficients from (2, 10)

ELECTROLYTE	Q	I (MAX)	S
AGNO3	2.550	0.0	0.012
CSAC	5.590	3.5	0.037
CSHR	0.060	5.0	0.028
CSCL	0.160	6.0	0.036
CSJ	0.410	3.0	0.001
CSOM	7.340	1.0	*
CSNO3	2.620	1.4	*
HCL	6.690	6.0	0.050
HCL	6.100	16.0	0.092
HCLH4	8.200	6.0	0.044
HCL04	9.300	16.0	0.189
HNH3	3.660	3.0	0.001
KAC	5.050	3.5	0.027
KBN	1.150	5.5	0.003
KBRH3	2.000	0.5	*
KCL	0.920	4.5	0.006
KCLO3	1.700	0.7	0.012
KONS	0.610	5.0	0.012
KF	2.110	4.0	0.025
KHMAL	0.720	5.0	0.006
KH2PO4	2.540	1.0	*
KHSUC	0.020	4.5	0.017
KI	1.620	4.5	0.011
KNO3	2.330	3.5	0.008
KOH	4.770	6.0	0.029
KTOL	1.750	3.5	0.029
LIAC	2.810	4.0	0.003
LIBR	7.270	6.0	0.018
LIBR	7.800	20.0	0.144
LICL	5.620	6.0	0.025
LICL	5.650	20.0	0.148
LIOM	0.080	4.0	0.018
LINH3	3.800	6.0	0.040
LINO3	3.400	12.0	0.111
LITOL	0.840	4.5	0.011
NAAC	4.200	3.5	0.016
NABR	2.900	4.0	0.017
NABRH3	0.600	2.5	0.003
NACL	2.230	6.0	0.041
NACLH3	0.410	3.5	0.007
NACLH4	1.300	6.0	0.005
NACNS	2.940	4.0	0.009
NAF	0.370	1.0	*
NAFORM	1.830	3.5	0.011
NAHMAL	0.010	5.0	0.005
NAHSUC	0.000	5.0	0.018
NAH2PO4	1.500	0.0	0.062
NAJ	4.060	3.5	0.007
NANO3	0.300	6.0	0.014
NAHN	3.000	6.0	0.006

ELECTROLYTE	Q	I (MAX)	S
NAOH	3.950	29.0	0.226
NAPROP	5.540	3.0	0.032
NATOL	0.800	4.0	0.025
NH4CL	0.820	6.0	0.013
NH4NH3	1.150	6.0	0.013
NHAC	5.390	3.5	0.028
RHBR	0.460	5.0	0.007
RHCL	0.620	5.0	0.014
RBI	0.450	5.0	0.012
RBNH3	2.490	4.5	0.004
TLAC	0.730	6.0	0.004
TLNO3	4.600	0.4	*

HIGHER ELECTROLYTES	Q	I (MAX)	S
ALCL3	1.920	10.8	0.028
AL2(SO4)3	0.360	15.0	0.016
BAAC2	0.600	10.5	0.003
BABR2	1.920	6.0	0.021
BACL2	1.480	5.4	0.027
BACL042	1.900	15.0	0.055
BAI2	2.840	6.0	0.019
BANH32	0.520	1.2	*
HES04	0.400	10.0	0.055
CACL2	2.400	18.0	0.103
CACL042	3.450	18.0	0.065
CAI2	3.270	6.0	0.011
CANH32	0.930	18.0	0.037
CA(NO3)2	0.900	60.0	0.049
CONH32	1.530	7.5	0.043
COS04	0.016	14.0	0.049
CECL3	1.410	12.0	0.022
COBR2	3.080	15.0	0.014
COCL2	2.250	12.0	0.039
COI2	3.870	18.0	0.038
CONH32	2.000	15.0	0.023
CHCL3	1.720	7.2	0.022
CR(NO3)3	1.510	8.4	0.028
CR2(SO4)3	0.430	18.0	0.033
CS2S04	0.160	5.4	0.010
CUCL2	1.400	6.0	0.014
CUNH32	1.830	18.0	0.022
CUS04	0.000	5.0	0.008
EUCL3	1.490	12.0	0.022
FFCL2	2.100	6.0	0.008
K2CR04	0.163	10.5	0.018
K2S04	0.250	2.1	0.001
KJFE(CN)6	0.400	8.4	0.036
K4FE(CN)6	0.300	4.0	0.040
LACL3	1.410	12.0	0.022
LI2S04	0.570	9.0	0.014
HGAC2	0.830	12.0	0.007

ELECTROLYTE	Q	I (MAX)	S
MGRH2	3.500	15.0	0.096
MGCL2	2.900	15.0	0.103
MGCL042	4.150	12.0	0.057
MGI2	4.640	6.0	0.045
MGNH32	2.320	15.0	0.026
MGS04	0.150	12.0	0.040
MNCL2	1.600	18.0	0.075
MNS04	0.140	16.0	0.052
NA2CR04	0.410	12.0	0.043
NA2FUM	0.880	6.0	0.001
NA2MAL	0.120	9.0	0.039
NA2S203	0.180	10.5	0.023
NA2S04	0.190	12.0	0.029
NDCL3	1.420	12.0	0.020
NH42S04	0.250	12.0	0.037
NICL2	2.330	15.0	0.007
NIS04	0.025	10.0	0.029
PBCLH42	2.250	18.0	0.024
PBNH32	0.970	6.0	0.010
PRCL3	1.400	12.0	0.020
RB2S04	0.007	5.4	0.010
SCCL3	1.680	10.8	0.023
SMCL3	1.470	12.0	0.021
SRHR2	2.340	6.0	0.006
SRCL2	1.950	12.0	0.042
SRCLH42	2.840	18.0	0.013
SR12	3.030	6.0	0.009
SRNH32	0.300	12.0	0.043
U02CL2	2.400	9.0	0.050
U02CL042	5.640	16.5	0.064
U02NH32	2.900	0.0	0.034
U02S04	0.060	8.0	0.257
YCL3	1.550	12.0	0.021
ZNCL2	0.800	18.0	0.096
ZNCL042	4.300	12.0	0.063
ZNH32	2.280	18.0	0.027
ZNS04	0.050	8.0	0.257

ABBREVIATIONS

- Q Value of exponent q in Equation 3
- I(MAX) Maximum value of ionic strength at which Equation 3 compared against experimental data
- S Estimated standard deviation in $[\ln(Eq.3)/\ln(exp)] - 1$
- AC Acetate
- FOR Formate
- FUM Fumarate
- MAL Maleate
- PROP Propionate
- SUC Succinate
- TOL p-toluene sulphonate

* q determined from 1 data point activity coefficient data from (2, 10)

Analytical Expression. For convenience in computer calculations, the following analytical expression has been developed to fit all the isotherms of Figure 1:

$$\Gamma^{\circ} = [1 + B(1 + 0.1 I)^q - B]\Gamma^* \quad (3)$$

where

$$B = 0.75 - 0.065q \quad (3a)$$

$$\log_{10} \Gamma^* = \frac{-0.5107\sqrt{I}}{1 + C\sqrt{I}} \quad (3b)$$

$$C = 1 + 0.055q \exp(-0.023I^3) \quad (3c)$$

Inspection shows that this equation, relating the reduced activity coefficient Γ° to ionic strength I , involves a single parameter q , and that fixing q determines an entire isotherm. A simple program suitable for a calculator such as an H.P. 25 or equivalent for calculating Γ_{12}° from Equation 3 when given I and q , or for calculating q when given Γ° and I , is presented in the Appendix. Equation 3 is also the source of the q values for various electrolytes presented in Table 1. That is, each q value here is an average of individual q 's calculated from selected experimental data points found in the literature. The estimated standard deviations listed in Table 1 are usually at four different I values obtained by determining the error in Γ between experimental and calculated values as found from Equation 3.

Effect of Temperature. So far, Figure 1 and Equation 3 have been presented as applying only at 25°C. Further study shows, however, that isotherms at all temperatures from -20°C to 150°C and beyond fall into this curve family (7) and therefore also follow Equation 3. The values of q for any given electrolyte vary systematically with temperature in accordance with the following equation:

$$\frac{q_T - q_{25}}{t - 25} = aq + b^* \quad (4)$$

where the constants a and b* are as follows: for sulfates (except H₂SO₄), a is -0.0079 and b is -0.0029; for all other electrolytes, a is -0.005 and b* is 0.0085. Thus, for HCl, when I is 8, Γ° is reported by Akerlof and Teare (1) to be 5.9 at 25°C, hence q is 6.23 as determined from Figure 1, Equation 3 or the computer program of the Appendix. Substituting into Equation 3 and solving at 50°C, q is found to be 5.66, making Γ° equal to 4.7 by Equation 1 (or Figure 1) versus Akerlof and Teare's experimental value of 4.5.

Vapor Pressures

Having determined the appropriate q value in Equation 3 for a pure electrolyte solution of interest, the corresponding vapor pressure of water at the same temperature as a function of I and log Γ° can be determined from the Gibbs-Duhem equation (3) as follows:

$$\log (a_w)_{z_1 z_2} = -[0.0156 I_{12}/(Z_1 Z_2)] - (0.036) \int_0^{\Gamma_{12}^\circ} Id \log \Gamma_{12}^\circ \quad (5)$$

Knowing the value of q for the electrolyte under consideration, and assuming Equation 3 to apply, then the last term on the right side of Equation 5 can be integrated directly. Obviously, (a_w^o)_{z₁z₂} can be evaluated from Equation 5 at any temperature for any electrolyte whose q value is known. A Fortran program is presented in the Appendix for evaluating (a_w^o)_{z₁z₂} from Equation 5, knowing I and q for the electrolyte in question.

It is often convenient to have a graphical representation of Equation 5 to supplement the calculational procedures of the Appendix. For this purpose, water activities of pure solutions of 1:1 electrolytes are designated as (a_w^o)'. Values of (a_w^o)' calculated from Equation 5 are plotted as dotted lines on

Figure 2. To illustrate, the activity coefficient, Γ° , is known to be 7.41 for a 10 molal HCl solution at 50°C. From Figure 2 or from the Fortran program of Appendix B, $(a_w^\circ)'$ for this solution is 0.44, which compares well with the experimental value of 0.43.

To obtain the activity of water over pure solutions of higher electrolytes from Figure 2, the following relation (obtained directly from Equation 5, (3) is used:

$$\log (a_w^\circ) = (0.0156)(I)\left(1 - \frac{1}{Z_1 Z_2}\right) + \log (a_w^\circ)' \quad (6)$$

To illustrate at 25°C, NiCl_2 is a 2:1 electrolyte for which Γ° is 1.72 when the ionic strength I is 12 (a 4.0 molal solution). At these values of I and Γ° , $(a_w^\circ)'$ is 0.52 from Figure 3. Substituting into Equation 6 $\log (a_w^\circ)$ for NiCl_2 is -0.190 or $a_w^\circ = 0.645$ which is in fair agreement with 0.635 calculated from the reported osmotic coefficient ϕ of 2.10 (see nomenclature). A further comparison of experimental water activities and values obtained from Figure 2 with Equation 6 used for higher electrolytes, is shown in Table 2. Agreement is generally seen to be within a few percent. Clearly the computer program shown in the Appendix could have been used here equally well.

Activity Coefficients in Mixtures

At any given ionic strength, the reduced activity coefficient of electrolyte 12 in a multicomponent (mixed) aqueous solution, namely Γ_{12} , is usually different from its pure solution value. In mixed solutions, Γ_{12} can be estimated from pure solution values of Γ° for the various cation-anion pairs that can be formed, with all Γ° values determined at the temperature and total ionic strength of the mixture. Upon identifying the cations "i" with the odd subscripts 1, 3, 5, etc., and anions "j" with even subscripts 2, 4, 6, etc., calculating I_i , I_j and V_{ij} values as defined in the nomenclature, $\log \Gamma_{12}$ is obtained by the following equation, applicable to solutions of two, three, four and by extension of any number of ions.

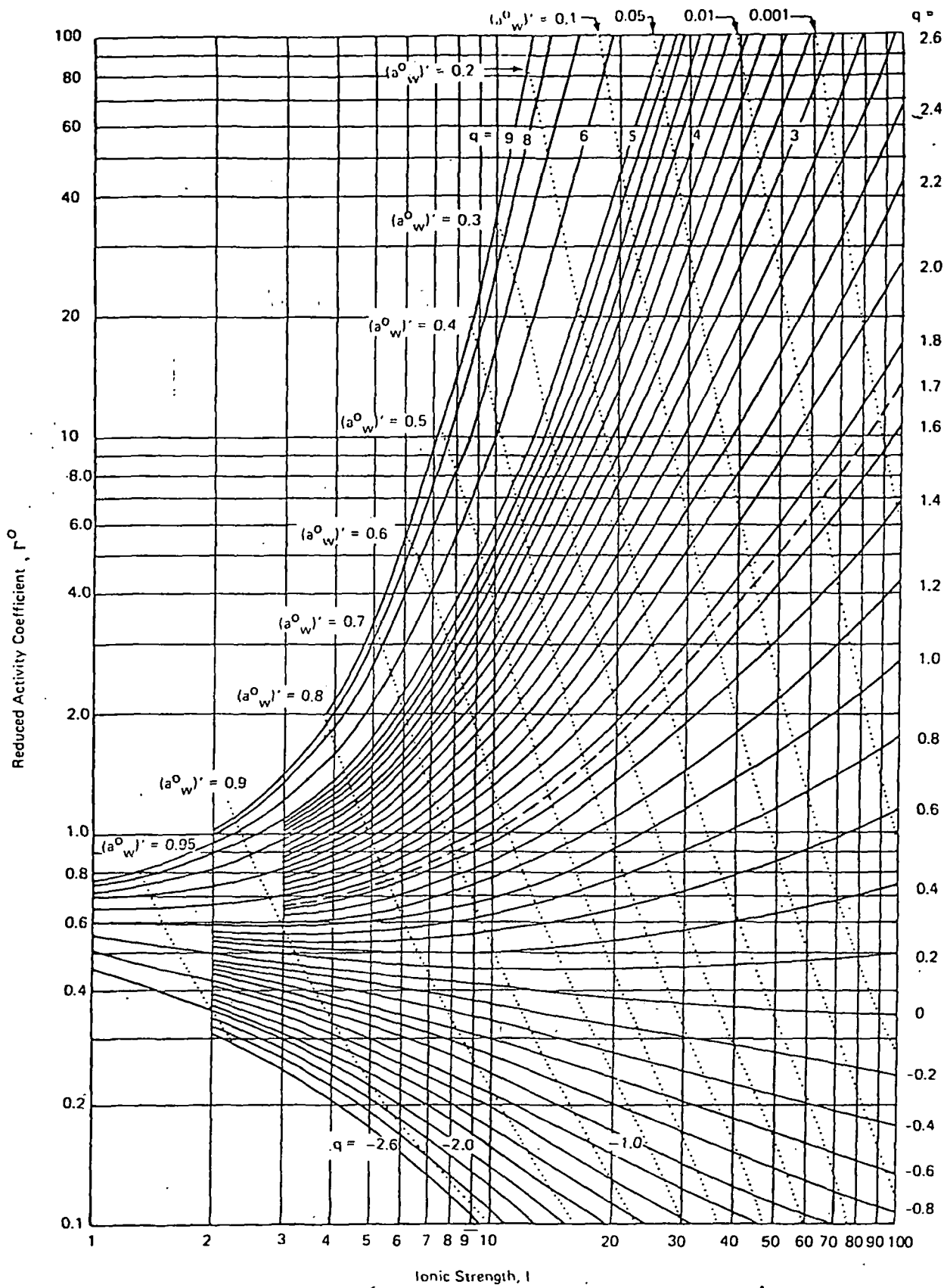


FIGURE 3 ISOTHERMS OF Γ° VERSUS I SHOWING LINES OF CONSTANT WATER ACTIVITIES FOR 1:1 ELECTROLYTES
 For higher electrolytes, $(a_w^0)'$ values read from this figure are used in Equation 6 to determine water activities.

TABLE 2

CALCULATED VERSUS EXPERIMENTAL VALUES OF WATER ACTIVITIES AT 25°C

<u>Electrolyte</u>	<u>Ionic Strength I</u>	<u>a_w (experimental)*</u>	<u>a_w from Figure 3 and Eq. 6</u>
AgNO ₃	12	0.855	0.86
NH ₄ NO ₃	20	0.678	0.67
NaOH	20 27.5	0.136 0.07	0.15 0.06
HCl	16	0.174	0.17
CaCl ₂	30	0.180	0.17
Pb(ClO ₄)	30	0.178	0.17
"	36	0.113	0.13
NH ₄ NO ₃	27.5	0.62	0.60
MgCl ₂	17.4	0.33	0.38
LiCl	19.6	0.11	0.10

* Largely calculated from the osmotic coefficient ϕ (see nomenclature).

$$\log \Gamma_{12} = \frac{Z_1}{Z_1+Z_2} (V_{12}I_2 \log \Gamma_{12}^\circ + V_{14}I_4 \log \Gamma_{14}^\circ + \dots) / I_T + \frac{Z_2}{Z_1+Z_2} (V_{21}I_1 \log \Gamma_{21}^\circ + V_{23}I_3 \log \Gamma_{23}^\circ + \dots) / I_T \quad (7)$$

or in general for any specific electrolyte identified by cation numbered

$$\log \Gamma_{ij} = \frac{Z_i}{Z_i+Z_j} (V_{i2}I_2 \log \Gamma_{i2}^\circ + V_{i4}I_4 \log \Gamma_{i4}^\circ + \dots) / I_T + \frac{Z_j}{Z_i+Z_j} (V_{j1}I_1 \log \Gamma_{j1}^\circ + V_{j3}I_3 \log \Gamma_{j3}^\circ + \dots) / I_T \quad (8)$$

If only ions 1, 2, and 3 are present, then the second term on the right side of Equation 7 disappears, since I_4 is now zero. Similarly if ions 5 and 6 are added to the system, then the term $V_{16}I_6 \log \Gamma_{16}^\circ$ is added in the first parenthesis of Equation 7, $V_{25}I_5 \log \Gamma_{25}^\circ$ is added in the second parenthesis. Equation 7 is an extended version of that originally presented (4), and is applicable to all mixtures, regardless of the magnitude of Z_1 , Z_2 , etc. As expected when all cations carry the same charge and all anions the same charge (e.g. NiCl_2 , CuCl_2 , FeCl_2), Equation 7 simplifies to that previously published:

$$\log \Gamma_{12} = 0.5 (Y_2 \log \Gamma_{12}^\circ + Y_4 \log \Gamma_{32}^\circ + X_1 \log \Gamma_{12}^\circ + X_3 \log \Gamma_{32}^\circ) \quad (9)$$

where the ionic strength fractions X and Y are defined in the nomenclature. In practice, simplified Equation 9 predicts activity coefficients in three-ion solutions of singly and doubly charged ions with apparently no greater error, and in some cases less error than the more complex Equations 7-8.

However, Equations 7-8 appear superior in predicting activity coefficients for solutions containing either more than three ions or having ions carrying more than a double charge. To illustrate the applicability of Equation 7 to a three-ion system, consider a mixed solution, saturated at 25°C with NaNO₃ which is 5.30 molal in Na⁺, 15.84 molal in NO₃⁻ and 5.27 molal in Ca⁺⁺. It follows by definition that the total ionic strength, I_T, for this solution is 0.5(5.30)(1²)+0.5(15.84)(1²)+0.5(5.27)(2²)=21.1. Designating Na⁺, NO₃⁻ and Ca⁺⁺ as ions 1, 2, and 3, then V₁₂ and V₂₃ are respectively 2.0 and 2.25, while log Γ₁₂^o and log Γ₃₂^o are respectively -0.60 (4) and -0.081 (2). Substituting into Equation 7, Γ₁₂ for NaNO₃ in this mixed solution is 0.45 versus a value calculated from the solubility product of 0.38 (4).

Three ion systems such as just illustrated are often encountered, and a program which can be used with an HP 25 or equivalent is presented in the Appendix.

Vapor Pressures Over Multicomponent Solutions

Corresponding to the above activity coefficient equations, the water activity for the mixed solution just discussed can be calculated from the "pure" solution activities of water, (a_w^o)₁₂, (a_w^o)₁₄, (a_w^o)₃₂; etc., at the total ionic strength and temperature of the mixed solution. For a 4-ion system, log (a_w)_{mix} becomes:

$$\log (a_w)_{\text{mix}} = W_{12} \log (a_w^o)_{12} + W_{14} \log (a_w^o)_{14} + W_{32} \log (a_w^o)_{32} + W_{34} \log (a_w^o)_{34} + r \quad (10)$$

where the weighting factors W_{ij}, and residue, r, are defined in the nomenclature. For similarly charged electrolytes such as MgCl₂ in CaBr₂ the residue term is

zero and $W_{ij} = X_i Y_j$ which yields the following previously published equation (5) for a four-ion system.

$$\begin{aligned} \log (a_w)_{\text{mix}} = & X_1 Y_2 \log (a_w^\circ)_{12} + X_1 Y_4 \log (a_w^\circ)_{14} \\ & + X_3 Y_2 \log (a_w^\circ)_{32} + X_3 Y_4 \log (a_w^\circ)_{34} \end{aligned} \quad (11)$$

Calculation of Salt Solubility

Solubilities of an electrolyte in its pure and mixed solutions are related by the so-called thermodynamic solubility product, $(K_t)_{\text{sp}}$ which is constant for a specific electrolyte at a given temperature in all its saturated solutions, whether pure or "mixed." Thus, for mixed and pure saturated solutions of an electrolyte containing n water of crystallization per mole, the solubility products are related as follows (8):

$$(m_1)^{v_1} (m_2)^{v_2} (\gamma_{12})^{v_{12}} (a_{\text{mix}})^{n_0} = (m_1^\circ)^{v_1} (m_2^\circ)^{v_2} (\gamma_{12}^\circ)^{v_{12}} (a_w^\circ)^{n_0} \quad (12)$$

In addition, the relevant solubility product equation for systems in which the number of waters of hydration n is not the same in pure and mixed solutions is given by:

$$(m_1)^{v_1} (m_2)^{v_2} (\gamma_{12})^{v_{12}} (a_{\text{mix}})^n = (m_1^\circ)^{v_1} (m_2^\circ)^{v_2} (\gamma_{12}^\circ)^{v_{12}} (a_w^\circ)^{n_0} k_c \quad (13)$$

The free energy change between crystals with n and n_0 waters of hydration is accounted for by the term k_c (as defined in the nomenclature) with examples of the use of the above equation given in reference (5).

The above solubility product equations have been further extended (6) to double salts containing three or more ions such as glaserite $(K_3Na(SO_4)_2)$.

Precision

Errors in estimating activity coefficients for various mixed electrolytes in aqueous solutions have been found to be generally within 20%. Further errors can be introduced when Γ° values are predicted from vapor pressure lowering, extrapolated over large ranges of ionic strength in Figure 2, or large temperature ranges by Equations 4 or 5. In addition, significant deviations from these curves can be found (9) for some electrolytes such as zinc and cadmium chlorides, bromides, and iodides, sulfuric acid, and thorium nitrate. Thus the relations shown here should be used only when direct experimental evidence is not available.

APPENDIX

For ease in calculations, several programs are presented below for determining the exponent q in Equation 3 and calculating Γ° , Γ_{mix} , and a_w .

Finding Exponent q

Given the ionic strength I and the reduced activity coefficient Γ° , a simple program is presented in Table A-1 for use with the Hewlett Packard HP-25 programmable calculator to find the exponent q in Equation 3. Before running the program, the following values are placed in the registers R : ionic strength I in R_0 , first trial value of exponent q in R_1 , reduced activity coefficient Γ° in R_2 , -0.023 in R_3 , $+0.055$ in R_4 , $+0.065$ in R_5 , -0.5107 in R_6 , enter into R_7 one-half of the fractional error limit in calculating Γ , say 0.001 if a value within 0.2% is desired, as used in the calculation below. Upon running the program, the final value D in the display is given by

$$D = \left| \frac{\Gamma^\circ(\text{nth trial})}{\Gamma^\circ \text{ in Register 2}} \right| - \text{value stored in Register 7.} \quad \text{Eq. A}$$

The value of q for use in Equation 3 is then obtained from Register 1. For example, suppose that the value of q is desired for HCl knowing that $\Gamma^\circ = 5.9$ (entered in Register 2) at an ionic strength = 9 (entered into Register 0). Upon entering the first trial value of q , say 7.0 in Register 1 and then running the program (which takes normally less than two minutes) the value in the display is found to be -8.77×10^{-5} in accordance with Equation A. By recalling the value q from Register 1 q is found to be 6.23 (+0.2%).

TABLE A-1
 DETERMINING EXPONENT "q" GIVEN I & Γ°

LINE	CODE	KEY ENTRY
00		
01	2401	RCL 1
02	2405	RCL 5
03	61	X
04	04	4
05	1522	g 1/x
06	51	+
07	31	Enter
08	31	Enter
09	01	1
10	41	-
11	2400	RCL 0
12	73	.
13	01	1
14	61	X
15	01	1
16	51	+
17	2401	RCL 1
18	1403	f y^x
19	61	X
20	41	-
21	2406	RCL 6
22	2400	RCL 0
23	03	3
24	1403	f y^x
25	2403	RCL 3
26	61	X
27	1507	g e^x
28	2404	RCL 4
29	61	X
30	2401	RCL 1
31	61	X
32	01	1
33	51	+
34	2400	RCL 0
35	1402	f \sqrt{x}
36	1522	g 1/x
37	51	+
38	71	\div
39	1508	g 10^x
40	61	X
41	2402	RCL 2
42	71	\div
43	1407	f ln
44	234101	STO - 1
45	1503	g ABS
46	2407	RCL 7
47	41	-
48	1551	g ≥ 0
49	1301	GTO 01

Calculating Γ°

To calculate a value of Γ given the ionic strength and the exponent q , the program shown in Table A-1 is modified by replacing Step 41 with the statement GTO 00. Registers 2 and 7 are not used whereas the other registers have the same values as discussed in the program in Table A-1. For example, upon running the program with $I=8$ and $q = 6.23$ entered in Registers 0 and 1 respectively, the final value in the display is $\Gamma^\circ = 5.91$, which is within 0.2% of the value used in the example above.

Fortran Program for Γ° and a_w

For calculating Γ° and the activity of water, given a value of q , Γ° and the water activity can be obtained from a computer program developed in Fortran language and shown in Table A-2. Data entry is achieved on a standard 80-column data card containing the following data..

-
- Col 1- 5 Temperature of solution °C;
 - Col 6-10 Z_1 ;
 - Col 11-15 Z_2 ;
 - Col 16-20 ionic strength (lowest value if more than 1 value of Γ° , a_w° desired);
 - Col 21-25 highest value of ionic strength (if more than one value of Γ° and a_w° desired*);
 - Col 26-30 increment in ionic strength*;
 - Col 31-35 value of exponent q in Equation 3;
 - Col 36-40 largest value of q if more than one value to be calculated;*
-

* If only one value of Γ and a_w are desired for a given I , set these equal to zero.

- Col 41-45 increment in q if Γ and a_w desired for more than 1 value of q ;
- Col 46-50 stoichiometric coefficient, v .

Upon entering these values into the program by reading them off the data card, values of the activity of water are calculated.

Calculating Γ_{12}

To facilitate calculating the activity coefficient in a mixture of three ions a program for use with the HP-25 is shown in Table A-3. Values to be entered into the registers R are as follows: Γ_{12} in R_0 , Γ_{14}° in Register 1, I_1 in Register 2, I_2 in Register 3, I_3 in Register 4, Z_1 in Register 5, Z_2 in Register 6, Z_3 in Register 7. Upon running the program the value shown in the display is Γ_{12} in the mixed solution. Based on the example following Equation 9, values into the registers are $R_0 = 0.25$, $R_1 = 0.083$, $R_2 = 2.65$, $R_3 = 7.92$, $R_4 = 10.54$, $R_5 = 1$, $R_6 = 1$, $R_7 = 2$. Program execution then yields a value in the display of $\Gamma_{12} = 0.45$ in accordance with Equation 7.

TABLE A-2: FORTRAN PROGRAM FOR CALCULATING r^0 AND a_w GIVEN q

```

REAL I, IMAX, MOL, NU, LG11, LG22, LGR, LOGAN, QMAX
MM=5
NR=8
14 FORMAT(1H1,2X,1HT,5X,3H Q ,4X,2HM ,7X,2HI ,3X,4HLA11,4X,4HLAZZ,
12X,4HZPZM,1X,9HGAMSMALL ,8H LGAMRED,2X,7H PHI ,2X,2HAW)
LMAX=5H
READ(MR,25)TC,A,B,XI,IMAX,DELI,C,QMAX,UELO,NU
25 FORMAT(10F5,2)
19 I=XI
LINE=0
WRITE(MM,14)
16 CONTINUE
CALL ANGAM(A,B,C,I,TC,D,E,MOL,LG11,LG22)
ZZZ=A*B
MOL=2.*I/(NU*ZZZ)
G=U.*ZZZ
LGR=ALOG10(G)
IF(I)31,30,31
30 PHI=1.
GO TO J2
31 CONTINUE
PHI=-63.9HJ+ZZZ*LGZZ/I
32 WRITE(MM,15)TC,C,MOL,I,LG11,LG22,A,B,G,LGR,PHI,E
15 FORMAT(F5,1,2F7,3,3F8,3,1X,2F2,0,1X,1PE9,3,8PF7,3,F8,4,F7,4)
LINE=LINE+1
IF(LINE=LMAX)41,41,40
40 WRITE(MM,14)
LINE=0
41 I=I+DELI
IF(I=IMAX)16,16,17
17 C=C+DELO
IF(C=QMAX)19,19,18
18 CALL EXIT
END
1
0001 SUBROUTINE ANGAM(Z1,Z2,N25,MUT,T,Y,AW,NT,LG11,LG22)
0002 REAL N25,NT, MUT,LG11,LG22
0003 DIMENSION CONST (510)
0004 MM=5
0005 NT=N25
0006 12 AT=N,25 * N,005*NT
0007 BT=1,-AT
0008 XMAX=MUT
0009 INT =XMAX/0.4 +1
0010 EVEN=2*INT
0011 DELX=XMAX/EVEN
0012 DO 1 I=1,INT
0013 II=2*I -1
0014 CONST(II)=4,
0015 II=2*I
0016 1 CONST(II)=2,
0017 IMAX=2*INT
0018 CONST(IMAX)=1,
0019 SUMLG=0
0020 X=DELX
0021 DO 2 I=1,IMAX
0022 CUM=0,02J*X **J
0023 EXX=1,+(NT* 0,055)*EXP(CUM)
0024 DNM=1,+EXX* SORT(X)
0025 GSTAR=1H,*(=(0,5107*SORT(X)/DNM))
0026 G = (RT*(1,+0,1*X)**NT+AT)*GSTAR
0027 YLG=CONST(I)*ALOG10(G)
0028 SUMLG=SUMLG + YLG
0029 2 X=X+DELX
0030 Y=G
0031 LG11 = 0,012* DELX * SUMLG
0032 LG11=LG11-MUT*(0,0156 +0,036*ALOG10(G))
0033 ZZZ=Z1+Z2
0034 LG22 = LG11 + 0,0156*MUT*(ZZZ -1,)/ZZZ
0035 AW =1H, **LG22
0036 RETURN
0037 END

```

TABLE A-3
 DETERMINING Γ_{MIX} FROM EQUATION 7

<u>Line</u>	<u>Code</u>	<u>Key Entry</u>
00		
01	2403	RCL 3
02	2406	RCL 6
03	71	÷
04	2402	RCL 2
05	2405	RCL 5
06	71	÷
07	51	+
08	2405	RCL 5
09	2406	RCL 6
10	51	+
11	1502	$9x^2$
12	61	X
13	2400	RCL 0
14	1408	f log
15	61	X
16	2406	RCL 6
17	2407	RCL 7
18	51	+
19	1502	$g x^2$
20	2407	RCL 7
21	71	÷
22	2402	RCL 4
23	61	X
24	2401	RCL 1
25	1408	f log
26	61	X
27	51	+
28	02	2
29	71	÷
30	2405	RCL 5
31	2406	RCL 6
32	51	+
33	71	÷
34	2402	RCL 2
35	2403	RCL 3
36	51	+
37	2404	RCL 4
38	51	+
39	1474	f Pause
40	71	÷
41	1508	10^x
42	-1300	GTO 00

NOMENCLATURE

- a_w = activity of water, $(a_w^\circ)_{12}$ being for a pure solution of an electrolyte identified by subscript, $(a_w)_{\text{mix}}$ being for mixed solution. (a_w°) is derived from the Gibbs-Duhem expression and is equal to the activity of water for 1:1 electrolytes.
- $\exp(x)$ = e^x
- F = molal free energy of formation from the elements, F_{n_0} , referring to crystals carrying n_0 moles water of hydration per mole electrolyte, F_n , referring to crystals carrying n moles water of hydration per mole electrolyte, and F_w being the free energy of liquid water, namely -56.69 Kcal/g-mol at 25°C.
- I = ionic strengths indicated by the subscript. The ionic strengths I_1, I_2, \dots , of the individual ions are $0.5 m_1 Z_1^2$, $0.5 m_2 Z_2^2$, and so forth. The total ionic strength I_T equals $0.5 (m_1 Z_1^2 + m_2 Z_2^2 + m_3 Z_3^2 + \dots)$. For a pure system, I_T equals $0.5 m_{12} \nu_{12} Z_1 Z_2$. The cationic strength I_c of a solution is $(I_1 + I_3 + \dots)$, the anionic strength I_a is $(I_2 + I_4 + \dots)$.
- k_c = $\exp(-\Delta F_c/RT)$
- \log, \ln = logarithm to base 10 and base e respectively
- m = molality, in g-mol/1000 g water. The ions or electrolyte referred to are indicated by subscript.
- n = moles of water of crystallization per mole of anhydrous electrolyte in a solid, n_0 and n being used to distinguish between solids in equilibrium with saturated pure and mixed solutions, respectively.
- r = residue term = $0.0156 I_T (W_{12} X_1 Y_2 / Z_1 Z_2 + W_{23} X_3 Y_2 / Z_2 Z_3 + \dots) - .0156 [I_1 / Z_1^2 + I_2 / Z_2^2 + I_3 / Z_3^2 + I_4 / Z_4^2 + \dots]$.
- R = 1.987 cal/(g mole $^\circ K$)
- V_{ij} = weighting factor $0.5(Z_i + Z_j)^2 / (Z_i Z_j)$.
- W_{ij} = $X_i Y_j [(Z_i + Z_j)^2 / Z_i Z_j] (I_c / I_T) (I_a / I_T)$.
- X = cationic fraction, as indicated by subscript i, e.g., I_1 / I_c or I_3 / I_c .
- Y = anionic fraction, as indicated by subscript j, e.g., I_2 / I_a or I_4 / I_a .

Nomenclature (Continued)

- Z = absolute number of unit charges on the ion, indicated by the subscript. Thus Z is unity for Na^+ , also for NO_3^- , but is 3 for Al^{3+} , also for PO_4^{3-} . Similarly charged electrolytes are those with similar charges on cations and anions such as MgCl_2 in CaBr_2 or NaCl in KCl . Dissimilarly charged electrolytes are those where either a) all cations do not have the same charge or b) all anions do not have the same charge; examples include a mixture of Na_2SO_4 in MgCl_2 or NaCl in MgCl_2 .
- γ = mean ionic activity coefficient for the electrolyte indicated by the subscript, γ_{12}° being for the pure solution and γ_{12} for the mixed solution.
- Γ = reduced activity coefficient, namely $\gamma_{12}^{1/Z_1 Z_2}$ for the electrolyte indicated by the subscript. The term Γ_{12}° , refers to pure solutions, Γ_{12} to mixed solutions.
- ΔF_c = free energy change of crystal hydration = $F_n - F_n(n_o - n)F_w$.
- ν = moles of ions formed upon complete dissociation of 1 mol of electrolyte. Thus, ν_1 is for the indicated cation, ν_2 is for the indicated anion, while ν_{12} is the total number of ions namely $(\nu_1 + \nu_2)$. To illustrate, ν_{12} is 2 for NaCl and 5 for $\text{Al}_2(\text{SO}_4)_3$.
- ϕ = osmotic coefficient (6, 13) = $-(63.9Z_1Z_2 \log a_w^\circ)/I$

Subscripts

- 1,3,5... = odd numbers refer to cations
2,4,6... = even numbers refer to anions
w = water
mix = values for a multicomponent solution.

Superscript

- 0 = "pure" electrolyte solution (i.e., binary solution)
' = for 1:1 electrolyte - see a_w

Other Symbols

- 1:1 = electrolytes with singly charged ions where $Z_1 = 1$ and $Z_2 = 1$
M:N = electrolytes having ion charges given by $Z_1 = M$, $Z_2 = N$

LITERATURE CITED

1. Akerlof, G., and J. W. Teare, "Thermodynamics of Concentrated Aqueous Solutions of Hydrochloric Acid," J. Am. Chem. Soc. 59, 1855 (1937).
2. Harned, H. S., and B. B. Owen, "Physical Chemistry of Electrolyte Solutions," 3rd Ed., App A, Reinhold, New York, N.Y. (1958)
3. Kusik, C. L., and H. P. Meissner, "Vapor Pressures of Water over Aqueous Solutions of Strong Electrolytes," Ind. Eng. Chem. Process Des. Develop., 12, 112 (1973).
4. Meissner, H. P., and C. L. Kusik, "Activity Coefficients of Strong Electrolytes in Multicomponent Aqueous Solutions," AIChE. J., 18, 2294 (1972).
5. Meissner, H. P., and C. L. Kusik, "Aqueous Solutions of Two or More Strong Electrolytes," Ind. Eng. Chem. Process Des. Develop., 12, 205 (1973).
6. Meissner, H. P., and C. L. Kusik, to be submitted to AIChE. J. (1977)
7. Meissner, H. P., et. al., "Activity Coefficients of Strong Electrolytes in Aqueous Solutions - Effect of Temperature," AIChE. J., 18, 3661 (1972).
8. Meissner, H. P., and N. A. Peppas, "Activity Coefficients - Aqueous Solutions of Polybasic Acids and Their Salts," AIChE. J., 19, 4806 (1973).
9. Meissner, H. P., and J. W. Tester, "Activity Coefficients of Strong Electrolytes in Aqueous Solutions," Ind. Eng. Chem. Process Des. Develop., 11, 1128 (1972).
10. Robinson, R. A., and R. H. Stokes, "Electrolyte Solutions," 2nd Ed., Academic Press, New York (1959).

Activity-Composition Relationships for Pyrope-Grossular Garnet

B. J. Hensen*, R. Schmid**, and B. J. Wood

Department of Geology, Manchester University, Manchester

Received May 13, 1975 / Accepted May 15, 1975

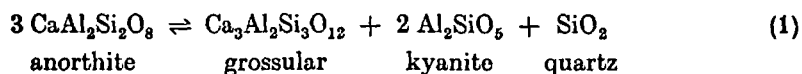
Abstract. Activity coefficients (γ) for grossular in pyrope-grossular garnet have been determined experimentally using the divariant assemblage garnet-anorthite-sillimanite (kyanite)—quartz. Values of γ for garnets with 10–12 mole % grossular have been obtained at 1000°, 1100°, 1200° and 1300° C at pressures between 15 and 21 Kb. The data are consistent with a symmetrical regular solid model for grossular-pyrope solid solutions. The interaction parameter (W) increases linearly with decreasing temperature and is given by $W = 7460 - 4.3 T$ cals (T in °K). A solvus in the pyrope-grossular solid solution is predicted with a temperature of critical mixing of $629^\circ \text{C} \pm 90^\circ \text{C}$.

Introduction

The mixing properties of garnet solid solutions have been discussed by various authors (e.g. Saxena [1], Ganguly [2], Wood [3]) but no quantitative experimental data have been available to date. In view of the potential of garnet bearing assemblages as indicators of pressure-temperature (PT) conditions of metamorphism, a better understanding of the composition-activity relationships in garnets is of major interest.

In the present paper we report an experimental study of the activity of grossular component in pyrope-grossular garnet at high pressure and temperature.

Using the end member reaction



the activities of $\text{Ca}_3\text{Al}_2\text{Si}_3\text{O}_{12}$ component in Ca—Mg garnets in the assemblages garnet_{ss}—anorthite—kyanite—quartz and garnet_{ss}—anorthite—sillimanite—quartz can be calculated at a range of pressures and temperatures from the relationship

$$(P_0 - P_1) \Delta V_0 = RT \ln a_{\text{Ca}_3\text{Al}_2\text{Si}_3\text{O}_{12}}^g \quad (2)$$

where P_0 is the equilibrium pressure for reaction (1) at the temperature of interest (T in °K), ΔV_0 is the volume change of reaction (1) at room temperature, P_1 is the pressure of interest, $a_{\text{Ca}_3\text{Al}_2\text{Si}_3\text{O}_{12}}^g$ is the activity of grossular component in the pyr-

* Present address: School of Applied Geology, University of New South Wales, Kensington, N.S.W. 2033, Australia.

** Present address: ETH Zürich, Switzerland.

ope-grossular solid solution and R is the gas constant¹. By determining garnet compositions at various temperatures and pressures the activity coefficient for grossular component can be obtained from the relation for 3-site Mg—Ca mixing:

$$a_{\text{Ca}_2\text{Al}_2\text{Si}_2\text{O}_{11}}^{\text{gt}} = (X_{\text{Ca}_2\text{Al}_2\text{Si}_2\text{O}_{11}} \gamma_{\text{Ca}_2\text{Al}_2\text{Si}_2\text{O}_{11}})^3$$

where $X_{\text{Ca}_2\text{Al}_2\text{Si}_2\text{O}_{11}}$ is the mole fraction of grossular component in the garnet solid solution and $\gamma_{\text{Ca}_2\text{Al}_2\text{Si}_2\text{O}_{11}}$ is the activity coefficient of grossular in the garnet solid solution.

Assuming the garnet to be a symmetrical regular solution (Thompson, [4]) the interaction (or Margules) parameter (W) can be calculated by

$$W = \frac{RT \ln \gamma_{\text{Ca}_2\text{Al}_2\text{Si}_2\text{O}_{11}}}{(1 - X_{\text{Ca}_2\text{Al}_2\text{Si}_2\text{O}_{11}})^2} \quad (3)$$

and the critical temperature of mixing is given by

$$T_c = \frac{W}{2R} \quad (4)$$

The anorthite breakdown reaction (1) is well known from the work of Hays [5], Hariya and Kennedy [6] and Newton [7]. Because the accuracy of the activity data depends critically on the position of the anorthite reaction boundary a check on this boundary has been carried to ensure internal consistency of the data used to calculate the activity coefficients.

Experimental Technique

The experiments were carried out in conventional, $\frac{1}{2}$ inch, Boyd and England [8] type piston cylinder apparatus, using talc and boron-nitride as pressure media.

Temperatures were controlled to within 5°C of the quoted values using Pt/Pt—13% Rh thermocouples.

The 'hot piston out' procedure was used throughout; the run is taken to a pressure 5 kb in excess of the desired value and taken to temperature before the pressure is brought back to the final value. Pressures reported are uncorrected values. The apparatus has been calibrated with respect to other laboratories at 1200°C and 1300°C and 15–20 Kb and very good agreement with previously published data has been found (Hensen and Barton [9]).

Starting materials were run in unwelded Pt-capsules. Samples were moistened by breathing for runs at 1000° and 1100°C . Run times were around 1 hr at 1300°C , 5 hrs at 1200°C and varied from 17–25 hrs at 1000° and 1100°C .

The material used in the experiments consisted of 55% of a glass of composition anorthite₄₀ensatic₆₀ (molar) plus 27% sillimanite (Brandewyn Springs, Del. by courtesy of Dr. P. M. Bell) and 18% excess purified quartz. This mixture was seeded with 4–8% garnet bearing high pressure assemblage to provide the starting material for most runs. A reversal using crystalline starting materials only has also been carried out.

In view of the fact that consistent, reproducible and, as demonstrated in one instance, reversible data could be obtained it is believed that equilibrium was closely approached in the experimental runs.

All runs were checked optically and by powder X-ray photography to ensure they contained the full mineral assemblage of interest. This is of major importance as it is not unusual at temperatures of 1200°C and above for quartz or anorthite to disappear owing to partial melting. In such cases the garnet composition is no longer fixed and cannot be used for the determination of activity coefficients.

¹ Standard states for all components are taken to be the pure phases at the pressure and temperature of interest.

Table 1. Run data and grossular quartz

Run No.	Temp. (°C)	Press. (Kb)
94	1300	16
79	1300	21
67	1200	15
81	1200	16.5
89	1200	18.5
101	1200	19
65	1100	15
77	1100	17.3
83	1100	18.5
80	1000	17
85 ^c	1000	17

^a See introduction for definition.

^b Accuracy in a_0 measurement.

^c In this run kyanite occurred.

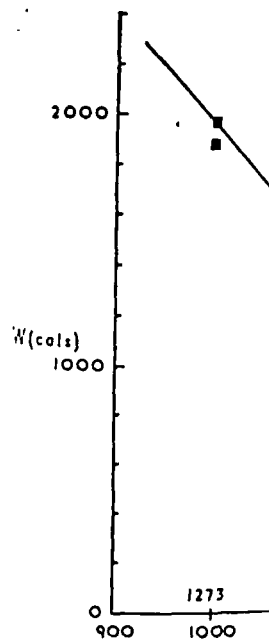


Fig. 1. Plot of the interaction parameter W to the data is shown on the curve.

Experimental Data

The experimental results and calculated interaction parameter

ent¹. By determining garnet
the activity coefficient for
on for 3-site Mg—Ca mixing

component in the garnet solid
grossular in the garnet solid

solution (Thompson, [4] the
related by

(3)

(4)

from the work of Hays [5],
the accuracy of the activity
the reaction boundary a check
consistency of the data used

oyd and England [8] type piston
media.

and values using $Pt/Pt-13\% Bi$

run is taken to a pressure 5 kb in
the pressure is brought back to
the apparatus has been calibrated
-20 Kb and very good agreement
Barton [9]).

bles were moistened by breathing
at 1300° C, 5 hrs at 1200° C and

glass of composition anorthite,
s, Del. by courtesy of Dr. P. M.
eded with 4-8% garnet bearing
for most runs. A reversal using

demonstrated in one instance,
um was closely approached in the

graphy to ensure they contained
portance as it is not unusual at
to disappear owing to partial
ixed and cannot be used for the

ure phases at the pressure and

Table 1. Run data and garnet composition in the assemblage garnet-anorthite-sillimanite-quartz

Run No.	Temp. (°C)	Press. (Kb)	Cell edge ^b a ₀ (Å)	Garnet composition (mole fraction of grossular component)		γ ^a	W (cals)
				X-ray	microprobe		
94	1300	16	11.502	0.11	0.11	1.154	565
78	1300	21	11.544	0.22		1.153	731
67	1200	15	11.497	0.10	0.11	1.353	1092
31	1200	16.5	11.507	0.12		1.408	1293
83	1200	18.5	11.530	0.18		1.260	1006
101	1200	19	11.534	0.19	0.19	1.287	1126
65	1100	15	11.503	0.11	0.11	1.554	1581
77	1100	17.3	11.523	0.16	0.16	1.527	1637
83	1100	18.5	11.541	0.21		1.418	1527
80	1000	17	11.537	0.20	0.20	1.656	1994
85 ^c	1000	17	11.547	0.22		1.574	1886

^a See introduction for definition of symbols.

^b Accuracy in a₀ measurement is better than 0.005 Å.

^c In this run kyanite occurs instead of sillimanite.

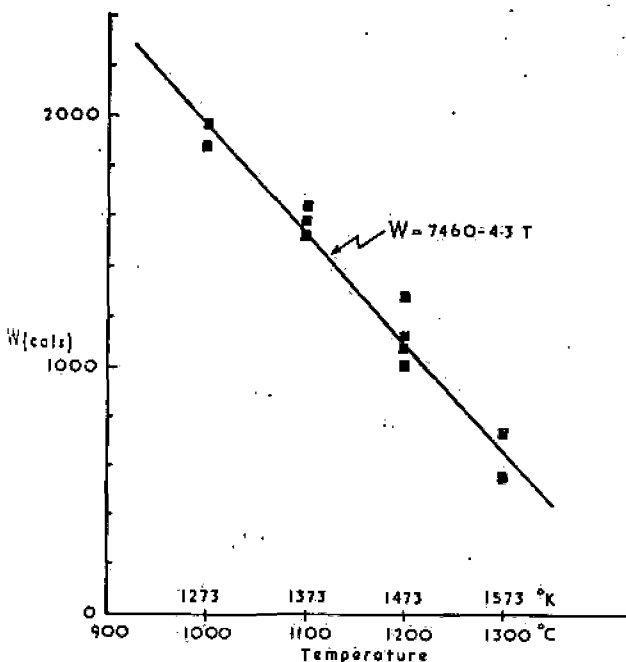


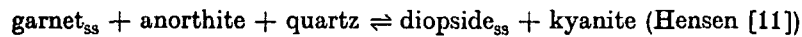
Fig. 1. Plot of the interaction parameter (W) against temperature. A linear least squares fit to the data is shown on the diagram

Experimental Data

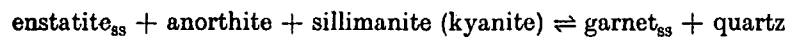
The experimental results are given in Table 1 and Fig. 1 shows a plot of the calculated interaction parameter W against temperature. The grossular content of

the garnet in the assemblage garnet-anorthite-sillimanite-quartz has been determined from cell edge measurements obtained from X-ray powder photographs. In addition electron microprobe analyses of a number of runs have been carried out using the TPD probe with non-dispersive detection system. (Reed and Ware [10]). The results of these analyses agree well with the X-ray data (Table 1). However, the microprobe revealed that compositions approximating the seed composition ($X_{\text{Gross}} \approx 0.21$) sometimes persist in cores in garnets of the composition indicated by the X-ray data. This shows that although garnet of a certain composition grows from the fine grained low pressure assemblage (that forms from the glass on heating) the rate of diffusion within garnet is too low to allow complete equilibration between cores and rims.

The reason that no data are reported above 17 Kb at 1000° C and 21 Kb at 1300° C is that above these pressures the assemblage garnet—anorthite—kyanite—quartz is no longer stable owing to the univariant reaction



At low pressure the assemblage of interest is limited by the reaction



Experimental data on these reactions will be published shortly (Hensen [12]).

Several experimental runs in Table 1 have the assemblage garnet—anorthite—sillimanite—quartz though they crystallised in the kyanite stability field. The fact that these experimental assemblages are metastable does not affect their usefulness for the activity calculations. This is well illustrated by two runs at 1000° C—17 Kb (Table 1) one of which was seeded with kyanite². The calculated interaction parameter (W) is the same, within experimental error, for the latter run (assemblage garnet—anorthite—kyanite—quartz) as for the former (assemblage garnet—anorthite—sillimanite—quartz). This also is good evidence that the results represent equilibrium data.

The garnet compositions obtained experimentally were compared with the activities, calculated using expression (2), and the resulting activity coefficients are shown in Table 1. The following data were used to calculate the activities of grossular component in pyrope grossular solid solution.

a) The anorthite breakdown curve (1) according to Hariya and Kennedy [6]:
 $\Delta V_0 = 66 \text{ cc}$. The reaction is given by $P = -1200 + 23.3T$ (P in bars, T in °C)

b) The equivalent metastable reaction



$$\Delta V_0 = 54.4 \text{ cc}; P = -460 + 24.2T \quad (P \text{ in bars, } T \text{ in } ^\circ\text{C}).$$

The expression for this reaction was calculated using the following data for the kyanite-sillimanite phase boundary

$$\Delta V_0 = 5.8 \text{ cc}; P = -6500 + 21T \quad (P \text{ in bars, } T \text{ in } ^\circ\text{C}).$$

These data for the kyanite-sillimanite boundary are consistent with the piston-out data of O'Hara and Richardson [13] and the hydrostatic data of Richardson *et al.* [14]. A reversal on this boundary in our apparatus at 1300° C gave a value of 20.5 ± 0.5 Kb in excellent agreement with O'Hara and Richardson [13] (Hensen and Barton [9]).

2 The starting material for this run consisted of garnet—clinopyroxene—kyanite—sillimanite—quartz.

A reversal of the anorthite—quartz boundary at 29.5 Kb agreeing with the model of [6].

The interaction (or W) obtained at each temperature is compared to experimental error and model, *c.f.* Thompson [11] for garnet compositions. The asymmetry in the pyrope—grossular temperature dependence of the data gives $W = 7460 - 4(T - T_0)$ for this linear equation.

Discussion of Errors

The internal consistency of the data in Eq. (2) is the main source of error. The pressure uncertainty is about 10%. The checks carried out on the sillimanite phase boundary are due to the uncertainty in the data.

Errors due to uncertainty in the activity coefficients are of ± 0.01 in W from an error of ± 0.01 in a_i . The total error in W is of about 4%. Comparison of the data with the model of [6] shows that the data are in good agreement with the model.

Conclusions

The experimental data show a significant positive dependence of W on temperature. Assuming a model given by $W = 7460 - 4(T - T_0)$, marking the top of a 10% error in W .

A critical temperature for univariant reactions between pyrope and grossular indicate a solvus temperature of about 629 ± 90° C.

The present data are in good agreement with the data for a temperature close to 629 K calcs that is independent of the critical temperature of 629 ± 90° C. The reason for the differences (or experiments for the pyrope—grossular phase assemblages reported in the literature).

More information on the pyrope—grossular system will be required for natural rocks.

Preliminary results for the almandine—grossular system are also available.

ite-quartz has been determined by x-ray powder photographs. The results of runs have been summarized in Table 1. However, the seed composition of a certain composition that forms from the glass to allow complete equilibrium.

at 1000° C and 21 Kb, as garnet—orthite—kyanite reaction

anite (Hensen [11])

the reaction

garnet_{ss} + quartz

shortly (Hensen [12])

large garnet—orthite—

anite stability field. This

table does not affect the

illustrated by two runs at

kyanite². The calculated

experimental error, for the latter

is for the former. (assum-

ptions is good evidence that

were compared with the

activity coefficients

to calculate the activities of

[Hariya and Kennedy [6]]

$3.3T$ (P in bars, T in °C)

quartz. (3)

°C).

The following data for the

T in °C).

is consistent with the piston

data of Richardson

at 1300° C gave a value

Richardson [13] (Hensen

ene—kyanite—sillimanite

A reversal of the orthite breakdown curve (1) at 1300° C gave a value between 29.1 and 29.5 Kb agreeing well with the value of 29.1 given by Hariya and Kennedy [6].

The interaction (or Margules) parameters are also given in Table 1. The values obtained at each temperature show minor random variation, which can be attributed to experimental error, and are consistent with a symmetrical regular solution model, *c.f.* Thompson [4]. In view of the fact that only a relatively small range of garnet compositions could be studied (reasons given above) the possibility of asymmetry in the pyrope-grossular solvus cannot be excluded. A significant near-linear temperature dependence of W is evident from the data. A least Squares fit of the data gives $W = 7460 - 4.3T$ cal (in °K). As shown in figure 1 the data fit this linear equation remarkably well.

Discussion of Errors

The internal consistency of the data is very good. Uncertainty in the ΔP values in Eq. (2) is the main possible source of error for the W values. At 1000° C a pressure uncertainty in ΔP of 0.25 Kb has a corresponding error in W of around 10%. The checks carried out on the orthite breakdown curve (1) and the kyanite-sillimanite phase boundary, mentioned above, give confidence that the error due to the uncertainty in ΔP is small, perhaps in the order of 5-10%.

Errors due to uncertainties in garnet composition are relatively small. The uncertainty of ± 0.01 in the mole fraction of the grossular component resulting from an error of $\pm 0.005 \text{ \AA}$ in the cell edge measurements produces an error in W of about 4%. Compounded error in W is believed to be better than 10%.

Conclusions

The experimental data demonstrate that pyrope-grossular solid solutions exhibit a significant positive deviation from ideality that increases with decreasing temperature. Assuming a symmetrical regular solution the interaction parameter is given by $W = 7460 - 4.3T$ cal (T in °K). The temperature of critical mixing (T_c), marking the top of the pyrope-grossular solvus, equals $629 \pm 90^\circ \text{ C}$ (assuming a 10% error in W).

A critical temperature of 629° C is consistent with recent experimental data on univariant reactions in the system CaO-MgO-Al₂O₃-SiO₂ (Hensen [12]) that indicate a solvus temperature above 600° C.

The present data are consistent with those presented by Ganguly and Kennedy [2] for a temperature close to 600° C. They give an approximate value of $W \approx 3.8 \pm 0.2 \text{ K cal}$ that is independent of temperature. Ganguly and Kennedy [2] predict a critical temperature of $694 \pm 55^\circ \text{ C}$ which overlaps with the present estimate of $629 \pm 90^\circ \text{ C}$. The reason that coexisting garnets are unknown from natural occurrences (or experiments for that matter) lies in the fact that other, mainly hydrous, phase assemblages replace Ca-Mg garnet at temperatures below 750-800° C.

More information on the mixing properties of almandine-grossular and almandine-pyrope will be required before the present data can be quantitatively applied to natural rocks.

Preliminary results by Cressoy (personal communication) indicate near ideality for almandine-grossular solid solution in agreement with the estimate of Ganguly [2].

Activity Coefficients of Strong Electrolytes in Multicomponent Aqueous Solutions

SUBJ
GCHM
ACS

EQUILIB. MODELS / CONC. SOL.

H. P. MEISSNER

Chemical Engineering Department
Massachusetts Institute of Technology, Cambridge, Massachusetts 02139

C. L. KUSIK

Arthur D. Little, Inc., Cambridge, Massachusetts 02140

The quantity Γ_{12} here called the reduced activity coefficient is related to γ_{12} the mean activity coefficient of a strong electrolyte 12 as follows:

$$\Gamma_{12} = \gamma_{12}^{1/z_1 z_2}$$

where z_1 and z_2 are the charge numbers on the ions. The value of Γ_{12} for electrolyte 12 in an aqueous solution containing the three ions 1, 2, and 3, such as Na^+ , Cl^- , and Ba^{++} , is to be calculated as follows:

$$\log \Gamma_{12} = \log \Gamma_{12}^\circ + \frac{1}{2}(X_3) \log (\Gamma_{32}^\circ / \Gamma_{12}^\circ)$$

Here Γ_{32}° and Γ_{12}° are for the indicated electrolytes, namely NaCl and BaCl_2 in this example, at the total ionic strength of the mixture. The term X_3 represents the fraction $m_3 z_3^2 / (m_1 z_1^2 + m_3 z_3^2)$ in which m represents the molality of the indicated ion. Fair success is usually attained with this equation in predicting γ , even at high electrolyte concentrations.

Similar equations are proposed for aqueous solutions containing four or more ions.

Values of γ , the mean activity coefficient of an individual strong electrolyte in an aqueous solution of two or more strong electrolytes, are required in calculating the ionic reaction equilibria in aqueous solutions. Of particular interest are γ values in relatively concentrated solutions (brines, waste streams, etc.) such as are encountered in industrial chemistry, in hydrometallurgy, in electrochemistry, in biochemical systems and the like. Experimental data on γ in mixed systems are difficult to obtain and relatively few direct measurements have been published. The object here is to consider a method for approximating the values of such activity coefficients, applicable in all concentrations of mixed aqueous solutions at 25°C.

In the systems under discussions, the cations are designated by the subscripts 1, 3, 5, 7, etc., while the anions are 2, 4, 6, 8, etc., with corresponding ion molalities being m_1, m_2, m_3 , etc., and ion charges being z_1, z_2, z_3 , etc. The mean activity coefficient of any single electrolyte 12 in solution is designated at γ_{12}° , while its mean activity coefficient in a "mixed" solution containing more than one anion and one cation is γ_{12} . The total ionic strength μ_T of solutions, regardless of the number of dissolved electrolytes, is then $\frac{1}{2}(m_1 z_1^2 + m_2 z_2^2 + m_3 z_3^2 + \dots)$. Similarly, in ionic strength units, the cationic strength μ_c is $\frac{1}{2}(m_1 z_1^2 + m_3 z_3^2 + m_5 z_5^2 + \dots)$, while the anionic strength μ_a is $\frac{1}{2}(m_2 z_2^2 + m_4 z_4^2 + m_6 z_6^2 + \dots)$. Obviously, μ_c and μ_a are equal only when all ion charges are of equal magnitude. By definition, the total ionic strength is μ_T , where $\mu_T = \mu_c + \mu_a$.

In ionic strength units, the fraction of the cations present represented by cation 1 is X_1 , where

$$X_1 = 1/2(m_1 z_1^2 / \mu_c)$$

Similarly, the fraction of the anions present represented by anion 2 is Y_2 , where

$$Y_2 = 1/2(m_2 z_2^2 / \mu_a)$$

In any solution containing a single electrolyte, X_1 and Y_2 are unity.

For mixed systems, these definitions are conveniently illustrated with a solution containing 1 g.-mole Na_2SO_4 and 1 g.-mole AlCl_3 in 1000 g. water. The ions Na^+ , SO_4^{--} , Al^{+++} and Cl^- are arbitrarily designated as 1, 2, 3, and 4 respectively; consequently, the molalities m_1, m_2, m_3 and m_4 are respectively 2, 1, 1, and 3, while the corresponding z values are 1, 2, 3, and 1. In ionic strength units, μ_c is $1/2(2 \cdot 1^2 + 1 \cdot 3^2)$ or 5.5, μ_a is $1/2(1 \cdot 2^2 + 3 \cdot 1^2)$ or 3.5, hence μ_T is (5.5 + 3.5) or 9. In these units, the ion fractions are as follows: X_1 is $1/2(2 \cdot 1^2) / 5.5$ or 0.18; X_3 is $1/2(1 \cdot 3^2) / 5.5$ or 0.82; Y_2 is $1/2(1 \cdot 2^2) / 3.5$ or 0.57; and Y_4 is $1/2(3 \cdot 1^2) / 3.5$ or 0.43. It is clear that the mixed solution just discussed could have been prepared in many other ways, as by dissolving 2 g.-moles of NaCl , $1/3$ g.-mole of AlCl_3 and $1/3$ g.-mole of $\text{Al}_2(\text{SO}_4)_3$ in 1000 g. of water, or by dissolving 1 g.-mole NaCl , $1/6$ g.-mole of $\text{Al}_2(\text{SO}_4)_3$, $2/3$ g.-moles of AlCl_3 and $1/2$ g.-mole of Na_2SO_4 in 1000 g. of water, etc.—The values of m, μ, X and Y for the individual ions are of course independent of how this solution is prepared.

Electrolytes are often characterized by their ion charges, in that a salt like NaCl or KBr is a 1:1 electrolyte, CaCl_2 is a 2:1 electrolyte, CuSO_4 is a 2:2 electrolyte, etc. For any electrolyte, it has been found useful (5) to designate the "reduced" activity coefficient, namely $(\gamma_{12}^{1/z_1 z_2})$, as Γ_{12} in a "pure" solution and Γ_{12} in a "mixed" solution. For a 1:1 electrolyte, γ is identical with Γ , and γ° with Γ° , but these equalities obviously do not hold for electrolytes containing ions having charges greater than unity.

Am. Inst. Chem. Eng. J.
AICHE Journal (Vol. 18, No. 2)

UNIVERSITY OF UTAH
RESEARCH INSTITUTE
EARTH SCIENCE LAB.

Γ° IN PURE SYSTEMS

In this development it will become evident that to predict γ for a strong electrolyte in a mixed solution of any given ionic strength, it is necessary to know the value of Γ° or of γ° for this same electrolyte in a pure solution of the same total ionic strength and the same temperature. Sometimes the only experimental Γ° or γ° values available are at ionic strengths other than that of interest, in which case extrapolation is undertaken with the aid of Figure 1. This extrapolation is based on the finding (5) that curves of Γ° versus μ for most strong electrolytes fall fairly well into the curve family of Figures 1 and 2, with only one known point required to locate a curve. Thus experimental values of Γ° for $\text{Pb}(\text{NO}_3)_2$ are 0.50 and 0.31 at ionic strengths of 1.0 and 6.0 respectively (6). Locating the point where μ is unity and Γ° is 0.5 on Figure 1 and following the curve thus identified to where μ is 6, Γ° is found to be 0.29, or within 10% of the experimental value. To establish a value for Γ° in the supersaturated region, it is merely necessary to follow this same curve out to the desired ionic strength. In general, errors in extrapolation become greater as extrapolation from low μ values to values in excess of 10 is undertaken. To minimize such errors, the range of μ involved in an extrapolation should be kept as small as possible.

Often, no known values for Γ° or γ° are available at any concentration for the strong electrolyte under study. In this event, methods of prediction for Γ° outlined elsewhere (5), or in later paragraphs of this paper may be useful.

Γ IN MIXTURES

The limited direct experimental measurements available in the literature on activity coefficients in mixed solutions are reviewed and methods of correlations are discussed by Hala et al. (2) as well as by Harned and Robinson (4). Most of these studies involve solutions of two electrolytes having a common ion, such as HCl and NaCl. These solutions are usually made by adding μ_{12} ionic strength units of electrolyte 12 and μ_{32} ionic strength units of electrolyte 32 to 1000 g. of water, in such proportions that the total ionic strength μ_T , namely $(\mu_{12} + \mu_{32})$, is constant at some value. In such systems, Harned showed that as a first approximation at a constant total ionic strength, experimental data on γ can be correlated as follows:

$$\log \gamma_{12} = \log \gamma_{12}^\circ + \alpha \mu_{32} / \mu_T \quad (1)$$

$$\log \gamma_{32} = \log \gamma_{32}^\circ - \alpha \mu_{12} / \mu_T \quad (2)$$

Here α is constant at any fixed value of μ_T , but can vary with μ_T , while γ_{12}° and γ_{32}° are the activity coefficients for the pure electrolytes at μ_T .

A second possible source of activity coefficient values in mixed solutions is from solubility product calculations in saturated solutions. That is, the solubility product of any 1:1 electrolyte 12 in its pure saturated solution is $(\gamma_{12}^\circ m_{12}^\circ)^2$, where m_{12}° is the molality and γ_{12}° is its corresponding activity coefficient determined experimentally or by estimation (5). The solubility product of 12 in a mixed system saturated with 12 is $\gamma_{12}^2 (m_1 m_2)$, where m_1 and m_2 are the ion molalities. Equating these two solubility product expressions and rearranging

$$\gamma_{12} = \frac{\gamma_{12}^\circ m_{12}^\circ}{(m_1 m_2)^{1/2}} \quad (3)$$

Thus a pure saturated solution of KNO_3 is 3.79 molal, for which γ° is 0.24 (6). In a solution saturated with both

KNO_3 and NaNO_3 the respective molalities of these two salts are 4.65 and 11.8, hence with ions K^+ , NO_3^- and Na^+ designated as 1, 2, and 3, m_1 is 4.65 and m_2 is $(4.65 + 11.8)$ or 16.45. Substituting into Equation (3), the value of γ_{KNO_3} based upon solubility products is $(3.79 \times 0.24) / (4.65 \times 16.45)^{1/2}$ or 0.122. Since this solution happens also to be saturated with NaNO_3 , its activity coefficient can be determined in an analogous way.

A similar calculation using solubility data usually cannot be carried out to test the success in predicting γ for electrolytes containing ions with z values greater than unity. That is, the solubility product relation of Equation (3) applies only when the electrolyte involved exists as a pure solid, containing no water of crystallization. Unfortunately, solid salts whose ions carry more than a single charge are almost invariably hydrated when in contact with their saturated solutions. Thus Equation (3) applies primarily

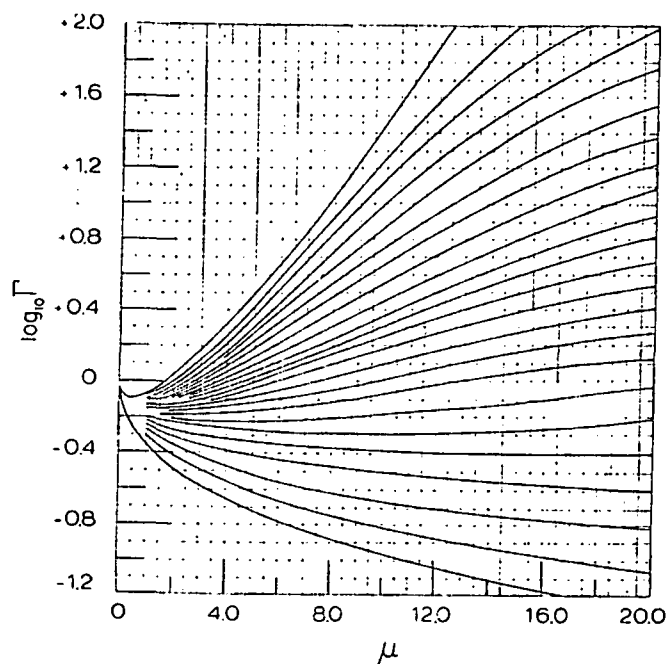


Fig. 1. Generalized plot of the reduced activity coefficient Γ versus ionic strength μ over the ionic strength range of 1.0 to 20.

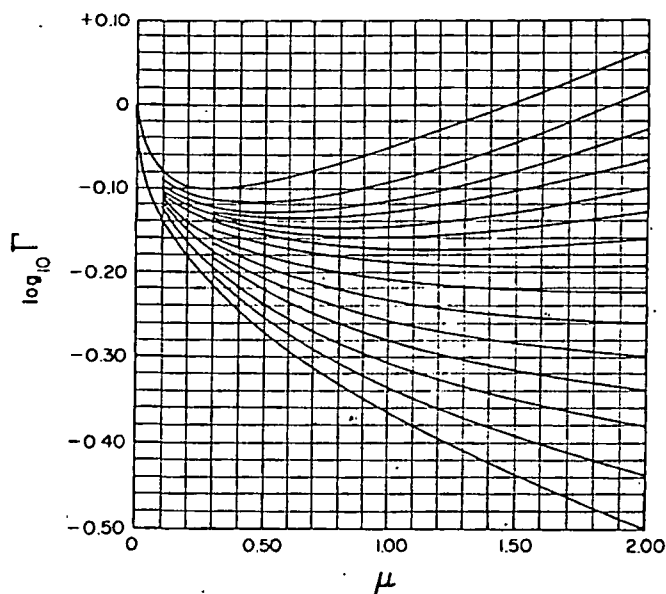


Fig. 2. Generalized plot of Γ versus μ over the ionic strength range of 0.1 to 2.0. This graph supplements the information on Figure 1.

to 1:1 salts, since most of these as solids do not contain water of hydration. Similarly, Equation (3) cannot be used for testing when the solid electrolyte exists in solid solution or as a double salt.

PROPOSED RELATIONS

Brønsted (1) proposed that the value of the mean activity coefficient for electrolyte 12 in a mixed solution depends primarily upon the interaction between cation 1 and each anion present, namely ions 2, 4, 6, etc., and on the interaction between anion 2 and each cation present, namely cations 1, 3, 5, etc. As a first approximation the interaction of ions with like charge is small and can be neglected. To extend this reasoning, assume:

1. The energy of interaction between cation 1 and the anions present is measured by F_1 , where F_1 is defined as

$$F_1 = \frac{1}{2} (Y_2 \log \Gamma_{12}^\circ + Y_4 \log \Gamma_{14}^\circ + Y_6 \log \Gamma_{16}^\circ + \dots) \quad (4)$$

All Γ° are at the total ionic strengths of the mixture.

2. The energy of interaction between anion 2 and the cations present is F_2 , where

$$F_2 = \frac{1}{2} (X_1 \log \Gamma_{12}^\circ + X_3 \log \Gamma_{32}^\circ + X_5 \log \Gamma_{52}^\circ + \dots) \quad (5)$$

where the Γ° values are again taken at the total ionic strengths of the mixture.

3. The mean activity coefficients of 12 in the mixture is then related to F_1 and F_2 as follows:

$$\log \Gamma_{12} = F_1 + F_2 \quad (6)$$

Thus substitution of Equations (4) and (5) into Equation (6) leads directly to values of the reduced activity coefficient Γ_{12} in mixed solutions.

Similar relations are presented below for calculating activity coefficients of electrolytes formed by other possible combinations of ions. Thus in a system containing ions 3, 4, 5 and 6 in addition to ions 1 and 2:

$$F_3 = \frac{1}{2} (Y_2 \log \Gamma_{32}^\circ + Y_4 \log \Gamma_{34}^\circ + Y_6 \log \Gamma_{36}^\circ + \dots) \quad (7)$$

$$F_4 = \frac{1}{2} (X_1 \log \Gamma_{14}^\circ + X_3 \log \Gamma_{34}^\circ + X_5 \log \Gamma_{54}^\circ + \dots) \quad (8)$$

$$F_5 = \frac{1}{2} (Y_2 \log \Gamma_{52}^\circ + Y_4 \log \Gamma_{54}^\circ + Y_6 \log \Gamma_{56}^\circ + \dots) \quad (9)$$

$$F_6 = \frac{1}{2} (X_1 \log \Gamma_{16}^\circ + X_3 \log \Gamma_{36}^\circ + X_5 \log \Gamma_{56}^\circ + \dots) \quad (10)$$

Using the convention of numbering the cation first, the reduced activity coefficients for various ion combinations then are of the form:

$$\log \Gamma_{32} = F_3 + F_2 \quad (11)$$

$$\log \Gamma_{34} = F_3 + F_4 \quad (12)$$

$$\log \Gamma_{14} = F_1 + F_4 \quad (13)$$

$$\log \Gamma_{52} = F_5 + F_2, \text{ etc.} \quad (14)$$

The extensions of these equations to systems containing more than six ions is obvious. The equations proposed above are presumed to apply to saturated as well as unsaturated solutions. For saturated solutions, unlike Equation (3), they apply regardless of what forms may be taken by the solid phases. That is, these solid phases may be unhydrated or hydrated salts, double salts, solid solutions, etc.

Errors to be expected in using these equations are indi-

cated by comparing calculated values of the activity coefficient with corresponding experimental values for various systems. In the typical cases now discussed, solubility data on pure and mixed solutions are from Seidell-Linke (7), while experimental values for activity coefficients are from the appendices of Harned and Owen (3) and from Robinson and Stokes (6). It is often necessary to estimate γ° and Γ° values for pure supersaturated solutions, which is done by extrapolating known values of Γ° using Figure 1. All examples presented here involve aqueous solutions at 25°C.

THREE ION SYSTEMS

Two cations and one anion. Only the three ions, 1, 2, and 3 are present when dissolving electrolytes 12 and 32 in water. Obviously, Equations (6) and (11) apply here, with all terms other than those involving X_1 , Y_2 , and X_3 in Equations (4), (5), and (7) being zero. Substituting Equations (4), (5), and (7) into Equations (6) and (11):

$$\log \Gamma_{12} = \frac{1}{2} (X_1 \log \Gamma_{12}^\circ + Y_2 \log \Gamma_{12}^\circ + X_3 \log \Gamma_{32}^\circ) \quad (15)$$

$$\log \Gamma_{32} = \frac{1}{2} (X_1 \log \Gamma_{12}^\circ + Y_2 \log \Gamma_{32}^\circ + X_3 \log \Gamma_{32}^\circ) \quad (16)$$

In this system, Y_2 is unity and X_1 equals $(1 - X_3)$, hence the above equations become

$$\log \Gamma_{12} = \log \Gamma_{12}^\circ + 0.5X_3 \log (\Gamma_{32}^\circ / \Gamma_{12}^\circ) \quad (17)$$

$$\log \Gamma_{32} = \log \Gamma_{32}^\circ - 0.5X_1 \log (\Gamma_{32}^\circ / \Gamma_{12}^\circ) \quad (18)$$

These equations, in which $\log \Gamma_{12}$ is linear in X_3 and $\log \Gamma_{32}$ is linear in X_1 , have the following characteristics:

1. The slopes of these equations are both numerically equal to $\log \Gamma_{32}^\circ / \Gamma_{12}^\circ$, but are of opposite sign.

2. The obvious requirement that Γ must become equal to Γ° in pure solution is satisfied, in that $\log \Gamma_{12}$ equals $\log \Gamma_{12}^\circ$ when X_1 is unity and X_3 is zero, and $\log \Gamma_{32}$ equals $\log \Gamma_{32}^\circ$ when X_1 is zero and X_3 is unity.

3. When a solution of electrolyte 32 contains only a trace of 12 for a given value of μ_T , that is, X_1 is zero while Y_2 and Y_3 are both unity, Equation (15) becomes:

$$\Gamma_{12}^{tr} = (\Gamma_{12}^\circ \cdot \Gamma_{32}^\circ)^{1/2} \quad (19)$$

Similarly, for a trace of 32 in 12, from Equation (16)

$$\Gamma_{32}^{tr} = (\Gamma_{12}^\circ \cdot \Gamma_{32}^\circ)^{1/2} \quad (20)$$

Thus, for a given μ_T , Γ_{12}^{tr} and Γ_{32}^{tr} are equal hence

$$(\gamma_{12}^{tr})^{1/2i_2} = (\gamma_{32}^{tr})^{1/2i_3} \quad (21)$$

It is interesting to note that Equation (21) is in agreement with the equation developed by Harned and Robinson (4) using a different line of reasoning. Calculated values of γ_{12}^{tr} and γ_{32}^{tr} from Equations (19) and (20) are compared with experimental values in the upper part of Table 1. Inspection indicates that in general errors of not over 10% are encountered in predicting γ_{HCl}^{tr} and γ_{NaCl}^{tr} in various three-ion systems with chloride as the common anion. Agreement, however, is poor for $AlCl_3$ and $LaCl_3$ in their trace solutions in aqueous HCl.

4. For mixtures of two 1:1 salts, X_3 obviously equals $\mu_{32} / (\mu_{12} + \mu_{32})$; consequently, Equation (17) becomes similar to Equation (1) and Equation (18) becomes similar to Equation (2). It follows that the slope α in the Harned equation equals $\frac{1}{2} \log (\gamma_{32}^\circ / \gamma_{12}^\circ)$. In a mixture of two electrolytes having unlike charges, such as when both a 1:1 and a 2:1 salt are present, X_3 is obviously no longer identical with $\mu_{23} / (\mu_{12} + \mu_{23})$. For such systems,

success in correlating experimental data using Equation (17) is nevertheless reasonable, as indicated by the following few paragraphs.

Equations (15) through (21) deal with three-ion systems having a common anion. An analogous set of equations can be written for three ion systems involving ions 1, 2 and 4, with ion 1 as the common cation. Examples here are mixtures of NaCl with NaClO₃, with Na₂SO₄, etc. The errors to be expected can again be judged from the data presented in the bottom half of Table 1.

A further test of these relations involves comparing values for γ in saturated solutions calculated by Equation (3) from solubility products, with values of γ calculated by Equation (17):

1. By Equation (17): A solution 5.27 molal in Ca(NO₃)₂ and 5.3 molal in NaNO₃ is saturated with NaNO₃ but not Ca(NO₃)₂. The ionic strength of the anions in this solution is $\frac{1}{2}(5.3 \times 1^2 + 2 \times 5.27 \times 1^2)$ or 7.9. The ionic strength of the cations is $\frac{1}{2}(5.3 \times 1^2 + 5.27 \times 2^2)$ or 13.2; the total ionic strength is (7.92 + 13.2) or 21.1. Ionic strengths at which experimental activity coefficient data are available are 18 for Ca(NO₃)₂ where Γ° is 0.77, and 6 for NaNO₃, where Γ° is 0.37. Using Figure 1 to extrapolate to a μ_T of 21.1, Γ° is 0.85 for Ca(NO₃)₂ and 0.25 for NaNO₃. The value of $X_{Ca^{++}}$ in this solution is $(5.27 \times 2^2)/(2 \times 13.2)$ or 0.8. Substituting into Equation (17), Γ and γ for NaNO₃ are found to be 0.40.

2. The ionic strength of a pure saturated solution of NaNO₃ at 25°C. is 10.8, where γ° by Figure 1 for NaNO₃ is found to be 0.32. Substituting into Equation (3), γ for NaNO₃ in the mixed solution described above is $(0.32 \times 10.8)/[(5.3)(5.3 + 2 \times 5.27)]^{1/2}$ or 0.38. This is within 10% of the value calculated above from Equation (17).

Using the procedure just illustrated, solubility data have been used to test the extent to which the equations proposed here can be used to predict γ values of 1:1 electrolytes in saturated mixed solutions of high as well as lower ionic strength. In most cases, at ionic strengths from perhaps 10 to 30, agreement between predicted values and

those based upon solubility product calculations lies within 25%, with an average error of about 15%. Errors are generally smaller at lower total ionic strengths. When the proper solubility data are available, it is suggested calculated values from Equation (17), etc., on a given system be tested by comparing results with those calculated from Equation (3).

ESTIMATING Γ° IN PURE SYSTEMS

In the absence of direct measurements, values of γ° and Γ° for an electrolyte 32 can be estimated by Equations (3) and (17), given suitable solubility data for a 1:1 electrolyte like NaCl or KNO₃ in mixed solution with electrolyte 32. To illustrate, the value of Γ°_{32} will be estimated for Ca(NO₃)₂ in a solution known to be saturated with NaNO₃ (6.1 molal) and 3.40 molal in Ca(NO₃)₂. Since in a pure saturated solution, NaNO₃ is 10.8 molal, with γ° and Γ° values of 0.32, then in the mixed solution by Equation (3):

$$\gamma_{NaNO_3} = 10.8 \times 0.32 / [(6.1)(6.1 + 2 \times 3.40)]^{1/2} = 0.39$$

The total ionic strength of this mixed solution is 16.3, at which Γ°_{12} for NaNO₃ is 0.29 while X for Ca⁺⁺ is 0.69. Substituting these values into Equation (17), Γ° for electrolyte 32 is found to be about 0.69, versus an experimental value (3) of 0.735.

FOUR ION SYSTEMS

Two types of four-ion systems exist: those containing two cations and two anions, and those containing three cations and one anion, or one cation and three anions.

Two cations and two anions. These solutions are made by dissolving electrolytes 12 and 34 in water after which 32 or 34 may or may not be added. In all cases, four different ion pairs are identifiable, namely 12, 32, 34, and 14, respectively involving Equations (6), (11), (12), and (13). Remembering that both $(X_1 + X_3)$ and $(Y_2 + Y_4)$ equal unity, then by combining Equations (4), (5), and

TABLE 1. EXPERIMENTAL VERSUS PREDICTED VALUES OF γ^{tr}

Cl⁻ as Common Anion

12	32	μ_T	γ_{12}°	γ_{32}°	exptl. ^o	γ_{12}^{tr}	calc. ^{oo}	exptl. ^o	γ_{32}^{tr}	calc. ^{oo}
HCl	LiCl	2	1.009	0.921	0.986		0.96	—		0.96
HCl	NaCl	2	1.009	0.668	0.878		0.82	—		0.82
HCl	KCl	2	1.009	0.573	0.781		0.76	—		0.76
HCl	CsCl	2	1.009	0.496	0.641		0.71	—		0.71
HCl	CaCl ₂	0.3	0.588	0.326	0.578		0.58	0.334		0.34
NaCl	MgCl ₂	3	0.714	0.569	0.77		0.73	0.636		0.54
NaCl	CaCl ₂	6	0.965	0.79	0.935		0.93	—		0.86
NaCl	SrCl ₂	3	0.714	0.465	0.705		0.70	0.536		0.49
HCl	AlCl ₃	3	1.318	0.33	0.85		0.95	0.45		0.87
HCl	AlCl ₃	12	7.25	3.37	3.96		3.30	—		—
HCl	LaCl ₃	1	0.809	0.282	0.655		0.73	0.256		0.38
HCl	ThCl ₄	3	1.318	0.14	0.895		0.90	—		0.65

Na⁺ as Common Cation

12	14	μ_T	γ_{12}°	γ_{14}°	exptl. ^o	γ_{12}^{tr}	calc. ^{oo}	exptl. ^o	γ_{14}^{tr}	calc. ^{oo}
NaCl	Na ₂ SO ₄	6	0.985	0.154	0.62		0.62	—		0.39
NaCl	Na ₂ SO ₄	1	0.655	0.31	0.60		0.60	—		0.36
NaCl	NaAcetate	3	0.714	0.99	0.833		0.84	—		0.84
NaCl	NaNO ₃	6	0.985	0.37	0.61		0.60	—		0.60
NaCl	NaClO ₃	6	0.985	0.675	0.815		0.82	—		0.82

^o Primarily from (3) and (6).

^{oo} Calculated from Equations (19) and (20).

(6) and rearranging

$$\log \Gamma_{12} = \log \Gamma_{12}^{\circ} + \frac{1}{2} X_3 (\log \Gamma_{32}^{\circ} - \log \Gamma_{12}^{\circ}) + \frac{1}{2} Y_4 (\log \Gamma_{14}^{\circ} - \log \Gamma_{12}^{\circ}) \quad (22)$$

As an illustration, consider the solution containing the ions Na^+ , Cl^- , NH_4^+ , and SO_4^{2-} , respectively designated as 1, 2, 3, and 4, with molalities of 5.04, 7.76, 5.18, and 1.23. Under these conditions, the solution is known to be saturated with NaCl , NH_4Cl and $\text{Na}_2\text{SO}_4 \cdot 10 \text{H}_2\text{O}$. As discussed earlier, Equation (3) may be applied without modification to NaCl and NH_4Cl but not to $\text{Na}_2\text{SO}_4 \cdot 10 \text{H}_2\text{O}$. A pure saturated solution of NaCl is 6.14 molar, with values for γ° and Γ° of unity, consequently in the mixed solution by Equation (3):

$$\gamma_{\text{NaCl}} = 6.14 \times 1 / (5.04 \times 7.76)^{1/2} = 0.98$$

Alternatively, γ_{NaCl} may be calculated from Equation (22). At the total ionic strength of this solution of 11.5, Γ° values are found to be 1.75 for NaCl , by extrapolation using Figure 1, 0.56 for NH_4Cl , and 0.36 for Na_2SO_4 . By Equation (22), Γ and γ for NaCl in this mixture are 0.97, which is in good agreement with the results of Equation (3):

Since this solution is also saturated with NH_4Cl , calculations similar to those just presented for the activity coefficient of NaCl can be repeated for NH_4Cl . The values of γ for NH_4Cl are found to be 0.67 by Equation (3) and 0.64 by Equation (22), which again represents fair agreement.

Three cations and one anion. Such a solution is prepared by adding electrolytes 12, 32 and 52 such as KCl , CaCl_2 and MgCl_2 to water. Values of Γ for these ion pairs can be calculated from Equations (6), (11) and (14). For electrolyte 12, by combining Equations (4), (5), and (6)

$$\log \Gamma_{12} = \frac{1}{2} (X_1 \log \Gamma_{12}^{\circ} + X_3 \log \Gamma_{32}^{\circ} + X_5 \log \Gamma_{52}^{\circ} + Y_2 \log \Gamma_{12}^{\circ}) \quad (23)$$

where Y_2 is, of course, unity. Analogous equations for Γ can of course be written for electrolytes 32 and 52. An example here is a solution containing CaCl_2 , which is in equilibrium with both solid KCl and solid Carnallite, namely $\text{KMgCl}_3 \cdot 6 \text{H}_2\text{O}$. This solution is 0.67 molar in KCl , 2.54 molar in CaCl_2 and 1.97 molar in MgCl_2 corresponding to a total ionic strength of 14.2. A pure saturated solution of KCl is 4.9 molar, where Γ° is 0.59, consequently by Equation (3):

$$\gamma_{\text{KCl}} = 0.59 \times 4.9 / [0.67(0.67 + 2 + 1.97 + 2 \times 2.54)]^{1/2} = 1.13$$

Alternatively, at this total ionic strength, Γ° for KCl (by extrapolation using Figure 1) is 0.65, for CaCl_2 is 1.9 and for MgCl_2 is 3.3. Similarly, X values for K^+ , Ca^{++} , and Mg^{++} are respectively 0.036, 0.544 and 0.42, while Y for Cl^- is unity. Substituting into Equation (23), γ for KCl is found to be 1.22, which again compares reasonably with the value found by Equation (3).

FIVE ION SYSTEMS

Only limited solubility data are available on solutions containing five or more ions. The following relation, developed by combining Equations (4), (5), and (6) applies to a five-ion system involving the cations 1 and 3, and the anions 2, 4, and 6:

$$\log \Gamma_{12} = \frac{1}{2} (X_1 \log \Gamma_{12}^{\circ} + X_3 \log \Gamma_{32}^{\circ} + Y_2 \log \Gamma_{12}^{\circ} + Y_4 \log \Gamma_{14}^{\circ} + Y_6 \log \Gamma_{16}^{\circ}) \quad (24)$$

An example here is a solution which is 5.4 molar in NaCl , 0.22 molar in KClO_4 and 2.4 molar in NaNO_3 (these salts being respectively designated as 12, 34, and 16). This solution is saturated with both NaCl and KClO_4 . At this solution's total ionic strength of 8.0, Γ° values are as follows: 1.20 for salt 12, 0.63 for salt 32, 0.34 for salt 16 and 0.74 for salt 14. Substituting into Equation (24) and using the appropriate X and Y values the activity coefficient γ_{12} is found to be 0.96, which compares with 0.95 found by solubility product calculations based on Equation (3).

PRECISION

The errors to be expected in predicting γ values by the equations proposed here become larger at higher values of μ_T . Further errors are introduced when Γ° values are predicted as discussed earlier and when extrapolating Γ° over large ranges of μ_T by use of Figure 1. The relations proposed here for estimating activity coefficients for strong electrolytes should therefore not be used when direct experimental data are available.

NOTATION

- F = interaction term in Equations (4), (5), (7), etc.
- m = molality, g.-moles/1,000 g. water
- X_1 = for cation 1, $X_1 = m_1 z_1^2 / \mu_c$
- Y_2 = for anion 2, $Y_2 = m_2 z_2^2 / \mu_a$
- z = ion charge; 1 for Na^+ , 2 for SO_4^{2-} , 3 for Al^{+++} , etc.
- α = constant, Equations (1) and (2)
- γ = mean activity coefficient of an electrolyte in a multicomponent solution
- γ° = mean activity coefficient of an electrolyte in a pure solution
- γ^{tr} = activity coefficient of an electrolyte present in trace communications in a multicomponent solution
- Γ = $\gamma^{1/z_1 z_2}$
- Γ° = $(\gamma^{\circ})^{1/z_1 z_2}$
- μ_a = ionic strength of anions, namely $\frac{1}{2} (m_2 z_2^2 + m_4 z_4^2 + \dots)$
- μ_c = ionic strength of cations, namely $\frac{1}{2} (m_1 z_1^2 + m_3 z_3^2 + m_5 z_5^2 + \dots)$
- μ_T = total ionic strength, namely $(\mu_a + \mu_c)$

Subscripts

Cations are indicated by 1, 3, 5, etc., anions are indicated by 2, 4, 6, etc. Electrolytes are identified by subscripts such as 34, indicating cation 3 and anion 4.

LITERATURE CITED

1. Brønsted, J. N., *J. Am. Chem. Soc.*, **42**, 761, (1920); 45, 2898 (1923).
2. Hala, E., J. Pick, V. Fried, O. Vicini, "Vapor Liquid Equilibrium," 2nd ed., Pergamon Press, New York (1968).
3. Harned, H. S., and B. B. Owen, "The Physical Chemistry of Electrolyte Solutions," 3rd ed., Appendix A, Reinhold, New York (1958).
4. Harned, H. S., and R. A. Robinson, "Multicomponent Electrolyte Solutions," p. 17, Pergamon Press, New York (1968).
5. Meissner, H. P., and J. W. Tester, "Activity Coefficients of Strong Electrolytes in Aqueous Solution," *Ind. Eng. Chem. Process Design Develop.*, **11**, 128 (1972).
6. Robinson, R. A., and R. H. Stokes, "Electrolyte Solutions," Appendix 8.1, Butterworth's, London (1955).
7. Seidell, A., and W. F. Linke, "Solubilities, Inorganic and Metal-Organic Compounds," 4th ed., Vol. I & II, Am. Chem. Soc., Washington, D.C. (1965).

Manuscript received June 10, 1971; revision received August 27, 1971; paper accepted September 10, 1971.

Activity Coefficients of Strong Electrolytes in Aqueous Solution—Effect of Temperature

UNIVERSITY OF UTAH
RESEARCH INSTITUTE
EARTH SCIENCE LAB.

SUBJ
GCH1
ACSE

H. P. MEISSNER

Chemical Engineering Department
Massachusetts Institute of Technology, Cambridge, Massachusetts 02139

C. L. KUSIK

Arthur D. Little, Inc.,
Cambridge, Massachusetts 02140

JEFFERSON W. TESTER

Chemical Engineering Department
Massachusetts Institute of Technology, Cambridge, Massachusetts 02139

The reduced activity coefficient Γ for an individual strong electrolyte in aqueous solution is defined as $\gamma_{\pm}^{1/z_{\pm}}$ where γ_{\pm} is the mean ionic activity coefficient and z_{+} and z_{-} are the charges on the cations and anions respectively. A generalized relation at 25°C between Γ and μ , the ionic strength, is shown graphically in Figure 1 (Meissner and Tester, 1972). Since there is usually only minor curve cross over in this family of curves, the entire curve for any strong electrolyte can be located on Figure 1 from a single value of Γ at 25°C available at a μ of 2 or higher.

Given the necessary data, a family of curves similar to that of Figure 1 could presumably be constructed at any temperature resulting, however, in a multiplicity of charts. The object here is to propose a general method whereby Figure 1 alone can be used for predicting values of γ_{\pm} for any strong electrolyte in aqueous solution over temperatures ranging from 0° to 150°C and higher.

TEMPERATURE VERSUS Γ

Values of γ_{\pm} at other than 25°C are reported in the literature for few electrolyte solutions. The change of γ_{\pm} with temperature can, of course, be calculated from partial molal enthalpies of solution using the familiar thermodynamic relations (for example, Robinson and Stokes, 1955), but few such enthalpy measurements are reported. Fortunately, abundant data exist on the vapor pressures of water over solutions of many electrolytes at various concentrations and temperatures (International Critical Tables, 1926; Smithsonian Physical Tables, 1954). The quantity γ_{\pm} can be determined from these vapor pressures by use of the familiar Gibbs-Duhem equation, written as follows for aqueous electrolytes of molality m (Pitzer and Brewer, 1961; Harned and Owen, 1958).

$$d \ln \gamma_{\pm} = - d \ln m - \frac{55.5}{\nu m} d \ln a_w \quad (1)$$

Here a_w is the activity of water, namely the ratio of water's vapor pressure over the solution divided by the vapor pressure of pure water at the temperature in question. Similarly, ν is the number of moles of ions formed upon complete dissociation of one mole of the electrolyte in question.

Equation (1) is relatively simple to integrate for any given temperature over the concentration range from 0.01 molal (in the Debye-Huckel region where γ_{\pm} can be directly calculated) to any higher concentration. Examina-

tion of the isothermal curves of Γ versus μ so calculated for solutions of various electrolytes leads to the following observations:

1. As a first approximation, for temperatures from 0°C to over 100°C, isothermal curves of $\log \Gamma$ versus μ for 40 typical strong electrolytes were found to remain members of the curve family of Figure 1. Therefore, to locate a curve for, say CaBr_2 on Figure 1 at a temperature such as 80°C, it is merely necessary to have available a known value of $\log \Gamma$ at 80°C for some value of μ above 2. Locating this point on Figure 1, the entire curve can be drawn immediately.

2. A change in temperature has no effect upon γ_{\pm} values at any given ionic strength for solutions of those electrolytes represented by the dotted curve of Figure 1. Thus, this dotted curve applies to all temperatures, from the freezing point to the boiling point.

3. For a system whose curve at 25°C of $\log \Gamma$ versus μ lies either above or below the dotted curve on Figure 1, a change in temperature at constant μ in the range of from

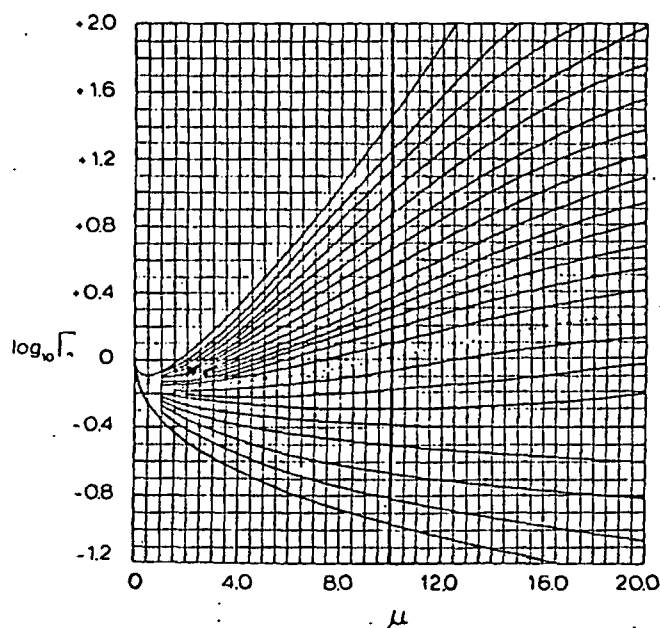


Fig. 1. Generalized isothermal lines of the reduced activity coefficient Γ versus the ionic strength μ . The dotted line, which passes through the point where $\log \Gamma$ is 0 when μ is 10, separates the regions of positive and negative temperature dependence.

0°C to 150°C will cause a shift in Γ . For systems whose curves lie above the dotted curve on Figure 1, an increase in temperature always results in a diminution in Γ . For systems with curves below this dotted curve, an increase in temperature causes an increase in Γ .

For a solution of any given strong electrolyte at a given μ , the quantity $\log \Gamma_T$ is found to be a unique function of $\log \Gamma_{25^\circ\text{C}}$. At a constant μ of 10, this function becomes linear, in that at a fixed temperature T , a plot of $\log \Gamma_T$ versus $\log \Gamma_{25^\circ\text{C}}$ for various electrolytes forms a straight line. This is illustrated by Figure 2, on which points of $\log \Gamma_{100^\circ\text{C}}$ [calculated from Equation (1)] are plotted against $\log \Gamma_{25^\circ\text{C}}$ for selected electrolytes. It was also found that at any fixed μ , the quantity $\log \Gamma_T$ generally varies in a linear fashion with temperature. Thus for HCl in a solution in which μ (and also molality) equals 10, Akerlof and Teare (1937) showed experimentally that $\log \Gamma$ diminishes by (0.059 ± 0.001) for each increase of 10°C in temperatures between 0°C and 50°C.

The following empirical equation, which applies only at a μ value of 10 and temperatures in the range of 0° to 150°C, expresses the foregoing analytically:

$$\log(\Gamma_T)_{\mu=10} = \{1 - 0.0050(T - 25)\} \log(\Gamma_{25^\circ\text{C}})_{\mu=10} \quad (2)$$

Note that $\log \Gamma_{25^\circ\text{C}}$ is zero when μ equals 10 for the dotted curve of Figure 1, and so as expected from Equation (2) any change in temperature leaves Γ_T equal to $\Gamma_{25^\circ\text{C}}$, namely unity. Similarly, for points above the dotted line of Figure 1, by Equation (2), an increase in temperature causes Γ_T to diminish relative to $\Gamma_{25^\circ\text{C}}$. Again for points lying below the dotted line by Equation (2), Γ_T increases relative to $\Gamma_{25^\circ\text{C}}$ as temperature increases. It is therefore obvious that, knowing the curve on Figure 1 which applies to the electrolyte in question at 25°C, the curve for any other temperature can be immediately located by use of Equation (2). To illustrate: $\log \Gamma$ at 25°C for HCl is reported to be 1.6179 at a μ value of 16 (Akerlof and Teare, 1937). Locating this point on Figure 1 and moving down the curve thus identified, $\log \Gamma$ at 25°C and a μ of 10 is found to be 0.96. Substituting into Equation (2) $\log \Gamma$ at 50°C and a μ of 10 is 0.84 compared to an experimental value of 0.8699. Following up the corresponding curve on Figure 1 ($\log \Gamma = 0.84$; $\mu = 10$) to where μ equals 16, $\log \Gamma$ is here shown to be 1.42, versus an experimental value of 1.373.

DISCUSSION

Only limited experimental data are available on activity coefficients of electrolytes in aqueous solutions at higher ionic strengths and temperatures other than 25°C. Few direct tests of these methods for relating γ_{\pm} of an electrolyte to temperature can therefore be made, and other test procedures must be adopted. Thus, the values of $\log \Gamma_{100^\circ\text{C}}$ at an ionic strength of 10 calculated by Equation (1) from isothermal vapor pressure data at 100°C for selected electrolytes, plotted as points on Figure 2, fall reasonably close to the line on this figure for Equation (2). Agreement between the points and the line is usually within 20% of the value calculated by Equation (1), although in some cases as with BeSO_4 the error is as great as 45%. Such errors encountered with Equation (2) tend to diminish at T values below 100°C. This behavior is observed despite the finding that when μ is 10, $\log \Gamma_T$ is often only approximately linear in T , and for some materials, such as NaOH , $\log \Gamma$ shows a shallow maximum between 0° and 100°C. In these latter cases, however, the

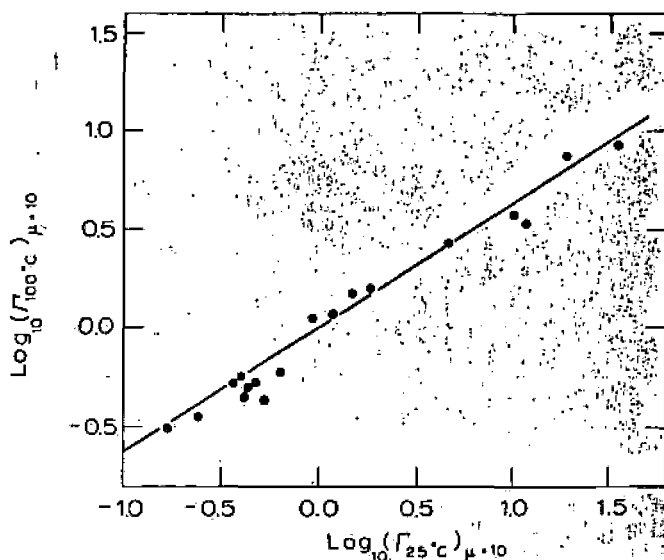


Fig. 2. $\log \Gamma_{100^\circ\text{C}}$ versus $\log \Gamma_{25^\circ\text{C}}$ at a μ value of 10. Moving from left to right, the points are for the following compounds: NH_4NO_3 , PbSO_4 , Na_2SO_4 , K_2CrO_7 , NH_4Cl , MnSO_4 , NiSO_4 , BeSO_4 , $\text{Ca}(\text{NO}_3)_2$, KI , AlCl_3 , NaCl , CaBr_2 , NaI , LiCl , HCl , LiBr .

curves of $\log \Gamma$ versus μ lie relatively close to the dotted curve of Figure 1, so that \log of $\Gamma_T/\Gamma_{25^\circ\text{C}}$ is small at worst. Other sources of error are discussed elsewhere (Meissner and Tester, 1972; Meissner and Kusik, 1972). This method is therefore to be used only when experimental data are not available.

As temperatures increase, isotherms for all electrolytes move towards the dotted line of Figure 1, with some indication that they may all fall together on this dotted line at all temperatures over about 250°C. Equation (2), however, has been tested only up to 150°C and obviously cannot be used much above this temperature.

Mixture rules have been presented (Meissner and Kusik, 1972) for estimating γ_{\pm} values at 25°C of an electrolyte in an aqueous solution containing several other electrolytes. To apply these rules at 25°C, information is required on Γ values of individual electrolytes in "pure" solution at 25°C. These same rules are applicable without modification to any other temperature, given information on Γ for the individual electrolytes in pure solution at this new temperature. Thus, by use of Figure 1 and Equation (2), the mixture rules formulated for 25°C can be extended to other temperatures.

LITERATURE CITED

- Akerlof, G., and J. W. Teare, "Thermodynamics of Concentrated Aqueous Solutions of Hydrochloric Acid," *J. Am. Chem. Soc.*, 59, 1855 (1937).
- Harned, H. S., and B. B. Owen, "Physical Chemistry of Electrolyte Solutions," 3rd ed., Reinhold, New York (1958).
- International Critical Tables, Vol. 3, pp. 361-380, McGraw-Hill, New York (1926).
- Meissner, H. P., and J. W. Tester, "Activity Coefficients of Strong Electrolytes in Aqueous Solution," *Ind. Eng. Chem. Process Design Develop.*, 11, 128 (1972).
- Meissner, H. P., and C. L. Kusik, "Activity Coefficients of Strong Electrolytes in Multicomponent Aqueous Solutions," *AIChE J.*, 18, 294 (1972).
- Pitzer, K. S., and L. Brewer, "Thermodynamics," 2nd ed., McGraw-Hill, New York (1961).
- Robinson, R. A., and R. H. Stokes, "Electrolyte Solutions," Butterworths, London (1955).
- Smithsonian Physical Tables, Smithsonian Inst. Publ., pp. 374-5, 9th Rev. ed. Wash. D. C. (1954).

SUBJ
GCHM
AHL

Annealing History Limits for Inhomogeneous, Native Gold Grains as Determined from Au-Ag Diffusion Rates *

GERALD K. CZAMANSKE, GEORGE A. DESBOROUGH, AND FRASER E. GOFF

Abstract

Quantitative study of intrinsic inhomogeneities in native gold grains from three deposits in the western United States has revealed concentration profiles that represent the integrated sum of natural diffusion plus original chemical heterogeneity. By assuming that measured natural concentration gradients result solely from diffusion, upper limits may be placed on the temperature-time annealing history of the gold nuggets. This assumption focuses on the end member case in which an initial step-discontinuity is assumed between measured extremes of concentration.

Concentration changes of up to 30 weight percent Ag indicate probable deposition temperatures of less than 300°C for electrum from Copper Basin, Arizona, and Alder Gulch, Montana. The gold in the Homestake, South Dakota, deposit probably was formed at temperatures well under 400°C.

In support of this study, new data for interdiffusion in the Au-Ag system were obtained from a series of annealing experiments followed by electron microprobe analysis. The interdiffusion coefficient, \bar{D} , in the range 10^{-10} to 10^{-17} cm² sec⁻¹ was determined from measured profiles across synthetic alloy pairs held at eight fixed temperatures from 297° to 799°C, for periods ranging from 32 hours to 730 days.

Introduction

WHILE using the electron microprobe to analyze native gold grains and nuggets from many districts in the western United States, Desborough and his co-workers (1972) discovered abrupt variations in composition within many specimens. These variations are not related to specimen surfaces and clearly have not resulted from postdepositional processes such as those postulated by Desborough (1970) for certain placer deposits. Rather, such compositional variations are interpreted to reflect changes in the composition of the fluids from which the grains originally grew, causing gold-silver alloys of different compositions to form contiguous growth zones with time. Initial variations in alloy composition could have been either abrupt or gradual and may have been more or less modified by diffusion. The persistence of compositional heterogeneity in natural gold grains suggests that, for many deposits, limitations can be placed on the thermal history of gold deposition and annealing, based on diffusion rates for the Au-Ag system. Such an approach would not only be specific for the economic mineral, gold, but, being intrinsic to the nuggets, might also allow limits to be placed upon the subsequent thermal history of nuggets in ancient placer deposits.

A search of the metallurgical literature for diffusion data on the Au-Ag system showed that diffusion coefficients were well established at temperatures above 650°C. At such elevated temperatures, one may employ "classical techniques," because the substantial diffusion rates permit mechanical milling of the diffusion couple for bulk chemical or radioisotope analysis (e.g., Johnson, 1942; Mallard et al., 1963). The only lower temperature data known to us are at 394°C from application of a high-temperature electrochemical method by Raleigh and Crowe (1969) and in the range 200° to 260°C from an elegant study of Cook and Hilliard (1969) based on rate of decay of composition modulations in vapor-deposited films.

Although the low-temperature data of Cook and Hilliard agree well with extrapolations of the higher temperature diffusion coefficients of Johnson (1942) (see Fig. 5), we elected to proceed with a systematic electron microprobe study of Au-Ag diffusion. We hoped to establish unequivocally that electron microprobe analyses of gradients in natural gold specimens are reliable and may be used for our intended purposes. This experimental study of interdiffusion in the Au-Ag system is outlined in the Appendix.

The work of Goldstein and co-workers (e.g., Goldstein et al., 1965; Goldstein and Ogilvie, 1965), who studied interdiffusion of Ni-Fe in meteorites, has many parallels to ours in terms of goals, experimental techniques, and methods of attack.

* Publication authorized by the Director, U. S. Geological Survey.

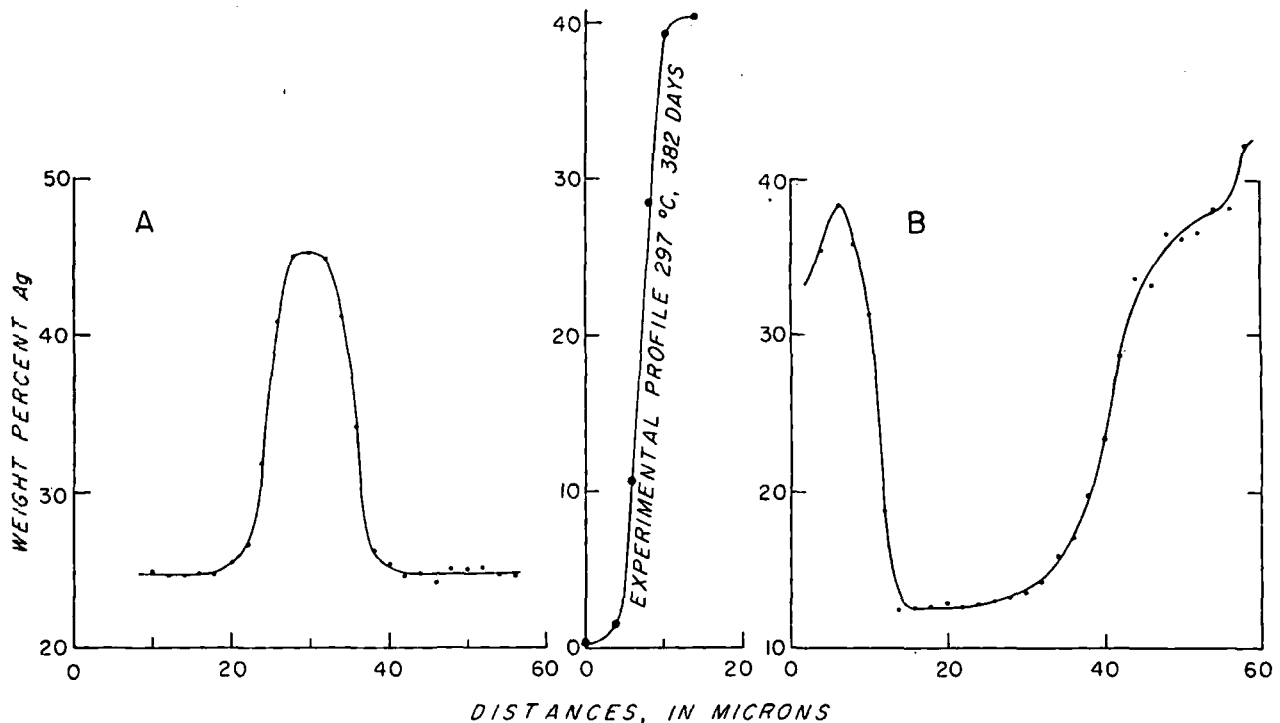


FIG. 1. Measured natural concentration gradients in electrum from Alder Gulch, Montana (compare with experimental profile at 297°C).

Compositional Gradients in Natural Gold Specimens

Concentration gradients were measured in coarse gold specimens from three localities: (1) Alder Gulch, Virginia City district, Madison County, Montana; (2) Copper Basin, Yavapai County, Arizona; and (3) Homestake mine, Lawrence County, South Dakota. (For discussion of the geology of these localities and the compositions of the gold therefrom, see Desborough et al., 1972.) High Ag content and associated sulfides indicate that gold from these deposits is hydrothermal in origin. Several specimens from each locality were analyzed and usually more than one traverse was made on each grain. Analyses were made using standards and operating conditions identical to those outlined in the Appendix for the experimental diffusion couples.

Typical concentration profiles for natural specimens from Alder Gulch and Copper Basin are shown in Figures 1 and 2. We interpret profiles such as these to be related to conditions of initial gold deposition and/or subsequent annealing. Ultimately, the existence of a concentration profile must indicate that the chemistry of the solution depositing the electrum changed in such a way as to cause electrum of different compositions to be deposited

contiguously. From the experimental Au-Ag diffusion data, it is clear that moderate temperatures (150° to 500°C), whether related to the primary environment of deposition or to the thermal regime associated with a later geologic event, will promote significant diffusion and tend to homogenize initial compositional differences. In some cases, it may be possible to make interpretations involving not only the primary site of gold deposition, but also the history of a secondary environment, e.g., that of an ancient placer deposit.

Individual profiles, such as those for Alder Gulch and Copper Basin (Figs. 1 and 2), may represent single crystals (in a crystallographic sense) which had primary compositional gradients or polycrystalline grains in which gradients mark the site of original crystal boundaries. Inasmuch as sharp concentration gradients without crystallographic discontinuity are possible in Au-Ag alloys, the profiles need not represent polycrystalline grains. Differences in composition within studied specimens produce marked color contrasts, and etching such heterogeneous grains is not enlightening. In fact one may postulate that it is of little consequence whether the grains are single crystals or polycrystalline aggregates, so long as one may assume that the process of diffusion has not been retarded, for example, by crystal boundary impurities. The results of our

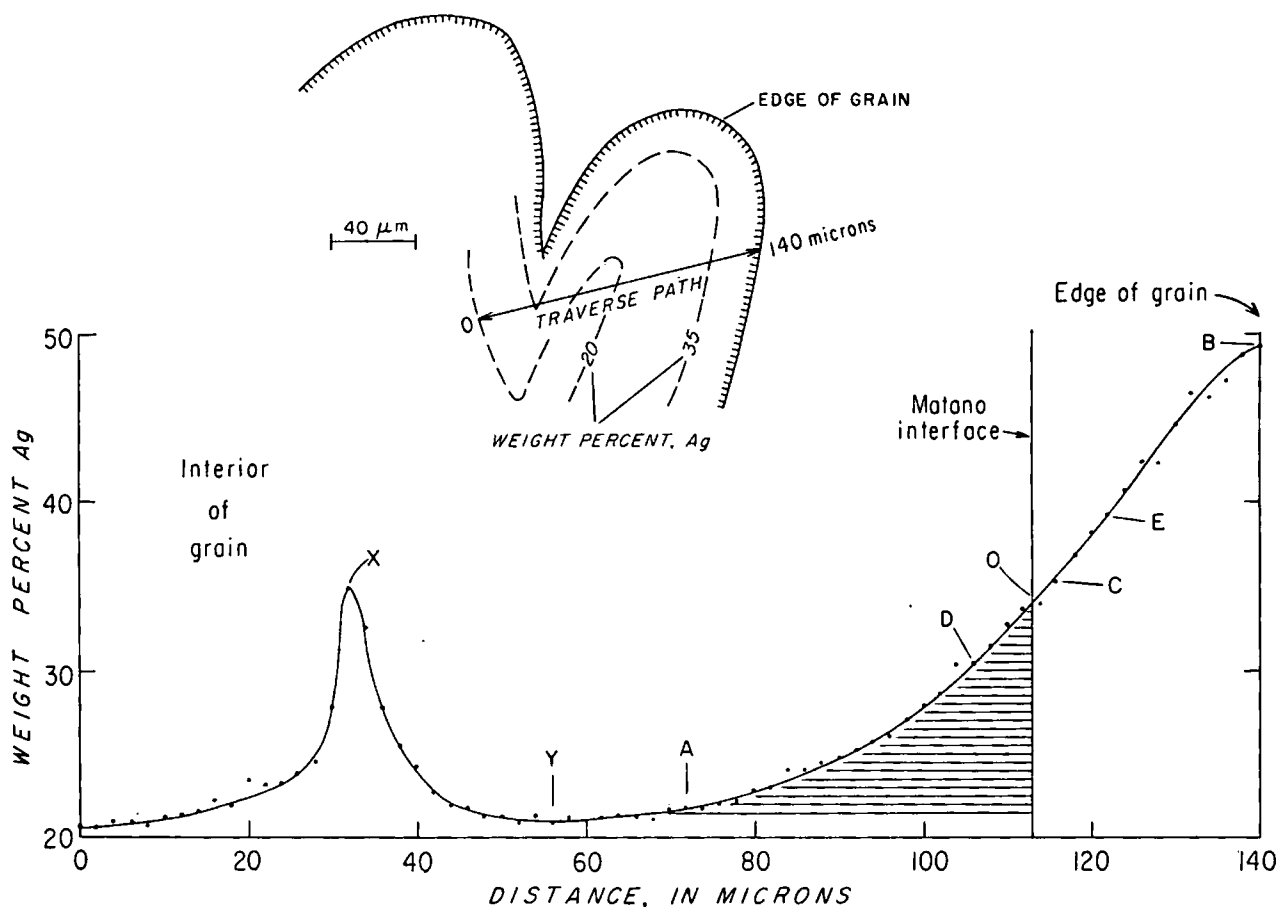


Fig. 2. Measured natural concentration gradients in electrum from Copper Basin, Arizona, showing elements of annealing history analysis and sketch of traverse path. See text for explanation of symbols.

experimental work support this conclusion (see Appendix).

A related consideration, therefore, is whether diffusion rates in natural samples might be so affected by intragranular impurities as to preclude valid comparison with experimental data, e.g., Shewmon, 1963, p. 111-113. The most direct way to check this is to anneal representative specimens in order to establish actual interdiffusion rates. Accordingly, profiles for several samples from Alder Gulch and Copper Basin were measured, after which the grains were removed from mounting media, annealed at 700°C, and the profiles remeasured. In this way, application of data for the pure Au-Ag system to our natural samples has been justified.

The analysis which we propose here establishes only an upper limit to the annealing or thermal history of a given specimen because typically one cannot differentiate composition gradients reflecting primary deposition from gradients produced by later diffusion. The relevant parameters for diffusion are temperature and time. The method of analysis

which we have chosen forces us to assume an initial discontinuity in composition, and we may only conclude that a gradient could not represent more than X years of annealing at Y degrees Celsius (see Table 1). As a corollary, the steepest concentration gradients measured for specimens judged to represent uniform conditions provide the closest estimate of the actual annealing time (at a given temperature) for that occurrence. A series of gradients measured on a single suite of specimens may differ for several reasons, the most obvious being that the ideal situation, in which vertically oriented compositional heterogeneities are traversed at right angles, will not always be realized. Profiles will then appear flatter than they should, and annealing times calculated from them will be too long. Differences in growth rate on different crystal surfaces are another source of variation and will be reflected through any subsequent annealing history. An example from Copper Basin (Fig. 2) is discussed below.

Steep concentration gradients typical of specimens

TABLE 1. Maximum Annealing Periods Permitted by Measured Concentration Gradients in Natural Electrum

Locality	Grain (Profile)	Composition Change (wt % Ag)	Temperature (°C)	Time (years)
Copper Basin	22 ¹ (XY)	35 → 21	396	0.3
			297-300	30-160
			200	280,000
Copper Basin	22 ¹ (AB)	21 → 49	396	8
			297-300	700-4,000
			200	7,000,000
Copper Basin	8 (left limb) ²	31 → 19	396	2.5
			297-300	220-1,200
			200	2,200,000
Copper Basin	8 (right limb)	22 → 40	396	2
			297-300	190-1,100
			200	1,900,000
Alder Gulch	7 ³ (left limb)	25 → 45	396	0.1
			297-300	8-50
			200	83,000
Alder Gulch	6 ⁴ (left limb)	38 → 13	396	0.08
			297-300	7-40
			200	67,000
Alder Gulch	6 ⁴ (right limb)	13 → 38	396	0.4
			297-300	35-190
			200	340,000
Homestake	HB-5	15.2 → 18.7	396	0.8
			297-300	70-400
			200	690,000

¹ The traverse of grain 22 is shown as Figure 2.

² The terms left limb and right limb refer to the two sides of a concentration disturbance as plotted, e.g., see Figures 1A and B.

³ The traverse of grain 7 is shown as Figure 1A.

⁴ The traverse of grain 6 is shown as Figure 1B.

from Alder Gulch (Fig. 1), show that within 4 microns the Ag content of the electrum typically changes by 14 to 19 weight percent. Both of these profiles were taken across portions of specimens showing obvious heterogeneity and both terminate within specimen boundaries. From these and other profiles in electrum from Alder Gulch, it is clear that changes in electrum composition were extreme and irregular, with extensive development of electrum with 12-14, 24-25, 32-40, and 45-46 weight percent Ag. These four plateaus are interpreted to represent four distinct and relatively enduring environments of deposition, and perhaps of ore solution composition. The effects of diffusion have been slight if there was initially a step discontinuity between the composition of adjacent areas, nil if the measured profiles reflect the gradient as initially deposited.

Samples from Copper Basin typically show less steep compositional gradients, which would suggest a longer and/or higher temperature annealing history (Table 1). However, the compositional profile shown as Figure 2 reveals that, in fact, changing conditions of primary deposition are in large measure responsible for measured gradients. This particular traverse took a path shown by the inset

sketch; that is, it crossed an area in which two grains grew asymmetrically, perhaps because they impinged on one another, or because ore-forming solutions had poorer access to the area between grains. Other specimens from Copper Basin show that the concentration gradient measured in the interval A-B (Fig. 2) is typical.

Asymmetrical growth caused compression of the compositional gradient, as contoured in the plan sketch of Figure 2; that is, during each increment of time Δt , the growth increment Δ_{X-Y} associated with profile X-Y was distinctly less than growth increment Δ_{A-C} associated with the development of A-C (the compositionally equivalent portion of profile A-B). In consequence, profile X-Y is steeper than A-C, although it is interpreted to have developed over a similar time interval. As noted earlier, concentration profile X-Y allows the more precise limits to be placed on the thermal history of the Copper Basin electrum. Furthermore, the indication that much of the broad compositional profile A-B is a primary rather than a thermal feature comes solely from the existence of the steeper profile X-Y. The fact that profile A-B continues to the margin of the grain cannot be construed as evidence that this gradient is a growth phenomenon; this gradient

would develop under the conditions set forth in Table 1 from the situation in which there was a step discontinuity, 21 → 49 weight percent Ag, at the approximate position of the Matano interface (Fig. 2).

Establishment of Time-Temperature Limits

Diffusion coefficients in two-component, alloy systems that exhibit concentration-dependent diffusion are readily calculated using the Boltzmann-Matano method (cf. Shewmon, 1963). Application of this method in our study is unusual because initial and boundary conditions are not rigorously established. Regardless of the means of analysis employed, however, uncertainty as to the sharpness of the primary, chemical discontinuities is inescapable. Thus, the assumption of an initial step discontinuity seems acceptable within the stated limitations. The condition of a constant composition plateau at either end of the profile is often realized or is readily approximated for natural specimens. Clearly, the requirement that the Boltzmann-Matano solution be applied only to systems in which there is no volume change on mixing is fulfilled for electrum. In fact, the molar volumes of Au and Ag differ by less than 0.6 percent (Robie et al., 1966). If there was volume change on mixing, the treatment of Wagner (1969) is required to obtain correct results (e.g., Greskovich and Stubican, 1970).

The equation relevant to the Boltzmann-Matano solution is

$$D(c') = -\frac{1}{2t} \left(\frac{dx}{dc} \right)_{c'} \int_0^{c'} x \, dc \quad (1)$$

where $D(c')$ = diffusion coefficient in cm^2/sec at concentration c'

c = concentration in any consistent units

t = time in sec

x = distance in cm

\int = integral sign.

This equation is usually solved by graphic methods, by determining the Matano interface (Fig. 3) which provides a reference point for calculation of the integral term. This is the plane that makes equal the two graphic areas bounded by itself and the diffusion profile, i.e., the two horizontal lined areas of Figure 3.

Recent determinations of D_{Ag} and D_{Au} in Ag-Au alloys (e.g., Mallard et al., 1963) have generally been done with radioactive tracers and thin-film techniques. Use of the electron microprobe, however, gives compositions at points in the diffusion profile and tells nothing of relative diffusion rates of Ag and Au to attain that profile; in this case, one

is restricted to the determination of an interdiffusion coefficient, \bar{D} . For the practical purpose of evaluating the time dependence of concentration profiles, the single coefficient is as useful as more detailed information on intrinsic diffusivities.

The process of setting time limits to the thermal history of compositionally heterogeneous gold specimens such as those from Alder Gulch (Fig. 1) and Copper Basin (Fig. 2) may be visualized by consideration of the right-hand portion of the concentration profile for Copper Basin (Fig. 2). By algebraic rearrangement of equation (1), one may obtain

$$t = \frac{(\text{factor})}{D(c')}, \text{ where "factor"} = \frac{-\int_0^{c'} x \, dc}{2 \left(\frac{dc}{dx} \right)_{c'}} \quad (2)$$

In this study, this equation was solved by hand to give approximate annealing times for a set of reasonable geologic temperatures (see Table 1), for a representative number of measured natural profiles such as A-B and X-Y of Figure 2.

Consider the portion of the traverse A-B that may be considered to represent the diffusion profile that could result in time if there were initially a steplike change in composition from 21 to 49 weight percent silver at approximately the plane labeled Matano interface. Because the point c' (eq. 2) at which the diffusion coefficient is to be evaluated may be chosen at will along the profile, it was generally taken at 0, the intersection of the profile and the Matano interface. With this designation, the integral term (eq. 2) is equivalent to the horizontally lined area of Figure 2 and has units of microns \times weight percent. Similarly, the derivative term (dc/dx) in equation (2) can be approximated as the slope of the profile at 0, as evaluated by the coordinates of the two points D and E; the slope has units of weight percent/microns. Specifically, for profile A-B (Fig. 2), the area (integral) involved is 193 microns \times weight percent and the slope (derivative) is 0.54 weight percent/micron. Hence

$$\begin{aligned} \text{"Factor"} &= \frac{(193)(10^{-8})}{2(0.54)} = 1.8 \times 10^{-6} \\ \text{and } t &= \frac{1.8 \times 10^{-6}}{\bar{D}} \quad (3) \end{aligned}$$

where 10^{-8} is a conversion factor for square microns to square centimeters, t is the time in seconds, and \bar{D} is the interdiffusion coefficient. Because values of the interdiffusion coefficient are temperature dependent (Table 2), one merely selects those values corresponding to possible temperatures of gold deposi-

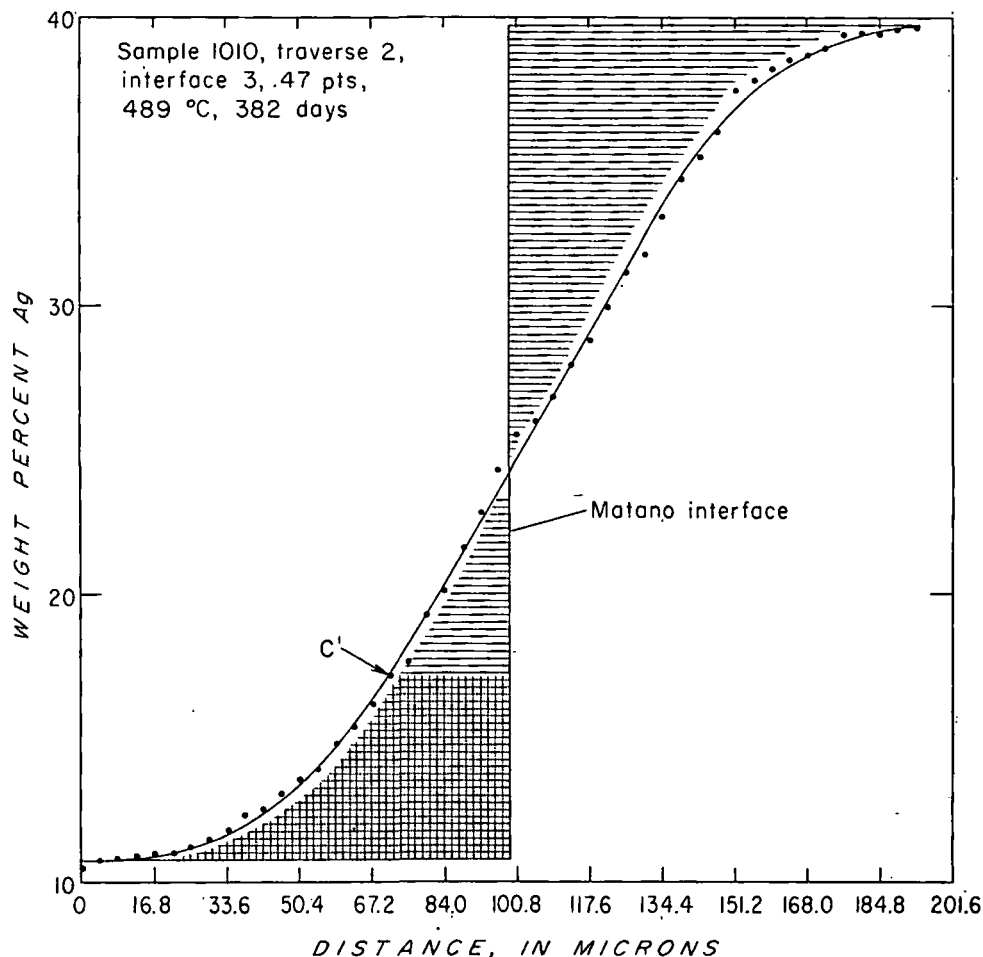


FIG. 3. Example of measured experimental diffusion profile showing elements of Boltzmann-Matano analysis. See text for explanation of symbols.

tion in order to generate corresponding values for t through equation (3). Values so derived for representative grains from each district are presented in Table 1.

Because our experimental data differ somewhat

from interpolation of available published data (Fig. 5), some choice of values for the interdiffusion coefficient \bar{D} is required. We have attempted, in Table 1, to give an indication of the effect of uncertainty in \bar{D} on estimates of annealing

TABLE 2. Summary of Values Obtained for the Interdiffusion Coefficient, \bar{D} , at a Concentration of 35 Atomic Percent Ag

Temperature, °C	Annealing Time	$\ln \bar{D}$	\bar{D} , cm ² sec ⁻¹
297	382 days	-37.1 ± 0.2	8.0 ± 1.7 × 10 ⁻¹⁷ ¹
297	730 days	-37.1 ± 0.4	7.4 ± 3.0 × 10 ⁻¹⁷
396	382 days	-32.6 ± 0.4	7.0 ± 2.8 × 10 ⁻¹⁶ ²
396	730 days	-32.8 ± 0.3	5.7 ± 1.7 × 10 ⁻¹⁶
489	193 days	-28.3 ± 0.4	5.1 ± 2.1 × 10 ⁻¹³
489	382 days	-28.7 ± 0.3	3.4 ± 1.1 × 10 ⁻¹³
595	33 days	-25.7 ± 0.3	6.9 ± 2.1 × 10 ⁻¹²
595	67 days	-26.0 ± 0.4	5.1 ± 2.2 × 10 ⁻¹²
701	142 hours	-23.7 ± 0.3	5.1 ± 1.5 × 10 ⁻¹¹
799	32 hours	-21.8 ± 0.2	3.4 ± 0.7 × 10 ⁻¹⁰

¹ Error estimates for 297°C data are the average absolute error.

² Error estimates for computer reduced data represent approximately 2σ from third iteration (e.g., Fig. 4).

time by rather arbitrarily using our measured values for calculations at 396° and 297°C and values corresponding to the drawn data curve of Figure 5 for calculations at 300° and 200°C. Our values for the interdiffusion coefficient being somewhat larger, the calculated maximum annealing times are shorter, as is reflected in Table 1, for the temperature 297–300°C. The disparity between our 396°C value and an interpolated 400°C value would not be as great (see Fig. 5).

Several points can be made from consideration of Table 1. The first set of Copper Basin data, corresponding to profile X-Y on grain 22, sets the limit to the thermal history there, as discussed earlier. Other data from Copper Basin, of which grain 22 A-B and particularly grain 8 are typical, indicate that much of the apparent "diffusion" record at Copper Basin is really a record of relatively slow change in the composition of gold as deposited. If it is reasonable to assume that it takes tens to hundreds of years to form and cool an ore deposit, as suggested for example by Clark (1959) and Silberman et al. (1972), one may conclude that grain 22 must have formed at less than 300°C. A similar conclusion applies to the deposit at Alder Gulch and, perhaps surprisingly, to that at the Homestake mine.

Desborough et al. (1972) have discussed variation of the Ag content of Homestake gold within and among numerous analyzed crystals. Our analysis, as reported in Table 1, supports their conclusion that Slaughter (1968) is correct in viewing the gold mineralization at Homestake as epithermal. If the gold at Homestake were early and high-temperature or had passed through the metamorphic history of the Homestake Formation, intragranular heterogeneity would not be expected.

In general agreement with our temperature estimates, Nash (1972) presents convincing evidence, from fluid inclusion studies of gangue minerals associated with epithermal gold in Nevada, that epithermal gold deposition typically takes place in the temperature range $250^{\circ} \pm 50^{\circ}\text{C}$.

For a specific application of our way of thinking, one may consider two recent papers on the composition of Witwatersrand gold. Schidrowski (1968) and Saager (1969) have published reports that emphasize, among other things, the limited range in Ag content represented by Witwatersrand gold and the fact that they found no evidence of intergranular heterogeneity in gold composition. Saager's proposals regarding initial homogenization of the gold during transportation and sedimentation are difficult to accept. Both Saager and Schidrowski consider the homogenization effects of "pseudohydrothermal" transport and reconstitution, which is a part of the

modified placer theory they accept for the evolution of the Witwatersrand deposits. We believe that uniformity of gold composition is permissive of virtually any history: the gold could have been deposited at any temperature from solutions so constant in composition that no detectable inter- or intragranular variation ever existed, or the postulated thermal metamorphism of the placer deposits may have obliterated original heterogeneity.

Limitations and Applications

The salient aspects of our diffusion studies in the synthetic and natural Au-Ag system can be summarized as follows:

(1) Preserved Au-Ag gradients in native gold are not necessarily products of diffusion, as we have no method of distinguishing diffusion from depositional gradients.

(2) Preserved gradients, regardless of origin, provide maximum time-temperature limits on the annealing history of gold nuggets. When temperatures can be independently fixed, analysis in terms of diffusion provides a limit for the duration of elevated temperature.

(3) Chemical inhomogeneity in native gold reflects changes in the chemistry of ore fluids and may be useful in evaluation of processes of ore deposition.

(4) Gold grains subjected to metamorphism should show no chemical inhomogeneity. Relative age relations of gold-quartz veins in metamorphic rocks should be determinable.

(5) Low-silver rims on placer grains have such steep gradients that their formation within the hydrothermal regime is unlikely (e.g., Desborough, 1970).

Many of the problems encountered in geothermometry of ore deposits relate to the difficulties of establishing paragenetic and/or equilibrium relationships among ore and gangue mineral phases. The search for measurable chemical or physical parameters intrinsic to individual ore mineral species is just beginning, but seems of great potential. Recently, Stanton and Gorman (1968) and Stanton and Willey (1972) have established useful physical bases for geothermometry that relate directly to ore minerals. With refined analytical technology now available, measurement of minor and trace elements and isotopic variation may be expected to provide data on chemical heterogeneity that can be interpreted according to the diffusion-initial variation model described here for an ideal and simple system. Eventually, knowledge of diffusivities of elements and isotopes within individual mineral species may permit refined time-temperature estimates based on: (1) consideration of several components

within an individual ore-mineral phase and/or (2) comparison of data from each of several coexisting ore-mineral phases. Because constituents of mineral phases are known to have widely different diffusivities (e.g., Barton and Skinner, 1967, fig. 7.1), this technique may be broadly applicable.

The existence of isotopic variations within ore-mineral crystals is well established (e.g., Ault, 1959; Austin and Slawson, 1961; Cannon et al., 1963; Rye and Czamanske, 1969; and Pinckney and Rafter, 1972). The potential for monitoring changes in isotopic ratio with the ion probe is an exciting corollary of our study.

Acknowledgments

For perceptive reviews, we thank J. T. Nash, H. R. Shaw, and R. A. Yund. D. A. Stevenson provided helpful advice.

G. K. G. AND F. E. G.

U. S. GEOLOGICAL SURVEY
MENLO PARK, CALIFORNIA 94025

G. A. D.

U. S. GEOLOGICAL SURVEY
FEDERAL CENTER
DENVER, COLORADO 80225

December 14, 1972; April 6, 1973

REFERENCES

- Abramowitz, M., and Stegun, I. A., eds., 1964, Handbook of mathematical functions with formulas, graphs, and mathematical tables: Washington, D.C., Natl. Bur. Standards, Applied Math. Series, 55, 1046 p.
- Ault, W., 1959, Isotopic fractionation of sulfur in geochemical processes, in Abelson, P. H., ed., Research in geochemistry: New York, John Wiley and Sons, Inc., 511 p.
- Austin, C. F., and Slawson, W. F., 1961, Isotopic analysis of single galena crystals: a clue to history of deposition: *Am. Mineral.*, v. 46, p. 1132-1140.
- Barton, P. B., Jr., and Skinner, B. J., 1967, Sulfide mineral stabilities, in Barnes, H. L., ed., *Geochemistry ore deposits*: New York, Holt, Reinhart and Winston, 670 p.
- Cannon, R. S., Jr., Pierce, A. P., and Delevaux, M. H., 1963, Lead isotope variation with growth zoning in a galena crystal: *Science*, v. 142, p. 574-576.
- Clark, S. P., Jr., 1959, Thermal calculations pertaining to ore deposition: *Carnegie Inst. Washington Year Book* 58, p. 157-160.
- Cook, H. E., and Hilliard, J. E., 1969, Effect of gradient energy on diffusion in gold-silver alloys: *Jour. Applied Phys.*, v. 40, p. 2191-2198.
- Desborough, G. A., 1970, Silver depletion indicated by microanalysis of gold from placer occurrences, *Western United States: ECON. GEOL.*, v. 65, p. 304-311.
- Heidelberg, R. H., Raymond, W. H., and Tripp, J., 1972, Primary distribution of silver and gold in native gold from six deposits in the Western United States: *Mineralium Deposita*, v. 7, p. 321-334.
- Goldstein, J. I., Hanneman, R. E., and Ogilvie, R. E., 1965, Diffusion in the Fe-Ni system at 1 atm and 40 Kbar pressure: *Am. Inst. Mining Metall. Petroleum Engineers Trans.* v. 23, p. 812-820.
- Goldstein, J. I., and Ogilvie, R. E., 1965, The growth of Widmanstätten pattern in metallic meteorites: *Geochim. et Cosmochim. Acta*, v. 29, p. 893-920.
- Greskovich, C., and Stubican, V. S., 1970, Change of molar volume and interdiffusion coefficients in the system MgO-Cr₂O₃: *Jour. Amer. Ceramic Soc.*, v. 53, p. 251-253.
- Johnson, W. A., 1942, Diffusion experiments on a gold-silver alloy by chemical and radioactive tracer methods: *Am. Inst. Mining Metall. Petroleum Engineers Trans.*, v. 147, p. 331-347.
- Mallard, W. C., Bardner, A. B., Bass, R. F., and Slifkin, L. M., 1963, Self-diffusion in silver-gold solid solutions: *Phys. Rev.*, v. 129, p. 617-625.
- Mathews, J., and Walker, R. L., 1965, *Mathematical methods of physics*: New York, W. A. Benjamin, Inc., 475 p.
- Maurice, F., 1970, Utilisation de la microsonde dans les études de diffusion: *Jour. de Microscopie*, v. 9, p. 296-299.
- Nash, J. T., 1972, Fluid inclusion studies of some gold deposits in Nevada: *U. S. Geol. Survey Prof. Paper* 800-C, p. 15-19.
- Pinckney, D. M., and Rafter, T. A., 1972, Fractionation of sulfur isotopes during ore deposition in the Upper Mississippi Valley zinc-lead district: *ECON. GEOL.*, v. 67, p. 315-328.
- Raleigh, D. O., and Crowe, H. R., 1969, Electrochemical methods for the measurement of high-temperature diffusion in metals: *Jour. Electrochem. Soc.*, v. 116, p. 40-48.
- Robie, R. A., Bethke, P. M., Toulmin, M. S., and Edwards, J. L., 1966, X-ray crystallographic data, densities, and molar volumes of minerals, in Clark, S. P., Jr., ed., *Handbook of physical constants*: *Geol. Soc. America Mem.* 97, p. 27-74.
- Rye, R. O., and Czamanske, G. K., 1969, Experimental determination of sphalerite-galena sulfur isotope fractionation and application to the ores at Providencia, Mexico: *Geol. Soc. America Abst. with Prog.*, Pt. 7, p. 195-196.
- Saager, R., 1969, The relationship of silver and gold in the basal reef of the Witwatersrand system, South Africa: *Mineralium Deposita*, v. 4, p. 93-113.
- Schidrowski, M., 1968, The gold fraction of the Witwatersrand conglomerates from the Orange Free State Goldfield (South Africa): *Mineralium Deposita*, v. 3, p. 344-363.
- Shewmon, P. G., 1963, *Diffusion in solids*: New York, McGraw-Hill Book Co., 203 p.
- Silberman, M. L., Chesterman, C. W., Kleinhampl, F. J., and Gray, C. H., Jr., 1972, K-Ar ages of volcanic rocks and gold-bearing quartz-adularia veins in the Bodie Mining District, Mono County, California: *ECON. GEOL.*, v. 67, p. 597-604.
- Slaughter, A. L., 1968, The Homestake mine, in Ridge, J. D., ed., *Ore Deposits of the United States 1933-1967* (Graton-Sales vol.): New York, Am. Inst. Mining Metall. Petroleum Engineers, p. 1436-1459.
- Stanton, R. L., and Gorman, H., 1968, A phenomenological study of grain boundary migration in some common sulfides: *ECON. GEOL.*, v. 63, p. 907-923.
- Stanton, R. L., and Willey, H. G., 1972, Experiments on a specimen of galena ore from Coeur d'Alene, Idaho: *ECON. GEOL.*, v. 67, p. 776-788.
- Wagner, C., 1969, The evaluation of data obtained with diffusion couples of binary single-phase and multiphase systems: *Acta Metall.*, v. 17, p. 99-107.

Appendix

Experimental Methods

Synthesis

Au-Ag alloys for this study were prepared from Johnson and Matthey Spectrographic Grade Ag bar and Au sheet from the Stieff Company. Spectrographic analysis of the gold indicates only 100 ppm Ag, 200 ppm Cu, and 3 ppm Pd as impurities. Appropriate proportions of the metals to produce alloys at 10 weight percent intervals from pure Au to 50

weight percent Ag were weighed into clean 8 mm I.D. and 12 mm O.D. quartz tubes. Each tube was attached to a vacuum system and passed through a furnace port and the contents were melted. After several minutes of agitation under dynamic evacuation, the tubes were sealed off with an oxy-hydrogen flame. Alloy melts were held at approximately 1,100°C for two weeks and agitated vigorously once each day to promote homogeneity. After quenching in ice water, the large ingots (average weight, 5–6 gm) were divided by using a jeweler's saw nippers. Resulting chunks of alloy were pressed between the hardened dies of a hydraulic press to produce flat wafers 6 mm in diameter by 0.3 to 0.5 mm thick. The wafers were trimmed if necessary, carefully washed in dilute HCl, resealed in the original silica tubes, and placed in a furnace at approximately 800°C for annealing. They were held at this temperature for four months to coarsen grain sizes and thereby approach ideal, single-crystal diffusion models. Crystal or grain sizes of the annealed, starting alloys and a sample reacted at 396°C were determined by etching polished surfaces with dilute KCN solutions and measuring crystal boundary intercept distances using a micrometer ocular at a magnification of $\times 250$ in reflected light. The average grain size for the annealed alloys is greater than 200 $m\mu$. The average grain size for a typical 396°C diffusion join after 382 days annealing time was about 260 $m\mu$ with grains ranging from 25 to 900 $m\mu$ over a distance of about 6 mm.

In comparison to conventional methods of preparing alloy couples, in which single crystals are grown and surfaces are carefully lapped, our preparation procedures were crude. This approach was taken partly from want of ready access to crystal growth apparatus and partly from an over-riding desire perhaps to simulate more closely nonideal geological conditions, rather than ideal laboratory conditions. When coupled with analysis of a large number of profiles, this procedure is shown below to give data with considerable scatter, but adequate to support our study and on the average in reasonable agreement with data available in the literature.

Assembly

At the suggestion of Prof. D. A. Stevenson, Stanford University, contact between alloy wafers was maintained at temperature by confining wafer sandwiches in machined, sintered molybdenum jigs. Mo was chosen for this purpose because it has an extremely low thermal expansion coefficient (4.9×10^{-6}). The Mo jig acts as a vise in that the higher thermal expansion coefficients of the alloys ($13\text{--}17 \times 10^{-6}$) provide a force to promote and maintain intimate contact between alloy wafers. Briefly

described, the jig resembles a threaded vial 13 mm in diameter by 35 mm long, with an internal well 7 mm in diameter and 16 mm deep. The vial is internally threaded to take a screw top that is machined such that a flat face projects into the well. Typically, three to five alloy wafers formed a "sandwich" and three such sandwiches were placed in a single jig, individual sandwiches being separated by flat Mo wafers 1 and 2 mm thick. After some trial and error to observe wafer deformation, all vials were snugly tightened by hand. Each jig was then placed in a clean silica tube, evacuated, sealed, and held at temperature for times indicated in Table 2. The wafer assemblages for runs at 297°, 396°, and 489°C, the principal focus of this study, were Au-Ag₁₀-Ag₃₀-Ag₄₀-Ag₅₀, Au-Ag₂₀-Ag₃₀-Ag₅₀, and Au-Ag₁₀-Ag₁₀-Ag₅₀-Ag₂₀, where subscripts denote weight percent Ag in the alloy. No case of wafer sandwich parting occurred and few instances of imperfect wafer contact were detected. Pairs of jigs (silica tubes) for the 297°, 396°, and 489°C runs lay side-by-side in furnaces controlled by solid state controllers. Drift of these furnaces over a two year period was less than 5°C; their short-period variation is nil.

Analysis

Au-Ag alloy sandwiches were prepared for analysis by mounting them in epoxy, sawing the epoxy button in half normal to the wafer surfaces with a jeweler's saw, grinding to a flat surface with silicon carbide, and polishing with diamond pastes (6, 3, and 1 $m\mu$) on a lap wheel. Final buffing was done with 0.3 and 0.05 $m\mu$ alumina suspended in dilute solutions of chromic acid. This final polishing provides a surface that is essentially free of alloy smearing developed during grinding and polishing. Reference standards and samples were prepared by the same method.

Analyses were performed on an Applied Research Laboratories model EMX-SM electron microprobe operated at 15 kv, with a sample current of 3×10^{-8} amperes referenced to pure gold. This relatively low accelerating voltage was used to minimize effective beam diameter, as well as matrix effects. Counting intervals of about 20 seconds were determined by integrated beam current termination. Silver and gold were analyzed with ADP crystals, using the silver L_{α} and gold M_{α} lines. Silver was determined independently on two channels using sealed proportional detectors while gold was analyzed simultaneously on a flow proportional detector.

Typically, three sets of profiles were measured across sandwiches, perpendicular to the diffusion interfaces, using an automatic step-scanning motor which provides for sequential point analyses with a

nominal fixed distance between each point, e.g., 2, 4, 6, and 10 $m\mu$. The accuracy of these intervals was checked by traversing a measured distance of 400 $m\mu$; corrected step intervals used in the following analysis are 2.0, 4.2, 6.1, and 11.7 $m\mu$, the choice depending on steepness of gradient. Electron beam diameter was smaller than the smallest step interval and probably of the order of 1 $m\mu$. Focus of the specimen (and therefore the electron beam) was monitored visually during all analyses.

Reference standards were the identical alloys prepared for the experimental diffusion study. Use of these alloys as standards has shown that compositional inhomogeneities within and between wafers are within the limits of measurement with the microprobe.

Calculation of Interdiffusion Coefficients

To calculate \bar{D} at concentration c' , one obtains the reciprocal of the tangent to the diffusion profile at c' and calculates the area associated with c' , as represented by the cross-hatched pattern of Figure 3. For each of our profiles, $\bar{D}(c')$ was calculated for each c' (i.e., each point in the profile) except those near the ends of the profile, where the integral approaches zero. Because of the great quantity of data, approximately 3,000 determinations representing 114 separate diffusion profiles, the calculations were made by computer.

The consistency of the raw data plus the generous number of points in each profile justified calculation of areas (and subsequent positioning of the Matano interface) by using straight-line segments between points to represent the profile. Because area calculations are sensitive to minor shifting of the interface, our program equalized areas to within two percent by successive iterations. Clearly, however, the reciprocal of the slope at various points on the profile cannot be readily obtained from such a curve, as the derivative should be calculated for a smoothly curving function. As a practical approximation to this, we elected to use the Lagrange Interpolation Formula over consecutive 5-point arrays (e.g., Mathews and Walker, 1965), with evaluation of the tangent at the midpoint.

Given five points with Cartesian coordinates (X_1, Y_1) , (X_2, Y_2) , (X_3, Y_3) , (X_4, Y_4) , and (X_5, Y_5) , we have

$$Y(X) = Y_1 \frac{(X-X_2)(X-X_3)(X-X_4)(X-X_5)}{(X_1-X_2)(X_1-X_3)(X_1-X_4)(X_1-X_5)} + \dots + Y_5 \frac{(X-X_1)(X-X_2)(X-X_3)(X-X_4)}{(X_5-X_1)(X_5-X_2)(X_5-X_3)(X_5-X_4)} \quad (1)$$

$$\frac{dY}{dX} = Y_1 \frac{d[(X-X_2), \dots, (X-X_5)]}{dX(X_1-X_2), \dots, (X_1-X_5)} + \dots + Y_5 \frac{d[(X-X_1), \dots, (X-X_4)]}{dX(X_5-X_1), \dots, (X_5-X_4)} \quad (2)$$

The derivatives in the first, second, fourth, and fifth terms on the right side of equation (2) at $X=X_3$ can be evaluated by the following process, as shown for the first term:

$$\begin{aligned} & \frac{d}{dX} [(X-X_2), \dots, (X-X_5)]_{X=X_3} \\ &= (X-X_2)(X-X_4)(X-X_5) \frac{d}{dX} (X-X_3) \\ &+ (X-X_3) \frac{d}{dX} [(X-X_2)(X-X_4)(X-X_5)]_{X=X_3} \end{aligned} \quad (3)$$

Therefore

$$\frac{d}{dX} [(X-X_2), \dots, (X-X_5)]_{X=X_3} = (X-X_2)(X-X_4)(X-X_5)1 + 0 \quad (4)$$

Because data are obtained by the microprobe at regular intervals (11.7 $m\mu$, 6.1 $m\mu$, etc.) through one traverse the derivative of the third term in equation (2) is zero. Thus the final equation is:

$$\begin{aligned} & \left. \frac{dY(X)}{dX} \right|_{X=X_3} \\ &= \frac{Y_1(X_3-X_2)(X_3-X_4)(X_3-X_5)}{(X_1-X_2)(X_1-X_3)(X_1-X_4)(X_1-X_5)} \\ &+ \frac{Y_2(X_3-X_1)(X_3-X_4)(X_3-X_5)}{(X_2-X_1)(X_2-X_3)(X_2-X_4)(X_2-X_5)} \\ &+ 0 + \frac{Y_4(X_3-X_1)(X_3-X_2)(X_3-X_5)}{(X_4-X_1)(X_4-X_2)(X_4-X_3)(X_4-X_5)} \\ &+ \frac{Y_5(X_3-X_1)(X_3-X_2)(X_3-X_4)}{(X_5-X_1)(X_5-X_2)(X_5-X_3)(X_5-X_4)} \end{aligned} \quad (5)$$

The greatest errors occur near the ends of the individual profiles where the integral is small and the reciprocals large. These aberrant values show up on plots such as Figure 4 as "tails" of points extending above and below the major belt of points at compositions corresponding to those of the starting alloys (i.e., the ends of each diffusion profile as indicated on Fig. 4).

Data handling

Microprobe data for samples annealed at temperatures from 396° to 799°C were converted from tape to cards and processed by computer to return values in weight percent by direct comparison with count data for the series of standard Au-Ag alloys.

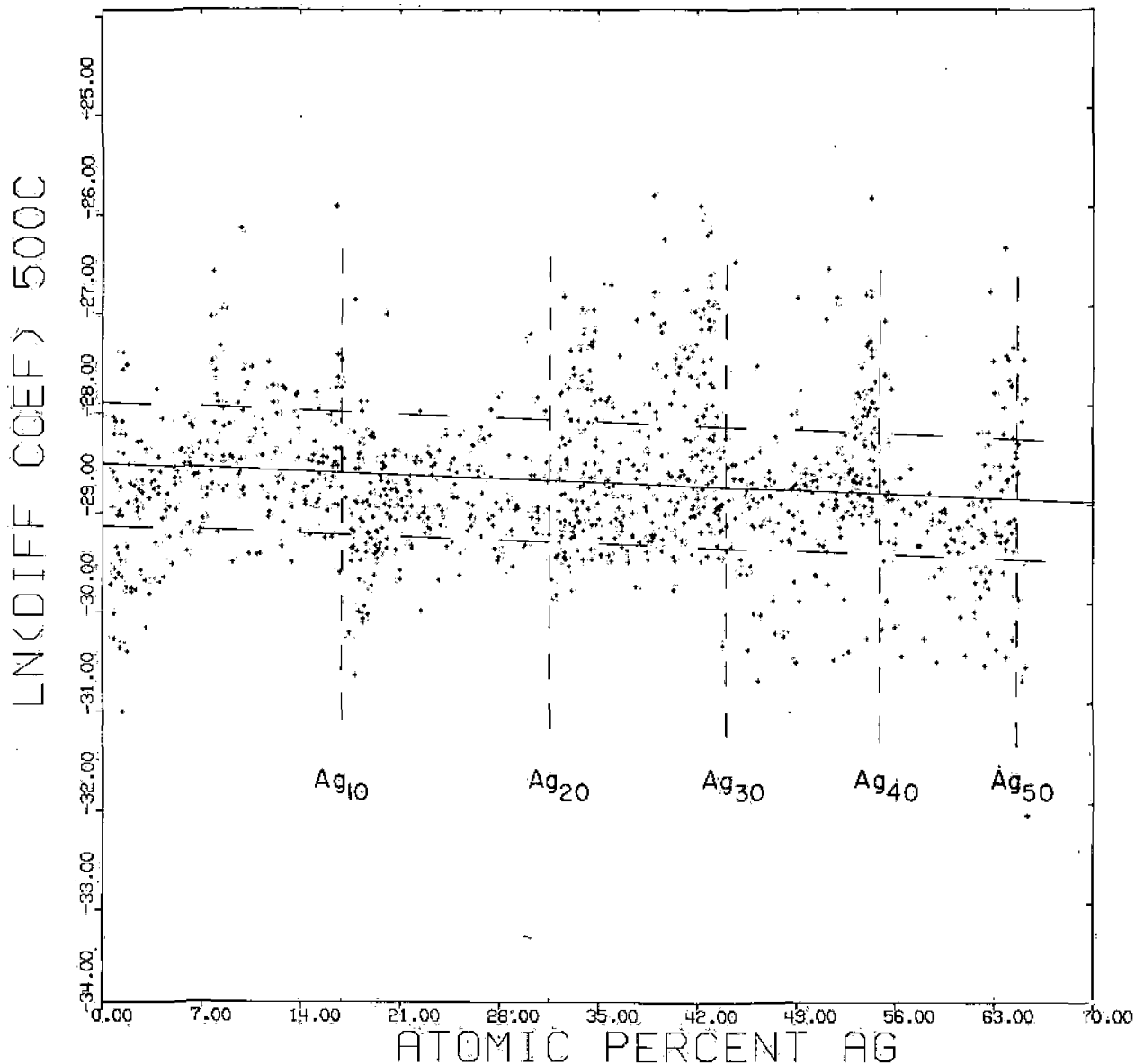


FIG. 4. Example of computer plot of $\ln \bar{D}$ versus atomic percent Ag showing refined least-squares data fit. Limits of 2σ relating to third (final) iteration are shown by subhorizontal, long-dashed lines. Vertical dashed lines represent initial wafer compositions in weight percent Ag. (Actual temperature—489°C.)

A modified version of U. S. Geological Survey Computer Program B-890, Curve Calibration (Linear) and Analysis of Unknowns, was used to produce both card and printed output of weight percent silver for the two channels used on the microprobe. This second set of cards was edited to eliminate data of constant value corresponding to areas between interfaces. Data for individual profiles were run through our Diffusion Program, which first averaged compositions from the two channels and then calculated values for \bar{D} as outlined in the preceding section. In addition to re-

turning a listing of diffusion coefficients calculated for each point in a profile, the program punched a third set of cards associating each calculated value of \bar{D} with measured atomic percent Ag.

The least-squares fit of $\ln \bar{D}$ versus atomic percent Ag and final plots such as Figure 4 were obtained by processing the third card set through supplementary programs allowing the fixing of appropriate limits of $\ln \bar{D}$. In order to exclude clearly spurious data associated with the "tails" of diffusion profiles, we calculated a fit to all data points, rejected points deviating more than 2σ from this line, repeated the

fitting and 2σ rejection, and found the final fit by a third iteration. This iterative fitting resulted in rejection of an average of 35 percent of calculated data points. Approximate limits to accepted data are shown in Figure 4.

For the 297°C profiles, which contained six points at best in the diffusion profile, diffusion coefficients were calculated by hand calculator rather than by computer because the sparsity of data produced large errors in derivatives and areas. For the 382-day experiments, data for seven interfaces yield an average value of $\bar{D} = 8.0 \pm 1.7 \times 10^{-17}$; for the 730-day experiments, data for nine interfaces give $\bar{D} = 7.4 \pm 3.0 \times 10^{-17}$. It must be emphasized that diffusion profiles for the 297°C experiments are steep (note Fig. 1) and that some artificial broadening of the profile may be caused by electron beam spreading despite the low accelerating voltage used. This should cause calculated \bar{D} values to be too high, and they are, although they are not anomalously high in comparison to our 396° and 489°C data points (note Fig. 5) where beam spreading should not be a factor. The use of deconvolution techniques in an attempt to improve our 297°C data is not warranted in terms of our dependence upon those data.

Our results are summarized in Table 2 and plotted on Figure 5. With the exception of the 297°C data, the reported values of \bar{D} are for 35 atomic percent silver. We chose to report \bar{D} for a composition of 35 atomic percent silver for three reasons: (1) it is about midway in the range we investigated experimentally (Fig. 4); (2) it is within the range of many of the natural profiles we studied (Table 1); and (3) it is not far from 50 atomic percent Ag, the most Au-rich composition for which high and low temperature values of \bar{D} are available. Precise studies of Au-Ag diffusion (e.g., Mallard et al., 1963, and Raleigh and Crowe, 1969) show a variation in D_{Au} and D_{Ag} with composition, such that measurably lower diffusivity values are typical in 50-65 atomic percent Ag relative to pure Au or pure Ag. A similar relation should hold for \bar{D} , because $\bar{D} \approx X_2 D_1 + X_1 D_2$ for an ideal solid solution. For 396° and 489°C where data are most plentiful and extend over the full composition range, our least squares fit shows comparable variation in \bar{D} with composition (e.g., Fig. 4). At higher temperatures, where data are less plentiful and pertain to a restricted range of compositions, lower diffusivities at 50-65 atomic percent Ag are not clearly indicated. Because of the resultant uncertainty in the slope of the least squares fit, we therefore feel that our most accurate interdiffusion values are at 35 atomic per-

cent Ag, in the middle of the compositional range studied.

In order to make a more rigorous analysis of our data for the compositional dependence of the interdiffusion coefficient and to check our overall method of analysis we chose another method modeled after simple treatments for a pair of infinite solids (Shewmon, 1963; Johnson, 1942). Essentially, this method involves the use of a probability or error function to derive a single interdiffusion coefficient for each profile by reducing the diffusion profile to a straight line and fitting it. This method is strictly applicable only when diffusion coefficients are not concentration dependent. In order to make an estimate of the overall composition dependent variation of the interdiffusion coefficient, we have had to use our couples of most closely spaced initial composition, i.e., 0-10, 10-20, etc., with the assumption that interdiffusion is not concentration dependent. Because of the relative paucity of data at other temperatures this analysis was restricted to the 396° and 489°C data.

The proper solution of the diffusion equation

$$\frac{\partial c}{\partial t} = \bar{D} \frac{\partial^2 c}{\partial x^2} \text{ (constant composition)} \quad (6)$$

is

$$\frac{c_x - c_0}{c_1 - c_0} = \frac{1}{2} \left\{ 1 - \phi \left[\left(\frac{x}{2(\bar{D}t)^{1/2}} \right) \right] \right\} \quad (7)$$

where \bar{D} = the interdiffusion coefficient in cm^2/sec
 t = time of experiment in seconds

ϕ = the probability integral (error function)

c_0 = minimum concentration of Ag in profile

c_1 = maximum concentration of Ag in profile

c_x = concentration of Ag after a time t at a distance x along the profile.

For simplicity, let us set

$$Z = \frac{c_x - c_0}{c_1 - c_0} \quad (8)$$

and

$$y = \frac{x}{2(\bar{D}t)^{1/2}} \quad (9)$$

Then

$$\phi(y) = 1 - 2Z \quad (10)$$

A smooth fit to diffusion profiles such as Figure 3 can be calculated by varying the value assigned to \bar{D} in equation (7), but this process for finding \bar{D} is not convenient. Because y is proportional to x , one can obtain \bar{D} more easily by solving the error function $\phi(y)$ for y at each x , plotting the resulting pairs, and finding the slope of the line which best fits these points (e.g., Johnson, 1942, p. 335). The

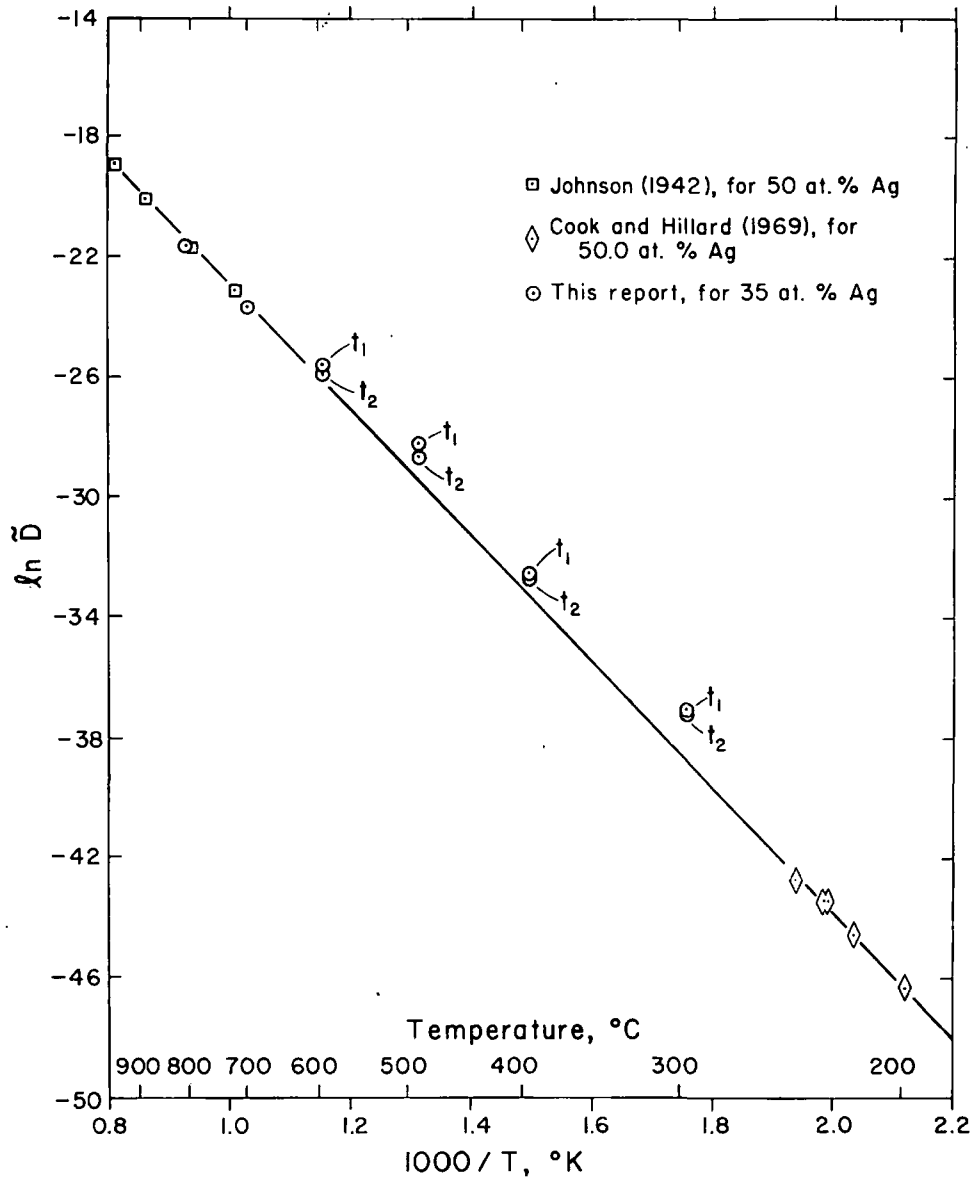


FIG. 5. Plot of literature data and new data, this report, in terms of $\ln \tilde{D}$ versus $1,000/T$; t_1 and t_2 refer to shorter and longer reaction times, respectively.

process is similar to plotting Z versus x on probability paper.

Solving the error function for x is somewhat difficult because

$$\phi(y) = \frac{2}{(\pi)^{1/2}} \int_0^y e^{-u^2} du \quad (11)$$

cannot be integrated by any direct means. Fortunately, a close approximation of $\phi(y)$ can be derived by calculating the Taylor Series expansion of the derivative and then integrating the result, term by term. Because the limits of $\phi(y)$ in our problem are $-1 < \phi(y) < 1$, the series is best

evaluated at zero. We have

$$e^{-u^2} = 1 - u^2 + \frac{u^4}{2} - \frac{u^6}{6} \quad (12)$$

$$\begin{aligned} [\phi(y)] \frac{\pi^{1/2}}{2} &= \int_0^y e^{-u^2} du \\ &\approx \int_0^y \left(1 - u^2 + \frac{u^4}{2} - \frac{u^6}{6} \right) du \\ &= y - \frac{y^3}{3} + \frac{y^5}{10} - \frac{y^7}{42}. \quad (13) \end{aligned}$$

We can now revert the series of equation (13) to

simplify the calculation of y , for if

$$\frac{\pi^{\frac{1}{2}}}{2} [\phi(y)] = y - \frac{y^3}{3} + \frac{y^5}{10} - \frac{y^7}{42} \quad (14)$$

then

$$y = A \left[\frac{\pi^{\frac{1}{2}}}{2} \phi(y) \right] + C \left[\frac{\pi^{\frac{1}{2}}}{2} \phi(y) \right]^3 + E \left[\frac{\pi^{\frac{1}{2}}}{2} \phi(y) \right]^5 + G \left[\frac{\pi^{\frac{1}{2}}}{2} \phi(y) \right]^7. \quad (15)$$

The coefficients solved by appropriate equations (see Abramowitz and Stegun, 1964) are

$$\begin{aligned} A &= 1.0 \\ C &= 0.333333 \\ E &= 0.233333 \\ G &= 0.153968. \end{aligned}$$

A computer program was devised to find y at each X using equation (15). These values were then analyzed by a least squares fit to determine the slope of the line from which

$$\bar{D} = \frac{1}{t(2 \cdot \text{slope})^2}. \quad (16)$$

The results of this analysis suggest that, over the composition range 10 to 50 atomic percent Ag, values of \bar{D} decrease from 4.8×10^{-13} to 2.6×10^{-13} $\text{cm}^2 \text{sec}^{-1}$ at 489°C and from 7.3×10^{-15} to 2.4×10^{-15} $\text{cm}^2 \text{sec}^{-1}$ at 396°C . Values of $\ln \bar{D}$ obtained by this method at 35 atomic percent Ag agree well with those obtained by our initial procedure: 489°C , -28.75 ± 0.2 ; at 396°C , -33.25 ± 0.34 (compare Table 2).

Figure 5 relates data for 35 atomic percent Ag from our study to available data for 50 atomic percent Ag; comparison of the two is not straight-

forward. The data of Mallard et al. and Raleigh and Crowe are interpreted to indicate an increase in the disparity between values for \bar{D} at 35 and 50 atomic percent Ag (for convenience \bar{D}_{35} and \bar{D}_{50}) as a function of decreasing temperature. We estimate from Mallard et al. that, at 700°C , \bar{D}_{35} is 10 to 15 percent larger than \bar{D}_{50} . From our own data, as well as that of Raleigh and Crowe, \bar{D}_{35} may be 25 to 50 percent larger than \bar{D}_{50} . Referring to Figure 5, it therefore seems that our highest temperature data may in fact indicate diffusivities 5 to 15 percent lower than expected, whereas our lower temperature data indicate diffusivities somewhat higher than would be expected. For example, even point t_2 at 396°C represents an interdiffusion coefficient 65 percent larger than that obtained from the drawn curve. (Recall that we presumed the 297°C data points to plot anomalously high because of analytical difficulties.) Values of the activation energy, Q , calculated from the Arrhenius Equation, $D = D_0 e^{-Q/RT}$ (where $-Q/R$ would be the slope of the best fit through our data in Fig. 5), are 10 to 15 percent smaller than literature values because of the systematic differences between our values for \bar{D}_{35} and those predicted from the work of Mallard et al. and Cook and Hilliard (1969). These differences most probably relate to the strain caused by specimen loading or confinement techniques, or to the relative importance of intergranular versus intracrystalline diffusion.

In summary, it appears that our techniques of specimen preparation have provided values for interdiffusion in the Au-Ag system which agree fairly well with those from earlier investigations and would be adequate to establish a basis for interpretation of natural gradients. The data do not compare as well with previous studies as we had expected, but we are not sure why.

2
SUBJ
GCHM
AMOT

Dup
**UNIVERSITY OF UTAH
RESEARCH INSTITUTE
EARTH SCIENCE LAB.**

A Model of the Dump Leaching Process that Incorporates
both Physics and Chemistry

L. M. Cathles
Ledgemont Laboratory
Kennecott Copper Corporation
Lexington, Massachusetts 02173

J. Apps
Kennecott Copper Corporation
Metal Mining Division, Research Center
Salt Lake City, Utah 84111

Text of paper presented at
AIChE Symposium
on
Modeling and Analysis of
Dump and In-Situ Leaching Operations
August 19, 1974

A Model of the Dump Leaching Process that Incorporates
both Physics and Chemistry

Abstract

Air convection is essential to the successful dump leaching of sulfide waste. In this paper the validity of this statement is first demonstrated. Then a simple one dimensional model is developed that includes air convection as well as the chemistry of sulfide dissolution. The model is calibrated by comparing model predictions to the observed leaching history of a test dump. Parameters in the model are varied to show how the dump might have leached if it had been thicker, if more leach fluid had been passed through the dump, if the waste had contained more pyrite, etc.

Definition of Symbols Used

α	Coefficient of thermal expansion of air including effects of changing water vapor saturation.
β	Coefficient describing the change in air density due to oxygen depletion. (See equation (14)).
C_g	Heat capacity of gas phase in dump including effects of variable water saturation, gm/cm ³ .
C_l	Heat capacity of mobile liquid phase in dump, cal/gm-°C.
C_T	Heat capacity of dump as a whole, cal/gm-°C.
E_{DS}^* , E_{DNS}^*	Activation energies describing, through equation (11), the temperature dependence of τ_{DS} , τ_{DNS} . kcal/mole.
E_{CS}^* , E_{CNS}^*	Activation energies describing, through equation (11), the temperature dependence of τ_{CS} , τ_{CNS} . kcal/mole.
FPY	Moles of pyrite leached per mole of sulfide copper leached.
G_S	Initial sulfide grade of dump, wt % Cu.
G_{NS}	Initial non-sulfide grade of dump, wt % Cu.
g_o	Gravitational acceleration, cm/sec ² . (Usually ~ 980 cm/sec ²).
H	Height of dump, cm.
H_i	Thickness of ith layer of dump, cm.
\bar{H}_i	Dimensionless thickness of ith layer of dump. $\bar{H}_i = H_i/H$
K_T	Thermal conductivity of dump as a whole (total dump), cal/cm-°C-sec.
k_{AVE}	Average permeability of the dump, cm ² . (1 Darcy $\approx 10^{-8}$ cm ²).
N	Number of layers into which dump has been arbitrarily broken for sake of computation (usually 20).
μ_g	Viscosity of the gas phase in the dump, poise.
$[O_2]_{STP}^g$	Concentration of oxygen in air under standard conditions of temperature and pressure, gm/cm ³ .

Definition of symbols used, cont.

$[O_2]^g$	Concentration of oxygen in gas phase of dump, gm/cm ³ .
$[\bar{O}_2]^g$	Normalized oxygen concentration in gas phase of dump. $[\bar{O}_2]^g = [O_2]^g / [O_2]_{STP}^g$.
ΔP	Pressure drop across (bottom to top) the dump, dynes/cm ² . (10 ⁶ dynes/cm ² ~ 1 atmosphere).
ϕ	Interblock porosity of dump (usually ~25%).
R_A	Rate of heat generation, kcal/cm ³ -dump-sec.
R_{O_2}	Rate of oxygen consumption, gmO ₂ /cm ³ -dump-sec.
R_{Cu}	Rate of copper leaching, gmCu/cm ³ -dump-sec.
ρ_R	Density of waste particles, gm/cm ³ .
ρ_T	Density of the dump as a whole ("Total" dump), gm/cm ³ . ($\rho_T = \rho_R (1 - \phi)$).
ρ_l	Density of liquid phase of dump (water), gm/cm ³ .
ρ_g	Density of gas phase in dump including effect of variable water vapor saturation, gm/cm ³ .
ρ_{oo}	Density of air at standard temperature and pressure, gm/cm ³ .
T	Temperature of dump at any particular location. Temperature of water, rock, and gas phases assumed identical. °C.
τ_{DS} , τ_{DNS}	Time to leach typical waste particle completely of <u>Sulfide</u> or <u>Non-Sulfide</u> copper assuming rate of leaching is limited by <u>Diffusion</u> of oxidant or acid into the particle.
τ_{CS} , τ_{CNS}	Time to leach typical waste particle completely of <u>Sulfide</u> or <u>Non-Sulfide</u> copper assuming the rate of leaching is controlled by the shrinking surface area of the sulfide or non-sulfide copper (" <u>Chemical</u> " control).
V_g	Darcy gas velocity through dump, cm ³ gas/cm ² dump-sec.
V_l	Darcy velocity of water passing through the dump. Average rate over application periods and rest cycles is used. cm ³ water/cm ² dump-sec.
X_{NS}	Fraction of initial non-sulfide copper remaining in dump or given layer of dump.

Definition of symbols used, cont.

X_S Fraction of initial sulfide copper remaining in the dump or a given layer of the dump.

X_i Distance of center of i th layer of dump from base of dump, cm.

INTRODUCTION

Sulfides must be oxidized before their metal values may be put into solution. The conceptual basis of the model of dump leaching presented here is simply that the exothermic sulfide oxidation reactions generate heat and consume oxygen from the air, and by so doing drive air convection through the dump. This air convection is the only significant source of oxidant to the dump.

A counter current flow system is envisioned:

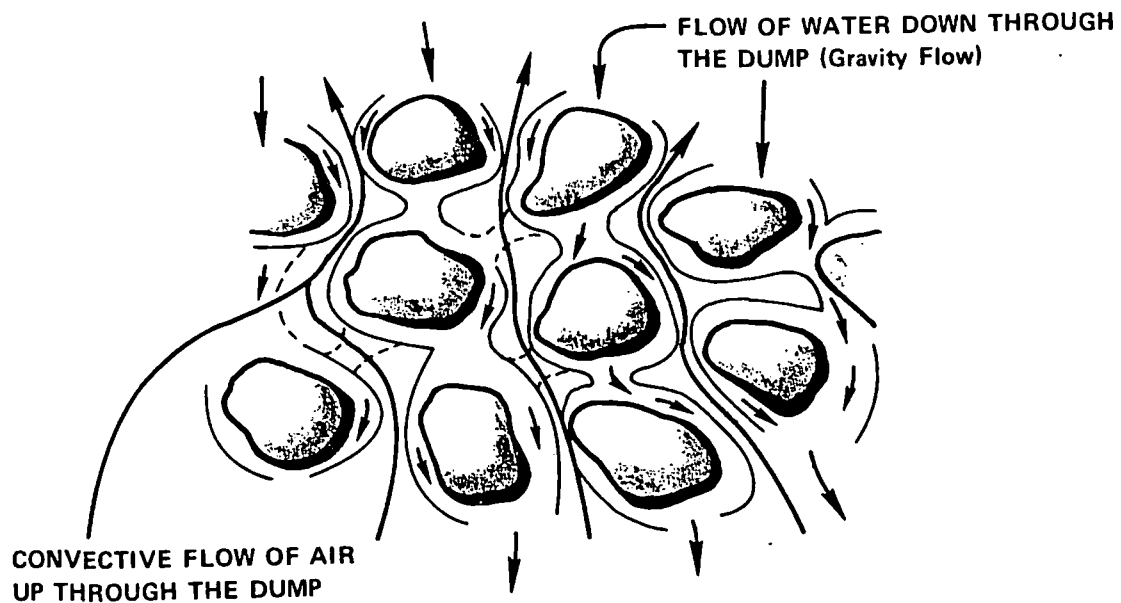
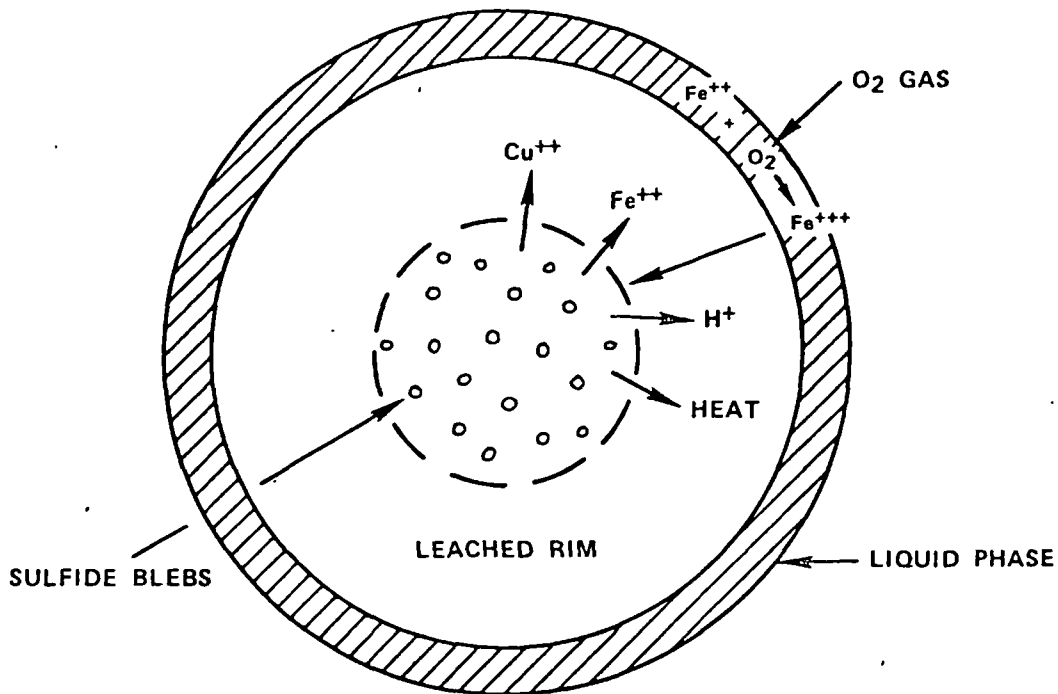


Figure 1: There is a counter-current interlocking flow of air and water through a leach dump. The flow of water is usually intermittent.

In detail, the oxygen leaves the gas phase within the dump by dissolving in the liquid phase where it oxidizes ferrous to ferric iron. The ferric iron diffuses into the ore fragments and oxidizes the sulfide minerals*:



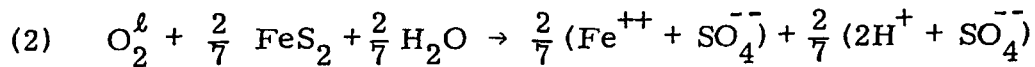
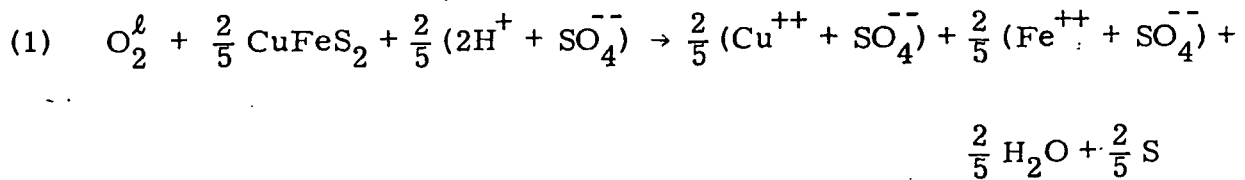
CROSS SECTION OF WASTE PARTICLE

Figure 2: Idealization of the leaching of a single waste particle.

Acid, Fe^{+++} , and heat are produced along with Cu^{++} . As the leached rim grows, the rate of leaching drops.

* At 1/5 atmosphere P_{O_2} and the temperatures involved in dump leaching, oxygen is not very soluble in water ($< 8.6 \times 10^{-3}$ gm/liter). Typical ferric iron concentrations in leach dumps run ~ 1 gm/liter. These relative concentrations ensure Fe^{+++} will be the oxidizing agent in the diffusion controlled processes envisioned above.

If pyrite and chalcopyrite are the only sulfide minerals, then from the chemical reactions



it can be seen that for every mole (64 gm) of sulfide copper leached, 5/2 mole (5/2 · 32 gm) of oxygen will be consumed. If FPY moles of pyrite are leached per mole of sulfide copper, an additional 7/2 FPY moles (7/2 · 32 · FPY gm) of O₂ will be consumed. Thus for every gram of sulfide copper leached, the following number of grams of O₂ will be consumed.

$$(3) \quad gmO_2 \text{ consumed} = (1.25 + 1.75 \text{ FPY}) \text{ gm sulfide Cu leached}$$

Actually the amount of oxygen consumed per gram of sulfide copper leached is somewhat greater than this, if account is taken of the oxidant required to precipitate, as jarosite, the iron exchanged for copper during cementation (2.5 lb. Fe/lb. Cu) and the iron produced in leaching the chalcopyrite and pyrite. Further, if the excess acid produced by the oxidation of pyrite is neutralized by reaction with gangue of biotite composition* a bit more iron is generated, oxidized, and precipitated. With these additions (3) becomes:

$$(4) \quad gmO_2 \text{ consumed} = (1.75 + 1.91 \text{ FPY}) \text{ gm sulfide Cu leached}$$

* Biotite has been found to be more reactive by a factor of ~100 than other gangue minerals in a porphyry copper intrusive.

Waste material typically contains 10 to 100 moles of pyrite for every mole of sulfide copper. Thus pyrite is by far the most important oxidant consumer.

A liter of air contains 0.28 gm O₂. Figure 3 shows that (4) requires far more air than water to flow through a waste dump if the effluent solutions are to contain the copper concentrations typically observed*. For the particular dump we shall consider, at least 80 times more air passed through the dump than water. That is, for each liter of leaching solution leaving the dump with a net gain of .25 gm/l (2 lb. Cu/1000 gal.) copper, 80 liters of air are required to supply the oxidant necessary for the chemical reactions involved.

Equations (1) and (2) not only tell us the amount of oxidant consumed per gram of copper leached, but also the heat generated per gram of copper leached. (The enthalpy of reaction, ΔH_R , of equation (1) is -108.8 kcal; the ΔH_R for equation (2) is -94.9 kcal). If we again take into account the heat consumed in the precipitation of jarosite, require acid and iron balance, and assume 2.5 lb. Fe are exchanged per pound of Cu at the precipitation plant:

(5) Kilocalories produced = (2.89 + 5.41 FPY) gm sulfide Cu leached

Again it can be seen pyrite oxidation will in all probability be the most significant source of heat. The rate at which a waste dump heats up is quite a direct measure of FPY.

Equations (4) and (5) contain the fundamentals of a model of the dump leaching process. Sulfide oxidation reactions consume oxygen from the air in a dump. Since O₂ is a heavy component in air, the oxygen depleted air is light. The same is true of increases in water saturation. Buoyant forces

* Leach solutions cannot carry significant oxidant with them as they move through the dump.

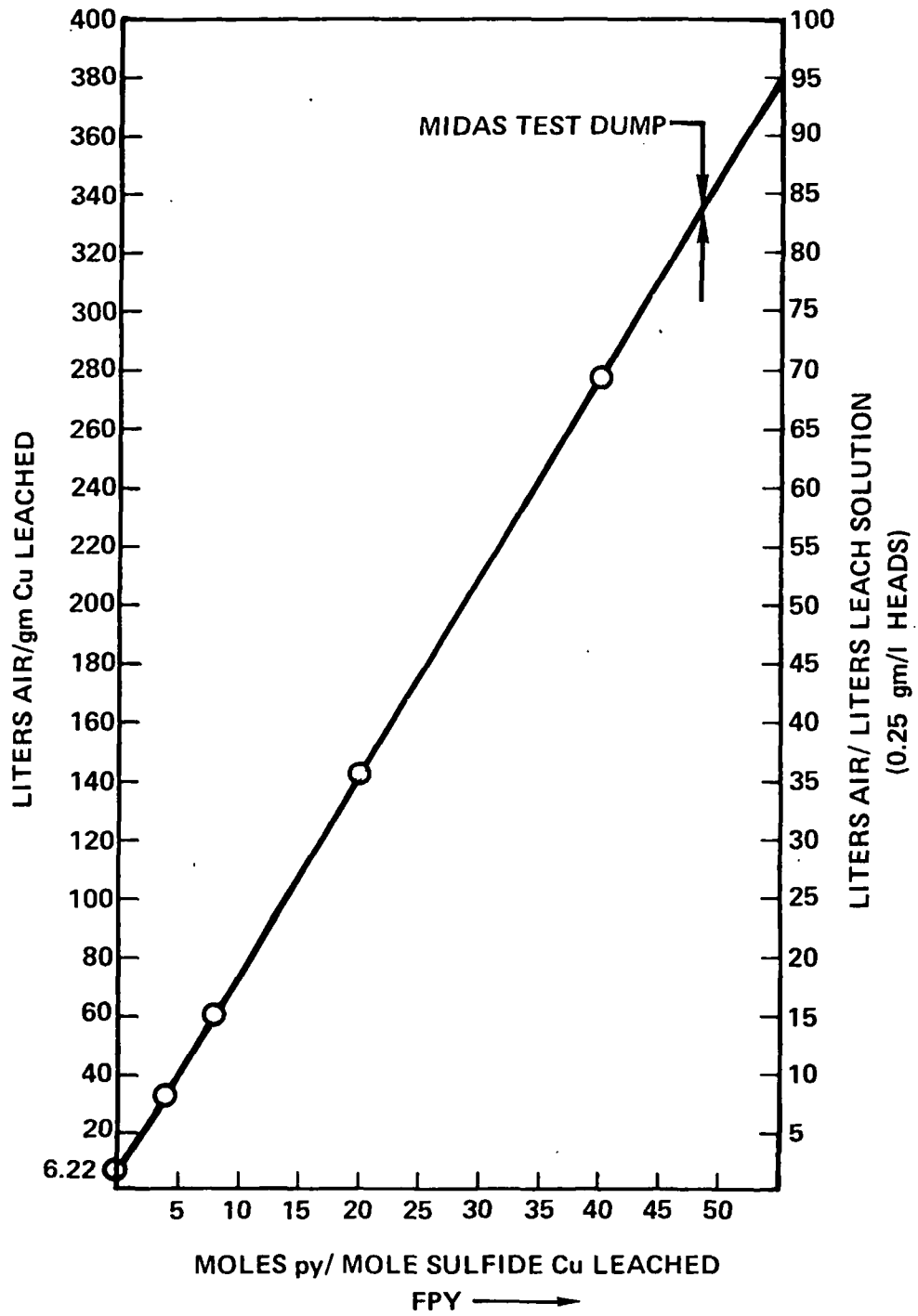


Figure 3: Equation (4) requires that far more air flow through a dump than water if sulfide copper is to be effectively leached.

tend to produce air convection. Furthermore the oxidation reactions are exothermic. The heating also promotes air convection.

In the next section we generalize (4) and (5) slightly to take into account copper sulfides other than chalcopyrite and non-sulfide copper. We briefly discuss processes that control the rate of leaching, and develop a simple one dimensional flow model. The section after next compares the model of leaching behavior of a small test dump. The last section speculates on the answers to several "what if" questions, using the model.

A MODEL OF THE DUMP LEACHING PROCESS

Because sulfide leaching is dominated by the leaching of pyrite (4) and (5) are quite easy to generalize. Provided FPY is taken as the moles of pyrite oxidized per mole of sulfide copper oxidized, and provided FPY is greater than ~ 4 , (4) and (5) will hold to good approximation even if sulfide minerals other than chalcopyrite are present.

We assume sulfide oxidation takes place in a dump only where the air filled pores of the dump contain oxygen and that the oxidation proceeds at a rate independent of the actual oxygen concentration. Experiments show the rate of bacterial conversion of Fe^{++} to Fe^{+++} in the presence of air is nearly independent of oxygen concentration until the oxygen in the air is nearly depleted. Sulfide leaching tends to be less than first order in Fe^{+++} concentration.

By contrast non-sulfide copper is leached with acid alone. Acid generated by pyrite oxidation anywhere in the dump is recirculated through the dump in normal operation. Therefore, non-sulfide copper leaching should take place everywhere in the dump at a rate independent of the presence or absence of nearby oxygen.

Suppose the fraction of sulfide copper remaining in the dump after some leaching is X_S , and the fraction of non-sulfide copper in the dump is X_{NS} . Let the original sulfide copper grade be G_S gm Cu/gm waste and the original non-sulfide copper grade be G_{NS} . Then the rate at which copper is leached from the dump, \mathcal{R}_{Cu} [gm Cu/cm³ dump-sec], may be expressed:

$$(6) \quad \mathcal{R}_{Cu} = \rho_R (1 - \phi) \left(G_S \frac{dX_S}{dt} + G_{NS} \frac{dX_{NS}}{dt} \right)$$

Similarly the rate of oxygen consumption, \mathcal{R}_{O_2} (gmO₂/cm³ dump-sec), and the rate of heat generation, \mathcal{R}_A [kcal/cm³ dump-sec], may be expressed, from (4) and (5):

$$(7) \quad \mathcal{R}_{O_2} = \rho_R (1 - \phi) G_S \frac{dX_S}{dt} (1.75 + 1.91 \text{ FPY})$$

$$(8) \quad \mathcal{R}_A = \rho_R (1 - \phi) G_S \frac{dX_S}{dt} (2.89 + 5.41 \text{ FPY})$$

ρ_R is the density of the rock waste (commonly about 2.7 gm/cm³), ϕ is the interblock porosity of the dump (commonly ~25%). $\rho_R (1 - \phi)$ is the bulk density of the dump as a whole, which for $\rho_R = 2.7$ gm/cm³ and $\phi = .25$, equals 1.7 tons/yd³.

The rate of leaching $\frac{dX_S}{dt}$ and $\frac{dX_{NS}}{dt}$ may be conveniently described by a "shrinking core" model. If we assume a mixed chemical and diffusion controlled model, and if τ_D is the time required to leach a waste particle completely when the process is solely diffusion controlled, and τ_C the time to leach a waste particle completely when the process is controlled by the decreasing surface area of the shrinking unleached core, then:

$$(9) \quad \frac{dX_S}{dt} = \frac{-3X_S^{2/3}}{6 \tau_{DS} X_S^{1/3} (1 - X_S^{1/3}) + \tau_{CS}}$$

$$(10) \quad \frac{dX_{NS}}{dt} = \frac{-3X_{NS}^{2/3}}{6 \tau_{DNS} X_{NS}^{1/3} (1 - X_{NS}^{1/3}) + \tau_{CNS}}$$

Given values for τ_{DS} , τ_{CS} , τ_{DNS} , τ_{CNS} , (9) and (10) determine the rate of leaching at any point in the dump at any stage of leaching. X_{NS} and X_S can be updated after each increment model of leaching. Model time increments may be taken as short as desired.

Both τ_C and τ_D can be given physical meaning and their values computed "theoretically". When this is done $\tau_{CS}^{20^\circ C} = 903$ mo, and $\tau_{DS}^{20^\circ C} = 1590$ mo. In addition τ_C and τ_D may be given a temperature dependence:

$$(11) \quad \tau(T) = \tau(T = 0^\circ C) \text{ EXP} \left(\frac{1000 \cdot E^*}{2} \frac{T}{(273)(273 + T)} \right)$$

This introduces activation energies E^*_{DS} , E^*_{CS} , E^*_{DNS} , E^*_{CNS} . From the literature reasonable guesses for E^*_{DS} and E^*_{DNS} would be 5.0 kcal/mole. E^*_{CS} and E^*_{CNS} might range from 14.0 kcal/mole to 20.0 kcal/mole, the activation energies reported by various authors for the leaching of pyrite (Mathews, C., Robins, 1972; Smith and Shumate, 1970).

The most serious approximation in (9) and (10) is probably the assumption that the dump is composed of waste particles of only one size. This may not be as serious an approximation as it might at first seem, given the tendency of small ore particles to clump together and leach as if they were a larger aggregate, and the tendency for large ore particles to have large enough cracks that they leach like somewhat smaller particles (Auck and Wadsworth 1973).

Given (6) - (11), the heat balance in a waste dump may be described by:

$$(12a) \quad \rho_T C_T \frac{\partial T}{\partial t} = -(\rho_l C_l V_l + \rho_g C_g V_g) \cdot \nabla T + R_A + K_T \nabla^2 T$$

Where ρ and C are the density and heat capacity of the total dump (subscript T) and the liquid (subscript l) and gas (subscript g) phase of the dump. V_l is the darcy liquid velocity (i. e. $\text{cm}^3 \text{water} / \text{cm}^2 \text{dump surface-sec}$ passed through the dump). V_g is the darcy air velocity through the dump (i. e. $\text{cm}^3 \text{air} / \text{cm}^2 \text{dump area - sec}$). K_T is the thermal conductivity of the dump, taken to be $5 \times 10^{-3} \text{ cal/cm-}^{\circ}\text{C-sec}$. For calculations $\rho_T C_T = .6$, $\rho_l C_l = 1.0$, and $\rho_g C_g = 1.3 \times 10^{-3} (.126 + .0283 T)$, where T is the temperature of the dump. This last expression takes into account the thermal effects of evaporation. It was assumed the air in the dump was always saturated with water; account was taken of the increase in water saturation values with increasing air temperature, T , and the effect, through the latent heat of boiling, this would have on the heat capacity or heat carrying ability of air.

For a one dimensional dump (i. e. air and water flow restricted to be vertical only), (12a) simplifies to:

$$(12b) \quad \rho_T C_T \frac{\partial T}{\partial t} = (\rho_l C_l V_l - \rho_g C_g V_g) \frac{\partial T}{\partial z} + R_A + K_T \frac{\partial^2 T}{\partial z^2}$$

One dimensional convective air flow through a dump may be described:

$$(13) \quad V_g = \frac{k_{AVE}}{\mu_g} \frac{\Delta P}{H}$$

H is the height of the dump, μ_g is the viscosity of air = 1.9×10^{-4} poise. ΔP is the pressure drop across the dump in dynes/cm². ΔP may be expressed:

$$(14) \quad \Delta P = \rho_{OO} g_0 H \sum_i \bar{H}_i (\alpha (T_i) T_i + \beta (1 - [\bar{O}_2]^g))$$

Here ρ_{OO} is the density of air at STP, g_0 is the gravitational constant, $\bar{H}_i = \frac{H_i}{H}$, is the normalized thickness of the ith incremental level of the dump. $\alpha (T_i)$ is the temperature dependent coefficient of thermal expansion which, like the heat capacity, includes the effects of changing water vapor saturation. β is a coefficient which describes the decrease in air density due to oxygen depletion ($\beta = 2.83 \times 10^{-2}$). $[\bar{O}_2]^g = [O_2]^g / [O_2]_{STP}^g$. k_{AVE} the average permeability of the dump, may be expressed:

$$(15) \quad k_{AVE} = \frac{1}{\sum_i \bar{H}_i / k_i}$$

Any distance x_i from the base of the dump, where fresh air is assumed to enter, the oxygen concentration in the dump will be:

$$(16) \quad [\bar{O}_2]^g = 1 - \frac{R_{O_2} x_i}{V_g [O_2]^g_{STP}}$$

Equations (12b), (13) and (16) represent a model of the dump leaching process that includes both physics (air convection) and chemistry. The equations can be solved using an implicit finite difference scheme. The method used was to start the dump leaching at some starting temperature and loop between (13) and (16) until a steady state O_2 profile and air velocity was attained. Then (12) was used to determine the temperature of the dump at $t + \Delta t$. Δt was generally taken to be one month. The average rate of fluid application was used, an approximation that is probably valid so long as the leach cycle is less than three months. The ambient temperature was varied seasonally in a manner appropriate to the location of the dump (temperature measurements were available from a mine station). The surface temperature of the dump was also varied seasonally but at a higher average temperature and over a more restricted range. Air convection kept the dump surface warmer than the surroundings. Snow was observed to melt more quickly on the dump than in the surrounding areas.

Given a set of parameters and operating procedures (rate of application of water), the finite difference model computes the leach history of the model dump. The per cent copper leached per month (or the effluent copper heads can be computed easily)*:

* The dump is considered to be broken into N layers. V_l is measured in cm^3 water/ cm^2 -dump-sec which equals the average application rate in gal/ ft^2 -hr times 1.13×10^{-3} .

$$(17) \quad \frac{\% \text{ Cu}}{\text{month}} = \frac{dx}{dt} (2.68 \times 10^6 \frac{\text{sec}}{\text{mo}}) = 2.68 \times 10^6$$

$$\sum_{\text{dump}} \frac{(G_{NS} \frac{dX_{NS}^i}{dt} + G_S \frac{dX_S^i}{dt})}{N (G_S + G_{NS})}$$

$$(18) \quad \text{HEADS [gpl Cu]} = \rho_R^{(1-\phi)} H \sum_{\text{dump}} \frac{(G_{NS} \frac{dX_{NS}^i}{dt} + G_S \frac{dX_S^i}{dt})}{N V_\ell} \cdot 1000$$

The cumulative per cent leached, $1 - X_{TOT}$ is just:

$$(19) \quad \% \text{ Cu Leached} = 1 - \frac{(G_{NS} X_{NS} + G_S X_S)}{G_{NS} + G_S}$$

The next section compares the rate of leaching and the cumulative leaching of a test dump to the rate of leaching and cumulative leaching computed by the model through equations (17) and (19).

CALIBRATION OF THE MODEL

Figure 4 shows a cross section of the Midas test dump, built by the Utah Copper Division of Kennecott Copper Corporation at Bingham Canyon, Utah. The dump was about 400 feet long, 200 feet wide. The average depth was 20 feet with a maximum depth of 40 feet. Fifty-eight leach ponds covered the top of the dump. The waste tonnage beneath the ponds was about 93,000 tons (assuming 1.7 tons/yd³). The waste itself was 60% quartzite material and 40% intrusive. The average grade of the waste was .145% copper. 80% of the copper was sulfide, dominantly chalcopyrite, the rest was non sulfide copper.

Leaching of the dump began on April 9, 1969. Prior to this there had been some runoff through the dump but very low copper extraction. Figure 5 shows the leaching after water application was slow at first, increased rapidly to a maximum about 5 months after the start of leaching, and then fell steadily, with some fluctuations that appear correlated with the season (maximum in summer). Figure 4 shows that by August 1969 the internal dump temperature had risen to 130°F (54°C). There was substantial oxygen depletion as the air convected through the dump. It can also be seen that the air convected in along the high permeability base of the dump and then up through the dump - the one dimensional model is not inappropriate for this case.

As time went on the location of maximum dump temperature shifted from the far end of the dump (as shown in Figure 4) to about the same distance from the near end.

The parameters used in the model are listed in Table I.

Figure 4: August 1969 temperature and oxygen distribution in the Midas test dump (built and operated by the Utah Copper Division, Kennecott Copper Corporation at Bingham Canyon, Utah).

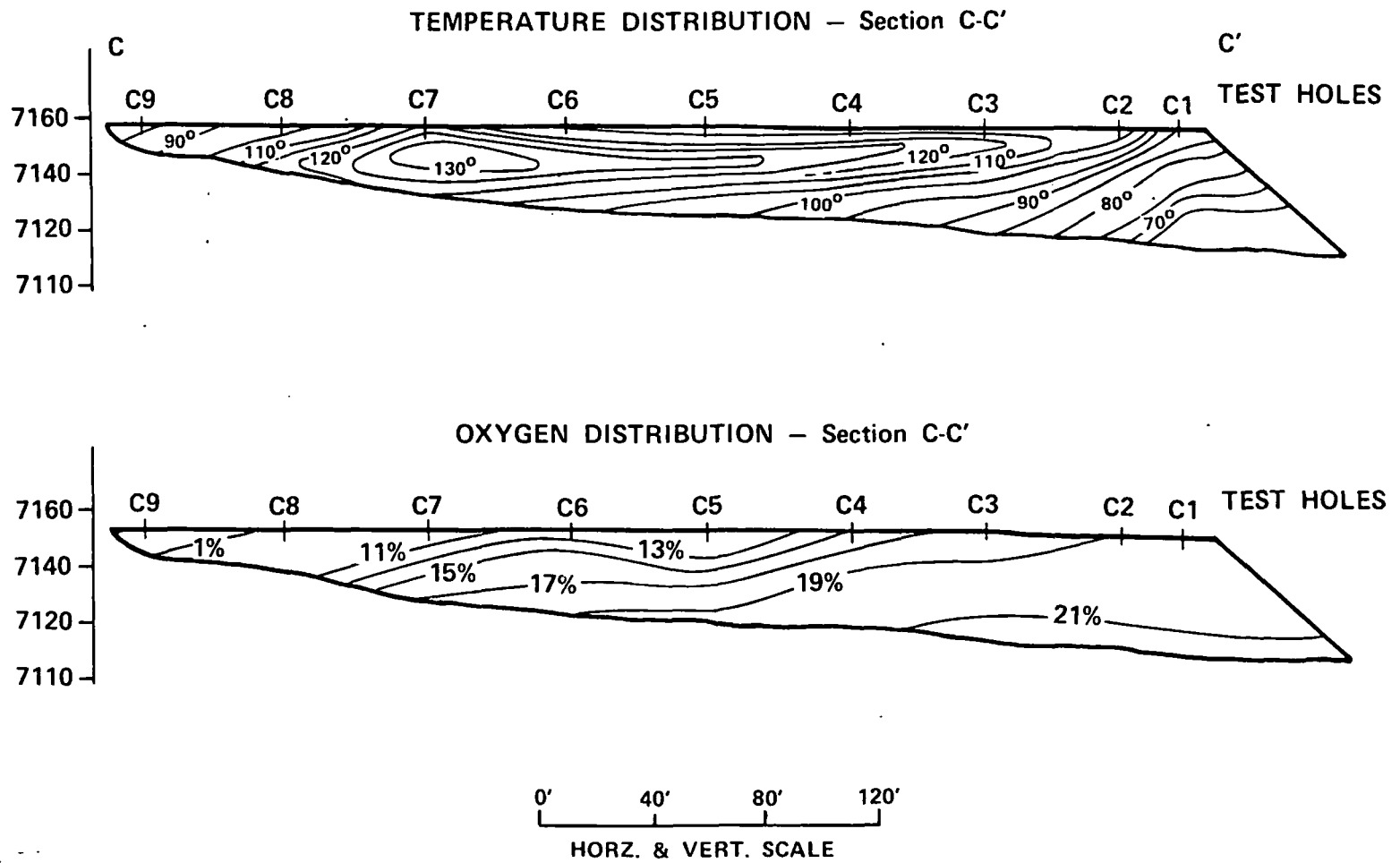


TABLE I: Parameters used for the model shown in Figure 6

H	Height of dump	22ft
FPY	Moles pyrite leached/mole cu leached	47
k'	Dump permeability k_{AVE}	1000 darcys
V_l	Rate of water application	.02 gal/ft ² -hr
G_s	Dump sulfide copper grade	.116 wt %
G_{NS}	Dump non-sulfide copper grade	.029 wt %
τ_{DS}	Diffusional sulfide leach time (20°C)	1700 months
τ_{CS}	Leach time for sulfide copper under surface area rate control (20°C)	200 months
τ_{DNS}	Diffusional non-sulfide leach time (20°C)	500 months
τ_{CNS}	Leach time for non-sulfide copper under surface area rate control (20°C)	300 months
E_{DS}^*, E_{DNS}^*	Activation energies for diffusion	5.0 kcal/mole
E_{CS}^*, E_{CNS}^*	Activation energies for chemical leaching reactions	18.0 kcal/mole

Figure 6 compares the calibrated model leach history to the leach history of the Midas test dump shown in Figure 5. The match in general is quite good. In addition to the leach history similarity, the model dump reached 51°C internal temperature by August 1969 and then decreased in temperature to about 14°C, as did the far end of the Midas test dump. In August 1969 the effluent oxygen concentration was 9% in good agreement with observation (see Figure 4). The values of τ_{CS} and τ_{DC} are quite close to the values anticipated (compare Table I and last section).

The initial rise in extraction rate is due to the heating up of the dump. This feature is not peculiar to the Midas test dump, and can be observed in the leach history of many dumps. The fall in leaching rate after the first seven months of leaching is due to the fact the more accessible copper has been leached and Fe^{+++} must diffuse through already leached areas to reach the remaining copper. The fall in dump temperature also contributes to the decline in leaching rate.

Thermal boundary conditions were chosen: The base of the dump was fixed at 20°C . The top surface temperature was allowed to vary:

$$T(\text{mo}) = 10^{\circ}\text{C} - 10 \cdot \text{Cos} ((\text{mo}-1) \pi/6)$$

where mo runs from 1 to 12 and is the number of the calendar month. Thus the top surface of the dump was assumed to vary seasonably between 32°F and 68°F , a slightly more restricted and hotter range than the ambient temperature variation of 19°F to 63°F . The temperature at the base of the dump also fluctuated somewhat.

The assumption of a constant 20°C basal temperature is a matter of convenience and is probably subject to some error. Both boundary conditions are plausible and probably not too far wrong, however.

The starting temperature of the model dump was 10°C . The Midas Test Dump was built in winter so the dump was initially at least this cold.

VARIATIONS FROM THE BASE MODEL

It is of interest to vary the model parameters to see what effect they may have on the rate of copper extraction. Table II lists the parameters of Table I and shows the per cent increase in copper extraction after 24 months of leaching that results from a given per cent alteration in the listed parameter.

PARAMETER	VARIATION	INCREASE IN COPPER RECOVERED IN 24 MONTHS
✓ H	+10%	8.9%
✓ FPY	+10%	6.2%
τ_{DS}	-10%	6.2%
✓ G_s	+10%	4.8%
E_{DS}^*	+10%	2.7%
τ_{CS}	-10%	1.8%
✓ V_ℓ	-10%	1.3%
τ_{DNS}	-10%	1.3%
E_{CS}^*	+10%	.9%
G_{NS}	+10%	.9%
τ_{CNS}	-10%	.4%
E_{DNS}^*	+10%	.4%
Starting Temp	+10%	.4%
E_{CNS}^*	+10%	.0%
k'	+10%	.0%
	-10%	-.4%

TABLE II: The parameters in the first column are varied as shown in the second (see Table I for definitions of symbols). The effect on the total amount of copper extracted in 24 months is shown in the last column. The parameters that are checked effect the rate of leaching primarily by allowing the dump to attain higher temperatures.

The reader is cautioned that the variations in leach rate shown in Table II are based only on what is in the model. Much may go on in a waste dump that has not been included, as yet, in the model. Secondly not all the parameters listed in Table II are mutually independent. For example increasing FPY at a constant sulfide copper grade will cause τ_{DS} to increase substantially. Lastly the combination of parameters that models, successfully, the Midas test dump

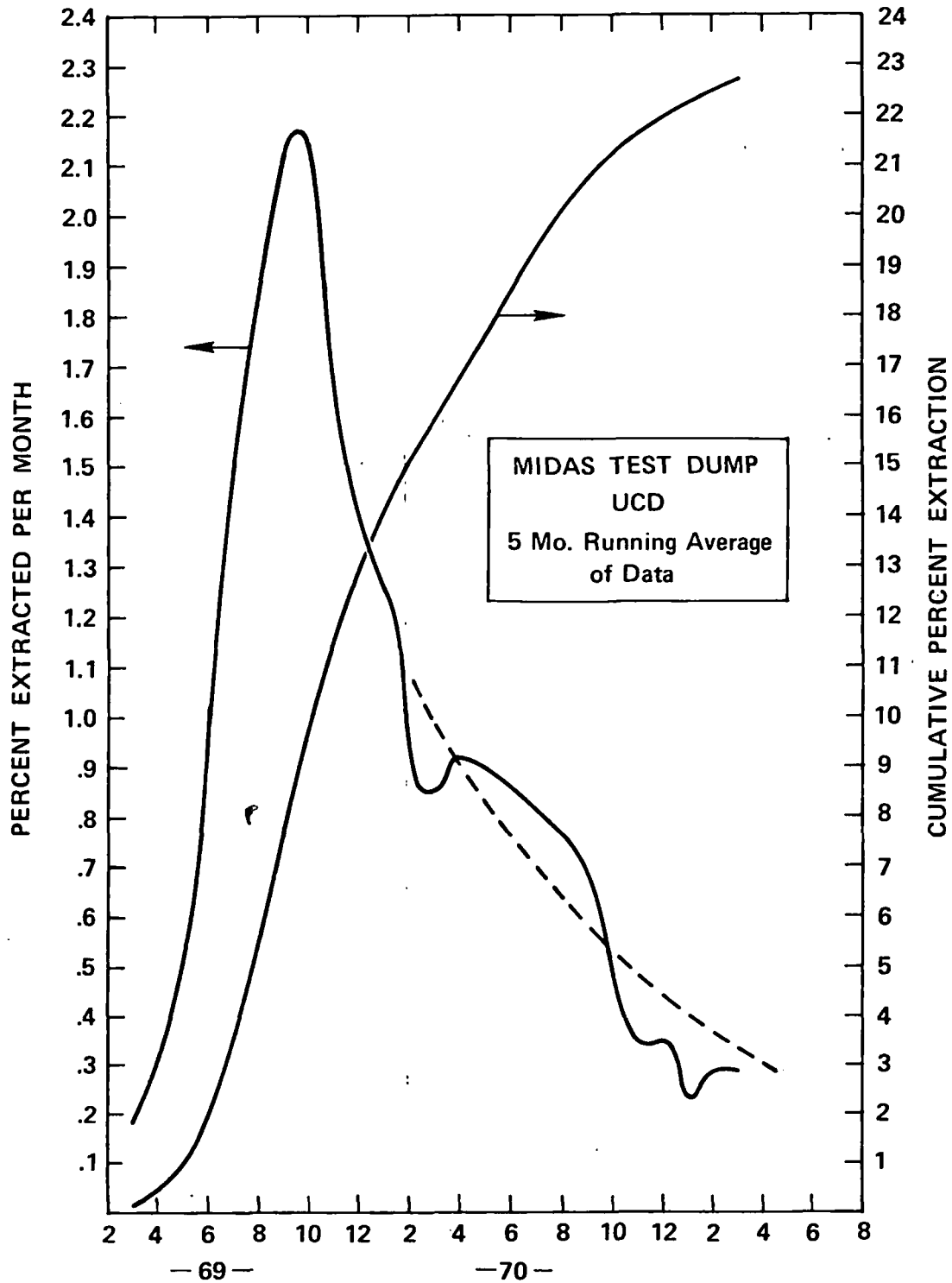


Figure 5: The rate of extraction (% per month) and cumulative extraction of copper from the Midas test dump. Leaching began on April 9, 1969. The data is averaged using a five month running average.

MIDAS TEST DUMP 5 MONTH RUNNING AVERAGE

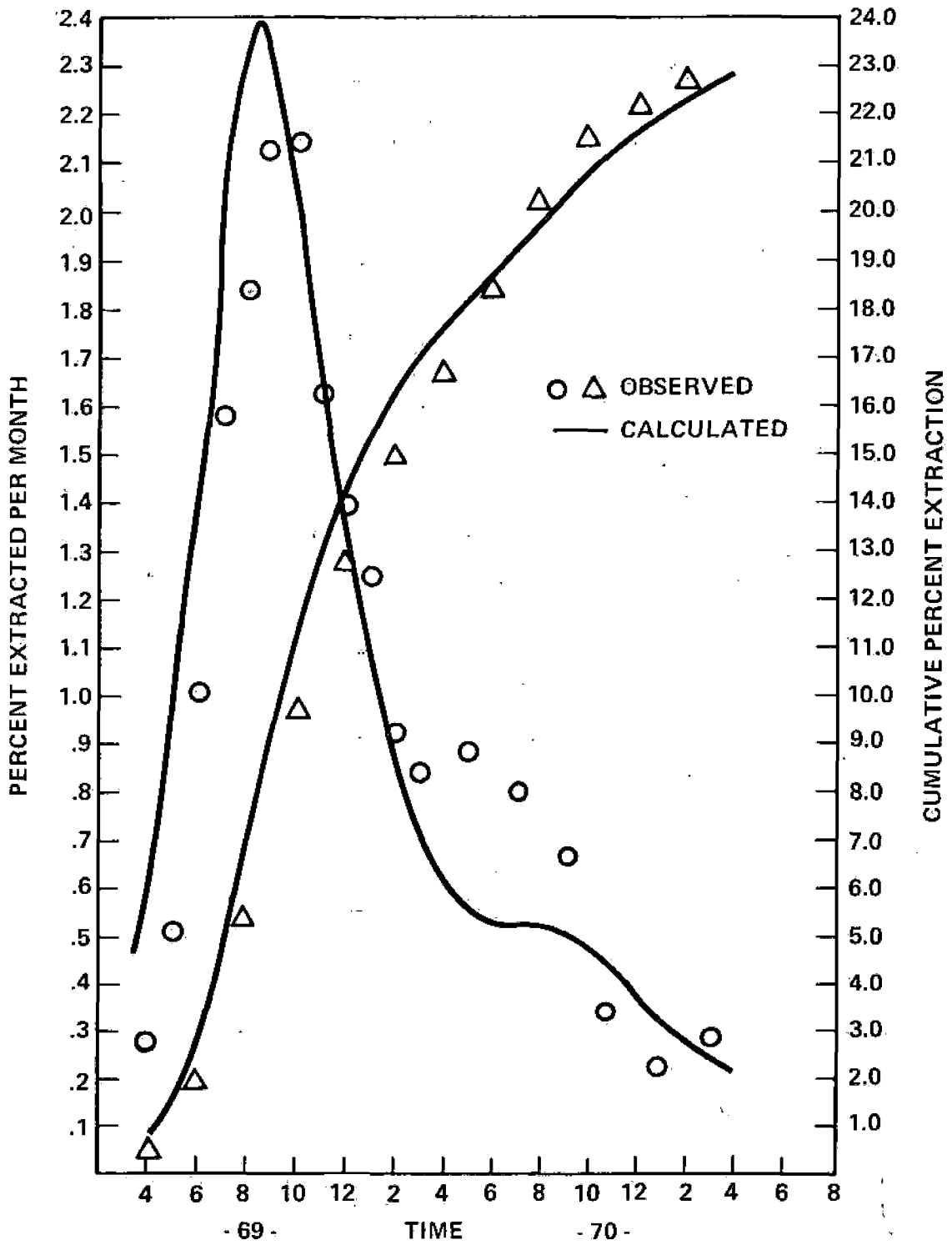


Figure 6: Comparison of observed and calculated dump behavior.

is not necessarily a unique set or the correct set. Data from more than one test dump is needed to resolve these uncertainties.

The lack of dependence of leach rate on permeability simply indicates the dump was shallow and permeable enough not to be oxygen starved anywhere. Had the dump been thicker (~100'), a significant dependence of leach rate on permeability would be noted.

ACKNOWLEDGEMENTS

The authors would like to thank Kennecott Copper Corporation for permission to present this paper. The authors would also like to thank the Utah Copper Division and in particular Messrs. Southard, Pernichele and Ream for permission to use the Midas Test Dump data as a base case for this study. Enough recognition cannot be given to the extensive, careful work of these individuals and others that was required to collect the high quality data so easily cited in this paper.

BIBLIOGRAPHY

- Auck, Y. T., and M. E. Wadsworth: Physical and Chemical Factors in Copper Dump Leaching, 1973 AIME International Symposium on Hydrometallurgy, p. 645-700, 1973.
- Mathews, C. T., and R. G. Robins: Australian Chemical Engineering, 1972 August, p. 21-25.
- Smith, E. E., and K. S. Shumate: Sulfide to Sulfate Reaction Mechanism, Water Pollution Control Research Series 14010 FPS 02/70, U.S. Government Printing Office, 1970.

The Application of Oxygen and Hydrogen Isotope Studies to Problems of Hydrothermal Alteration and Ore Deposition*

HUGH P. TAYLOR, JR.

Abstract

$^{18}\text{O}/^{16}\text{O}$ and D/H analyses of hydrothermal minerals and fluid inclusions can provide data on temperatures and attainment of equilibrium, but they are principally useful as isotopic tracers in determining the origin of the H_2O involved in ore deposition. This results from the fact that different sources of H_2O in the earth's crust, namely primary magmatic, metamorphic, oceanic, connate, and meteoric, all exhibit characteristic δD and/or $\delta^{18}\text{O}$ values. Recent studies have provided quantitative data emphasizing the importance of meteoric H_2O in many hydrothermal fluids. Epizonal igneous intrusions emplaced into permeable country rocks (e.g., highly fractured volcanic areas) act as gigantic "heat engines" that set up long-lived hydrothermal convection systems that persist throughout the crystallization and cooling of the intrusion. The amounts of magmatic water in such systems are negligible compared with the very large amounts of heated meteoric ground water. Certain epithermal ore deposits and their associated propylitic alteration zones in volcanic terranes (western Cascades, Tonopah, Comstock, Goldfield, the San Juans) were formed by such low- ^{18}O meteoric fluids; the very high water/rock ratios imply that such ore-bearing fluids are relatively dilute water. If the country rocks are less permeable, as in many porphyry copper environments, less outside water is available and dominantly magmatic-hydrothermal fluids are isotopically identified as the source of the biotite-K feldspar alteration in the core zones of the porphyry stocks. A less pronounced meteoric-hydrothermal circulation, perhaps involving Na-Ca-Cl brines in the country rocks, is set up outside the stock. Such solutions are responsible for the pyrite-sericite and hypogene clay alteration zones in the outer portions of the stock. These zones tend to collapse and encroach on the central zone with time and the Cu ore bodies commonly occur near this boundary. At a much later stage, after erosion, supergene clay formation may occur and this can also be distinguished from the hypogene clay alteration by means of $\delta^{18}\text{O}$ and δD analyses.

Introduction

The purpose of this review paper is to examine the basic principles of hydrogen and oxygen isotope geochemistry that bear on the problems of hydrothermal alteration and ore deposition. Although isotopic analyses can, in principle, provide determinations of the temperatures of formation of hydrothermal mineral assemblages, the prevalence of isotopic disequilibrium in such assemblages severely restricts this application. At present the most useful application lies in using D/H and $^{18}\text{O}/^{16}\text{O}$ analyses as indicators of the origin and history of the H_2O in hydrothermal fluids.

Inasmuch as H_2O is the dominant constituent of ore-forming fluids, a knowledge of its origin is fundamental to any theory of ore formation.

* Contribution No. 2436 of the Division of Geological and Planetary Sciences, California Institute of Technology, Pasadena, California 91103.

The other materials in solution also provide important evidence, but variations in dissolved salts and gases tell us principally something about the P-T history of the solution and about the types of rocks with which the fluid came into contact. The ultimate source of the H_2O can only be deciphered by studying some geochemical parameter based on the water molecules themselves. Stable isotope analyses provide just such a parameter, because natural waters of various origins exhibit systematic differences in their deuterium and oxygen-18 contents. To apply these techniques to ore deposits we first need to understand the natural isotopic variations in the various waters that conceivably could be involved in ore deposition; then we must find a way of determining the isotopic composition of the fluid that formed a given mineral deposit.

There are two ways of determining $^{18}\text{O}/^{16}\text{O}$ and D/H ratios of natural hydrothermal fluids: (1) by

direct measurement of the fluid itself in a geothermal area or of fluid inclusions in the minerals of an ore deposit, and (2) by isotopic analysis of mineral assemblages, calculation of temperatures of formation utilizing various geothermometers, and finally, calculation of D/H and $^{18}\text{O}/^{16}\text{O}$ ratios of waters in equilibrium with the assemblages at their temperatures of formation.

Although both approaches have been utilized, there are problems involved in the actual application of either of the above techniques, particularly with respect to whether or not the isotopic ratios are preserved during subsequent cooling of the ore deposit. The water that is present in fluid inclusions of oxygen-bearing minerals, for example, undergoes exchange with the host mineral during cooling, thus changing the $^{18}\text{O}/^{16}\text{O}$ ratio of the fluid (Sugisaki and Epstein, 1968, unpub. data; Rye and O'Neil, 1968). Even nonoxygen-bearing minerals may contain secondary fluid inclusions that are not representative of the original fluid from which the mineral formed, especially if the mineral is highly fractured or full of imperfections.

The following discussions are not meant to be an exhaustive review of all the literature on this subject. Instead, the basic principles will be emphasized and the examples to be used will largely be drawn from previous work by the writer, his students, and his colleagues. The general approach is to illustrate the overwhelming amount of isotopic evidence gathered in recent years showing the importance of waters other than primary magmatic water in natural hydrothermal fluids. In particular, heated meteoric ground waters will be shown to be a very important constituent of many ore-forming fluids. The suggestion that meteoric waters might be important in hypogene ore deposition is a very old one and was, in fact, much in vogue until J. F. Kemp, W. Lindgren, and other geologists made such an apparently convincing case for the magmatic-hydrothermal theory about 1910. Early workers such as Van Hise (1902), Ransome (1909), and Lawson (1914) strongly supported the idea of deep circulation and heating of such surface waters, but it is only with the development of stable isotope geochemistry in recent years that it has become possible to supply proof for such ideas and to contradict much of the dogma that has arisen concerning magmatic-hydrothermal solutions.

Equilibrium Isotope Fractionations

Although we shall not dwell on isotope geothermometry in this paper, if we are to be able to calculate isotope ratios of hydrothermal fluids

it is necessary to discuss the state of our present knowledge concerning D/H and $^{18}\text{O}/^{16}\text{O}$ fractionation factors for mineral-gas-water systems. Gas- H_2O fractionations as a function of temperature can be accurately calculated by the methods of statistical mechanics, but in general, mineral- H_2O fractionations at high temperatures must be experimentally determined in the laboratory. The latter approach is usually extremely difficult and time-consuming and a great deal of further work is necessary; successful experiments have so far been made in very few laboratories throughout the world.

First, some basic definitions: the isotope data are reported as δD or $\delta^{18}\text{O}$, where:

$$\delta = \left(\frac{R_{\text{sample}}}{R_{\text{standard}}} - 1 \right) 1,000$$

and R_{sample} is D/H or $^{18}\text{O}/^{16}\text{O}$ in the sample and R_{standard} is the corresponding ratio for the standard. We are not concerned with absolute ratios, only with relative deviations from a standard material, and the most convenient standard for both oxygen and hydrogen is ocean water. A particular set of ocean water values, designated Standard Mean Ocean Water (SMOW) by Craig (1961) is the most common standard in present-day use. Thus, a δ -value = +10 would mean that the sample is 10 per mil (10 parts per thousand) or 1 percent richer in deuterium or ^{18}O than SMOW. Negative numbers signify relative depletions in the heavy isotopes.

The accuracy of determination of δD is about an order of magnitude worse than for $\delta^{18}\text{O}$ (± 1 per mil versus ± 0.1 per mil). However, the natural variations in D/H are much greater than for $^{18}\text{O}/^{16}\text{O}$; hence, a 10 per mil variation represents a very large $\delta^{18}\text{O}$ change but only a small δD change.

Another term in common use is α , the fractionation factor or isotopic partition coefficient for two minerals or two chemical compounds (species *A* and species *B*):

$$\alpha_{AB} = R_A/R_B.$$

Note that from the definition of δ , it follows that:

$$\ln \alpha_{AB} = \ln \left(1 + \frac{\delta_A}{1,000} \right) - \ln \left(1 + \frac{\delta_B}{1,000} \right).$$

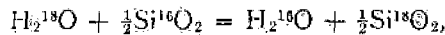
Inasmuch as $\ln(1 + \epsilon) \approx \epsilon$, if $\epsilon \ll 1$, we obtain the approximate relationship:

$$1,000 \ln \alpha_{AB} \approx \delta_A - \delta_B.$$

For δ -values $\leq |10|$, this approximate relationship holds up very well and we can treat isotopic distribution coefficients by simply subtracting

δ -values, which is very convenient. However, for larger fractionations, as typically occur in the case of D/H ratios, this can lead to errors; in such cases the fractionation factors should be divided out to insure accuracy.

If an isotopic exchange reaction is written such that only one of a set of exchangeable atoms in each compound takes part, using as an example the quartz-H₂O system:



then it can be shown (Urey, 1947) that $\alpha \equiv K$, the equilibrium constant for the reaction as written. Urey (1947) and Bigeleisen and Mayer (1947) showed that $\ln K$ for an isotopic exchange reaction involving perfect gases closely follows $1/T^2$ dependence over a wide temperature range and must approach zero at some very high temperature. Many mineral-H₂O fractionations also approximately follow $1/T^2$ dependence, and this is the reason for presenting the data in Figures 1, 2, 3, and 4 in the form of plots of $1,000 \ln \alpha$ versus $10^6/T^2$.

Some calculated ¹⁸O/¹⁶O fractionation curves of geological interest are given in Figure 1, together with an experimental determination of the liquid water-vapor water equilibrium. Three classes of curves are shown in Figure 2: (1) a summary of the available information on mineral-H₂O experimental calibration curves; (2) some recent estimates by Bottinga and Javoy (1973) of the positions of these curves, based partly on theoretical and partly on empirical considerations; and (3) some empirical estimates from data obtained on natural mineral assemblages. Also shown for comparison is a single calculated curve for calcite-H₂O, based on some of the calculated curves shown in Figure 1.

The estimates by Bottinga and Javoy (1973) agree quite well with most of the calibration curves in Figure 2, except for the quartz-H₂O curve of Clayton et al. (1972). The latter authors, however, have pointed out the experimental difficulties encountered in the quartz-H₂O system and better agreement is obtained with a set of their data that involves partial equilibration and extrapolation to complete equilibrium. This latter calibration curve, $1,000 \ln \alpha = 3.57(10^6/T^2) - 2.73$, is the one that has been used in most isotope geothermometry involving quartz (e.g., Taylor, 1967; Shieh and Taylor, 1969a and b; Taylor and Coleman, 1968). Use of the quartz-H₂O calibration equations of Clayton et al. (1972) typically gives geologically unreasonable temperatures of formation of mineral assemblages. Therefore, either their equations are in error, the other mineral-H₂O

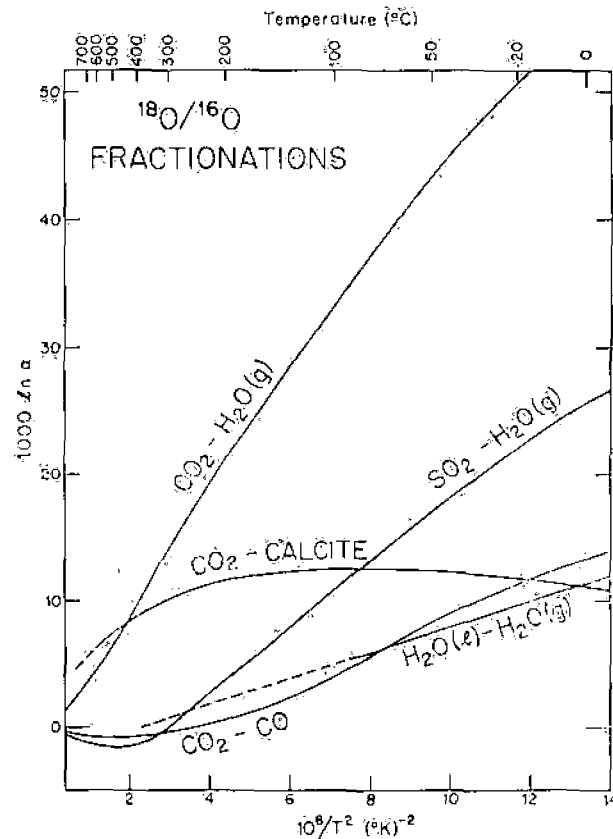


FIG. 1. Calculated equilibrium oxygen isotope fractionation factors as a function of temperature for CO₂-H₂O and CO₂-calcite (Bottinga, 1968), SO₂-H₂O and CO₂-CO (Urey, 1947), together with the experimentally determined curve for liquid water-vapor water (Horibe and Craig, in Craig, 1963, solid line; Bottinga and Craig, 1968, dashed line).

curves are wrong, or isotopic "temperatures" do not tell us much of anything about the original temperatures of formation of natural mineral assemblages. At present, it is not readily obvious which of the above possibilities we should choose. However, note that at any temperature, the scatter in the various quartz-H₂O curves shown in Figure 2 would lead to only about a 1 per mil variation in the calculated $\delta^{18}\text{O}$ values of a hydrothermal fluid in equilibrium with quartz.

There is at least one way to partially reconcile the quartz-H₂O curve of Clayton et al. (1972) with the other curves on Figure 2. The waters utilized in the experiments of Clayton et al. (1972) were not analyzed directly; they were done by the standard technique involving CO₂ equilibration at 25°C, assuming a CO₂-H₂O(l) fractionation factor of 1.0407. There are some indications now that a better value for this fractionation factor might be about 1.0412 or higher, based on several recent studies. This would cause an up-

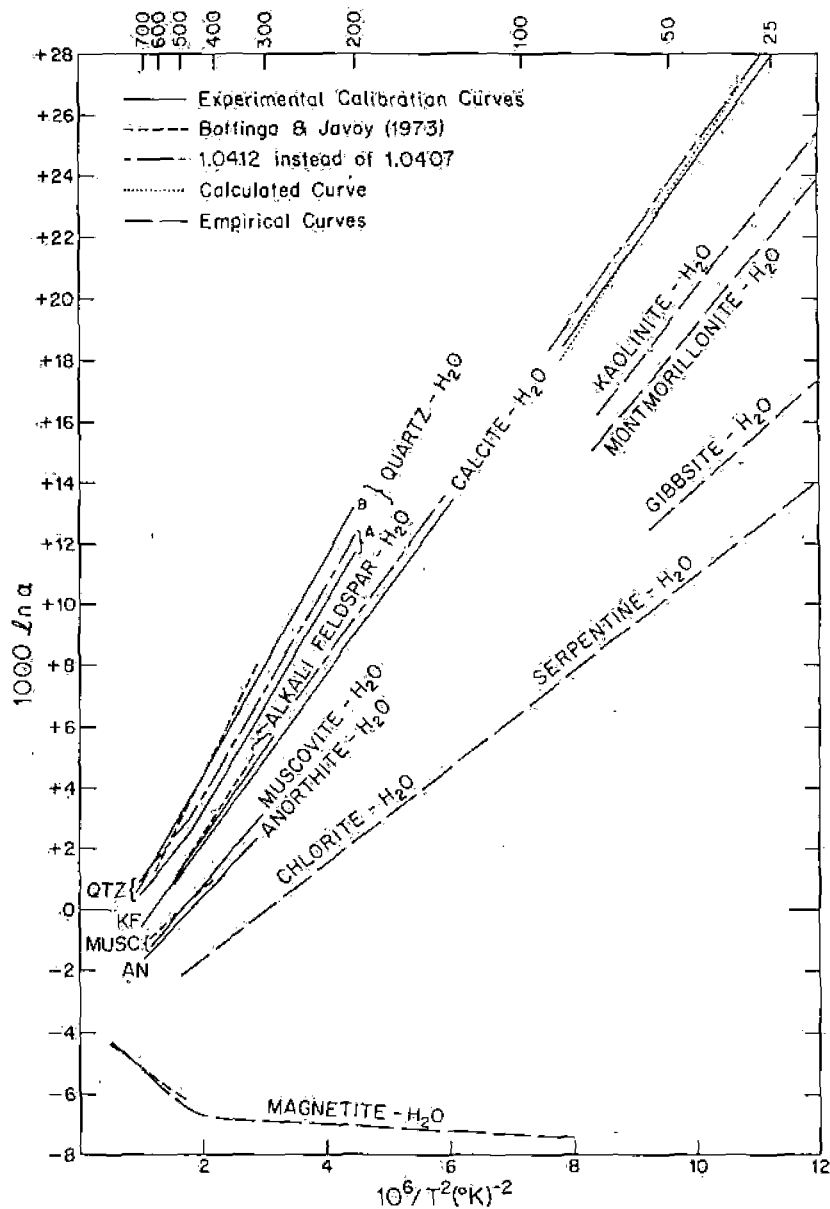


FIG. 2. Experimentally determined equilibrium oxygen isotope fractionation curves for various mineral-H₂O systems: calcite-H₂O (O'Neil et al., 1969); quartz-H₂O (B = "partial" exchange experiments, A = "complete" exchange experiments, Clayton et al., 1972); alkali feldspar (KF)-H₂O and anorthite (AN)-H₂O (O'Neil and Taylor, 1967); and muscovite-H₂O (O'Neil and Taylor, 1969). Also shown are some empirically derived curves: magnetite-H₂O (high-T portion = Anderson et al., 1971, low-T portion = Wenner and Taylor, 1971); serpentine-H₂O and chlorite-H₂O (Wenner and Taylor, 1971); kaolinite-H₂O (Savin and Epstein, 1970a); and gibbsite-H₂O (Lawrence and Taylor, 1971). In addition, some calculated curves of Bottinga and Javoy (1973) and Bottinga (1968, calcite-H₂O) are indicated, together with two readjusted experimental curves based on changing the CO₂-H₂O (*f*) fractionation factor at 25°C from 1.0407 to 1.0412 (see text).

ward shift of the quartz-H₂O curve of Clayton et al., in Figure 2, bringing it into closer agreement with the other quartz-H₂O curves. Except

for calcite-H₂O, the other curves on Figure 2 are not affected, either because the H₂O was analyzed directly (O'Neil and Taylor, 1967; 1969), or be-

cause the curves are based on empirical considerations of $^{18}\text{O}/^{16}\text{O}$ data on natural mineral assemblages.

In summary, in spite of the difficulties, the experimentally determined calibration curves on Figure 2 represent the most reliable means of calculating the $\delta^{18}\text{O}$ values of H_2O in equilibrium with a mineral assemblage at a given temperature. The other curves shown on Figure 2 are not independent; they are basically determined by these experimental curves in conjunction with data on natural mineral assemblages. Pressure is not a factor, because the equilibrium isotopic fractionations are solely temperature dependent. The composition of the aqueous fluid may, however, be important. This problem is discussed by Taylor (1967, p. 131) and recent work by Truesdell (1971) has shown that salinity variations may require adjustments to be made in calculated $\delta^{18}\text{O}$ values of hydrothermal waters. However, in view of the other variables involved, these difficulties are of second order and will be ignored in further discussions.

Some calculated D/H fractionation curves of geological interest are given in Figure 3. Note the enormously larger values of $1,000 \ln \alpha$ in these systems compared to the $^{18}\text{O}/^{16}\text{O}$ systems. The curves show, for example, that at equilibrium at about 400°C , H_2O will be about 400 per mil richer in deuterium than coexisting H_2 gas. This means that if equilibrium is maintained and a hydrothermal fluid encounters a strongly reducing environment, some of the H_2O will be reduced to H_2 and the latter will have a very low δD value. By material balance the remaining H_2O will have to become richer in deuterium. Therefore, reactions of this type represent possible means of changing the δD values of the H_2O in a natural hydrothermal fluid and, for the above example, the equations governing this change are given by:

$$\begin{aligned} \delta D_{\text{H}_2\text{O}}^f - \delta D_{\text{H}_2}^i &\approx 400 \\ x\delta D_{\text{H}_2\text{O}}^f + y\delta D_{\text{H}_2}^i &= \text{constant} = \delta D_{\text{H}_2\text{O}}^i \end{aligned}$$

where x and y are, respectively, the mole fractions of H_2O and H_2 in the final (f) mixture, and the initial (i) material is assumed to be 100 percent H_2O . If $\delta D_{\text{H}_2\text{O}}^i$ is -70 , and as little as 5 percent of the H_2O is reduced to H_2 , the δD of the H_2O in the final hydrothermal fluid will be increased by 20 per mil to $\delta D_{\text{H}_2\text{O}}^f = -50$. Any OH-bearing minerals in equilibrium with this hydrothermal fluid will therefore also be enriched in deuterium by 20 per mil (providing they constitute only a tiny part of the total hydrogen reservoir; if an appreciable fraction of the total hydrogen in the

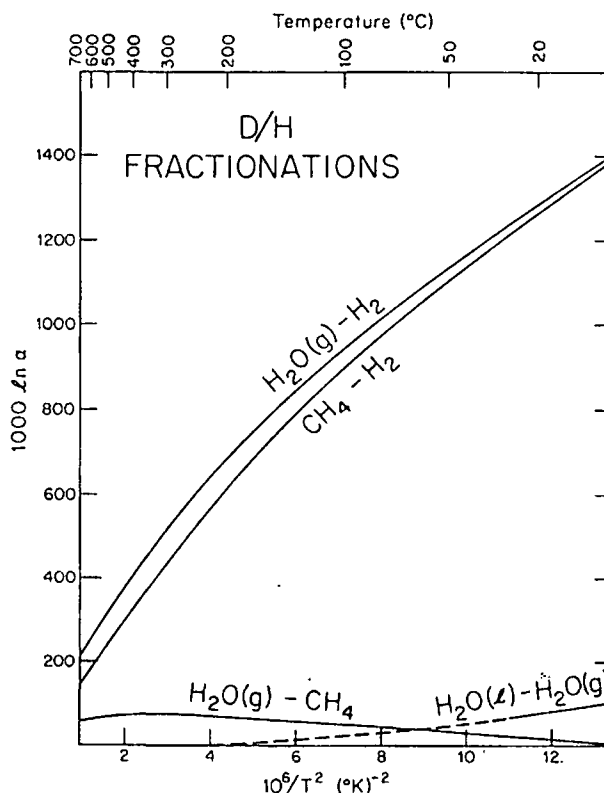


FIG. 3. Calculated equilibrium hydrogen isotope fractionation factors as a function of temperature for $\text{H}_2\text{O}-\text{H}_2$, CH_4-H_2 , and $\text{H}_2\text{O}-\text{CH}_4$ (Bottinga, 1969), together with the experimental liquid water-vapor water equilibrium curve (Merlivat and Nief, unpub. data, 1965, solid line; Merlivat et al., 1963, dashed line).

system is tied up in such minerals, the above equations become slightly more complicated).

The reverse of the above situation occurs if an H_2 -bearing hydrothermal fluid encounters an oxidizing environment. Then the H_2O will become depleted in deuterium. Generally, all of the above effects will be small in natural hydrothermal systems because the amounts of H_2O involved are so huge and the buffering capacities of the rocks are limited. Also, at the normal oxygen fugacities encountered in natural ore-forming solutions (e.g., Meyer and Hemley, 1967; Barnes and Czamanske, 1967), only minuscule amounts of H_2 will be formed (Eugster and Skippen, 1967). In particular, if carbon is present in the system, then under reducing conditions methane generally will be an enormously more important constituent than H_2 gas and, as shown on Figure 3, the $\text{H}_2\text{O}-\text{CH}_4$ fractionation is never larger than 70 per mil. To produce a $+20$ per mil change in the H_2O analogous to the example given above would require that 30 percent of the H_2O in hydrothermal fluid react with carbon species to make methane. This

could perhaps happen in a system containing abundant graphite (Eugster and Skippen, 1967), coal, or petroleum, but is unlikely in most hydrothermal environments.

Hydrogen isotope fractionation factors in silicate-H₂O systems have been investigated at high temperatures in only one laboratory study (Suzuoki and Epstein, 1970, 1974). Some of the results of Suzuoki and Epstein on biotite, muscovite, chlorite, serpentine, and kaolinite are incorporated into Figure 4, together with some empirical estimates of the low-temperature fractionation factors for some of these minerals based on data from natural mineral assemblages.

The most important results of the studies by Suzuoki and Epstein (1970, 1974) are that the D/H fractionations among silicates are mainly a function of the Mg, Al, and Fe contents in the minerals. Water concentrates deuterium relative to all OH-bearing silicates and Mg-rich and Al-rich minerals concentrate deuterium relative to Fe-rich minerals. This helps explain why muscovite in natural mineral assemblages is invariably richer in D than coexisting biotite, and why coexisting biotite and hornblende generally have similar δD values (they also generally have similar Mg/Fe ratios).

Above 400°C, the various silicate-H₂O D/H fractionation curves determined by Suzuoki and

Epstein (1974) form subparallel lines on a plot of $1,000 \ln \alpha$ versus $10^6/T^2$ (Fig. 4). Below 400°C the positions of the curves are unknown, but if the low-temperature estimates of Savin and Epstein (1970a), Lawrence and Taylor (1971), and Wenner and Taylor (1973) are reasonably accurate, all the hydrogen isotope fractionation curves must flatten out, as shown on Figure 4.

If the curves shown in Figure 4 are approximately valid, it means that hydrogen isotope geothermometry on silicate minerals is virtually impossible. However, if one can independently estimate temperatures of formation (e.g., by ¹⁸O/¹⁶O geothermometry), the curves can be used to calculate accurately the δD values of coexisting H₂O. The major problem in applying these curves to natural mineral assemblages lies in whether or not the primary δD values in a mineral assemblage are preserved during later geological events. This is a more serious problem for D/H than for ¹⁸O/¹⁶O, as discussed in more detail below.

Isotopic Variations in Natural Waters.

Meteoric waters

The isotopic variations of H₂O in rain, snow, glacier ice, streams, lakes, rivers, and most low-temperature ground waters are extremely system-

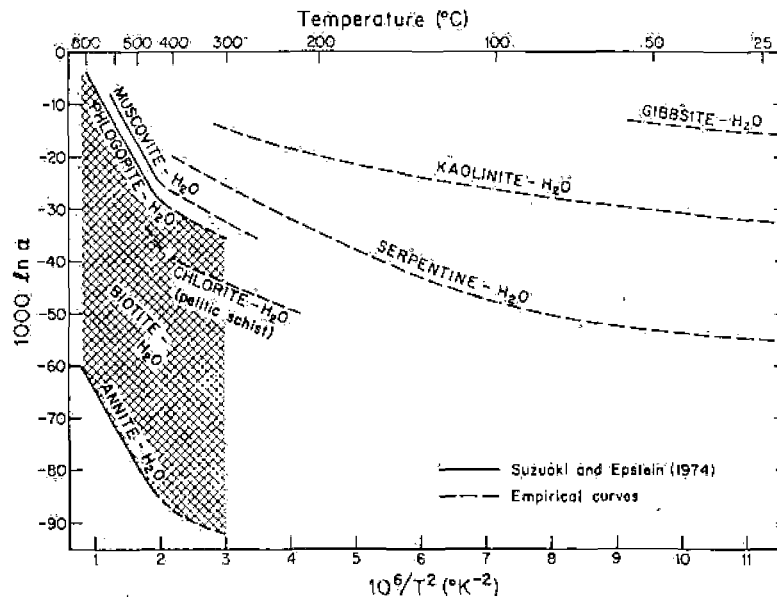


FIG. 4. Equilibrium hydrogen isotope fractionation curves for various mineral-H₂O systems. For temperatures above 400°C, the curves are based on laboratory experiments of Suzuoki and Epstein (1970, 1974). For temperatures below 400°C, the curves are based on empirical extrapolations to estimated values at earth-surface temperatures (Savin and Epstein, 1970a; Lawrence and Taylor, 1971; Wenner and Taylor, 1973) and on some preliminary laboratory experiments by Sheppard and Taylor (unpub. data, 1969) on kaolinite-H₂O at 300°C.

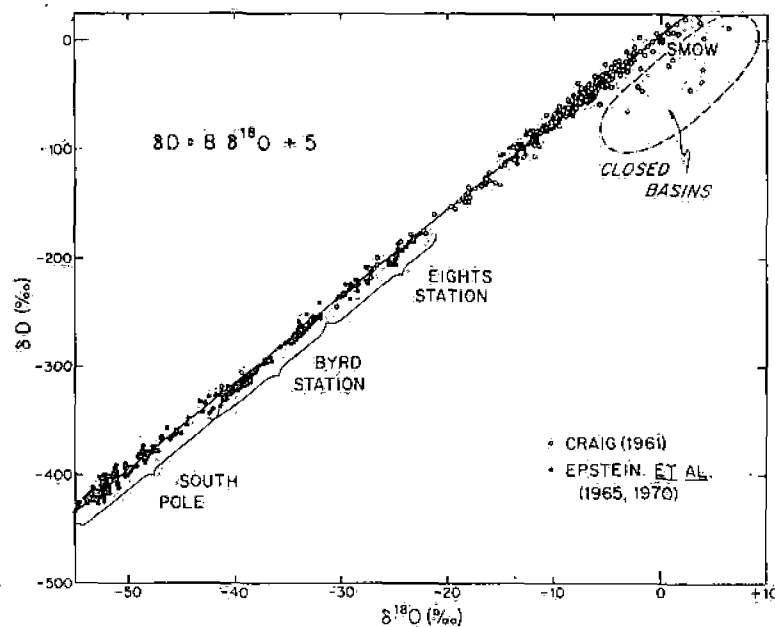


FIG. 5. Plot of δD versus $\delta^{18}O$ for various meteoric surface waters. The data of Craig (1961) define a line with the equation: $\delta D = 8\delta^{18}O + 10$. These data together with the corrected data of Epstein et al. (1965, 1970) define the virtually identical line shown on the graph with $\delta D = 8\delta^{18}O + 5$. Eights Station, Byrd Station, and South Pole are localities in Antarctica. The closed basins represent lakes where there has been strong evaporation.

atic; the higher the latitude or elevation, the lower are the δD values and $\delta^{18}O$ values of the waters. These effects were discovered by Epstein and Mayeda (1953) and Friedman (1953); they were later refined by Craig (1961), who showed that to a very close approximation all meteoric waters follow the equation:

$$\delta D \approx 8\delta^{18}O + 10 \text{ (in per mil)}$$

Recent work by Epstein et al. (1965, 1970) on the Antarctic ice sheet has extended the range of δD and $\delta^{18}O$ of meteoric H_2O down to values as low as -440 and -55 , respectively (Fig. 5). Throughout the entire isotopic range, the samples of water and ice form a very tight linear grouping. The Craig-Epstein meteoric water line ($\delta D = 8.0\delta^{18}O + 5$) shown on Figure 5 is virtually indistinguishable from the original Craig (1961) line and, considering that there is some scatter in the data points, we shall continue to use the latter in the discussions that follow.

The linear relationship between δD and $\delta^{18}O$ arises because condensation of H_2O from the earth's atmosphere is essentially an equilibrium process and the D/H fractionation is proportional to the $^{18}O/^{16}O$ fractionation. For example, at $25^\circ C$, relative to liquid water, H_2O vapor is depleted in ^{16}O by about 9 per mil and depleted in deuterium by 72 per mil (Horibe and Craig, in Craig, 1963;

Mérlivat and Nief, unpub. data, 1965). Both of these fractionations increase proportionally with decreasing temperature and this is essentially where the factor of eight arises in the slope of the meteoric H_2O line (Figs. 1 and 3).

Thus, water condensed from atmospheric vapor in an air mass will be richer in ^{18}O and D than the vapor and by simple material-balance any subsequent precipitation from the same air mass must be lower in ^{18}O and D than this initial condensate. Thus, as the air mass leaves the ocean and progresses across the continents, it becomes steadily lower in ^{18}O and deuterium. This leads to pronounced geographic and topographic isotopic effects on the rain and snow and, although there are seasonal changes as well as variations from storm to storm, the average δD values of surface waters on the continents are consistent enough so that a rough isotopic contour map for the North American continent can be drawn, as shown in Figure 6. Note that a practically identical contour map could be drawn for $\delta^{18}O$ just by changing the δ -values according to the aforementioned meteoric water equation (i.e., $\delta D = -90$ would be replaced by $\delta^{18}O = -12.5$, and so forth).

The only fresh surface waters which do not lie close to the meteoric water line are those which have undergone appreciable evaporation in arid regions, such as the waters labelled closed basins

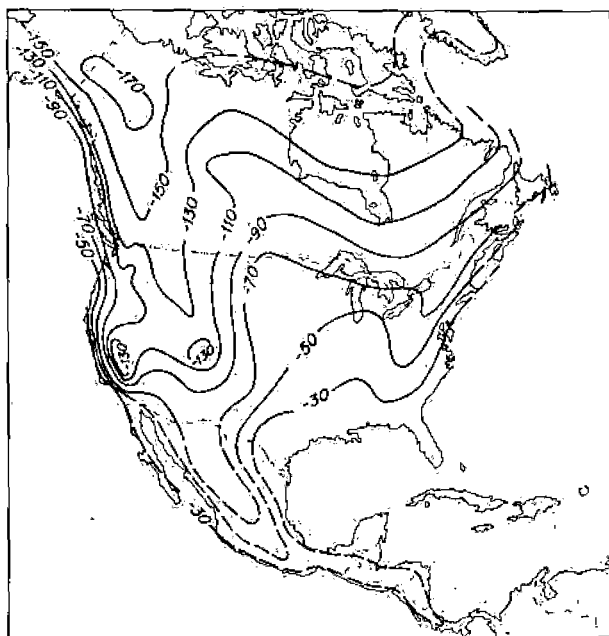


FIG. 6. Map of North America showing contours of the approximate average δD values of meteoric surface waters, based principally on data of Friedman et al. (1964), Dansgaard (1964), and Hitchon and Krouse (1972). Because of the linear relationship between δD and $\delta^{18}O$ in meteoric waters (Fig. 5), this figure can serve equally well as a $\delta^{18}O$ contour map if $\delta D = -30$ is replaced by $\delta^{18}O = -5.0$, $\delta D = -50$ by $\delta^{18}O = -7.5$, and so forth.

on Figure 5. Another example would be rain falling through very dry air. These rare exceptions are attributed to kinetic isotope effects accompanying the evaporation (Craig, 1963). The reason why kinetic isotope effects in the $H_2O(g)$ - $H_2O(l)$ system are so different from the equilibrium effects is because the former depend largely upon the motions of the molecules involved and thus on the square roots of their masses. Note that HDO has a mass of 19, whereas $H_2^{18}O$ has a mass of 20. Therefore, instead of the hydrogen isotope effects being an order of magnitude larger (as at equilibrium), they may in fact be less than the ^{18}O effects (i.e., $\sqrt{19/18}$ versus $\sqrt{20/18}$).

Ocean waters

The isotopic composition of present-day ocean water is exceedingly uniform at $\delta^{18}O = 0$ and $\delta D = 0$. This is why it represents a useful isotopic standard (SMOW on Fig. 5). Only in areas such as the Red Sea (Craig, 1966) where there has been appreciable evaporation and an increase in salinity do you get $\delta^{18}O$ values as high as +2 and δD values as high as +11. Also, if there is appreciable dilution with fresh waters, there can be small isotopic changes in the opposite direction, particularly in the Arctic and Antarctic.

The major isotopic problem concerning sea water is how constant has its isotopic composition been through geologic time? We know that if we melted all the ice sheets in the world, the $\delta^{18}O$ value might become as low as -1 and the δD value as low as -10. At least throughout most of Phanerozoic time, the isotopic composition of ocean water has probably fluctuated within those limits and paleotemperature studies on carbonate fossils indicate that the ocean has had a $\delta^{18}O \approx 0$ throughout the Mesozoic and Cenozoic (Urey et al., 1951; Lowenstam, 1961).

The assumption that the isotopic composition of sea water has been essentially constant with time is important, obviously, if sea water is itself involved in processes of hydrothermal alteration or ore deposition. Equally important, however, is the fact that the isotopic composition of the oceans controls the isotopic composition of all meteoric waters as well. The intercept of the meteoric water line must shift if the isotopic composition of ocean water shifts in any direction other than parallel to the meteoric water line. We can be reasonably confident that the meteoric water line has been in its present position for the last 150 million years (± 1 per mil for ^{18}O , ^{16}O and ± 10 per mil for D/H), but prior to that time the position of the meteoric water line is intimately tied into the problem of the isotopic evolution of ocean waters.

There are major uncertainties concerning the isotopic composition of ocean water in the Precambrian. Conceivably, there may have been $\delta^{18}O$ depletions of as much as 20 per mil in the Precambrian oceans (e.g., Perry, 1967), but detailed discussion of these problems is beyond the scope of this paper. It is the opinion of the present writer, however, that based mainly on recent work of Knauth and Epstein (1971), the oceans were roughly similar to the present-day isotopic composition, at least throughout much of the late Precambrian. Nonetheless, this is an immensely difficult subject and it would perhaps not be amiss in this review to mention briefly the principal theories as to how the isotopic compositions of the oceans evolved to their present state.

Most magmatic waters in equilibrium with igneous rocks at high temperatures will have $\delta^{18}O \approx +6$ to +8 and $\delta D \approx -50$ to -80 (see below). If the oceans originated from such waters, why are they now at zero? The apparent $\delta^{18}O$ shift is probably due to the steady removal of ^{18}O -rich oxygen from the oceanic reservoir in the form of cherts ($\delta^{18}O \approx +30$ to +38), carbonates ($\delta^{18}O \approx +25$ to +30), and other authigenic minerals such as clays ($\delta^{18}O \approx +18$ to +25). A lot of

heavy oxygen is now locked up in such sediments and their metamorphic equivalents. On the basis of material balance calculations by Silverman (1951) and Savin and Epstein (1970b), the volume of high- ^{18}O sediment on earth can apparently account for an ^{18}O depletion of about 6 per mil in the oceans. By this model, if the oceans have grown progressively with time, they conceivably could have remained essentially constant in $\delta^{18}\text{O}$. However, if the volume of the oceans has remained constant for the last 3,000 to 3,500 m.y., this model would require a progressive $\delta^{18}\text{O}$ shift of about 1 per mil every 500 m.y.

Another process that will have an influence on the isotopic composition of the oceans is the interaction of sea water with submarine rocks during the hydrothermal alteration and weathering that follow sea-floor volcanism. Very large amounts of sea water take part in these reactions, particularly at mid-ocean ridges. Considering that recent plate tectonic theories require a fairly rapid addition of new igneous rocks at the spreading centers, the $\delta^{18}\text{O}$ of the oceans may in large part be controlled by the temperatures of these hydrothermal reactions (Muehlenbachs and Clayton, 1972; Wenner and Taylor, 1973). If this is so, the $\delta^{18}\text{O}$ of the oceans may be "buffered" near a value of zero.

It has been suggested that the apparent enrichment of ocean water by 60 to 70 per mil in δD relative to magmatic water is due to progressive loss of dissociated H atoms or ions from the upper atmosphere over geologic time (Kokubu et al., 1961). The H atoms definitely can escape from the earth and H would be preferentially lost relative to D. It is at present difficult to make a quantitative evaluation as to whether this process is adequate to account for the apparent δD shift in the oceans. It is possible that the oceans never began with a $\delta\text{D} \approx -65$ in the first place; they may always have had $\delta\text{D} \approx 0$. If this is true, how then do we explain why almost all igneous rocks, including those such as basalts and kimberlites that definitely come from the mantle, have much lower δD values? A plausible answer lies in the fact that most authigenic OH-bearing minerals precipitated from ocean-water fractionate hydrogen isotopes such that they have δD values of about -50 to -80 (Savin and Epstein, 1970a and b, also see Fig. 10 below). Is this just a coincidence that this is identical to the "normal" magmatic range of values? Perhaps not, in the light of the recent theories of sea-floor spreading in which much of this type of material is probably being carried down into the mantle along subduction zones. If such processes have worked

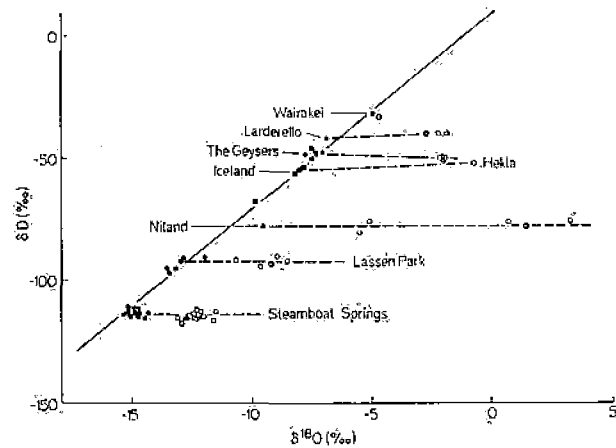


FIG. 7. Plot of δD versus $\delta^{18}\text{O}$ for near-neutral, chloride-rich geothermal waters (open circles) and local precipitation (dark symbols) from a variety of hot spring areas throughout the world (after Craig et al., 1956; Craig, 1963). Localities: Wairakei, New Zealand; Larderello, Italy; Niland (Salton Sea), The Geysers and Lassen Park, California; Hekla, Iceland; and Steamboat Springs, Nevada. The diagonal line is the meteoric water line.

throughout most of geologic time, the δD values of igneous rocks may in large part simply be reflecting the isotopic composition of recycled marine hydroxyl minerals carried down into the mantle. This would remove any need to call upon a massive escape of H from the upper atmosphere, although such a process must have been going on to some extent.

This brief summary concerning the isotopic compositions of ancient oceans should at least acquaint the reader with certain pitfalls in applying stable isotopic techniques to Precambrian ore deposits. However, it must be emphasized that at least for Mesozoic and Cenozoic deposits there are no problems whatsoever in this regard. We know that δD and $\delta^{18}\text{O}$ of ocean waters were essentially constant during that time period.

Geothermal waters

The $\delta^{18}\text{O}$ and δD variations in hot waters and steam from various geothermal areas throughout the world are shown in Figures 7 and 8, after data by Craig et al. (1956) and Craig (1963). These two figures clearly show that essentially all of the H_2O in these geothermal, hot spring areas is of surface derivation. In almost all cases the hot water or steam shows a characteristic ^{18}O shift to higher $\delta^{18}\text{O}$ values as a result of isotopic exchange with silicate and carbonate country rocks, all of which start out with $\delta^{18}\text{O}$ values higher than $+5.5$. Wairakei, New Zealand, is unique in showing no ^{18}O exchange effects at all, either because of rapid circulation or because the rocks

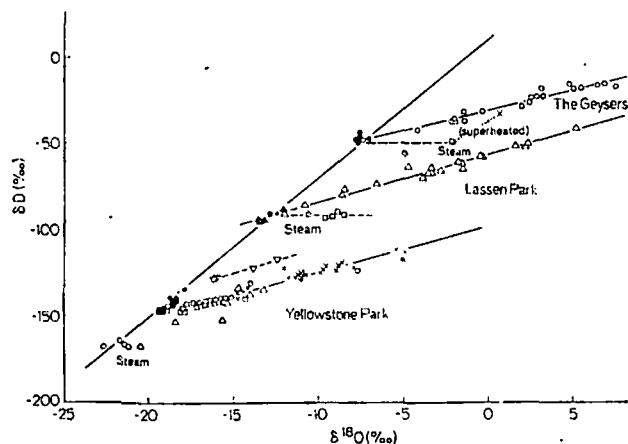


FIG. 8. Plot of δD versus $\delta^{18}O$ for acid geothermal waters and steam from hot spring areas at The Geysers and Lassen Park in California and Yellowstone Park, Wyoming (after Craig, 1963). The dark symbols represent local, unheated, meteoric waters at the three localities.

have previously all been depleted in ^{18}O by prior exchange with the meteoric waters.

In contrast to the $^{18}O/^{16}O$ ratios, the D/H values of the hot waters in these geothermal areas are not controlled by the exchange process; this is because the rocks contain so little initial hydrogen compared to the amounts of the H_2O

involved. Instead, the δD values either remain constant, identical to the local meteoric waters (Fig. 7), or are systematically enriched in deuterium along linear trends having a slope of about three (see Fig. 8). The latter is due to nonequilibrium evaporation of steam at temperatures of 70° to $90^\circ C$ (Craig, 1963).

"Connate" formation waters (brines)

Oil-field brines at one time were largely thought to represent connate water or original trapped sea water. However, isotopic evidence obtained by Clayton et al. (1966) and Hitchon and Friedman (1969) show that meteoric ground waters are a major constituent of these brines in the mid-continent region of North America (Fig. 9). These circulating ground waters have increased in salinity either because of solution of evaporites and/or because of shale-membrane filtration. Therefore, the term "connate" should probably not be applied to such waters and "modified connate" or "formation water" should be used instead.

These formation waters show a very wide range in $\delta^{18}O$, δD , and salinity, but the waters within a given sedimentary basin are usually isotopically

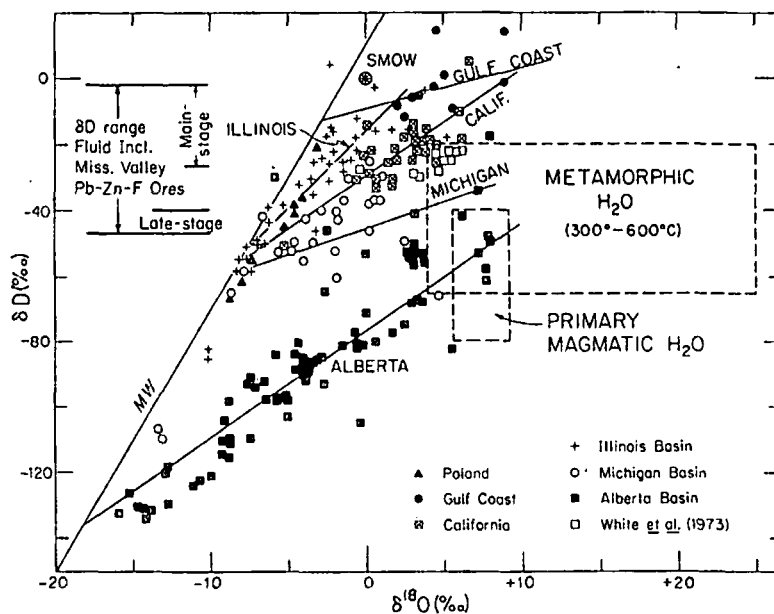


FIG. 9. Plot of δD versus $\delta^{18}O$ for oil-field brines (formation waters) from the midcontinent region of the United States (Gulf Coast, Illinois, and Michigan basins, Clayton et al., 1966), the Alberta basin in Canada (Hitchon and Friedman, 1969), the California Tertiary (Kharaka et al., 1972), and Poland (Dowgiallo and Tongiorgi, 1972). Also shown are the calculated fields of primary magmatic and metamorphic waters (see text), analyses of some possible modern metamorphic waters from the California coast ranges (White et al., 1973), and the range of δD in fluid inclusions from some Mississippi-Valley Pb-Zn ore deposits (Hall and Friedman, 1963). MW = meteoric water line.

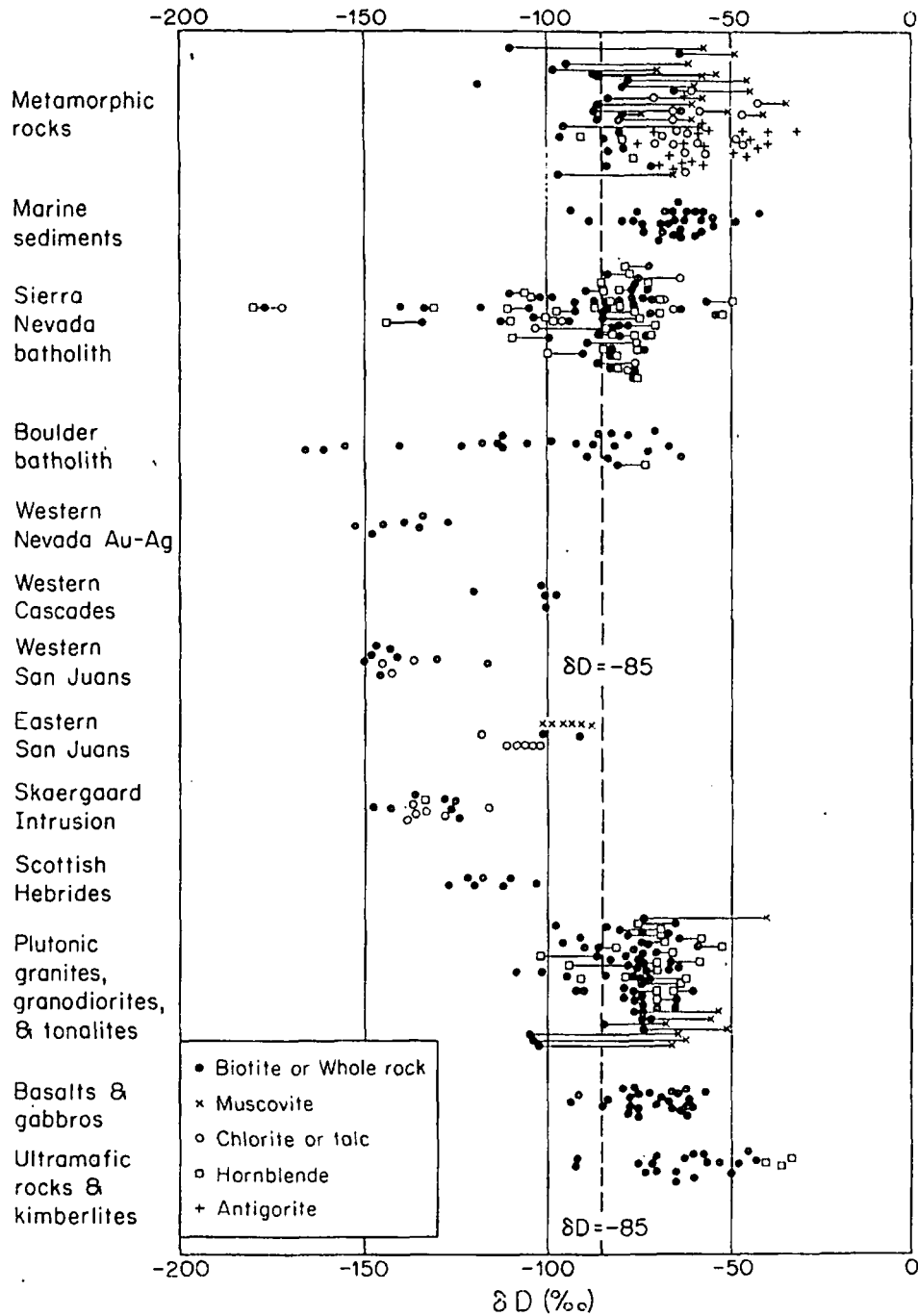


FIG. 10. A compilation of available δD analyses of minerals from igneous, metamorphic, and hydrothermally altered rocks from a variety of localities (Taylor and Epstein, 1966, 1968; Shieh and Taylor, 1969a and b; Wenner and Taylor, 1973, 1974; Turi and Taylor, 1971a; Savin and Epstein, 1970a and b; Godfrey, 1963; Sheppard and Taylor, 1974; Taylor, 1973, 1974; O'Neil et al., 1973; Bethke et al., 1973; Taylor and Forester, 1973; Kuroda et al., 1974; Kokubu et al., 1961; Friedman, 1967; Sheppard and Epstein, 1970; Sheppard et al., 1971; and Moore, 1970).

distinct. Just as with the surface meteoric waters, there is a general decrease in δD (and to a lesser extent $\delta^{18}O$) as one moves to higher latitudes.

For example, the Gulf Coast formation waters are appreciably richer in δD and $\delta^{18}O$ than the Alberta Basin waters (Fig. 9). Within a given

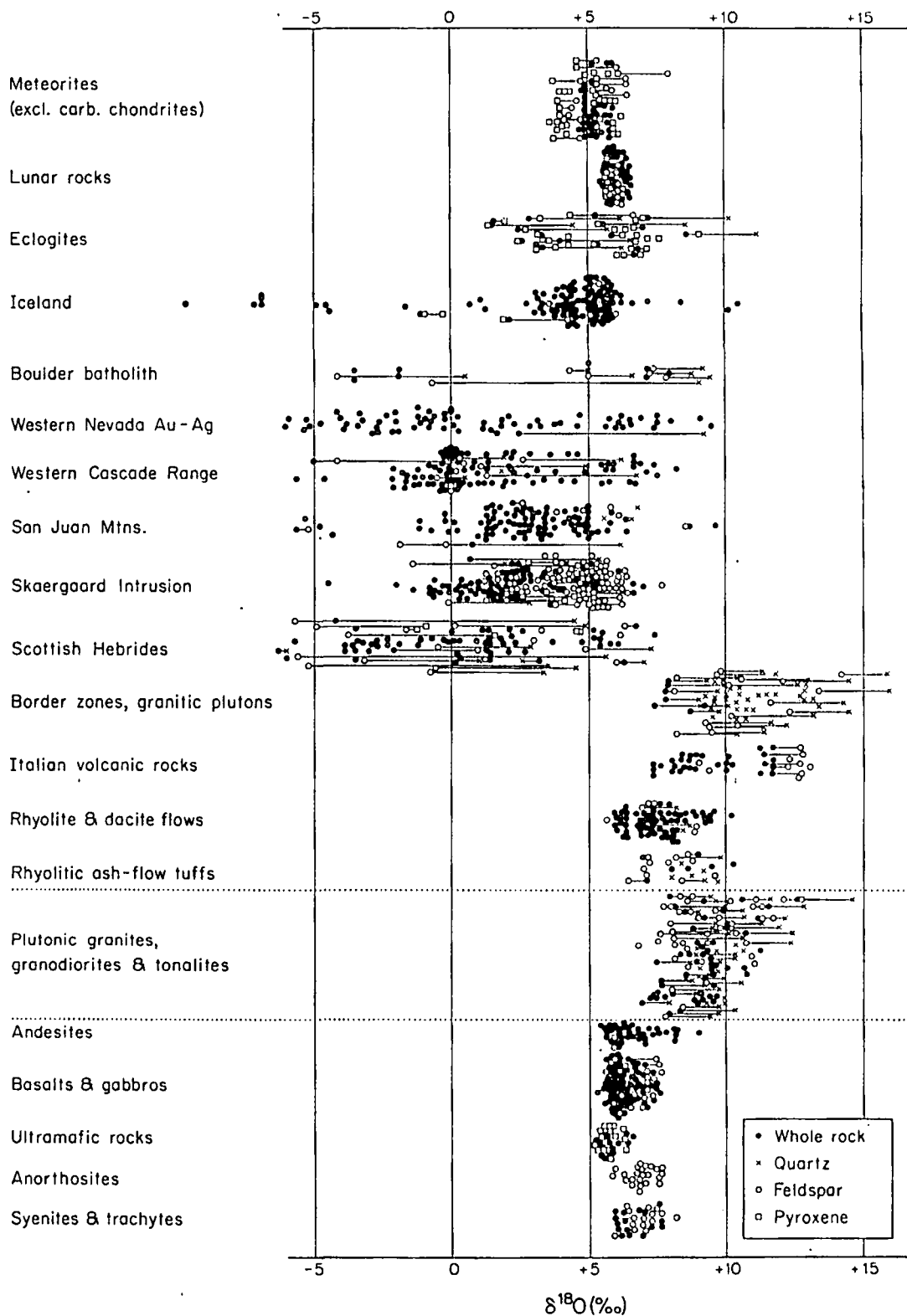


FIG. 11. A compilation of $\delta^{18}\text{O}$ analyses of minerals and whole-rock samples of igneous rocks from a variety of localities. This figure is a modification of figure 8 of Taylor (1968), but it also includes additional data by Taylor et al. (1965), Reuter et al. (1965); Omura et al. (1972), Taylor and Epstein (1970a and b), Epstein and Taylor (1971, 1972), Vogel and Garlick (1970), Garlick et al. (1971), Sheppard and

basin the highest $\delta^{18}\text{O}$ values are typically associated with the highest temperatures and salinities, but in contrast to the near-neutral, chloride-type geothermal waters (Fig. 7) the δD values of the brines are not constant; instead, although they show a great deal of scatter, the δD values generally increase with salinity and $\delta^{18}\text{O}$ content. This is a result of mixing of the meteoric waters with true connate waters or waters of other origins, of exchange with hydroxyl-bearing clay minerals in the rocks, of fractionation effects such as membrane-filtration, and/or of reactions involving petroleum hydrocarbons.

All sedimentary basins probably contain formation waters analogous to those found in wells from the midcontinent of North America. Isotopic analyses of such waters from Poland and from Tertiary sedimentary rocks in California are also shown on Figure 9. Such formation waters are probably the most common type of pore solution in deeply buried, unmetamorphosed sedimentary-rock sections and they may in certain cases represent important ore-forming fluids. Hall and Friedman (1963), for example, showed that fluid inclusions in minerals from Mississippi-Valley type Pb-Zn ores have δD values and salinities that are practically identical to nearby formation waters (Fig. 9).

Metamorphic waters

All the waters so far discussed represent materials for which we can obtain actual samples for isotopic analysis. However, for some other geologically important waters, isotopic data can only be indirectly obtained. Metamorphic pore waters are an example, because except for the possibility of making measurements on the fluid inclusions present in certain minerals, we must use calculations to obtain the isotopic composition of the H_2O coexisting with the rocks at the temperature and pressure at which metamorphism takes place.

Calculations of this type will be valid if the temperatures of metamorphism are known fairly accurately, because isotopic equilibrium between silicates and H_2O is certainly obtained above 200°C , considering the large time intervals involved in regional metamorphism. There is little published information on the D/H ratios of metamorphic minerals, but utilizing what is available (Fig. 10), together with the tentative fractionation

curves shown in Figure 4, a generalized field of metamorphic waters is shown on Figure 9.

Typically, regional metamorphic waters appear to have a relatively restricted range of δD (-20 to -65) but a wide range of $\delta^{18}\text{O}$ ($+5$ to $+25$). Even considering the paucity of hydrogen isotope data it is remarkable that minerals of metamorphic rocks from a wide variety of areas have such uniform δD values. Metamorphic muscovites are richer in D than coexisting chlorites, which are in turn richer in D than coexisting biotites and hornblendes (Taylor and Epstein, 1966). However, all of these metamorphic minerals typically have δD values in the narrow range -35 to -90 per mil. The few samples shown on Figure 10 with $\delta\text{D} < -90$ are from contact metamorphic zones of epizonal intrusions (Shieh and Taylor, 1969a and b); these samples probably have interacted to a certain extent with heated meteoric waters.

Metamorphosed sedimentary rocks and their constituent minerals have a wide range in $\delta^{18}\text{O}$ simply because they retain in large part their original sedimentary $\delta^{18}\text{O}$ values during metamorphism. Shales, limestones, and cherts all tend to be very rich in ^{18}O ($\delta = +15$ to $+35$), whereas rocks such as sandstones, graywackes, arkoses, and volcanogenic sediments tend to be low in ^{18}O ($\delta = +8$ to $+13$).

There is a possibility that some metamorphic waters actually do make their way to the earth's surface. White et al. (1973) have identified some isotopically unusual geothermal waters in the California coast ranges, which are a rare exception to the above mentioned rule that hot spring waters are everywhere wholly of surface derivation. These anomalous waters are plotted on Figure 9 and they overlap our calculated field of metamorphic waters. White et al. (1973) concluded that these waters are true metamorphic waters that have penetrated to the surface from some undetermined depth. It is of interest that these waters are also isotopically similar to the calculated waters that formed some antigorites in certain coast range ultramafic bodies (Wenner and Taylor, 1973).

Magmatic waters

Magmatic waters present some of the same problems referred to above concerning metamor-

Taylor (1974), Garlick and Epstein (1966), Taylor (1971, 1973, 1974), O'Neil et al. (1973), Forester and Taylor (1972), Taylor and Forester (1971, 1973), Turi and Taylor (1971a and b, unpub. data, 1974), Shieh and Taylor (1969a and b), Matsuhisa et al. (1972, 1973), Anderson et al. (1971), Wenner and Taylor (1973), Muehlenbachs and Clayton (1972), and Sheppard et al. (1971). Note that in Iceland, all the samples with $\delta^{18}\text{O} < +2$ are hydrothermally altered basalts or xenoliths, but many of the other samples were erupted as low- ^{18}O magmas (Muehlenbachs et al., 1972).

phic waters. Nowhere, even in H_2O gas samples from active volcanoes, can we be absolutely certain that we are obtaining H_2O that has come directly from a pristine, uncontaminated magma. As before, we can, however, calculate the isotopic composition of the H_2O that would have coexisted with the various igneous minerals at magmatic temperatures. Inasmuch as magmas only exist over a restricted temperature range of about 700° to $1,100^\circ C$ and because most volcanic and plutonic igneous rocks typically have very uniform $\delta^{18}O$ values (+5.5 to +10.0, Fig. 11) and δD values (-50 to -85 , Fig. 10), the "normal" isotopic range for magmatic H_2O (Fig. 9) is much more restricted than the range for metamorphic H_2O .

True magmas with unusual oxygen isotopic compositions well outside the normal range do exist, however. Some of these rare examples are fresh volcanic flows on Iceland (Muehlenbachs et al., 1972) that have $\delta^{18}O$ values as low as +2 and, at the other end of the spectrum, unaltered flows from some Pleistocene volcanoes north of Rome, Italy, which have $\delta^{18}O$ values as high as +13 (Turi and Taylor, unpub. data 1974). Any magmatic H_2O coming from such anomalous magmas would have $\delta^{18}O$ values outside the "normal" range.

The total δD range of magmas is at present not so well understood, although it is likely that 95 to 99 percent of all magmas in the world originally had δD values in the range -50 to -85 (Fig. 10). The term "primary magmatic water" (Fig. 9) is thus defined somewhat arbitrarily as the calculated H_2O in equilibrium with these "normal" igneous rocks at $T \geq 700^\circ C$. Direct analyses of volcanic gases from active volcanoes in Iceland show H_2O with δD in this range, for example (Arnason and Sigurgeirsson, 1968). Also, a δD value of -60 was obtained for the original H_2O in a carefully studied, recent, chilled, submarine basalt flow from Hawaii (Moore, 1970).

Nonetheless, quite a significant number of plutonic biotites (and hornblendes) are known with δD values ranging down to -170 (Fig. 10). These low- δD values are commonly thought to be a result of post-crystallization exchange between the rocks and heated meteoric ground waters, but in most instances we cannot rule out the possibility that the δD values are a characteristic of the magmas themselves. Even if the latter is true, it is probable that the low- δD values were acquired during direct or indirect interaction with meteoric waters after the magmas penetrated upward to shallow levels in the earth's crust (see below).

It is unfortunately very difficult at present to develop criteria to decide whether the low- δD

values are a magmatic phenomenon or are a result of later exchange. With oxygen isotopes this is feasible because the different minerals in an assemblage undergo ^{18}O exchange at vastly different rates (e.g., quartz versus feldspar). For example, the low- ^{18}O igneous rocks shown on Figure 11 are known to have been produced by high-temperature interaction with low- ^{18}O meteoric ground waters and in many of these rocks the quartz has essentially a "normal" $\delta^{18}O$ value whereas the coexisting feldspar in the same assemblage has been depleted in ^{18}O by several per mil (compare the lengths of the tie lines between quartz and feldspar for the "normal" rocks in Figure 11 with those for the ^{18}O -depleted rocks). In laboratory hydrothermal experiments, quartz is known to be much more resistant to isotopic exchange than is feldspar (O'Neil and Taylor, 1967; Clayton et al., 1972).

In the case of hydrogen isotopes these types of differential exchange effects are not so obvious. However, there does seem to be a tendency for the hornblendes in the low- D rocks to have consistently lower δD values than coexisting biotites, whereas in the "normal" igneous rocks these two minerals have very similar δD values. If it could be shown in the laboratory that hornblende undergoes D/H exchange with hot H_2O more easily than does biotite, the data in Figure 10 could be interpreted as indicating that at least some of the D/H exchange in the natural samples occurred after crystallization of the biotite and hornblende.

Supergene Alteration

In this paper, the isotopic effects accompanying supergene ore formation will be discussed before taking up hypogene ore deposition. This is done because in supergene ore deposits there is no question concerning the origin of the ore-forming solutions (namely meteoric surface waters) or the approximate temperature of ore deposition (25° to $60^\circ C$). We shall show that, given favorable circumstances, stable isotope techniques can clearly distinguish between supergene and hypogene mineral assemblages.

Let us first consider the isotopic data that have been obtained on certain other materials formed at surface temperatures. In Figure 12 we show the variations in $\delta^{18}O$ and δD values of present-day soils formed on igneous parent rocks from various parts of the United States (Lawrence and Taylor, 1971). Soils in the more northerly regions are depleted in both ^{18}O and deuterium and there is a clear parallelism with the isotopic variations in coexisting meteoric waters. Note that the clay-rich soils all plot very close to a curve labeled

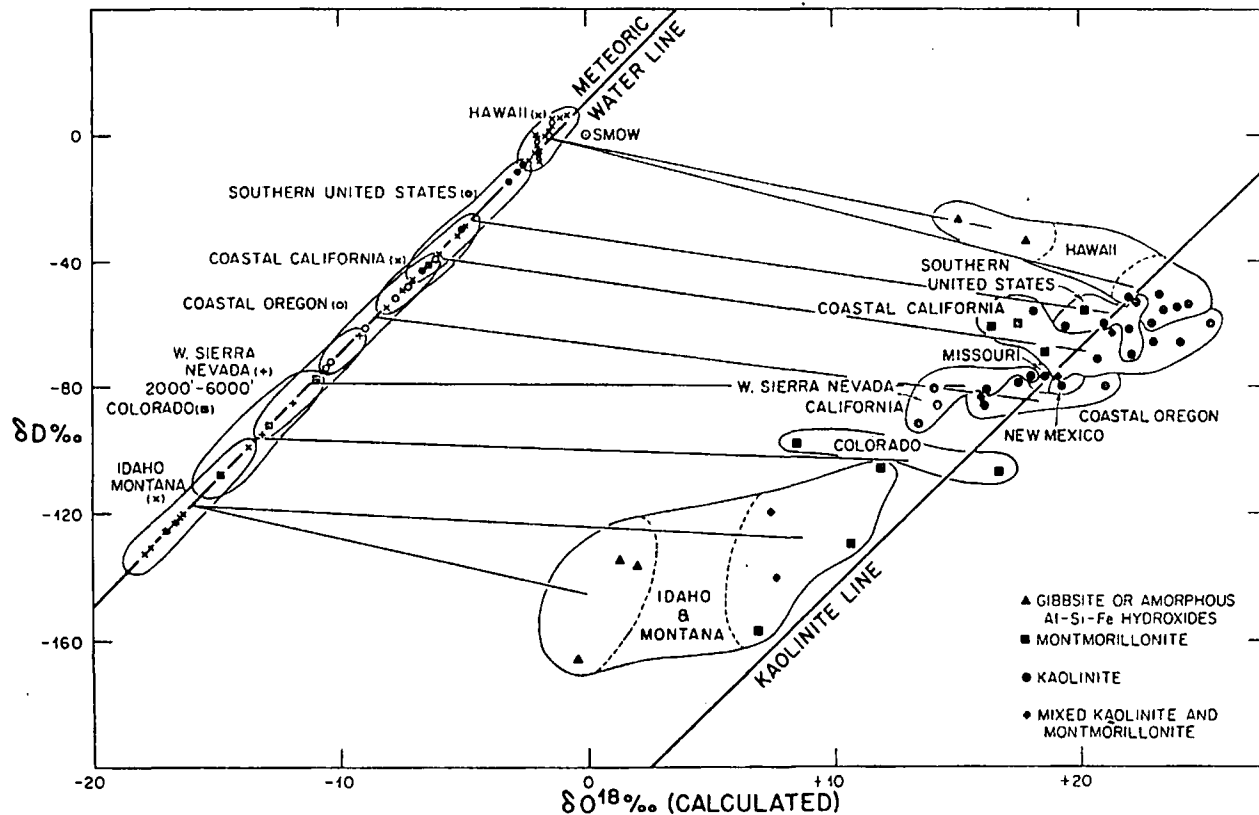


FIG. 12. Plot of δD versus $\delta^{18}O$ for clay minerals and hydroxides from modern soils formed on igneous parent rocks in the United States, after Lawrence and Taylor (1971). The $\delta^{18}O$ values are only approximate because they are calculated from the bulk soil analyses by subtracting out the isotopic contribution due to parent-rock minerals. Also shown is the kaolinite line of Savin and Epstein (1970a) and some typical meteoric waters from various regions. Most of the meteoric waters shown were analyzed only for δD or $\delta^{18}O$, not both; they are, however, plotted on the meteoric water line.

"kaolinite line," this represents the locus of isotopic data points obtained in pure kaolinites from weathering zones (Savin and Epstein, 1970a). The latter data, together with Figure 12 and the data of Lawrence and Taylor (1972), imply that kaolinites and montmorillonites formed during weathering are in approximate isotopic equilibrium with their coexisting meteoric waters and that the fractionation factors are such that these clays are ~ 27 per mil enriched in ^{18}O and ~ 30 per mil depleted in deuterium relative to the water from which they formed. Note on Figure 12 that soils rich in hydroxide minerals (e.g., gibbsite) plot to the left of the clay-rich soils; this is presumably because the gibbsite- H_2O isotopic fractionation factors differ appreciably from those for kaolinite and montmorillonite (Figs. 2 and 4).

In the light of the above relationships we should also expect supergene clay minerals to plot in the vicinity of the "kaolinite line" if they form in equilibrium with meteoric H_2O at earth-surface temperatures. Sheppard et al. (1969) showed this to be the case, if allowance is made for the fact that temperatures of supergene deposition may

range up to 50° to $60^\circ C$ because of the large amount of heat produced by oxidation of pyrite during the production of the acid supergene solutions. All of the presently available isotopic analyses of clay minerals from ore deposits are plotted on Figure 13 and, based on geologic relations, the probable supergene clays are distinguished by a different symbol from the hypogene clays. Note that all of these supergene clays either plot on the "kaolinite line" or slightly to the left of it; this shift to the left is readily explained by slightly higher temperatures of formation than are involved in surface weathering.

Not only do the isotopic compositions of the clays of apparent supergene origin correlate with the meteoric water relationship, but the probable hypogene clays do also. This is because meteoric water was present and important in the hypogene-hydrothermal system responsible for argillic alteration. The range of the D/H and $^{18}O/^{16}O$ in supergene clays are clearly different from hypogene clays. Therefore, we can use oxygen and hydrogen data to

low-
The
pointed,

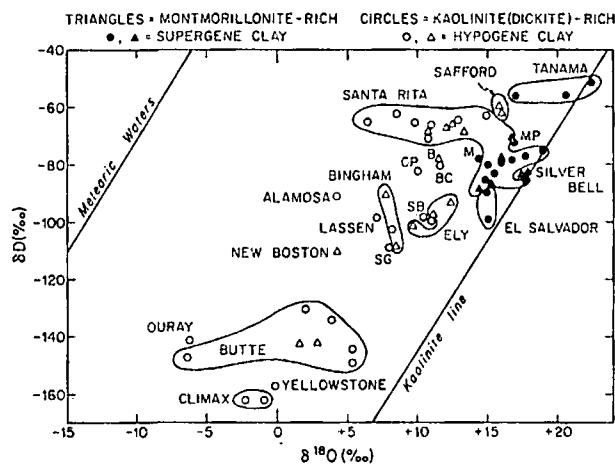


FIG. 13. Plot of δD versus $\delta^{18}O$ for hypogene and supergene clay minerals from various ore deposits, modified after figure 5 of Sheppard et al. (1969), with the deletion of the halloysite data and addition of new data from Silver Bell, Arizona (Lawrence, 1970); the Alamosa River stock, Colorado (Taylor, 1974); and Climax, Colorado (Hall et al., 1973). MP = Mineral Park, M = Morenci, B = Bethlehem, CP = Cerro de Pasco, SB = Sulphur Bank, BC = Bond Creek, SG = St. George.

supergene and hypogene clay minerals. In theory this should also be possible for any other O- and H-bearing supergene mineral as well.

In favorable regions, such as at the Santa Rita deposit in southern New Mexico, $\delta^{18}O$ data alone might possibly be used to distinguish between supergene and hypogene clays; in general, however, both types of analyses must be carried out. The clay data at Santa Rita are shown in Figure 14, modified after Sheppard et al. (1969). Note the clear relationship between depth and isotopic composition (particularly $\delta^{18}O$ value). Essentially all of the deeper samples (below 5,000 ft. elevation) have $\delta^{18}O = 6.4$ to 14.9 and $\delta D = -62$ to -71 , whereas the shallow samples have $\delta^{18}O = 14.5$ to 18.9 and $\delta D = -71$ to -88 . On a δD - $\delta^{18}O$ diagram, such as Figure 13, there is a clear-cut gap between the shallow supergene samples at Santa Rita and the deep hypogene samples.

Most of the supergene clay samples shown in Figure 13 are mid- to late Tertiary in age, based on geological relationships at the various deposits (see table 2, Sheppard et al., 1969). In general, most of these clays appear not to be in equilibrium with present-day ground waters. Instead, their high- δD values seem to reflect a warmer, more temperate environment. The same type of climatic distinction can be inferred from some kaolinites formed during Tertiary surface weathering in the western United States (Lawrence, 1970). If one calculated the isotopic compositions of the meteoric waters in equilibrium with these various low-temperature clay deposits, one obtains a map

such as that in Figure 6, but with the δD contours shifted about 10 to 20 per mil higher than the present-day contours (also see Fig. 32 below).

The data on Tertiary supergene and weathering clays are important in that they demonstrate that none of these very fine-grained ancient clays have completely equilibrated with present-day ground waters, even though they have been exposed to such waters for hundreds of thousands of years. The problem of preservation of isotopic ratios (particularly D/H) in such fine-grained minerals is a very critical one, if isotopic analyses of such minerals are to be used in interpreting hydrothermal alteration processes. Although we cannot at present rule out the possibility of isotopic exchange at temperatures of 100° to $150^\circ C$ or higher, there are a variety of lines of evidence which indicate that low-temperature exchange is very slow, even for hydrogen isotopes. This statement needs to be qualified somewhat for montmorillonite, because Lawrence and Taylor (1972) showed that clay minerals containing interlayer water were more susceptible to such exchange effects than minerals like kaolinite. In addition, they showed that the mineral halloysite, in which the hydroxyls are directly in contact with easily removable interlayer water, does not preserve its D/H ratio for more than a few days; all hydrogen isotope analyses of halloysite are meaningless as a method for interpreting the conditions of its formation. Furthermore, Wenner and Taylor (1974) demonstrated that antigorite serpentine, a very fine-grained hydrous silicate with a crystal structure somewhat analogous to many of the clay minerals, seems to preserve its original $\delta^{18}O$ and δD values extraordinarily well during subsequent low-temperature geologic events.

Note that if any of the hypogene clays shown on Figure 13 had exchanged appreciably with low-temperature ground waters, the data points would all have moved to the right and downward and all should now plot in the vicinity of the kaolinite line. Even the montmorillonites do not do this to a significant degree, although they do plot closer to the kaolinite line than do the kaolinites and dickites. They thus may have suffered some partial isotopic exchange.

Interactions between Meteoric Ground Waters and Igneous Intrusions

In recent years it has become well established by means of oxygen and hydrogen isotope analyses that certain epizonal igneous intrusions have interacted on a very large scale with meteoric ground waters. In favorable terranes, namely in highly jointed, permeable, flat-lying volcanic rocks, these

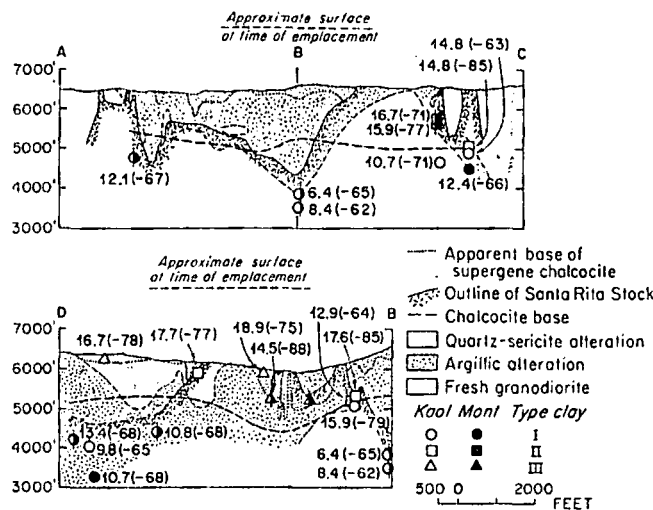


FIG. 14. Modification of figure 2 of Sheppard et al. (1969) showing $\delta^{18}\text{O}$ and δD (parentheses) analyses of clay minerals along two vertical sections through the mineralized porphyry stock at Santa Rita, New Mexico. The upper section A-B-C trends roughly N-S along the E edge of the stock. The lower section B-D trends E-W through the center of the stock. Type I: deepest clays from beneath the chalcocite base, which represents the bottommost occurrence of trace amounts of supergene chalcocite. Type II: intermediate-depth clays from between the actual chalcocite base and the apparent chalcocite base, which is the lowermost occurrence of obvious chalcocite in hand specimen. Type III: shallowest clays from above the apparent chalcocite base.

intrusions act as gigantic "heat engines" that provide the energy necessary to promote a long-lived convective circulation of any mobile H_2O in the country rocks surrounding the igneous body. These systems may represent the "fossil" equivalents of the deep portions of modern geothermal water systems such as occur at Wairakei, New Zealand; Steamboat Springs, Nevada; and Yellowstone Park, Wyoming (e.g., Banwell, 1961; White, 1968).

The interaction and transport of large amounts of meteoric ground waters or ocean waters through hot igneous rocks produce a depletion of ^{18}O in the igneous rocks and a corresponding ^{18}O enrichment or " ^{18}O -shift" in the water. Fortunately, primary unaltered igneous rocks throughout the world display a relatively narrow range of $\delta^{18}\text{O}$, typically only +5.5 to +10.0 (Fig. 11). This provides a datum whereby we can discern the effects of any processes that drastically affect the $\delta^{18}\text{O}$ value of an igneous rock. It is also fortunate that the only other commonly occurring natural process that is known to produce ^{18}O -depletions in igneous rocks is strong decarbonation and loss of CO_2 from carbonate-bearing rocks. However, there do exist a few low- ^{18}O eclogites (Vogel and Garlick, 1970; Garlick et al., 1971) whose origin is not yet understood (Fig. 11). In any case,

inasmuch as the deuterium contents of meteoric ground waters are always lower than ocean water, and in many cases are lower than the primary magmatic waters in igneous rocks, detailed geologic observations combined with $^{18}\text{O}/^{16}\text{O}$ and D/H analyses usually allow a clear-cut decision to be made between the possibilities mentioned above.

Low- ^{18}O igneous rocks produced by interaction with meteoric ground waters have now been observed in the Skaergaard intrusion; in the Stony Mountain ring-dike complex and San Juan volcanic field of Colorado; in the Scottish Hebrides; in Iceland; in the western Cascades; in the Ag-Au deposits at Tonopah, Goldfield, and the Comstock Lode, Nevada; in Bodie, California; and in portions of the Boulder batholith and the southern California batholith (Taylor and Epstein, 1963, 1968; Taylor, 1968, 1971, 1973, 1974; Taylor and Forester, 1971, 1973; Forester and Taylor, 1972; Sheppard and Taylor, 1974; Muehlenbachs et al., 1972; O'Neil et al., 1973). Some of these $\delta^{18}\text{O}$ and δD data are shown in Figures 10 and 11, for comparison with the "normal" isotopic values from igneous rocks.

The igneous complexes that are abnormally low in ^{18}O characteristically display the following geological, petrological, and isotopic features. (1) The intrusions are emplaced into young, highly jointed,

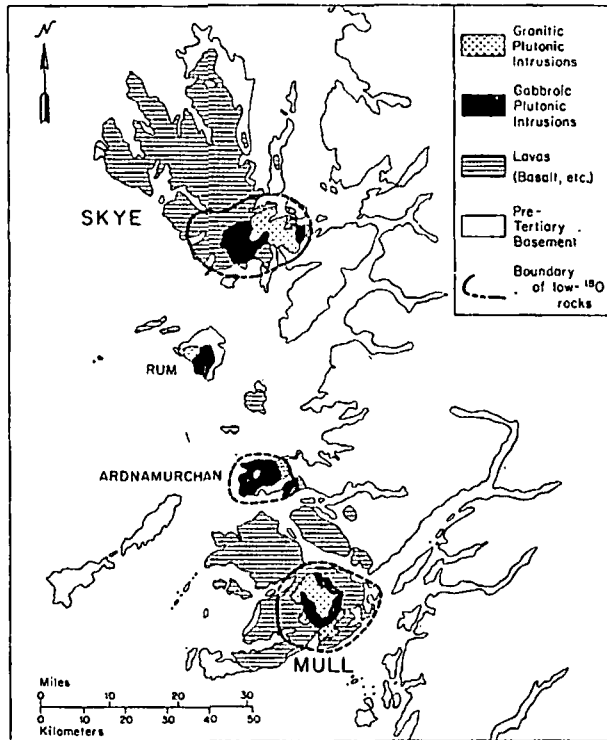


FIG. 15. Generalized geologic map of western Scotland, showing the islands of the Inner Hebrides, and the generalized outer boundaries of low- ^{18}O igneous rocks at three Tertiary volcanic centers (after Taylor, 1968; Taylor and Forester, 1971). All of the rocks within the heavy oval lines have been depleted in ^{18}O by 1 to 15 per mil, with an average whole-rock $\delta^{18}\text{O}$ value of about +0.5 at Skye, +2.0 at Ardnamurchan, and -1.0 at Mull.

volcanic rocks that are very permeable to ground-water movement. (2) In a given rock, the feldspars are commonly depleted in ^{18}O to a greater degree than the other coexisting minerals and the feldspars very commonly show a "clouding" or turbidity (particularly the alkali feldspars). (3) The primary igneous pyroxenes and olivines are usually partially altered to uraltic amphibole, chlorite, Fe-Ti oxides, and/or epidote; locally, this process has gone to completion and only pseudomorphs of the primary igneous minerals remain. (4) Granophyric (micrographic) intergrowths of turbid alkali feldspar and quartz are ubiquitous. (5) Mirolitic cavities are locally present in the intrusives and veins filled with quartz, alkali feldspar, epidote, chlorite, or sulfides are very common in both the intrusives and the surrounding country rocks. (6) The OH-bearing minerals invariably have abnormally low δD values relative to "normal" igneous rocks (Fig. 10).

In certain cases, the characteristic petrographic features outlined above are minor or totally absent (e.g., fresh unaltered olivine). This usually indicates that the hydrothermal alteration occurred

at very high temperatures and/or that the minerals crystallized directly from low- ^{18}O magmas. These low- ^{18}O magmas are themselves probably produced by some process of exchange with meteoric waters, although as will be discussed below, this does not simply involve direct interaction with the meteoric waters.

In the following discussion we shall review the various occurrences of low- ^{18}O igneous rocks and describe in more detail the basic processes involved. It is important to grasp how widespread these effects are, as well as to understand the large scale at which they operate. These meteoric-hydrothermal phenomena involve truly enormous amounts of surface waters and are responsible for the hydrothermal alteration of very large volumes of rocks.

Scottish Hebrides

The evidence for interaction between meteoric ground waters and epizonal igneous intrusions was first discovered at the Skaergaard intrusion (Taylor and Epstein, 1963), but its enormous scale and pervasive effect were first recognized in the Tertiary volcanic centers of Skye, Mull, and Ardnamurchan in western Scotland (Taylor, 1968). Later work by Taylor and Forester (1971) established the extent of the ^{18}O effects around each intrusive complex (Fig. 15). Within the boundaries outlined on Figure 15, essentially all the rocks have been depleted in ^{18}O , some by as much as 13 per mil. The average ^{18}O depletion is about 6 to 7 per mil at both Skye (~150 sq. mi.) and Mull (~150 sq. mi.), but only about 4 per mil at Ardnamurchan (~30 sq. mi.). The effects are smaller at Ardnamurchan because it is a smaller center, but also probably because the country rocks there are largely Precambrian basement rocks; such rocks are less permeable than the overlying highly jointed lavas. The only Hebrides intrusion that shows no appreciable ^{18}O depletion is the Beinn an Dubhaich granite at Skye; this is one of the youngest intrusions and it also was emplaced into Cambrian dolomite rather than into plateau lavas.

Each of the centers shown on Figure 15 represents a complex history of ring-dike intrusion, caldera collapse, and explosive volcanic activity. In general, the oldest ring dikes have suffered the most ^{18}O depletion, presumably because they have been affected by several overlapping meteoric-hydrothermal convection systems. Each new intrusion acts as a separate "heat engine" that can provide the energy to keep the convective circulation going.

Taylor and Forester (1971) showed that the Pb and Sr isotope relationships at Skye have probably been markedly disturbed by the meteoric-hydrothermal activity. The hydrothermal processes have apparently been responsible for some of the systematics in the Pb and Sr isotope patterns attributed by Moorbath and Bell (1965) and Moorbath and Welke (1969) to primary magmatic variations.

From the δD values obtained for some of these rocks (Taylor and Epstein, 1968), we can estimate that the δD values of the early Tertiary meteoric waters in this region were about -85 and thus that the initial $\delta^{18}O$ values of the H_2O were about -11 to -12 . In spite of the abundance of meteoric-hydrothermal solutions in these volcanic centers, no ore deposits have been found; either they never existed or they have been eroded away.

Skaergaard intrusion

The oxygen and hydrogen isotope studies of the Skaergaard intrusion by Taylor and Epstein (1963, 1968), Taylor (1968), and Taylor and Forester (1973) provide some insight into the mechanism of interaction between circulating ground waters and igneous intrusions, mainly because this is a beautifully layered intrusion that has a simple geometrical shape and has been intensively investigated by many mineralogists and geochemists since the pioneering work of Wager and Deer (1939). Also, it is relatively young (Eocene) and is favorably situated in northerly latitudes where the meteoric ground waters are quite low in deuterium. In addition, this intrusion cuts across a profound unconformity in the country rocks, wherein highly jointed plateau basalts are lying on a Precambrian gneissic basement (see Figs. 17 and 18). Thus, the upper part of the intrusion is emplaced against rocks which can be expected to be highly permeable to ground-water movement, whereas the country rocks surrounding the lower part of the intrusion should be relatively impermeable. At the time of emplacement, the depth from the surface to the unconformity is estimated to have been about 5 km (Wager and Deer, 1939).

Some of the $^{18}O/^{16}O$ data obtained by Taylor and Forester (1973) are plotted on Figure 16, which shows four traverses across the contact, one low in the intrusion starting in gneiss, another at the unconformity, and two others somewhat higher up in the intrusion where the country rocks are plateau basalts. The isotopic differences among the various traverses are readily apparent. Most of the ^{18}O analyses were done on plagioclase because, of the minerals in these rocks, plagioclase

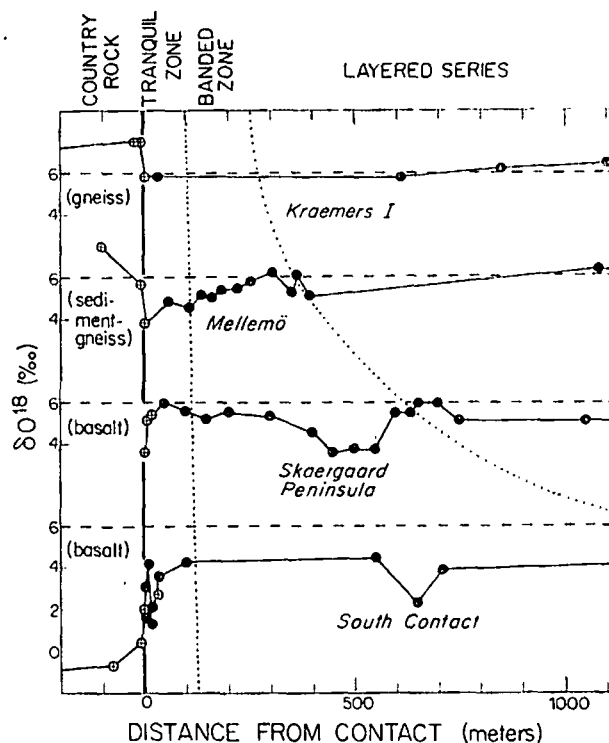


FIG. 16. Graph showing how the $\delta^{18}O$ values of plagioclase (dark circles) and whole-rock samples (crosses) vary along three traverses across the western contact of the Skaergaard intrusion and one traverse across the southern contact (after Taylor and Forester, 1973).

is the one that is known to be the most susceptible to oxygen isotope exchange with hydrothermal fluids. Figure 16 exhibits three main points: (1) The $\delta^{18}O$ variations are very chaotic and commonly change abruptly across a short horizontal distance, particularly within the border zones of the higher traverses. (2) There is a systematic tendency for the samples to be more depleted in ^{18}O in the higher traverses, particularly right at the margins of the intrusion. (3) The plagioclase of the lowermost traverse (against gneiss) has essentially a "normal" igneous $\delta^{18}O$ value $\approx +6$ throughout.

Figure 17 is a map of the Skaergaard intrusion showing $\delta^{18}O$ contours of plagioclase throughout the intrusion, as well as a few $\delta^{18}O$ and δD values of the country rocks. Note that the rocks were tilted about 25° to 30° to the south after intrusion and crystallization. The $\delta^{18}O$ contours cut directly across the primary igneous layering in the intrusion and in the northwest part of the body all the $\delta^{18}O$ determinations have "normal" igneous values ($\sim +6$). The $\delta^{18}O = +6$ contour, in fact, closely follows the trace of the basalt-gneiss unconformity projected through the intrusion. The plagioclase samples stratigraphically above this

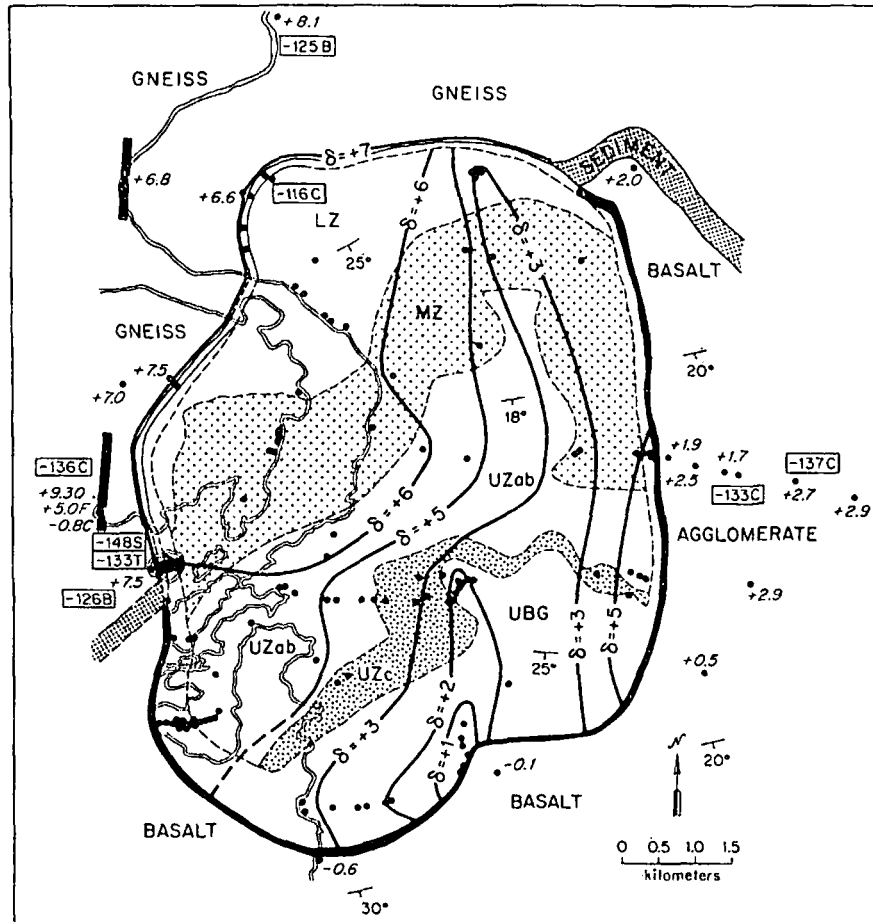


FIG. 17. Generalized geologic map of the Skaergaard intrusion, east Greenland (after Wager and Deer, 1939), showing $\delta^{18}\text{O}$ contours of plagioclase throughout the intrusion. The $\delta^{18}\text{O}$ values in the country rocks are either on whole-rock samples or on quartz (Q), alkali feldspar (F), and chlorite (C). The δD values (rectangular boxes) are on chlorite (C), stilpnomelane (S), tremolite (T), or biotite (B). The isotopic data are from Taylor and Forester (1973). The thick black lines trending N-S on the west side of the intrusion indicate a red alteration zone along a major vertical fracture system in the gneiss. LZ = Lower Zone, MZ = Middle Zone, UZab = Upper Zone, UZc = Uppermost Zone, of the layered series. UBG = Upper Border Group.

$\delta^{18}\text{O} = +6$ contour have all been depleted in ^{18}O to varying degrees and the $\delta^{18}\text{O}$ values in general tend to become steadily lower as one moves stratigraphically upward (south) through the intrusion.

All of the above features are exactly what one would expect if hot meteoric H_2O gained access to the Skaergaard intrusion mainly through the permeable basalts. This is shown schematically in Figure 18. The ground waters in the plateau basalts are heated at the margins of the intrusion. Because of lowered density, they start to rise. A hydrothermal convective circulation system is set up and, after the border zone of the gabbro magma solidifies and fractures, the hot H_2O penetrates into and exchanges with the intrusion. The

convective circulation is driven by cooler water that flows radially in toward the heat source under hydrostatic pressure. At the presumed depth of the unconformity, a column of water would exert a pressure of about 500 bars, whereas the lithostatic pressure in the still-liquid core of the intrusion would be about 1.5 kbars. The circulating ground waters do not significantly affect the lower part of the intrusion because the gneissic basement is relatively impermeable; any H_2O that penetrates from the basalts into the fractured, solid intrusion will be heated and must rise.

A post-Skaergaard, major, east-west, vertical dike swarm cuts the plateau basalts south of the Skaergaard intrusion. In some areas, the outcrops are 90 to 95 percent dikes with only minor

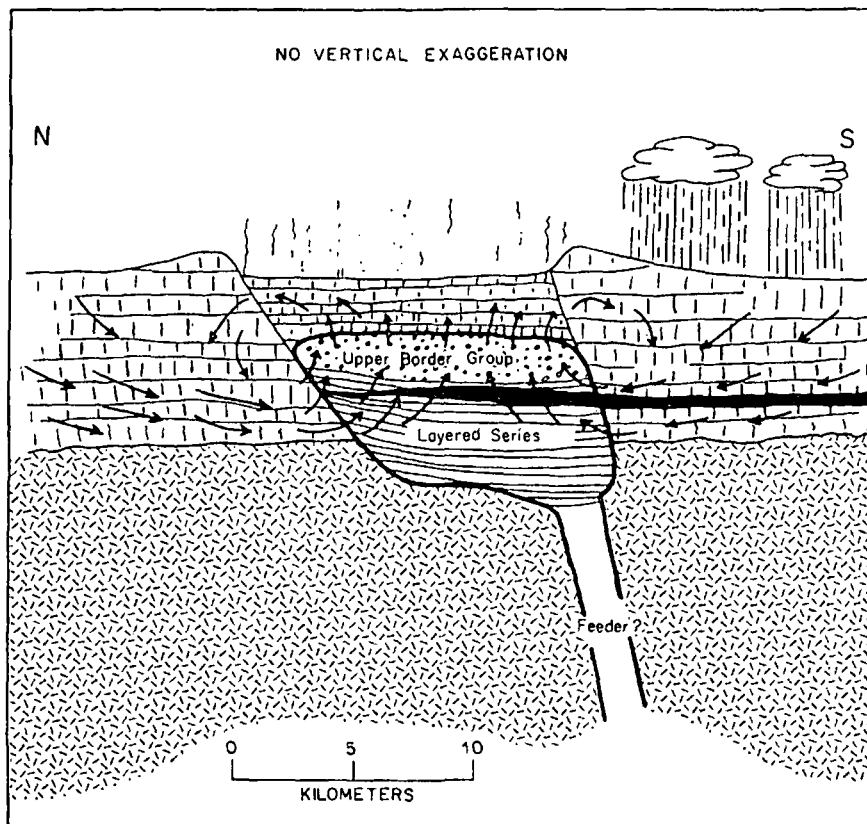


FIG. 18. Schematic geologic cross section of the Skaergaard intrusion, showing the meteoric-hydrothermal circulation pattern in the plateau lavas above the granite-gneiss basement. Only minor amounts of meteoric-hydrothermal H_2O penetrated the gneissic basement along fractures.

screens of basaltic country rock. All of the rocks (dikes plus basalts) are hydrothermally altered and depleted in ^{18}O , with δ -values of 0 to -2 . This shows that sheet-like intrusions can also set up convective circulation systems if they are closely spaced, abundant, and intruded over a short time interval.

A question of great interest in these types of studies is whether or not any considerable amount of meteoric H_2O is able to diffuse directly into the liquid magma, because this is at least one of the plausible ways in which the rare low- ^{18}O magmas might be produced (see below). In the case of the Skaergaard intrusion, this can be answered definitively in the negative because of the following relationships. (1) Except in the "normal" northwest corner of the intrusion, the plagioclase-pyroxene ^{18}O fractionations are either abnormally small or negative; in other words, plagioclase was differentially depleted in ^{18}O relative to the pyroxene, indicating that essentially all of the ^{18}O -depletion in the plagioclase occurred after the layered cumulates were formed. (2) Blocks of coarse-grained UBG gabbro in the Lower

Zone of the Skaergaard intrusion contain abnormally ^{18}O -depleted plagioclase, whereas the cumulates in which they are embedded contain "normal" plagioclase with $\delta^{18}O > +6$. This is interpreted to mean that the hydrothermal convective circulation was operating early in the history of the intrusion and that these blocks of Upper Border Group material exchanged with the low- ^{18}O waters before they broke off and fell to the bottom of the magma chamber. (3) Even though all the rocks in the upper parts of the Skaergaard intrusion are depleted in ^{18}O , the greatest ^{18}O depletions are found in alteration zones along joints and fractures.

Thus, even though a meteoric-hydrothermal convection system was apparently established soon after emplacement of the Skaergaard intrusion, these solutions produced little if any ^{18}O depletion of the liquid magma throughout practically the entire period of crystallization, which must have lasted thousands of years. It is, in fact, difficult to envisage how large quantities of H_2O could migrate into the magma from an essentially hydrostatic fissure system in the country rocks. The

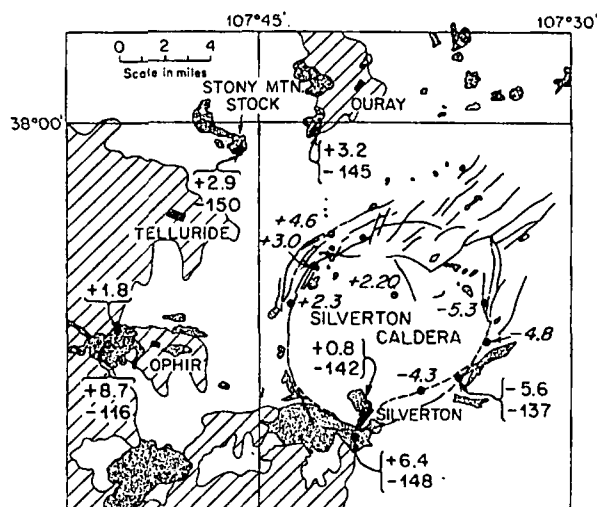


FIG. 19. Generalized geologic map of the western San Juan Mountains, Colorado, after Luedke and Burbank (1968), showing some $\delta^{18}\text{O}$ and δD values (Taylor, 1974) of volcanic country rocks (italic numbers) and intrusive igneous rocks. Stippled pattern = intrusive stocks; diagonal pattern = sedimentary rocks; blank pattern = volcanic rocks. The Stony Mountain stock (Fig. 20) is located 4 miles NE of Telluride.

magma must be under a lithostatic pressure that is a factor of 2.5 to 3 higher than the hydrostatic pressure in the fissure system. The fractures which provide the major conduits for H_2O circulation outside the intrusion obviously cannot be present in the immediate contact zone at the edge of the magma body; otherwise they would be forcibly filled with magma. Therefore, if H_2O is to gain access directly to the magma, it must be by grain-boundary diffusion up a thermal gradient through the hot contact zone and into the magma. Once the H_2O is inside the magma chamber, convective circulation of the silicate melt can aid the diffusion process in distributing this H_2O through the interior of the magma body. Nonetheless, such diffusion is likely to be a relatively slow process, even given the fact that the Skaergaard magma was initially undersaturated with respect to H_2O .

The difficulties outlined above are compounded by the fact that as far as ^{18}O effects are concerned, very large amounts of H_2O are required to produce any significant $\delta^{18}\text{O}$ lowering of the magma. First of all, any H_2O finally able to diffuse into the magma would probably have already undergone a significant ^{18}O shift to much higher $\delta^{18}\text{O}$ values than those characteristic of the cool ground waters in the surrounding terrane. In the case of the Skaergaard intrusion, it would be remarkable if such H_2O had a $\delta^{18}\text{O}$ much lower than -5 at the time of influx into the silicate melt. To produce even a modest $\delta^{18}\text{O}$ lowering of a magma from a "normal" value of about $+6$ to a value of $+4$

with such H_2O would require a water/rock ratio of about 0.25. This is equivalent to about 15 wt percent H_2O and is far more H_2O than can be dissolved in a basaltic magma at such shallow depths in the earth's crust, thereby implying that most of this H_2O would have to diffuse or bubble through the magma chamber and then out again!

It is therefore doubtful that direct influx of low- ^{18}O meteoric H_2O into a magma chamber can by itself account for more than about a one per mil lowering of the $\delta^{18}\text{O}$ of a large magma body. Taken together with the fact that we see no evidence whatsoever of such ^{18}O depletion in the main Skaergaard magma, this independently argues that essentially all of the very large ^{18}O depletion (i.e., $\delta^{18}\text{O} < 0$) in igneous rocks occur after solidification, when the rocks are coherent enough to fracture. This may, however, not apply to the thin sheets of granophyric melt formed during the very latest stages of crystallization of the Skaergaard magma; these sheets have a high surface-to-volume ratio and therefore such small magma bodies are more susceptible to external exchange.

San Juan Mountains, Colorado

Western San Juan Mountains: The isotopic compositions of samples from the Tertiary volcanic-intrusive terrane of the western San Juan Mountains are very depleted in both ^{18}O and deuterium relative to "normal" igneous rocks (Fig. 19). This is particularly true of samples collected in the deeply eroded Animas River Canyon along the eastern ring fracture of the Silverton caldera, where the average $\delta^{18}\text{O}$ value is -5 per mil. This represents a depletion in ^{18}O of 10 to 12 per mil during exchange with heated meteoric ground waters.

These meteoric-hydrothermal solutions were not totally pervasive throughout the area shown in Figure 19, however. A sample from the center of the large quartz monzonite stock just southwest of Silverton is only about 2 per mil lower than "normal" for a quartz monzonite and its quartz-alkali feldspar ^{18}O fractionation of 2.2 per mil is just 0.5 to 1.0 per mil larger than "normal." Thus, only minor quantities of meteoric-hydrothermal solutions penetrated into the center of this stock. Nonetheless, such amounts of H_2O are more than enough to have overwhelmed the small amounts of primary magmatic water that may have been originally present in the biotite, as shown by its very low δD value (-145).

In addition to the above example, which is a large stock emplaced along the boundary between the permeable volcanic terrane and a Paleozoic

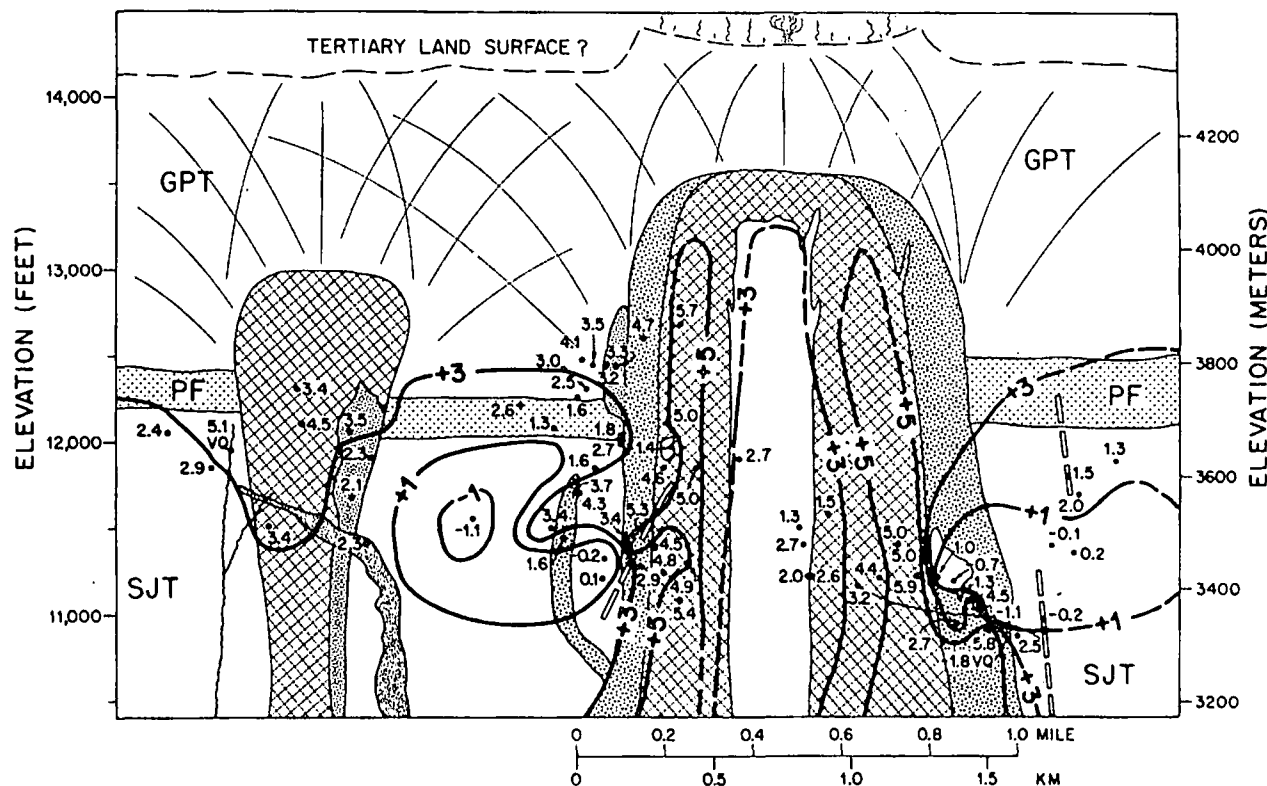


FIG. 20. Generalized geologic section through the Stony Mountain ring-dike complex, Colorado (see Fig. 19), showing $\delta^{18}\text{O}$ values of whole-rock samples and approximate $\delta^{18}\text{O}$ contours at -1 , $+1$, $+3$, and $+5$ (after Forester and Taylor, 1972). The cross-hatched pattern represents gabbro, coarse stipple = outer diorite, fine stipple = monzonite, blank core = inner diorite, wavy pattern = late rhyolite, SJT = San Juan tuff, PF = Picayune formation, GPT = Gilpin Peak tuff, wavy lines = veins, and rectangular bars = dikes.

sedimentary-rock section, certain other igneous rocks from the San Juan Mountains (including a stock west of Ophir shown in Fig. 19) also show little or no ^{18}O depletion (see Taylor, 1974). All of these represent intrusions into the sedimentary-rock section, which apparently was much less permeable to ground-water flow than was the volcanic section. Of such samples, only a single propylitically altered specimen collected at an intrusive contact near the boundary between the volcanic rocks and the sedimentary rocks show any clear-cut ^{18}O depletion ($\delta^{18}\text{O} = +1.8$, left side of Fig. 19).

Stony Mountain ring-dike complex: A detailed study of one of the western San Juan intrusive centers, emplaced wholly into the volcanic-rock section at Stony Mountain, six miles southwest of Ouray, was made by Forester and Taylor (1972). As shown in Figure 20, significant $\delta^{18}\text{O}$ variations were produced during the interaction of heated meteoric ground waters with this composite stock, which is very well exposed over a vertical elevation of more than 2,000 feet. Although the bulk of the $\delta^{18}\text{O}$ variations in the Stony Mountain complex are clearly due to exchange between

heated meteoric ground waters and solidified igneous rocks, Forester and Taylor (1972) concluded that a low- ^{18}O magma must have formed the inner diorite that forms the core of the ring-dike complex.

The $\delta^{18}\text{O}$ values of all the whole-rock samples at Stony Mountain were projected onto the cross section of Figure 20, assuming cylindrical symmetry in the vicinity of the main ring complex. For example, a gabbro sample located halfway between the outer and central diorites would be rotated into the plane of the cross section and be plotted halfway between the two diorites but at its proper elevation.

The most pertinent features of the data shown in Figure 20 are the following. (1) The rocks most highly depleted in ^{18}O are the volcanic rocks near the intrusive contacts. (2) The central diorite intrusion has a unique low- $\delta^{18}\text{O}$ value, less than 3 per mil, much lower than the gabbro which completely encloses it. (3) The finer grained rocks are generally depleted in ^{18}O with respect to the coarser grained rocks (Fig. 21). (4) The most intensely hydrothermally altered rocks tend to have the lowest $\delta^{18}\text{O}$ values; the outer diorite shows the largest variation observed in any single rock

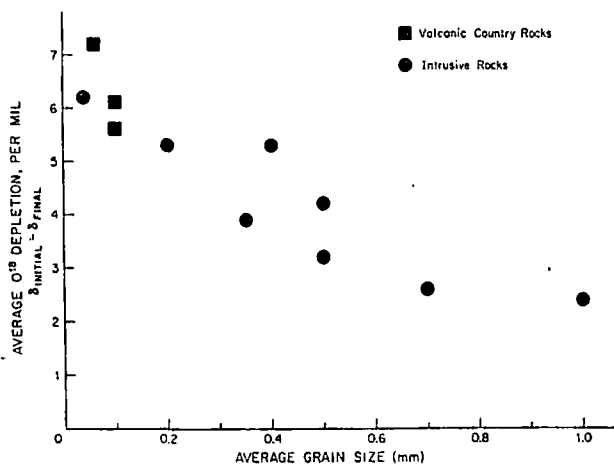


FIG. 21. Plot of average ^{18}O depletion in various types of the Stony Mountain complex versus average grain size in these rock types (after Forester and Taylor, 1972).

unit, from $\delta = -1.1$ to $+5.8$. The latter sample contains exceedingly fresh phenocrysts and groundmass, whereas the low- ^{18}O sample is 60 to 70 percent altered to a propylitic assemblance. (5) Quartz typically has $\delta^{18}\text{O} = +6$ to $+8$ and is more resistant to exchange than any other mineral studied; the $\Delta_{\text{quartz-feldspar}}$ value of 9.4 in a rhyolite is larger than that observed in any other rock yet analyzed, except for a granite from Skye (Taylor, 1968), indicating that during hydrothermal exchange the feldspar in the rhyolite was depleted in ^{18}O by at least 8 per mil while the quartz was virtually unaffected. The $^{15}\text{O}/^{16}\text{O}$ data on coexisting minerals in the Stony Mountain area and similar localities suggest that, other things being equal, the order of increasing resistance of ^{18}O exchange in such environments is alkali feldspar-plagioclase-pyroxene-biotite-magnetite-quartz. (6) The San Juan tuff, although having the same general grain size as the overlying volcanic units, has an appreciably lower average $\delta^{18}\text{O}$, suggesting that it might be the principal aquifer and route of influx for the circulating meteoric ground waters.

A major question is why does the central diorite intrusion have such a uniformly low- $\delta^{18}\text{O}$ value? There is no ready way to explain how the low- ^{18}O aqueous fluids were able to travel through the gabbro and outer diorite shells and only exchange appreciably with the central diorite core. Also, the central diorite is relatively fresh and unaltered; its primary igneous texture, a pronounced "trachytic" flow-foliation, is perfectly preserved.

Forester and Taylor (1972) therefore concluded that the inner diorite was in fact emplaced as a low- ^{18}O magma. This could have come about through some process of mixing and exchange

between meteoric H_2O and a silicate melt in a deeper magma chamber. If the original H_2O had a $\delta^{18}\text{O} \approx -14$ (a reasonable value based on the δD analyses and the meteoric water equations) and the initial diorite magma had a $\delta^{18}\text{O} = +7.5$, it would require mixing or exchanging an amount of H_2O equal to about 15 wt percent of the silicate melt. Obviously, the melt could not contain this much H_2O at any one time, so the meteoric water would either have had to diffuse from the country rocks into and then out of the melt, or it would have had to bubble through the melt, assuming the magma was saturated with H_2O . Because of prior exchange with the country rocks, the H_2O entering the magma would almost surely have had a higher $\delta^{18}\text{O}$ than -14 ; thus much more H_2O is required than is shown by this example.

Other, perhaps more plausible, ways in which such low- ^{18}O magmas might be produced are: (1) by direct melting of water-rich country rocks above a magma chamber—rocks that had already been hydrothermally altered and strongly depleted in ^{18}O by the meteoric-hydrothermal circulation system found above the intrusive body; (2) by large-scale assimilation and dissolution of such low- ^{18}O rocks directly into the magma; (3) by sinking of low- ^{18}O xenoliths through the magma chamber—because the H_2O in the abundant hydrous minerals would certainly be driven off into the magma; also, in hydrous magmas such xenoliths rapidly exchange ^{18}O with their host magma (Shieh and Taylor, 1969b), even though they may show no evidence of dissolution by the silicate melt; and finally (4) by direct exchange between the liquid magma and ^{18}O -depleted country rock at the edge of the magma chamber or along a fissure through which the magma penetrates.

Direct melting of hydrothermally altered roof-rocks above a magma chamber emplaced into a thick volcanic pile would be favored by the large amounts of circulating H_2O present in such an environment. If these melted rocks at the top of the chamber remain separate from the underlying magma (because of lower density or low mixing rates), such melts conceivably could have $\delta^{18}\text{O}$ values as low as any of the hydrothermally altered rocks from which they formed. However, if any of the assimilation mechanisms are solely involved, one would not expect such extreme ^{18}O depletions in the magmas. It is of interest that in Iceland, where the clearest evidence of low- ^{18}O magmas has been found, none of the magmas have $\delta^{18}\text{O}$ values $< +2$ per mil (Muehlenbachs et al., 1972; also see Fig. 11).

Note that the more complicated the intrusive igneous history, the more likely it is that one or

all of the above four mechanisms will be actuated. In particular, multiple intrusion, ring-dike formation, repeated cauldron subsidence, and periodic explosive activity would all be expected to be accompanied by such developments as are outlined above. The lack of ^{18}O depletion of the main mass of Skaergaard magma may be due to the fact that the Skaergaard intrusion represents almost an end-member example of a single, simple, textbook intrusion of basaltic magma that subsequently underwent a relatively straightforward sequence of fractional crystallization.

Eastern San Juan Mountains: Taylor (1974) carried out isotopic analyses on several samples from the composite granodiorite-quartz monzonite Alamosa River stock from the southeast part of the San Juan volcanic field. The K-Ar age of this stock is 29.1 m.y. (Lipman et al., 1970), similar to the ages of intrusion in the western San Juans.

The $\delta^{18}\text{O}$ values of samples from the Alamosa River stock are all low relative to "normal" igneous rocks, although the ^{18}O depletions are not quite so extreme as those described above from the western San Juans. The observed whole-rock $\delta^{18}\text{O}$ values range down to +1.5. Therefore, the same general type of meteoric-hydrothermal convective system must have been set up after emplacement of this stock, but judging by the observed isotopic effects in the stock and in its country rocks, this system either involved meteoric water with a higher $\delta^{18}\text{O}$ value or the amounts of water involved were less.

There is a very extensive kaolinitic alteration zone present on the north side of the Alamosa River stock, extending toward the Summitville mining district. The $\delta^{18}\text{O}$ values of two kaolinite samples from this part of the stock are 3.9 and 4.2 with a δD of -91.

An interesting aspect of the hydrogen isotope data reported by Taylor (1974) is that the samples from the eastern San Juans are markedly richer in deuterium than those from the Silverton area only 80 miles to the northwest (~ -105 versus -140 , respectively). It is clear from the $\delta^{18}\text{O}$ data that meteoric-hydrothermal systems were important in both localities and also the time of formation of the calderas and associated epizonal intrusions was late Oligocene to early Miocene in both areas (Lipman et al., 1970). Therefore, the meteoric ground waters in the two areas apparently had markedly different δD values about 25 to 30 m.y. ago. This circumstance conceivably could be explained as follows. (1) The elevation of the volcanic plateau in the Silverton area may have been appreciably higher than in the Platoro area, perhaps resulting in greater snowfall in the

Silverton area and thus a lower δD in the integrated annual local precipitation. Although less extreme, this is actually the case today in the two areas. (2) The topographic barriers in the mid-Tertiary may have been such that the western San Juans obtained most of their rainfall and snowfall from Pacific storms, whereas the southeastern San Juans obtained most of their precipitation from air masses formed over the Gulf of Mexico. This pattern is also generally true today in the two areas and it leads to higher deuterium values in the surface waters of northern New Mexico (see Friedman et al., 1964, and the map in Fig. 6). (3) The meteoric-hydrothermal fluids in the two areas may have had different histories. For example, if a sedimentary rock section underlies the volcanic field in the eastern San Juans, a formation water (brine?) from such a section may have been involved in the convective circulation. Such formation waters typically contain a major meteoric H_2O component but have heavier δD values than the local meteoric waters (Fig. 9). (4) The emplacement of intrusive igneous rocks, together with their accompanying meteoric-hydrothermal convective systems, could have persisted to much younger ages in the western San Juans than in the eastern San Juans. The lighter δD values in the west may have been produced by late-Tertiary ground waters that were isotopically more similar to those of the present-day.

Ore deposits: Very little isotopic data is presently available on the ore deposits in the western San Juan volcanic field, but, by analogy with data obtained on other epithermal mineral deposits in volcanic terranes, it is practically certain that most of these ore deposits were formed from hydrothermal fluids that contained a significant component of meteoric ground water. This statement is supported by the low- ^{18}O quartz obtained from a sample of ore from a vein in the Gold King mine near the center of the Silverton caldera (Fig. 19). The $\delta^{18}\text{O}$ value of this quartz (+2.2) indicates formation from a hydrothermal fluid with $\delta^{18}\text{O} \approx -5$ to -10 , if the temperature of deposition was somewhere in the range 200° to 400°C . Such a low- ^{18}O fluid must be dominantly (or wholly!) of ground-water origin. Even more definite statements of this sort can be made concerning a vein dickite from the Ouray area ($\delta^{18}\text{O} = -6.2$, $\delta\text{D} = -141$; see Sheppard et al., 1969).

Hydrothermal veins cut all the rock types at Stony Mountain (Fig. 20), and at least in some cases these veins contain very low ^{18}O quartz (e.g., $\delta = -1.8$). Also, some rocks very close to the veins are markedly depleted in ^{18}O (an outer diorite sample 0.5 m from the aforementioned

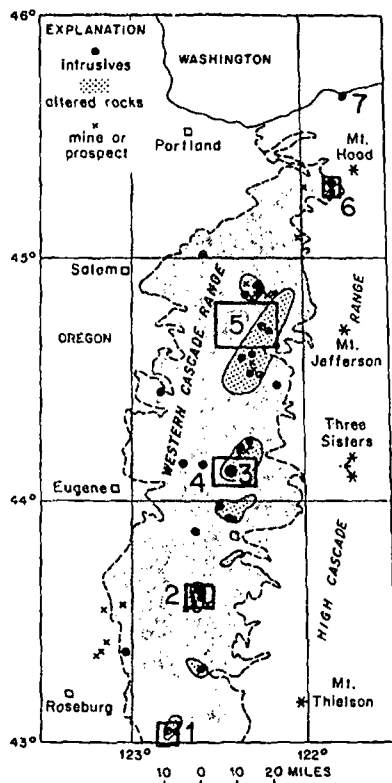


FIG. 22. Map of part of western Oregon (after Taylor, 1971, modified after Peck et al., 1964) showing the Tertiary volcanic rocks of the western Cascade Range (dark, fine stippled pattern), the intrusions emplaced into these volcanic rocks, and the areas of propylitic (coarse stipple) that surround the intrusions. 1 = South Umpqua River locality, 2 = Bohemia district, 3 = Nimrod area, 4 = Vida stock, 5 = Detroit area, 6 = Laurel Hill stock, 7 = Shellrock intrusion.

quartz vein has a $\delta^{18}\text{O} = -1.1$). Another possible example is the central diorite sample with $\delta = +1.3$; it was collected within 10 m of a major vein system in the district.

Several areas of ore mineralization are found in the eastern San Juans in the vicinity of the Alamosa River stock, notably the Summitville district to the north and the Platoro district to the southeast. By analogy, these areas of hydrothermal alteration and ore deposition also very likely involve fluids that contain a dominant meteoric-water component. Note that based on the D/H data of Taylor (1974), the δD value of this meteoric water would have been about -60 to -70 , implying an initial $\delta^{18}\text{O}$ of about -9 rather than the -14 suggested in the Silverton area.

It is interesting that the Creede Ag-Pb-Zn-Cu deposit, which also occurs in San Juan volcanic rocks only 40 km northwest of the Alamosa River stock, was apparently formed from meteoric-hydrothermal solutions with $\delta^{18}\text{O} \approx -6$ to -1 and

$\delta\text{D} \approx -60$ (Bethke et al., 1973). Therefore, all of the above arguments concerning the problems of origin of such solutions also apply to Creede, but this does suggest that whatever the origin of these relatively deuterium-rich meteoric-hydrothermal waters in the eastern San Juan volcanic field, they probably were widespread in this region during late Oligocene-early Miocene time.

Western Cascade Range, Oregon

A series of low- ^{18}O dioritic to granodioritic intrusive bodies are found in the western Cascade Range in Oregon (Fig. 22; see also Taylor, 1971; Peck et al., 1964; Buddington and Callaghan, 1936). These intrusions range in size from a few meters to four km. There are no major ore deposits in these areas, but every one of the intrusive localities has some associated mineralization, notably the Bohemia mining district (Fig. 23) from which about \$1,000,000 in gold was removed from 1870 to 1940.

As shown in Figure 24, all of the volcanic country rocks in the vicinity of the intrusive bodies have been strongly depleted in ^{18}O . The low- ^{18}O zones extend outward at least 2.5 to 3.0 stock diameters away from the nearest intrusive contact. Distances are plotted in this manner in order to take into account the fact that the larger intrusions are in general surrounded by correspondingly larger meteoric-hydrothermal convection systems. The areas of low- ^{18}O rocks correspond very well with the areas of propylitic alteration shown on Figure 22.

Not only are the volcanic country rocks depleted in ^{18}O , all the intrusive bodies are as well; South Umpqua River: $\delta^{18}\text{O} = +2.3$ to $+4.9$; Nimrod: $+0.1$ to $+5.5$; Detroit: -1.7 to $+0.5$; Laurel Hill: -2.1 to $+0.7$; and Vida: $+4.3$ to $+4.6$. These variations are shown in detail in Figure 23 for one of the areas, the Bohemia mining district. Approximate $\delta^{18}\text{O}$ contours for the intrusives and the volcanic country rocks have been drawn on Figure 23. The contour pattern is very systematic and coincides approximately with the pattern of propylitic alteration mapped by Peck et al. (1964). The major ore deposit in the area occurs within the $\delta = 0$ contour, at the south end of the Champion Creek stock. It seems to make little isotopic difference whether the local rocks are intrusives or country rocks, except that there is a general increase in $\delta^{18}\text{O}$ as one moves toward the centers of both the Champion Creek and Brice Creek stocks. This is clearly a result of smaller water-rock ratios in the central portions of each stock.

The low- ^{18}O aureoles in Oregon are similar to what is observed in the San Juan Mountains, but

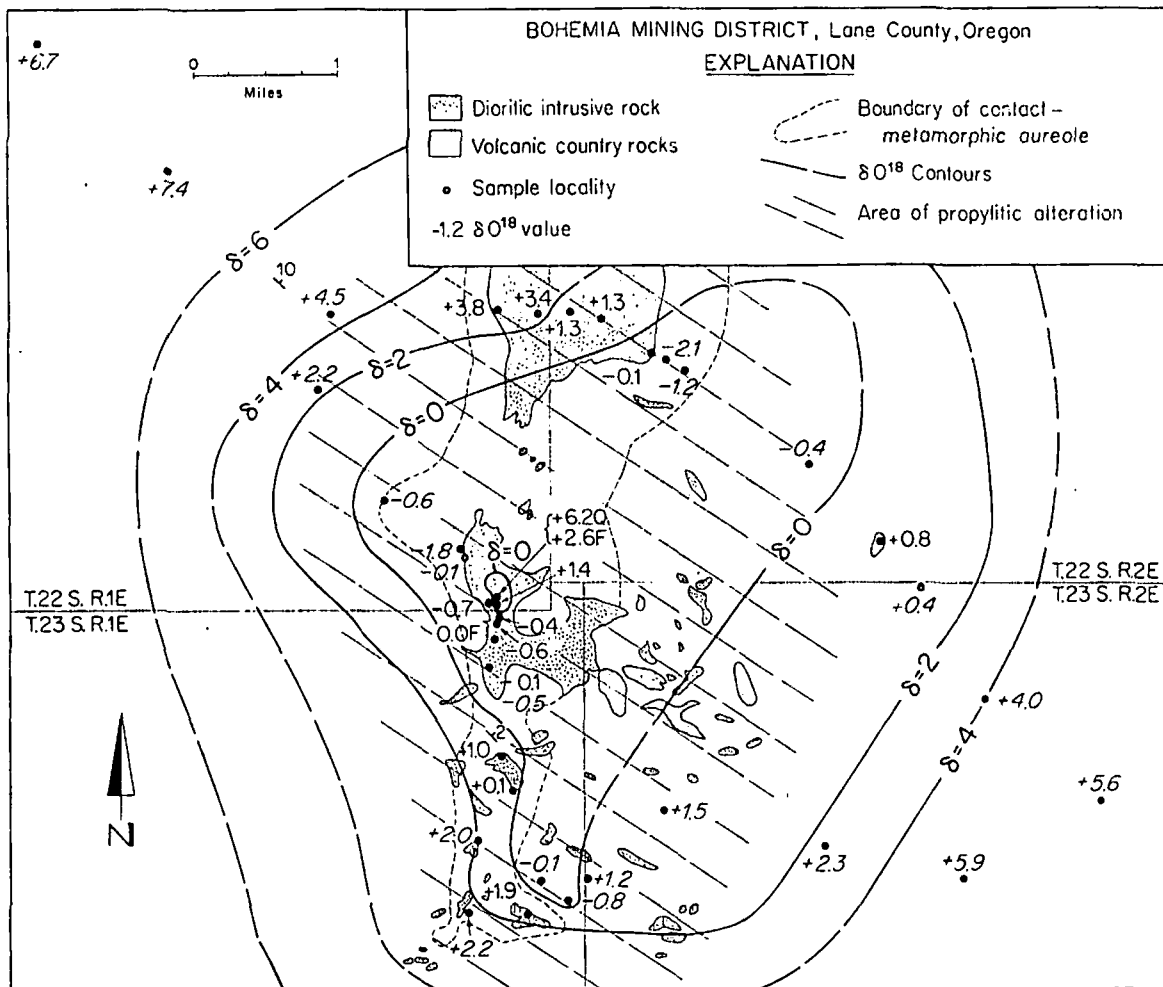


FIG. 23. Generalized geologic map of the Bohemia mining district, Oregon, showing $\delta^{18}O$ values of volcanic country rocks (italic numbers) and intrusive bodies (modified after fig. 4, Taylor, 1971). The Brice Creek stock is at the top and the Champion Creek stock is in the center of the map. Q = quartz, F = plagioclase.

they are much broader than the ones in the Scottish Hebrides; at the latter localities the effects are confined to within about 0.5 "stock" diameters (Fig. 15). The 0.5 number is somewhat misleading, because the diameters of the Scottish "stocks" are assumed to be those of an entire ring-dike complex rather than any single intrusion. Nevertheless, there is no doubt that the low- ^{18}O areas in Oregon are correspondingly much broader than in Scotland, particularly the Nimrod and Detroit areas (3 and 5 on Fig. 22). One possible reason for this may be that at the present erosion level the Hebrides intrusions lie very close to the unconformity between the plateau lavas and the Precambrian basement, whereas the Oregon samples are all underlain by thousands of feet of permeable volcanic rocks. It is also likely that whereas the Scottish intrusions are probably cylindrical in shape with near-vertical contacts, the

Oregon stocks represent either myriads of small plugs or the eroded tops of large intrusions with irregular, gentle, outward-dipping contacts (e.g., note the many small intrusions to the east of the Champion Creek stock in Fig. 23).

Western Nevada Au-Ag Districts

A number of important epithermal Au-Ag deposits in the western United States occur in environments similar to those described above in the San Juan Mountains and western Cascades. In particular, this is true of the geologic setting and petrographic and mineralogical features exhibited by the altered volcanic rocks in the Tonopah, Goldfield, and Comstock Lode districts in western Nevada. Because of these similarities, Taylor (1973) investigated the oxygen and hydrogen isotope variations in these areas in the

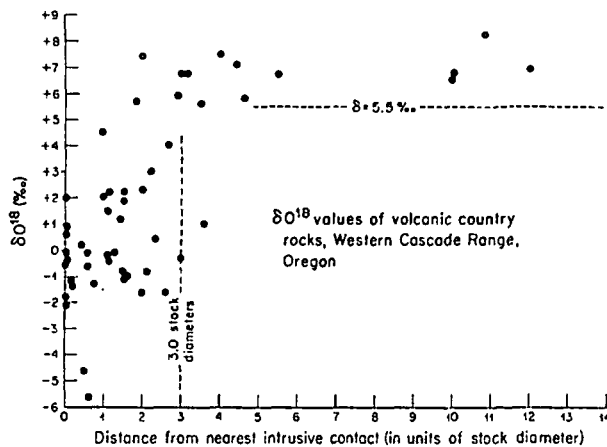


FIG. 24. Plot of whole-rock $\delta^{18}\text{O}$ values of volcanic country rocks from the western Cascade Range versus distance from the closest intrusive contact (measured in units of stock diameter, see text). This is figure 8 of Taylor (1971).

hope of finding ^{18}O and deuterium depletions similar to those described above. As shown in Figures 10 and 11, this was indeed found to be the case. O'Neil et al. (1973) also demonstrated the existence of similar effects in the Bodie district near the California-Nevada border, and O'Neil and Silberman (1973) have shown that this also applies to a large number of other epithermal precious metal deposits in the Great Basin.

Each of the above ore deposits occurs in an extensive area of low- ^{18}O propylitically altered volcanic rocks. All of the hydrothermal vein minerals such as quartz and adularia that are associated with ore deposition also have remarkably low $\delta^{18}\text{O}$ values. At Tonopah, both preore and postore vein quartz samples show a very narrow range of $\delta^{18}\text{O}$ from -5.1 to -1.8 per mil and even the very latest stage, tiny, euhedral quartz crystals that line vugs have $\delta^{18}\text{O} = -3.2$ to $+0.7$ (Taylor, 1973). Using the preferred fractionation curves shown in Figure 2, a quartz-adularia pair at Tonopah gives an isotopic temperature of 285°C . Various other lines of evidence also suggest temperatures of about 250° to 300°C at this deposit and, if these temperatures are valid, we can calculate from the quartz data that the ore-forming fluid at Tonopah had a $\delta^{18}\text{O} \approx -13$. A similar value was calculated for Bodie by O'Neil et al. (1973). Inasmuch as the D/H determinations at Tonopah and Bodie indicate that these fluids had δD values of about -100 , this means that not only are these fluids derived from meteoric waters, they are practically pristine, unexchanged meteoric waters that apparently have not undergone the characteristic ^{18}O shift shown by most of the geothermal waters on Figures 7 and 8. In this sense, they would be analogous to the

Wairakei geothermal waters and they must represent long-continued circulation through fractures where the wall rocks had been previously depleted in ^{18}O .

It is clear that these epithermal Au-Ag deposits are formed from meteoric-hydrothermal systems analogous to the other areas described above. The only difference is probably that in western Nevada the intrusive stocks (or associated volcanic country rocks) through which the meteoric waters circulated contained higher initial concentrations of the precious metals. The isotopic characteristics of these ore fluids imply that the solutions probably carried very low concentrations of the heavy metals and that extremely large amounts of water were involved. This is compatible with the chemical data on fluid inclusions from such deposits, which indicate only about one percent NaCl equivalent or less (Nash, 1972).

At the Comstock Lode and Bodie there are outcrops of low- ^{18}O intrusive stocks that were in part the source of the heat necessary to drive the meteoric-hydrothermal convection systems. These stocks are petrographically almost indistinguishable from analogous intrusions in the western Cascades and San Juan Mountains. However, at Tonopah and Goldfield there are no outcrops of such epizonal intrusions and they must be inferred to exist at depth. Nolan (1935) postulated the existence of such a stock at Tonopah and from the topography of the ore zone he indicated that it probably lay beneath the center of the district in the vicinity of the Mizpah shaft; Nolan's data are reproduced in Figure 25. In Figure 26, the $\delta^{18}\text{O}$ data obtained on the altered volcanic rocks are contoured in a fashion similar to that shown in Figure 23

TABLE 1. Calculated "Temperatures" of Isotopic Exchange between H_2O and Volcanic Country Rocks. (A simple closed-system model, see text, and a constant water/rock ratio is assumed throughout the hydrothermal system. Under these conditions, the $\delta^{18}\text{O}$ contours in Figures 23 and 26 also represent isotherms.)

$\delta_{\text{Rock}}^{18}\text{O}$	Temperature ($^\circ\text{C}$)	
	$\delta\text{H}_2\text{O}_i = -9$, $w/r = 1.0$ (Bohemia district)	$\delta\text{H}_2\text{O}_i = -14$, $w/r = 2.0$ (Tonopah district)
+6	110°	65°
+5	135°	80°
+4	165°	90°
+3	200°	105°
+2	245°	120°
+1	305°	140°
0	395°	160°
-1	540°	185°
-2	875°	215°
-3	—	250°
-4	—	295°
-5	—	355°
-6	—	440°

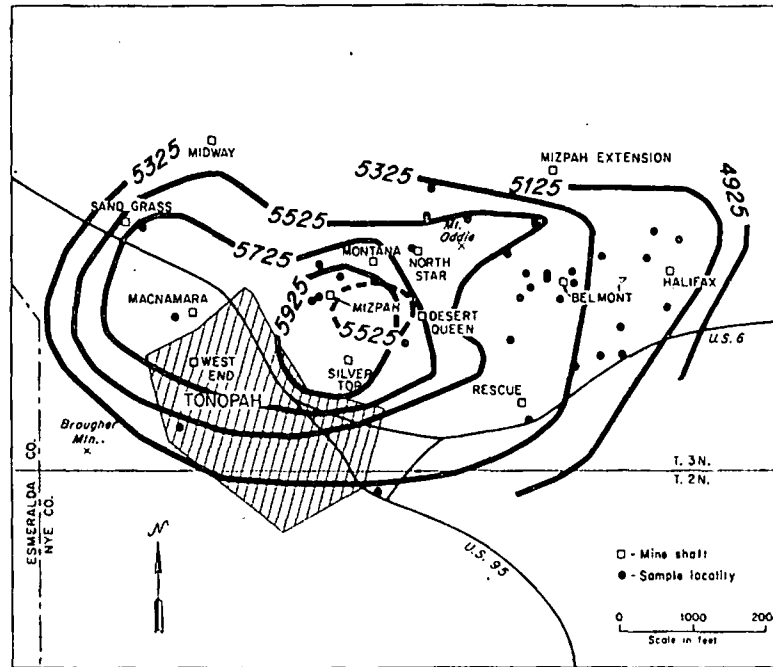


FIG. 25. Map of the Tonopah mining district, Nevada, modified after Nolan (1935). The sample localities are those of Taylor (1973). The solid contours indicate the elevations (in feet) of the upper surface of the productive ore zone in the vein systems at Tonopah. The single broken contour represents the elevation of the apex of the bottom surface of this productive ore zone.

for the Bohemia district. Note that although the sampling is incomplete, there is a clear suggestion that the area of lowest $\delta^{18}\text{O}$ values at Tonopah coincides pretty well with the apex of the productive ore zone as outlined by Nolan (1935). This low- ^{18}O zone represents either (a) the locus of the highest temperature solutions in the district, and/or (b) the zone where the most H_2O was pumped through. Either (a) or (b) is compatible with the suggestion that the hidden stock is located beneath the center of the district, because the high-temperature plume of upward-moving meteoric H_2O should be centered above the heat source (see below).

The $\delta^{18}\text{O}$ contours shown in Figures 23 and 26 suggest the intriguing possibility that whole-rock $\delta^{18}\text{O}$ analyses might be used for prospecting purposes. Much work remains to be done before such an idea can be taken seriously, but it is worth pointing out that ^{18}O measurements of this type are now very routine. Once a laboratory is set up, it is feasible to consider analyzing at least a hundred samples in a month.

Amounts of Meteoric H_2O Involved in the Hydrothermal Systems

We know the initial $\delta^{18}\text{O}$ values of unaltered basaltic and andesitic igneous rocks with a good

deal of accuracy: $\approx +6.5 \pm 1$ per mil. Using D/H analyses of the alteration mineral assemblages or of fluid inclusions, we can apply the meteoric water equation and calculate the initial $\delta^{18}\text{O}$ of the meteoric waters at any given locality. Given the above parameters together with some temperature information, it is then possible to calculate the total amount of water involved in each meteoric-hydrothermal system as follows:

$$w \delta_{\text{H}_2\text{O}}^i + r \delta_{\text{Rock}}^i = w \delta_{\text{H}_2\text{O}}^f + r \delta_{\text{Rock}}^f$$

where i = initial value; f = final value after exchange; w = at. percent of meteoric water oxygen in the total system; r = at. percent of exchangeable rock oxygen in the bulk system.

In order to complete the calculation one must assume that $\delta_{\text{H}_2\text{O}}^f$ is determined by isotopic equilibration with the rocks at the temperature of hydrothermal alteration. Then:

$$w/r = \frac{\delta_{\text{Rock}}^f - \delta_{\text{Rock}}^i}{\delta_{\text{H}_2\text{O}}^f - (\delta_{\text{Rock}}^f - \Delta)}$$

where $\Delta = \delta_{\text{Rock}}^f - \delta_{\text{H}_2\text{O}}^f$. Note that for a given set of initial conditions, if w/r is a constant, then δ_{Rock}^f is determined solely by Δ , which is only a function of temperature. Conversely, if the temperature is constant, δ_{Rock}^f is controlled only by the w/r ratio.

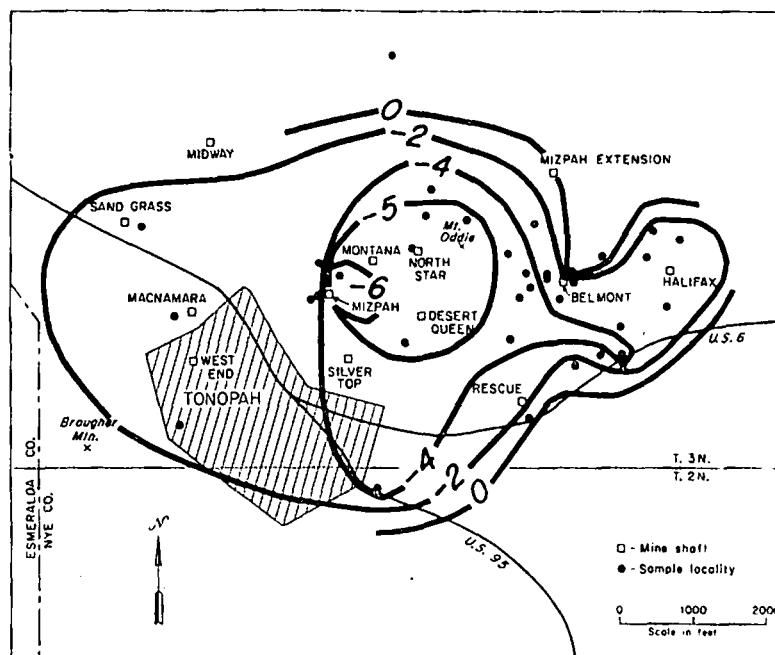


FIG. 26. Map of the Tonopah mining district, Nevada, showing approximate $\delta^{18}\text{O}$ contours of whole-rock samples of the altered volcanic rocks (based on data of Taylor, 1973). Note the rough correspondence between the $\delta^{18}\text{O}$ contours and the elevation contours shown in Figure 25.

If we make the reasonable approximation that in these systems δ_{Rock} at equilibrium is equal to the $\delta^{18}\text{O}$ value of plagioclase (An_{30}), then we can utilize the feldspar- H_2O geothermometer to calculate Δ at any temperature ($\Delta \approx 2.68(10^6/T^2) - 3.53$; O'Neil and Taylor, 1967).

Figure 27 shows how these types of calculations apply to some of the hydrothermal systems discussed in the present paper. For simplicity we shall consider only two initial meteoric water compositions, -9 and -14 . The former value should closely approximate the $\delta_{\text{H}_2\text{O}}^i$ in the western Cascades and eastern San Juans, while the latter value fits the situation in the western San Juans, the western Nevada Au-Ag areas, and the Skaergaard intrusion. The Scottish Hebrides occurrences are not plotted on Figure 27, because $\delta_{\text{H}_2\text{O}}^i$ had an intermediate value ≈ -11 to -12 in those localities.

The principal features illustrated by Figure 27 are that a wide range in water/rock ratios is required in these systems, from essentially zero up to values of 3 to 4. The average values at any one locality are seldom greater than one, however. Note that these calculations give us the total, integrated amounts of H_2O that migrated through the rocks from the beginning of the hydrothermal system to its conclusion. They nevertheless only represent minimum values of w/r , because appreciable H_2O may move through the rocks without

exchanging (i.e., along previously exchanged fracture systems, as indicated by the extremely low- ^{18}O vein quartz at Tonopah).

The volume of heated meteoric H_2O in a typical hydrothermal system is thus approximately equal to the volume of hydrothermally altered rock. Hundreds to thousands of cubic miles of rock are involved, so enormous amounts of meteoric H_2O are also demanded. The amounts are not unreasonable, however, considering the permeability of the jointed volcanic rocks and the tens of thousands of years over which individual hydrothermal systems probably persist. Assuming normal amounts of rainfall, only about five percent of the local annual precipitation needs to be added to the deep circulation systems.

The most difficult problem in these systems is in fact not the amounts of H_2O , but the large quantities of heat energy that are necessary to drive the convection systems. A simple calculation shows that even if the propylitically altered country rocks are only heated from about 50°C to an average temperature of 250°C , then with a specific heat of 0.3 cal/g , approximately 60 cal/g of heat must be added throughout the alteration zone. With $w/r \approx 1$, about 0.5 g of H_2O have to be heated for every g of rock, thus increasing this to about 160 cal/g of altered rock. From a magma body initially intruded as a liquid at 950°C , the maximum amount of heat that can be obtained

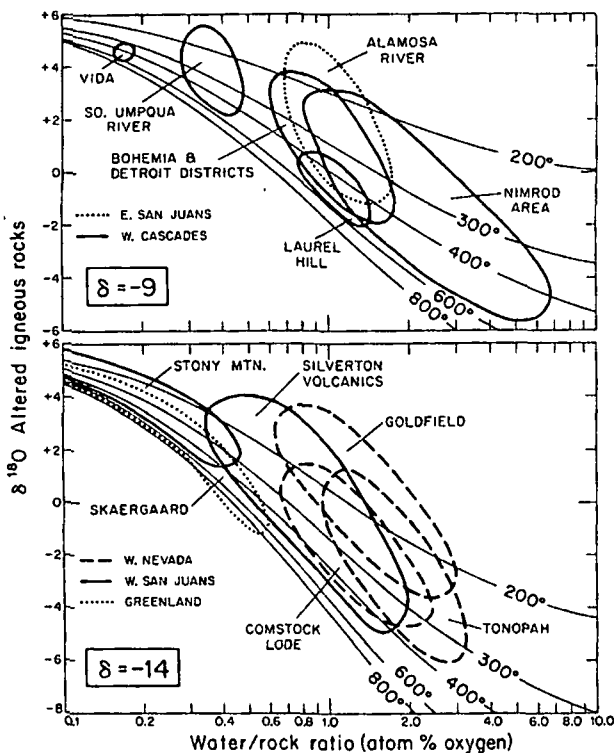


FIG. 27. Plot of whole-rock $\delta^{18}\text{O}$ values versus water/rock ratios for various localities discussed in this paper. Only two values of $\delta_{\text{H}_2\text{O}}$ are shown, -9 and -14 . The method of calculation of the isotherms is described in the text.

during crystallization and cooling to 300°C is only 275 cal/g (this includes about 80 cal/g for the latent heat of crystallization). Some heat is also available from the exothermic hydration reactions that occur during hydrothermal alteration, perhaps about 30 cal/g . Taking this all into account, a cylindrical stock of magma only contains enough heat to produce an alteration aureole about 0.4 to 0.5 stock diameters wide. This calculated value is somewhat smaller than the observed situation in the Scottish Hebrides (Fig. 15) and is much smaller than is indicated for the western Cascades in Figure 24.

The above discrepancy between calculation and observation can probably only be explained in three ways. (1) The stocks are not cylindrical, but broaden in cross-sectional area with depth. (2) The alteration zones are underlain by hidden intrusive bodies that do not crop out. (3) The intrusions do not represent a single injection of magma, but instead represent episodic addition of new magma from below, as would be expected in a volcanic conduit to the surface. All three of these explanations may have some validity, but the latter is almost certainly important with respect to ring-dike complexes such as Stony Mountain

and the Scottish Hebrides. These areas represent the deeply eroded cores of volcanoes and the repeated intrusion and resupply of new magma that are known to take place in such localities probably removes any heat-balance problem.

Of all the intrusive bodies so far studied, the one whose three-dimensional shape is best known is the Skaergaard intrusion; also, the circulation pattern of meteoric H_2O is best understood here, and explanation (3) cannot possibly apply because this intrusion essentially represents a single injection of magma (Wager and Deer, 1939). As shown in Figure 27, the water/rock ratios calculated for the Skaergaard intrusion are, in fact, very low and are compatible with the above facts. Also, the hydrothermal alteration effects attributable to the Skaergaard intrusion only extend about 0.3 to 0.4 stock diameters eastward from the contact shown in Figure 17 (Taylor and Forester, 1973).

Comparison with a Modern Geothermal System

Figure 28 shows the measured present-day temperature distributions in the modern geothermal system at Wairakei, New Zealand (Banwell, 1961; Elder, 1965). This is a volcanic area similar to some of the areas of hydrothermal alteration described above, the H_2O is entirely of meteoric origin, and there is also some associated epithermal Au mineralization. Note that the main upward movement of H_2O at Wairakei is localized in a narrow zone directly above the hypothetical magmatic heat source and that the isotherms form

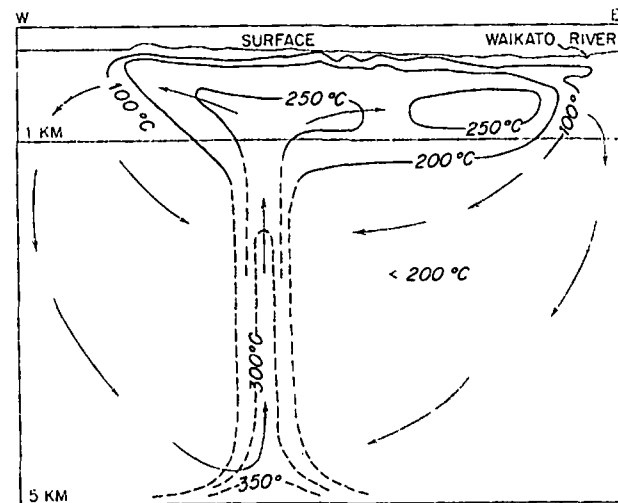


FIG. 28. Vertical section through the modern geothermal system at Wairakei, New Zealand, showing actual measured (solid lines) and estimated (dashed lines) isotherms down to a depth of 5 km beneath the surface (modified after Banwell, 1961, and Elder, 1965). The approximate flow lines of the meteoric water are shown with arrows.

a "mushroom-shaped" plume. At any particular depth the isotherms form a series of concentric ovals, with temperature increasing toward the center.

If the water/rock ratios were roughly constant throughout the areas shown for the Bohemia and Tonopah districts in Figures 23 and 26, then the $\delta^{18}\text{O}$ contours as shown would also represent isotherms, with the temperature increasing toward the center of each district. Table 1 shows some calculated temperature values for these "fossil" isotherms, based on assuming various constant values for w/r. The calculated temperature gradients seem to be fairly reasonable and there is an apparent correspondence between these "fossil" isotherms and those measured at Wairakei.

Unfortunately, it is not strictly valid to assume constant w/r ratios throughout the alteration zones. For instance, we might equally well have assumed a constant temperature, in which case the $\delta^{18}\text{O}$ contours would represent contours of constant w/r, also increasing toward the center of the district. At Wairakei, the higher temperatures in the rising plume of H_2O are also associated with higher w/r ratios because more H_2O is pumped through that region. Thus, both effects probably go hand-in-hand and the $\delta^{18}\text{O}$ contours in Figures 23 and 26 would represent neither exact isotherms nor exact contours of constant w/r, but some combination of the two extremes.

Porphyry Copper Deposits

We have shown above that in volcanic terranes deep circulation and interaction between surface waters and epizonal intrusions is to be expected and is a common phenomenon. Profound and extensive $\delta^{18}\text{O}$ effects are produced because the meteoric-water/rock ratios are very high. What happens, however, if the country rocks are sedimentary rocks or Precambrian crystalline rocks where the permeabilities are not so great? The $\delta^{18}\text{O}$ effects will be smaller and they may be so small, given the natural isotopic variations in igneous rocks, that no clear-cut $\delta^{18}\text{O}$ changes may be discernible. However, even if the $\delta^{18}\text{O}$ effects are very small, the δD values of fluid inclusions or of OH-bearing minerals will be affected by the influx of external waters, because the initial H_2O concentrations of most igneous rocks are so small.

Another problem exists with D/H ratios, however. This is the fact that the most common meteoric waters on earth have δD values that are similar to primary magmatic waters (Fig. 9). Over much of the North American continent (Fig. 6), the surface meteoric waters and the saline formation waters (Fig. 9) have δD values of -40

to -90 ; the latter values are too close to the range of magmatic values to provide any test of discrimination.

Because of the obstacles mentioned above, studies of intrusive bodies that involve a small water/rock ratio can only be definitive in certain geographic areas. Favorable regions would include submarine environments where $\delta\text{D} \approx 0$ or northerly regions such as Montana or British Columbia where $\delta\text{D}_{\text{H}_2\text{O}}$ can be lower than -130 . Areas of high elevation can in principle also be used, but generally it is difficult to ascertain the original surface elevation above a specific ore deposit. At least for Tertiary ore deposits, latitude is a much more definite variable than original surface elevation.

A proper approach then might be to examine a certain class of ore deposits that occur over a wide geographic area. The isotopic composition of minerals formed by magmatic-hydrothermal solutions would be expected to be independent of latitude, whereas the minerals formed from meteoric hydrothermal or "connate"-hydrothermal solutions should show the proper latitudinal dependence in δD (and perhaps to some extent in $\delta^{18}\text{O}$). The above approach was utilized by Sheppard et al. (1969, 1971) and Sheppard and Taylor (1974) in their studies of porphyry copper deposits in North America. Their isotopic data are reproduced in Figure 29.

The δD values of hypogene clay minerals and sericites from the deposits shown on Figure 29 become lower as one moves north from Arizona and New Mexico (Santa Rita, Safford, Copper Creek, Mineral Park) to Utah, Colorado, and Nevada (Bingham, Ely, Climax, St. George) to Montana, Idaho, and Washington (Butte, Wickes, Spokane, Ina). It is thus clear that the δD values of these minerals are a result of interaction with meteoric waters, the only question is whether or not they represent the original δD values of the sericites and clays or are a result of later exchange.

The possibility of later exchange cannot be totally ruled out, but in order to explain all of the δD - $\delta^{18}\text{O}$ relationships this would have to be a pervasive exchange with heated meteoric waters, not simply partial low-temperature exchange with ground waters (see supergene discussion above).

The δD values of the hypogene clays and sericites at a given deposit such as Santa Rita are much more uniform than would be expected on the basis of variable degrees of partial exchange with such groundwaters. Therefore, the D/H data require that a geothermal H_2O circulation system was present at each deposit. In addition, the very low $\delta^{18}\text{O}$ values in sericites and clays from some

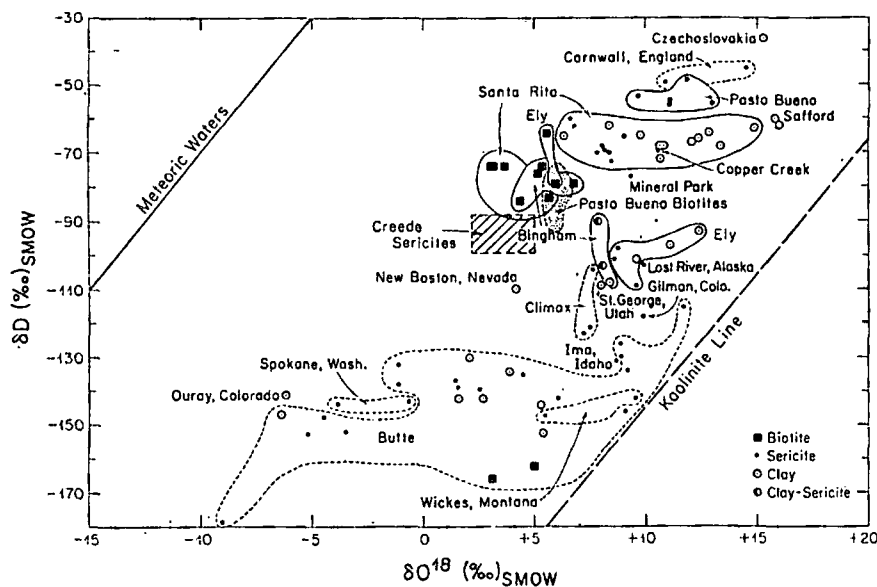


FIG. 29. Plot of δD versus $\delta^{18}O$ for various hydrothermal minerals from ore deposits (modified after fig. 2 of Sheppard et al., 1971). The field of Creede, Colorado, sericites is from Bethke et al. (1973), the Butte data are from Sheppard and Taylor (1974), and the Pasto Buena data are from Landis (1972).

of the northerly deposits (Butte, Spokane) independently argue that these effects are not due to secondary exchange, as also does the similarity in δD values of sericites of vastly different grain size from the Climax deposit (Sheppard et al., 1971, p. 524, 538).

In striking contrast to the sericites and clays, the δD and $\delta^{18}O$ values of the hydrothermal biotites from porphyry copper deposits form a very tight grouping similar to "normal" igneous biotites (Fig. 29) and show no relationship to latitude. Biotites from the El Salvador deposit in Chile also have identical isotopic compositions (S. M. F. Sheppard, pers. commun.). The only biotites that do not fall within this narrow range are the very fine grained EDM biotites from Butte; the latter are thought to have exchanged D/H with the low- δD , main-stage ore fluids at Butte, because the samples come from areas where there has been intense, subsequent main-stage mineralization (Sheppard and Taylor, 1974).

The hydrothermal biotites in porphyry copper deposits thus all appear to have formed from H_2O with an isotopic composition plotting well within the hypothetical field of primary magmatic waters (compare Figs. 9 and 31), whereas the clays and sericites appear to have formed from heated meteoric waters of some type. The amounts of H_2O , however, are less than in the low- ^{18}O volcanic intrusive terranes discussed previously. This implies that somewhat similar, but less extensive, hydrothermal convective circulation systems are

also established around the epizonal porphyry copper stocks, but that the K-silicate alteration assemblages in the cores of the stocks are not related to these external systems. These concepts are shown diagrammatically in Figure 30.

Magmatic-hydrothermal solutions under lithostatic pressure are formed during the late stages of crystallization in the upper, interior portions of a porphyry stock. Outside the stock a meteoric-hydrothermal circulation is established under hydrostatic pressures that are probably only one-third to one-half as high as the pressures inside the stock. These external waters might be either meteoric ground waters or saline formation waters, because the latter also display the proper isotopic dependence on latitude (Fig. 9). Both hydrothermal systems are simultaneously present early in the history of the stock, but the external system will persist even after the magmatic-hydrothermal system fades away. With time, as the "heat engine" of the stock cools off, the external hydrothermal system very likely collapses onto the hydrothermally altered rocks formed by the internal system; the argillic and sericite-pyrite alteration zones will then be locally superimposed upon the K-feldspar-biotite alteration zones or upon the fresh intrusive.

As shown in Figure 30, the major locus of chalcopyrite deposition tends to be along the boundary between the two different types of hydrothermal systems (Lowell and Guilbert, 1970). The reasons for this localization are not known,

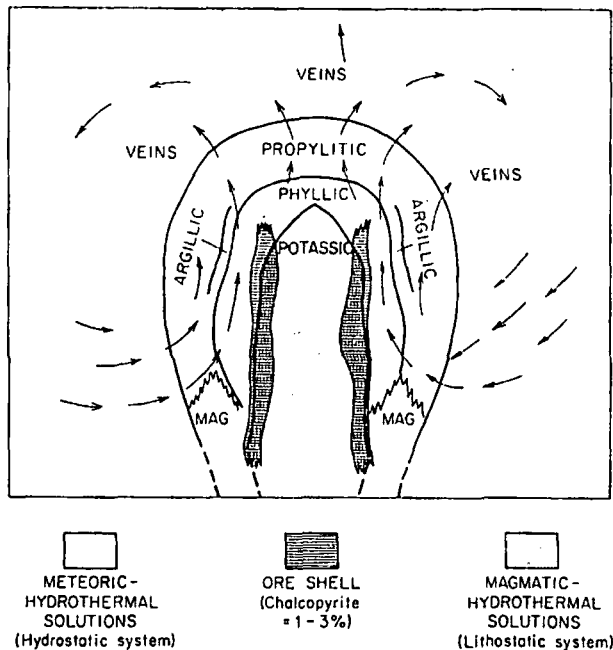


FIG. 30. Schematic cross section through a typical porphyry copper deposit (modified after Lowell and Guilbert, 1970), showing the two types of hydrothermal fluids generated in such environments, as determined from D/H and $^{18}\text{O}/^{16}\text{O}$ measurements (Sheppard et al., 1969, 1971).

but it is plausible that it might be the result of the drastic changes in pressure, temperature, pH, salinity, etc., that must occur across this boundary during hydrothermal alteration.

The above model envisages that, although the H_2O has at least two major sources, the source of the S, Cu, and other heavy metals in these systems is basically the porphyry stock itself, with some minor contribution of materials leached from surrounding country rocks. The size and intensity of the external hydrothermal system varies considerably in known porphyry copper deposits, from "wet" types (e.g., Bingham, Morenci) having high pyrite-to-chalcopyrite ratios and surrounded by enormous halos of pyrite-sericite-quartz, to "dry" deposits (e.g., Bethlehem) with relatively minor sericite-pyrite zones (Lowell and Guilbert, 1970). These variations in size of the external system are to be expected because the permeabilities and amounts of H_2O available in the country rocks must be quite variable.

Other Ore Deposits

Figure 31 shows a plot of the calculated waters in equilibrium with various hydrothermal alteration assemblages given in Figure 29, at their presumed temperatures of formation. Also included are data from other ore deposits at Creede,

Providencia, Tonopah, and Bluebell. The hydrothermal fluids at most of the ore deposits (shown on Fig. 31) clearly must have contained a dominant meteoric water component. However, a few of the deposits in addition to the porphyry copper K-silicate assemblages exhibit calculated waters that plot within the range of primary magmatic H_2O ; for such deposits the isotopic data are compatible with a magmatic origin, but except for localities at high latitudes the isotope analyses then will be ambiguous and inconclusive as to the ultimate origin of the hydrothermal fluids.

The major isotopic characteristic of many of the calculated hydrothermal fluids shown on Figure 31 is that, at a given locality, there is commonly a very wide range in $\delta^{18}\text{O}$ but a narrow range of δD (Bluebell is the best example; Ohmoto and Rye, 1970). This is exactly what is seen for modern geothermal waters of meteoric origin that have undergone the type of ^{18}O shifts shown on Figures 7 and 8. This reinforces the conclusion that meteoric waters are the dominant source of the H_2O , particularly in volcanic localities such as Tonopah and Creede, where the calculated waters plot near the meteoric water line and thus can have undergone only minor ^{18}O shifts.

If an ore deposit shows a large δD range in its calculated waters, this generally will mean that more than one source of H_2O is involved. As pointed out above, there are ways to change the δD value of a hydrothermal fluid by boiling (Fig. 8) or by oxidation-reduction reactions involving large production or consumption of coexisting H_2 gas in the fluid. Except in unusual cases, however, these effects will be small and in any individual case they are predictable if a careful study is made of the ore deposit. Considering the complex environments of many ore deposits, it is not unreasonable that two (or three or more) different types of H_2O might be involved either simultaneously or at different stages in the history of ore deposition at a given locality, as for example was shown for the porphyry copper deposits. This is therefore the most probable explanation of major δD fluctuations in the calculated hydrothermal fluids in most ore deposits and it may also explain some of the $\delta^{18}\text{O}$ variations, although the latter can change so readily through exchange with the large available rock-oxygen reservoir that only very detailed studies can sort out these effects.

Excluding the porphyry copper deposits, which have already been dealt with, the only individual deposits shown on Figure 31 that exhibit a large δD range are Butte and Climax (see Hall et al., 1973). The large δD range at Butte is real, but most of the samples show only a narrow range

of δD ; excluding two anomalous sericites and the two EDM biotites (probably exchanged, see above), all the other Butte samples shown on Figure 29 have a δD range of only about 20 per mil. Thus most of the ore deposition and alteration at Butte can be pretty well attributed to a single type of meteoric-hydrothermal fluid (Sheppard and Taylor, 1974). The Climax molybdenum deposit, however, seems to require at least two major sources of H_2O , one that is meteoric in origin and another that may be magmatic (Sheppard et al., 1971; Hall et al., 1973).

In summary, it is useful to mention briefly a few of the other ore deposits for which δD and $\delta^{18}O$ analyses have been made.

Pasto Bueno, Peru

A very complete isotopic, fluid inclusion, and mineralogical study was done by Landis (1972) on this tungsten-base metal deposit associated with an intrusive stock emplaced into sedimentary rocks. Landis showed that at least two types of H_2O were involved, one with a δD as high as -29 and the other a meteoric water component with a δD lower than -90 . He concludes that the high-D water is probably magmatic, but that a metamorphic origin cannot be excluded. A "connate" formation water is also a possibility because a value of -29 seems abnormally high for a primary magmatic H_2O (see Fig. 9). The isotopic compositions of hydrothermal sericites and biotites from Pasto Bueno are plotted on Figure 29. Note that the biotites are isotopically similar to the biotites of porphyry copper deposits.

The calculated $\delta^{18}O$ values of fluids associated with the early greisen start out in the magmatic range, but during most of ore deposition the fluids fluctuate between $+2$ and $+6$, compatible only with a major meteoric water component in the system. The δD of the hydrothermal fluid at Pasto Bueno shows two pronounced "dips" in the middle of the paragenetic sequence. These "dips" both coincide with the deposition of wolframite and it is likely that both effects are a result of periodic influx of the meteoric-water component into the vein systems. At the very latest stages of mineralization, the meteoric-water component becomes completely predominant and the δD values dip below -110 .

Echo Bay, Northwest Territories, Canada

An isotopic and mineralogic study by Robinson and Ohmoto (1973) on this Precambrian U-Ni-Ag-Cu vein deposit emplaced into volcanic tuffs showed that the ore-forming fluid was probably

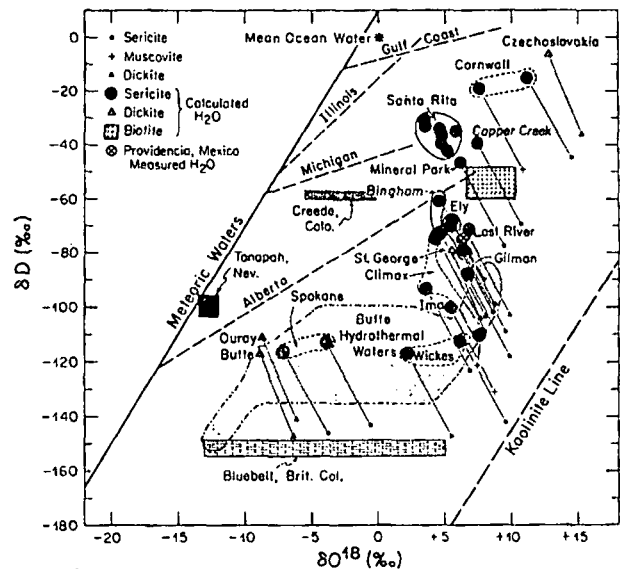


FIG. 31. Plot of δD versus $\delta^{18}O$ for calculated hydrothermal waters from a variety of ore deposits, mainly from western North America. This is modified after figure 10 of Sheppard et al. (1971) with the addition of data for Creede (Bethke et al., 1973), Tonopah (Taylor, 1973), and Bluebell (Ohmoto and Rye, 1970). The calculations are based on a variety of methods of estimating the temperatures of formation of the different mineral assemblages, as discussed in the above references. The biotite "box" shown represents the waters that would have coexisted in equilibrium with the hydrothermal biotites from Ely, Bingham, and Santa Rita at $650^{\circ}C$. Also shown are the trend lines for oil-field formation waters from various sedimentary basins in the mid-continent of North America (from Fig. 9).

sea water. Circulation and heating of the ocean water to 100° to $250^{\circ}C$ is thought to have been produced by intrusion of diabase about 1,450 m.y. ago. The calculated $\delta^{18}O$ value of the H_2O is $+1.0 \pm 2.5$ per mil, practically identical to present-day ocean water.

Kuroko massive sulfide deposits, Japan

Ohmoto et al. (1970) have shown that $\delta^{18}O$ and δD analyses of these "black ore" deposits in volcanic rocks indicate involvement of ocean water in the hydrothermal fluids. It may well be that many volcanogenic massive sulfide deposits are formed in submarine environments from heated ocean waters or brines derived therefrom, such as the Red Sea hot brine (Craig, 1966). Other probable examples of such marine-hydrothermal interactions are the massive sulfide deposits associated with the Troodos ophiolite complex on Cyprus (S. M. F. Sheppard, pers. commun.).

Providencia, Mexico

Rye (1966) and Rye and O'Neil (1968) showed that the δD and $\delta^{18}O$ values of the hydrothermal

fluids responsible for these Pb-Zn deposits were remarkably uniform at $\delta^{18}\text{O} \approx +7$ and $\delta\text{D} \approx -75$, in spite of wide fluctuations in salinity. This fits the characteristics of a magmatic-hydrothermal fluid almost perfectly and this is the origin preferred by Rye (1966). Unfortunately, the δD values of surface meteoric waters in this region of Mexico are very similar as well and so the isotope data are not strictly conclusive. This ambiguity is particularly a problem in such limestone terranes because the high- $\delta^{18}\text{O}$ values and ready exchangeability of limestones will allow circulating meteoric-hydrothermal water to attain $\delta^{18}\text{O}$ values as high as $+6$.

Darwin, California

Rye and Hall (1971) analyzed minerals from this Ag-Pb-Zn ore deposit (late Cretaceous?) associated with contact metamorphosed carbonate rocks. They concluded that the ore fluids had $\delta\text{D} \approx -60$ to -70 and $\delta^{18}\text{O} \approx +4$ to $+7$, reasonably consistent with a magmatic-hydrothermal origin. However, heated meteoric waters in this region also may have attained similar values (see Figs. 6 and 32).

Casapalca, Peru

Sawkins and Rye (1970) are able to make a much more convincing case for magmatic-hydrothermal ore deposition in this Ag-Pb-Zn deposit, because the deposit is very young (≈ 5 m.y. old), the calculated isotopic compositions of the ore fluids lie within the primary magmatic range ($\delta^{18}\text{O} \approx +7$ to $+8$, $\delta\text{D} \approx -50$ to -65), and the present-day local meteoric waters are very light. However, heated formation waters in the Casapalca area also conceivably could have attained these isotopic compositions. Low- δD and $\delta^{18}\text{O}$ values in the later stages of mineralization indicate an influx of meteoric waters into the hydrothermal system.

Mississippi Valley-type Pb-Zn deposits

The one very important type of ore deposit that unquestionably has formed from heated formation waters are these relatively low-temperature deposits from the midcontinent region of North America. Hall and Friedman (1963, 1969) and Pinckney and Rye (1972) have shown that the isotopic compositions of these ore fluids are identical to those of nearby oil-field brines (see Fig. 9) and many other lines of evidence support this correlation.

Bluebell, British Columbia

An important isotopic study of this Pb-Zn replacement deposit in limestones was made by Ohmoto and Rye (1970). This deposit occurs in a geographic area that is very favorable for distinguishing between magmatic and meteoric waters and, as shown in Figure 31, because of this it is possible to state that the Period III late-stage, vug period of ore deposition only involved meteoric-hydrothermal waters with a remarkably uniform δD value of -152 ± 5 , but a very wide range of $\delta^{18}\text{O}$ and salinity. The end-stages of deposition at Bluebell cannot have involved any significant magmatic component; the fluids may have formed from heated meteoric waters that circulated through an evaporite sequence.

Ducktown, Tennessee

Addy and Ypma (1973) have measured the δD and $\delta^{18}\text{O}$ values of muscovites, chlorites, and biotites from this massive sulfide copper deposit. There are indications that this stratiform ore body has undergone metamorphism and, inasmuch as the measured isotopic compositions of the OH-bearing minerals are similar to those of typical metasediments shown in Figure 10, they are compatible with this hypothesis.

Tertiary Meteoric Waters in the United States

Because of the almost ubiquitous presence of meteoric H_2O in many intrusive-volcanic areas of hydrothermal alteration and because of its identification as a major component at least at some stage of ore deposition in so many localities, it is instructive to combine these data with analyses of Tertiary supergene mineral assemblages (Sheppard et al., 1969) and Tertiary weathering deposits (Lawrence, 1970). If this is done, there are enough data to make a very rough map of the isotopic compositions of Tertiary meteoric waters in the western United States. Obviously, this should strictly be done only for certain precise ages in the Tertiary, but there are at present not sufficient data available to do this. Ultimately, such finer subdivisions may be possible.

The calculated δD values of Tertiary meteoric waters are plotted on the map in Figure 32 and they demonstrate that, during much of the Tertiary, the basic geographic pattern of δD and $\delta^{18}\text{O}$ in surface precipitation must have been similar to the present-day pattern. However, comparison with Figure 6 shows that the Tertiary δD contours tend to be shifted toward heavier values by about 10 to 15 per mil (1 to 2 per mil in ^{18}O).

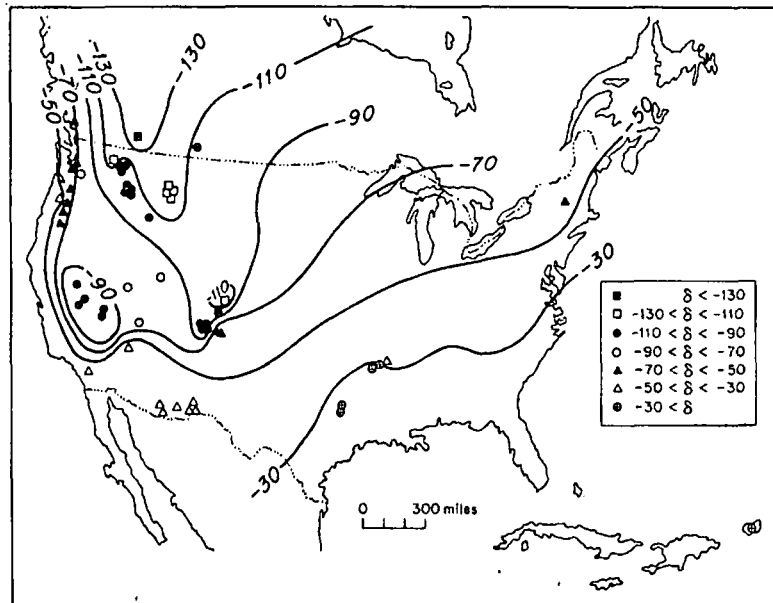


FIG. 32. Map of the United States, showing calculated δD values of Tertiary meteoric waters based on (1) data from various Tertiary meteoric-hydrothermal systems discussed in the present paper, and (2) data on Tertiary supergene clays and weathering deposits, from studies by Sheppard et al. (1971) and Lawrence (1970). Highly approximate Tertiary δD contours are drawn on the map. The Tertiary δD values are consistently about 10 to 15 per mil higher than the present-day δD values of surface waters shown in Figure 6, indicating either that during much of the Tertiary the climate was warmer and more temperate or that there was a general lowering of the topographic barriers that exist today.

This is compatible with the abundant evidence for a warmer, more temperate Tertiary climate based on extensive kaolinitic weathering deposits in the Pacific northwest (data on some of these deposits are used in drawing the contours on Fig. 32; Lawrence, 1970) and on other climatic evidence (Axelrod, 1964). Although it is very approximate at present, Figure 32 at least shows the consistency of the isotopic data from different geologic environments and demonstrates beyond any shadow of a doubt that we truly are observing meteoric H_2O in the Tertiary ore deposits and hydrothermal alteration systems.

Conclusions

Oxygen and hydrogen isotope studies have shown that the most common types of water in hydrothermal systems in the uppermost two to four miles of the continental crust are meteoric ground waters and "connate" formation waters or combinations of the two. The most common type of water in analogous submarine hydrothermal systems is sea water.

Magmatic waters and metamorphic waters are of course dominant in deep-seated plutonic complexes, but in most such areas there is little

mineralogical evidence for the massive introduction of H_2O and hydrogen metasomatism that is such a ubiquitous feature of most hydrothermal ore deposits. In large part this difference is a result of the much higher temperatures involved. The H_2O is mostly tied up in primary OH-bearing minerals of the igneous and metamorphic assemblages. Nevertheless, wherever there are thermal anomalies in the earth's crust (e.g., around every igneous intrusion) there will be a tendency for a hydrothermal convective circulation system to be set up. This will be restricted only by the smaller availability of H_2O in deep-seated rocks and also by the much lower permeabilities of such rocks at high pressures. Favoring these effects, however, is the fact that much larger volumes of the crust are involved, temperatures are much higher, and the time scale over which the processes occur is markedly longer.

Isotopic evidence for important, large-scale interactions between plutons and externally derived metamorphic waters has been presented by Taylor (1970), Shieh and Taylor (1969a), and Turi and Taylor (1971a and b). Enormous hydrothermal transfers and exchange of material have apparently taken place in these deep-seated plutonic complexes, but the effects mainly show up only in the $\delta^{18}O$

values, because the δD values of magmatic and metamorphic waters overlap (Fig. 9). Unfortunately, except in favorable circumstances where there happens to be a juxtaposition of rocks with markedly different $\delta^{18}O$ values, even the $\delta^{18}O$ effects may not be sufficiently large to give conclusive answers. Whereas in the upper levels of the crust, waters with a great variety of origins and isotopic compositions exist, in the deep-seated plutonic complexes the only waters available are of magmatic or metamorphic origin, and these tend to attain similar isotopic compositions at the very highest grades of metamorphism.

Summing up, even though this report has stressed the importance of waters of surface origin in hydrothermal systems, the writer does not want to leave the impression that magmatic and metamorphic waters are not important. The opposite in fact is true; considering the earth as a whole, the latter types of H_2O are by far the most important sources of hydrothermal solutions. However, most hydrothermal ore deposits are apparently formed at relatively shallow levels of the earth's crust where a whole variety of waters can play an important role and it is just in such environments that the techniques of hydrogen and oxygen isotope geochemistry show promise of being able to help solve significant problems.

Acknowledgments

I wish to thank S. M. F. Sheppard and S. Epstein for stimulating discussions of this work. Financial support of the National Science Foundation, Grant Number GA 30997X, is also gratefully acknowledged.

DIVISION OF GEOLOGICAL AND PLANETARY
SCIENCES
CALIFORNIA INSTITUTE OF TECHNOLOGY
PASADENA, CALIFORNIA 91109

REFERENCES

- Addy, S. K., and Ypma, P. J. M., 1973, Metamorphism of sulfide deposits and the metamorphogenic circulation of pure water at Ducktown, Tennessee: *Geol. Soc. America Ann. Mtg., Abstracts with Programs*, p. 529-530.
- Anderson, A. T., Jr., Clayton, R. N., and Mayeda, T. K., 1971, Oxygen isotope thermometry of mafic igneous rocks: *Jour. Geology*, v. 79, p. 715-729.
- Arnason, B., and Sigurgeirsson, T., 1968, Deuterium content of water vapor and hydrogen in volcanic gas at Surtsey, Iceland: *Geochim. et Cosmochim. Acta*, v. 32, p. 807-813.
- Axelrod, D. J., 1964, The Miocene Trapper Creek flora of southern Idaho: *Calif. Univ. Publ. Geol. Sci.*, v. 51, p. 1-148.
- Banwell, C. J., 1961, Geothermal drillholes—physical investigations: U. N. Conf. New Sources of Energy, Paper G53.
- Barnes, H. L., and Czamanske, G. K., 1967, Solubilities and transport of ore minerals, in Barnes, H. L., ed., *Geochemistry of hydrothermal ore deposits*: New York, Holt, Rinehart, and Winston, p. 334-381.
- Bethke, P. M., Rye, R. O., and Barton, P. B., Jr., 1973, Hydrogen, oxygen, and sulfur isotopic compositions of ore fluids in the Creede district, Mineral County, Colorado: *Geol. Soc. America Ann. Mtg., Abstracts with Programs*, p. 549.
- Bigeleisen, J., and Mayer, M. G., 1947, Calculation of equilibrium constants for isotopic exchange reactions: *Jour. Chem. Physics*, v. 15, p. 261.
- Bottinga, Y., 1968, Calculation of fractionation factors for carbon and oxygen isotopic exchange in the system calcite-carbon dioxide-water: *Jour. Phys. Chemistry*, v. 72, p. 800-808.
- 1969, Calculated fractionation factors for carbon and hydrogen isotope exchange in the system calcite-carbon dioxide-graphite-methane-hydrogen-water vapor: *Geochim. et Cosmochim. Acta*, v. 33, p. 49-64.
- and Craig, H., 1968, High temperature liquid-vapor fractionation factors for H_2O - HDO - H_2O^{18} [abs.]: *Am. Geophys. Union Trans.*, v. 49, p. 356.
- Bottinga, Y., and Javoy, M., 1973, Comments on oxygen isotope geothermometry: *Earth Planet. Sci. Letters*, v. 20, p. 250-265.
- Buddington, A. F., and Callaghan, E., 1936, Dioritic intrusive rocks and contact metamorphism in the Cascade Range in Oregon: *Am. Jour. Sci.*, v. 31, p. 421-449.
- Clayton, R. N., Friedman, I., Graf, D. L., Mayeda, T. K., Meents, W. F., and Shimp, N. F., 1966, The origin of saline formation waters: I. Isotopic composition: *Jour. Geophys. Research*, v. 71, p. 3869-3882.
- Clayton, R. N., Muffler, L. J. P., and White, D. E., 1968, Oxygen isotope study of calcite and silicates of the River Ranch No. 1 Well, Salton Sea geothermal field, California: *Am. Jour. Sci.*, v. 266, p. 968-979.
- Clayton, R. N., O'Neil, J. R., and Mayeda, T., 1972, Oxygen isotope exchange between quartz and water: *Jour. Geophys. Research*, v. 77, p. 3057-3067.
- Craig, H., 1961, Isotopic variations in meteoric waters: *Science*, v. 133, p. 1702-1703.
- 1963, The isotopic geochemistry of water and carbon in geothermal areas, in Tongiorgi, E., ed., *Nuclear geology on geothermal areas*, Spoleto: Pisa, Consiglio Nazionale della Ricerca, Laboratorio de Geologia Nucleare, p. 17-53.
- 1966, Isotopic composition and origin of the Red Sea and Salton Sea geothermal brines: *Science*, v. 154, p. 1544-1548.
- Boato, G., and White, D. E., 1956, Isotopic geochemistry of thermal waters: *Proc. 2nd Conf. Nuclear Processes in Geologic Settings*, Nat'l Research Council, Nuclear Sci. Ser. Rept. 19, p. 29-38.
- Craig, H., Gordon, L., and Horibe, Y., 1963, Isotopic exchange effects in the evaporation of water: *Jour. Geophys. Research*, v. 68, p. 5079-5087.
- Dansgaard, W., 1964, Stable isotopes in precipitation: *Tellus*, v. 16, p. 436-468.
- Dowgiallo, J., and Tongiorgi, E., 1972, The isotopic composition of oxygen and hydrogen in some brines from the Mesozoic in northwest Poland: *Geothermics*, v. 1, p. 67-69.
- Elder, J. W., 1965, Physical process in geothermal areas, in *Terrestrial heat flow*: *Geoph. Mon. 8*, NAS-NRC No. 1288, Amer. Geophys. Union, p. 211-239.
- Epstein, S., and Mayeda, T., 1953, Variation of O^{18} content of waters from natural sources: *Geochim. et Cosmochim. Acta*, v. 4, p. 213-224.
- Epstein, S., Sharp, R. P., and Gow, A. J., 1965, Six-year record of oxygen and hydrogen isotope variations in South Pole firn: *Jour. Geophys. Research*, v. 70, p. 1809.
- 1970, Antarctic ice sheet: Stable isotope analyses of Byrd station cores and interhemispheric climatic implications: *Science*, v. 168, p. 1570-1572.
- Epstein, S., and Taylor, H. P., 1971, O^{18}/O^{16} , Si^{30}/Si^{28} , D/H , and C^{13}/C^{12} ratios lunar samples: *Proc. 2nd Lunar Sci. Conf.*, M.I.T. Press, v. 2, p. 1421-1441.
- 1972, O^{18}/O^{16} , Si^{30}/Si^{28} , C^{13}/C^{12} , and D/H studies of Apollo 14 and 15 samples: *Proc. 3rd Lunar Sci. Conf.*, *Geochim. et Cosmochim. Acta Supp.* 3, v. 2, p. 1429-1454.

- Eugster, H. P., and Skippen, G. B., 1967, Igneous and metamorphic reactions involving gas equilibria, in Abelson, P. H., ed., *Researches in geochemistry*: New York, John Wiley and Sons, v. 2, p. 492-520.
- Forester, R. W., and Taylor, H. P., 1972, Oxygen and hydrogen isotope data on the interaction of meteoric ground waters with a gabbro-diorite stock, San Juan Mountains, Colorado: *Internat. Geol. Cong.*, 24th, Montreal 1972, sec. 10, *Geochemistry*, p. 254-263.
- Friedman, I., 1953, Deuterium content of natural water and other substances: *Geochim. et Cosmochim. Acta*, v. 4, p. 89-103.
- 1967, Water and deuterium in pumice from the 1959-60 eruption of Kilauea volcano, Hawaii: *U. S. Geol. Survey Prof. Paper 575-B*, p. B120-B127.
- Rediel, A. C., Schoen, B., and Harris, J., 1964, The variation in the deuterium content of natural waters in the hydrologic cycle: *Rev. Geophysics*, v. 2, p. 177-224.
- Garlick, D. G., and Epstein, S., 1966, The isotopic composition of oxygen and carbon in hydrothermal minerals at Butte, Montana: *ECON. GEOL.*, v. 61, p. 1325-1335.
- Garlick, D. G., MacGregor, I. D., and Vogel, D. E., 1971, Oxygen isotope ratios in eclogites from kimberlites: *Science*, v. 172, p. 1025-1027.
- Godfrey, J. D., 1962, The deuterium content of hydrous minerals from the east-central Sierra Nevada and Yosemite National Park: *Geochim. et Cosmochim. Acta*, v. 26, p. 1215-1245.
- Hall, W., and Friedman, I., 1963, Composition of fluid inclusions, Cave-in-Rock fluorite district, Illinois, and Upper Mississippi Valley zinc-lead district: *ECON. GEOL.*, v. 58, p. 886-911.
- 1969, Oxygen and carbon isotopic composition of ore and host rock of selected Mississippi Valley deposits: *U. S. Geol. Survey Prof. Paper 650-C*, p. C140-C148.
- and Nash, J. T., 1973, Fluid inclusion and light stable isotope study of the Climax molybdenum deposits, Colorado: *Geol. Soc. Amer. Ann. Mtg.*, Abstracts with Programs, p. 649-650.
- Hitchon, B., and Friedman, I., 1969, Geochemistry and origin of formation waters in the western Canada sedimentary basin—I. Stable isotopes of hydrogen and oxygen: *Geochim. et Cosmochim. Acta*, v. 33, p. 1321-1349.
- Hitchon, B., and Krouse, H. R., 1972, Hydrogeochemistry of surface waters of the Mackenzie River drainage basin, Canada, III. Stable isotopes of oxygen, carbon, and sulfur: *Geochim. et Cosmochim. Acta*, v. 36, p. 1337-1358.
- Kharaka, Y. K., Berry, F. A. F., and Friedman, I., 1973, Isotopic composition of oil-field brines from Kettleman North Dome, California, and their geologic implications: *Geochim. et Cosmochim. Acta*, v. 37, p. 1899-1903.
- Knauth, L. P., and Epstein, S., 1971, Oxygen and hydrogen isotope relationships in cherts and implications regarding the isotopic history of the hydrosphere: *Geol. Soc. America Ann. Mtg.*, Abstracts with Programs, p. 624.
- Kokubu, N., Mayeda, T., and Urey, H. C., 1961, Deuterium content of minerals, rocks and liquid inclusion from rocks: *Geochim. et Cosmochim. Acta*, v. 21, p. 247-256.
- Kuroda, Y., Suzuoki, T., Matsuo, S., and Kanisawa, S., 1974, D/H fractionation of coexisting biotite and hornblende in some granitic rock masses: *Earth Planet. Sci. Lett.* (in press).
- Landis, G. P., 1972, Geologic, fluid inclusion, and stable isotope studies of a tungsten-base metal ore deposit, Pasto Bueno, northern Peru: Ph.D. thesis, Univ. Minn., 160 p.
- Lawrence, J. R., 1970, O^{18}/O^{16} and D/H ratios of soils, weathering zones and clay deposits: unpub. Ph.D. thesis, California Inst. Technology, 263 p.
- and Taylor, H. P., 1971, Deuterium and oxygen-correlation: Clay minerals and hydroxides in Quaternary soils compared to meteoric waters. *Geochim. et Cosmochim. Acta*, v. 35, p. 993-1003.
- 1972, Hydrogen and oxygen isotope systematics in weathering profiles: *Geochim. et Cosmochim. Acta*, v. 36, p. 1377-1393.
- Lawson, A. C., 1914, Is the Boulder "batholith" a laccolith? A problem in ore genesis: *Univ. Calif. Publ. Geol. Sci.*, v. 8, p. 1-15.
- Lipman, P. W., Steven, T. A., and Mehnert, H. H., 1970, Volcanic history of the San Juan Mountains, Colorado, as indicated by potassium-argon dating: *Geol. Soc. America Bull.*, v. 81, p. 2329-2352.
- Lowell, J. D., and Guilbert, J. M., 1970, Lateral and vertical alteration-mineralization zoning in porphyry ore deposits: *ECON. GEOL.*, v. 65, p. 373-408.
- Lowenstam, H. A., 1961, Mineralogy, O-18/O-16 ratios, and strontium and magnesium contents of recent and fossil brachiopods and their bearing on the history of the oceans: *Jour. Geology*, v. 69, p. 241.
- Luedke, R. G., and Burbank, W. S., 1968, Volcanism and caldera development in the western San Juan Mountains, Colorado, in Epis, R. C., ed., *Cenozoic volcanism in the southern Rocky Mountains*: Colorado Sch. Mines Quart., v. 63, p. 175-208.
- Matsuhisa, Y., Honma, H., Matsubaya, O., and Sakai, H., 1972, Oxygen isotopic study of the Cretaceous granitic rocks in Japan: *Contr. Mineralogy Petrology*, v. 37, p. 65-74.
- Matsuhisa, Y., Matsubaya, O., and Sakai, H., 1973, Oxygen isotope variations in magmatic differentiation processes of the volcanic rocks in Japan: *Contr. Mineralogy Petrology*, v. 39, p. 277-288.
- Merlivat, L., Botter, R., and Nief, G., 1963, Fractionnement isotopique au cours de la distillation de l'eau: *Jour. Chim. Physique*, v. 60, p. 56-59.
- Merlivat, L., and Nief, G., 1965, Fractionnement isotopique lors des changements d'état solide-vapeur et liquide-vapeur de l'eau a des temperatures inferieurs a 0°C: unpublished manuscript.
- Meyer, C., and Hemley, J. J., 1967, Wall rock alteration, in Barnes, H. L., ed., *Geochemistry of hydrothermal ore deposits*: New York, Holt, Rinehart, and Winston, p. 166-235.
- Moorbath, S., and Bell, J. D., 1965, Strontium isotope abundance studies and rubidium-strontium age determinations on Tertiary igneous rocks from the Isle of Skye, northwest Scotland: *Jour. Petrology*, v. 6, p. 37-66.
- Moorbath, S., and Welke, H., 1969, Lead isotope studies on igneous rocks from the Isle of Skye, northwest Scotland: *Earth Planet. Sci. Lett.*, v. 5, p. 217-230.
- Moore, J. G., 1970, Water content of basalt erupted on the ocean floor: *Contr. Mineralogy Petrology*, v. 28, p. 272-279.
- Muchlenbachs, K., Anderson, A. T., and Sigvaldason, G. E., 1972, The origins of O^{18} -poor volcanic rocks from Iceland: *Am. Geophys. Union Trans. [abs.]* v. 53, p. 566.
- Muchlenbachs, K., and Clayton, R. N., 1972, Oxygen isotope studies of fresh and weathered submarine basalts: *Can. Jour. Earth Sci.*, v. 9, p. 172-184.
- Nash, J. T., 1972, Fluid inclusion studies of some gold deposits in Nevada: *U. S. Geol. Survey Prof. Paper 800-C*, C15-C-19.
- Nolan, T. B., 1935, The underground geology of the Tonopah mining district, Nevada: *Nevada Univ. Bull.* v. 29, no. 5, 49 p.
- Ohmoto, H., and Rye, R. O., 1970, The Bluebell Mine, British Columbia. I. Mineralogy, paragenesis, fluid inclusions, and the isotopes of hydrogen, oxygen, and carbon: *ECON. GEOL.*, v. 65, p. 417-437.
- Ohmoto, H., Kajiwarra, Y., and Date, J., 1970, The Kuroko ores in Japan: products of sea water?: *Geol. Soc. America Ann. Mtg.*, Abstracts with Programs, p. 640-641.
- O'Neil, J. R., Clayton, R. N., and Mayeda, T., 1969, Oxygen isotope fractionation in divalent metal carbonates: *Jour. Chem. Physics*, v. 51, p. 5547-5558.
- O'Neil, J. R., and Silberman, M. L., 1973, Stable isotope relations in epithermal Au-Ag deposits, western U. S. A., *Geol. Soc. America Ann. Mtg.*, Abstracts with Programs: p. 758.
- Fabbri, B. P., and Chesterman, C. W., 1973, Stable isotope and chemical relations during mineralization in the Bodie mining district, Mono County, California: *ECON. GEOL.*, v. 68, p. 765-784.
- O'Neil, J. R., and Taylor, H. P., Jr., 1967, The oxygen isotope and cation exchange chemistry of feldspars: *Am. Mineralogist*, v. 52, p. 1414-1437.

- 1969, Oxygen isotope fractionation between muscovite and water: *Jour. Geophys. Research*, v. 74, p. 6012-6022.
- Onuma, N., Clayton, R. N., and Mayeda, T. K., 1972, Oxygen isotope temperatures of "equilibrated" ordinary chondrites: *Geochim. et Cosmochim. Acta*, v. 36, p. 157.
- Peck, D. L., Griggs, A. B., Schlicher, A. G., Wells, F. G., and Dole, H. M., 1964, Geology of the central and northern parts of the western Cascade Range in Oregon: U. S. Geol. Survey Prof. Paper 449, 56 p.
- Perry, E. G., 1967, The oxygen isotope chemistry of ancient cherts: *Earth Planet. Sci. Letters*, v. 3, p. 62-66.
- Pinkney, D. M., and Rye, R. O., 1972, Variation of O^{18}/O^{16} , C^{13}/C^{12} , texture and mineralogy in altered limestone in the Hill mine, Cave-in-Rock District, Illinois: *ECON. GEOL.*, v. 67, p. 1-18.
- Ransome, F. L., 1909, The geology and ore deposits of Goldfield, Nevada: U. S. Geol. Survey Prof. Paper 66, 258 p.
- Reuter, J. H., Epstein, S., and Taylor, H. P., 1965, O^{18}/O^{16} ratios of some chondritic meteorites and terrestrial ultramafic rocks: *Geochim. et Cosmochim. Acta*, v. 29, p. 481-488.
- Robinson, B. W., and Ohmoto, H., 1973, Mineralogy, fluid inclusions, and stable isotopes of the Echo Bay U-Ni-Ag-Cu deposits, Northwest Territories, Canada: *ECON. GEOL.*, v. 68, p. 635-656.
- Rye, R. O., 1966, The carbon, hydrogen, and oxygen isotopic composition of the hydrothermal fluids responsible for the lead-zinc deposits at Providencia, Zacatecas, Mexico: *ECON. GEOL.*, v. 61, p. 1399-1427.
- and O'Neil, J. R., 1968, The O^{18} content of water in primary fluid inclusions from Providencia, North-Central Mexico: *ECON. GEOL.*, v. 63, p. 232-238.
- Rye, R. O., and Hall, W. E., 1971, Carbon, hydrogen, oxygen, and sulfur isotope study of the Darwin Ag-Pb-Zn deposits, Southern California [abs.]: *ECON. GEOL.*, v. 66, p. 1269.
- Savin, S. M., and Epstein, S., 1970a, The oxygen and hydrogen isotope geochemistry of clay minerals: *Geochim. et Cosmochim. Acta*, v. 34, p. 25-42.
- 1970b, The oxygen and hydrogen isotope geochemistry of ocean sediments and shales: *Geochim. et Cosmochim. Acta*, v. 34, p. 43-64.
- Sawkins, F. J., and Rye, R. O., 1970, The Casapalca Ag-Pb-Zn-Cu deposit, Peru: An ore deposit formed by hydrothermal solutions of deep-seated origin? [abs.] *Geol. Soc. America Ann. Mtg., Abstracts with Programs*, p. 674-675.
- Sheppard, S. M. F., and Epstein, S., 1970, D/H and O^{18}/O^{16} ratios of minerals of possible mantle or lower crustal origin: *Earth Planet. Sci. Letters*, v. 9, p. 232-239.
- Sheppard, S. M. F., Nielsen, R. L., and Taylor, H. P., 1969, Oxygen and hydrogen isotope ratios of clay minerals from porphyry copper deposits: *ECON. GEOL.*, v. 64, p. 755-777.
- 1971, Hydrogen and oxygen isotope ratios in minerals from porphyry copper deposits: *ECON. GEOL.*, v. 66, p. 515-542.
- Sheppard, S. M. F., and Taylor, H. P., Jr., 1974, Hydrogen and oxygen isotope evidence for the origin of water in the Boulder batholith and the Butte ore deposits, Montana: *ECON. GEOL.*, v. 69, p. 926-946.
- Shieh, Y. N., and Taylor, H. P., Jr., 1969a, Oxygen and hydrogen isotope studies of contact metamorphism in the Santa Rosa range, Nevada, and other areas: *Contrib. Mineralogy Petrology*, v. 20, p. 306-356.
- 1969b, Oxygen and carbon isotope studies of contact metamorphism of carbonate rocks: *Jour. Petrology*, v. 10, p. 307-331.
- Silverman, S. R., 1951, The isotope geology of oxygen: *Geochim. et Cosmochim. Acta*, v. 2, p. 26-42.
- Suzuoki, T., and Epstein, S., 1970, Hydrogen isotope fractionation factors (α 's) between muscovite, biotite, hornblende, and water: *Am. Geophys. Union Trans.*, v. 51, p. 451-452.
- 1974, Hydrogen isotope fractionation between OH-bearing silicate minerals and water: *Geochim. et Cosmochim. Acta* (in press).
- Taylor, H. P., Jr., 1967, Oxygen isotope studies of hydrothermal mineral deposits, in Barnes, H. L., ed., *Geochemistry of hydrothermal ore deposits*: New York, Holt, Rinehart, and Winston, p. 109-142.
- 1968, The oxygen isotope geochemistry of igneous rocks: *Contr. Mineralogy Petrology*, v. 19, p. 1-71.
- 1970, Oxygen isotope studies of anorthosites with special reference to the origin of bodies in the Adirondack Mountains, New York, in *Origin of anorthosites*: N. Y. State Museum Science Service Memo. 18, p. 111-134.
- 1971, Oxygen isotope evidence for large-scale interaction between meteoric ground waters and Tertiary granodiorite intrusions, western Cascade Range, Oregon: *Jour. Geophys. Research*, v. 76, p. 7855-7874.
- 1973, O^{18}/O^{16} evidence for meteoric-hydrothermal alteration and ore deposition in the Tomopah, Comstock Lode, and Goldfield mining districts, Nevada: *ECON. GEOL.*, v. 68, p. 747-764.
- 1974, Oxygen and hydrogen isotope evidence for large-scale circulation and interaction between ground waters and igneous intrusions, with particular reference to the San Juan volcanic field, Colorado: *Carnegie Inst. Washington, Conference on Geochemical Transport and Diffusion* (in press).
- and Coleman, R. G., 1968, O^{18}/O^{16} ratios of coexisting minerals in glaucophane-bearing metamorphic rocks: *Geol. Soc. America Bull.*, v. 79, p. 1727-1756.
- Taylor, H. P., Jr., Duke, M. B., Silver, L. T., and Epstein, S., 1965, Oxygen isotope studies of minerals in stony meteorites: *Geochim. et Cosmochim. Acta*, v. 29, p. 489-512.
- Taylor, H. P., Jr., and Epstein, S., 1963, O^{18}/O^{16} ratios in rocks and coexisting minerals of the Skaergaard intrusion: *Jour. Petrology*, v. 4, p. 51-74.
- 1966, Deuterium-hydrogen ratios in coexisting minerals of metamorphic and igneous rocks [abs.]: *Am. Geophys. Union Trans.*, v. 47, p. 213.
- 1968, Hydrogen isotope evidence for influx of meteoric ground water into shallow igneous intrusives [abs.]: *Geol. Soc. America Ann. Mtg., Abstracts with Programs*, p. 294.
- 1970a, O^{18}/O^{16} ratios of Apollo 11 lunar rocks and minerals: *Proc. Apollo 11 Lunar Sci. Conf.*, *Geochim. et Cosmochim. Acta Supp.* 1, v. 2, p. 1613-1626.
- 1970b, Oxygen and silicon isotope ratios of lunar rock 12013: *Earth Planet. Sci. Letters*, v. 9, p. 208-210.
- Taylor, H. P., Jr., and Forester, R. W., 1971, Low- O^{18} igneous rocks from the intrusive complexes of Skye, Mull, and Ardnamurchan, western Scotland: *Jour. Petrology*, v. 12, p. 465-497.
- 1973, An oxygen and hydrogen isotope study of the Skaergaard intrusion and its country rocks: *Am. Geophys. Union Trans.* [abs.], v. 54, p. 500.
- Truesdell, A. H., 1971, Nonideality of oxygen isotope fugacity in salt solutions at elevated temperatures—geochemical implications [abs.]: *Geol. Soc. America Ann. Mtg., Abstracts with Programs*, p. 735.
- Turi, B., and Taylor, H. P., 1971a, An oxygen and hydrogen isotope study of a granodiorite pluton from the Southern California batholith: *Geochim. et Cosmochim. Acta*, v. 35, p. 383-406.
- 1971b, $^{18}O/^{16}O$ ratios of the Johnny Lyon granodiorite and Texas Canyon quartz monzonite plutons, Arizona and their contact aureoles: *Contr. Mineralogy Petrology*, v. 32, p. 138-146.
- Urey, H. C., 1947, The thermodynamic properties of isotopic substances: *Jour. Chem. Soc.*, p. 562-581.
- Lowenstam, H. A., Epstein, S., and McKinney, C. R., 1951, Measurement of paleotemperatures and temperatures of the Upper Cretaceous of England, Denmark, and the southeastern United States: *Geol. Soc. America Bull.*, v. 62, p. 399.
- Van Hise, C. R., 1902, Some principles controlling the deposition of ores, in *The genesis of ore deposits*: *Am. Inst. Mining Eng. Trans.*, v. 23 and 24, p. 282-432.
- Vogel, D. E., and Garlick, G. D., 1970, Oxygen-isotope ratios in metamorphic eclogites: *Contr. Mineralogy Petrology*, v. 28, p. 183-191.

Wager, L. R., and Deer, W., 1939, Geological investigations in East Greenland. Part. III. The petrology of the Skaergaard intrusion, Kåmgerdlugsuaq: Medd. Grønland, v. 105, no. 4, p. 1-353.

Wenner, D. B., and Taylor, H. P., Jr., 1971, Temperatures of serpentinization of ultramafic rocks based on O^{18}/O^{16} fractionation between coexisting serpentine and magnetite: Contr. Mineralogy Petrology, v. 32, p. 165-185.

— 1973, Oxygen and hydrogen isotope studies of the serpentinization of ultramafic rocks in oceanic environ-

ments and continental ophiolite complexes: Am. Jour. Sci., v. 273, p. 207-239.

— 1974, $^{18}O/^{16}O$ and D/H studies of serpentinization of ultramafic rocks: Geochim. et Cosmochim. Acta (in press).

White, D. E., 1968, Hydrology, activity, and heat flow of the Steamboat Springs thermal system, Washoe County, Nevada: U. S. Geol. Survey Prof. Paper 458-C, p. C1-C109.

— Barnes, I., and O'Neil, J. R., 1973, Thermal and mineral waters of non-meteoritic origin, California coast ranges: Geol. Soc. America Bull., v. 84, p. 547-560.



SUBJ
GCHM
ARS

1
2
3
4
5
6
7
8
9
10
11
12
13
14
15
16
17
18
19
20

Activity Relations and Stabilities in Alkali Feldspar
and Mica Alteration Reactions

by

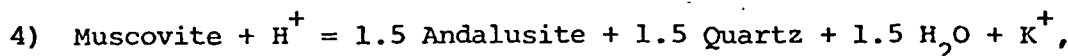
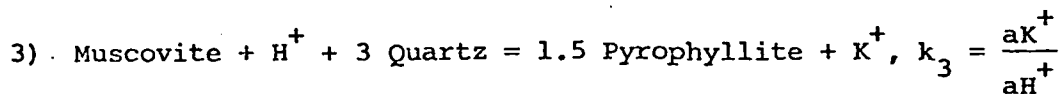
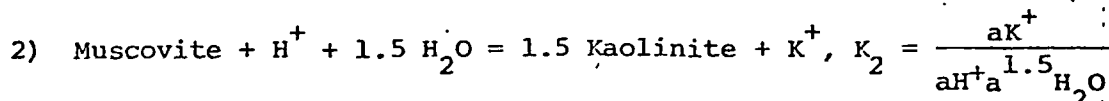
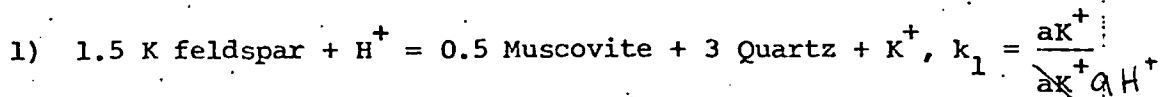
J. J. Hemley and J. W. Montoya*

U.S. Geological Survey, Reston, Virginia

*The Anaconda Co., Tucson, Arizona

Experimental concentration ratios for alkali feldspar and mica hydrolysis equilibria have been given in earlier papers (Hemley, 1959, Hemley and Jones, 1964). Corresponding activity values and equilibrium constants are also of interest and may be estimated from information that has accumulated on the solid phases and the aqueous electrolytes. Recent information has been presented by Shade (1974), but some additional discussion is appropriate.

Taking the K-bearing system as an example, the appropriate reactions are:



$$k_4 = \frac{a\text{K}^+ a^{1.5} \text{H}_2\text{O}}{a\text{H}^+}$$

The equilibrium constants of reactions (2) and (4) are also defined by the ion activity ratio, $a\text{K}^+/a\text{H}^+$, if the reference state pressure of water is taken as the confining pressure at any temperature and only dilute solutions are involved. The ion activity ratios for the reactions may be derived from the experimental concentration curves of fig. 1 by correcting for the effects of non-ionization at the elevated pressure-temperature conditions of the experiments. The broken curves of figs. 1 and 2 represent such corrections at and above 300°C.

The dissociation constants used for the calculations converts to molal units, are given in table 1. They are based on conductance studies and are from Franck (1956) for KCl, HCl, and KOH, from Quist and Marshall (1962) for NaCl and from Quist (1970) for H₂O. For NaOH a relationship between NaOH and NaCl similar to that observed between KOH and KCl was assumed. A computer solution of the appropriate set of simultaneous equations was made; for the K system these are:

$$k_{KCl} = \frac{aK^+ aCl^-}{aKCl}$$

$$k_{HCl} = \frac{aH^+ aCl^-}{aHCl}$$

$$k_{KOH} = \frac{aK^+ aOH^-}{aKOH}$$

$$k_w = aH^+ aOH^-$$

$$mK^+ + mH^+ = mCl^- + mOH^-$$

$$\Sigma K = mKCl + mK^+ + mKOH$$

$$\Sigma Cl = mKCl + mHCl + mCl^-$$

Because two equilibria must be considered at each temperature, the simplifying approximation $\Sigma K = \Sigma Cl$ cannot be used. As indicated, the dissociation of KOH is involved in the calculations, but its contribution to solution composition is negligible. Thus, the experimental concentration ratios of fig. 1, determined after quenching, represent the quantity $\frac{K^+ + KCl}{H^+ + HCl}$ at the pressure-temperature conditions of the experiment. At intermediate and high basicities, however, or in systems involving more stable hydroxy complexes, e.g., $MgOH^+$, such

complexes may produce appreciable errors in quench results that are difficult to evaluate.

Calculated activities for a 1 molal solution are given in table 2. It will be noted that the above equations do not specify mean or individual ion activity coefficients and thus embrace only the dominant effect of complexing at the high pressure-temperature conditions of the experiments. Ionic activity coefficients cannot confidently be calculated at the high pressure-temperature conditions involved, but should constitute a minor part of the data correction. The work of Lietzke, Marshall and others, e.g., Lietzke et al. (1965), indicate, for example, that ion activity coefficient ratios in mixed electrolytes at elevated temperatures should generally be close to unity. Activity ratios, therefore, such as define the phase boundaries in figs. 1 and 2, are probably very close to the correct values, even though ion activities themselves may be a few tenths of a log unit smaller than the values given in table 2. The observed constancy in total KCl/HCl ratio with change in concentration is consistent with such behavior.

At and below 300°C, the broken curves in figs. 1 and 2 were calculated thermodynamically from the relations $\Delta G^\circ = \Delta H^\circ - T\Delta S^\circ$ and $\Delta G^\circ = -RT \ln k$, where k is the equilibrium constant of the reaction. Thermodynamic data for the solids at 298.15°K are from Robie and Waldbaum (1968), except for montmorillonite and paragonite, which are from Ulbrich and Merino (1974). G°_f , H°_f and S° at 298.15K are respectively for montmorillonite ($\text{Na}_{.33}\text{Al}_{2.33}\text{Si}_{3.67}\text{O}_{10}(\text{OH})_2$), - 1277.76 kcal/mole, -1366.84 kcal/mole and 62.8 Gb/mole and for paragonite -1320.76 kcal/

mole, -1412.05 kcal/mole and 65.03 Gb/mole. Adularia, low albite and natural 2M micas were the minerals used in the final equilibration runs and in the calculations. No change in the minerals was detected after the runs, but purely surficial recrystallization, to which the aqueous phase would respond, must always occur to some extent.

Extrapolations of ΔH° and ΔS° to higher temperatures were made using the heat capacity data compiled by Helgeson (1969), or in the absence of such information, from summation of C_p of the oxides. Free energy data for water at elevated pressure and temperature are from Fisher and Zen (1971) for those reactions involving H_2O . For the ions, average heat capacities from Criss and Cobble (1964) were used. Pressure corrections for the solids to 1 kb assumed constant molar volumes, i.e., $\Delta G = V\Delta P$. Partial molal volumes of the ions were taken from the work of Ellis and McFadden (1972). Pressure corrections on the free energy of the solids and ions are relatively small.

The uncertainties in the data points calculated from conductance data are difficult to evaluate, but are probably at least ± 0.1 log units at 400° and 500°, and greater at 300° where evaluation of dissociation constants is more difficult. Similar small uncertainties exist for the thermodynamic points in the diagrams because of the scarcity of experimental data on ionic C_p and \bar{v} values at appropriate elevated pressure-temperature conditions, but larger changes may result

from current reevaluation of the free energies of formation of some of the solids. Because of such uncertainties in the thermodynamic data base, the experimental results are not used in this discussion to generate new thermodynamic numbers for any of the solid phases.

High Temperature Stability Relations

At high temperatures in the diagrams the mica fields diminish and eventually disappear due to convergence of the hydrolysis curves at the point of thermal dehydration. This change defines the isobaric invariant point for the assemblage feldspar-mica-andalusite-quartz. Above 500°C, runs were made at 550 and 580°C in the K-bearing system and the curves are drawn through the points. These data probably represent a close approach to equilibrium although successive or replicate equilibration runs, such as were made at lower temperatures, were not carried out. Both synthetic and natural muscovite were used. The implied muscovite breakdown temperature at about 600°C is in agreement with results of Day (1973). The experimental precision for the andalusite-mica values at 500°C in figures 1 and 2 is ± 0.17 log units, compared to ± 0.10 log units for the other 500° points. Average precision for the diagram as a whole in the earlier work was ± 0.12 log units, and was based upon three or four replicate equilibration runs per point.

Data along the metastable extension of the mica-pyrophyllite boundaries, as given in the earlier papers, define, of course, wider muscovite and paragonite fields at high temperatures. The generation of any pyrophyllite in the assemblage tends to bias experimental results toward that curve, which was a problem encountered in some runs. In

the very low ratio, high temperature region, dilute solutions (e.g., 0.5 m KCl) were found advantageous in establishing and following pH trends, as the system is not then swamped with very high total acidity. In all experiments, the solution was equilibrated with excess solids.

Thermal stabilities of the hydrous aluminosilicates as shown in fig. 1 are in accordance with earlier work (Reed and Hemley, 1966, Kerrick, 1967, Hemley, 1967). The pyrophyllite value could be somewhat lower within experimental precision, but probably not as low as the recent value proposed by Haas and Holdaway (1973).

The muscovite field in the activity diagram should trend and terminate essentially as indicated in fig. 1. The marked curvature of the experimental concentration curves toward higher acidity at very high temperatures indicates that HCl is becoming much less dissociated relative to KCl, and the fact that the calculated activity ratio does not fall at the apex of the field may be due to a number of influences. These include error in the dissociation constants used, the effect of individual ion activity coefficients, and possible complexing in the mixed electrolyte not covered in the single electrolyte equilibria. This would include speciation involving aqueous Al and Si, although significant effects due to these constituents at the concentrations involved are unlikely.

A further possibility, noted in an earlier discussion (Hemley, 1959), is the development of a two-fluid phase field at the highest temperatures studied. Undissociated HCl would partition in favor of

the more gaseous fluid and a very low KCl/HCl ratio would then be observed in the quenched aqueous product. In view of the data of Sourirajan and Kennedy (1962), this alternative does not appear likely as runs at 1 kb are above a two phase region in this temperature range.

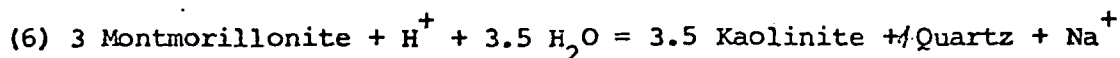
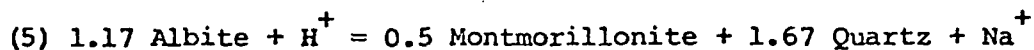
In the Na system, the upper stability limit of paragonite was anticipated in the temperature region above 500°C, and only two exploratory runs involving paragonite were made, both at 550°C. These showed a marked shift to low ratios similar to that noted in the K system. As regards the thermal stability of paragonite, Chatterjee (1972) has bracketed the boundary for 1 kb at 470-490°C, and Gusynin and Ivanov (1970) report 500 ± 5°C. The experiments here considered do not resolve the problem inasmuch as natural, well crystallized paragonite, exchanged with aqueous NaCl hydrothermally to eliminate K, was used in the runs, and such material would be expected to persist metastably in the run times involved at 500°C (7-14 days). It is not improbable, however, that synthetic hydrous phases, such as used by foregoing investigators, would tend to show low dehydration temperatures because of grain-size effects and crystal imperfections.^{1/} Even reversed experimental data might therefore be biased toward a low decomposition temperature because the upper bracket is too low. Reversals recycled at least once on the same sample, thus involving well-annealed and well-crystallized material, are desirable for proof of stability change. Until more work is done, however, the paragonite-bearing assemblages at 500°C in fig. 2 probably should be considered at or near their upper limit of stability.

^{1/}Moreover, the present authors have observed that paragonite synthesized from gels at 500°C has minor expanding character, not noticeable without glycol treatment because the basal peak present corresponds to the normal 001 spacing of paragonite.

Low Temperature Stability Relations

The diverging trends of the concentration and activity curves in the diagrams illustrate the increasing occurrence of ion association or complexing with increasing temperature, and the increase is greater for HCl than for the alkali chlorides. Also plotted in fig. 1 are corresponding activity ratio calculations from Usdowski and Barnes (1972) and Shade (1974), for the K feldspar-muscovite-quartz equilibrium. All values are strongly dependent, of course, upon the values of the dissociation constants used. The 400° to 600° points are from Shade, the 30° and 300° points are from Usdowski and Barnes, and the 200° point is their point from Hemley (1959). At 200° complete dissociation was assumed, hence its location on the experimental curve. With regard to the 200° data, it is apparent that if the thermodynamically calculated value is correct, the experimental point must be somewhat in error. An increase in relative stability of muscovite, however, over the present thermodynamically accepted value, will shift the K feldspar-muscovite-quartz curve to the right and bring the experimental and thermodynamic points in fig. 1 into better agreement. Of course, a curve calculated for sanidine rather than adularia would also be shifted to the right, e.g., 0.37 log units at 25°C. A most pertinent consideration in this problem, although of less importance in the K- than in the Na-bearing system, is the composition and structural nature of the solid phases typically present in natural or in experimental systems, relative to that thermodynamically stable at a given PTX condition.

Some liberties are obviously taken in interpreting the activity curves for the Na-bearing system. The reactions involving montmorillonite used in the calculations are as follows:



The Na montmorillonite-kaolinite-quartz trend is particularly divergent from the experimental curve. The chosen composition and estimated thermodynamic values of the montmorillonite may be significantly in error, but assuming montmorillonite is the stable phase at low temperature, the trend suggests marked Cp and compositional change of montmorillonite toward paragonite with increase in temperature. This is in suggested agreement with experimental findings. At 300°C, a fully expanding montmorillonite is produced by albite hydrolysis decomposition and is quite persistent, even in 4m NaCl. The assemblages were, of course, too fine grained for electron probe work or mineral separation and analysis. However, analysis of montmorillonite of initially so-called ideal composition, equilibrated in runs of the same duration (2 months) and solution composition as the mineral equilibration studies, showed montmorillonite with an Na formula content of 0.6, i.e. in partial transition toward paragonite. In a long run (9 months) a regular 1:1 mixed-layer montmorillonite-paragonite was formed. Calorimetric data, yet to be obtained for these phases, will help clarify relationships. In the meantime, conclusions expressed in the earlier work remain, namely, that the stability limit of Na montmorillonite is not established relative to either paragonite, a more

hydrous Na-mica, or a mixed-layer phase, and is depressed by higher aqueous Na concentration. It probably does not range as high as 300°, and a considerably lower temperature is more likely, such as between 100 and 200°C. The curves are terminated at 1 atm. rather than 1 kb at 25°C.

The experimental studies considered in this paper present an excellent example of the problem of using $\log k$ vs $\frac{1}{T}$ plots for extrapolation to different temperatures. Such a procedure yields a near linear plot provided $\int \Delta C_p dT$ is small relative to the total enthalpy change of reaction. Whether or not ΔC_p is constant is not defined by the curve, although, of course, if ΔC_p were zero the curve would be linear. A relatively small $\int \Delta C_p dT$ often characterizes reactions, but in systems involving an aqueous phase changes in state and speciation can have an appreciable effect on heat capacity and therefore on the slope and curvature of the plot. The effect is particularly great where aqueous densities are changing rapidly. In fig. 3 $\log k$ vs $\frac{1}{T}$ plots are shown for the experimentally-based portions of the solid and dashed curves of fig. 1 from 300° to 500°C. Both yield essentially straight lines in this temperature interval, but greatly different slopes because they correspond to different reactions (ionic and largely non-ionic). The ionic curves must, of course, be used for the long 25°C extrapolation since all species are ionized at low temperature. The experimental and calculated curves converge at low temperatures as in fig. 1.

Although thermodynamic considerations indicate that the slopes of the extrapolated curves would flatten somewhat with decreasing temperature, the width of the field of muscovite, hence its relative stability and

negative value of G_f° at 25°C is greater than that corresponding to the calculated thermodynamic points of fig. 1. Similarly, ΔH° for reaction (1), as given by the slope of the curve in fig. 3, is -7322 cal/mole H^+ , as compared to -6080 from tabulated thermodynamic data.

Conclusions

Activity ratio curves for the alkali feldspar and mica hydrolysis reactions have been presented based on conductance studies and on thermodynamic data. The agreement is good considering the uncertainties involved. Stability fields are thus illustrated in terms of both activities and concentrations, with the fields essentially superimposed at low temperatures. The activity relations are of interest as they are independent of electrolyte character, i.e., concentration and anion make-up, and provide the basis for more meaningful extrapolation to other temperatures, whereas concentration relations are of interest as they provide a more direct reading of change in chemical masses in geologic processes. The latter must always be considered, therefore, in quantitative evaluations of metasomatic processes. The ratio of the activity and concentration curves defines the total or stoichiometric activity coefficient of the reactions, inclusive of complexing, at any given temperature.

ACKNOWLEDGEMENTS

I am grateful to John Tanida and Todd Huffman of the U. S. Geological Survey and James Staten of the Anaconda Co. for assistance in the computer calculations. E-an Zen, Alfred Truesdell, Paul Barton, and Edwin Roedder of the U. S. Geological Survey kindly reviewed the manuscript, but any errors remaining are those of the author.

REFERENCES

- Chatterjee, N.D., 1972, The upper stability limit of the assemblage paragonite + quartz and its natural occurrences: *Contr. Mineral. and Petrol.*, v. 34, p. 288-303.
- Criss, C.M. and Cobble, J.W., 1964, The thermodynamic properties of high temperature aqueous solutions - IV Entropies of ions up to 200° and the correspondence principle: *Am. Chem. Soc. Jour.*, v. 86, p. 5385-5390; V the calculation of ionic heat capacity up to 200°: *Entropies and heat capacities above 200°*, v. 86, p. 5390-5393.
- Day, H.W., 1973, Redetermination of the stability of muscovite + quartz: *Am. Mineralogist*, v. 58, p. 255-262.
- Ellis, A.J. and McFadden, I.M., 1972, Partial molal volumes of ions in hydrothermal solutions, *Geochim. et Cosmochim. Acta*, v. 36, p. 413-427.
- Fisher, J.R. and Zen, E-an, 1971, Thermochemical calculations from hydrothermal phase equilibrium data and the free energy of H₂O: *Am. Jour. Sci.*, v. 270, p. 297-314.
- Franck, E.U., 1956, Hochverdichteter wasserdampf II, ionendissoziation von KCl in H₂O bis 750°C, III, ionendissoziation von HCl, KOH and H₂O in überkritischem wasser: *Zeitschrift für Physikalische Chemie*, Bd. 8, p. 107-206.

Gusynin, V.F. and Ivanov, I.P., 1970, Stability of Paragonite in the system $\text{SiO}_2\text{-NaAlSi}_3\text{O}_8\text{-H}_2\text{O}$: Geochim. Int'l. v. 7, p. 578-587.

Haas, H. and Holdaway, M.J., 1973, Equilibria in the system $\text{Al}_2\text{O}_3\text{-SiO}_2\text{-H}_2\text{O}$ involving the stability limit of pyrophyllite and thermodynamic data on pyrophyllite: Amer. Jour. Sci., v. 273, p. 449-464.

Helgeson, H.C., 1969, Thermodynamics of hydrothermal systems at elevated temperatures and pressures: Am. Jour. Sci., v. 567, p. 729-804.

Hemley, J.J., 1959, Some mineralogical equilibria in the system $\text{K}_2\text{O-Al}_2\text{O}_3\text{-SiO}_2\text{-H}_2\text{O}$: Am. Jour. Sci., v. 257, p. 241-270.

Hemley, J.J. and Jones, W.R., 1964, Chemical aspects of hydrothermal alteration with emphasis on hydrogen ion metasomatism: Econ. Geol., v. 59, p. 238-369.

Hemley, J.J., 1967, Stability relations of pyrophyllite, andalusite, and quartz at elevated pressures and temperatures (abs): Am. Geophys. Union Trans., v. 48, p. 224.

Lietzke, M.H., Hupf, H.B., and Stoughton, R.W., 1965, The thermodynamic properties of HCl-NaCl mixtures, J. Phys. Chem., v. 69, p. 2395-2399.

Quist, A.S., 1970, The ionization of water to 800°C and 4000 bars, J. Phys. Chem., v. 74, p. 3396.

Quist, A.S. and Marshall, W.L., 1968, Electrical conductances of aqueous sodium chloride solutions from 0 to 800° and at pressures to 4000 bars: J. Phys. Chem., v. 72, p. 684-703.

Reed, B.L. and Hemley, J.J., 1966, Occurrences of pyrophyllite in the Kekiktuk Conglomerate, Brooks Range, northeastern Alaska: U.S. Geol. Survey Prof. Paper 550-C, p. 162-166.

Robie, R.A. and Waldbaum, D.R., 1968, Thermodynamic properties of minerals and related substances at 298.15°K (25.0°C) and one atmosphere (1.013 bars) pressure and at higher temperatures: U. S. Geological Survey Bull. 1259, 256 p.

Shade, J.W., 1974, hydrolysis reactions in the SiO_2 -excess portion of the system $\text{K}_2\text{O}-\text{Al}_2\text{O}_3-\text{SiO}_2-\text{H}_2\text{O}$ in chloride fluids at magmatic conditions, Econ. Geol. v. 69, p. 218-229.

Sourirajan, S. and Kennedy, G.C., 1962, The system $\text{H}_2\text{O}-\text{NaCl}$ at elevated temperatures and pressures, Am. Jour. Sci., v. 260, p. 115-141.

Ulbrich, H.H. and Merino, E., 1974, An examination of standard enthalpies of formation of selected minerals in the system $\text{SiO}_2-\text{Al}_2\text{O}_3-\text{Na}_2\text{O}-\text{K}_2\text{O}-\text{H}_2\text{O}$: Am. Jour. Sci., v. 274, p. 510-542.

Fig. 1. Concentration and calculated activity ratio curves in the system $K_2O-Al_2O_3-SiO_2-H_2O$. Solid symbols from conductance data. Open symbols from thermodynamic data. Vertical bar indicates 1 atm. at 25°C and saturated water vapor pressure above 100°C.

5-
6
7
8
9
10-
11
12
13
14
15-
16
17
18
19
20
21
22
23
24

9.1177

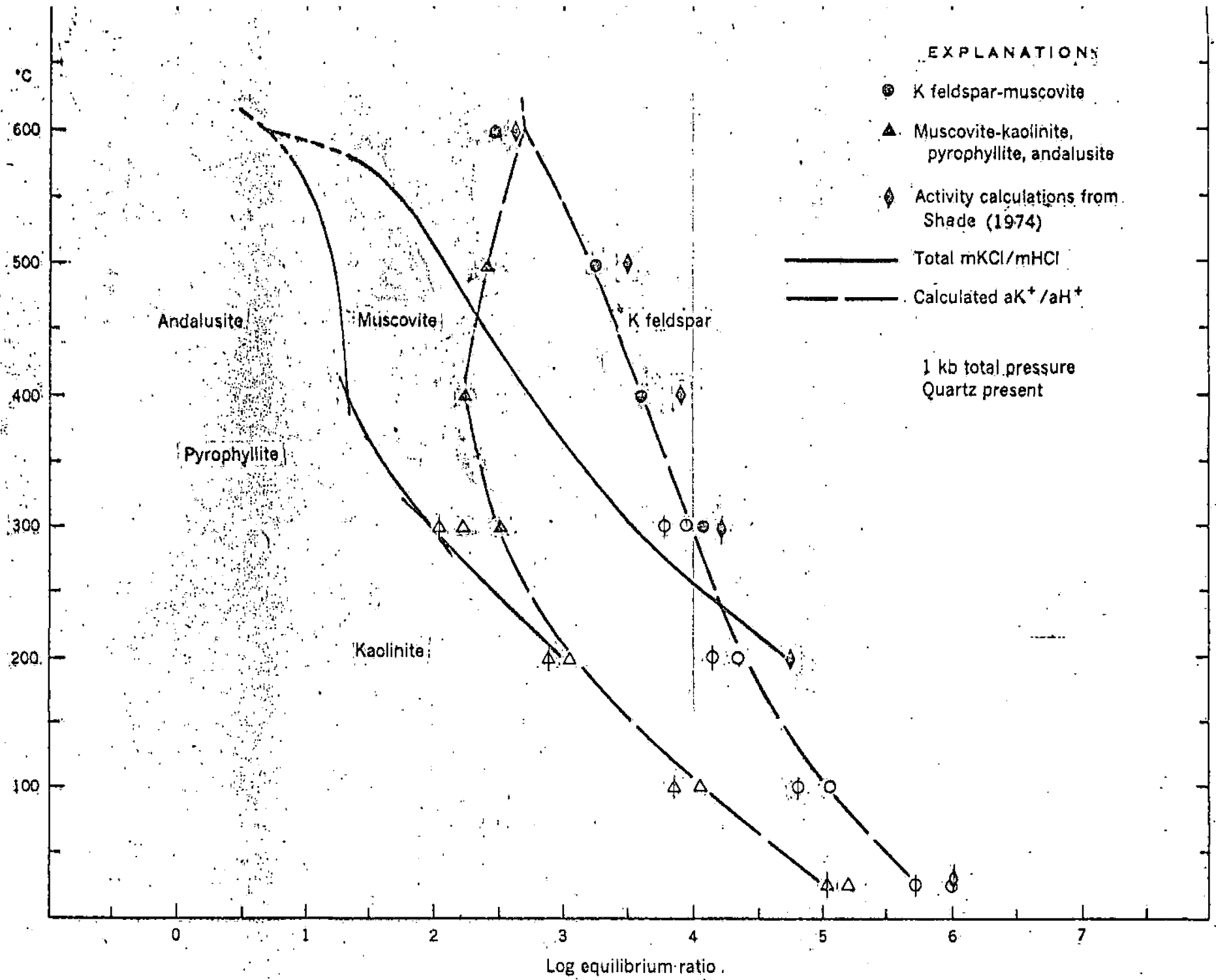
1 Fig. 2. Concentration and calculated activity ratio curves in the
2 system $\text{Na}_2\text{O}-\text{Al}_2\text{O}_3-\text{SiO}_2-\text{H}_2\text{O}$. Solid symbols from conductance data.
3 Open symbols from thermodynamic data. Vertical bar indicates 1 atm. at
4 25°C and saturated water vapor pressure above 100°C .

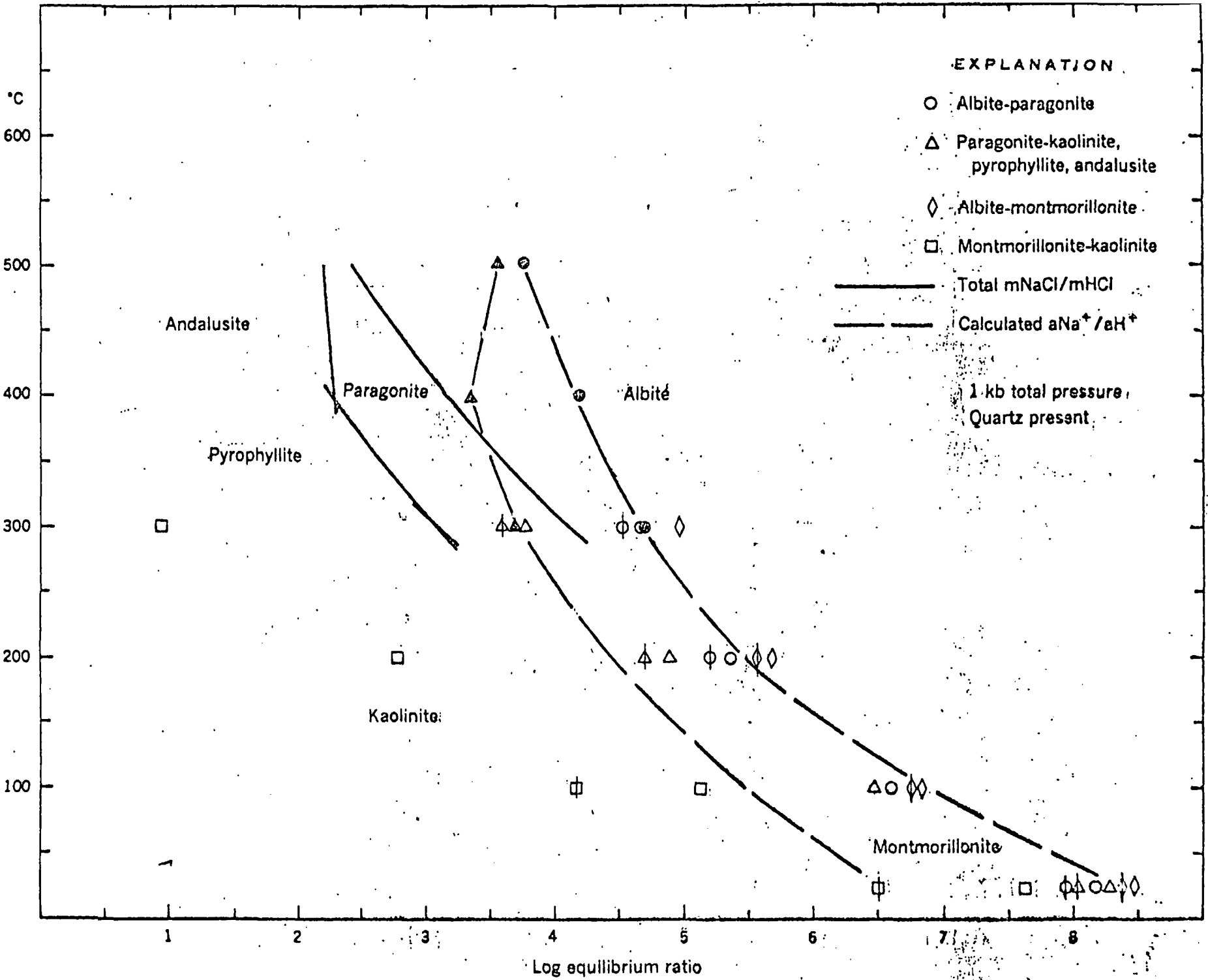
5-
6
7
8
9
10-
11
12
13
14
15-
16
17
18
19
20-
21
22
23
24
25

1 Fig. 3. Log k vs $\frac{1}{T}$ plot of experimental concentration data and
2 activity ratios calculated from concentration data, as shown in fig.

3 1. Activity data are extrapolated to low temperatures.
4

5-
6
7
8
9
10-
11
12
13
14
15-
16
17
18
19
20
21
22
23
24
25





1

2

3

4

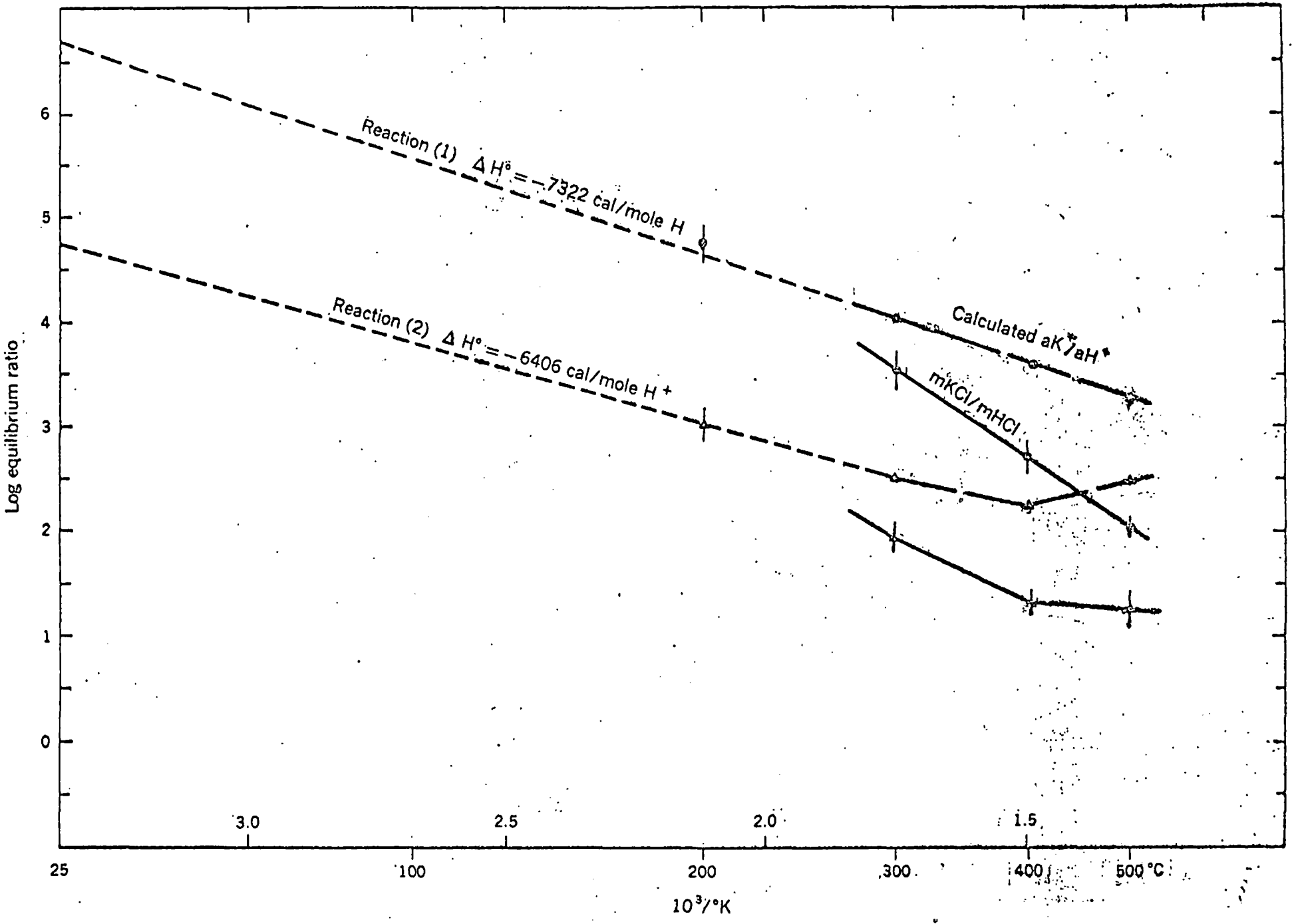
5

6

7

8

Log equilibrium ratio



Aqueous Solutions of Two or More Strong Electrolytes

Vapor Pressures and Solubilities

SUBJ
GCHM
AST

UNIVERSITY OF UTAH
RESEARCH INSTITUTE
EARTH SCIENCE LAB.

Herman P. Meissner*

Department of Chemical Engineering, Massachusetts Institute of Technology, Cambridge, Mass. 02139

Charles L. Kusik

Arthur D. Little Inc., Cambridge, Mass. 02140

A relationship is presented for determining the vapor pressure of water over aqueous solutions containing more than one strong electrolyte. Illustrations present use of this relationship in determining the solubility in such mixed solutions of electrolytes whose crystals are hydrated.

The activity coefficients of strong electrolytes in aqueous solutions can be predicted at various temperatures and ionic strengths by recently published methods (Meissner and Kusik, 1972; Meissner and Tester, 1972; and Meissner et al. 1972). Vapor pressure of water over such solutions, containing only one dissolved electrolyte, can also be predicted (Kusik and Meissner, 1973). The object here is to extend these procedures to the calculation of water vapor pressures over aqueous solutions of more than one electrolyte, and to illustrate application of these methods to the estimation of the solubility of electrolytes whose crystals are hydrated.

Mixed Solutions

A solution of an electrolyte 12 is here called "pure" or "mixed," depending on whether other electrolytes are present. Mixed solutions are described as containing cations 1, 3, 5, and so forth, and anions 2, 4, 6, and so forth. It is convenient to characterize these solutions in terms of the individual ions, using the definition of ionic strength presented in the nomenclature table. To illustrate, consider a solution which is 2 *m* in NaCl and 2 *m* in Na₂SO₄. Designating Na⁺, Cl⁻, and SO₄²⁻ as ions 1, 2, and 4, the ionic strengths μ_1 , μ_2 , and μ_4 are 0.5 (6 × 1²), 0.5 (2 × 1²), and 0.5 (2 × 2²), or 3, 1, and 4, respectively. The anionic strength of the solution itself, namely μ_a equals ($\mu_2 + \mu_4$) or 5, the cationic strength is μ_c or 3, making μ_T , the solution's total ionic strength, equal to ($\mu_a + \mu_c$) or 8. Finally, again using the definitions in the nomenclature table, the anionic strength fractions Y_2 and Y_4 in this system are, respectively, 0.2 and 0.8, while the cationic strength fraction X_1 is unity.

Mixed Solution Vapor Pressure

The activity of water, designated as $(a_w^\circ)_{12}$ over a pure solution of electrolyte 12 and $(a_w^\circ)_{\text{mix}}$ over a mixed solution is defined as the ratio p/p° , namely, the ratio of the partial pressure of water over the solution and over pure water at the temperature in question. In a mixed solution $(a_w^\circ)_{\text{mix}}$ can be calculated from $(a_w^\circ)_{12}$, $(a_w^\circ)_{14}$, $(a_w^\circ)_{23}$, and so forth, all taken at the total ionic strength and temperature of the mixed solution, as follows:

$$\log (a_w^\circ)_{\text{mix}} = X_1 Y_2 \log (a_w^\circ)_{12} + X_1 Y_4 \log (a_w^\circ)_{14} + X_1 Y_6 \log (a_w^\circ)_{16} \dots + X_3 Y_2 \log (a_w^\circ)_{32} + X_3 Y_4 \log (a_w^\circ)_{34} + X_3 Y_6 \log (a_w^\circ)_{36} \dots + X_5 Y_2 \log (a_w^\circ)_{52} + X_5 Y_4 \log (a_w^\circ)_{54} + X_5 Y_6 \log (a_w^\circ)_{56} \dots \quad (1)$$

The derivation of this equation is outlined in later paragraphs.

For a mixed aqueous solution of NaCl and KCl, here called electrolytes 12 and 32, respectively, Equation 1 obviously simplifies to

$$(a_w^\circ)_{\text{mix}} = [(a_w^\circ)_{\text{NaCl}}^{X_1 Y_2}] [(a_w^\circ)_{\text{KCl}}^{X_3 Y_2}] \quad (2)$$

Thus a solution which is 5.09 *m* in NaCl and 2.31 *m* in KCl is saturated with both salts at 30°C, and has a total ionic strength of 7.4; consequently X_{Na^+} is 0.69, Y_{Cl^-} is 1.0, and X_{K^+} is 0.31. At 30°C and a total ionic strength of 7.4, a solution containing only NaCl or only KCl is supersaturated. The activities of electrolytes and the vapor pressures of water over these two pure supersaturated solutions are readily estimated by the methods previously discussed (Kusik and Meissner, 1973; Meissner and Tester, 1972; Meissner et al., 1972). For example, starting with literature values for γ° of 0.67 and 0.57, respectively, for a solution of pure NaCl and pure KCl at 25°C at an ionic strength of 2, then by extrapolation to an ionic strength of 7.4, $(a_w^\circ)_{\text{NaCl}}$ and $(a_w^\circ)_{\text{KCl}}$ are, respectively, 0.71 and 0.78. Substituting into Equation 2, $(a_w^\circ)_{\text{mix}}$ is predicted to be 0.73 vs. an experimental value of 0.722 (Adams and Mertz, 1929). Water activities over several other saturated aqueous solutions of two 1:1 electrolytes having a common ion are tabulated in Table I. Inspection shows fair success again to be attained.

A more interesting application of Equation 1 lies in calculating water vapor pressures over multi-ion solutions. Thus, a synthetic brine with a measured vapor pressure of 18.35 mm Hg at 26°C has the following ion molalities: 2.36 Mg²⁺, 1.13 SO₄²⁻, 0.83 K⁺, 5.75 Cl⁻, and 2.46 Na⁺. When we designate these ions as 1, 2, 3, 4, and 5, respectively, Equation 1 becomes:

$$(a_w^\circ)_{\text{mix}} = (a_w^\circ)_{12}^{X_1 Y_2} (a_w^\circ)_{14}^{X_1 Y_4} (a_w^\circ)_{32}^{X_3 Y_2} (a_w^\circ)_{34}^{X_3 Y_4} \times (a_w^\circ)_{52}^{X_5 Y_2} (a_w^\circ)_{54}^{X_5 Y_4} \quad (3)$$

To solve, it is necessary first to determine $(a_w^\circ)_{12}$, $(a_w^\circ)_{14}$, and so forth, each at the total ionic strength of the mixture, namely 0.5 (2.36 × 2² + 1.13 × 2² + 0.83 × 1² + 5.75 × 1² + 2.46 × 1²), or 11.47. In sequence for the six terms as written on the right-hand side of Equation 3, the values of a_w° (calculated by the methods outlined previously) are 0.95 for MgSO₄, 0.62 for MgCl₂, 0.93 for K₂SO₄, 0.65 for KCl, 0.89 for Na₂SO₄, and 0.51 for NaCl. Similarly, values of X_1 , Y_2 , X_3 , Y_4 , and X_5 are, respectively, 0.742, 0.44, 0.065, 0.56, and

0.193. Substituting into Equation 3, $(a_w)_{\text{mix}}$ is 0.73, making the water vapor pressure equal to 18.4 mm Hg, very close to the experimental value of 18.35 as reported above.

Solubility

The ionic activity product equation, which relates the solubilities of electrolyte 12 in pure and in mixed saturated solution, is usually written as follows:

$$(m_1^\circ)^{\nu_1}(m_2^\circ)^{\nu_2}(\gamma_{12}^\circ)^{\nu_{12}} = (m_1)^{\nu_1}(m_2)^{\nu_2}(\gamma_{12})^{\nu_{12}} \quad (4)$$

The symbols used here are again defined in the nomenclature table. For low concentrations with very insoluble electrolytes, γ_{12}° and γ_{12} are both unity, whereupon Equation 4 reduces to the familiar solubility product equation. For systems of higher concentration, these electrolyte activity coefficients can be predicted with reasonable success by the method of Meissner and Tester (1972) and Meissner and Kusik (1972). However, Equation 4 applies only to electrolytes like NaCl and KCl which as solids contain no waters of crystallization. This equation must be modified for application to saturated solutions in which the solid phases are hydrated, as is normally the case with electrolytes whose ion charges exceed unity. For convenience, the moles of water per mole of electrolyte in the crystal are here called n_o when in contact with pure saturated solution, and n when in contact with mixed saturated solution. For such hydrated solids, when n_o and n are identical:

$$(m_1^\circ)^{\nu_1}(m_2^\circ)^{\nu_2}(\gamma_{12}^\circ)^{\nu_{12}}(a_w^\circ)_{12}^{n_o} = (m_1)^{\nu_1}(m_2)^{\nu_2}(\gamma_{12})^{\nu_{12}}(a_w)_{\text{mix}}^{n_o} \quad (5)$$

Occasionally, n_o and n are unequal. Thus, for pure sodium carbonate, the solid phase in contact with pure saturated solution at 25°C is $\text{Na}_2\text{CO}_3 \cdot 10\text{H}_2\text{O}$, but in contact with a mixed saturated solution containing 11% NaCl is $\text{Na}_2\text{CO}_3 \cdot 7\text{H}_2\text{O}$ (International Critical Tables, 1928 IV, p 301), making n_o and n equal to 10 and 7, respectively. For such cases, the solubility relationship becomes:

$$(m_1^\circ)^{\nu_1}(m_2^\circ)^{\nu_2}(\gamma_{12}^\circ)^{\nu_{12}}(a_w^\circ)^{n_o} = (m_1)^{\nu_1}(m_2)^{\nu_2}(\gamma_{12})^{\nu_{12}}(a_w)_{\text{mix}}^n \exp(-\Delta F_c/RT) \quad (6)$$

where (see nomenclature table for definitions):

$$\Delta F_c = F_{n_o} - F_n - (n_o - n)F_w \quad (7)$$

Values of the free energies in Equation 7 are presented in the standard references or can be calculated from water activities for saturated solutions in which both crystal species are present.

The derivation of Equations 4, 5, and 6 is presented in later paragraphs. It is worth noting that when n_o and n are equal, then Equation 6 reduces to Equation 5. In mixed solutions containing only small amounts of other electrolytes, n_o and n are usually identical; consequently Equation 5 applies. When concentrations of both pure and mixed solutions are low because of low solubilities, then $(a_w^\circ)_{12}$ and $(a_w)_{\text{mix}}$ are both substantially unity, and both Equations 5 and 6 reduce to Equation 4. Extension of the thoughts above indicate that Equation 6 applies also to situations where the left-hand side as well as the right-hand side represent mixed solutions.

FeCl₂ Solubility

Consider the problem of determining how much HCl can be dissolved at 25°C in a 1.4 *m* solution of ferrous chloride (here called electrolyte 12) before solid $\text{FeCl}_2 \cdot 4\text{H}_2\text{O}$ starts to precipitate. From the literature, a pure saturated solution of this tetrahydrate at 25°C has a molality of 5.07; hence μ is

Table I. Activities of Water at 30°C in Solutions Saturated with Two Salts Having a Common Ion

	Electrolyte molalities		Water activity in mixed solution		
			Calculated from Equation 1	Experimental (Adams and Mertz, 1929)	
NaCl	5.09	KCl	2.31	0.73	0.722
NaCl	4.11	NaNO ₃	8.55	0.64	0.676
KCl	2.05	NH ₄ Cl	5.74	0.77	0.735
KCl	4.74	KNO ₃	2.70	0.82	0.786

Table II

System	Solid phases	Molalities	
		Na ₂ SO ₄	NaCl
I	Na ₂ SO ₄ · 10H ₂ O	1.97	0
II	Anhydrous Na ₂ SO ₄ and NaCl	0.69	5.51

15.21. Here γ_{12} and (a_w°) are, respectively, 3.8 and 0.55, found by extrapolation (Kusik and Meissner, 1973; Meissner and Tester, 1972), when we know that Γ_{12}° is 0.9 for a pure (unsaturated) FeCl_2 solution at 25°C when μ is 6 (Harned and Owen, 1958). Substituting into the left side of Equation 5, we get:

$$(m_1^\circ)^{\nu_1}(m_2^\circ)^{\nu_2}(\gamma_{12}^\circ)^{\nu_{12}}(a_w^\circ)_{12}^{n_o} = (5.07)(2 \times 5.07)^2(3.8)^3(0.55)^4$$

The foregoing product, which is numerically 2617, must equal the right side of Equation 5, or

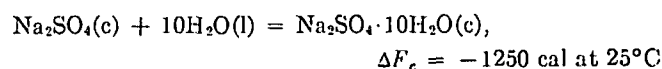
$$2617 = (1.4)(2 \times 1.4 + m_{32})^2(\gamma_{12})^3(a_w)_{\text{mix}}^4 \quad (8)$$

Here m_{32} represents the moles of HCl which must be present to form the desired saturated solutions of ferrous chloride. In these solutions, by definition, μ_T equals $(1.4 \times 3 + m_{32})$. By trial, various values of m_{32} are assumed and corresponding values of γ_{12} are obtained by the method of Meissner and Kusik (1972). Values of $(a_w)_{\text{mix}}$ are calculated by Equation 1. Equation 8 is in balance when m_{32} is 6.6 at which point μ is, of course, 11.8, γ_{FeCl_2} is 8.6, and $(a_w)_{\text{mix}}$ is 0.43. Agreement with the experimental value for m_{32} of 7 *m* (Seidell and Linke, 1965) is thus within 6%.

Errors

Errors may be encountered in applying Equations 5 and 6, not only because of inaccuracies in estimating values of activity coefficients and vapor pressures, but because these terms are raised to powers, magnifying such inaccuracies. For example in Table II, systems at 25°C, solution I is pure while solution II is saturated with both sodium sulfate and sodium chloride (International Critical Tables, Vol. 4, p 288, 1926). There is some disagreement in the values for Na₂SO₄ molality in saturated solution II, inasmuch as they are alternatively reported in the International Critical Tables as 0.82 on page 287 of Vol. 4, and as 0.595 on page 982 of Seidell and Linke.

The molality, m_{II} , of sodium sulfate in solution II will now be calculated by trial from Equation 6 and compared with the experimental value in Table II. The free energy of hydration of anhydrous sodium sulfate is reported (Rossini, 1952) as follows:



Values of n_o and n for the decahydrate and the anhydrous salt in this equation are, respectively, 10 and 0. From Robinson and Stokes (1959), $\gamma_{Na_2SO_4}$ for pure solution I is 0.155, while (a_w°) is 0.96 as estimated by the method of Kusik and Meissner (1973), making the left side of Equation 6 equal to $(1.97 \times 2)^2(1.97)(0.55)^2(0.96)^{10}$ or 0.076.

Similarly, when we know $\gamma_{Na_2SO_4}$ for solution I, its value in a mixed solution which is 5.5 m in NaCl, as in solution II, can be determined by the methods of Meissner and Kusik (1972). Thus, when m_{II} is assumed to be 0.46, then μ_T is 6.89 while $\gamma_{Na_2SO_4}$ is 0.32. By trial, Equation 6 is in balance as follows when m_{II} is 0.46:

$$0.076 = (2 m_{II} + 5.51)^2(m_{II})(0.32)^2 \exp(-1250/1.99 \times 298)$$

There appears to be a significant difference between this calculated value for m_{II} and the average of the experimental values reported earlier. Caution should obviously be used in applying Equations 5 and 6, especially when either n or n_o is large.

Derivation of Equation 1

For a system of two 1:1 electrolytes 12 and 32, having ion 2 as the common ion, the Gibbs-Duhem equation is:

$$-55.5 d \ln (a_w)_{mix} = m_{12} \nu_{12} d \ln m_{12} \gamma_{12} + m_{32} \nu_{32} d \ln m_{32} \gamma_{32} \quad (9)$$

Separating and rearranging the right-hand side of Equation 9 give us:

$$-55.5 d \ln (a_w)_{mix} = \nu_{12} d m_{12} + \nu_{32} d m_{32} + m_{12} \nu_{12} d \ln \gamma_{12} + m_{32} \nu_{32} d \ln \gamma_{32} \quad (10)$$

Hold the ratio m_{12}/m_{32} constant and Equation 10 is integrated from zero to the final electrolyte concentration. Natural logarithms are converted to base 10 logarithms, the quantities of the form $m_{12} \nu_{12} z_1 z_2$ are replaced by $2 \mu_{12}$, and $d \log \gamma_{12}$ is replaced by $z_{12} d \log \Gamma_{12}$, whereupon:

$$-55.5 \log (a_w)_{mix} = \frac{\mu_{12} + \mu_{32}}{2.3 z_1 z_2} + 2 \int \mu_{12} d \log \Gamma_{12} + 2 \int \mu_{32} d \log \Gamma_{32} \quad (11)$$

But from Meissner and Kusik (1972), for a three-ion system:

$$d \log \Gamma_{12} = 0.5 (X_1 d \log \Gamma_{12}^\circ + Y_2 d \log \Gamma_{12}^\circ + X_3 d \log \Gamma_{32}^\circ) \quad (12)$$

$$d \log \Gamma_{32} = 0.5 (X_1 d \log \Gamma_{12}^\circ + Y_2 d \log \Gamma_{32}^\circ + X_3 d \log \Gamma_{32}^\circ) \quad (13)$$

From Kusik and Meissner (1973), the activity for water over the pure electrolyte solutions are, respectively,

$$-55.5 \log (a_{mix}^\circ)_{12} = \frac{\mu_T}{z_1 z_2} + 2 \int \mu_T d \log \Gamma_{12}^\circ \quad (14)$$

$$-55.5 \log (a_{mix}^\circ)_{32} = \frac{\mu_T}{z_3 z_2} + 2 \int \mu_T d \log \Gamma_{32}^\circ \quad (15)$$

By definition for this system of 1:1 electrolytes:

$$\mu_{12} = X_1 \mu_T; (\mu_{12} + \mu_{32}) = Y_2 \mu_T; \mu_{32} = X_3 \mu_T \quad (16)$$

For this three-ion system, of course, Y_2 is unity, and

$$X_1 Y_2 + X_3 Y_2 = 1.0 \quad (17)$$

Substituting Equations 12 and 13 into Equation 11, eliminating the integrals by using Equations 14 and 15, and combining with Equation 16, yield Equation 2 for a three-ion system. It is obvious that this derivation can be extended to multi-ion systems of 1:1 electrolytes, yielding Equation 1. This derivation is rigorous for systems in which all cations have the same charge, and all anions have the same charge, as in a solution of NH_4Cl and KNO_3 , or a solution of $CaCl_2$ and $MgCl_2$. When cations and/or anions have unequal charges, as in a solution of HCl and $FeCl_2$, or $NaCl$ and Na_2SO_4 , then Equation 1 is still a good first approximation as indicated by the foregoing examples.

Derivation of Equations 4 and 5

In these derivations, the standard state for water is the pure liquid and for the electrolyte is in its familiar pure hypothetical solution in which both the mean ionic molality and activity are unity. For each equation, the derivation is based on the reversible isothermal transfer of electrolyte (and any associated waters of crystallization) by two alternative paths from the standard states just listed to the same solid crystalline form. Providing the crystals produced are identical, the free energy changes over these two paths must be equal:

Path I. Starting with the standard states just mentioned, transfer 1 mol of electrolyte plus n_o moles of water into the saturated pure solution, simultaneously allowing the hydrated crystals to precipitate. Obviously n_o is zero for an anhydrous crystal. Since the free energy change of forming crystals from saturated solutions is always zero, the molal free energy change over this path is obviously $RT [\ln (m_1^\circ)^{\nu_1} (m_2^\circ)^{\nu_2} (\gamma_{12}^\circ)^{\nu_{12}} + n_o \ln (a_w^\circ)_{12}]$.

Path II. Again starting from the standard states mentioned above, transfer 1 mol of electrolyte plus n moles of water into the saturated mixed solution, simultaneously allowing the crystals to precipitate. Since this free energy change of crystal formation from saturated solution is again zero, the molal free energy change over this path is $RT [\ln (m_1)^{\nu_1} (m_2)^{\nu_2} (\gamma_{12})^{\nu_{12}} + n \ln (a_w)_{mix}]$.

Equation 4 is derived by equating these free energy changes for paths I and II above, recognizing that n_o and n are both zero since the crystals precipitating are anhydrous. By neglecting second-order terms, the derivation of Equation 5 proceeds along similar lines for the case when the solid phases are hydrated, with n_o and n being equal.

When n_o and n are not identical, as in Equation 6, then the crystals precipitated from the pure solution of path I above are not identical with those from the mixed solution of path II. Before the free energy changes of these two paths can be equated, allowance must be made for rehydrating the crystals of path II from n to n_o . The free energy change of this crystal hydration step is of course given by Equation 7. It is obvious that Equation 6 results when the molal free energy changes of the two completed paths are equated.

Nomenclature

(a_w) = activity of water, $(a_w^\circ)_{12}$ being for a pure solution of an electrolyte identified by subscript, $(a_w)_{mix}$ being for mixed solution

ΔF_c = free energy change of crystal hydration, as in Equation 7

F' = molal free energy of formation from the elements, F_{n_o} , referring to crystals carrying n_o moles water of hydration per mole electrolyte, F_n , referring to crystals carrying n moles water of hydration per mole electrolyte, and F_w

being the free energy of liquid water, namely -56.69 Kcal/g-mol at 25°C

m = molality, in g-mol/1000 g solvent; m° referring to pure solutions and m to mixed solutions. The ions or electrolyte referred to are indicated by subscript

n = moles of water of crystallization per mole of anhydrous electrolyte in a solid, n_0 and n being used to distinguish between solids in equilibrium with saturated pure and mixed solutions, respectively

X = cationic fraction, as in μ_1/μ_c or μ_3/μ_c

Y = anionic fraction, as in μ_2/μ_a or μ_4/μ_a

z = number of unit charges on the ion, indicated by the subscript. Thus z is unity for Na^+ , also for NO_3^- , but is 3 for Al^{3+} , also for PO_4^{3-}

ν = moles of ions formed upon complete dissociation of 1 mol of electrolyte. Thus, ν_1 is for the indicated cation, ν_2 is for the indicated anion, while ν_{12} is the total number of ions namely $(\nu_1 + \nu_2)$. To illustrate, ν_{12} is 2 for NaCl and 5 for $\text{Al}_2(\text{SO}_4)_3$

γ = mean ionic activity coefficient for the electrolyte indicated by the subscript, γ_{12}° being for the pure solution and γ_{12} for the mixed solution

Γ = reduced activity coefficient, namely $\gamma_{12}^{1/\nu_{12}}$ for the electrolyte indicated by the subscript. The term, Γ_{12}° , refers to pure solutions, Γ_{12} to mixed solutions

μ = ionic strengths indicated by the subscript. The ionic

strengths μ_1, μ_2, \dots , of the individual ions are $0.5 m_1 z_1^2, 0.5 m_2 z_2^2$, and so forth. The total ionic strength μ_T equals $0.5 (m_1 z_1^2 + m_2 z_2^2 + m_3 z_3^2 + \dots)$. For a pure system, μ_T equals $0.5 m_{12} \nu_{12} z_1^2 z_2^2$. The cationic strength μ_c of a solution is $(\mu_1 + \mu_3 + \dots)$, the anionic strength μ_a is $(\mu_2 + \mu_4 + \dots)$

Literature Cited

- Adams, J. R., Mertz, A., *Ind. Eng. Chem.*, **21**, 305 (1929).
Harned, H. S., Owen, B. B., "Physical Chemistry of Electrolyte Solutions," 3rd ed., Reinhold, New York, N. Y., 1958.
International Critical Tables, McGraw-Hill, New York, N. Y., 1926.
Kusik, C. L., Meissner, H. P., "Vapor Pressures of Water Over Aqueous Solutions of Strong Electrolytes," *Ind. Eng. Chem. Process Des. Develop.*, **12**, 112 (1973).
Meissner, H. P., Kusik, C. L., "Activity Coefficients of Strong Electrolytes in Multicomponent Aqueous Solutions," *A.I.Ch.E. J.*, **18**, 2294 (1972).
Meissner, H. P., Kusik, C. L., Tester, J. W., "Activity Coefficients of Strong Electrolytes in Aqueous Solutions—Effect of Temperature," *ibid.*, p 3661.
Meissner, H. P., Tester, J. W., "Activity Coefficients of Strong Electrolytes in Aqueous Solutions," *Ind. Eng. Chem. Process Des. Develop.*, **11**, 1128 (1972).
Robinson, R. A., Stokes, R. M., "Electrolyte Solutions," 2nd ed., Academic Press, New York, N. Y., 1959.
Rossini, F. D., "Selected Values of Thermodynamic Properties," *Circ. 500*, Natl. Bur. Stand., 1952.
Seidell, S., Linke, W. F., "Solubilities," Vol. II, 4th ed., Amer. Chem. Soc., Washington, D. C., 1965.

RECEIVED for review September 11, 1972
ACCEPTED December 11, 1972

Joe

SUBJ
GCHM
BTE

UNIVERSITY OF UTAH
RESEARCH INSTITUTE
EARTH SCIENCE LAB.

Jour. Research U.S. Geol. Survey
Vol. 4, No. 1, Jan.-Feb. 1976, p. 41-47

BEHAVIOR OF TRACE ELEMENTS DURING MAGMATIC PROCESSES—
A SUMMARY OF THEORETICAL MODELS AND THEIR APPLICATIONS

By JOSEPH G. ARTH, Reston, Va.

Abstract.—Progress in understanding the behavior of trace elements during the processes that produce igneous rocks has been made possible by the parallel development of theoretical models to describe that behavior and analytical techniques that permit precise measurement of trace-element concentrations in igneous rocks and minerals. The result of this progress is that trace-element studies may now be used to place strong limits on both the degree of partial melting or fractional crystallization involved in the production of a given magma and the identity and quantity of the residual phases. A summary of quantitative trace-element theory and partition coefficient data for igneous rocks is presented.

Trace-element studies are now widely used by petrologists and geochemists in the study of igneous rocks, yet many geologists wonder about the basis or validity of petrogenetic conclusions drawn from these studies. While many aspects of trace-element behavior remain unknown, significant progress has been made in both the theory and its experimental and geologic verification. In this paper, the quantitative theory of trace-element behavior during the processes of partial melting and fractional crystallization is summarized for the geologist who has not closely followed the development of this powerful new tool. A simple example of the use of the equations is given, as well as a compilation of phenocryst-groundmass partition coefficient data.

The theoretical models that have been proposed assume as a starting point that trace elements form dilute solid solutions and behave in accordance with Henry's law. This assumption cannot be made, however, where an element, although low in abundance, is a stoichiometric constituent of a phase (for example, zirconium in zircon). Application of Henry's law also depends on the assumption of equilibrium or near-equilibrium conditions. At equilibrium the chemical potential, μ , of element i in phase α equals the chemical potential of i in phase β :

$$\mu_i^\alpha = \mu_i^\beta.$$

This can be restated in terms of the activity, a , and the chemical potential for the standard state, μ° , as:

$$\mu_i^\alpha + RT \ln a_i^\alpha = \mu_i^\beta + RT \ln a_i^\beta.$$

Algebraic manipulation yields the equation

$$\exp\left(\frac{\mu_i^\alpha - \mu_i^\beta}{RT}\right) = a_i^\beta / a_i^\alpha = k.$$

The first part of this equation is constant if the temperature, pressure, and bulk composition are constant, so that the ratio of activities will equal a constant, k . The activities can be restated in terms of elemental concentrations, c , and activity coefficients, γ , to produce the following:

$$\gamma_i^\beta c_i^\beta = k \gamma_i^\alpha c_i^\alpha.$$

According to Henry's law the activity coefficients have a constant value which is independent of concentration so long as the solution is dilute, so that

$$\frac{c_i^\alpha}{c_i^\beta} = \frac{\gamma_i^\beta}{k \gamma_i^\alpha} = K^{\alpha/\beta}.$$

The quantity $K^{\alpha/\beta}$ is called the distribution coefficient and simply represents the concentration ratio of a trace element between two equilibrated phases. The concentration of a trace element in a magma, therefore, is expected to reflect the value of the distribution coefficient between the magma and the solid phases with which it coexists. The expected effects on the distribution coefficient of temperature, pressure, crystallographic site, and magma composition have been discussed by McIntire (1963) and Banno and Matsui (1973), but are experimentally confirmed for only a few elements in a few minerals and over very limited ranges of temperature, pressure, and composition.

PARTIAL MELTING

Equations describing the behavior of trace elements during partial melting were formulated by Schilling and Winchester (1967) and Gast (1968). Shaw (1970) later devised less complicated expressions which describe three possible partial-melting mechanisms: (1) continuous removal of melt from the residual solid, (2) continuous removal of melt from the residual solid followed by collection of this melt in a single

completely mixed chamber, and (3) continuous equilibrium of the liquid phase with the residual solid until removal of the liquid from the solid (sometimes referred to as "batch" melting). When small fractions of material are melted, the equations for each mechanism yield similar results. When large fractions of material are melted (>25 percent) results of the equations vary considerably. As the continuous removal of infinitesimal amounts of liquid (Nos. 1 and 2) is often considered physically unlikely, mechanism 3 may be the most geologically realistic for large bodies of magma of uniform composition.

For partial melting in which the liquid phase remains in equilibrium with the residual solid phases until it is removed (No. 3), equation 15 of Shaw (1970) gives

$$\frac{c^L}{c_0} = \frac{1}{D_0 + F(1-P)} \quad (1)$$

where F is the fraction of melting, c_0 the initial trace-element concentration of the solid, and c^L the trace-element concentration of the liquid. D_0 is the bulk distribution coefficient for the starting assemblage and is given by Shaw's equation 6 as

$$D_0 = \sum X_n^0 K^{n/L} + \sum Y_n^0 K^{n/L} + \dots \quad (2)$$

where X_n^0 is the initial weight fraction of phase n , Y_n^0 the initial weight fraction of phase β , and $K^{n/L}$ is the solid-liquid distribution coefficient for phase n , $K^{\beta/L}$ the solid-liquid distribution coefficient for phase β . The term P is given by

$$P = p^a K^{a/L} + p^b K^{b/L} + \dots \quad (3)$$

where p^a , p^b , and so forth are the fraction of liquid contributed by each phase during melting. For the unusual case when simple modal melting takes place (in other words, when the percentage of each phase in the solid does not change during melting), $P = D_0$, and equation 1 reduces to

$$\frac{c^L}{c_0} = \frac{1}{D_0 + F(1-D_0)} \quad (4)$$

In figure 1, c^L/c_0 is plotted against the extent of partial melting for residues having D_0 values of 0 to 10. When the bulk distribution coefficient approaches zero, equation 1 reduces to

$$\frac{c^L}{c_0} = \frac{1}{F} \quad (5)$$

so that the concentration of an element in the liquid depends solely on the extent of partial melting. Where $D_0 = 0$ (fig. 1), an upper limit is provided for the concentration that can result by partial melting of a given solid. When two elements have small distribution coefficients, the ratio of these elements in the liquid will

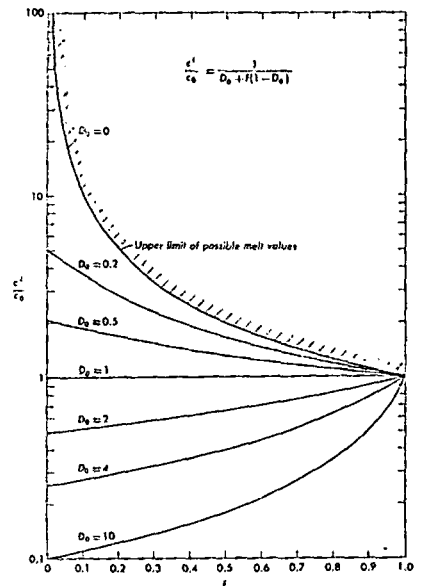


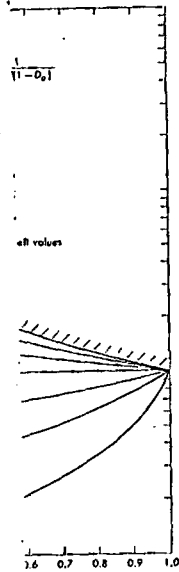
FIGURE 1.—Illustration of the behavior of a trace element during partial melting predicted by the "modal melting" equation of Shaw (1970) for liquid which is in continuous equilibrium with residual solid until it is removed as a "batch." F , fraction of melting; c_0 , initial trace-element concentration of the solid; c^L , trace-element concentration of the liquid; D_0 , bulk distribution coefficient for the starting assemblage.

be the same as that in the parent. Where F approaches 0 or is much smaller than D_0 , equation 1 or 4 reduces to

$$\frac{c^L}{c_0} = \frac{1}{D_0} \quad (6)$$

The larger the value of D_0 , the greater will be the extent of melting for which this relation holds. For example, when $D_0 = 10$ (fig. 1), c^L/c_0 has a value of about 0.1 for nearly 30 percent melting.

Also of importance during partial melting is the influence of minor phases. No phase, major or minor, that is present in an assemblage before melting will exert any control on the trace-element content or ratios of the melt if it is not a residual phase when the melt is separated. A consequence of this is that the modal



of a trace element during "modal melting" equation 5 in continuous equilibrium with the starting assemblage; D_0 = element concentration in the liquid; D_0 = starting assemblage.

Where F approaches 1 or 4 reduces

(6)

greater will be the relation holds. For c/c_0 has a value of melting. partial melting is the case, major or minor, before melting will not content or ratios phase when the melt is that the modal

FRACTIONAL CRYSTALLIZATION

Equations governing trace-element behavior during fractional crystallization assume equilibrium either between the surface of the crystallizing phases and the melt or between the total solid and the melt. The surface equilibrium models are based on the quantitative description of the distillation process developed by Rayleigh (1893) as applied to crystal growth from solution by Doerner and Hoskins (1925). These equations were first applied to magmatic differentiation by Neumann (1948), Holland and Kulp (1949), and Neumann, Mead and Vitaliano (1951), and were refined by Greenland (1970) and Albarède and Bottlinga (1972).

The equation describing trace-element behavior during fractional crystallization given by Greenland (1970) may be written (for the simplified case of crystallization of phases in constant proportions with constant distribution coefficients) as

$$\frac{c_L}{c_0} = F^{D_0/(D_0-1)} \tag{8}$$

F' is the fraction of liquid remaining, c_0 is the concentration of the original melt, c_L is the concentration in the differentiated liquid, and D_0 is the bulk distribution coefficient given by

$$D_0 = W^s K^{s/l} + W^l K^{l/l} + \dots \tag{9}$$

where K is the solid-liquid partition coefficient and W^s represents the weight fraction of a in the precipitating phases (fig. 2). As in the case of partial melting, when D_0 approaches zero,

$$\frac{c_L}{c_0} \approx \frac{1}{F'} \tag{10}$$

so that the concentration of an element depends only on the extent of solidification. Thus, the line marked $D_0 = 0$ (fig. 2) forms an upper limit to the concentration that a fractionated liquid may contain for a given percentage crystallized. If, on the other hand, D_0 is very large, then the liquid will be very strongly depleted. This is illustrated by the line marked $D_0 = 10$ in figure 2.

It is of interest to compare the relative magnitude of depletion and enrichment that occurs during surface-equilibrium fractional crystallization with that which occurs during partial melting. For a large value of D_0 or D_0' (for example, D_0 or $D_0' = 10$), fractional crystallization (fig. 2) can produce a greater depletion in the melt than partial melting (fig. 1). Similarly, for a value of D_0 or D_0' which is less than 1 (for example, D_0 or $D_0' = 0.5$), fractional crystallization (fig. 2)

melting model can be used to predict liquid concentrations when the identity of early melting phases is unknown, but when the mineralogical composition of the residue can be exactly specified for the specific degree of melting at which the separation of liquid occurs.

In applying the equations discussed above, the most useful results are obtained when the trace elements studied have a broad range of distribution coefficients for the various rock-forming minerals. If an element has a value of D_0 that approaches zero for a given residual mineral assemblage, equation 5 provides an estimate of the extent of partial melting. If an element has a value of $K^{s/l}$ that is large for one residual mineral and small for the other residual minerals, then a determination of the percentage of that mineral in the residue can be made for small degrees of melting, because equation 2 can be approximated as $D_0 \approx X_0^s K^{s/l}$, and equation 6 can be written as

$$X_0^s = \frac{c_0}{c^s K^{s/l}} \tag{7}$$

If the distribution coefficients are significantly different for two trace elements in a single mineral, the presence of that mineral in the residue can be determined. For example, consider the behavior of K and Rb during partial melting of an ultramafic assemblage containing olivine, pyroxene, and amphibole, when K is present in trace amounts. Both olivine and pyroxene have solid-liquid distribution coefficients for K and Rb that are close to zero (table 1), whereas the amphibole-liquid coefficient for K is close to one and that for Rb is about 0.3. Thus, during partial melting, residual olivine and pyroxene will retain almost no Rb or K, while residual amphibole rejects Rb more strongly than K. The result is a liquid that is enriched in Rb more than K and that has a lower K:Rb ratio than that of the parent assemblage. Thus, a low K:Rb ratio in a magma may suggest the presence of residual amphibole. If amphibole does not remain in the residue but is all reacted or melted, the K:Rb ratio will be close to that of the parent as neither olivine nor pyroxene retain K or Rb.

If K and Rb were major elements in this example, early melting of amphibole, which usually has a high K:Rb ratio, would produce a small fraction of melt of high K:Rb ratio. The high ratio for the melt would be lowered to that of the original parent solid as melting continued. It is thus important to determine whether the elements under consideration are major or trace elements for the composition in question. Unfortunately, criteria for this distinction in real magma systems are yet to be adequately defined.

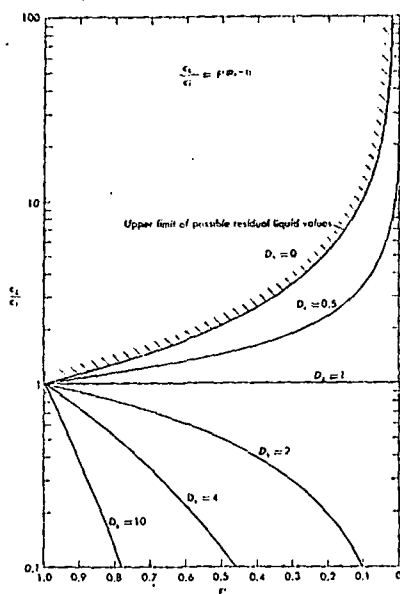


FIGURE 2.—Illustration of the behavior of a trace element predicted by a Rayleigh fractionation model for fractional crystallization from a liquid of phases in constant proportions and having constant distribution coefficients. F , fraction of liquid remaining; c_0 , concentration of the original melt; c_l , concentration in the differentiated liquid; D_0 , bulk distribution coefficient for the residual solid.

can produce greater enrichment than partial melting (fig. 1).

The second description of fractional crystallization assumes equilibrium between the total crystallizing solid and melt. This is expressed as

$$\frac{c_l}{c_0} = \frac{1}{F' + D_0(1-F')} \quad (11)$$

with symbols as previously defined. This equation is analogous to the total equilibrium partial melting models (eq. 1); figure 1 can be used to represent this case graphically if the abscissa scale is reversed to read from 1.0 to 0 and D_0 values are read as D_0' values. The surface-equilibrium model may be more applicable to rapidly cooling, shallowly emplaced magmas, whereas the total equilibrium model may better de-

scribe plutonic conditions where the cooling of an intruded magma is extremely slow, so that the crystallizing phases may be in total equilibrium with the melt (Rittman, 1973, p. 18).

DISTRIBUTION COEFFICIENTS

Quantitative application of the models above depends strongly on the availability of accurately determined distribution coefficients. Several approaches have been utilized in attempting to determine the absolute value of distribution coefficients, the principal ones including experimental studies in the mineral-aqueous vapor system, microprobe studies of strongly doped experimentally grown crystals and quench glass, and measurement of concentrations in separated phenocrysts and groundmass from volcanic rocks. Some of the severe problems incurred in utilizing the mineral-aqueous vapor system are illustrated by Zielinski and Fyfe (1974). Microprobe studies may prove useful, although doping of the experimental materials in sufficient quantity to detect the trace elements by microprobe may remove them from the concentration levels at which Henry's law is thought to apply. Phenocryst-matrix studies such as those of Philpotts and Schmetzler (1970) provide a body of "real world" data. These data are thought to approximate the true values, but they incur problems such as the effects of crystal zonation, as illustrated by Albarde and Bottinga (1972).

Rb, Sr, Ba, and rare-earth elements are among the most useful at this time because their phenocryst-matrix coefficients have been precisely measured for a variety of minerals in various rock types. The data for Rb, Sr, Ba, and rare earths are summarized in tables 1-3. The average and range for the determinations are given. Many partition coefficients vary in value by more than an order of magnitude; but refinement should be possible after careful evaluation has been made of the effects of temperature, pressure, crystallographic site, and magma composition. In spite of the large range of values, rare-earth elements, when considered as a group, show remarkably consistent partition coefficient patterns for a given mineral (see, for example, Schmetzler and Philpotts, 1970). Residues containing these minerals will thus produce characteristic fractionations in the rare-earth patterns of associated magmas.

NEED FOR ANALYTICAL PRECISION

The usefulness of trace elements is enhanced by their large range of natural abundance, especially when they are measured precisely and accurately, as for example, when the method of isotope-dilution mass-spec-

he cooling of an in-
so that the crystal-
equilibrium with the melt

CIENTS

e models above de-
of accurately deter-
Several approaches
g to determine the
icients, the principal
ies in the mineral-
studies of strongly
als and quench glass,
in separated pheno-
crystic rocks. Some
of tilizing the mineral-
ed by Zielinski and
may prove useful,
al materials in suffi-
lements by micro-
concentration levels
apply. Phenocryst-
ilipotts and Schnetz-
l world" data. These
the true values, but
fects of crystal zonal-
and Bottinga (1972).
rents are among the
e their phenocryst-
isely measured for a
ck types. The data
are summarized in

e for the determina-
coefficients vary in
agnitude; but refine-
mentful evaluation has
ature, pressure, crys-
tallization. In spite of
arth elements, when
markedly consistent
given mineral (see,
otts, 1970). Residues
s produce character-
-istic patterns of asso-

PRECISION

is enhanced by their
ec, especially when
accurately, as for ex-
-cess-dilution mass-spec-

TABLE 1.—Partition coefficients for basaltic and andesitic rocks

	Olivine			Orthopyroxene			Clinopyroxene			Augite			Biotite			Hornblende			Phlo- pate			Plagioclase			Car- not*	
	Avg	Low	High	Avg	Low	High	Avg	Low	High	Avg	Low	High	Avg	Low	High	Avg	Low	High	Avg	Low	High	Avg	Low	High		
Ce	0.000	0.000	0.000	0.021	0.002	0.025	0.070	0.013	0.026	0.13	0.07	0.21	0.02	0.20	0.004	0.31	0.034	0.12	0.023	0.23	0.023	0.023	0.023	0.023	0.023	0.023
Nd	0.063	0.03	0.10	0.29	0.06	0.53	1.2	0.65	1.8	3.1	1.7	4.3	0.6	2.3	1.0	2.0	0.42	0.81	0.23	0.20	0.23	0.023	0.023	0.023	0.023	0.023
Ba	0.066	0.03	0.11	0.54	0.14	1.00	1.8	0.90	2.6	3.0	2.0	7.4	1.0	3.2	1.4	3.3	0.31	0.67	0.21	0.17	0.20	0.023	0.023	0.023	0.023	0.023
Eu	0.068	0.05	0.10	0.54	0.22	0.79	1.4	0.91	2.6	3.1	2.7	7.5	0.84	2.9	1.1	3.0	0.31	0.67	0.21	0.17	0.20	0.023	0.023	0.023	0.023	0.023
Gd	0.077	0.04	0.12	0.91	0.32	1.71	1.9	0.95	2.7	3.1	2.7	8.7	1.6	5.3	2.4	1.1	0.30	0.63	0.17	0.17	0.21	0.023	0.023	0.023	0.023	0.023
Dy	0.099	0.06	0.11	1.5	0.34	2.53	2.1	1.05	3.1	3.5	3.0	1.0	2.3	6.1	3.1	1.0	0.30	0.53	0.19	0.19	0.21	0.023	0.023	0.023	0.023	0.023
Er	0.11	0.05	0.12	2.3	0.70	4.6	1.7	1.07	3.3	3.5	4.0	1.0	3.2	5.5	2.1	1.0	0.31	0.63	0.19	0.19	0.21	0.023	0.023	0.023	0.023	0.023
Yb	0.14	0.09	0.23	3.4	1.1	6.7	1.0	0.92	2.3	3.2	4.3	1.0	4.0	4.9	2.3	0.8	0.12	0.67	0.06	0.06	0.11	0.023	0.023	0.023	0.023	0.023
La	0.016	0.009	0.020	0.42	0.11	0.81	1.3	0.71	1.9	2.6	2.7	0.95	1.5	4.3	2.2	0.2	0.16	0.50	0.045	0.045	0.11	0.023	0.023	0.023	0.023	0.023

* Garnet values obtained by multiplying average garnet/clinopyroxene of reference 6 by average augite/liquid of this table.
 † References are as follows:
 1. Higuchi and Nagasawa (1969).
 2. Osima and others (1968).
 3. Philpotts and Schmetzler (1970).
 4. Schmetzler and Philpotts (1965).
 5. Schmetzler and Philpotts (1970).
 6. Philpotts and others (1971).
 Refer-
 ences: 1, 2, 4, 5 ----- 2, 3, 5 ----- 3, 5 ----- 2, 3, 4, 5 ----- 3, 5 ----- 1, 3, 4, 5 ----- 2, 5 ----- 1, 3, 5 -----

TABLE 2.—Partition coefficients for dacitic rocks
(Data represent one determination per mineral)

	Garnet	Biotite	Plagioclase	Hornblende
Ce	0.35	0.037	0.21	0.899
Nd	5.3	0.44	1.7	2.90
Sm	2.66	0.58	1.3	3.09
Eu	1.60	1.45	2.11	3.44
Gd	10.5	0.82	0.90	5.48
Dy	28.6	0.67	0.80	6.20
Er	42.8	1.02	0.81	5.94
Yb	39.9	1.79	0.77	4.89
La	29.0	1.85	0.92	4.53
K	0.020	0.23		
Rb	0.085	3.26	0.48	
Sr	0.15	1.2	2.64	
Ba	0.17	6.30	3.6	
References*	1, 2	1, 2	1, 2	3

* References are as follows:
 1. Philpotts and Schmetzler (1970).
 2. Schmetzler and Philpotts (1970).
 3. Artib, unpub. data, 1973.

TABLE 3.—Partition coefficients for rhyolitic rocks
(Figures in parentheses indicate number of determinations)

	Hyperthene		Clinopyroxene		Hornblende		K-feld- spar	Bio- tite	Phlo- pate	Apatite		Zircon		Plagioclase	
	(4)	(1)	(2)	(1)	(3)	(1)				(1)	(4)	(2)	(4)		
	Avg	Low	High	Avg	Low	High	Avg	Low	High	Avg	Low	High	Avg	Low	High
Ce	0.15	0.082	0.26	0.29	0.36	0.65	1.52	1.38	1.77	0.044	0.32	0.23	34.7	18.0	52.5
Nd	22	12	35	1.11	0.91	1.25	4.26	4.03	4.49	0.023	0.29	0.34	57.1	27.4	83.1
Ba	37	16	38	1.61	1.52	1.81	5.77	7.1	8.1	0.018	0.26	0.30	62.8	29.3	80.8
Eu	17	0.93	27	1.50	1.11	2.01	5.14	4.5	5.9	1.13	2.4	2.6	30.4	20.5	50.2
Gd	34	23	49	1.82	1.5	2.2	10.0	8.3	10.5	0.911	2.8	3.3	36.3	23.2	75.0
Dy	46	33	55	1.93	1.23	2.08	13.0	12.3	12.5	0.96	2.9	2.9	46.2	23.6	69.2
Er	53	33	73	1.80	1.07	2.25	12.9	10.5	11.0	0.966	3.5	3.7	37.2	20.9	51.2
Yb	85	72	99	1.75	1.14	2.04	8.3	7.15	9.0	0.912	4.1	4.7	22.9	12.1	37.0
La	90	76	114	1.54	1.28	1.91	5.5	4.4	6.3	0.966	3.3	3.1	20.2	11.2	20.2

* References are as follows:
 1. Nagasawa and Schmetzler (1971).
 2. Higuchi and Nagasawa (1969).
 3. Nagasawa (1970).
 4. Philpotts and Schmetzler (1970).
 5. Schmetzler and Philpotts (1970).
 6. Noble and Hedge (1970).

trometry is used. The need for accurate and precise
data is perhaps best illustrated by a simple hypothet-
ical example. Two laboratories measure the concentra-
tion of Rb in a sample from a large homogeneous body
of basalt. The precise laboratory reports Rb and Sr
values of 5.0±0.1 ppm and 150±3 ppm, whereas the
second laboratory, using a less precise technique, reports
Rb and Sr values of 5±4 ppm and 150±30 ppm. Near
the basalt is a large uniform dacite flow, the origin of
which is not clear, but two hypotheses have been ad-
vanced: (1) partial melting at great depth of a rock of
composition similar to that of the basalt at the surface,
leaving a residue containing equal amounts of garnet
and clinopyroxene or (2) fractional crystallization of
equal amounts of plagioclase and clinopyroxene from

the basaltic liquid. Each laboratory produces a Rb and Sr measurement for the dacite, the first reporting 35 ± 0.7 ppm Rb and 500 ± 10 ppm Sr, the second reporting 35 ± 4 ppm Rb and 500 ± 100 ppm Sr. The result of calculating each of these two models is shown in figure 3. The precise data suggest that neither simple mechanism is correct, whereas the imprecise data allow that the partial melting model is a possibility. Clearly, the validity of conclusions based on imprecise analytical data is subject to question, yet a surprising number of geochemists continue to publish and allow publication of data of poor precision and accuracy. One might argue that we do not yet know partition coefficients sufficiently well to justify rock analyses of great precision. However, we never will know distribution coefficients well without precise and accurate measurement, and when and if we do attain this goal, only the precise data in the literature will be of any value.

REFERENCES CITED

- Albarede, F., and Bottinga, Y., 1972, Kinetic disequilibrium in trace element partitioning between phenocrysts and host lava; *Geochim. et Cosmochim. Acta*, v. 36, no. 2, p. 141-156.
- Banno, Shohet, and Matsui, Yoshio, 1973, On the formulation of partition coefficients for trace elements distribution between minerals and magma; *Chem. Geology*, v. 11, no. 1, p. 1-15.
- Doerner, H. A., and Hoskins, W. M., 1925, Coprecipitation of radium and barium sulfates; *Am. Chem. Soc. Jour.*, v. 47, p. 662-675.
- Gast, P. W., 1968, Trace element fractionation and the origin of tholeiitic and alkaline magma types; *Geochim. et Cosmochim. Acta*, v. 32, no. 10, p. 1057-1086.
- Greenland, L. F., 1970, An equation for trace element distribution during magmatic crystallization; *Am. Mineralogist*, v. 55, nos. 3-4, p. 455-465.
- Higuchi, Hideo, and Nagasawa, Hiroshi, 1969, Partition of trace elements between rock-forming minerals and the host volcanic rocks; *Earth and Planetary Sci. Letters*, v. 7, p. 281-287.
- Holland, H. D., and Kulp, J. L., 1949, The distribution of accessory elements in pegmatites—I. Theory; *Am. Mineralogist*, v. 34, nos. 1-2, p. 35-60.
- McIntire, W. L., 1963, Trace element partition coefficients—A review of theory and applications to geology; *Geochim. et Cosmochim. Acta*, v. 27, no. 12, p. 1209-1254.
- Nagasawa, Hiroshi, and Schmetzler, C. C., 1971, Partitioning of rare earth, alkali and alkaline earth elements between phenocrysts and acidic igneous magma; *Geochim. et Cosmochim. Acta*, v. 35, no. 3, p. 953-968.
- Nagasawa, Hiroshi, 1970, Rare earth concentrations in zircons and apatites and their host dacites and granites; *Earth and Planetary Sci. Letters*, v. 9, no. 4, p. 332-364.
- Neumann, Heinrich, 1948, On hydrothermal differentiation; *Econ. Geology*, v. 43, no. 2, p. 77-83.
- Neumann, Heinrich, Mead, Judson, and Vitaliano, C. J., 1954, Trace element variation during fractional crystallization

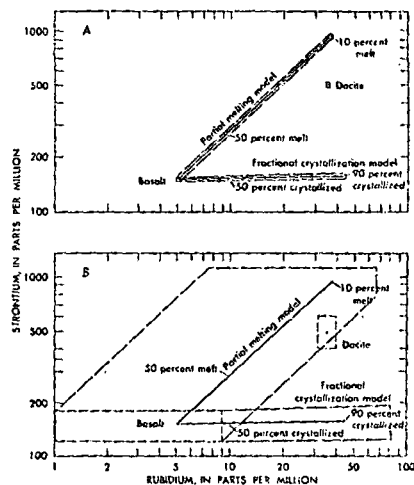


FIGURE 3.—Illustration of the need for precise analyses, as explained in the text. A, Model constructed from precise data. B, Model constructed from imprecise data. Solid lines represent model values; dashed lines, the uncertainties based only on the precision of the analyses, but not including uncertainties in the partition coefficients.

as calculated from the distribution law; *Geochim. et Cosmochim. Acta*, v. 6, nos. 2-3, p. 90-96.

Noble, D. C., and Hedge, C. E., 1970, Distribution of rubidium between saffie sanidine and natural silicic liquid; *Contrib. Mineralogy and Petrology*, v. 29, no. 3, p. 232-241.

Omura, N., Higuchi, H., Wakita, H., and Nagasawa, H., 1968, Trace element partition between two pyroxenes and the host volcanic rocks; *Earth and Planetary Sci. Letters*, v. 5, 47-51.

Philpotts, J. A., and Schmetzler, C. C., 1970, Phenocryst-matrix partition coefficients for K, Rb, Sr and Ba, with applications to anorthosite and basaltic gneiss; *Geochim. et Cosmochim. Acta*, v. 34, p. 307-322.

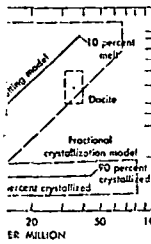
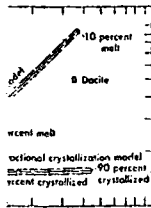
Philpotts, J. A., Schmetzler, C. C., and Thomas, H. H., 1972, Petrogenetic implications of some new geochemical data on eclogitic and ultrabasic inclusions; *Geochim. et Cosmochim. Acta*, v. 36, no. 10, p. 1151-1194.

Rayleigh, J. W. S., 1896, Theoretical considerations respecting the separation of gases by diffusion and similar processes; *Philos. Mag.*, v. 42, p. 77-107.

Rittman, Alfred, 1973, Stable mineral assemblages of igneous rocks, Springer-Verlag, p. 16-19.

Schilling, J. G., and Winchester, J. W., 1967, Rare-earth fractionation and magmatic processes, in *Remond, S. K., ed., Mantles of the Earth and terrestrial planets*; London and New York, Interscience Publishers, p. 267-283.

DISSESSES



precise analyses, as expected from precise data. Solid lines represent estimates based only on not including uncer-

tion law: *Geochim. et Cosmochim. Acta*, v. 34, p. 231-240.

Distribution of rubidium in siliceous liquid: *Contr. Mineral. Petrol.*, v. 3, p. 234-241.

and Nagasawa, H., 1963, Two pyroxenes and the Planetary Sci. Letters.

1970, Phenocryst-matrix relationships and Ba, with applications: *Geochim. et Cosmochim. Acta*.

Thomas, H. H., 1972, New geochemical data on the evolution of the Earth: *Geochim. et Cosmochim. Acta*, v. 36, p. 1023-1030.

considerations respecting the evolution of the Earth and similar processes: *Geochim. et Cosmochim. Acta*.

assemblages of igneous rocks: *Geochim. et Cosmochim. Acta*.

1967, Rare-earth fractionation in the Earth and other planets: *Geochim. et Cosmochim. Acta*, v. 31, p. 267-283.

ARTH

Schneizler, C. C., and Philippotts, J. A., 1968, Partition coefficients of rare-earth elements and barium between igneous matrix material and rock-forming-mineral phenocrysts—1, in Abrens, I. H., ed., *Origin and distribution of the elements*: Oxford, England, and New York, Pergamon Press, p. 929-938.

Schneizler, C. C., and Philippotts, J. A., 1970, Partition coefficients of rare-earth elements between igneous matrix

material and rock-forming-mineral phenocrysts—11: *Geochim. et Cosmochim. Acta*, v. 34, no. 3, p. 331-340.

Shaw, D. M., 1970, Trace element fractionation during anatexis: *Geochim. et Cosmochim. Acta*, v. 34, no. 2, p. 237-243.

Zielinski, R. A., Frey, F. A., 1974, An experimental study of partitioning of a rare-earth element (Gd) in the system diopside-aqueous vapour: *Geochim. et Cosmochim. Acta*, v. 38, p. 545-565.

UNIVERSITY OF UTAH
RESEARCH INSTITUTE
EARTH SCIENCE LAB.

EQUILIB MODELS/
CONC SOLUTIONS

CALCULATING ACTIVITY COEFFICIENTS IN HYDROMETALLURGY -
A REVIEW

CHARLES L. KUSIK and HERMAN P. MEISSNER

*A.D. Little, Inc., Cambridge, Mass. (U.S.A.)
Department of Chemical Engineering, Massachusetts Institute of Technology, Cambridge,
Mass. (U.S.A.)*

(Received June 25, 1974; accepted October 1, 1974)

ABSTRACT

Kusik, C.L. and Meissner, H.P., 1975. Calculating activity coefficients in hydrometallurgy - a review. *Int. J. Miner. Process.*, 2: 105-115.

Recent developments for estimating activity coefficients of electrolytes both in pure and multicomponent aqueous solutions are reviewed with good success generally attained up to saturation. Examples are presented to illustrate applications of these methods in calculating ion concentrations, vapor pressures, and solubility limits, for some problems encountered in hydrometallurgy.

INTRODUCTION

Equilibrium calculations of strong electrolyte concentrations in aqueous solution reactions, such as in leaching, metal pickling, causticising, and in hydrometallurgical operations generally, have been handicapped by a lack of activity coefficient data. The Debye-Hückel equation for predicting such activity coefficients unfortunately applies only in very dilute pure solutions having concentrations far below those of common industrial interest. The object here is to review new methods for predicting such activity coefficients over normally encountered ranges of temperatures, and for concentrations often up to saturation. Success with recently published methods is usually well within 20%. Application to typical metallurgical problems is illustrated.

The quantities involved in the correlations discussed here are the so-called reduced activity coefficient, Γ° , and concentrations expressed as μ , the ionic strength. These quantities are related to γ° ; the mean ionic activity coefficient for the pure electrolyte in question, and to its molality m , as follows:

$$\Gamma^\circ = (\gamma^\circ)^{1/z_+ z_-} \quad (1)$$

$$\mu = 0.5 m (v_+ z_+^2 + v_- z_-^2) \quad (2)$$

where v_+ and v_- are respectively numbers of moles of cations and anions formed per mole of electrolyte upon complete dissociation, while z_+ and z_-

SUDJ
GCHM
CAC

Inspection of Fig.1 indicates the isotherms to fall onto a single curve family, with little curve cross-over, so that when one value of Γ° for a strong electrolyte is known at a given concentration, the entire curve for this material can be estimated. Thus assume that γ° is to be predicted for a 9 *m* aqueous solution of KOH, knowing that when μ is 2, $\gamma^\circ = 0.863$ (Robinson and Stokes, 1959, p. 494) corresponding to a value of $\log \Gamma^\circ = -0.064$. Locating this known point on Fig.1 and extrapolating to a μ of 9, $\log \Gamma^\circ$ is found to be 0.66 corresponding to a γ° of 4.57 which is within 5% of the reported value for γ° value of 4.72 at this concentration (Robinson and Stokes, 1959, p.504).

Location of the proper curve to use in Fig.1 for a given strong electrolyte obviously requires knowledge of at least one value of $\log \Gamma^\circ$ at a given ionic strength. Much of the literature data on experimental values of γ° is reviewed by Harned and Owen (1958) and by Robinson and Stokes (1959). Unless otherwise indicated, values for activity coefficients are taken from these sources. Lacking experimental values, Γ° can be estimated from data on vapor pressure lowering of aqueous solutions of the electrolyte in question (Kusik and Meissner, 1972). In the absence of all such data, Γ° can be predicted by the method of Meissner and Tester (1972), or by the method of Bromley (1973).

EFFECT OF TEMPERATURE

As has been pointed out (Meissner et al., 1972) the isotherms of Fig.1 apply not only at 25°C, but at all temperatures between 0° and 150°C and higher. However, a given electrolyte's isotherm at 25°C does not necessarily coincide with that at some other temperature. Only those points which lie on the dashed "reference" line of Figs.1 and 2, designated by the subscript "ref", are relatively unaffected by temperature, and for such points $(\partial \log \Gamma_{\text{ref}} / \partial T)_\mu$ is obviously zero. The effect of temperature upon $\log \Gamma_T^\circ$ can be estimated at any fixed ionic strength below 20 by the following equation (Meissner and Peppas, 1973):

$$\log \Gamma_T^\circ = (1.125 - 0.005t) \log \Gamma_{25^\circ\text{C}}^\circ - (0.125 - 0.005t) \log \Gamma_{\text{ref}} \quad (3)$$

where $\log \Gamma_T^\circ$, $\log \Gamma_{25}^\circ$, and $\log \Gamma_{\text{ref}}$ are all at the ionic strength in question while the solution temperature t is in degrees centigrade. To illustrate application of eq.3: when μ is 16, $\log \Gamma^\circ$ for HCl is reported by Harned and Owen (1958) to be 1.6179 at 25°C. From the dashed line of Fig.1, $\log (\Gamma_{\text{ref}})$ is 0.18 when μ is 16. Substituting into eq.3 and solving at 50°C, $\log \Gamma_{50}^\circ$ is found to be 1.39, versus Harned and Owen's experimentally reported value of 1.373 at these conditions.

It is to be noted in passing that, as expected, when Γ_{ref} and Γ_{25}° are identical, then Γ_T° and Γ_{ref} are likewise identical in eq.3.

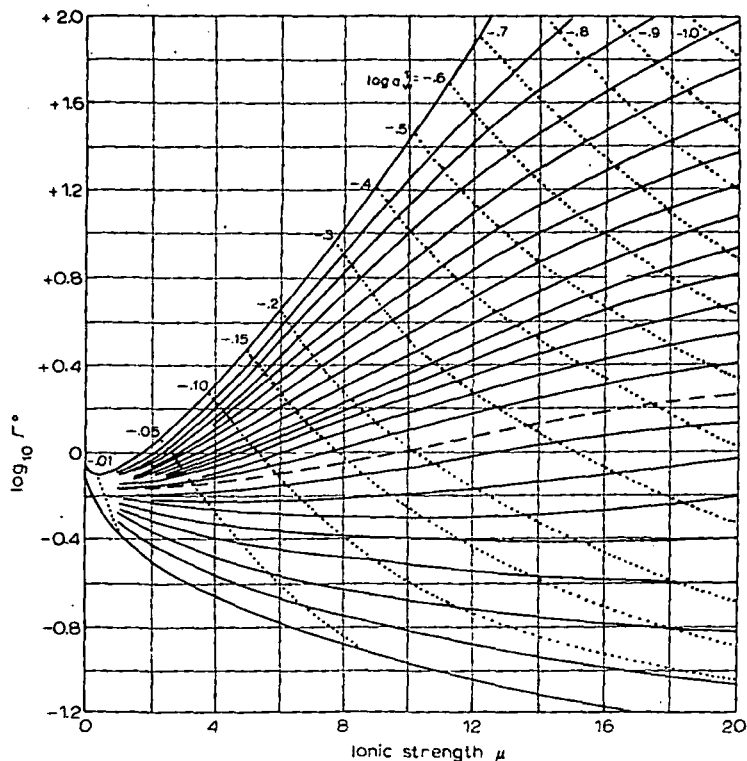


Fig.2. Activities of water for aqueous solutions of pure electrolytes plotted over Fig.1. For 1:1 electrolytes values of $\log(a_w^1)$ are equal to $\log(a_w)$ and thus the dotted curves with $\log(a_w^1)$ constant represent conditions with constant vapor pressure of water. For higher electrolytes, $\log(a_w^1)$ values read from this figure are used in eq.4 to determine activities of water.

VAPOR PRESSURES

Having located the isothermal curve of the activity coefficient of a single electrolyte in aqueous solution versus concentration on Fig.1, points on the corresponding curve of water vapor pressure as a function of concentration for such a solution can be determined from the Gibbs-Duhem equation. Curves so calculated for the water vapor pressure in solution of single 1:1 electrolytes in water are presented in Fig.2 (Kusik and Meissner, 1972), superimposed on the activity coefficient curves of Fig.1. Results are shown in terms of the water activity, (a_w^1) , defined in the usual manner as the isothermal water vapor pressure ratio of the electrolyte solution to pure water. It should be noted that these isothermal curves for $\log(a_w^1)$ apply at any temperature and indicate that at given values of Γ° and μ , all such 1:1 electrolytes have the same value of (a_w^1) , regardless of the temperature T . To illustrate application of these curves, a pure saturated solution of NaNO_3 at 25°C has an ionic

strength of 10.8 hence $\log \Gamma^\circ$ is -0.46 (Harned and Owen, 1958). For this condition, $\log (a_w^1)$ is found to be -0.13 from Fig.2 which is the same as the experimental value. Similarly at 50°C , an HCl solution which has an ionic strength of 10 has a value for $\log \Gamma^\circ$ of 0.87 . From Fig.2, $\log (a_w^1)$ for this condition is -0.365 , which again equals the experimental value.

At a given value of μ and $\log \Gamma^\circ$, water activities (and vapor pressures) of the higher electrolytes differ from those of the 1:1 electrolytes. Water activities for these higher electrolytes, namely $(a_w^\circ)_{z_1 z_2}$, can nevertheless be estimated from the curves of Fig.2 for the 1:1 electrolytes by use of the following equation (Kusik and Meissner, 1972):

$$\log (a_w^\circ)_{z_1 z_2} = 0.0156\mu \left(1 - \frac{1}{z_1 z_2}\right) + \log (a_w^1) \quad (4)$$

To illustrate at 25°C , CaCl_2 is a 2:1 electrolyte for which $\log \Gamma^\circ$ is 0.385 when μ is 15 (a 5 *m* solution). At these values of μ and $\log \Gamma^\circ$, $\log (a_w^1)$ is -0.39 from Fig.2. Substituting into eq.4 $\log (a_w^\circ)_{z_1 z_2}$ for CaCl_2 is 0.525 which is in fair agreement with the experimental value of 0.575 .

It is evident that knowing the vapor pressure of a solution of a 1:1 electrolyte at a given ionic strength and temperature, the corresponding value of $\log \Gamma^\circ$ can be directly determined from Fig.2 and the associated isotherms for this electrolyte located in Fig.1. For higher electrolytes, determination of $\log \Gamma^\circ$ from vapor pressure data requires recourse to eq.4 along with Fig.2. As pointed out earlier, such a procedure can be used for curve identification of a given electrolyte on Fig.1 when no experimental data on γ° are available.

ACTIVITY COEFFICIENTS IN MIXTURES

The reduced activity coefficient of electrolyte 12 in a mixed aqueous solution of total ionic strength μ_T can be estimated from pure solution values (Γ°) of the various individual electrolytes present, determined at the ionic strength and temperature of the mixture (Meissner and Kusik, 1972). For the simple case of solutions involving not more than two cations and two anions, in which four ion combinations can obviously be identified, the equations are as follows:

$$\log \Gamma_{12} = 0.5 (X_1 \log \Gamma_{12}^\circ + Y_2 \log \Gamma_{12}^\circ + X_3 \log \Gamma_{32}^\circ + Y_4 \log \Gamma_{14}^\circ) \quad (5)$$

$$\log \Gamma_{32} = 0.5 (X_1 \log \Gamma_{12}^\circ + Y_2 \log \Gamma_{32}^\circ + X_3 \log \Gamma_{32}^\circ + Y_4 \log \Gamma_{34}^\circ) \quad (6)$$

$$\log \Gamma_{14} = 0.5 (X_1 \log \Gamma_{14}^\circ + Y_2 \log \Gamma_{12}^\circ + X_3 \log \Gamma_{34}^\circ + Y_4 \log \Gamma_{14}^\circ) \quad (7)$$

$$\log \Gamma_{34} = 0.5 (X_1 \log \Gamma_{14}^\circ + Y_2 \log \Gamma_{32}^\circ + X_3 \log \Gamma_{34}^\circ + Y_4 \log \Gamma_{34}^\circ) \quad (8)$$

where X and Y , the ionic strength fractions, are defined in the nomenclature (see p.114). These equations, applying at any temperature, are readily extended to systems containing more than four ions. To illustrate the applicability to a three ion system, consider a mixed solution, at 25°C saturated with NaNO_3

which is 5.27 *m* in $\text{Ca}(\text{NO}_3)_2$ and 5.3 *m* in NaNO_3 . It follows by definition that the total ionic strength, μ_T , for this solution is 21.1. Designating Ca^{2+} , NO_3^- and Na^+ ions as 1, 2 and 3, then X_1 , Y_2 , and X_3 are respectively 0.8, 1.0, and 0.2, while Y_4 is, of course, zero in this case. Substituting into eq.6, Γ for NaNO_3 in this mixed solution is 0.40, versus a value calculated from the solubility product of 0.38.

VAPOR PRESSURES OVER MIXED SOLUTIONS

The water activity for the mixed solution just discussed containing 3 or 4 ions can be calculated from the activities of water over pure solutions at the ionic strength and temperature of the mixture. Thus taking $(a_w^\circ)_{12}$, $(a_w^\circ)_{14}$, $(a_w^\circ)_{32}$, etc., at the total ionic strength and temperature of this mixed solution, then $\log(a_w)_{\text{mix}}$ becomes (Meissner and Kusik, 1973):

$$\log(a_w)_{\text{mix}} = X_1 Y_2 \log(a_w^\circ)_{12} + X_1 Y_4 \log(a_w^\circ)_{14} + X_3 Y_2 \log(a_w^\circ)_{32} + X_3 Y_4 \log(a_w^\circ)_{34} \quad (9)$$

To illustrate an application, a solution saturated at 30°C with both NaCl and KCl is 5.09 and 2.3 *m* in these two salts, respectively. Since (a_w°) values for NaCl and KCl, namely salts 12 and 32, are respectively 0.71 and 0.78 at this solution temperature and total ionic strength, then the water activity over the mixed solution, $(a_w)_{\text{mix}}$, is 0.73 by eq.9 versus an experimental value of 0.72 (Adams and Mertz, 1929). Eq.9 is again readily extended to systems of more than four ions.

As stated earlier (Meissner and Kusik, 1973, p.207) eqs.5 through 9 above rigorously satisfy the Gibbs-Duhem relations only for electrolyte mixtures in which all cations have the same charge, and all anions have the same charge, as in solutions of NaNO_3 and NH_4Cl ; or $\text{Ca}(\text{NO}_3)_2$ and MgCl_2 . For such systems, Bromley (1973) has made a similar observation. However, eqs. 5 through 9 fit available experimental data in substantially all multicomponent systems reasonably well, including those in which ion charges do not satisfy the above criteria.

SOLUBILITY

Consider two saturated solutions of the strong electrolyte 12, in which the solid phase in each solution carries *n* moles of water of crystallization. For example, one aqueous solution is saturated with FeCl_2 at 25°C. The second solution, again saturated with FeCl_2 at 25°C, contains some dissolved HCl. The solid phase present in both solutions is $\text{FeCl}_2 \cdot 4\text{H}_2\text{O}$, making *n* equal to 4. The applicable solubility product equation for electrolyte 12, namely FeCl_2 in this example, is then (Meissner and Kusik, 1973):

$$(m_1)^{\nu_1} (m_2)^{\nu_2} (\gamma_{12})^{\nu_{12}} (a_w)_{\text{mix}}^n = (m_1^\circ)^{\nu_1} (m_2^\circ)^{\nu_2} (\gamma_{12}^\circ)^{\nu_{12}} (a_w^\circ)^n \quad (10)$$

For solutions containing electrolytes carrying no waters of crystallization like AgCl, n is of course zero which for salts of low solubility, again like AgCl, activity coefficients are unity. In such systems, eq.10 reduces to the more familiar form of the solubility product equation:

$$(m_1)^{v_1} (m_2)^{v_2} = (m_1^{\circ})^{v_1} (\bar{m}_2^{\circ})^{v_2} \quad (11)$$

Eq.10 is easily extended to cases in which the solid phases in contact with the pure saturated solution and with the mixed solution are different hydrates of the same electrolyte. For example, in saturated aqueous solutions of Na_2CO_3 at 25°C , the solid phase present in pure saturated solutions is $\text{Na}_2\text{CO}_3 \cdot 10\text{H}_2\text{O}$, while in solutions also containing higher concentrations of NaCl, is $\text{Na}_2\text{CO}_3 \cdot 7\text{H}_2\text{O}$ (International Critical Tables, 1928, IV, p.301). Consequently n_0 and n_{mix} are 10 and 7 respectively. The derivation and proper form of eq.10 for such cases was discussed previously (Meissner and Kusik, 1973).

The use of the various relations just presented is further illustrated in the following examples.

Pickle liquor

A waste pickle liquor is 7 m in HCl. If also saturated at 25°C with $\text{FeCl}_2 \cdot 4\text{H}_2\text{O}$, what is the concentration of this electrolyte, knowing that the solubility of $\text{FeCl}_2 \cdot 4\text{H}_2\text{O}$ in pure water is 5.07 m ($\mu=15.21$)? For this pure saturated solution, $\gamma_{\text{FeCl}_2}^{\circ}$ is found, by using Fig.2, to be 3.8 from extrapolation of Harned and Owen's value (1958) for Γ° of 0.90 when μ is 6, while a_w is 0.55 as determined from Fig.2 and eq.4. Substituting into eq.10 and letting m_{12} and m_{32} be the concentration of ferrous chloride and HCl respectively in the mixed solution:

$$m_{12} (2m_{12} + m_{32})^2 \gamma_{12}^3 (a_w)_{12}^4 = (5.07) (2 \times 5.07)^2 (3.8)^3 (0.55)^4$$

or:

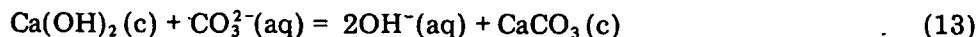
$$m_{12} (2m_{12} + 7)^2 \gamma_{12}^3 (a_w)_{12}^4 = 2617 \quad (12)$$

In these solutions, by definition, the total ionic strength, μ_T , equals $(3m_{12} + 7)$. By trial, various values of m_{12} are assumed, values of total ionic strength are calculated, and corresponding values of γ_{12}° , γ_{32}° , $(a_w^{\circ})_{12}$, $(a_w^{\circ})_{32}$, are found from Fig.2 and eq.4 as described above. Values of X_1 , Y_2 , X_3 are calculated and γ_{12} and a_{mix} are obtained from eqs.5 and 9. Upon substituting various values into eq.12 and solving, this equation balances when m_{12} is 1.65, (where μ is of course 11.95, γ_{FeCl_2} is 10 and a_{mix} is 0.35) compared to the experimental value for m_{12} of 1.4 m (Seidell and Linke, 1958).

Causticising

Caustic soda is often made industrially by adding an excess of solid hydrated

lime to a strong hot aqueous solution of sodium carbonate:



It is now desired to calculate the molalities of NaOH and Na₂CO₃ at equilibrium at 95°C in such a solution when the total ionic strength is 3.5. Since solubilities of CaCO₃ and Ca(OH)₂ are negligibly small, significant contributions to the ionic strength are made here only by the NaOH and Na₂CO₃ in solution, or:

$$\mu_T = m_{\text{NaOH}} + 3m_{\text{Na}_2\text{CO}_3} = 3.5 \quad (14)$$

It is obvious that the desired values of m_{NaOH} and $m_{\text{Na}_2\text{CO}_3}$ can be calculated from the equilibrium constant for eq.13:

$$K_{95^\circ\text{C}} = \frac{(m_{\text{OH}^-})^2}{(m_{\text{CO}_3^{2-}})} \cdot \frac{\gamma^4 \cdot m_{\text{NaOH}}}{\gamma^3 \cdot m_{\text{Na}_2\text{CO}_3}} \quad (15)$$

providing the activity coefficients and the equilibrium constant are known at 95°C. To determine $K_{95^\circ\text{C}}$ the value of $\Delta F_{25^\circ\text{C}}^\circ$ for reaction 13 is first calculated from the standard free energies of formation listed in Rossini et al (1952) for solid CaCO₃, solid Ca(OH)₂, and for both CO₃²⁻ and OH⁻ ions in their hypothetical solutions of unit activity at a mean ionic molality of unity. Since $\Delta F_{25^\circ\text{C}}^\circ$ equals $-RT \ln K$, $K_{25^\circ\text{C}}$ therefore equals 1,740 for reaction 13. Again from Rossini, ΔH° for reaction 13 is -0.93 kcal. Assuming this ΔH° to be independent of temperature, and integrating to 95°C with the van't Hoff equation, namely $(d \ln K/dT) = \Delta H/RT^2$, $K_{95^\circ\text{C}}$ is found to be 1,290. Values for $\log \Gamma_{25^\circ\text{C}}^\circ$ for Na₂CO₃ and NaOH, each in pure solution having an ionic strength of 3.5 are respectively -0.30 and -0.080 (Harned and Owen, 1958). Corresponding values of $\log \Gamma_{95^\circ\text{C}}^\circ$ for these two electrolytes are -0.25 and -0.105 , calculated from eq.3, knowing from Fig.2 that $\log \Gamma_{\text{ref}}^\circ$ is -0.15 when μ is 3.5. The activity coefficients of Na₂CO₃ and NaOH in the mixed solution in question at 95°C with μ equalling 3.5 can now be calculated from eqs. 5 and 7.

Solution is by trial and error, and is here illustrated with the assumed final value for $m_{\text{Na}_2\text{CO}_3}$ of 0.04, whereupon m_{NaOH} is 3.38 by eq.15. Designating Na⁺ as ion 1, CO₃²⁻ as 2, and OH⁻ as 4, the quantity Y_2 , namely $(4m_{\text{CO}_3^{2-}})/(4m_{\text{CO}_3^{2-}} + m_{\text{OH}^-})$, is 0.045 while Y_4 is 0.955 and X_1 is unity. Using the above found values in the mixture eqs. 5 and 7 and solving, $\Gamma_{\text{Na}_2\text{CO}_3}$ and Γ_{NaOH} are 0.66 and 0.78, respectively. Checking back on the initial assumption by substituting these values into eq.15, $K_{95^\circ\text{C}}$ calculates to 1,279, which is in reasonable agreement with the constant of 1,290 calculated from the Rossini free energy values above. Thus the equilibrium concentration of $m_{\text{Na}_2\text{CO}_3}$ and m_{NaOH} in this solution are calculated respectively to be 0.04 and 3.38, which compare with experimental values of 0.11 and 3.11 (Littman and Gaspari, 1956, run 218).

"Insoluble" salts

The solubility increase or decrease of an "insoluble" electrolyte by the addition of other salts has been explained by a "common ion" effect, salting in and salting out, etc. An interesting example is the case of CaSO_4 whose solubility increases with the ionic strengths in solutions of other soluble sulfates such as $(\text{NH}_4)_2\text{SO}_4$, despite the presence of the common ion.

Thus, using eq.10, consider the determination of the solubility of CaSO_4 at 25°C in a solution 3.17 m in $(\text{NH}_4)_2\text{SO}_4$ realizing that the stable solid phase is gypsum ($\text{CaSO}_4 \cdot 2\text{H}_2\text{O}$) having a solubility in pure water of 0.0154 m where $\mu = 0.062$ (Seidell and Linke, 1958, p.674). Recognizing that the activity coefficient of CaSO_4 is not readily available, Γ° for this salt is estimated from the known value of Γ° for CaCl_2 by the method of Meissner and Tester (1972), and found to be 0.51 when μ is 2 and 0.36 when μ is 0.062. Realizing that the water activity, a_w° , is about unity at the low ionic strength of a pure solution of CaSO_4 , and designating Ca^{2+} , SO_4^{2-} , and NH_4^+ as ions 1, 2, and 3 respectively, substitution in eq.10 yields:

$$(m_1)(m_2)(\gamma_{12})^2 (a_w)^\circ = (0.0154)(0.0154)(0.36)^2 (1)^2 = 3.07 \cdot 10^{-3} \quad (16)$$

The calcium ion concentration m_1 in the mixed solution must now be determined by trial and error by first assuming a value of m_{12} and calculating the total ionic strength, μ_T , of the mixed solution. At this total ionic strength the corresponding Γ° values of each pure salt and also the activity of water, a_w° , are determined from Fig.2 and eq.4. Values of Γ and a_w are then calculated in the mixed solution by eqs.5, 6 and 9, after which m_1 is obtained from eq.16.

Thus in a 3.19 m solution of $(\text{NH}_4)_2\text{SO}_4$ saturated with CaSO_4 , m_{12} is arbitrarily assumed to be 0.045 m , making a total ionic strength of 9.69. At this μ_T , $\log \Gamma^\circ$ for $(\text{NH}_4)_2\text{SO}_4$ is -0.455 (Robinson and Stokes, 1959, p.501), while $\log \Gamma^\circ$ for CaSO_4 is found by following the solid line on Fig.1 up from $\mu=2$ where Γ° is 0.51 as reported above, to $\mu=9.7$, where $\log(\Gamma^\circ)$ for CaSO_4 is -0.45 .

For the molalities assumed here, X_1 , X_3 and Y_2 are respectively 0.03, 0.97 and 1.0. For this mixed solution, the reduced activity coefficient Γ_{12} of CaSO_4 is calculated from eq.5 to be 0.0158. Using Fig.2 and eq.4 for pure solutions, the water activity in the mixed solution is found to be about 0.924 from eq.9. Substituting the above values into eq.16 the value of m_1 is now calculated:

$$(m_1)(3.2)(0.0158)^2 (0.924)^2 = 2.97 \cdot 10^{-3} \rightarrow m_1 = 0.045 \quad (17)$$

Since the initial value for m_1 chosen was also 0.045, this trial value is confirmed. For comparison, Seidell and Linke (1958) report that in a 3.19 m solution of $(\text{NH}_4)_2\text{SO}_4$ shows an experimentally determined solubility for CaSO_4 of 0.039 m . Thus, the error is seen to be about 15% which is well within the accuracy of the solubility data for CaSO_4 and errors that can be

encountered in calculating values of γ extrapolated from μ of 0.06 up to 9.7. Consequently by eq.10, the solubility of CaSO_4 can be expected to increase in concentrated $(\text{NH}_4)_2\text{SO}_4$ despite the presence of a common ion that tends to suppress solubility because:

(1) The water activity decreases from unity for pure CaSO_4 solutions to 0.90 in the mixed solution, with corresponding changes in the water vapor pressure.

(2) The CaSO_4 activity coefficient decreases from 0.36 in pure saturated solutions to 0.0158 in the mixed solution.

PRECISION

Errors in estimating activity coefficients for electrolytes in solutions have been found to be generally within 20%. Further errors can be introduced when Γ values are predicted from vapor pressure lowering, extrapolated over large ranges of ionic strength in Fig.1, or large temperature ranges by eq.3. Thus the relations shown here should be used only when direct experimental evidence is not available.

NOMENCLATURE

- (a_w) = activity of water, $(a_w^0)_{12}$ being for a pure solution of an electrolyte identified by subscript, $(a_w)_{\text{mix}}$ being for mixed solution. (a_w^1) is the activity of a 1:1 electrolyte at a given value of Γ^0 and μ , as in Fig.2.
- m = molality, in g-mol/1000 g solvent. The ions or electrolyte referred to are indicated by subscript.
- n = moles of water crystallization per mole of anhydrous electrolyte in a solid, n_0 and n being used to distinguish between solids in equilibrium with saturated pure and mixed solutions, respectively.
- X = cationic fraction, as in μ_1/μ_c or μ_3/μ_c .
- Y = anionic fraction, as in μ_2/μ_a or μ_1/μ_a .
- z = number of unit charges on the ion, indicated by the subscript. Thus z is unity for Na^+ , also for NO_3^- , but is 3 for Al^{3+} , also for PO_4^{3-} .
- v = moles of ions formed upon complete dissociation of 1 mol of electrolyte. Thus, v_1 is for the indicated cation, v_2 is for the indicated anion, while v_{12} is the total number of ions namely $(v_1 + v_2)$. To illustrate, v_{12} is 2 for NaCl and 5 for $\text{Al}_2(\text{SO}_4)_3$.
- γ = mean ionic activity coefficient for the electrolyte indicated by the subscript, γ_{12}^0 being for the pure solution and γ_{12} for the mixed solution.
- Γ = reduced activity coefficient, namely $\gamma_{12}^{1/z_1 z_2}$ for the electrolyte indicated by the subscript. The term Γ_{12}^0 , refers to pure solutions, Γ_{12} to mixed solutions.
- μ = ionic strengths indicated by the subscript. The ionic strengths μ_1, μ_2, \dots

Jour. Research U.S. Geol. Survey
Vol. 2, No. 3, May-June 1974, p. 271-278

THE CALCULATION OF AQUIFER CHEMISTRY IN HOT-WATER GEOTHERMAL SYSTEMS

By ALFRED H. TRUESDELL and WENDY SINGERS,
Mento Park, Calif., Chemistry Division, D.S.I.R., New Zealand

Abstract.—The temperature and chemical conditions (pH, gas pressure, and ion activities) in a geothermal aquifer supplying a producing bore can be calculated from the enthalpy of the total fluid (liquid + vapor) produced and chemical analyses of water and steam separated and collected at known pressures. Alternatively, if a single water phase exists in the aquifer, the complete analysis (including gases) of a sample collected from the aquifer by a downhole sampler is sufficient to determine the aquifer chemistry without a measured value of the enthalpy. The assumptions made are that the fluid is produced from a single aquifer and is homogeneous in enthalpy and chemical composition. These calculations of aquifer chemistry involving large amounts of ancillary information and many iterations require computer methods. A computer program in PL-1 to perform these calculations is available from the National Technical Information Service as document PB-219 376.

In active hydrothermal systems that have been drilled, mineral alteration and deposition can be related to observed temperatures and fluid compositions. Chemical analyses of water and steam produced from many types of geothermal systems are now available. However, analyses of fluids collected at the surface do not describe the chemistry of fluids as they occur at depth. The chemical differences between the fluids at the surface and in the deep aquifer are due to the decrease of pressure and temperature during production. Adiabatic expansion during passage up the drill hole may result in steam separation, cooling, and an increase in the concentration of the solutes in the water phase. Loss of dissolved CO_2 and H_2S from the water to the vapor increases the pH value of the water. The increase in pH and solute concentration and the decrease in temperature may cause the water to become supersaturated with calcite or silica minerals and may result in scaling of well casings. The continued production of a geothermal system is likely to decrease the reservoir pressures enough to form steam in the aquifer (Mahon, 1970). The resulting decrease in gas pressures, increase in aquifer pH, and temperature lowering may cause increased calcite deposition in the casing and possibly in the aquifer. Potential mineral deposition may be calculated if the chemistry of aquifer fluids is known.

Underground water temperatures may be calculated from known mineral solubility or ion exchange reactions that control water compositions; for example, quartz solubility (Fournier and Rowe, 1966; Mahon, 1966), Na:K ratios (White,

1965; Ellis, 1970), or Na:K:Ca ratios (Fournier and Truesdell, 1973). The assumptions underlying these calculations have been discussed by White (1970).

Thus, for practical reasons as well as to increase our knowledge of natural systems, it is of interest to calculate the chemical properties of geothermal fluids before they are changed during production. This is the purpose of the computer program described here.

ACKNOWLEDGMENTS

The computer program is a further development of the method of Ellis (1967, 1970) and was partly written in the laboratories of the Chemistry Division, Department of Scientific and Industrial Research (D.S.I.R.), New Zealand, while the author was on a training grant from the U.S. Geological Survey. The calculations have been discussed with A. J. Ellis, W. A. J. Mahon, Werner Giggenschach, and R. B. Glover of the D.S.I.R., New Zealand, and Ivan Barnes, L. J. P. Muffler, R. O. Fournier, and D. E. White of the U.S. Geological Survey. The program was initially written in Elliot-Algol.

ASSUMPTIONS

These calculations assume that fluid from a geothermal well (1) is produced from a single aquifer, (2) does not gain or lose significant heat or matter during passage up the well and through surface pipes to sampling points, and (3) maintains chemical equilibrium at each point of steam-water separation.

The first assumption that the fluid is produced from a single aquifer must be judged in each situation. In general, wells in which discharge enthalpy and silica contents indicate the same aquifer temperature are most probably from a single aquifer and existed in that aquifer as a single liquid phase. Two or more aquifers may, however, contribute fluids to a producing bore. This circumstance can be deduced from the drilling log, the ratios of gaseous components in the steam (Glover, 1970), or a comparison of the water composition with that of other wells in the field (Mahon, 1970).

The second assumption is most probably true for the well-studied and long-producing Wairakei, New Zealand, geothermal system in which the composition of produced fluids has been nearly constant over a decade of observation and in

which the mass of scale deposited is negligible (Mahon, 1970; Grindley, 1965, p. 58). Here also the conductive heat flow is small compared with the heat delivered to the surface in the fluid (Dawson and Dickinson, 1970; Grindley, 1965). This assumption is probably true also for many but not all other hot-water geothermal systems.

The assumption of chemical equilibrium is more difficult to justify. It has been observed that, in the aquifer, saturation with quartz is exactly maintained (Mahon, 1970), and most equilibria involving species dissolved in the aquifer water phase should be more rapid than saturation equilibria with a solid phase. However, during passage up the well and through the separator, CO_2 may not maintain an equilibrium distribution between the steam and water, as shown by Glover (1970), who found at Wairakei that the distribution coefficient for CO_2 between vapor and liquid water was about 70 rather than the equilibrium value of 460 (Ellis and Golding, 1963). The calculated total CO_2 based on analyses of the separated steam may be low by 2 percent or less. This would not significantly change the calculated CO_2 pressures or aquifer pH.

The difference between the actual total pressure in the aquifer and the saturated water-vapor pressure at the aquifer temperature is assumed to have a negligible effect on the equilibrium constants. The constants used in the program all refer to saturated water-vapor pressure conditions.

CHEMICAL AND PHYSICAL CHANGES ON PRODUCTION

The calculations performed in the program can be best illustrated by following the chemical and physical changes in the fluid produced from a representative aquifer. Analyses of water and gas samples from well 20 of the Wairakei, New Zealand, geothermal field are used as an example. The changes are discussed in the order that they occur; that is, from inaccessible conditions to the separated water and steam as analyzed. The program works backwards along the line of these changes and reconstructs the inaccessible states.

The calculated conditions prior to entering the bore are given in table 1. Note that the pH of 6.34 is nearly the neutral pH at the temperature 246°C and that virtually all boric and silicic acids and nearly all carbonic acid and hydrogen sulfide are undissociated. A substantial proportion of total sulfate exists as bisulfate ion, fluoride as neutral hydrogen fluoride, and ammonia as ammonium ion. Ion pairs such as NaCl , KCl , NaSO_4 and CaSO_4 are more stable than at low temperatures (see tables 4 and 5) and are present in moderate amounts. The enthalpy (enthalpy refers to specific enthalpy throughout) of the fluid is slightly less than that of water in equilibrium with steam (table 1), and a gas phase is probably not present.

The aquifer fluid flows toward and into the well along a gradient of decreasing pressure resulting from the lower density of the two-phase steam-water mixture in the well. The decrease in pressure causes steam separation and a decrease in temperature. These processes continue in the well and in the

Table 1.—Aquifer fluid adjacent to hole 20, Wairakei, New Zealand
[1 cal = 4.184 abs J]

Temperature	$^\circ\text{C}$	246
Pressure	bars abs	37.6
Enthalpy ¹	cal/g	252.8
pH ²		6.34
CO_2 partial pressure	bars	0.79
H_2S partial pressure	do	0.0093

Dissolved constituents	Concentrations in mmol/1,000 g H_2O
Li^+	1.5
Na^+	38.3
K^+	4.1
Rb^+025
Cs^+014
Ca^{+2}43
Mg^{+2}0
F^-29
Cl^-	42.9
Br^-05
I^-002
SO_4^{-2}079
H_3BO_3	1.74
H_2BO_3^-002
H_2CO_3^* CO_2aq	7.89
HCO_3^-35
CO_3^{-2}00001
H_4SiO_4^0	7.85
H_3SiO_4^-006
$\text{H}_2\text{SiO}_4^{-2}$00001
NH_4^+002
NH_3aq011
H_2Saq25
HS^-022
HF^0050
HSO_4^-0023
HCl^000006
NaCl^0	1.27
KCl^0097
MgSO_4^00
CaSO_4025
KSO_4015
NaSO_4^015
CaCO_3^00002
MgOH^+0

¹Saturated-water enthalpy is 254.6 cal/g.

²Neutral pH is 5.6 at 246°C .

steam-water separator, which was operated at a pressure of 16.3 bars absolute and a temperature of 202°C . With the decrease of pressure and temperature, the fluid separates into 10.1 percent steam with an enthalpy of 667.4 cal/g and 89.9 percent water with an enthalpy of 206.1 cal/g. (1 cal = 4.184 abs J.) The total enthalpy remains 252.8 cal/g ($0.101 \times 667.4 + 0.899 \times 206.1$) because no significant amount of heat has been lost in the passage up the well. The gases originally dissolved in the water have largely exsolved into the gas phase (experimental distribution coefficients for CO_2 and H_2S , tables 4 and 5, greatly favor the gas phase, particularly near 200°C). From the separator, the steam is collected and analyzed for CO_2 and H_2S . Collection and analysis methods

Table 2.—Analysis as reported on water and steam from well 20, Wairakei, New Zealand

Temperature of steam separation	°C.	202
Temperature of water separation	°C.	99 and 202
CO ₂ in high pressure steam	mmol/100 mol H ₂ O.	142
H ₂ S in high pressure steam	mmol/100 mol H ₂ O.	4.5
Water pH measured at 20°C		8.0

Dissolved constituents	Concentrations in water as analyzed at 20°C in mg/kg	Dissolved constituents	Concentrations in water as analyzed at 20°C in mg/kg
Li	14.8	Br	5.4
Na	1,260	I	.4
K	228	SO ₄	35
Rb	3.0	B	26
Cs	2.5	HCO ₃	7.7
Ca	25	CO ₃	0
Mg	0	SiO ₂	650
F	8.8	NH ₃	.3
Cl	2,164	H ₂ S	0

for steam and water are given in Ellis, Mahon, and Ritchie (1968). The gas analysis is given in table 2. The steam and water leave the separator in separate lines, and the water enters a silencer, which discharges to the atmosphere. In the silencer an additional 20 percent of the original water is flashed to steam, and the remaining water flows out the weir box where it is sampled. The proportions of steam and water at each separation point are calculated from an enthalpy balance with the assumption of constant enthalpy. The water sample in a capped polyethylene bottle is cooled and taken to the laboratory where it is analyzed and the pH is measured. The amount of CO₂ and H₂S dissolved in the water after separation is negligible relative to that which partitions into the gas phase and is not analyzed. The enthalpy of the whole fluid is calculated from measurements of the flows of steam and water under controlled conditions.

The properties of the water as analyzed are given in table 2. The steam and water analyses were made by the staff of the Chemistry Division, D.S.I.R., New Zealand. The water analysis has been recalculated in table 3 to show what species were present in the analyzed solution at 20°C. The water composition differs substantially from the composition of the aquifer fluid. The separation of steam has increased the concentration of mineral constituents that are insoluble in steam (compare Li⁺ in the tables). The separation of CO₂ and H₂S into the steam phase has increased the pH by 1.7 units.

The pH increase and temperature decrease have increased the ionization of weak acids, particularly boric acid, silicic acid, and carbonic acid. Ion pairs are generally less stable at lower temperatures (tables 4 and 5) and are thus less in evidence. The most important change is the partition of acid gases (CO₂, H₂S) into the steam with the resultant increase in pH. The aquifer pH, the activity coefficient of H⁺, and the potassium contents can be combined to calculate a K:H concentration ratio of 10^{3.83} which is similar to the extrapo-

Table 3.—Calculated composition at 20°C of separated well water from well 20, Wairakei, New Zealand

[Water pH measured at 20°C is 8.0]

Dissolved constituents	Concentrations in mmol/1,000 g H ₂ O	Dissolved constituents	Concentrations in mmol/1,000 g H ₂ O
Li ⁺	2.1	H ₃ SiO ₄ ⁻	.25
Na ⁺	54.9	H ₂ SiO ₄ ⁻²	.00009
K ⁺	5.85	NH ₄ ⁺	.017
Rb ⁺	.035	NH ₃ ^o	.0006
Cs ⁺	.019	H ₂ S	.0
Ca ⁺²	.62	HS ⁻	.0
Mg ⁺²	.0	HF ^o	<.000005
F ⁻	.47	HSO ₄ ⁻	<.000005
Cl ⁻	61.3	HCl ^o	<.000005
Br ⁻	.068	NaCl ^o	.05
I ⁻	.003	KCl ^o	.005
SO ₄ ⁻²	.315	MgSO ₄ ^o	.0
H ₃ BO ₃	2.26	CaSO ₄ ^o	.007
H ₂ BO ₃ ⁻	.15	KSO ₄ ⁻	.005
H ₂ CO ₃ ^o +CO ₂ aq	.003	NaSO ₄ ^o	.04
HCO ₃ ⁻	.126	CaCO ₃	.0002
CO ₃ ⁻²	.001	MgOH ⁺	.0
H ₄ SiO ₄ ^o	10.6		

lated, pressure-corrected experimental value of 10^{3.92} for water in equilibrium with K-mica, K-feldspar, and quartz near 250°C (Hemley, 1959; R. O. Fournier, oral. commun., 1972; Ellis and McFadden, 1972). This similarity suggests that mineralogical buffer systems are the major control on the pH of this aquifer fluid.

DATA REQUIRED

Data necessary to the calculation of aquifer chemistry consist of (1) a chemical analysis of the water separated from the water-steam mixture produced from the well, (2) the content of carbon dioxide and hydrogen sulfide in the separated steam, (3) the pressures of water and steam separation and the atmospheric pressure, and (4) the enthalpy of the whole fluid. The water analysis must include the pH, the temperature of pH measurement, and concentrations of all major dissolved constituents, particularly those that form weak acids or bases at low or high temperatures (HCO₃⁻, SO₄⁻², BO₂⁻, F⁻, SiO₂, and so forth. A silica analysis is essential because the temperature of the aquifer is calculated by assuming that the aquifer water phase is saturated with quartz (Mahon, 1966).

The CO₂ and H₂S contents of separated steam must be known because both of these gases dissolve in water to form weak acids and their separation from water raises the pH. The pressure of steam separation is introduced because the separation and collection of steam for gas analysis is most efficiently done at high pressure (to achieve a maximum gas to H₂O ratio) and the collection of water is usually from the silencer at atmospheric pressure (Ellis, Mahon and Ritchie, 1968). If the sample is from a downhole sampler, the water analysis and the CO₂ and H₂S contents are sufficient to

calculate the aquifer chemistry, provided that the fluid sampled was a single liquid phase.

AQUIFER TEMPERATURE CALCULATION

The temperature of an aquifer feeding a geothermal well is measured infrequently, and the measurements when made are uncertain. It has been shown (Fournier and Rowe, 1966; Mahon, 1966, 1970) to be preferable to calculate the aquifer temperature from the silica content of the discharge, assuming equilibrium with quartz in the aquifer, rather than to measure the temperature directly. The original silica content in the deep water must be calculated from analytical data allowing for concentration from steam separation and for the presence of steam in the aquifer. The calculation of the aquifer temperature requires enthalpy values of saturated steam and water at that temperature, and therefore an iteration procedure is necessary.

If the pH of the aquifer fluid is greater than about 7, some silica is present as silicate ions, and the indicated temperature from total silica will be too high. In this instance, concentrations of ionic silica species are calculated and subtracted from total silica concentrations because the silica concentration used for the temperature estimate is specifically $\text{SiO}_2(\text{aq})$.

CALCULATION OF THE EFFECTS OF STEAM SEPARATION AND EXCESS ENTHALPY

The enthalpies of the total fluid and of water and steam at the pressure and temperature of the aquifer and at each point of separation are necessary for calculating the proportion of water and steam separated and the degree of concentration of the dissolved mineral constituents in the water and of the dissolved gases in the steam. For these calculations, the program uses thermodynamic data for pure water from Keenan, Keyes, Hill, and Moore (1969). The effect of the low mineral contents (<0.3 wt percent NaCl) of most geothermal waters on the thermodynamic properties of water is negligible (J. L. Hass, written commun., 1971). The content of dissolved gases in steam from most geothermal discharges is low (<2 wt percent), and their effect on the thermodynamic properties has been neglected.

With the assumption of constant total enthalpy, the fraction of water or steam in the fluid can be calculated for any temperature (t) from the equations,

$$\text{fraction water} = \frac{\text{enthalpy of steam at } t - \text{fluid enthalpy}}{\text{enthalpy of vaporization at } t}$$

$$\text{and fraction steam} = \frac{\text{fluid enthalpy} - \text{enthalpy of water at } t}{\text{enthalpy of vaporization at } t}$$

If the enthalpy of the fluid is the same or lower than that of water saturated with steam at the aquifer temperature, then no steam is present in the aquifer, and the concentrations of mineral constituents owing to later steam separation are

calculated from the following:

$$\begin{aligned} \text{Original concentration} &= \text{concentration in complete discharge} \\ &= (\text{analyzed concentration in water}) \times (\text{fraction of water in separator 1}) \times (\text{fraction of water in separator 2}) \times (\text{fraction of water in silencer}). \end{aligned}$$

If, however, the enthalpy of the fluid is higher than that of steam-saturated water at the aquifer temperature, the presence of steam in the aquifer is indicated. The presence of steam causes the mineral constituents in the original waters as calculated above to be too low, so that the following correction factor is applied:

$$\begin{aligned} \text{Concentration in original water} \\ &= \frac{\text{concentration in complete discharge}}{\text{fraction of water in the aquifer}} \end{aligned}$$

The presence of steam is often the result of lowered pressure owing to extensive production. Because CO_2 and H_2S are strongly partitioned into the steam phase, the development of steam in the aquifer may result in a decrease in gas pressures and an increase in aquifer pH with the possibility of carbonate scale deposition in the aquifer and in the well casing.

Because of instrumental inaccuracies, measurement of the enthalpy of dillhole discharges is necessarily somewhat approximate; therefore, samples with fluid enthalpies within ± 28 cal/g (50 Btu/lb) of the enthalpy of water in equilibrium with steam at the aquifer temperatures are recalculated assuming exact equilibrium.

GAS PARTIAL PRESSURES

If the gas (CO_2 , H_2S) contents of the sampled steam and the fraction of steam in the fluid at the sampling point are known, the total gas contents of the aquifer fluids may be calculated. If a single liquid phase exists in the aquifer, the gas partial pressures may be calculated directly from experimental data on the solubility of gas in water at high temperatures (Ellis and Golding, 1963; Kozintseva, 1964). If both steam and water exist in the aquifer, a large fraction of the gas partitions into the aquifer steam phase, and the partial pressure of the gas is a quadratic function of the total gas content.

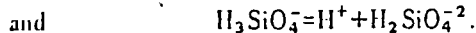
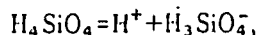
CHEMICAL MODEL

The calculation of the chemistry of the aquifer fluids requires knowledge of the total content of all solution components and of the dissociation constants of all weak acids and bases and all ion pairs. The total contents of components other than gases and hydrogen ions are easily calculated from the water analysis with allowance for the effects of steam separation and of steam in the aquifer as described earlier. The contents of dissolved gases in the water may be calculated from their solubilities, their contents in the separated steam, the steam fraction, and if there is excess enthalpy, from the fractions of steam and water in the aquifer. For the calculation

of the total content of hydrogen ion, the state of ionization of all weak acids and bases under the conditions of analysis must first be ascertained. This is done through the calculations of a chemical model (Garrels and Thompson, 1962; Ellis, 1967).

SOLUTION OF MASS ACTION AND MASS BALANCE EQUATIONS

In the chemical model for the water as analyzed, the analytical concentrations, experimental dissociation constants, mass balances, and the measured pH are used to calculate the distribution of weak acid species and experimental dissociation constants, and mass balance equations are used to calculate that of ion pairs. Weak acids dissociate to form hydrogen ions by equations such as those for silicic acid as follows:



The concentration of each species is determined by the total concentration, the pH, the activity coefficients of the species, and the equilibrium constants for distribution of species at chemical equilibrium. For the preceding reactions we can write the equilibrium equations as follows:

$$K_1 = \frac{m_{H_3SiO_4^-} \gamma_{H_3SiO_4^-} 10^{-pH}}{m_{H_4SiO_4} \gamma_{H_4SiO_4}}$$

$$K_2 = \frac{m_{H_2SiO_4^{2-}} \gamma_{H_2SiO_4^{2-}} 10^{-pH}}{m_{H_3SiO_4^-} \gamma_{H_3SiO_4^-}}$$

The mass balance equation for total silica (silicic acid and silicate ions) is

$$m_{Si \text{ total}} = m_{H_4SiO_4} + m_{H_3SiO_4^-} + m_{H_2SiO_4^{2-}}$$

The mass action equations can be combined with the mass balance equation to solve for $m_{H_4SiO_4}$.

$$m_{H_4SiO_4} = \frac{m_{Si \text{ total}}}{1 + \gamma_{H_3SiO_4^-} \left(\frac{K_1 10^{pH}}{\gamma_{H_2SiO_4^{2-}}} + \frac{K_1 K_2 10^{2pH}}{\gamma_{H_2SiO_4^{2-}}} \right)}$$

The value of $m_{H_4SiO_4}$ is then substituted into the mass action equations to solve for $m_{H_3SiO_4^-}$ and $m_{H_2SiO_4^{2-}}$. Activity coefficients are calculated from the extended Debye-Huckel equation as described later, and the ionic strength is calculated by iteration. Calculation of the concentration of ion pairs is accomplished by a slightly different procedure, which is illustrated by the calculation of the calcium ion species. The mass action expressions,

$$K_1 = \frac{m_{Ca^{+2}} \gamma_{Ca^{+2}} m_{SO_4^{2-}} \gamma_{SO_4^{2-}}}{m_{CaSO_4} \gamma_{CaSO_4}}$$

and

$$K_2 = \frac{m_{Ca^{+2}} \gamma_{Ca^{+2}} m_{CO_3^{2-}} \gamma_{CO_3^{2-}}}{m_{CaCO_3} \gamma_{CaCO_3}}$$

are combined with the mass balance expression,

$$m_{Ca \text{ total}} = m_{Ca^{+2}} + m_{CaSO_4} + m_{CaCO_3}$$

to produce an expression for free (uncomplexed) Ca^{+2} ion,

$$m_{Ca^{+2}} = \frac{m_{Ca \text{ total}}}{1 + \gamma_{Ca^{+2}} \left(\frac{m_{SO_4^{2-}} \gamma_{SO_4^{2-}}}{K_1 \gamma_{CaSO_4}} + \frac{m_{CO_3^{2-}} \gamma_{CO_3^{2-}}}{K_2 \gamma_{CaCO_3}} \right)}$$

The value of $m_{Ca^{+2}}$ may be substituted into the mass action expressions to solve for the ion pairs. In these equations $Ca \text{ total}$ is from the analysis, the dissociation constants depend only on temperature, and the activity coefficients are calculated from the ionic strength, which changes slowly during iteration. The molalities of the anions (SO_4^{2-} , CO_3^{2-}) are corrected in each iteration loop by summing the calculated species (for example, $m_{SO_4^{2-}} + m_{HSO_4^-} + m_{KSO_4^+} + \dots$) and comparing the sum with the analytical concentration of total anion. If the sum calculated differs from the analytical concentration by more than 0.1 percent, the free anion concentration is corrected by an amount depending on the difference. When all anions have been checked (and corrected if necessary), the program iterates if corrections have been made to any of them. Thus, the program leaves the loop when the concentrations of all species satisfy the mass balances to 0.1 percent.

TOTAL IONIZABLE HYDROGEN ION CONTENT

The total content of hydrogen ions in an aqueous solution includes not only free ions but also those in combination in weak acids and in water itself. Only part of these can be ionized under the range of conditions found in natural waters.

This part, the total "ionizable" hydrogen ion content, is calculated by summing the contents of H^+ ion and of all the undissociated and partly dissociated weak acids— HCO_3^- , HBO_2 , H_2S , NH_4^+ , HSO_4^- , HF , HCl , $H_3SiO_4^-$, H_4SiO_4 (two times), and H_2CO_3 (two times). When the total ionizable hydrogen ion content has been corrected for electrolyte concentration changes due to steam separation and the presence of aquifer steam as discussed earlier, the H_2S and CO_2 originally dissolved in the water are added (the CO_2 two times as H_2CO_3).

AQUIFER CHEMICAL MODEL

The aquifer chemical model is calculated using the analysis corrected for steam separation and aquifer steam contents, values of dissociation constants at the aquifer temperature and saturated water vapor pressure, and the total ionizable hydrogen ion content. The method of calculation of the chemical model is the same as before except that the pH is now a dependent rather than an independent variable. Because almost all of the hydrogen ion occurs in complexes, changes in the calculated pH cause relatively large changes in the anion mass balances, and the program converges very slowly. A change in the criteria of convergence from 1 percent to 0.1 percent of the anion mass balances doubles the number of

iterations and changes the final calculated pH by 0.1 to 0.15 units.

The correctness of the calculated model is dependent on the existence and validity of high-temperature quartz solubility values, gas solubility constants, and dissociation constants for the weak acids and bases and ion pairs present in the water. The data used in the program are given in tables 4 and 5 with their sources. They are of uneven quality, and as better data become available, the program can be easily updated. Tabular data are interpolated by a program written by P. C. Doherty of the U.S. Geological Survey. Single-ion activity coefficients have been calculated from the extended Debye-Hückel equation, with a small hydration coefficient (the "B." of Helgeson, 1969) assumed constant with temperature. This equation differs little from that suggested by Davies (1962). The ionic strength (I) of most geothermal waters is moderate ($<0.08m$), and the ionic activity coefficients are not very sensitive to the ion size (\bar{a}) and hydration parameters chosen. The equation used is:

$$\log \gamma_i = \frac{-A z_i^2 I^{1/2}}{1 + \frac{\bar{a}}{a_i} B I^{1/2}} + 0.04 I.$$

or Kravtsov
or Appendix II Berr

The constants A and B are from a tabulation by Helgeson (1967) and are for molal units. Values of \bar{a} are taken from Kielland (1937).

Table 4.—Solubility constants and dissociation constants in KA(1) and KT(1) arrays, analytical expressions

Reaction	Analytical expression if used (T in K, t in °C)	Log K		Note	Reference
		25°	250°		
1..... $H_2CO_3 \text{ app} = H^+ + HCO_3^-$	$\text{Log } K = -2382.3/T + 8.153 - 0.02194T$	-6.38	-7.88	(*)	Ryzhenko (1963).
2..... $H_2S = H^+ + HS^-$	$\text{Log } K = -3279.0/T + 11.17 - 0.02386T$	-6.94	-7.6		D'yachikova and Khodakovskiy (1968).
3..... $HBO_2 + OH^- = H_2BO_3^-$	$\text{Log } K = 1573.21/T + 28.6059 + 0.012078T - 13.2258 \log T$	+4.76	+1.98	(*)	Mesiner, Baes, and Sweeton (1972).
4..... $H_3SiO_4^- = H^+ + H_2SiO_4$	See table 5	-9.63	-9.63	(*)	Cobble (1964); Ryzhenko (1967).
5..... $HF = H^+ + F^-$	do	-3.18	-5.80	(*)	Ellis (1963).
6..... $HSO_4^- = H^+ + SO_4^{2-}$	$\text{Log } K = -557.2 + 61/T + 5.3505 - 0.0183412T$	-1.99	-5.31		Lietzké, Stoughton, and Young (1961).
7..... $H_2O = H^+ + OH^-$	$\text{Log } K = -4470.99/T + 6.0875 - 0.017067$	-13.995	-11.38		Harned and Owen (1958, p. 645).
8..... $NH_3(H_2O) = NH_4^+ + OH^-$	See table 5	-6.75	-6.06		Wright, Lindsay, and Deuga (1961).
9..... $HCl = H^+ + Cl^-$	do	-6.10	-6.7		Helgeson (1969).
10..... $NaCl = Na^+ + Cl^-$	do	+1.60	-25	(*)	Pearson, Copeland, and Benson (1963); Dunn and Marshall (1969); Hanna, Pethybridge, and Prue (1971).
11..... $KCl = K^+ + Cl^-$	do	+1.59	-1		Helgeson (1969); Hanna, Pethybridge, and Prue (1971).
12..... $MgSO_4 = Mg^{2+} + SO_4^{2-}$	do	-2.25	-5.7	(*)	Do.
13..... $CaSO_4 = Ca^{2+} + SO_4^{2-}$	do	-2.30	-4.1	(*)	Do.
14..... $K_2SO_4 = K^+ + SO_4^{2-}$	do	-8.3	-2.35	(*)	Quist and others (1963); Truesdell and Hostetler (1968).
15..... $Na_2SO_4 = Na^+ + SO_4^{2-}$	do	-8.3	-2.35	(*)	Do.
16..... $CaCO_3 = Ca^{2+} + CO_3^{2-}$	do	-2.30	-5.90	(*)	Helgeson (1969).
17..... $MgOH^+ = Mg^{2+} + OH^-$	do	-2.60	-4.65	(*)	Do.
18..... $H_3SiO_4^- = H^+ + H_2SiO_4$	$\text{Log } K = -3450/T + 6.34 - 0.02167$	-11.7	-11.5		Nayimov, Ryzhenko, and Kodakovskii (1971).
19..... $HCO_3^- = H^+ + CO_3^{2-}$	$\text{Log } K = -2730.7/T + 5.388 - 0.02199T$	-9.12	-11.34		Ryzhenko (1963).
KS..... $H_2S \text{ gas} = H_2S \text{ aq}$	$K = 357 + 15.688t - 0.030253t^2$	+2.86	+3.28		Kozintseva (1964).
K..... $CO_2 \text{ gas} + H_2O = H_2CO_3 \text{ app}$	See table 5	+3.21	+3.72	(*)	Ellis and Golding (1963).

* H_2CO_3 apparent includes H_2CO_3 and CO_2 aqueous.

† $H_2BO_3^-$ given in print out as BO_3^- . Reaction written by Mesiner, Baes, and Sweeton (1972) as $B(OH)_3 + OH^- = B(OH)_4^-$.

‡ Extrapolated above 200°C.

§ Extrapolated above 200°C. Agrees with Ryzhenko (1965) to 200°C.

¶ Extrapolated below 100°C.

* Assumed identical to K_2KSO_4 .

Table 5.—Log K(pK), and CO₂ and quartz solubility, data in tabular form interpolated by look-up subroutine [For reaction equations and source of data, see table 4]

t °C.	(4) H ₄ SiO ₄ ^o	(5) HF ^o	(8) NH ₃ (H ₂ O) ^o	(9) HCl ^o	(10) NaCl ^o	(11) KCl ^o	(12) MgSO ₄ ^o	(13) CaSO ₄ ^o	(14) KSO ₄ ^o	(16) CaCO ₃ ^o	(17) MgOH ⁺	CO ₂ solubility	Quartz solubility ¹ (p/m)
0	10.2	2.96	4.87	-7.5	-1.65	-1.65	2.05	2.3	0.65	3.0	2.50	700	2.4
10	9.94	3.00	4.80	-6.8	-1.63	-1.62	2.10	2.3	.71	3.05	2.58	1000	3.6
25	9.63	3.10	4.75	-6.1	-1.60	-1.59	2.25	2.3	.83	3.20	2.60	1630	6.6
35	9.48	3.25	4.70	-5.7	-1.40	-1.50	2.35	2.36	.90	3.27	2.63	2100	8.6
50	9.30	3.40	4.70	-5.0	-1.20	-1.40	2.60	2.40	1.00	3.40	2.7	2900	13.5
75	9.11	3.64	4.75	-3.8	-.90	-1.20	2.90	2.55	1.15	3.65	2.9	4000	27
100	9.03	3.85	4.85	-2.9	-.55	-1.00	3.20	2.7	1.30	3.90	3.1	5200	48
125	9.03	4.09	4.97	-2.0	-.55	-.90	3.55	2.9	1.45	4.15	3.33	6000	80
150	9.10	4.34	5.10	-1.23	-.45	-.75	3.90	3.1	1.60	4.50	3.6	6600	125
175	9.23	4.59	5.33	-.60	-.30	-.60	4.40	3.35	1.78	4.85	3.85	6800	190
200	9.36	4.89	5.53	-.07	-.15	-.40	4.80	3.6	1.93	5.20	4.1	6400	265
225	9.48	5.3	5.73	.30	.05	-.20	5.25	3.8	2.10	5.55	4.35	5900	367
250	9.63	5.8	6.0	.67	.25	.10	5.7	4.1	2.35	5.90	4.65	5300	490
275	9.83	6.2	6.3	.95	.60	.30	6.1	4.3	2.55	6.20	4.9	4600	615
300	10.2	6.8	6.75	1.2	.95	.6	6.4	4.5	2.75	6.45	5.15	3900	680
325	10.5	7.1	7.25	1.6	1.35	1.0	6.7	4.75	2.9	6.65	5.45	3100	720
350	11.0	7.4	8.0	2.5	2.0	1.7	7.0	5.0	3.1	7.0	5.7	2100	(750)

¹Quartz solubility in water at saturated water vapor pressure. 0°–240°C from Morey, Fournier, and Rowe (1962); 260°–325°C from Kennedy (1950). An incorrect 350° value is included because the look-up subroutine requires a monotonic function.

The algol version of this program (Truesdell and Singers, 1973) has just been published.

REFERENCES CITED

Cobble, J. W., 1964, The thermodynamic properties of high temperature aqueous solutions—[part] VI, Application of entropy correspondence to thermodynamics and kinetics: *Am. Chem. Soc. Jour.*, v. 86, p. 5394–5401.

Davies, C. W., 1962, Ion association: London, Butterworths, 190 p.

Dawson, G. B., and Dickinson, D. J., 1970, Heat flow studies in thermal areas of the North Island of New Zealand—U.N. symposium on the development and utilization of geothermal resources: *Geothermics special issue 2*, v. 2, pt. 1, p. 466–473.

Dunn, L. A., and Marshall, W. L., 1969, Electrical conductances and ionization behavior of sodium chloride in diokane-water mixtures at 100°C: *Jour. Phys. Chemistry*, v. 73, p. 2619–2622.

D'yachkova, I. B., and Khodakovskiy, I. L., 1968, Thermodynamic equilibria in the systems S-H₂O, Se-H₂O and Te-H₂O in the 25–300°C temperature range and their geochemical interpretations: *Geochemistry Internat.*, p. 1108–1125.

Ellis, A. J., 1963, The effect of temperature on the ionization of hydrofluoric acid: *Chem. Soc. [London] Jour.*, p. 4300–4304.

— 1967, The chemistry of some explored geothermal systems, Chapter 2 in Barnes, H. L., ed., *Geochemistry of hydrothermal ore deposits*: New York, Holt, Rinehart and Winston, p. 465–514.

— 1970, Quantitative interpretation of chemical characteristics of hydrothermal systems—U.N. symposium on the development and utilization of geothermal resources: *Geothermics special issue 2*, v. 2, pt. 1, p. 516–520.

Ellis, A. J., and Golding, R. M., 1963, The solubility of carbon dioxide above 100°C in water and in sodium chloride solutions: *Am. Jour. Sci.*, v. 261, p. 47–60.

Ellis, A. J., and McFadden, I. M., 1972, Partial molar volumes of ions in hydrothermal solutions: *Geochim. et Cosmochim. Acta.* v. 36, p. 413–426.

Ellis, A. J., Mahon, W. A. J., and Ritchie, J. A., 1968, Methods of collection and analysis of geothermal fluids. New Zealand Dept. Sci. and Indus. Research Chemistry Div. Rept. CD2103, 51 p.

Fournier, R. O., and Rowe, J., 1966, Estimation of underground temperatures from the silica content of water from hot springs and wet-steam wells: *Am. Jour. Sci.*, v. 264, p. 685–697.

Fournier, R. O., and Truesdell, A. H., 1973, An empirical Na-K-Ca geothermometer for natural waters: *Geochim. et Cosmochim. Acta.* v. 37, p. 1255–1275.

Garrels, R. M., and Thompson, M. E., 1962, A chemical model for sea water at 25°C and one atmosphere total pressure: *Am. Jour. Sci.*, v. 260, p. 57–66.

Glover, R. B., 1970, Interpretation of gas compositions from the Wairakei field over 10 years—U.N. symposium on the development and utilization of hydrothermal resources: *Geothermics, special issue 2*, v. 2, pt. 2, p. 1355–1366.

Grindley, G. W., 1965, The geology, structure, and exploitation of the Wairakei geothermal field Taupo, New Zealand: *New Zealand Geol. Survey Bull.* 75, 130 p.

Hanna, E. M., Pethybridge, A. D., and Price, J. D., 1971, Ion association and the analysis of precise conductivity data: *Electrochim. Acta.* v. 16, p. 677–686.

Harried, H. S., and Owen, B. B., 1958, The physical chemistry of electrolyte solutions: New York, Reinhold, 801 p.

Helgeson, H. C., 1967, Solution chemistry and metamorphism, in Abelson, P. H., ed., *Researches in geochemistry*, volume 2: New York, John Wiley and Sons, p. 362–404.

— 1969, Thermodynamics of hydrothermal systems at elevated temperatures and pressures: *Am. Jour. Sci.*, v. 267, p. 729–804.

Hendley, J. J., 1959, Some mineralogical equilibria in the system K₂O-Al₂O₃-SiO₂-H₂O: *Am. Jour. Sci.*, v. 257, p. 241–270.

Keenan, J. H., Keyes, F. G., Hill, P. G., and Moore, J. G., 1969, Steam tables, Thermodynamic properties of water including vapor, liquid, and solid phases: New York, John Wiley and Sons, 162 p.

Kennedy, G. C., 1950, A portion of the system silica-water: *Econ. Geology*, v. 45, p. 629–653.

Kielland, J., 1937, Individual ion activity coefficients of ions in aqueous solutions: *Am. Chem. Soc. Jour.*, v. 50, p. 1675–1678.

Kozintseva, T. N., 1964, Solubility of hydrogen sulfide in water at elevated temperatures: *Geochemistry Internat.*, p. 750–756.

Lietzke, M. H., Stoughton, R. W., and Young, T. F., 1961, The bisulfate acid constant from 25° to 225° as computed from solubility data: *Jour. Phys. Chemistry*, v. 65, p. 2247–2249.

Mahon, W. A. J., 1966, Silica in hot water discharged from drillholes at Wairakei, New Zealand: *New Zealand Jour. Sci.*, v. 9, 135–144.

— 1970, Chemistry in the exploration and exploitation of hydrothermal systems—U.N. symposium on the development and utilization of geothermal resources: *Geothermics, special issue 2*, v. 2,

- p. 2, p. 1310-1322.
- Mesmer, R. E., Baes, C. F., Jr., and Sweeton, E. H., 1972, Acidity measurements at elevated temperatures: VI. Boric acid equilibria: *Inorganic Chemistry*, v. 11, p. 537-543.
- Morcy, G. W., Fournier, R. O., and Rowe, J. J., 1962, The solubility of quartz in water in the temperature interval from 25° to 300°C: *Geochim. et Cosmochim. Acta*, v. 26, p. 1029-1043.
- Naymov, G. B., Ryzhenko, B. N., and Kodakovskii, I. L., 1971, *Spravochnik-termodinamicheskikh velichin dlia geology*: Moscow, Atomizdat, 239 p.
- Pearson, D., Copeland, C. S., and Benson, S. W., 1963, The electrical conductance of aqueous sodium chloride in the range 300° to 383°C: *Am. Chem. Soc. Jour.*, v. 85, p. 1044-1047.
- Quist, A. S., Franck, E. U., Jolley, H. R., and Marshall, W. L., 1963, Electrical conductances of aqueous solutions at high temperatures and pressures—[part] 1, The conductances of potassium sulfate-water solutions from 25° to 800°C and at pressures up to 4000 bars: *Jour. Phys. Chemistry*, v. 67, p. 2453-2459.
- Ryzhenko, B. N., 1963, Determination of dissociation constants of carbonic acid and the degree of hydrolysis of the CO_3^{2-} and HCO_3^- ions in solutions of alkali carbonates and bicarbonates at elevated temperatures: *Geochemistry*, no. 2, p. 151-164.
- 1965, Determination of the dissociation constant of hydrofluoric acid and the conditions for the replacement of calcite by fluorite: *Geochemistry Internat.*, v. 2, p. 196-200.
- 1967, Determination of the hydrolysis of sodium silicate and calculation of dissociation constants of orthosilicic acid at elevated temperatures: *Geochemistry Internat.*, v. 4 p. 99-107.
- Truesdell, A. H., and Hostetler, P. B., 1968, Dissociation constants of KSO_4 from 10°-50°C: *Geochim. et Cosmochim. Acta*, v. 32, p. 1019-1022.
- Truesdell, A. H., and Singers, Wendy, 1973, Computer calculation of downhole chemistry in geothermal areas: New Zealand Dept. Sci. Indus. Research, Chemistry Div. Rept. CD2136, 145 p.
- White, D. E., 1965, Saline waters of sedimentary rocks, in *Fluids in subsurface environments—a symposium*: Am. Assoc. Petroleum Geologists Mem. 4, p. 342-366.
- 1970, *Geochemistry applied to the discovery, evaluation, and exploitation of geothermal energy resources—U.N. symposium on the development and utilization of geothermal resources: Geothermics special issue 2, v. 1.*
- Wright, J. M., Lindsay, W. T., Jr., and Druga, T. R., 1961, The behavior of electrolytic solutions at elevated temperatures as derived from conductance measurements: Washington, D.C., U.S. Atomic Energy Comm. R&D WAPD-TM-204, 32 p.

SUBJ,
GCHM
CATE

CHEMICAL AND THERMAL EVOLUTION OF
HYDROTHERMAL FLUIDS, MERCUR GOLD
DISTRICT, TOOELE COUNTY, UTAH

(Running title: HYDROTHERMAL FLUIDS, MERCUR DISTRICT, UTAH)

by

Paul W. Jewell* and W. T. Parry

Department of Geology and Geophysics
University of Utah
Salt Lake City, Utah 84112

* Present Address: Department of Geological and Geophysical Sciences
Princeton University
Princeton, NJ 08544

**UNIVERSITY OF UTAH
RESEARCH INSTITUTE
EARTH SCIENCE LAB.**

ABSTRACT

The Mercur gold deposits of west-central Utah are hosted by the upper portion of the Topliff Member of the Mississippian Great Blue Limestone. Alteration exhibits a stratabound character which can be related to primary, sedimentary lithologies over a 60-80 m section of the Topliff Member.

Hydrothermal alteration at Mercur can be separated into four temporally overlapping stages. Stage I alteration consists of replacement of massive limestones with silica, sericite, and kaolinite by oxidizing, low pH (3.5-4.0) fluids at temperatures of 220-270°C. Stage I alteration is widely developed in a stratiform jasperoid body known as the Silver Chert, although other portions of the upper Topliff member are altered as well. Stage II alteration is characterized by decarbonation of silty limestones by fluids with pH and fO_2 values similar to Stage I fluids, but with less dissolved silica. Stage II fluids became progressively more reduced and less acid through reaction with carbonaceous limestones. Stage III consists of two vein or fracture filling assemblages: a) orpiment-pyrite-marcasite-organics, and b) calcite-realgar veins. Spatial relationships of calcite fluid inclusion filling temperatures indicate that vertical flow dominated the hydrothermal system in spite of the stratabound nature of the deposits. Stage III fluids appear to have been chemically similar to evolved Stage II fluids. Stage III fluids are restricted to portions of the upper Topliff member which are stratigraphically higher than the Silver Chert. Calcite of this stage was deposited at temperatures of 150-190°C. Stage IV alteration consists of barite and halloysite. Barite was deposited between 180-300°C as a result of progressively increasing temperature.

Salinities throughout the paragenesis remained relatively constant at 5-8 equivalent weight percent NaCl. Deposition of gold through the first three stages of the paragenesis was brought about by a decrease in temperature and increase in pH. Despite its relatively low solubility, AuCl_2^- is the most plausible complex for transporting the gold.

INTRODUCTION

The term "Carlin-type" deposit has been applied to a number of low grade, sediment-hosted gold deposits that have been discovered and brought into production in the western United States since the 1960s. Carlin-type deposits are characterized by replacement of carbonate and silty carbonate rocks by silica, pyrite, barite, various arsenic, mercury, antimony, and thallium minerals in addition to micron-size gold (Radtke and Dickson, 1974). All are believed to have formed in the upper few kilometers of the earth's crust under conditions which are analogous to present day geothermal systems.

The Mercur mining district of west-central Utah contains a number of gold deposits of this class. The district is located approximately 90 km southwest of Salt Lake City in the southwest portion of the Oquirrh Mountains, a typical north-south trending range of the Basin and Range physiographic province (Fig. 1). Two major ore bodies, Mercur-Sacramento and Marion Hill, are present in small hills in the center of the steep, east-west trending Mercur Canyon (Fig. 2). Initial production of silver in the Mercur district was from an interval of silicified limestone known as the Silver Ledge (Spurr, 1895), a term which was later changed to the Silver Chert. Fine gold was discovered in 1883 in a stratigraphic interval 30 m above the Silver Chert. Production terminated in 1917 after more than 1.2 million ounces of gold had been produced (Butler et al., 1920). The district was reopened in 1983 with Getty Mining Company as the principle operator.

The first geologic description of the Mercur district is given by

Spurr (1895). Butler et al., (1920) give a concise, accurate review of the geology, stratigraphy, and mineral production at Mercur. Gilluly's (1932) work remains the most comprehensive published study of the southern Oquirrh Mountains. Lenzi (1973) published data on the background geochemistry at Mercur. Tafuri (1976) describes the general geology, alteration, and mineralization at Mercur.

The investigation presented in this paper was undertaken to describe the thermal and chemical evolution of the ore forming fluids at Mercur, and to compare the Mercur hydrothermal system with modern geothermal systems and similar gold deposits in the western United States. Temporal and spatial relationships of the mineral assemblages were established by examination of outcrops and open pits at Mercur plus more detailed examination of 300 hand samples and 120 thin sections of surface and subsurface samples.

GEOLOGY

Rocks in the southwest portion of the Oquirrh Mountains are Upper Mississippian carbonate and clastic rocks and Tertiary igneous rocks. From oldest to youngest, the sedimentary formations are the Deseret Limestone (200 m thick), the Humbug Formation (190-200 m thick), the Great Blue Limestone (910-1150 m thick), and the Manning Canyon Shale (230-350 m thick). The relatively thick Great Blue Limestone is separated into three members. The lower 150-200 m of limestones and minor shales is named the Topliff Member following correlation with exposures of the type-section in the Tintic Mountains to the south (Morris and Lovering, 1961). The

upper portion of the Topliff Member is host to most of the Mercur ores and will be discussed in greater detail below. A 30-50 m thickness of shales and limestones overlying the Topliff was named the Long Trail Shale by Gilluly (1932). The upper portion of the Great Blue consists of 600-900 m of massive limestones with minor chert and shale which are unmineralized.

Two igneous rock units have been mapped in the southwest portion of the Oquirrh Mountains. The Porphyry Hill Monzonite is exposed 2-3 km north of the Mercur deposits and is reported by Gilluly (1932) and Proctor (1959) to be a porphyritic monzonite which occurs in sill-like bodies.

The Eagle Hill Rhyolite is a fine-grained, nonporphyritic unit with a distinctive white to pinkish color. Gilluly (1932) has mapped two semi-circular to elliptical intrusive stocks of this unit south of Mercur. Irregular, sill-like masses of the Eagle Hill Rhyolite can be seen in the Sacramento pit and in drill holes throughout the Sacramento Hill area (M. Bryant, T. Faddies, oral comm.). The Eagle Hill Rhyolite has a K-Ar age of 31.5 m.y. (Moore, 1968). The relative age of the Eagle Hill Rhyolite and the Mercur hydrothermal system is problematic due to ambiguous field relationships and the lack of minerals which are suitable for dating.

The structure of the Mercur district is dominated by the broad, northwest-trending, south-plunging Ophir anticline. The hinge of the anticline transects Mercur Canyon approximately 2 km west of the Mercur mine. Rocks in the Mercur area generally dip 20-30 degrees to the east. Two major east-west normal faults are recognized within the Mercur ore bodies (T. Faddies, R. Blair, oral comm.). The Carrie Steele fault crosscuts the Marion Hill ore body. The Lulu graben is a complex fault system south

of Mercur Hill with a displacement of approximately 15 m (R. Klatt, written comm.).

Upper Topliff Member in the vicinity of Mercur

Mineralization at Mercur is confined to the upper 60-80 m of the Topliff Member and lower portion of the Long Trail Shale. Descriptions given below are largely based on hand sample and petrographic observations from a deep, diamond drill hole spudded 0.75 km northeast of Mercur which encountered an unaltered to weakly altered Topliff section (Fig. 3). In discussing carbonate rocks, the classification of Dunham (1962) is used.

The Topliff Member is subdivided into the Magazine Sandstone, Barren Beds, Mercur Beds, and Upper Beds by Butler et al., (1920). The Magazine Sandstone can be roughly divided into two clastic sequences separated by a 5 m interval of mudstone, packstone, and shale. The lower sandstone interval overlies an unknown thickness of massive, medium-gray mudstone. The lower Magazine Sandstone is massive to porous, ochre to brown in color, and composed of fine-sand to coarse-silt sized quartz grains. Thin sections from this interval shows 35-45 percent subrounded, well-sorted quartz grains in a matrix of calcite, illite, and minor pyrite and iron oxides. The upper interval of the Magazine has a higher percentage of silt-sized sediment than the lower Magazine, and its coloration varies from gray to brown. A distinctive marker horizon at the top of the upper Magazine is a zone of worm burrows. The mudstone-packstone-shale sequence separating the upper and lower clastic units will be called the median limestone unit of the Magazine Sandstone.

Overlying the Magazine Sandstone is a 20-25 m thick section of limestones, silty limestones, and shales known collectively as the Barren Beds. The lower portion of the Barren Beds are largely mudstones, shales, and calcereous siltstones which grade upward into massive to moderately well-bedded mudstones. A distinctive, 2 m thick interval named the Apex vein by Butler et al., (1920) has been recognized 5-7 m above the top of the Magazine Sandstone. The Apex consists of interbedded mudstones and siltstones with distinctive, very delicate cross laminations and flaser bedding which aided in correlations between drill holes (Fig. 3).

The next stratigraphically higher interval in the upper Topliff Member is an 8 m thick sequence of porous, thin- to moderately-well bedded packstones, wackestones, and siltstone known as the Mercur Beds. The Mercur Beds are host for the highest amount of gold mineralization throughout the Mercur district. Alteration in the form of decalcification and minor silicification of the Mercur Beds is pervasive, even in the relatively unaltered, deep diamond drill hole north of Mercur (Fig. 3). In general, the Mercur Bed interval appears to have a higher porosity and greater amount of siltstone and shale than the rest of the upper Topliff carbonate. The original Mercur Beds appear to have been thinly bedded with abundant fenestrate bryozoa and diagenetic pyrite.

The uppermost subdivision of the Topliff is known as the Upper Beds. The Upper Beds consist of a 30-40 m thickness of limestones which grade from massive mudstones upward into massive wackestones and packstones interbedded with lesser amounts of siltstones and calcereous shales. Styolitic dissolution and intraformational breccias are common in this interval. Zones of interbedded siltstones and mudstones labeled the Middle

Streak and Upper Vein by Butler et al., (1920) are not distinguished in this paper as subunits of the Upper Beds.

The contact between the Topliff Member and overlying Long Trail Shale is not distinctive (Mercur geologic staff, written comm.). For the purposes of illustration in Figure 3, the contact is drawn at the base of a 2-3 m sequence of noncalcareous, black shale, 40 m above the top of the Mercur Beds. The Long Trail Shale has not been examined in detail by the authors, but it appears to consist of approximately equal amounts of carbonate and clastic rock.

Several generalizations of the entire upper Topliff section can be made on the basis of hand sample, core logging, and petrographic observations. The allochemical constituents are largely pelloids and fossil fragments. Fenestrate bryozoa are characteristic of the more thinly laminated lithologies, whereas the more massive mudstones and wackestones usually contain echinoids, crinoid fragments, and less commonly corals and brachiopods. The calcite mud is cryptocrystalline. The amount of fine-grained indigenous matter is sufficiently high to give the Great Blue Limestone its characteristic medium to dark gray color. Diagenetic pyrite is ubiquitous and ranges from euhedral cubes up to 1 cm in diameter down to individual grains, aggregates, and veinlets only microns in size. Quartz is usually well-rounded and very fine-grained (less than 50 μ in diameter). Lath-like illite grains up to 20 μ long are characteristic of the siltstones and shales. The illite is colorless in thin section and often displays a reticulated habit. X-ray analysis reveals the presence of kaolinite in unaltered Topliff samples. Petrographic identification of this mineral is difficult, but it appears to occur as fine-grained clots associated with the illite.

No phyllosilicate mineral other than illite and kaolinite has been found in unaltered Great Blue Limestone.

Whole rock chemical analyses of eight unaltered to weakly altered samples of the upper portion of the Topliff member (Table 1) suggest several generalizations. Massive limestones are essentially pure carbonates with less than 10 percent total silica, 0-2 percent alumina, and trace amounts of diagenetic pyrite. Relative amounts of kaolinite and illite are difficult to characterize, given the small number of samples (four) and the small percentages of clay minerals. Four thinly bedded, shaley limestones have silica values in the 30-40 percent range, and alumina values from 5-10 percent. Modal partitioning of elements shows that illite/kaolinite ratios are near unity. The amount of diagenetic pyrite is between 1 and 3 percent. The unaltered Topliff samples have organic carbon contents within the 0.2 to 1.0 percent range reported for unaltered Great Blue rocks near the mouth of Mercur Canyon (W. Tafuri, written comm.).

HYDROTHERMAL ALTERATION

Hydrothermal alteration is divided into four paragenetic stages.

Each stage is named according to the dominant mineral phases, even though there is overlap of mineral deposition in all of the stages (Fig. 4) with the exception of one portion of Stage III. The initial two alteration stages are characterized by complete replacement or dissolution of the host sedimentary rocks. The final two stages occur as mineral deposition in veins and open space fillings. The spatial relationships of the four alteration stages to the various lithologies are shown in Figure 4.

Stage I - Silica

Silicification of selected horizons of the Upper Topliff Member is the earliest and most widespread form of alteration at Mercur. The most conspicuous zone of this alteration is a 5-20 meter-thick interval of jasperoid known as the Silver Chert located immediately below the Magazine Sandstone. The Silver Chert jasperoid creates massive, outcrop-forming ledges on Marion Hill, Sacramento Hill, and less conspicuously, on Mercur Hill. In outcrop, the Silver Chert is typically aphanitic, dense, and medium- to light-gray, although brown and grayish-black varieties are not uncommon. Preservation of original sedimentary features is observed locally (Fig. 5a). The Silver Chert shows widespread brecciation (Fig. 5b), particularly in the Marion Hill area. Much of this brecciation is attributed to pre-mineralization karstification of limestones below the Magazine Sandstone throughout the southern Oquirrh Mountains (R. Blair, oral comm.). Matrix material consists of clay, barite, and clear crystalline quartz, although vugs and open space remain. A significant amount of tectonic breccia is found within the Silver Chert, although it is usually distinguishable from hydrothermal breccia by the presence of slickensides and fault gouge. Stage I silica is found in lesser amounts throughout the rest of the Upper Topliff Member. Silicification of the Magazine Sandstone is widespread and often makes determination of the Silver Chert-Magazine Sandstone contact difficult (e.g. drillhole GV-25, Fig. 3). Minor amounts of jasperoid are localized in the Mercur Beds and lower portion of the Barren Beds.

In thin section, a number of quartz textures typical of jasperoids (Lovering, 1972) are observed. The very earliest textures appear to consist of xenomorphic or "jigsaw" quartz grains of very ranges from submicroscopic to 150 μ . Relic sedimentary bedding and fossil casirregular size and shape (Fig. 5c). Size ranges from submicroscopic to 150 μ . Relic sedimentary bedding and fossil casts can be seen in thin section. The jigsaw-xenomorphic textured jasperoids typically contain submicropscopic iron oxide, allophane, and carbon(?) particles. The occurrence of silica-encapsulated carbon has been noted by Gilluly (1932). The very fine-grained nature of the carbonaceous and ferruginous matter associated with the Mercur jasperoids has prevented positive identification of these materials. Minor sericite and kaolinite occur as overgrowths and interstitial grains. Lovering (1972) has interpreted jasperoids with xenomorphic textures to be the result of crystallization from a silica gel.

The second texture observed consists of reticulated quartz grains which often achieve sizes up to 0.5 mm in length. The reticulated texture appears to be gradational with the xenomorphic texture in some jasperoid specimans. The reticulated quartz grains are tightly interlocked with little intergranular material. Small unidentified, birefringent minerals occur as inclusions in this type of quartz. Minute carbon(?) grains often outline crystal growth planes, a feature which indicates deposition of the silica as crystalline quartz. The final common quartz texture consists of discrete, euhedral quartz grains in a matrix of clay and iron oxides (Fig. 5d). Locally, the euhedral quartz displays cockscomb overgrowths on earlier developed silicification (Fig. 5e). This form of quartz contains small numbers of small (less than 10 μ diameter) fluid inclusions. The

euohedral quartz and clay appear to represent a transition to the next paragenetic stage.

Modal partitioning of whole rock analyses of the Silver Chert and Magazine Sandstone shows that quartz constitutes 85-97 percent of the totals (Table 1). Kaolinite appears to be the dominant phyllosilicate in the Silver Chert, whereas sericite is more common in the Magazine Sandstone.

Ore grade mineralization occurs in the Silver Chert and silicified Magazine Sandstone. Silica encapsulation of the gold has not been noted (R. Klatt, W. Tafuri, written comm.) suggesting that the gold was deposited following the major silica depositing stage.

Stage II - Argillic

Decarbonation of limestone and modification of pre-existing phyllosilicate minerals in the Upper Topliff Member constitutes the second alteration stage at Mercur. Argillic alteration postdates the silicification on the basis of matrix material in jasperoid breccias and crosscutting relationships observed in thin sections (Fig. 5f and 6a).

An x-ray diffraction survey of 17 samples representative of Stage II alteration as well as unaltered lithologies revealed that with the exception of two samples, kaolinite and sericite are the only phyllosilicate minerals at Mercur. In sample MH-9-174 (Mercur Beds, Mercur Hill) pyrophyllite was identified. In sample MH-9-275 (silicified Magazine Sandstone, Mercur Hill) a minor amount of smectite was found.

All stratigraphic intervals of the Upper Topliff Member are host for argillic alteration, although it is particularly well developed in the Mercur Beds, Upper Beds, and the lower portion of the Barren Beds.

Argillic alteration appears to be preferentially developed in silty and shaley lithologies, but replacement of massive limestones is also observed (Fig. 6b, c). Brecciation of argillic material and cementation by somewhat darker argillic material is common, although locally this lighter to darker sequence is reversed (Fig. 6d). Textures of the argillic material vary from punky, structureless masses to thinly laminated rock in which original sedimentary bedding and fossils are well preserved. Oxidation associated with this form of alteration is extremely varied and gives these rocks colorful red, maroon, brown, and olive colors. Catagorization of this oxidation within the paragenetic sequence is difficult since oxidizing conditions existed in both late and early hypogene fluids at Mercur, as well as in supergene fluids. The fact that the most decarbonated argillically altered rocks are also the least oxidized (Table 1) suggests that progressive alteration of this type was accomplished under more reduced conditions. This possibility is discussed in more detail below.

Microscopic examination of the argillic rocks shows sericite as discrete grains and aggregates which range from 20 μ to 0.1 mm in length and aggregates of irregular interlocking kaolinite crystals up to 15 μ . Sericite crystals viewed perpendicular to the c-axis have a pale green pleochrism. Sericite grains are observed crosscutting and conforming to the outline of quartz grains, suggesting that deposition of quartz and sericite was contemporaneous. Orientation of the sericite grains conforms to laminations in the rock. This, plus the sericite pleochroism, serves to distinguish hydrothermal sericite from sedimentary illite. Sericite has not been observed replacing illite in thin section. Deposition of silica during Stage II was minor. Silica values range up to 75-80 percent in totally decarbonated limestones

(Table 1). This twofold increase in silica contents of unaltered silty limestones is the result of dissolution of original carbonate (50-60% of the original total). In thin section, only minor silicification and quartz overgrowths on pre-existing quartz grains is observed. Chalcedony commonly replaces fossil casts within zones of argillic alteration or occurs as rinds on altered carbonate clasts (Fig. 5g).

Argillically altered rocks are locally mineralized with ore-grade gold and have a trace element signature (As-Tl-Hg) which is characteristic of gold mineralization. Visible arsenic minerals are not common in hand specimen. Pyrite is locally abundant in unoxidized argillically altered rocks, although the distinction between hydrothermal and diagenetic pyrite is difficult.

Stage III - Carbonate sulfide

Deposition of calcite, realgar, orpiment, pyrite, marcasite, and organic material characterizes the third stage of the Mercur paragenesis. This stage marks the transition from replacement of the host limestones to deposition in veins and open spaces and appears to coincide with the bulk of the gold mineralization (Mercur geologic staff, pers. comm.). It is typically developed in the Mercur Beds. Lesser amounts are found in the Upper Beds, and more rarely the Barren Beds and the median limestone of the Magazine Sandstone. The earliest assemblage of this alteration consists of orpiment, pyrite, marcasite, and organic material which form discrete veins and interconnected net-veined textures (Fig. 6a). In thin section, the orpiment occurs as poorly crystallized masses which are intergrown with very-fine grained pyrite, marcasite, and amorphous organic material

(Fig. 6b). Subhedral to euhedral calcite and realgar are common, but minor associates of this form of alteration. Sericite and quartz also appear in close spatial association with the orpiment-pyrite-marcasite-organics assemblage.

A second mineral association of this alteration assemblage consists of discrete veins of calcite and realgar up to 2 cm in width (Fig. 6c). The calcite and realgar occur in widely varying proportions although the calcite is usually the earlier of the two minerals. In thin section, vein selvages consist of drusy calcite with abundant organic contaminants. The vein centers typically consist of clear calcite and realgar. Both calcite and realgar contain fluid inclusions which are less than 15 μ in diameter. The calcite-realgar veins are the one mineral assemblage which appear as discrete occurrences with little overlap to earlier or later minerals of the paragenesis, although hydrothermal organic material and pyrite are typically found close to the veins. Three whole rock analyses of massive limestones with calcite realgar veins are given in Table 1. Chemical composition of the rock hosting the calcite-realgar veins is similar to that of massive, unaltered limestones, indicating that formation of the veins did not alter the enclosing rock.

A mercury-thallium trace element signature is also recognized in association with this stage of the paragenesis at Mercur. Despite the fact that Mercur derived its name from the German word for mercury, no mercury or thallium mineral phases were identified during this study.

Stage IV - Barite-Halloysite

The final hypogene alteration stage at Mercur consists of barite and halloysite. These minerals are found in all of the Mercur ore bodies, but are particularly well displayed on Marion Hill. Most barite-halloysite mineralization is confined to open spaces and veins in the Silver Chert although minor amounts are also present in all other units of the Upper Topliff member.

Halloysite is the earlier of the two minerals. Halloysite generally occurs as vitreous, white masses which are soft when hydrated. In thin section, the halloysite masses consist of minute, interlocking gray crystals.

Barite occurs as euhedral crystals which can be seen replacing Stage III calcite (Fig. 6e) and halloysite (Fig. 6f). In the Upper, Mercur, and Barren beds, barite is commonly observed in spatial association with the orpiment-pyrite-marcasite-organic Stage III mineral assemblage. Crystal length ranges from 0.1 mm to 3.0 cm. Fluid inclusion up to 25 μ in diameter are characteristic and often aid in identification of this mineral in thin section (Fig. 6g). Euhedral quartz crystals are a local but minor associate of the barite.

Stibnite is locally observed as open space fillings in the Silver Chert and an antimony signature is often found in other portions of the Topliff stratigraphy. The relative scarcity of stibnite makes its assignment in the paragenetic sequence tenuous (Fig. 4).

Late hypogene or supergene minerals

Jarosite is abundant throughout the Mercur district as veins and replacements of pyrite. Alternating deposition of jarosite and hematite is seen locally. Jarosite crystals are relatively coarse-grained (50-100 μ in diameter) and show a distinctive yellow-green pleochrism. On the basis of petrographic evidence alone, it is unknown whether the jarosite is hypogene or supergene.

Alunite has been observed in one thin section as well as being detected in association with jarosite by x-ray diffraction. Alunite overgrowths on jarosite crystals establishes the relative ages of the two minerals.

FLUID INCLUSIONS

Heating and freezing measurements of fluid inclusions in selected hydrothermal minerals in the Mercur gold deposit were made using a Chaixmeca combined heating and freezing stage. Nearly 200 individual inclusions representing three of the four major hypogene mineral assemblages were analyzed (Table 2). Standard thin sections were used to identify individual crystals which contained fluid inclusions. Doubly polished plates ranging in thickness from 100 μ to 1 mm were then prepared from these samples. Only those inclusions with characteristics which indicated a primary origin (see criteria in Roedder, 1979) were analyzed. Reproducibility of the heating measurements was ± 3.0 C and ± 0.4 C for the freezing point depressions. Calibration was made with standard organic materials of known melting

points (MacDonald and Spooner, 1981) and NaCl-H₂O solutions of known salinity.

Fluid inclusions from Stage I (silica) were found in euhedral quartz grains which occur as overgrowths on earlier xenomorphic and reticulated quartz. Care was taken to distinguish this early quartz from the much rarer quartz deposited in the barite-halloysite stage. In only one sample (GV-25-212, Table 2) were quartz grains clearly crosscut by a later hypogene mineral (realgar). Fluid inclusions in Stage I quartz are sparsely and irregularly distributed throughout individual quartz crystals. Diameters are generally less than 15 μ . All inclusions are two-phase, liquid dominant with no daughter minerals. Fluid inclusions in Stage III calcite were measured where calcite veins crosscut earlier hydrothermal minerals or contained realgar. The inclusions are abundant and evenly distributed, but generally quite small (2-10 μ) although 20-30 μ inclusions are not uncommon. All inclusions are two-phase, liquid dominant. The early, turbid form of calcite often made fluid inclusion measurements difficult. Most of the analyses in Table 2 are from clear calcite crystals located next to realgar crystals. Realgar also contained numerous small inclusions. The poor optical properties of realgar, particularly upon heating, prevented their use in this study.

Fluid inclusions are abundant in virtually all of the barite found at Mercur. Barite fluid inclusions exhibit a wide variety of shapes and sizes (up to 25 μ in diameter) and many appear empty or have a high vapor/liquid ratio. This feature can be explained as entrapment of varying proportions of liquid and vapor by a boiling fluid or as leakage through prominent cleavage planes in the barite. Heating measurements in barite were as reproducible as those in quartz and calcite and suggest that little leakage

has occurred in the liquid dominant inclusions which were measured. The standard deviations for barite filling temperatures are only slightly higher than those of quartz and calcite (Table 2). Measurement of homogenization temperatures of the vapor-rich inclusions was not possible.

Freezing measurements were performed on all three minerals, although the small size of most fluid inclusions often limited determination of the final melting point of the ice. Salinities (expressed as equivalent weight percent and molal NaCl in Table 2) were computed using the equations of Potter et al., (1978). Possible CO₂ clathrates were observed in three inclusions of one barite crystal (sample P-27-118) and the salinity measurements reported for that sample may be too high (Collins, 1979).

The depth at which the Mercur ore bodies formed cannot be determined unequivocally. Reconstruction of the amount of overlying rock is difficult since absolute age of the Mercur ore forming fluids is not known, and the youngest sedimentary rocks in the area are Pennsylvanian in age. The appearance of vapor-rich fluid inclusions in the last stage of the paragenesis suggests that boiling occurred between 200°C and 300°C. Using the data of Haas (1971), pressures between 20 and 80 bars would be expected for the boiling curve of this temperature interval. An average figure of 40 bars is chosen for thermodynamic calculations presented below. A pressure correction of 3-5°C has been applied to all fluid inclusion filling temperatures, using the data of Potter (1977). Initial temperatures of the Mercur fluids ranged from 220-270°C. The fluids apparently were progressively cooler through the next two stages of the paragenesis, as shown by temperatures of Stage III calcite (150-190°C). During the final

barite-halloysite stage, the fluids were heated to the 180-300°C temperature range.

Throughout the paragenesis at Mercur, the salinity of the fluids remained relatively constant at 5-8 equivalent weight percent NaCl (Table 2). Where heating and freezing measurements were accomplished on the same inclusions, a positive correlation is observed between temperature and salinity (Fig. 7). The positive correlation of barite filling temperatures and salinities may indicate that boiling caused an increase in salinity. The data are too few to make a similar conjecture about quartz (Fig. 7).

In all fluid inclusion measurements, the distance to the nearest crystal boundary was measured in an attempt to determine the temperature gradient of crystal growth. Stage I quartz crystals typically contained fewer than 5 measureable inclusions, and thus did not yield sufficient data to draw any conclusions concerning temperature gradients. Measurements of individual calcite grains yielded ambiguous results, in large part due to irregular crystal shapes. Three clearly defined, euhedral barite crystals gave reliable temperature data which could be plotted against distance to the edge of the crystal (Fig. 8). A barite crystal in sample P-27-156 with measured salinities of approximately 0.65 molal NaCl shows retrograde solubilities (relatively cool core growing outward to a relatively hot rim). Two other barite crystals (samples P-27-118 and M-9/22-5a) show little correlation between temperature and distance to the edge of the crystal. These two crystals were deposited at higher temperatures and salinities than sample P-27-156. These observations fit well with experimental barite solubilities (Blount, 1977 and accompanying references). As shown in Fig. 9, barite exhibits retrograde solubilities between 200°C

and 300°C and salinities of 0.25 to 1.0 molal NaCl. At similar temperatures and salinities above 1 molal NaCl, solubilities are constant to slightly prograde. These observations seem to confirm the previously stated thermal history in which the barite-halloysite stage occurred at temperatures higher than previous stages. Fluid inclusion studies at the Carlin gold deposit (Radtke et al., 1980) have shown a thermal history which has many similarities to the Mercur deposits. In both cases, early or main stage ore deposition at temperatures of 160°C to 200°C is followed by an acid-sulfate stage in which depositional temperatures are considerably higher (upper to 300°C).

A temperature versus present day elevation plot for calcite fluid inclusions is given in Figure 10. The positive correlation appears to indicate conductive cooling to the surface, a feature that has been observed in other epithermal ore deposits, (e.g. Creede Mining District, Robinson and Norman (1984)).

GEOCHEMISTRY

Stage I fluid chemistry

The Silver Chert and other silicified rocks of Stage I contain both sericite and kaolinite. pH of the early fluids can be established near the kaolinite/sericite boundary (Fig. 11).

Cation ratios can be roughly estimated using the Na-K-Ca geothermometer of Fournier and Truesdell (1973). This geothermometer is based on Na/K ratios determined by experimental feldspar-water equilibrations and regression analyses of Ca/Na and Ca/K ratios of natural thermal and non-thermal waters.

The solubility of carbonates for a given $p\text{CO}_2$ and pH controls the amount of calcium ion in solution (Fournier and Truesdell, 1973, p. 1262). The Na-K-Ca geothermometer appears to be valid for geothermal fluids in a variety of geologic settings, including thick sequences of sedimentary rocks such as those surrounding Mercur. For thermal waters at 240°C:

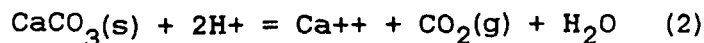
$$\log (a\text{Ca}^{++}) / \log(a\text{K}^+) = 0.5 \quad (1)$$

(Fournier and Truesdell, 1973, Fig. 3)

For thermal waters in equilibrium with sedimentary rocks between 200°C and 300°C, $a\text{K}^+/a\text{Ca}^{++}$ generally ranges from one to three (data from Cerro Prieto (Reed, 1975), Salton Sea (Muffler and White, 1969) and experimental work of Rosenbauer et al., 1983). Substituting these ratios into Equation 1 and then into the Na-K-Ca geothermometer for $T=240^\circ\text{C}$ gives an $a\text{K}^+$ range of 0.04 to 0.10 and an $a\text{Ca}^{++}$ range of 0.016 to 0.10 for a 1 molar solution. These values are used in Figure 11. At the kaolinite-muscovite boundary, a pH of 3.5 to 4.0 is indicated.

In all examples of Stage I alteration at Mercur, hematite is the dominant iron-bearing phase. This appears to be universally true in the Silver Chert horizon where pyrite has not been observed. Although pyrite is a very minor constituent of the massive limestones in Silver Chert equivalent rocks, the fact that hematite replaced pyrite during Stage I alteration establishes a minimum $\log(f\text{O}_2)$ of approximately -32 to -34, depending on the total sulfur and pH of the fluids (Fig. 11).

The complete dissolution of limestone during Stage I also helps to constrain the $p\text{CO}_2$ of the fluids according to the reaction:



Since $p\text{CO}_2$ is less than $p\text{TOTAL}$ (estimated to be approximately 40 bars), an upper limit for $p\text{CO}_2$ can be established. The mole fraction of CO_2 is found using Henry's Law:

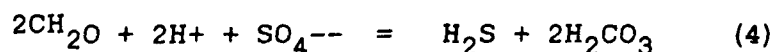
$$K * x\text{CO}_2 = p\text{CO}_2 \quad (3)$$

where the Henry's Law constant, K , is approximately 7000 for a 1.0 molal NaCl solution at 240°C (Ellis and Golding, 1963). At $p\text{CO}_2$ of 40 bars, $\log(x\text{CO}_2)$ is approximately -2.24 and $m\text{CO}_2$ is approximately 0.32. At the $f\text{O}_2$ values determined for Stage I fluids, $x\text{CO}_2$ is much greater than $x\text{CH}_4$ (see reactions of Table 3). Therefore, the total carbon of the system is no greater than 0.32 molal.

Stage II fluid chemistry

Silty and shaley limestones which are hosts to Stage II style alteration show a progressive evolution in terms of oxidation and change in clay mineralogy. As shown in Fig. 12, four unaltered silty limestone samples have calcite contents of 40-50% and illite to kaolinite ratios of 0.7 to 7.0. Oxidized, argillically altered limestones have variable amounts of calcite (2-50%), but sericite/kaolinite ratios which are lower than unaltered samples. A plausible interpretation is that early Stage II fluids were similar in composition to Stage I fluids, i.e. oxidizing and sufficiently acid to be in equilibrium with kaolinite. Whole rock analyses

of argillically altered silty limestones which are partially oxidized or reduced contain significantly less calcite (0-30%) and sericite to kaolinite ratios which range from unity to greater than 100 μ . This suggests that progressive alteration of the silty limestones produced fluids which were much less oxidized and in equilibrium with sericite rather than kaolinite. Reduction of the oxidizing fluids was accomplished by indigenous organic material in the limestones according to the reaction:



where CH_2O is a generalized formula for sedimentary organic matter. The reduced sulfur in solution would then be available to produce the iron and arsenic sulfides found in Stage II and III mineral assemblages.

The evolution of Stage I to Stage II silicate mineral assemblages is shown in terms of $a\text{SiO}_2(\text{aq})$ versus $a\text{K}^+/a\text{H}^+$ in Figure 13. Stage I fluids are supersaturated with quartz ($\log(a\text{SiO}_2(\text{aq}))$ greater than -2.1) and near the kaolinite-muscovite boundary. A decrease in temperature from 240°C to 160°C (as indicated by fluid inclusion filling temperatures) shifts the mineral equilibrium boundaries to lower values of $a\text{SiO}_2(\text{aq})$ and higher values of $a\text{K}^+/a\text{H}^+$. The final mineral assemblage is fixed along the muscovite-pyrophyllite boundary on the basis of modal partitioning of sample MH-9-174. Note that the fluid at this point is supersaturated with respect to chalcedony, a mineral which is found in association with argillic alteration. The change from 240°C to 160°C results in a positive $a\text{K}^+/a\text{H}^+$ shift of 0.5 log units.

Stage III fluid chemistry

Although gold deposition is found in association with the first two paragenetic stages at Mercur, its greatest concentrations are found with Stage III mineral assemblages. Mineral assemblage and metal solubility diagrams will be presented in more detail here to further define fluid parameters and shed light on the mechanism of gold deposition.

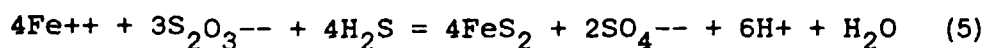
Although the fluid inclusion filling temperatures of Stage III calcite range between 153°C and 192°C, a temperature of 180°C is chosen for construction of Figures 14-17 in order to more closely approximate experimental work on iron and gold solubilities.

Distribution of carbon, sulfur, and arsenic aqueous species at 180°C is shown in Figure 14. The speciation of carbon and sulfur is well known (Ohmoto, 1972) while arsenic species are less established (Weissberg, 1966; Knight, 1977; Mironova and Zotov, 1980). The arsenic equilibrium constants given in Knight (1977) (Table 3) will be used in this study. For hydrothermal conditions at Mercur, orthoarsenic acid, $H_2As(OH)_5$, is the dominant species over a wide range of conditions (Fig. 14c). Aqueous arsenic species with a +5 valence are present only at very high $\log(fO_2)$ values (-25 to -30) at 180°C.

pH-oxygen fugacity condition. The two dominant Stage III mineral assemblages (pyrite-orpiment-organics-marcasite and calcite-realgar) are constrained to a pH of 3.5 to 5.2 on the basis of sericite coexistence with both Stage III mineral assemblages (Fig. 15). The calcite soluble/insoluble boundary within the muscovite field indicates pCO_2 and aCa^{++} values are similar to those hypothesized for Stage I fluids (aCa^{++} approximately 0.1 to 0.5 and pCO_2 near $pTotal$). The orpiment realgar boundary is drawn

for various values of total sulfur using the data of Craig and Barton (1973). Termination of this boundary is shown with a question mark at the point where XH_2S and XSO_4^{--} are approximately equal. At this boundary, As+++ oxide minerals are stable. The thermodynamic properties of As+++ oxides such as arsenolite and claudetite are only known to temperatures of 87°C (Chang and Bestul, 1971) and the tenuous extrapolation to higher temperatures is not attempted here. The most common oxidized mineral at Mercur is scorodite ($FeAsO_4 \cdot 2H_2O$) (T. Faddies, oral comm.), a mineral which contains +5 valent arsenic. Since the dominant arsenic valence under hypogene conditions hypothesized for Stage III fluids is +3 (Fig. 14c), the scorodite is probably supergene. The presence of realgar and orpiment and lack of hypogene As-oxides suggest that total sulfur values were less than approximately 0.001 molal since large sulfur values cause the calcite-realgar assemblage to fall outside the sericite field.

While the thermodynamic properties of marcasite have not been precisely determined, experimental work and observations in a variety of epithermal ore deposits (Rising, 1973; Robinson and Ohmoto, 1973) suggests marcasite typically forms near the pyrite-hematite boundary. At Mercur, this observation is corroborated by the spatial association of barite with the orpiment-pyrite-marcasite assemblage (see discussion of Stage IV fluids). Experimental work by El Dahhar and Barnes (1979) suggests that marcasite forms in acidic solutions (pH less than 4.4 at 25°C) in the presence of the thiosulfate ion according to the reaction:



The $S_2O_3^{--}$ ion is not stable in hydrothermal solutions above 200°C (Barnes, 1979), an observation that agrees with fluid inclusion data for Stage III fluids. By assuming that marcasite is stable near the pyrite-hematite boundary, further evidence is provided that the total sulfur of the fluids during Stage III was 0.001 to 0.0001 molar (Fig. 15).

The calcite-realgar assemblage which appears as discrete veins and veinlets formed at slightly higher pH and lower fO_2 than the orpiment-pyrite-organics-marcasite assemblage (Fig. 15). Calcite has a retrograde solubility with respect to temperature and a prograde solubility with respect to pressure (Holland and Malilin, 1979). The decrease in temperature hypothesized for the evolution from Stage I to Stage III is thus not a viable mechanism for the deposition of these veins. Although other mechanisms such as mixing with more dilute fluids cannot be discounted, a likely cause of these veins is a sudden decrease in pressure, such as a change from lithostatic to hydrostatic pressure. The fact that the calcite and realgar occur as veins and are not associated with other minerals in the paragenetic sequence lends further support for this mode of formation.

Metal solubilities. Metal solubility relationships of iron and gold computed as a function of pH and fO_2 are shown in Figures 16 and 17. At 180°C and mCl^- of 1.0, the dominant iron-bearing species is $FeCl^+$ (Crerar, et al., 1978). In Figure 17, values of this ion in equilibrium with pyrite and hematite have been contoured. As can be seen, a change from pH of 3.5, $\log(fO_2)$ of -34 (approximate conditions of Stage I fluids) to pH of 4.0, $\log(fO_2)$ of -40 results in no significant change in $FeCl^+$ solubilities until the pyrite-hematite boundary is reached. At this point, iron solubilities decrease approximately 1-2 log units.

The solubility of gold complexes and role in gold deposition have been a point of controversy for an extended period of time (Helgeson and Garrels, 1968; Boyle, 1969; Weisberg, 1969; Seward, 1973; Henley, 1973; Hattori, 1975; Casadevall and Ohmoto, 1977; Baronova and Ryzhenko, 1981; Henley and Ellis, 1983). Most authors consider gold to have a +1 valence under hypogene conditions and to be transported by either the AuCl_2^- complex or one of a variety of gold sulfide or bisulfide complexes. Equilibrium constants for AuCl_2^- and the $\text{Au}(\text{HS})_2^-$ (the most likely bisulfide complex) are given in Table 3. Seward (1973) states that $\text{Au}(\text{HS})^\circ$ probably causes significant complexing of gold at low pH. Unfortunately, there is no thermodynamic data for this complex.

In the pH- $f\text{O}_2$ range hypothesized for deposition of pyrite (Fig. 16) both gold chloride and gold bisulfide complexes have relatively low solubilities. The transition between oxidized and reduced sulfur species has been noted as a likely condition for gold deposition by other authors (Casadevall and Ohmoto, 1977; Henley and Ellis, 1983). Assuming that Stage I solutions were gold-bearing, AuCl_2^- is the most likely complex to have transported gold at Mercur. An isothermal change alone could decrease gold solubilities by more than two log units.

Stage IV fluid chemistry

With only two minerals in the final stage of hypogene mineralization at Mercur, only limited conclusions can be drawn about its chemistry. Halloysite is frequently considered to have a supergene origin (Miller, 1978). Although halloysite is bounded within the paragenetic sequence by mineral which are definitely hypogene (Fig. 4), a supergene origin

cannot be discounted. The occurrence of halloysite as vein and fracture fillings indicates that aluminum was mobile during its formation.

Precipitation of barite was probably accomplished by two mechanisms. Progressive heating of the fluids, as illustrated by temperature gradient measurements (Fig. 9) decreased the solubility of barite in solution. The lack of sulfide minerals in the barite-halloysite stage suggests that fluids at this point were oxidized. Conversion of H_2S to SO_4^{--} is also an effective mechanism to precipitate barite due to its very small solubility product (Table 3).

SUMMARY AND CONCLUSIONS

The mineralogical, fluid inclusion, and thermochemical data presented above provide a consistent picture of the spatial and temporal relationships of the Mercur gold deposits. A heat source initiated hydrothermal flow which was sufficiently vigorous to cause supersaturation of the fluids with respect to quartz at temperatures of approximately 250°C. Initial pH of the fluids was near 4 and $\log(fO_2)$ was between -32 and -34. Upon encountering the porous Magazine Sandstone in the vicinity of Mercur, precipitation of quartz, kaolinite, and sericite began. Massive limestones immediately below the Magazine Sandstone were jasperized to form the Silver Chert. Jasperization was possibly aided by prehydrothermal karstification of the limestones, although it may have been facilitated by the the process of "chemical brecciation" (Sawkins, 1969) whereby a change in rock composition can cause high internal stresses within the rock. Dissolution of limestones

and silty limestones in the Barren, Mercur, and Upper Beds was the second hydrothermal event at Mercur. Initial pH-fO_2 parameters were similar to those of the fluids which formed the Silver Chert jasperoid and silicified Magazine Sandstone, although the amount of silica deposited by these later solutions was considerably less. It is unknown whether Stage I and Stage II solutions represent separate hydrothermal events or were a part of a single hydrothermal event. Decarbonation of the silty limestones caused the Stage II fluids to become less acidic and reaction with sedimentary organic matter reduced the oxygen fugacity. The combination of these two changes brought about precipitation of pyrite and saturated the fluid with respect to calcite. The fact that sulfides are never observed in the Magazine Sandstone and Silver Chert supports the idea that reduction of the fluids was controlled by host lithology and composition. A sudden change in pressure, possibly caused by a breach of the convective system to the surface precipitated calcite and realgar.

The relatively high amounts of early, high temperature quartz progressing to minor amounts of late stage, low-temperature minerals suggest progressive thermal decay of the convecting hydrothermal system with time. During the waning stages of calcite deposition, cooling of the hydrothermal system was influenced by conduction to the surface.

The appearance of barite deposited at high temperatures late in the paragenetic sequence represents a rejuvenation of the hydrothermal system under pH-fO_2 conditions similar to those of the original fluids. Fluids during this stage were distinctly hotter than those of previous stages.

ACKNOWLEDGEMENTS

A Chevron Graduate Fellowship in Geology provided financial support for the senior author. Additional funding was provided by Getty Mining Company. Special thanks are due Robert Blair and William Tafuri for making their accumulated knowledge of Mercur available and the geologic staff at Mercur - Larry Kornze, Mike Bryant, Tom Faddies, Steve Johnson, and Jeff Goodwin - for bending over backward to help us during our visits to the mine. John Bowman and Greg Harper reviewed the manuscript and assisted with some of the lab work.

REFERENCES

- Baronova, N. N., and Ryshenko, 1981, Computer simulation of the Au-Cl-S-Na-H₂O system in relation to the transport and deposition of gold in hydrothermal processes: *Geochem. Inter.*, v. 18, p. 46-60.
- Barnes, H. L., 1979, Solubilities of ore minerals, in Barnes, H. L., ed., *Geochemistry of hydrothermal ore deposits*, 2nd ed.: New York, John Wiley and Sons, p. 404-460.
- Blount, C. W., 1977, Barite solubilities and thermodynamic quantities up to 300°C and 1400 bars: *Am. Min.*, v. 62, p. 942-952.
- Boyle, R. W., 1969, Hydrothermal transport and deposition of gold: *Econ. Geol.*, v. 64, p. 112-115.
- Butler, B. S., Loughlin, G. F., Heikes, V. C., and others, 1920, The ore deposits of Utah: U. S. Geol. Survey Prof. Paper 111, 672 p.
- Casadevall, T., and Ohmoto, H., 1977, Sunnyside mine, Eureka mining district, San Juan County, Colorado: Geochemistry of gold and base metal ore deposition in a volcanic environment: *Econ. Geol.*, v. 72, p. 1285-1320.
- Chang, S. S., and Bestul, A. B., 1971, Heat capacities of cubic, monoclinic, and vitreous oxides from 5-360°K: *Jour. Chem. Phys.*, v. 55, p. 933-946.
- Collins, P. L. F., 1979, Gas hydrates in CO₂-bearing fluid inclusions and the use of freezing data for estimation of salinity: *Econ. Geol.*, v. 74, p. 1435-1444.
- Craig, J. R., and Barton, P. B., Jr., 1973, Thermochemical approximations for sulfosalts: *Econ. Geol.*, v. 68, p. 493-506.

- Crerar, D. A., Susak, N. J., Borcisk, M., and Schwartz, 1978, Solubility of the buffer assemblage pyrite+pyrrhotite+magnetite in NaCl solutions from 200 to 350°C.: *Geochim. et Cosmochim. Acta*, v. 42, p. 1427-1439.
- Dunham, R. J., 1962, Classification of carbonate rocks according to depositional character, in Ham, W. E., ed., *Classification of carbonate rocks*: Am. Assoc. Petrol. Geologists Mem. No. 1, p. 108-121.
- El-Dahhar, M. A., and Barnes, H. L., 1979, Kinetics of marcasite formation (abstr.): *Am. Geophys. Union Trans.*, v. 60, p. 421.
- Ellis, A. J., and Golding, 1963, The solubility of carbon dioxide above 100°C in water and sodium chloride solutions: *Am. J. Sci.*, v. 261, p. 47-60.
- Fournier, R. O., and Truesdell, A. H., 1973, An empirical Na-K-Ca geothermometer for natural waters: *Geochim. et Cosmochim. Acta*, v. 37, p. 1255-1275.
- Gaudette, H. E., Flight, W. R., Loner, L., and Folger, D. W., 1974, An inexpensive method for determination of organic carbon in recent sediments: *J. Sed. Petrol.*, v. 44, p. 249-253.
- Gilluly, J., 1932, *Geology and ore deposits of the Stockton and Fairfield quadrangles, Utah*: U. S. Geol. Survey Prof. Paper 173.
- Haas, J. L., 1971, The effect of salinity on the maximum gradient of a hydrostatic system at hydrostatic pressure: *Econ. Geol.*, v. 66, p. 940-946.
- Hattori, K., 1975, Geochemistry of ore deposition at the Yatani lead-zinc and gold-silver deposit, Japan: *Econ. Geol.*, v. 70, p. 677-793.
- Helgeson, H. C., 1969, Thermodynamics of hydrothermal systems at elevated temperatures and pressures: *Am. J. Sci.*, v. 267, p. 729-804.

- Helgeson, H. C., and Garrels, R. M., 1968, Hydrothermal transport and deposition of gold: *Econ. Geol.*, v 63, p. 622-635.
- Helgeson, H. C., Delany, J. M., Nesbitt, M. W., and Bird, D. K., 1978, Summary and critique of the thermodynamic properties of rock-forming minerals: *Am. J. Sci.*, v. 276, 278 p.
- Henley, R. W., 1973, Solubility of gold in hydrothermal chloride solutions: *Chem. Geol.*, v. 11, p. 73-87.
- Henley, R. W., and Ellis, A. J., 1983, Geothermal systems ancient and modern: a geochemical review: *Earth-Sci. Rev.*, v. 19, p. 1-50.
- Holland, H. D., and Malinin, S. D., 1979, Solubility and occurrence of non-ore minerals in Barnes, H. L., ed., *Geochemistry of hydrothermal ore deposits*, 2nd ed.: New York, John Wiley and Sons, p. 461-508.
- Hutchinson, C. S., 1974, *Laboratory handbook of petrographic techniques*: New York, John Wiley and Sons, 527 p.
- Knight, J. E., 1977, A thermochemical study of alunite, enargite, luzonite, and tennantite deposits: *Econ. Geol.*, v. 72, p. 1321-1336.
- Lenzi, G. W., 1973, *Geochemical reconnaissance at Mercur, Utah*: Utah Geol. Min. Survey Spec. Studies 43, 16 p.
- Lovering, T. G., 1972, *Jasperoid in the United States - its characteristics, origin, and economic significance*: U.S. Geol. Survey Prof. Paper 710, 164 p.
- MacDonald, A. J., and Spooner, E. T. C., 1981, Calibration of a Linkan TH 600 programmable heating-cooling stage for microthermetric examination of fluid inclusions: *Econ. Geol.*, v. 76, p. 1248-1258.
- Miller, J. D., 1978, The formation of endellite and halloysite clay in

- argillic hydrothermal and supergene alteration processes: Ph.D. thesis, University of Utah, 148 p.
- Mironova, G. D., and Zotov, A. V., 1980, Solubility studies of the As(III) sulfide complexes at 90°C: *Geochem. Inter.*, v. 17, p. 46-54.
- Moore, W. J., 1968, Chronology of intrusion, volcanism, and ore deposition at Bingham, Utah: *Econ. Geol.*, v. 63, p. 612-621.
- Morris, H. T., and Lovering, T. S., 1961, Stratigraphy of the East Tintic Mountains, Utah: U. S. Geol. Survey Prof. Paper 361, 145 p.
- Muffler, L. P. J., and White, D. E., 1969, Active metamorphism of Upper Cenozoic sediments in the Salton Sea geothermal field and Salton Trough, southeastern California: *Geol. Soc. Am. Bull.*, v. 80, p. 157-182.
- Naumov, G. B., Ryshenko, B. N., and Khodahovsky, I. L., 1971, Handbook of thermodynamic data (translation of Russian report): U. S. Geol. Survey Report WRD 74-001.
- Ohmoto, H., 1972, Systematics of sulfur and carbon isotopes in hydrothermal ore deposits: *Econ. Geol.*, v. 67, p. 551-578.
- Potter, R. W., II, 1977, Pressure corrections for fluid inclusion homogenization temperatures based on the volumetric properties of the system NaCl-H₂O: *U. S. Geol. Survey Jour. Research*, v. 5, p. 603-607.
- Potter, R. W., II, Clynne, M. A., and Brown, D. L., 1978, Freezing point depression of aqueous sodium chloride solutions: *Econ. Geol.*, v. 73, p. 284-285.
- Proctor, P. D., 1959, Igneous rocks of the the Mercur area, in Bissell, H. J. ed., *Geology of the southern Oquirrh Mountains and Fivemile-northern Boulter Mountain area, Tooele and Utah Counties, Utah*: Utah Geol. Society Guidebook No. 14, p. 188-197.

- Radtke, A. S., and Dickson, F. W., 1974, Genesis and vertical position of fine-grained disseminated replacement-type gold deposits in Nevada and Utah, U. S. A., in Problems of ore deposition, v. 1, Volcanic ore deposits: Internat. Assoc. Genesis Ore Deposits (IAGOD), 4th Symposium, 1974, Varna, Bulgaria, Proc., v. 1, p. 71-78.
- Radtke, A. S., Rye, R. O., and Dickson, F. W., 1980, Geology and stable isotope studies of the Carlin gold deposit, Nevada: *Econ. Geol.*, v. 75, p. 642-672.
- Reed, M. J., 1975, Geology and hydrothermal metamorphism in the Cerro Prieto geothermal field, Mexico: Second U. N. Symp. on Development and Use of Geothermal Resources,
- Rising, B. A., 1973, Phase relations among pyrite, marcasite, and pyrrhotite below 300°C: Ph.D thesis, The Pennsylvania State University, 192 p.
- Robinson, B. W., and Ohmoto, H., 1973, Mineralogy, fluid inclusions, and stable isotopes of the Echo Bay U-Ni-Ag-Cu deposits: *Econ. Geol.*, v. 68, p. 635-656.
- Robinson, R. W., and Norman, D. I., 1984, Mineralogy and fluid inclusion study of the southern Amethyst Vein system, Creede Mining District, Colorado: *Econ. Geol.*, v. 79, p. 439-447.
- Roedder, E., 1979, Fluid inclusions as samples of ore fluids, in *Geochemistry of hydrothermal ore deposits*, 2nd edition: New York, John Wiley and Sons, p. 684-737.
- Rosenbaur, R. J., Bischoff, J. L., Radtke, A. S., 1983, Hydrothermal alteration of graywacke and basalt by 4 molal NaCl: *Econ. Geol.*, v. 78, p. 1701-1710.
- Sawkins, F. J., 1969, Chemical brecciation: an unrecognized method of breccia formation?: *Econ. Geol.*, v. 64, 613-617.

- Seward, T. M., 1973, Thio-complexes and the transport of gold in hydrothermal ore solutions: *Geochim. et Cosmochim. Acta*, v. 37, p. 379-399.
- Spurr, J. E., 1895, Economic geology of the Mercur Mining district, Utah: U. S. Geol. Survey 16th Ann Rept., pt. 2, p. 374-376.
- Tafari, W. J., 1976, Geology and geochemistry of the gold deposits at Mercur, Utah (abs.), in *Geology and exploration of fine-grained Carlin-type gold deposits*: Geol. Soc. Nevada and MacKay School of Mines Symposium, Reno, Nevada, p. 10.
- Weissberg, B. G., Dickson, F. W., and Tunnel, G., 1966, Solubility of orpiment As_2S_3 in $NaS-H_2O$ at 50-200°C and 100 to 1500 bars: *Geochim. et Cosmochim. Acta*, v. 30, p. 815-827.
- Weissberg, B. G., 1969, Solubility of gold in hydrothermal alkaline sulfide solutions: *Econ. Geol.*, v. 65, p. 551-556.

FIGURE CAPTIONS

Figure 1. Generalized geology of the southwestern portion of the Oquirrh Mountains, Utah (after Guilly, 1932).

Figure 2. Generalized geology in the vicinity of Mercur with location of principle ore deposits and drill holes used in this study (after Getty Mining Company maps).

Figure 3. Lithologic logs of upper portion of Topliff Member, Great Blue Limestone. DDH HS-4 is weakly to nonaltered, DDH MH-9 is weakly to moderately altered, and GV-25 is strongly altered. Datum is base of the Magazine Sandstone.

Figure 4. Paragenetic sequence and spatial distribution of hydrothermal alteration at Mercur.

Figure 5. Photographs of Stage I and Stage II lithologies.

A. Split core of Silver Chert from Marion Hill, DDH R-21-120. Note light colored banding which may be relic bedding. Scale bar is 5 cm.

B. Slabbed core of Silver Chert breccia, Marion Hill, DDH H-17-259.

j = Dark gray clasts are early jasperoid, s = amorphous silica-clay, c = crosscutting calcite veinlets. Scale bar is 2 cm.

C. Photomicrograph of xenomorphic quartz grains in Silver Chert horizon, Marion Hill, DDH P-27-149. Note bands of fine-grained minerals (allophane?) which crosscut crystal boundaries and suggest deposition of the silica as a gel prior to formation of individual quartz crystals. Scale bar

is 100 μ .

D. Photomicrograph of euhedral quartz in matrix of iron oxides and carbon(?). Silver Chert horizon, Marion Hill, DDH H-17-265. Scale bar is 0.5 mm.

E. Photomicrograph of xenomorphic (detrital?) quartz overprinted by later silica-clay clots. Lower portion of Barren Beds, Marion Hill, DDH H-17-202. Scale bar is 200 μ .

F. Photomicrograph of sericite aggregate overgrowth on quartz-sericite-kaolinite matrix. Mercur Beds, Mercur Hill, DDH ML-9-198. Scale bar is 200 μ .

G. Slabbed core section of mudstone being altered to argillic breccia. m = mudstone (dark strings are fenestrate bryozoa clasts), ch = chalcedony overgrowths on mudstone, a = argillic breccia. Note the crosscutting nature of the alteration to the original sedimentary bedding (shown by the bryozoa clasts). Mercur Beds, Golden Gate area, DDH GV-25-239. Scale bar is 0.5 cm.

H. Photomicrograph of oxidized argillic alteration being overprinted by later organic-rich alteration. Mercur Beds, Mercur Hill, DDH ML-9-198. Scale bar is 1 mm.

Figure 6. Photographs of Stage III and Stage IV lithologies.

A. Slabbed core section of argillic breccia. a = dark clasts of argillic material, in matrix of lighter argillic material, o = orpiment vein material. Mercur Beds, Mercur Hill, DDH MH-9-198. Scale bar is 5 mm.

B. Reflected light photomicrograph of Stage III orpiment-marcasite-organics mineral assemblage. m = marcasite, o = orpiment, org = organics. Mercur Beds, Mercur Hill, DDH ME-8-119. Scale bar is 200 μ .

C. Slabbed core section of calcite-realgar vein in massive mudstone.

r = realgar, p = pyrite. Note overgrowth of realgar on euhedral pyrite, which is probably diagenetic in origin. Barren Beds, Golden Gate area, DDH GV-25-284. Scale bar is 3 mm.

D. Photomicrograph of organic matter encased by Stage I quartz and crosscut by Stage III calcite. Mercur Beds, Golden Gate area, DDH GV-25-242.

Scale bar is 200 μ .

E. Photomicrograph of euhedral barite laths crosscutting Stage III calcite.

b = barite, c = calcite. Median limestone of Magazine Sandstone, Marion Hill, DDH R-21-104. Scale bar is 0.5 mm.

F. Photomicrograph of euhedral barite crystals in massive halloysite.

Square clast is Stage I jasperoid. Silver Chert, Marion Hill, DDH R-21-134.

Scale bar is 1 mm.

G. Photomicrograph of barite crystals with hematite coating and jarosite in vug of Silver Chert, Marion Hill, DDH H-17-237. Sequence of crystallization seems to be barite > hematite > jarosite. Scale bar is

200 μ .

H. Photomicrograph of Stage IV fluid inclusions in barite. Silver Chert horizon, Marion Hill, P-27-149. Scale bar is 10 μ .

Figure 7. Temperature versus salinity relationships for fluid inclusions at Mercur.

Figure 8. Temperature versus distance to the edge of crystal for three barite crystals. a) Sample P-27-156. b) Sample P-27-118. c) Sample 9/22-5a.

Figure 9. Barite solubilities in solutions of varying temperature and

salinity (after Blount (1977), Figure 1).

Figure 10. Calcite fluid inclusion filling temperatures plotted against present day elevation at Mercur.

Figure 11. pH versus $\log(fO_2)$ plot of Stage I hydrothermal fluids.

Figure 12. Percent calcite versus $\log(\text{sericite/kaolinite})$ plot for unaltered and argillically altered rocks at Mercur. Sericite/kaolinite ratios of 0.1 and 100 correspond to zero and infinity, respectively. Tie lines show unaltered/altered samples which are stratigraphically equivalent.

Figure 13. $\log(aSiO_2)$ versus $\log(aK^+/aH^+)$ plot of Stage I-Stage II and Stage III fluids at Mercur. Arrow shows change between starting and final fluid composition assuming a continuum between Stage I and Stage III fluids.

Figure 14. Aqueous speciation of Stage III fluids as functions of pH and fO_2 . a) Sulfur species. b) Carbon species. c) Arsenic species.

Figure 15. pH versus $\log(fO_2)$ plot of Stage III hydrothermal fluids.

Figure 16. pH versus $\log(fO_2)$ plot of $FeCl^+$ solubilities.

Figure 17. pH versus $\log(fO_2)$ plot of gold chloride and bisulfide complexes.

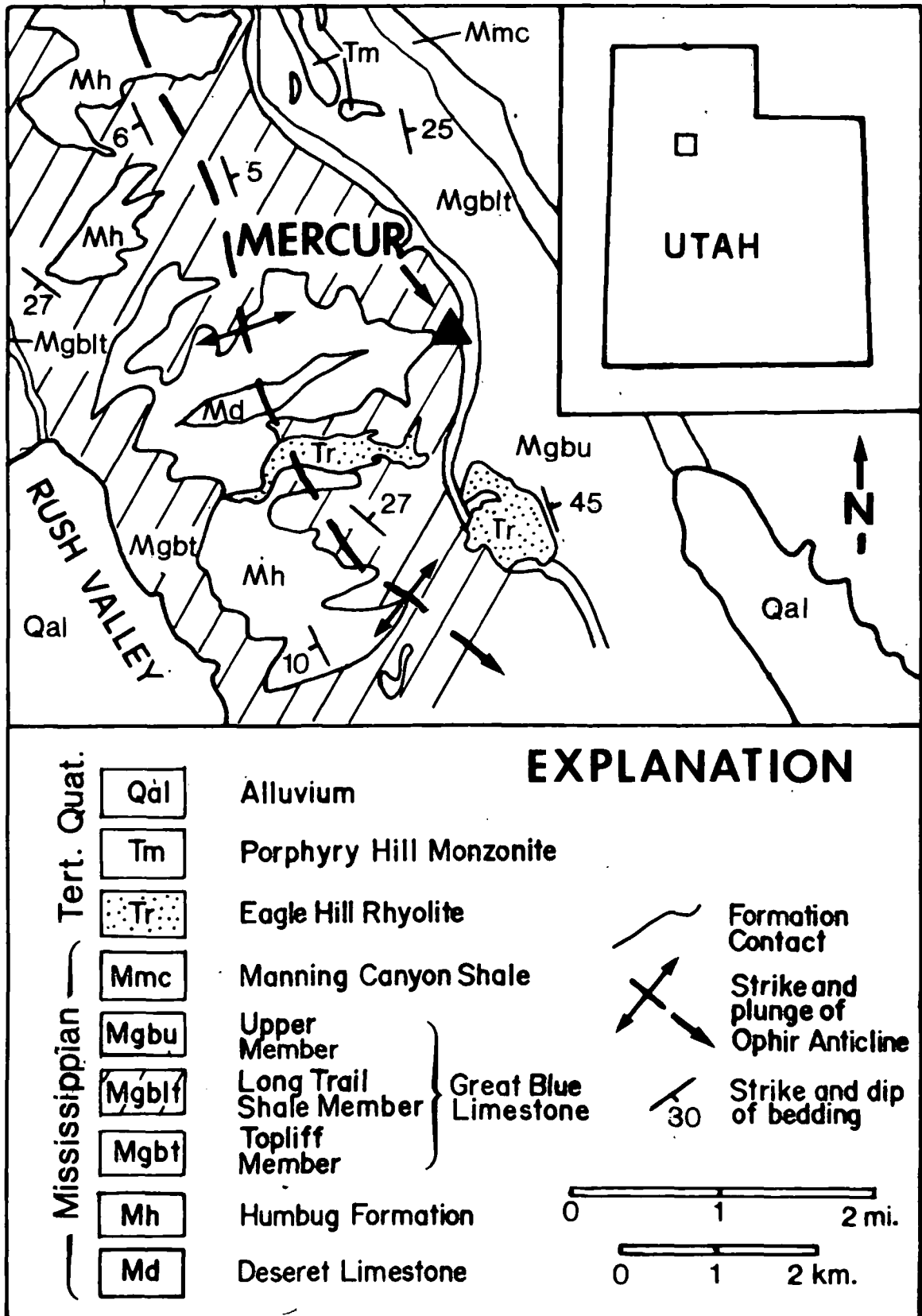


FIGURE 1

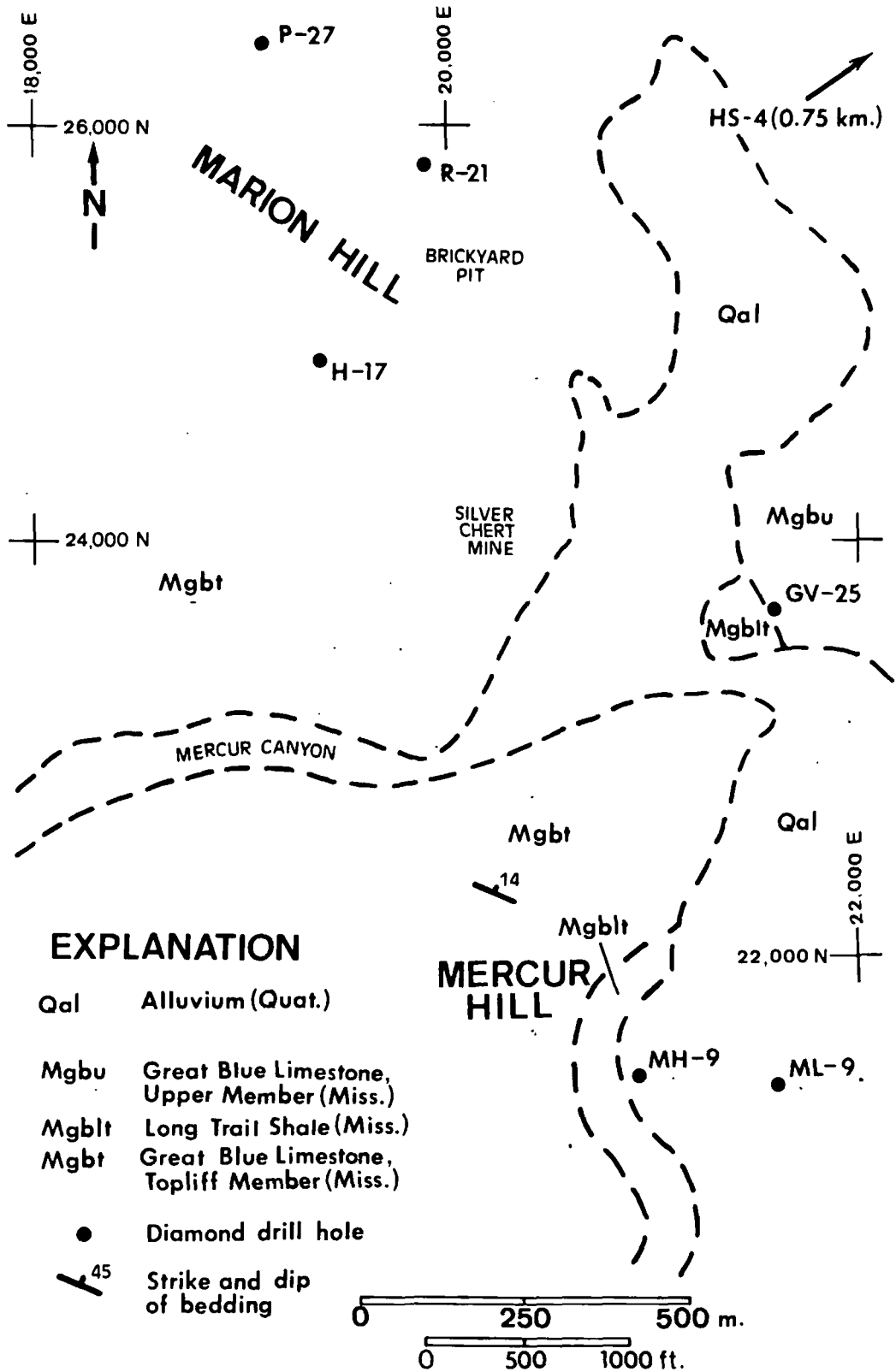


FIGURE 2

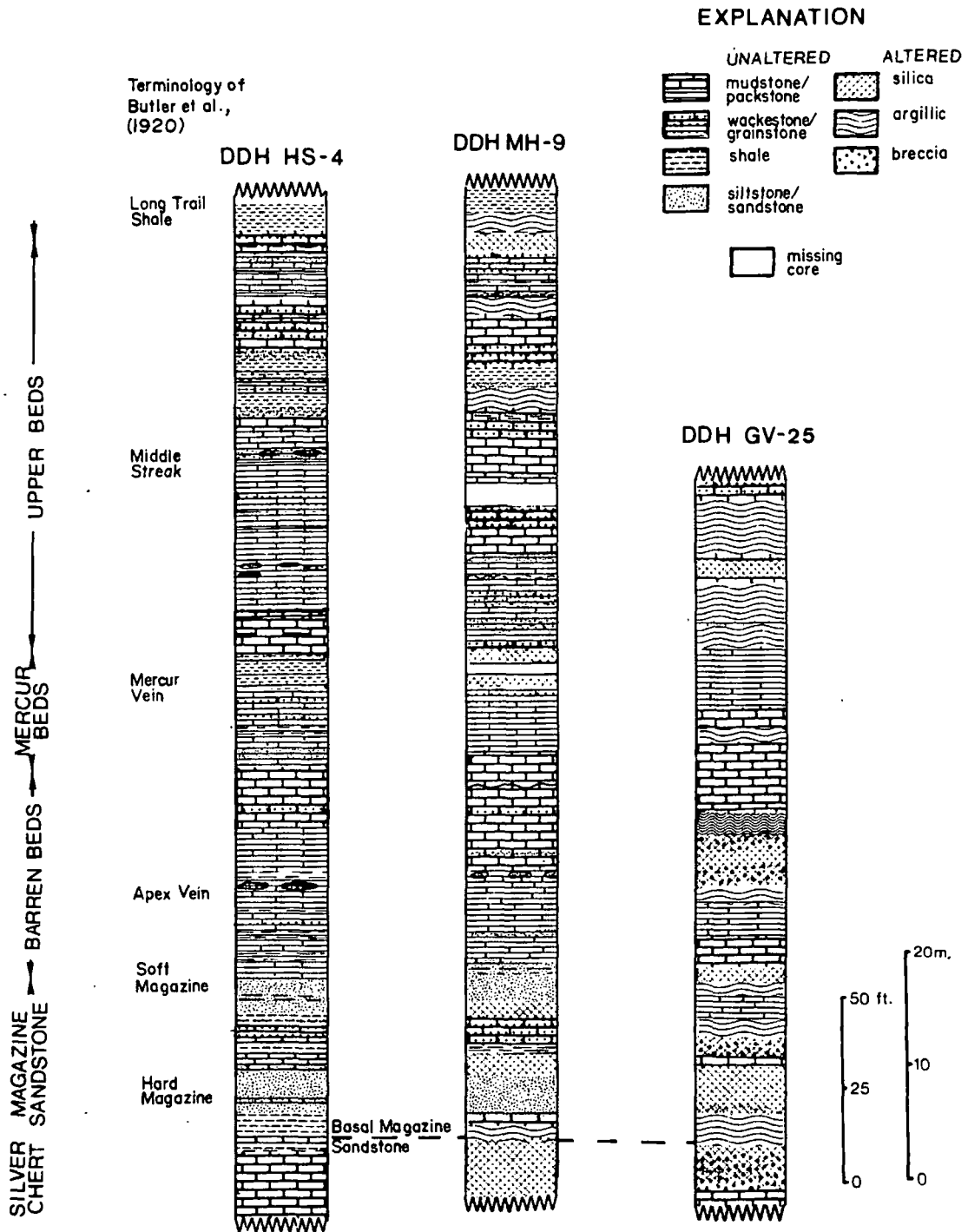


FIGURE 3

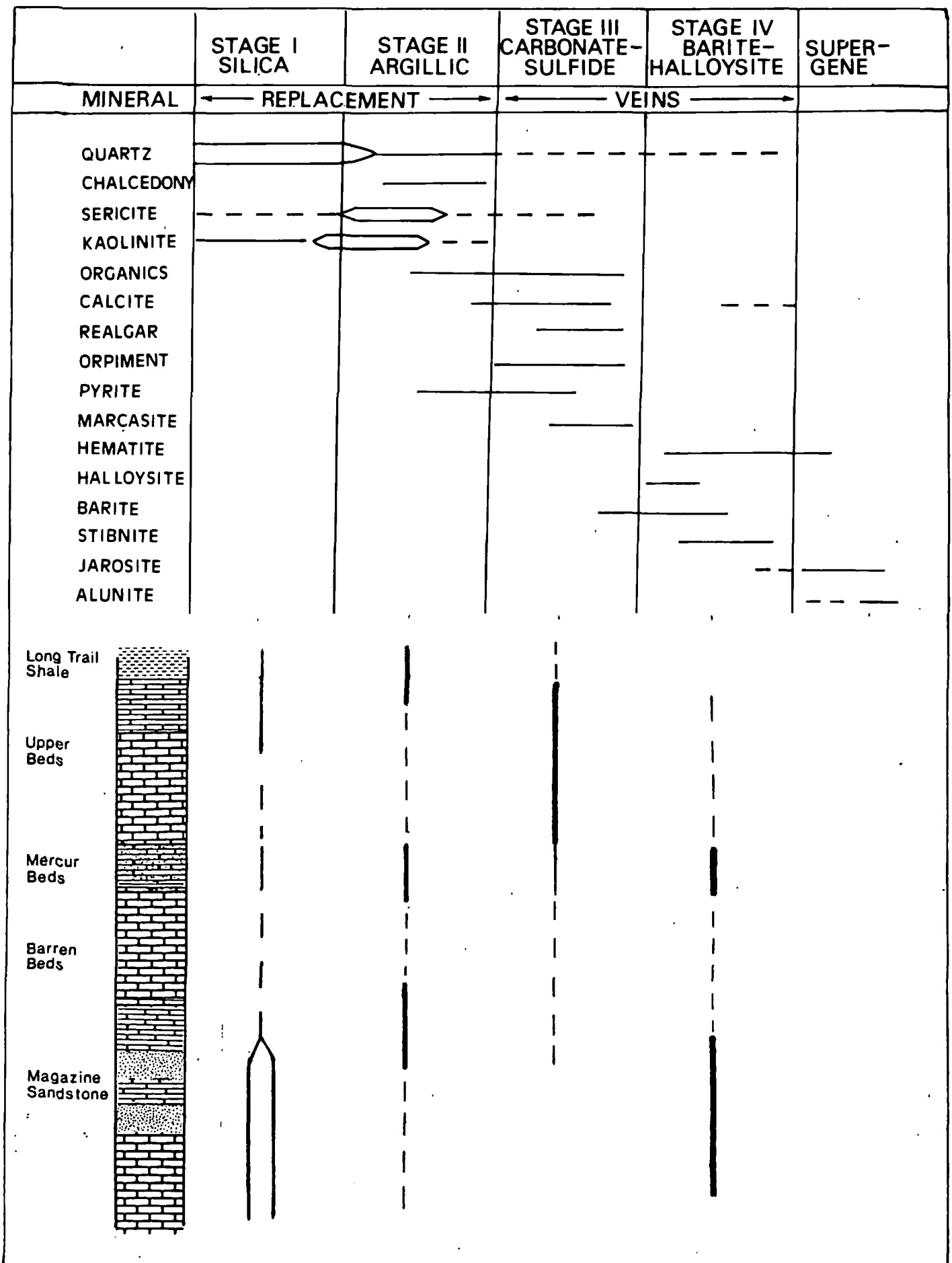


FIGURE 4.

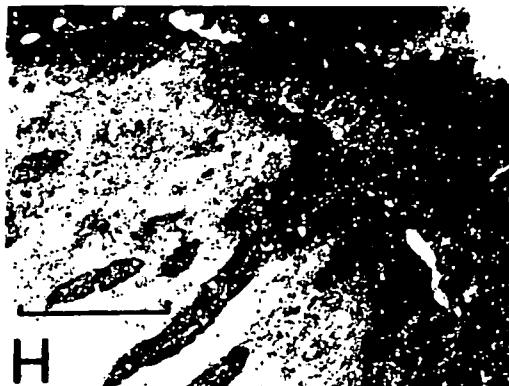
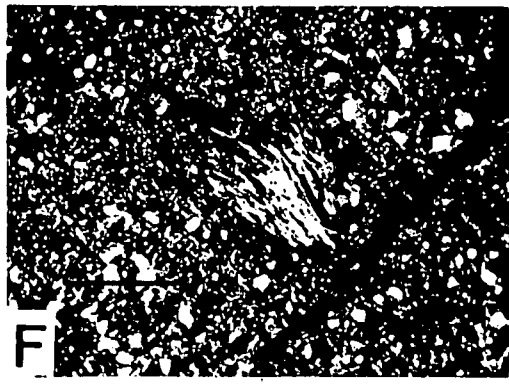
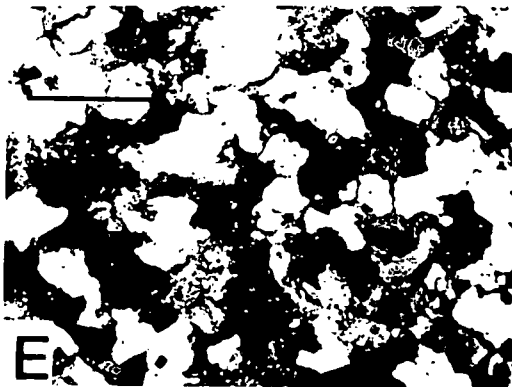
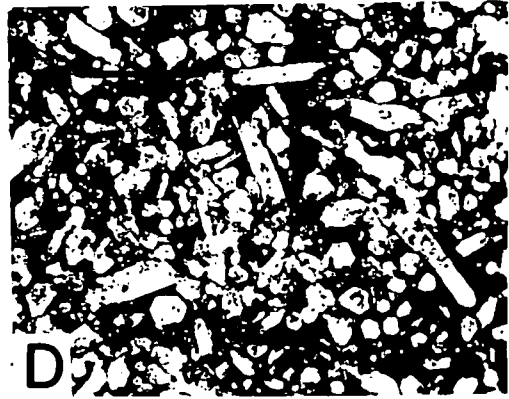
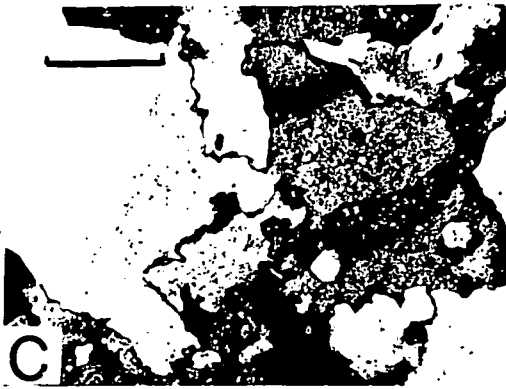
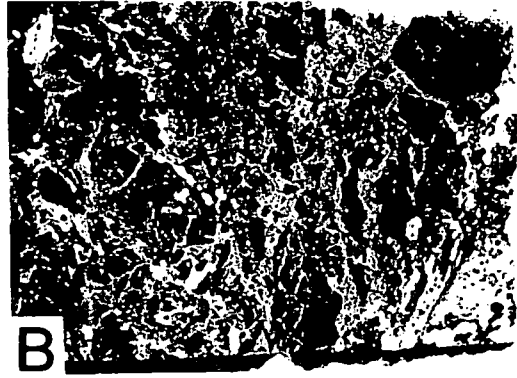


FIGURE 5.

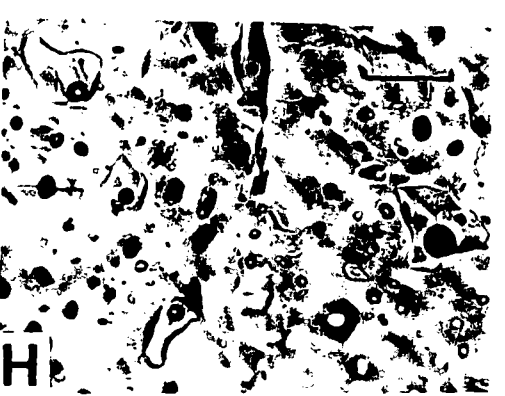
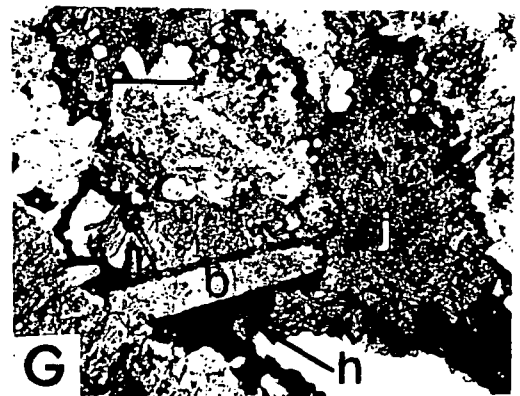
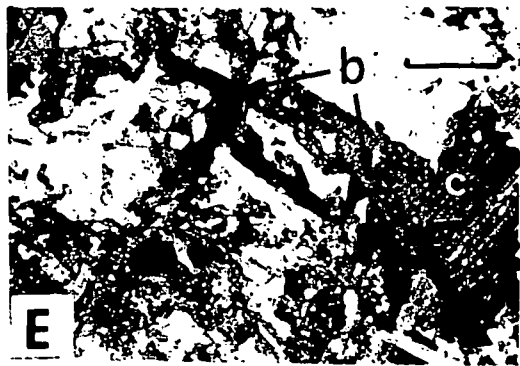
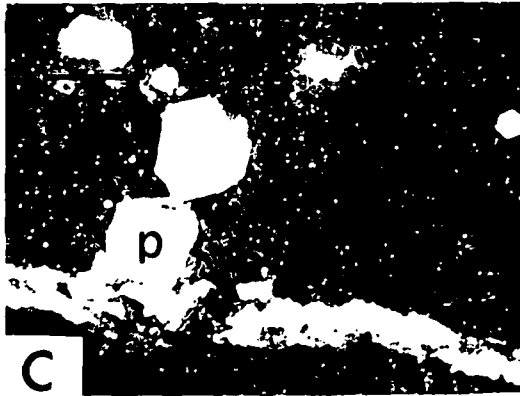
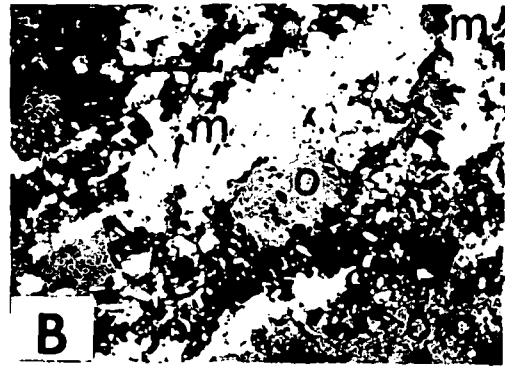
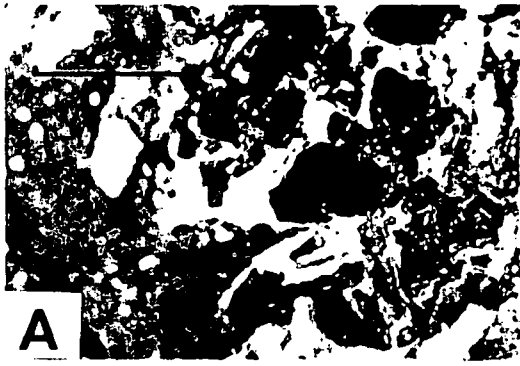


FIGURE 6.

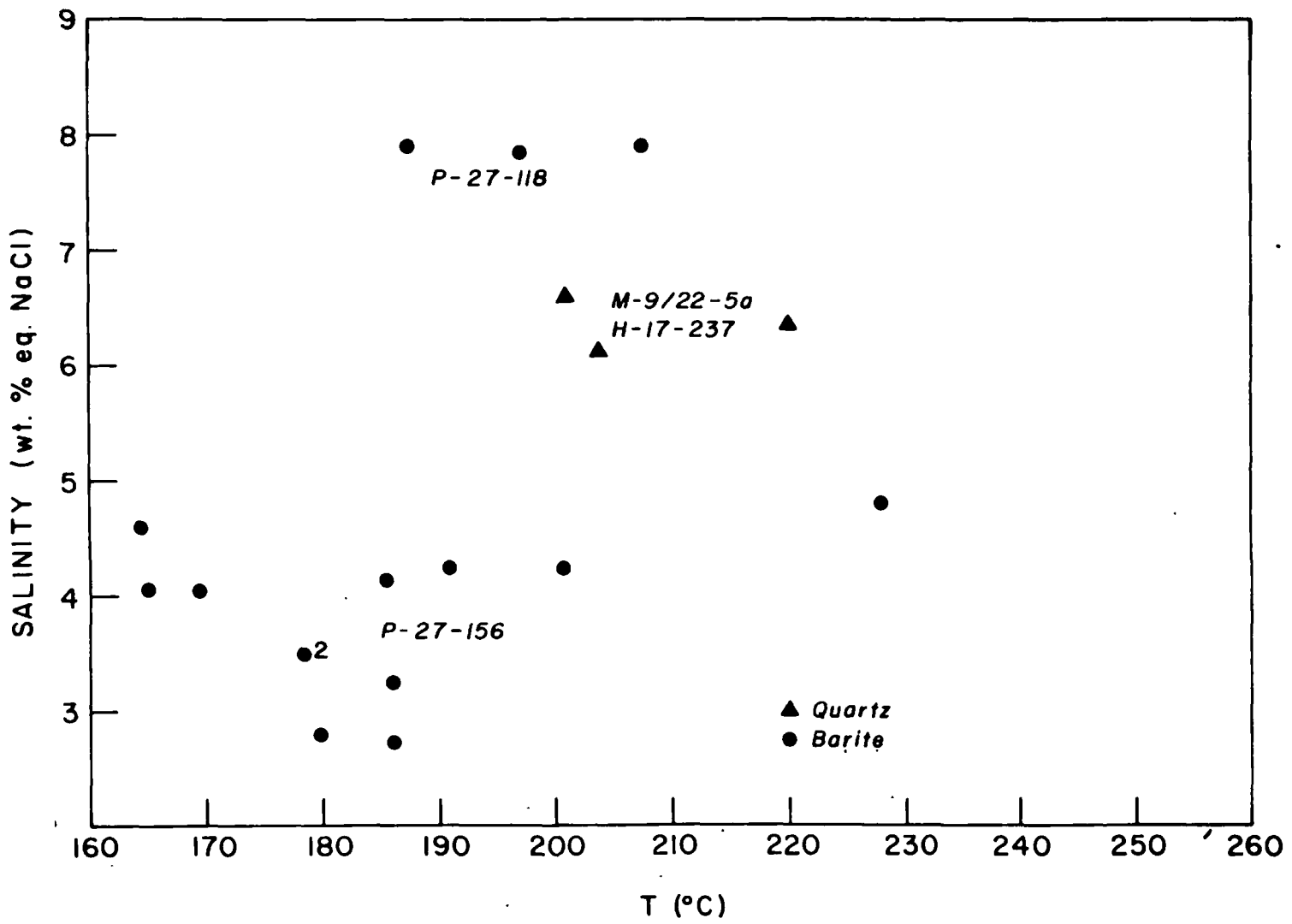


FIGURE 7.

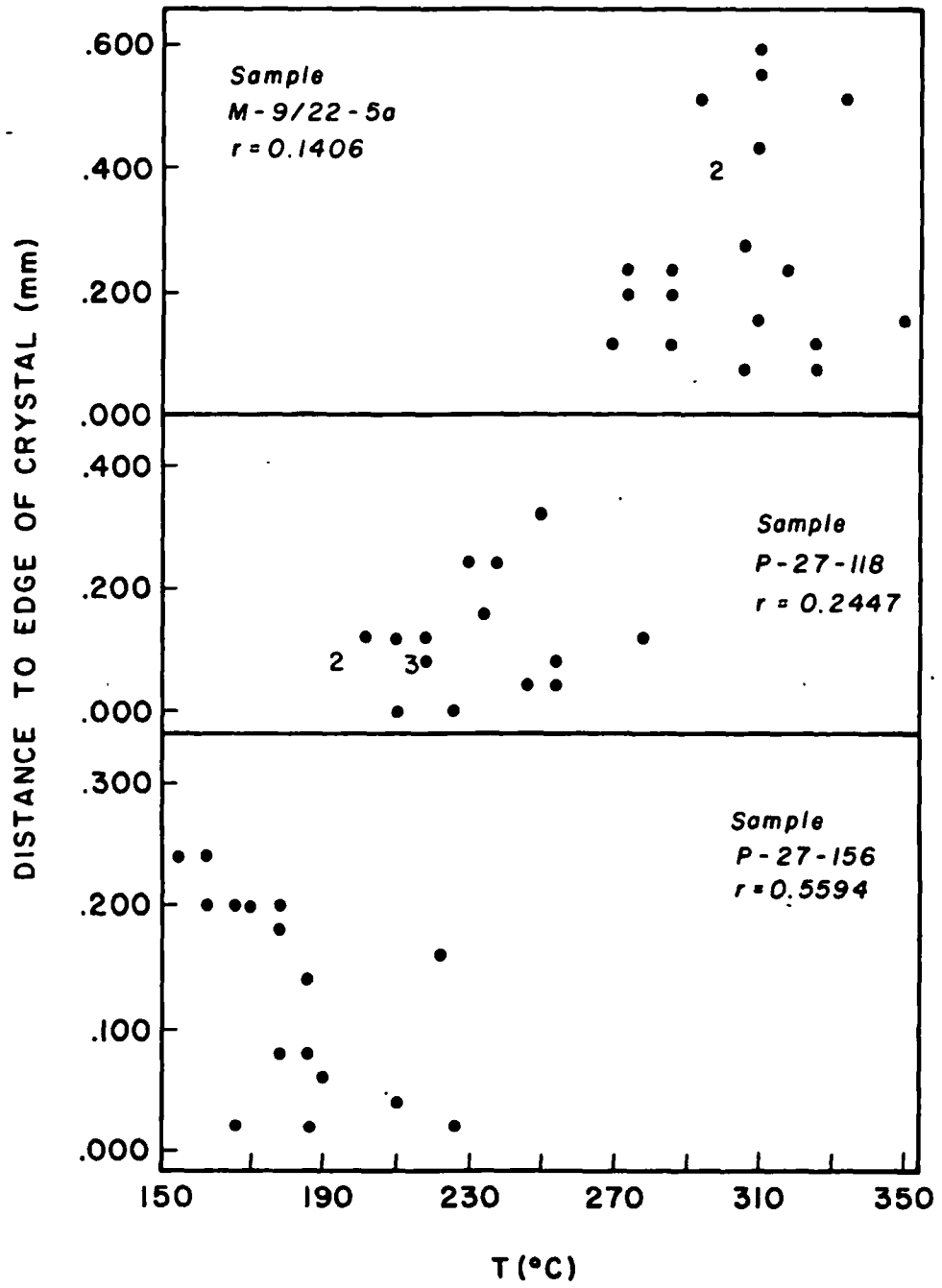


FIG. 8

FIGURE 8.

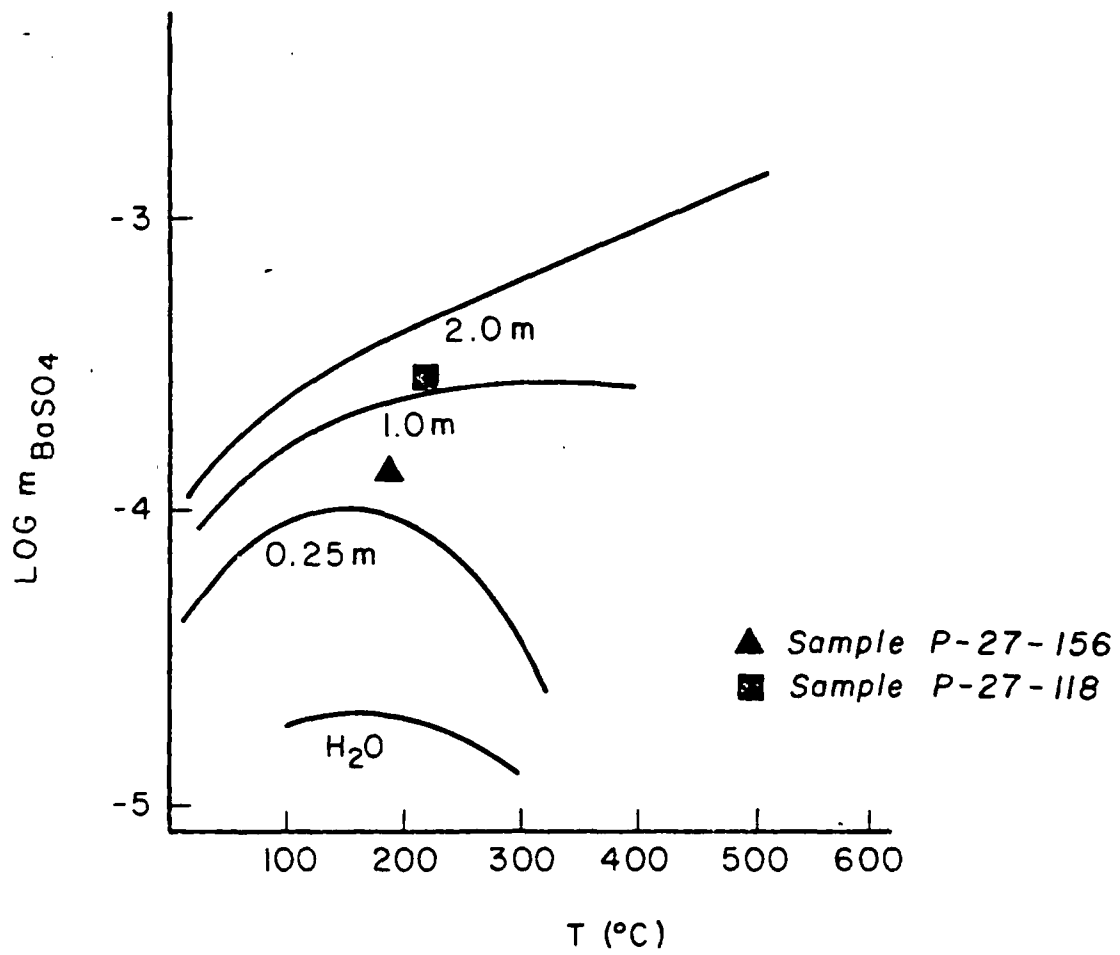


FIGURE 9

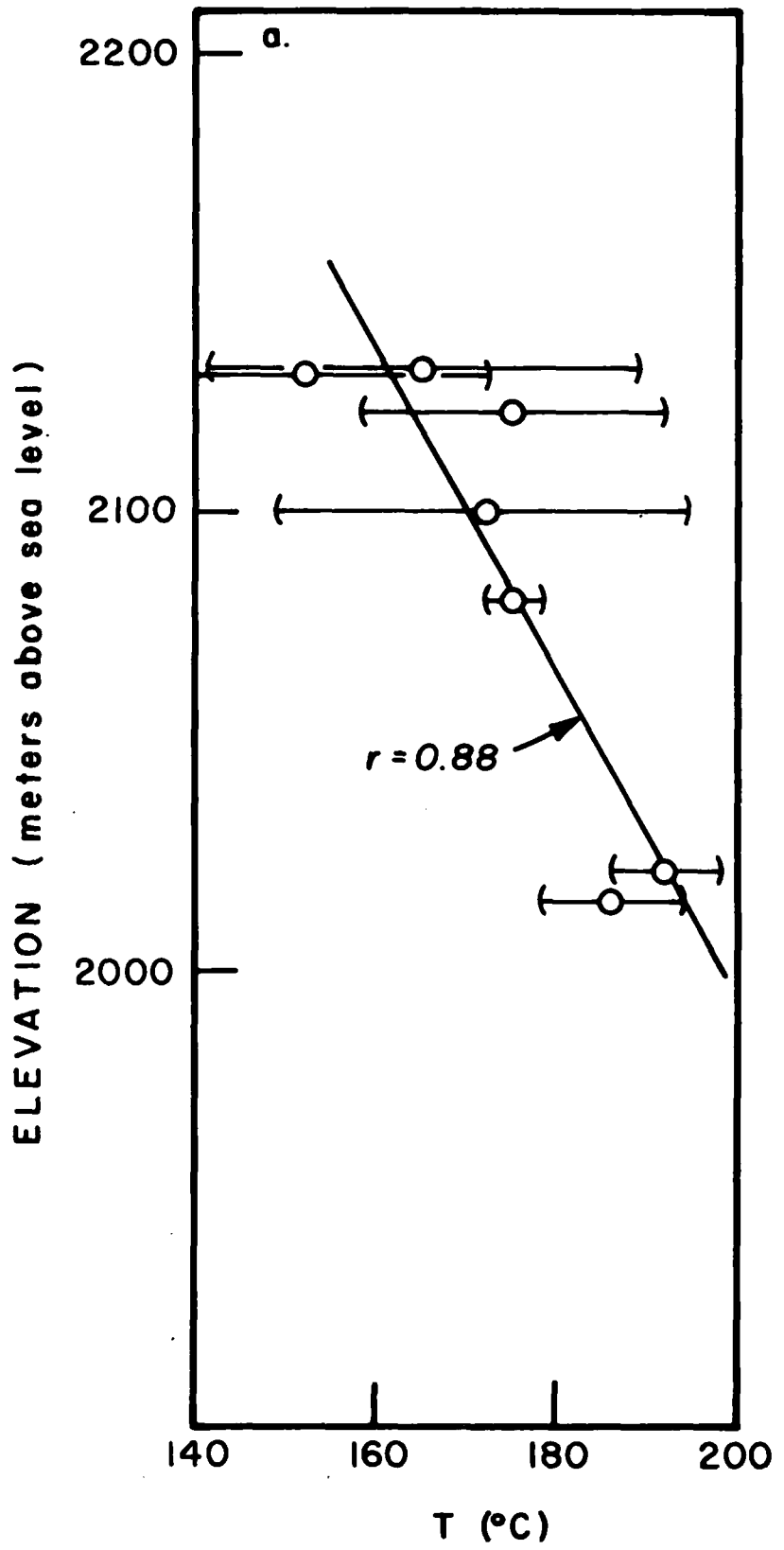


FIGURE 10.

FIGURE 11

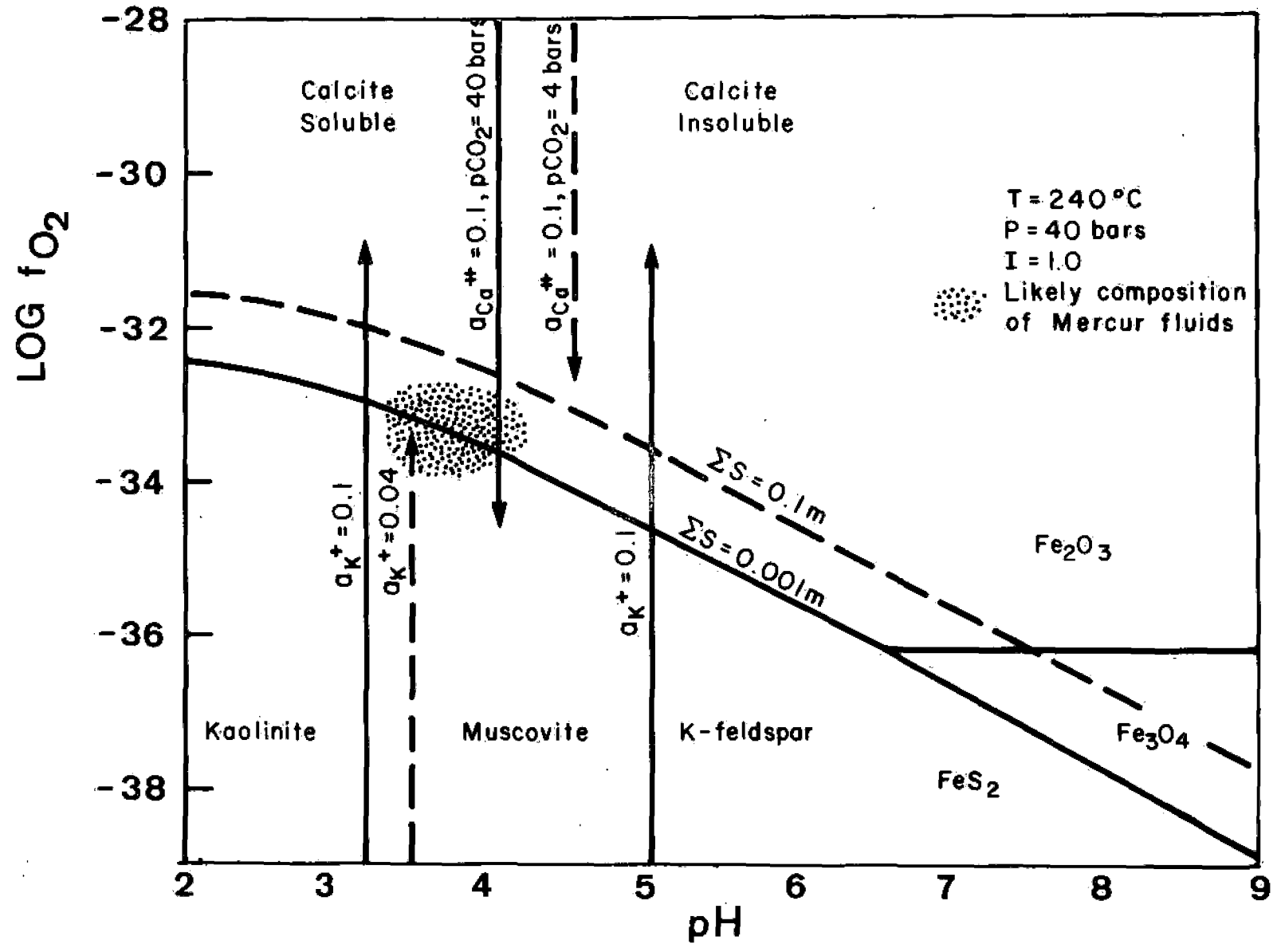
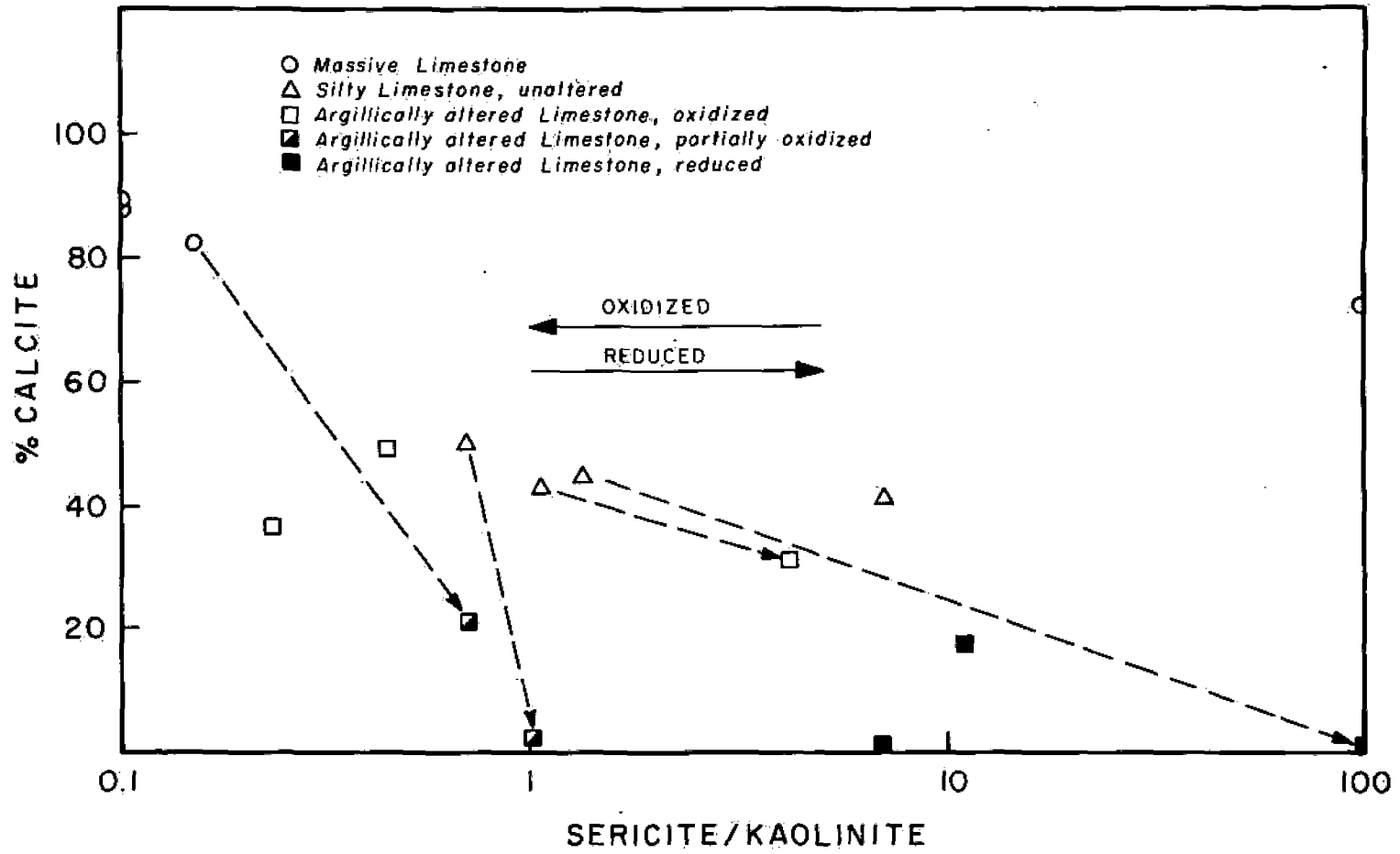


FIGURE 12



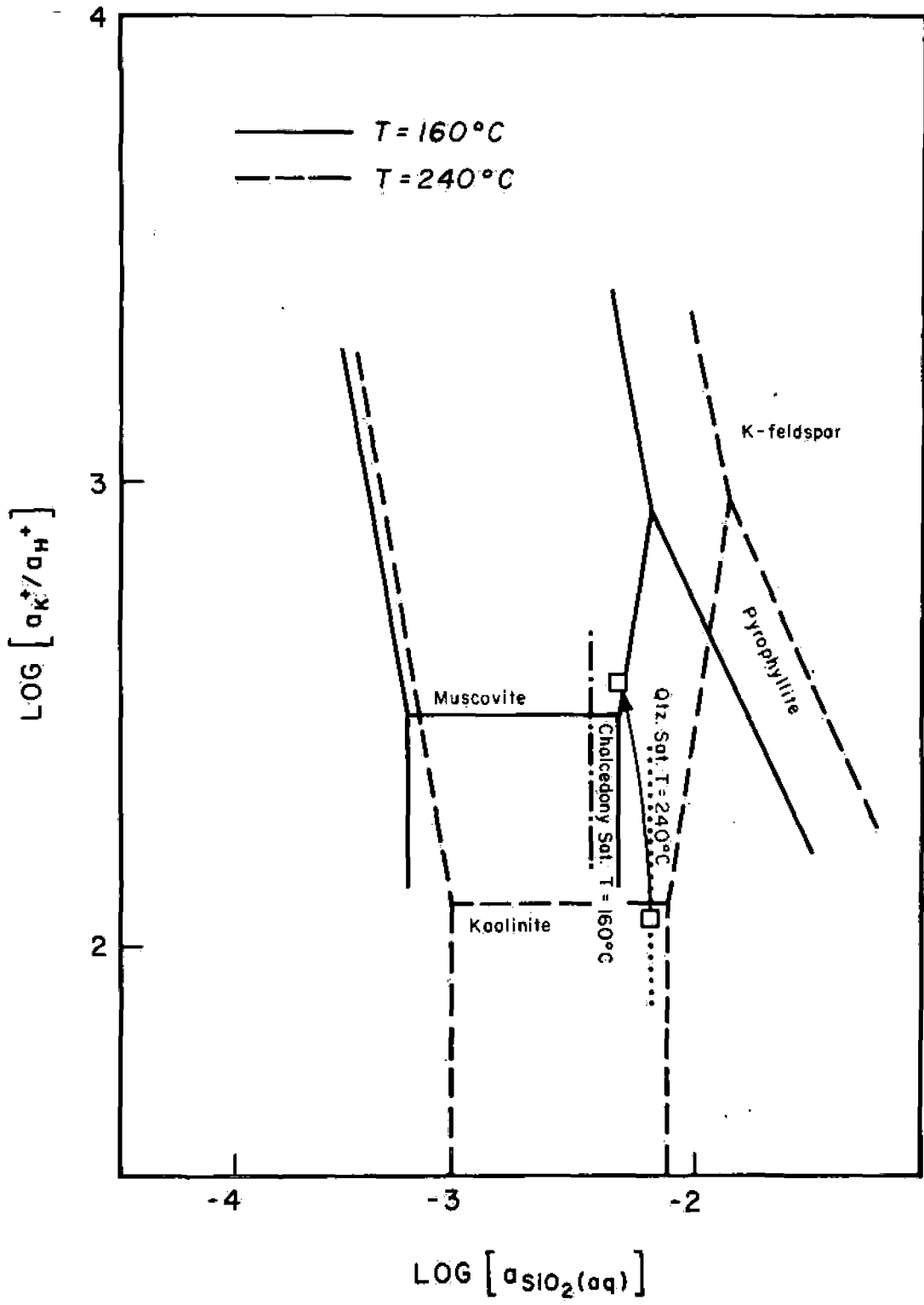


FIGURE 13 :

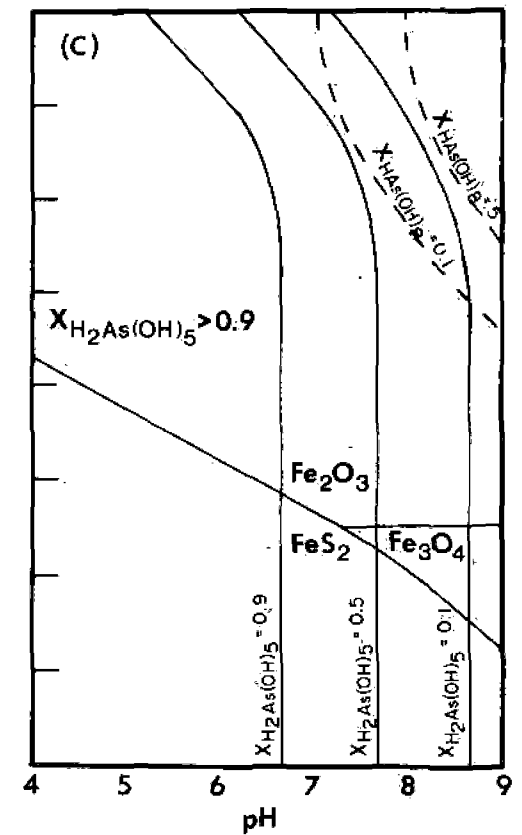
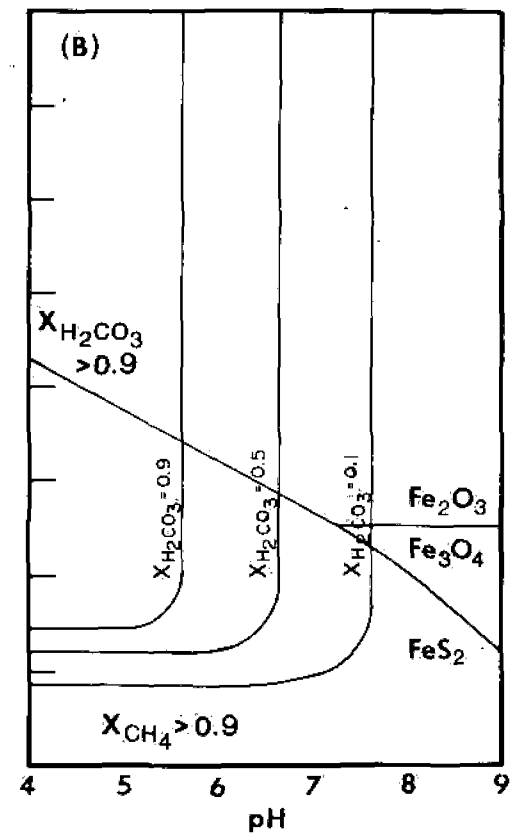
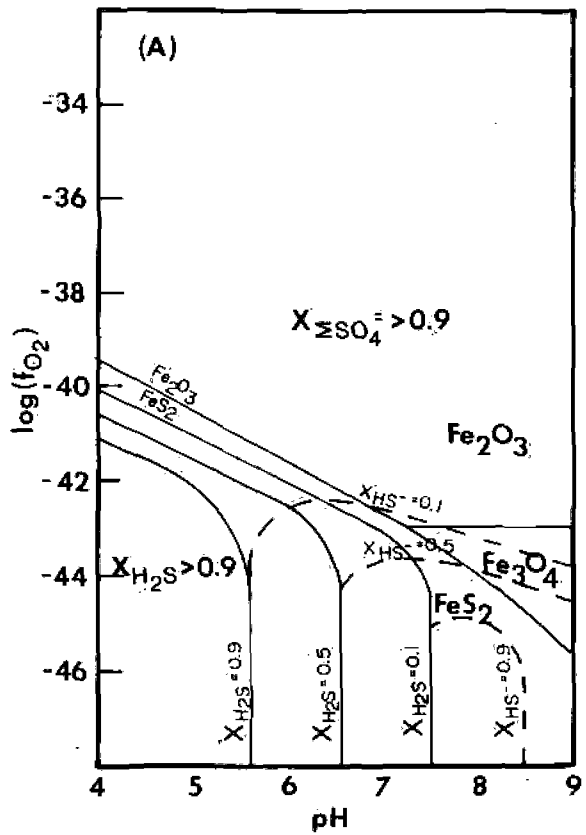


FIGURE 14.

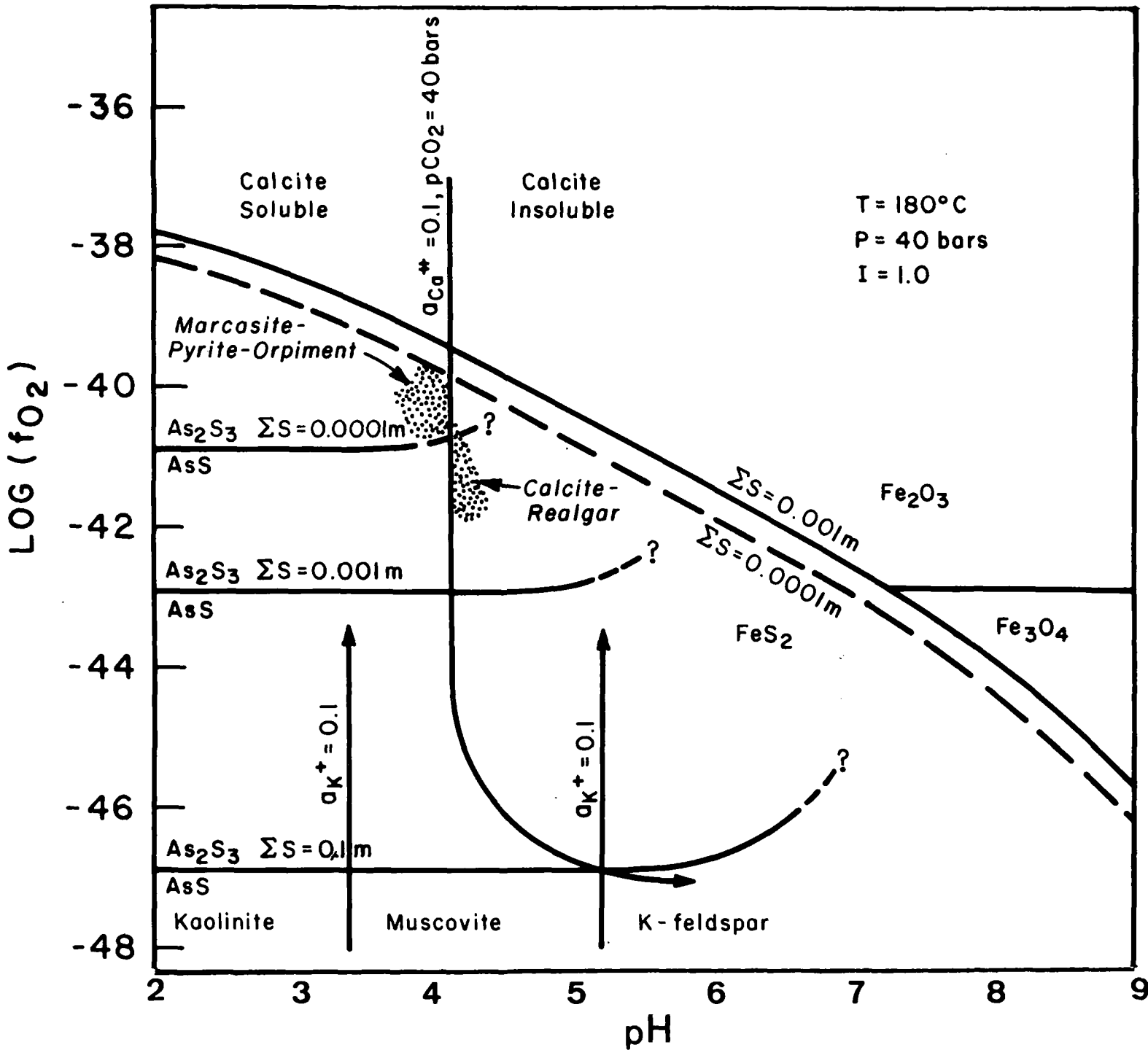


FIGURE 15

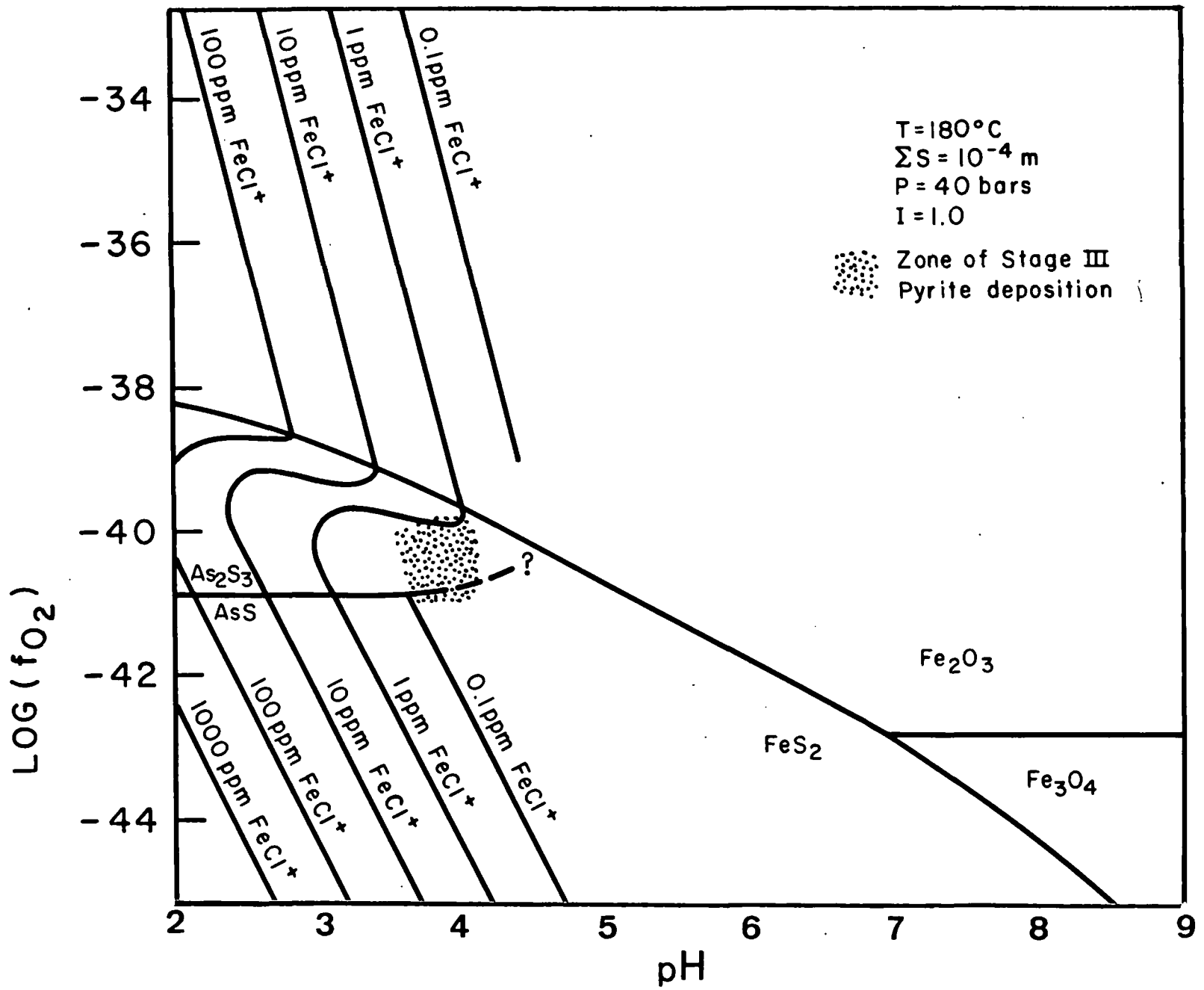


FIGURE 16

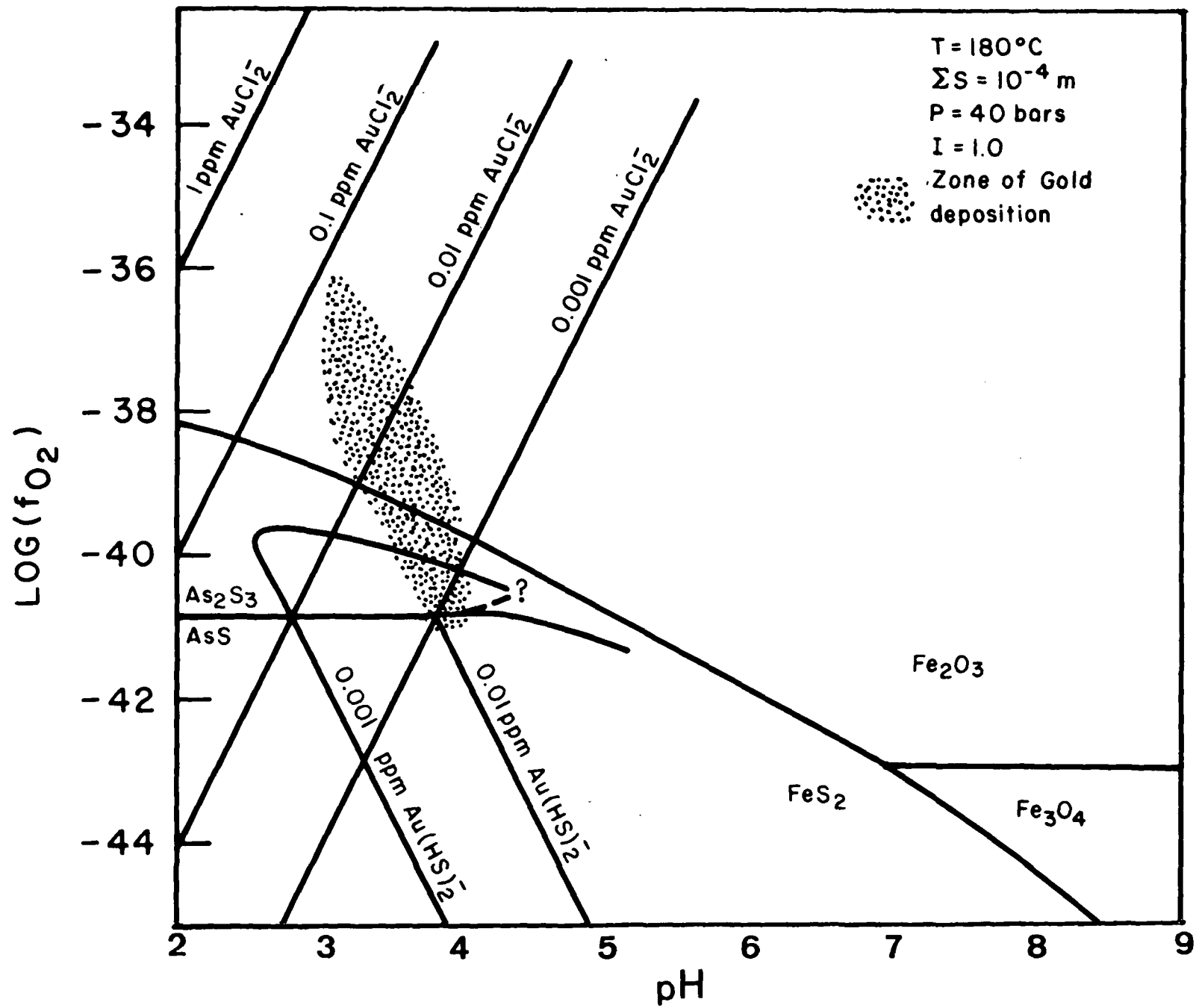


FIGURE 17

TABLE 1. Whole rock chemical analyses at Mercur (numbers in parentheses are one standard deviation).

	Massive Limestone	Silty Limestone	Silver Chert	Silicified Magazine Sandstone	Argillically altered limesto (oxidized)	Argillically altered limestone (partially-unoxidized)	Massive limestones with Stage III minerals
	n=4	n=4	n=3	n=3	n=3	n=5	n=3
SiO ₂	6.42 (1.11)	34.55 (3.36)	94.14 (3.86)	89.37 (2.25)	41.81 (2.14)	66.12 (13.89)	15.66 (6.32)
TiO ₂	0.06 (0.03)	0.34 (0.06)	0.16 (0.04)	0.45 (0.06)	0.34 (0.16)	0.41 (0.21)	0.14 (0.05)
Al ₂ O ₃	1.01 (0.82)	5.99 (1.21)	1.76 (0.59)	4.71 (0.99)	7.65 (3.36)	9.09 (2.39)	2.35 (0.94)
Fe ₂ O ₃			1.50 (1.27)	0.97 (0.45)	4.81 (3.74)		
FeO	0.89 (0.52)	2.12 (0.11)				3.51 (2.91)	1.06 (0.31)
MnO	0.13 (0.09)	0.09 (0.04)	0.01 (0.00)	0.01 (0.01)	0.08 (0.02)	0.02 (0.01)	0.19 (0.10)
MgO(1)	0.39 (0.14)	0.72 (0.27)	0.05 (0.01)	0.20 (0.10)			
CaO	50.65 (3.76)	29.37 (2.10)	0.01 (0.00)	0.41 (0.40)	22.23 (4.14)	4.79 (5.35)	43.23 (4.52)
K ₂ O	0.11 (0.14)	1.01 (0.35)	0.45 (0.42)	1.10 (0.25)	1.00 (0.97)	1.30 (0.61)	0.33 (0.33)
Na ₂ O(1)	0.00 (0.00)	0.05 (0.01)					
P ₂ O ₅	0.50 (0.14)	0.44 (0.03)	0.00 (0.00)	0.00 (0.00)	0.24 (0.09)	0.13 (0.06)	0.48 (0.04)
S ₂ O ₃ (2)			1.43 (1.04)	1.21 (0.86)	0.07 (0.01)		
S ⁻² (2)	0.36 (0.53)	1.55 (0.28)				3.61 (2.24)	1.32 (0.54)
H ₂ O(3)	0.65 (0.63)	2.69 (0.64)			3.21 (1.39)		
CO ₂ (4)	39.06 (1.22)	20.71 (1.74)			17.60 (2.79)		34.63 (3.38)
C(org)(5)	0.18 (0.14)	0.79 (0.50)			0.02 (0.03)	1.28 (0.84)	0.37 (0.29)
LOI			1.91 (1.07)	1.84 (1.44)		10.58 (4.36)	
Less O=S	0.08	0.34					0.30 (0.12)
Total	100.33	100.76	101.42	100.27	99.06	100.58	100.53
Quartz	5.13 (1.14)	24.63 (2.30)	92.08 (4.63)	82.96 (3.25)	31.55 (4.87)	54.02 (15.27)	12.47 (5.00)
Illite	1.21 (1.58)	11.12 (3.87)	0.71 (1.00)	9.18 (2.26)	11.12 (10.78)	14.48 (6.77)	3.64 (3.69)
Kaolinite	1.63 (1.99)	9.10 (1.21)	3.66 (0.93)	4.68 (1.07)	10.26 (6.19)	11.19 (6.66)	3.04 (2.65)
Calcite	89.10 (4.38)	44.69 (3.31)			39.26 (7.09)	8.25 (9.24)	77.84 (7.55)
Dolomite	1.77 (0.62)	3.23 (1.26)					
Pyrite	0.76 (1.01)	2.70 (0.34)				5.78 (4.44)	2.46 (1.01)
Jarosite			3.98 (3.07)	2.61 (0.73)			
Hematite			0.57 (0.71)				

- (1) Atomic absorption
- (2) LECO analysis
- (3) Total water by Penfield analysis (Hutchinson, 1974)
- (4) Acid evolution
- (5) Method of Gaudette, et al. (1974)

All other elements by x-ray fluorescence

2
 TABLE 2. Summary of Fluid Inclusion Data.

Sample	Stratigraphic Interval	Mineral	Stage in Paragenesis	Filling Temperatures			Salinity (eq. wt. NaCl)			
				Number	Range	Mean \pm S.D.	Number	Range	Mean	
GV-25-212	Upper Beds	Quartz	I - Silica	3	252-258	256.1	3.2			
GV-25-403	Silver Chert	Quartz	I - Silica	10	208-290	237.4	27.1			
H-17-237	Magazine Sandstone	Quartz	I - Silica	8	203-247	222.7	15.2	5	4.4-7.4	6.6
9/22-5b	Silver Chert	Quartz	I - Silica	5	233-257	269.5	32.8	2	6.4-7.4	6.9
GV-25-217	Upper Beds	Calcite	III - Carbonate Sulfide	2	188-197	192.2	6.4			
GV-25-242	Mercur Beds	Calcite	III - Carbonate/ Sulfide	7	175-196	186.8	8.1			
MH-9-128	Upper Beds	Calcite	III - Carbonate/ Sulfide	21	125-230	165.1	24.1			
MH-9-130	Upper Beds	Calcite	III - Carbonate/ Sulfide	2	133-167	152.6	20.5	5	5.8-8.9	7.2
MH-9-156	Mercur Beds	Calcite	III - Carbonate/ Sulfide	14	139-199	175.0	17.1			
MH-9-292	Median Beds Magazine Sandstone	Calcite	III - Carbonate/ Sulfide	2	174-178	176.1	3.3			
ML-9-153	Upper Beds	Calcite	III - Carbonate/ Sulfide	26	126-199	171.8	23.1	8	3.3-6.4	5.0
9/22-5a	Silver Chert	Barite	IV - Barite/ Halloysite	20	272-353	307.9	20.9			
F-27-118	Silver Chert	Barite	IV - Barite/ Halloysite	24	145-278	218.3	27.1	14	5.5-7.9	7.0
P-27-130	Silver Chert	Quartz	IV - Barite/ Halloysite	9	175-265	219.8	31.9			
P-27-130	Silver Chert	Barite	IV - Barite/ Halloysite	10	152-321	268.4	51.0			
P-27-149	Silver Chert	Barite	IV - Barite/ Halloysite	13	161-315	234.6	51.0			
P-27-156	Silver Chert	Barite	IV - Barite/ Halloysite	16	155-231	185.6	22.0	12	2.1-4.8	3.1

3
TABLE 3. Summary of Thermodynamic Data

Reaction	Equilibrium constant	
	160°C 40 bars	240°C 40 bars
$KAl_3Si_3O_{10}(OH)_2 + 2H^+ + H_2O = Al_2Si_2O_5(OH)_4 + 2K^+$	5.00	4.18 (a)
$KAl_5Si_3O_8 + 2H^+ = KAl_3Si_3O_{10}(OH)_2 + SiO_2(aq) + 2K^+$	-7.37	-5.34 (a)
$Al_2Si_2O_5(OH)_4 + SiO_2(aq) = Al_2Si_4O_{10}(OH)_2 + H_2O$	4.67	4.25 (a)
$Al_2Si_2O_5(OH)_4 + H_2O = 2Al(OH)_3 + 2SiO_2(aq)$	-6.44	-6.32 (a)
$KAl_5Si_3O_8 + 2H^+ = Al_2Si_4O_{10}(OH)_2 + 2K^+ + SiO_2(aq)$	1.43	2.09 (a)
$KAl_3Si_3O_{10}(OH)_2 + H^+ + 3H_2O = 3Al(OH)_2 + 2K^+$	-7.37	-7.09 (a)
$2KAl_3Si_3O_{10}(OH)_2 + 6SiO_2(aq) + 2H^+ = 3Al_2Si_4O_{10}(OH)_2 + 2K^+$	19.02	16.93 (a)
$SiO_2(\text{quartz}) = SiO_2(aq)$	-2.53	-2.24 (a)
$SiO_2(\text{chalcedony}) = SiO_2(aq)$	-2.53	-2.09 (a)

	180°C 40 bars	240°C 40 bars
$CaCO_3 + 2H^+ = Ca^{++} + H_2CO_3$	6.79	6.68 (a)
$Fe_2O_3 + 4H_2S(aq) + 1/2O_2 = FeS_2 + 4H_2O$	43.35	40.47 (a)
$Fe_3O_4 + 6H_2S(aq) + O_2 = 3FeS_2 + 6H_2O$	-47.47	-45.11 (a)
$2Fe_3O_4 + 1/2O_2 = 3Fe_2O_3$	21.44	18.13 (a)
$2AsS + H_2S(aq) + 1/2O_2 = As_2S_3 + H_2O$	26.25	24.42 (a)(b)
$Ba^{++} + SO_4 = BaSO_4$	-10.16	-10.77 (c)
$CO_2(aq) = CO_2(g)$	-2.15	-2.08 (d)
$CH_4(aq) = CH_4(g)$	3.14	2.92 (d)
$H_2S(aq) = H_2S(g)$	1.54	(a)
$H_2S(g) = H^+ + HS^-$	-8.46	-8.71 (a)
$SO_4^{--} + 2H^+ = H_2S(aq) + 2O_2$	-69.90	-56.83 (a)
$HSO_4^- = H^+ + SO_4^{--}$	-4.16	-5.11 (d)
$H_2CO_3 = H^+ + HCO_3^-$	-6.94	-7.54 (d)
$CH_4(g) + 2O_2 = H^+ + HCO_3^- + H_2O$	81.19	68.79 (a)
$H_2As(OH)_5 = H^+ + HAs(OH)_5^-$	-8.07	(e)
$H_2As(OH)_8^- = H^+ + HAs(OH)_8^{--}$	-7.64	(e)
$HAs(OH)_8^- + 2H^+ = H_2As(OH)_5 + 1/2O_2 + 2H_2O$	-1.75	(e)
$H_2O = H^+ + OH^-$	-11.28	-11.05 (a)
$FeS_2 + 2H^+ + Cl^- + H_2O = FeCl^+ + H_2S(aq) + 1/2O_2$	-27.20	-20.46 (f)
$Au(s) + 2Cl^- + 1/4O_2 + H^+ = 1/2H_2O + AuCl_2$	2.02	(g)
$Au(s) + H_2S(aq) + 1/4O_2 = 1/2H_2O + H^+ + Au(HS)_2^-$	6.64	(h)

- (a) Helgeson (1969); Helgeson et al., (1978)
 (b) Craig and Barton (1973)
 (c) Blount (1977)
 (d) Naumov et al., (1971)
 (e) Knight (1977)
 (f) Crerar et al., (1978)
 (g) Casadevall and Ohmoto (1977)
 (h) Seward (1973)

SUBJ
GCHM
CCD

[AMERICAN JOURNAL OF SCIENCE, VOL. 275, NOVEMBER, 1975. P. 1073-1088]

CHEMICAL COMPONENTS AND DIFFUSION

JOHN B. BRADY*

Department of Geological Sciences, Harvard University,
Cambridge, MA 02138

ABSTRACT. Chemical components for use in the description of a system involved in a diffusion process may be selected according to the same criteria followed in the selection of components for an equilibrium system. The various possible sets of components are not independent and may be interrelated through a component transformation. Actual components are preferred over nonvariable components, since they simplify descriptions and avoid theoretically nonmeasurable quantities. Two systems involved in an interdiffusion process may always be described using components that are actual components of both systems. For example, ternary reciprocal exchange of alkalis between alkali feldspars and dioctahedral alkali micas may be described using binary equations in terms of the exchange component, KNa_{-1} , which is an actual component of both minerals. Small quantities of additional components in approximately binary systems may have significant effects on measured diffusion coefficients, if neglected. Nevertheless, binary solutions to the continuity equation may be used, if the system is constrained in any of several ways to some binary or to a single set of boundary conditions.

INTRODUCTION

A phenomenological description of a diffusion process details the macroscopic changes of a thermodynamic system that result from mass transfer by diffusion. For any specific diffusion process, the form of the phenomenological description given will depend on a number of arbitrary decisions concerning the manner of presentation. For example, any of a large number of sets of chemical components may be used to specify composition changes, fluxes, et cetera, as in describing an equilibrium system. Because mass transfer is involved, a large number of possible reference frames are available, as in describing motion in any physical system. Also, one of many possible empirical diffusion constants must be selected, each of which may vary in magnitude with the choice of reference frame, components, and units. Of course the diffusion process is independent of any decision on matters of presentation. Thus, at least in principle, the various possible descriptions may all be interrelated.

One of the decisions concerning the form of a phenomenological description of a diffusion process, namely the selection of chemical components, is discussed in this paper. The other decisions, selection of reference frame and diffusion coefficient, are considered only briefly here, for an extensive treatment of these topics may be found elsewhere (Brady, 1975). The discussion begins with a brief statement of the equations commonly used to describe diffusion. This will serve both to emphasize the arbitrary choices involved in using these equations and to clarify the notation used in the rest of the paper.

MULTICOMPONENT DIFFUSION EQUATIONS

One-dimensional, steady-state, isothermal, isobaric diffusion in a homogeneous thermodynamic system of n components may be described by the equations

* Present address: Department of Geology, Smith College, Northampton, MA 01060

$$J_i^R = - \sum_{j=1}^n D_{ij}^{R,C} \left(\frac{\partial C_j}{\partial x} \right)_{P,T,t} \quad (i=1,2,\dots,n) \quad (1)$$

(Onsager, 1945). J_i^R is the flux of component i with respect to reference frame R . C_j is an arbitrary intensive variable, such as density or mole fraction, giving the system composition in terms of component j . x is distance, t time, P pressure, T temperature. $D_{ij}^{R,C}$ is an empirical constant, defined by equation (1), which relates the flux of component i with respect to reference frame R to the gradient of composition variable C_j . The units of $D_{ij}^{R,C}$ depend on the choice of units for J_i^R and the units of the composition variable C_j .

In order to avoid the necessity of comparing the multitude of possible diffusion coefficients it is convenient to express all flux equations in terms of "standard" diffusion coefficients, D_{ij}^0 (cm^2/sec), defined by

$$J_i^V = - \sum_{j=1}^{n-1} D_{ij}^0 \left(\frac{\partial \rho_j}{\partial x} \right)_{P,T,t} \quad (i=1,2,\dots,n-1) \quad (2)$$

(see Hooyman, and others, 1953; Brady, 1975). J_i^V is the flux of component i with respect to the mean volume reference frame in units of (moles of $i/\text{cm}^2\text{-sec}$). The mean volume reference frame is defined by the relation

$$\sum_{i=1}^n V_i J_i^V = 0 \quad (3)$$

where V_i is the partial molar volume of component i (see Hooyman, 1956; Kirkwood and others, 1960; Brady, 1975). ρ_j is the molar density of component j in units of (moles of j/cm^3). Since the fluxes J_i^V are connected by (3) and the molar densities ρ_j by the thermodynamic relation

$$\sum_{j=1}^n V_j d\rho_j = 0 \quad (\text{constant } P, T) \quad (4)$$

only $(n-1)$ fluxes and composition gradients are considered in (2) for an n -component system. Flux equations with respect to other reference frames R (mean molar frame, mean mass frame, et cetera) or using other compositional variables C_j (mole fractions, mass fractions, et cetera) may all be given in terms of the standard diffusion coefficients, D_{ij}^0 , if the appropriate thermodynamic relations and relative velocities are known (de Groot and Mazur, 1962; Brady, 1975).

Diffusion is generally a non-steady-state process and must be described by a form of the continuity equation. Assuming that there is *no volume change* and that the diffusion process is conservative, the continuity equation is given by

(Landau and Lifshitz,

$$\left(\frac{\partial \rho_i}{\partial t} \right)_{P,T,x} = \left(\frac{\partial}{\partial x} \right)_{P,T,t}$$

Equations (6) present a problem in real systems with n greater than 2. Independent of composition systems (Fuji) Equations (6) may be

$$\left(\frac{\partial \rho_i}{\partial t} \right)_{P,T,x}$$

Since most natural processes are independent of diffusion to considerations of will be concerned with although many of the component systems.

We may now have available for use in with some definition position that may be actually realizable sub describe a phase (into three types: available components (actual components) without destroying may be either added may not be added. Possible component compositional limits components and n

Of the two superior for the First, note that densities of components in the description

(i=1,2,...,n) (1)

$$\left(\frac{\partial \rho_i}{\partial t}\right)_{P,T,x} = -\left(\frac{\partial J_i^V}{\partial x}\right)_{P,T,t} \quad (5)$$

(Landau and Lifshitz, 1959) or using (2)

$$\left(\frac{\partial \rho_i}{\partial t}\right)_{P,T,x} = \left(\frac{\partial}{\partial x} \left[\sum_{j=1}^{n-1} D^{\circ}_{ij} \left(\frac{\partial \rho_j}{\partial x}\right)_{P,T,t} \right]\right)_{P,T,t} \quad (i=1,2,\dots,n-1) \quad (6)$$

Equations (6) present the major barrier to a generalized analysis of diffusion in real systems. No analytical solutions to (6) are known for systems with n greater than two. Only if the diffusion coefficients D°_{ij} are independent of composition are analytical solutions available for multicomponent systems (Fujita and Gosting, 1956; Kirkaldy, 1959; Oishi, 1965). Equations (6) may then be written in the more tractable form

$$\left(\frac{\partial \rho_i}{\partial t}\right)_{P,T,x} = \sum_{j=1}^{n-1} D^{\circ}_{ij} \left(\frac{\partial^2 \rho_j}{\partial x^2}\right)_{P,T,t} \quad (i=1,2,\dots,n-1) \quad (7)$$

Since most natural processes are non-steady-state and involve composition dependent diffusion coefficients, the bulk of diffusion literature is confined to considerations of binary systems. The following discussion, therefore, will be concerned primarily with examples from two-component systems, although many of the principles examined may be applied to multicomponent systems.

ACTUAL COMPONENTS

We may now proceed to evaluate the sets of chemical components available for use in the diffusion equations presented above. Let us begin with some definitions. A chemical component is a specific chemical composition that may or may not correspond to the composition of any physically realizable substance (Gibbs, 1928, p. 63). The components used to describe a phase (physically homogeneous substance) may be classified into three types: actual components, possible components, and nonvariable components (Gibbs, 1928, p. 64; Thompson, 1959). By definition *actual components* may be either added to or subtracted from a phase without destroying the homogeneity of that phase. *Possible components* may be either added or subtracted, but not both. *Nonvariable components* may not be added or subtracted, independently of other components. Possible components are a special case of actual components at some compositional limit of the phase. Therefore, I shall refer only to actual components and nonvariable components in the following discussion.

Of the two types of components, actual components are clearly superior for the description of diffusion processes, for several reasons. First, note that diffusion involves the addition or subtraction of quantities of components to or from a phase or system. If the components used in the description may not be independently added to or subtracted from

the phase of interest (that is, if they are nonvariable components), then "extra" equations of constraint must be carried in the description (for example, to ensure charge neutrality, stoichiometry, et cetera). While these additional equations do not invalidate the description, they may unnecessarily complicate it. A minimum number of equations of constraint are required if actual components are used.

A mineral is an n -component phase if all possible compositions of that mineral may be expressed by a linear combination of *not less than* n components (Thompson, 1959). Any set of n components sufficient to give all possible compositions of an n -component phase may be called an *ultimate* set of components for that phase (Gibbs, 1928, p. 79; Thompson, 1959). Any ultimate set of components for an n -component phase will consist of n independent actual components. Any set of components that includes even one nonvariable component must contain more than n components, if the set is to be sufficient to give all possible compositions of an n -component phase. Therefore, the minimum number of components need to be considered if an ultimate set of (actual) components is used.

The use of actual components also allows the empirical description considered here to be related to a more fundamental description in terms of chemical potential gradients, to which Onsager's reciprocal relations may be applied (Onsager, 1931a,b). Chemical potentials of actual components of a phase, ϕ , may be determined from the chemical composition of ϕ , if an equation of state for ϕ is known. However, the chemical potentials of nonvariable components of a phase, ϕ , may *not* be obtained from the composition of ϕ and an equation of state. They are specified only if ϕ is in equilibrium with other phases such that the total assemblage has as actual components the nonvariable components of ϕ . Other partial molar quantities of nonvariable components of ϕ , such as the partial molar volume V_i , are neither measurable nor specified by the presence of any assemblage in equilibrium with ϕ . This fact generally decreases the usefulness of any description in terms of nonvariable components and makes it difficult to utilize several mean velocity reference frames (Brady, 1975). All these considerations lead to the conclusion that a description in terms of an ultimate set of components is preferable to any other.

TRANSFORMATION OF COMPONENTS

While the description of a diffusion process in terms of one ultimate set of components is equivalent to a description in terms of another ultimate set, different sets of components may be convenient for different processes. It will be advantageous, therefore, to be able to interrelate two descriptions given in terms of different sets of components. This may be accomplished by following the procedures established for a transformation of the components used to describe an equilibrium system (for example, calculating a norm from a chemical analysis). For a recent discussion of component transformations see Greenwood (1975). See also Korzhinskii (1959, chap. II).

Chemical

To investigate the effect of a diffusion process in an iron-sulfur system, we choose the following set of components: Fe, S, and FeS. Either of these two sets of components would be suitable for describing the system in pyrrhotite (Fe_{1-x}S); both are suitable for describing the system in troilite (FeS). This particular example in the iron-sulfur system is probably limited by the geothermometer to a change in temperature of about 100°C.

The "new" component set consists of Fe and S by the stoichiometry of the reaction:

Equations (8) express the chemical potentials of one mole of Fe combined with one mole of S. We need to know, however, the chemical potentials of the system given the *total* number of moles of iron (n_{Fe}) and sulfur (n_{S}) is generally to start with the moles of iron (n_{Fe}) and sulfur (n_{S}) and pyrite (n_{FeS}).

Solving equations (9) for n_{Fe} and n_{S} gives

which is clearly not of the form of a mole fraction. Equations (9) and (10) show that the mole fractions N_{Fe} , N_{FeS} , and N_{S} in terms of the different sets of components are

$$N_{\text{Fe}} \equiv \frac{n_{\text{Fe}}}{n_{\text{Fe}} + n_{\text{S}} + n_{\text{FeS}}}$$

$$N_{\text{FeS}} \equiv \frac{n_{\text{FeS}}}{n_{\text{Fe}} + n_{\text{S}} + n_{\text{FeS}}}$$

Equations (10) may also be written in terms of the components, J_{FeS} and J_{FeS_2} components:

To investigate the effect of a transformation of components on the description of a diffusion process, let us consider as an example the binary system iron-sulfur. For "old" components we shall choose the physically realizable compositional limits of the system, Fe and S. For "new" components let us choose the compositions of troilite, FeS, and pyrite, FeS₂. Either of these two sets of components might be used to describe diffusion in pyrrhotite (Fe_{1-x}S); both are ultimate sets of components for pyrrhotite. This particular example may be of geological interest, for diffusion in pyrrhotite probably limits the rate of response of the pyrite-pyrrhotite geothermometer to a change in temperature.

The "new" components FeS and FeS₂ are related to the "old" components Fe and S by the stoichiometric relations



Equations (8) express the fact that one mole of FeS may be made from one mole of Fe combined with one mole of S, and similarly for FeS₂. What we need to know, however, is the *total* number of moles of FeS for a system given the *total* numbers of moles of Fe and S. The best procedure is generally to start with the inverse relations giving the total number of moles of iron (n_{Fe}) and sulfur (n_S) in terms of the numbers of moles of troilite (n_{FeS}) and pyrite (n_{FeS₂}). We have by inspection, then,

$$\begin{aligned} n_{\text{Fe}} &= n_{\text{FeS}} + n_{\text{FeS}_2} \\ n_{\text{S}} &= n_{\text{FeS}} + 2 n_{\text{FeS}_2} \end{aligned} \tag{9}$$

Solving equations (9) for n_{FeS} and n_{FeS₂} yields

$$\begin{aligned} n_{\text{FeS}} &= 2 n_{\text{Fe}} - n_{\text{S}} \\ n_{\text{FeS}_2} &= -n_{\text{Fe}} + n_{\text{S}} \end{aligned} \tag{10}$$

which is clearly not of the same form as (8).

Equations (9) and (10) may be used to obtain relations among the mole fractions N_{Fe}, N_{FeS}, et cetera to give the composition of the system in terms of the different sets of components:

$$N_{\text{Fe}} \equiv \frac{n_{\text{Fe}}}{n_{\text{Fe}} + n_{\text{S}}} = \frac{1}{2 + N_{\text{FeS}_2}} \tag{11}$$

$$N_{\text{FeS}} \equiv \frac{n_{\text{FeS}}}{n_{\text{FeS}} + n_{\text{FeS}_2}} = \frac{3 N_{\text{Fe}} - 1}{N_{\text{Fe}}}$$

Equations (10) may also be used to obtain the fluxes of the "new" components, J_{FeS}^R and J_{FeS₂}^R, from measurements of fluxes of the "old" components:

$$\begin{aligned} J_{\text{FeS}}^{\text{R}} &= 2 J_{\text{Fe}}^{\text{R}} - J_{\text{S}}^{\text{R}} \\ J_{\text{FeS}_2}^{\text{R}} &= -J_{\text{Fe}}^{\text{R}} + J_{\text{S}}^{\text{R}} \end{aligned} \tag{12}$$

where J_{FeS}^R is the total number of moles of FeS passing a unit cross section of reference frame R in unit time. Notice that all fluxes are given with respect to the *same* reference frame R. If a different reference frame is of interest, the above procedure must be combined with the procedures outlined in Brady (1975) for relating various reference frames.

Particular care should be exercised with regard to the reference frame used, for some reference frames depend on the choice of components. For example, the mean molar frame, N, for our "old" components is not identical with the mean molar frame, N', for our "new" components. Indeed, at any time during a diffusion process, the two mean molar frames will have a relative velocity such that

$$J_i^N = J_i^{N'} + \rho_i \bar{v}^{N'N} \quad (13)$$

where ρ_i is the molar density of component i and $\bar{v}^{N'N}$ is the local velocity of frame N' with respect to frame N. The mean molar frame N (for the components Fe and S) is defined by

$$J_{\text{Fe}}^N + J_{\text{S}}^N = 0 \quad (14)$$

and the mean molar frame N' (for the components FeS and FeS₂) by

$$J_{\text{FeS}}^{N'} + J_{\text{FeS}_2}^{N'} = 0 \quad (15)$$

(de Groot and Mazur, 1962). Adding (13) written for i = FeS to (13) written for i = FeS₂ and using (9), (12), and (15) we have

$$\bar{v}^{N'N} = \left(\frac{1}{\rho_{\text{FeS}} + \rho_{\text{FeS}_2}} \right) \left(J_{\text{FeS}}^{N'} + J_{\text{FeS}_2}^{N'} \right) = \frac{J_{\text{Fe}}^N}{\rho_{\text{Fe}}} \quad (16)$$

Substituting (16) into (13) written for component S yields

$$J_{\text{S}}^N = J_{\text{S}}^{N'} + \frac{\rho_{\text{S}}}{\rho_{\text{Fe}}} J_{\text{Fe}}^N \quad (17)$$

or using (14)

$$J_{\text{S}}^{N'} = J_{\text{S}}^N \left(1 + \frac{\rho_{\text{S}}}{\rho_{\text{Fe}}} \right) = \frac{J_{\text{S}}^N}{N_{\text{Fe}}} \quad (18)$$

It follows from (12), (14), and (18) that

$$J_{\text{FeS}}^{N'} = \frac{J_{\text{Fe}}^N}{N_{\text{Fe}}} \quad (19)$$

$$J_{\text{FeS}_2}^{N'} = \frac{J_{\text{S}}^N}{N_{\text{Fe}}}$$

A comparison of equations (19) and (12) will serve to demonstrate the importance of properly identifying the reference frames in use. Note also that $J_{\text{Fe}}^{N'} = 0$.

In contrast, the standard diffusion coefficient for a two component system, D° , does *not* depend on the choice of components.¹ This may be

¹The subscripts have been omitted from D°_{ij} since there is only one independent D°_{ij} for a binary system.

demonstrated by expressing diffusion coefficients D° and D°' respectively. The flux of component i in reference frame N is given by:

J_i^N

where \bar{V} is the volume of components. Using (20) along

$$J_{\text{FeS}}^{N'} = - \frac{D^{\circ'}}{\bar{V}'} \left(\frac{\partial N_{\text{FeS}}}{\partial x} \right)$$

where \bar{V}' is the volume of components. And noting that

$$\bar{V}' \equiv \frac{1}{n_{\text{FeS}}}$$

(21) becomes

Finally, evaluating the de

Thus, a description of diffusion of Fe and S may be readily extended to multicomponent systems. The same binary diffusion coefficients may be used for both sets of components.

This result appears to be only one standard diffusion coefficient for a set of components is used. The diffusion coefficient may be carefully labeled according to the reference frame and related to those obtained from similar problems concerning Cooper (1971), Cooper (1972), and Cooper (1973).

Buckley (ms) and others have shown that the use of actual diffusion coefficients for distances may be inconvenient as an example the example of thopyroxene. He points out that (where it is an actual

demonstrated by expressing the fluxes of (19) in terms of the binary diffusion coefficients D° and $D^{o'}$ for the "old" and "new" components, respectively. The flux of component i with respect to the mean molar reference frame N is given by (de Groot and Mazur, 1962, p. 252)

$$J_i^N = -\frac{D^\circ}{\bar{V}} \left(\frac{\partial N_i}{\partial x} \right)_{P,T,t} \quad (20)$$

where \bar{V} is the volume of the phase of interest per mole of "old" components. Using (20) along with the first equation of (19) we have

$$J_{FeS}^{N'} = -\frac{D^{o'}}{\bar{V}'} \left(\frac{\partial N_{FeS}}{\partial x} \right)_{P,T,t} = \frac{-D^\circ}{N_{Fe} \bar{V}} \left(\frac{\partial N_{Fe}}{\partial x} \right)_{P,T,t} = \frac{J_{Fe}^N}{N_{Fe}} \quad (21)$$

where \bar{V}' is the volume of the phase of interest per mole of "new" components. And noting that

$$\bar{V}' \equiv \frac{V}{n_{FeS} + n_{FeS_2}} = \frac{V}{n_{Fe}} = \frac{1}{\rho_{Fe}} = \frac{\bar{V}}{N_{Fe}} \quad (22)$$

(21) becomes

$$D^{o'} = \frac{D^\circ}{N_{Fe}^2} \left(\frac{d N_{Fe}}{d N_{FeS}} \right) \quad (23)$$

Finally, evaluating the derivative in (23) using (11) we obtain

$$D^{o'} = D^\circ \quad (24)$$

Thus, a description of diffusion in pyrrhotite in terms of the components Fe and S may be readily related to one in terms of FeS and FeS₂. The same binary diffusion coefficient D° will be obtained using either of these two ultimate sets of components.

This result appears to be quite general. For any binary system there is only one standard diffusion coefficient D° , regardless of which ultimate set of components is used. Unfortunately, this simple result may not be extended to multicomponent systems where each diffusion coefficient must be carefully labeled according to the components used for the composition gradient and related flux. However, the methods discussed above may be used to interrelate fluxes for different choices of components, and the diffusion coefficients obtained for one set of components can be related to those obtained for other sets of components. For discussions of similar problems concerning multicomponent systems see Gupta and Cooper (1971), Cooper (1974), and Schönert (1960).

EXCHANGE COMPONENTS

Buckley (ms) and Anderson and Buckley (1973, 1974) have argued that the use of actual components as "diffusing" components in some instances may be inconvenient, misleading, or inaccurate. Buckley (ms) cites as an example the exchange of Mg⁺² and Fe⁺² between garnet and orthopyroxene. He points out that while diffusion of FeSiO₃ in pyroxene (where it is an actual component) is meaningful, diffusion of FeSiO₃ in

radly
s of FeS passing a unit cross section
Notice that all fluxes are given
R. If a different reference frame
be combined with the procedure
ous reference frames.

with regard to the reference frame
on the choice of components. For
our "old" components is not
N', for our "new" components
cess, the two mean molar frames

$$\bar{v}^{N'} = 0 \quad (13)$$

nt i and $\bar{v}^{N'}$ is the local velocity
ie mean molar frame N (for the

$$= 0 \quad (14)$$

ponents FeS and FeS₂) by

$$= 0 \quad (15)$$

written for $i = FeS$ to (13) writ-
5) we have

$$J_{FeS}^{N'} + J_{FeS_2}^{N'} = \frac{J_{Fe}^N}{\rho_{Fe}} \quad (16)$$

ponent S yields

$$-J_{Fe}^N \quad (17)$$

$$) = \frac{J_S^N}{N_{Fe}} \quad (18)$$

$$(19)$$

will serve to demonstrate the
reference frames in use. Note also

efficient for a two component
of components.¹ This may be

since there is only one independent

garnet (where it is not an actual component) is not meaningful and conversely that the diffusion of $\text{Fe}_2\text{Al}_2\text{Si}_2\text{O}_{12}$ is meaningful in a garnet but not in a pyroxene. Buckley concludes from this that the total number of components needed to describe diffusion in a polyphase system is increased, if one is constrained to use actual components of the phases involved. Therefore, Buckley (ms) and Anderson and Buckley (1973, 1974) recommend the use of oxides of the elements for "diffusing" components. But the use of FeO as a "diffusing" component in garnet is little improvement over the use of FeSiO_3 . Neither is an actual component of garnet so that both have all the disadvantages of nonvariable components discussed above.

The difficulties in using actual components presented by Buckley (ms) are not encountered, if one begins with an appropriate selection of actual components for the phases or systems of interest. In the garnet-orthopyroxene example mentioned above, this would mean choosing the "negative" component FeMg_{-1} as one of the actual components for both minerals (see below). Indeed, there must always exist a set of actual components that contains the minimum number of components necessary to describe any diffusion process. To verify this, consider a generalized exchange of mass between two thermodynamic systems. Each of these two systems may be either a phase or a collection of phases. Any mass involved in the exchange must be subtracted from one of these systems and added to the other. There is no mass diffusing that is subtracted from one system and not added to the other. Therefore, it must be possible to describe the mass involved in the exchange using components that are actual components of *both* systems.²

For many mineral pairs (or assemblages) that might be involved in a diffusional exchange, the only actual components common to both minerals (or assemblages) are components that do not represent physically realizable compositions of the minerals (or assemblages) considered. This is perhaps best explained in terms of a simple example involving two phases in the same ternary system. Consider the exchange of Na and K between an alkali feldspar and a dioctahedral alkali mica. These two binary phases have only one actual component in common. Although not apparent on some commonly used compositional diagrams (fig. 1A), the intersection of the line of actual components for the alkali feldspars and the line of actual components for the muscovite-paragonite series gives the composition of the shared actual component, KNa_{-1} (fig. 1B). That KNa_{-1} is an actual component of both the alkali feldspars and the

² An actual component of an assemblage of phases is a component that may be both added to or subtracted from the assemblage without the addition of an extra phase (Thompson, 1959). An ultimate set of components for an *n*-component assemblage of phases is a set of *n* components sufficient to give all variations in the bulk composition of that assemblage. If one chooses ultimate sets of components for two systems such that the intersection of the two ultimate sets is as large as possible, then this intersection will be a set of actual components of *both* systems sufficient to describe all diffusional exchange between the two systems.

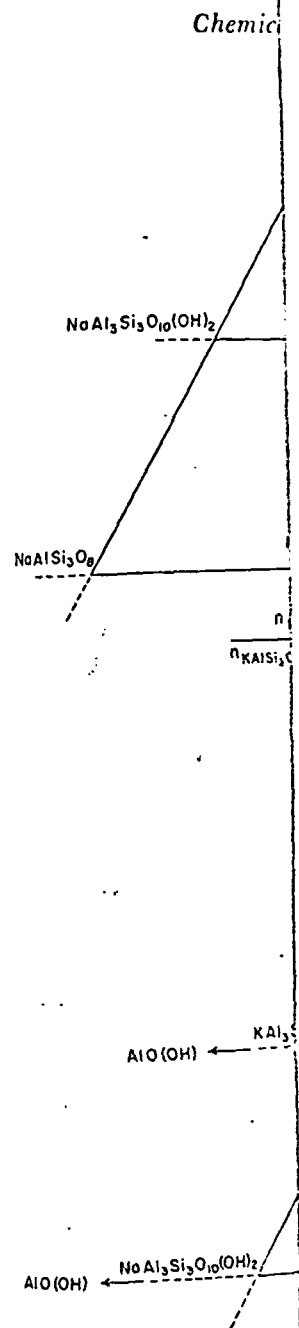


Fig. 1. Compositions of two different ternary systems: KAlSi_3O_8 and $\text{AlO}(\text{OH})$ (A) and KNa_{-1} (B).

not meaningful and com
ningful in a garnet but
that the total number of
polyphase system is in
ponents of the phases in
nd Buckley (1973, 1971)
"diffusing" components
garnet is little improve
al component of garnet
variable components dis

presented by Buckley
appropriate selection of
interest. In the garnet-
ould mean choosing the
al components for both
xist a set of actual com-
ponents necessary to
sider a generalized ex-
ms. Each of these two
ises. Any mass involved
ese systems and added
btracted from one sys-
ust be possible to de-
ponents that are actual

might be involved in a
common to both min-
t represent physically
ages) considered. This
ample involving two
change of Na and K
cali mica. These two
ommon. Although not
iagrams (fig. 1A), the
e alkali feldspars and
aragonite series gives
Na₋₁ (fig. 1B). That
li feldspars and the

ponent that may be both
tion of an extra phase
omponent assemblage of
in the bulk composition
or two systems such that
e, then this intersection
describe all diffusional

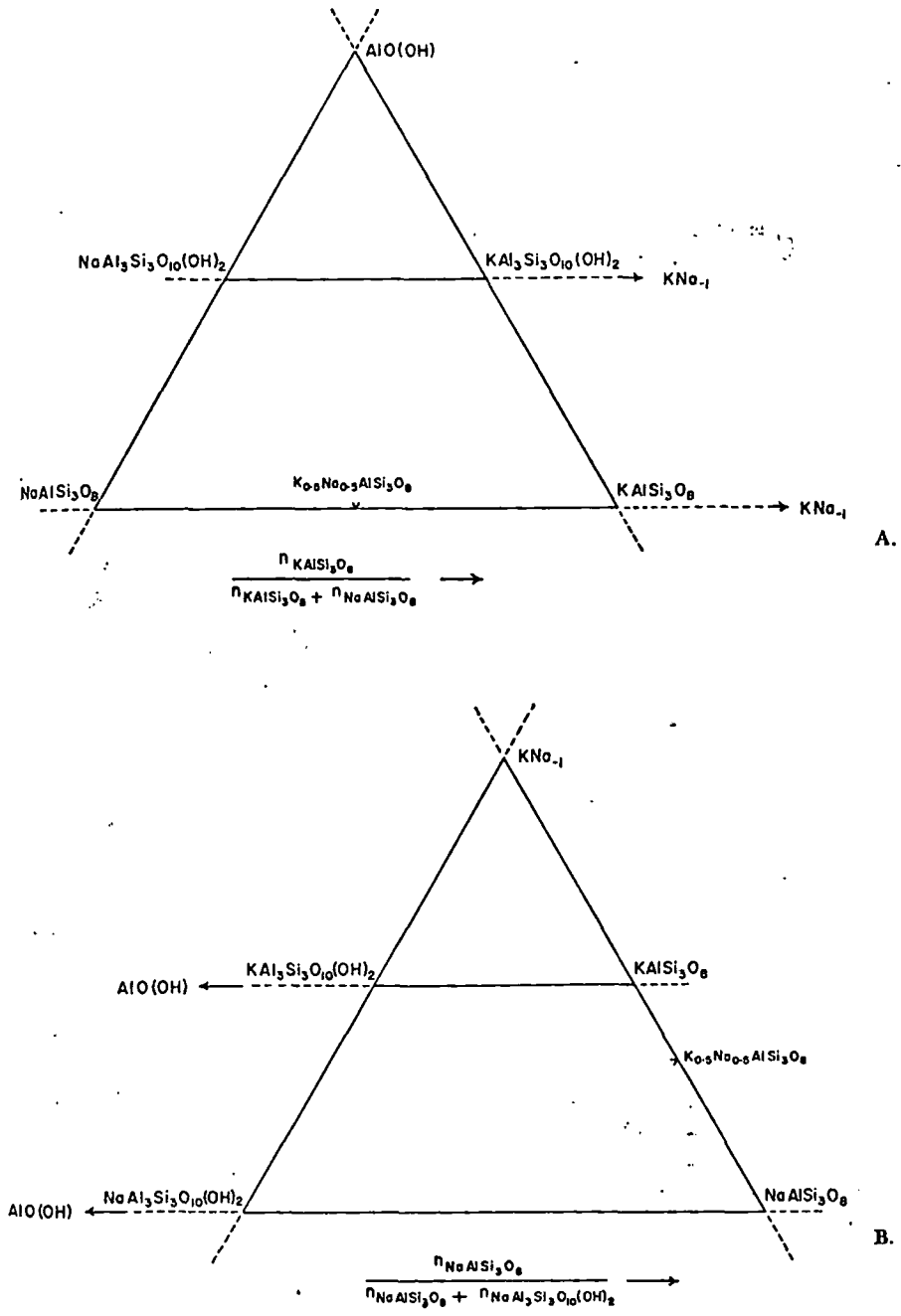
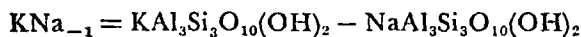
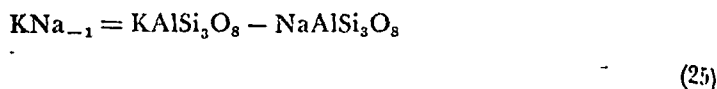


Fig. 1. Compositions of the alkali feldspars and dioctahedral alkali micas shown on two different ternary composition diagrams based on the components $NaAlSi_3O_8$, $KAlSi_3O_8$, and $AlO(OH)$ (A) and the components $NaAl_3Si_3O_{10}(OH)_2$, $NaAlSi_3O_8$, and KNa_{-1} (B).

dioctahedral alkali micas is evident from figure 1B and the stoichiometric relations



KNa_{-1} is an example of what I shall call an *exchange component*.³ It does not happen to correspond to the composition of any feldspar or mica but is just as valid as any other actual component. For example, the composition of any alkali feldspar may be expressed as a linear combination of KNa_{-1} and $\text{NaAlSi}_3\text{O}_8$. In fact, using KNa_{-1} as a component for alkali feldspars is analogous to using S as a component for pyrrhotite. S is given by the stoichiometric relation



and does not correspond to the composition of any pyrrhotite.

In many respects, the exchange component KNa_{-1} is an ideal "diffusing" component for the description of alkali exchange between feldspar and mica, or any other two alkali-bearing minerals. To begin with, the use of KNa_{-1} enables one to describe a ternary reciprocal exchange in terms of *one* diffusing component. Since KNa_{-1} is an actual component of both phases, constraints of stoichiometry and electrical neutrality are automatically satisfied. In addition, the driving force for alkali exchange is a gradient in the chemical potential of the exchange component, given by

$$\mu_{\text{KNa}_{-1}} = \mu_{\text{KAlSi}_3\text{O}_8} - \mu_{\text{NaAlSi}_3\text{O}_8} \quad (\text{in feldspar}) \quad (27)$$

$$\mu_{\text{KNa}_{-1}} = \mu_{\text{KAl}_3\text{Si}_3\text{O}_{10}(\text{OH})_2} - \mu_{\text{NaAl}_3\text{Si}_3\text{O}_{10}(\text{OH})_2} \quad (\text{in mica})$$

(see A. B. Thompson, 1974). Isothermal alkali exchange will cease only when the chemical potential of the exchange component is the same throughout the phases involved.

When described in terms of the flux of the exchange component, KNa_{-1} , alkali exchange between two binary phases in the same ternary system becomes mathematically equivalent to the case of interdiffusion in a binary system, when more than one phase is involved. The continuity equation has been solved for this latter case using the Boltzmann substitution (Jost, 1950, 1952, p. 75; Appel, 1968). The solution allows for a discontinuity in the concentration-distance profile but requires that the

³To my knowledge the use of exchange components like KNa_{-1} for the description of thermodynamic systems originates with J. B. Thompson, Jr. who demonstrates their convenient features in his lectures on phase equilibria (compare Thompson and Waldbaum, 1968, p. 1995; Waldbaum and Thompson, 1969, p. 1282). D. M. Burt (1972, 1974a, 1974b) has used exchange components extensively, calling them "exchange operators". For other examples of the use of "negative" components see Thompson (1972) or Korzhinskii (1959, chap. II).

magnitude of the discontinuity at $t = 0$ (compare Carslaw and Jaeger, 1959, p. 100).

For a one-dimensional diffusion of alkalis between an alkali feldspar and mica, the continuity equation (6) may be written as

$$\left(\frac{\partial \rho_{\text{KNa}_{-1}}}{\partial t} \right)_{\text{P.T.}}$$

If both the feldspar and mica are juxtapposed across a plane, the one-dimensional diffusion equation (6) may be written as (Carslaw and Jaeger, 1959) and Appel (1968)

$$D^\circ = \frac{-1}{2t}$$

$$D^\circ = \frac{1}{2t}$$

where $\rho_{\text{KNa}_{-1}}(+\infty)$ and $\rho_{\text{KNa}_{-1}}(-\infty)$ are the concentrations of the exchange component on one side of the interface.

Exchange components are useful for describing mineral pairs and assemblages such as Mg^{+2} between garnet and cordierite. Similar exchanges may be conveniently described in terms of the diffusion of exchange components in multiphase systems. In these cases, the use of exchange components is complete with

Few natural or experimental systems contain small quantities of exchange components. It is difficult to solve equations (6) for such systems. Yet if we neglect even a small amount of exchange components in binary systems as exact solutions, the results are nonreproducible results.

⁴Jost uses the correct form of equation (6) and [1.337] (1952) should be corrected in his paper, which agrees with Appel (1968).

magnitude of the discontinuity not change with time, for all time greater than $t = 0$ (compare Carslaw and Jaeger, 1947, p. 70).⁴

For a one-dimensional, isothermal, isobaric, isochoric exchange of alkalis between an alkali feldspar and a dioctahedral alkali mica, equation (6) may be written as

$$\left(\frac{\partial \rho_{KNa_{-1}}}{\partial t} \right)_{P,T,x} = \left(\frac{\partial}{\partial x} \left[D^\circ \left(\frac{\partial \rho_{KNa_{-1}}}{\partial x} \right)_{P,T,t} \right] \right)_{P,T,t} \quad (28)$$

If both the feldspar and mica are initially uniform in composition and juxtaposed across a planar boundary, appropriately oriented to ensure one-dimensional diffusion, then the solution to (28) modified after Jost (1950) and Appel (1968) is

$$D^\circ = \frac{-1}{2t} \left(\frac{dx}{d\rho_{KNa_{-1}}} \right) \int_{\rho_{KNa_{-1}}(-\infty)}^{\rho_{KNa_{-1}}} x d\rho_{KNa_{-1}} \quad (29)$$

$$D^\circ = \frac{1}{2t} \left(\frac{dx}{d\rho_{KNa_{-1}}} \right) \int_{\rho_{KNa_{-1}}}^{\rho_{KNa_{-1}}(+\infty)} x d\rho_{KNa_{-1}} \quad (30)$$

where $\rho_{KNa_{-1}}(+\infty)$ and $\rho_{KNa_{-1}}(-\infty)$ are the molar densities of KNa_{-1} far removed from the site of the diffusion. Equation (29) provides the solution for one side of the initial interface, and (30) for the other.

Exchange components may be readily applied to a great many other mineral pairs and assemblages. For example, the exchange of Fe^{+2} and Mg^{+2} between garnet and orthopyroxene discussed by Buckley (ms) may be conveniently described in terms of the exchange component $FeMg_{-1}$ as may similar exchanges between olivine and orthopyroxene or garnet and cordierite. Similarly, oxygen isotopic exchange may be described in terms of the diffusion of $O^{18}O^{16}_{-1}$. For diffusion in multicomponent, multiphase systems several exchange components may be used. In all these cases, the use of exchange components provides the simplest description complete with all the advantages of actual components.

APPROXIMATELY BINARY SYSTEMS

Few natural or experimental systems are strictly binary; nearly all contain small quantities of impurities (additional components). To deal rigorously with all these additional components would mean having to solve equations (6) for a multicomponent system, which is difficult at best. Yet if we neglect even very small quantities of impurities and treat nearly binary systems as exactly binary systems, we run the risk of encountering nonreproducible results. Indeed, there is abundant experimental evidence

⁴ Jost uses the correct approach but gives an incorrect result. His equations [4] (1950) and [1.337] (1952) should be modified to the mathematical form of (29) and (30) of this paper, which agree with Appel's result.

Brady
in figure 1B and the stoichiometric



$-NaAl_3Si_3O_{10}(OH)_2$
an exchange component.³ It does not consist of any feldspar or mica but is an exchange component. For example, the composition may be expressed as a linear combination of KNa_{-1} as a component for alkali feldspar and S is given as an exchange component for pyrrhotite.



of any pyrrhotite. The exchange component KNa_{-1} is an ideal "diffusion" component of alkali exchange between feldspar and mica. To begin with, the exchange is a ternary reciprocal exchange between KNa_{-1} and S . KNa_{-1} is an actual component of the exchange and electrical neutrality are maintained. The driving force for alkali exchange is the chemical potential of the exchange component, given by

$$\mu_{KNa_{-1}} \quad (\text{in feldspar}) \quad (27)$$

$$\mu_S \quad (\text{in mica})$$

alkali exchange will cease only when the exchange component is the same in both phases.

of the exchange component. In the case of interdiffusion in a ternary system, the solution is the same as in the case of interdiffusion in a binary system. The continuity of the exchange component is maintained using the Boltzmann substitution. The solution allows for a concentration profile but requires that the exchange component is the same in both phases.


components like KNa_{-1} for the description of the exchange. Thompson, Jr. who demonstrates their use (compare Thompson and Walden, p. 1282). D. M. Burt (1972, 1974a) calling them "exchange operators". For exchange components see Thompson (1972) or

that very small quantities of impurities may have a significant effect on the magnitude of measured diffusion coefficients (Shewmon, 1963). This is due to the fact that many impurities have associated defects such as vacancies which may greatly facilitate diffusion. Fortunately, however, there are several circumstances for which a binary approach will be useful even when the system examined is not constrained by stoichiometry to be binary. These will be considered in the following paragraphs assuming for simplicity that there is only one extra component (3) in addition to the two major components (1 and 2).

A case to which the binary equations may be correctly applied occurs when the quantity of component 3 (mole fraction of 3) in the phases involved does not vary during the diffusion process. If the mole fraction of 3, N_3 , does not change, then a binary description is quite correct, even if there is no stoichiometric constraint on 3. The diffusion coefficient determined, however, is valid only for the given constant N_3 and must be redetermined for other constant N_3 's. A constant mole fraction of component 3 during the diffusion process means either that the chemical potential of component 3, μ_3 , does not vary with N_2 at constant N_1 or that the diffusion of component 3 is very slow compared to the diffusion of components 1 and 2. The case of diffusion at constant N_3 , when the diffusion coefficients are all independent of composition, is a special case of ternary diffusion that was emphasized by Gupta and Cooper (1971). These authors pointed out that there will always be two directions in composition space (that is, two choices of component 3) for which diffusion will occur at constant N_3 . See also Cooper and Varshneya (1968) and Varshneya and Cooper (1972a,b,c).

If N_3 is not constant and the diffusion coefficients depend on composition, a binary solution may still be used if one is interested in only a *single* set of boundary conditions. Cooper (1968) has shown that for a semi-infinite diffusion couple with given boundary conditions, $N_2 (+\infty)$ and $N_2 (-\infty)$, the diffusion path (in composition space) will be unique. In other words, for each value of N_2 there will be a unique value of N_1 , N_3 , and D° (for the given boundary conditions). Therefore, a single experiment will suffice for a single set of specific boundary conditions, but other measurements will be necessary for other values of $N_2 (+\infty)$ and $N_2 (-\infty)$.

An alternative approach which may be used for some systems is to constrain an otherwise ternary system to behave as if it were binary by externally buffering the value of one or more chemical potentials. As an example let us consider diffusion in the common olivines. Although the compositions of many common olivines may be largely represented by a linear combination of the components $Mg_6(SiO_4)_3$ and $Fe^{+2}_6(SiO_4)_3$, most olivines contain some ferric iron as well. Assuming that charge balance is maintained by the introduction of vacancies, open square \square , on metal sites along with the ferric iron, we may represent the presence of ferric iron in olivine in terms of the component $\square_2 Fe^{+3}_4 (SiO_4)_3$. The



$Mg_6(SiO_4)_3$

Fig. 2. A ternary containing ferric iron of vacancies. The lines series of compositions $\gamma = 1/4$ have composition

ferric component a fine a ternary system.

A potentially this ternary olivine which radiate from labeled $\gamma = 1/4$ and tions with a constant such line may be re $Mg_6(SiO_4)_3$ and $Fe^{+3}_4(SiO_4)_3$ for different lines (t.

Assuming that a constant ferric-fer constant (for constant note the equilibrium

Substituting expressions into (31),

$$\mu_{Fe} = 1/2 \left[\mu^\circ_{Fe_6} \right]$$

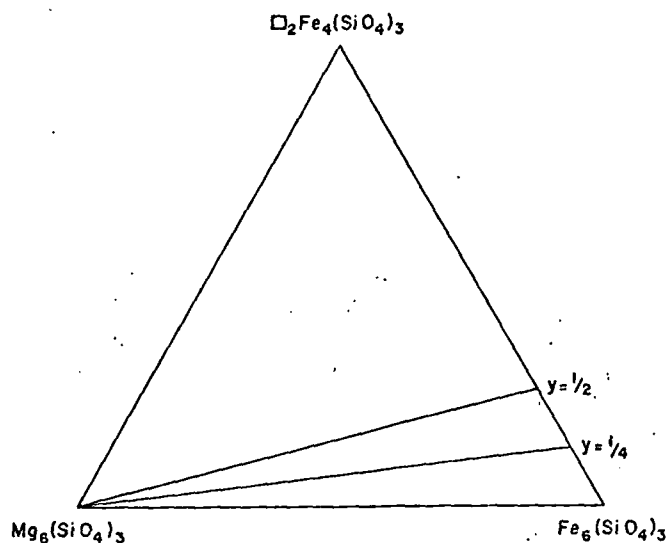


Fig. 2. A ternary composition diagram for the compositions of common olivines containing ferric iron, assuming that local charge balance is maintained by the presence of vacancies. The lines through the points labeled $y = 1/2$ and $y = 1/4$ each represent a series of compositions with the same ferric-ferrous ratio. The points labeled $y = 1/2$ and $y = 1/4$ have compositions given by the formula $Fe^{+2}_{6-3y} (\square Fe^{+3})_y (SiO_4)_3$.

ferric component along with the ferrous and magnesian components define a ternary system (fig. 2).

A potentially interesting set of binary subsystems contained within this ternary olivine system would correspond to the lines in figure 2 which radiate from the $Mg_6(SiO_4)_3$ corner (that is, those drawn to points labeled $y = 1/4$ and $y = 1/2$). Each of these lines is the locus of compositions with a constant ferric-ferrous ratio. All compositions along any one such line may be represented by a linear combination of the components $Mg_6(SiO_4)_3$ and $Fe^{+2}_{6-3y} (\square Fe^{+3})_y (SiO_4)_3$, where the y will be different for different lines (that is, for different ferric-ferrous ratios).

Assuming that the ternary olivines of figure 2 form an ideal solution, a constant ferric-ferrous ratio means that the chemical potential of Fe is constant (for constant pressure and temperature). To see that this is true note the equilibrium condition

$$\mu_{Fe} = 1/2 [\mu_{Fe_6(SiO_4)_3} - \mu_{\square_2Fe_4(SiO_4)_3}] \quad (31)$$

Substituting expressions for the chemical potentials in terms of mole fractions into (31), assuming ideality (Thompson, 1967, eq 4), yields

$$\mu_{Fe} = 1/2 \left[\mu^{\circ}_{Fe_6(SiO_4)_3} - \mu^{\circ}_{\square_2Fe_4(SiO_4)_3} + aRT \ln \left(\frac{N_{Fe_6(SiO_4)_3}}{N_{\square_2Fe_4(SiO_4)_3}} \right) \right] \quad (32)$$

ve a significant effect on s (Shewmon, 1963). This associated defects such as 1. Fortunately, however, 2. Every approach will be use 3. trained by stoichiometry, 4. following paragraphs as 5. a component (3) in addi.

6. correctly applied occurs 7. n of 3) in the phases in- 8. s. If the mole fraction of 9. m is quite correct, even 10. e diffusion coefficient de- 11. constant N_3 and must be 12. it mole fraction of com- 13. ither that the chemical 14. h N_2 at constant N_3 or 15. mpared to the diffusion 16. t constant N_3 , when the 17. osition, is a special case 18. pta and Cooper (1971). 19. y be two directions in 20. ment 3) for which diffu- 21. d Varshneya (1968) and

22. ficients depend on com- 23. one is interested in only 24. 8) has shown that for a 25. ry conditions, $N_2 (+\infty)$ 26. space) will be unique. 27. e a unique value of N_1 , 28. Therefore, a single ex- 29. oundary conditions, but 30. values of $N_2 (+\infty)$ and

31. l for some systems is to 32. as if it were binary by 33. emical potentials. As an 34. olivines. Although the 35. argely represented by a 36. $O_4)_3$ and $Fe^{+2}_6(SiO_4)_3$. 37. Assuming that charge 38. ancies, open square \square . 39. represent the presence 40. t $\square_2Fe^{+3}_4(SiO_4)_3$. The

If μ_{Fe} is constant, then $(N_{Fe_6(SiO_4)_3} / N_{\square_2Fe_4(SiO_4)_3})$ must also be constant and conversely, since the other terms in (32) have definite values at a given pressure and temperature (the μ° terms give the chemical potentials of the pure end members and α is a constant depending on the number of exchangeable sites per mole of the chosen components). Therefore, if we could externally constrain μ_{Fe} , possible olivine compositions would lie along one of the lines y in figure 2, and the diffusion is constrained to be binary.

An experiment corresponding to the desired conditions would entail controlling μ_{O_2} in addition to having an iron oxide present. If the olivines in the experiment were initially equilibrated separately at the μ_{O_2} of the diffusion run, and if the $Fe^{+2} \longleftrightarrow \square Fe^{+3}$ exchange is as rapid as the $Fe^{+2} \longleftrightarrow Mg^{+2}$ exchange, then the diffusion may be treated as binary (to the extent that the olivines are ideal). Buening and Buseck (1973) have measured Fe-Mg diffusion in olivines under conditions similar to those suggested here. They found a significant μ_{O_2} dependence of their measured binary diffusion coefficients. I suggest that what they have determined are binary diffusion coefficients for interdiffusion between forsterite and various fayalites with different ferric-ferrous ratios (that is, for different values of y (fig. 2)). A similar approach might be utilized to measure interdiffusion in other Fe-Mg solid solutions.

CONCLUSIONS

Of the many possible sets of components available for use in describing diffusion in an n -component system, an ultimate set of (actual) components is preferred because (1) a minimum number of equations of constraint are necessary, (2) a minimum number of components need be considered, and (3) inherently nonmeasurable quantities are avoided. Descriptions of diffusion in terms of one ultimate set of components may be easily transformed into descriptions in terms of another ultimate set of components. Special care must be exercised, however, when the reference frames used depend on the choice of components. The description of many diffusion problems may be simplified if one is willing to use actual components, which may contain negative amounts of atoms. Particularly convenient are "exchange components" like KNa_{-1} , as demonstrated above for the case of ternary reciprocal exchange between alkali feldspars and dioctahedral alkali micas. Small quantities of additional components in approximately binary systems may significantly affect diffusion processes and should not be neglected. However, solutions to the continuity equation for a two component system may be used if (1) the system is constrained by stoichiometry to be binary, (2) the system is constrained by kinetics to be binary, (3) the system is constrained to be binary by externally buffering certain chemical potentials, or (4) only one set of boundary conditions is of interest.

Special thanks belong to the lecturers and comments. Early drafts were improved by John M. Ferry, George V. Friends. This work is published in *Experimental Geology* and

- Anderson, D. E., and Buckley
Mineralogy and Petrology
1974, Modeling of
A. W., Giletti, B. J., Yoder
and kinetics: Washington
Appel, M., 1968, Solution for
system: Scripta Metallurg
Brady, J. B., 1975, Reference
p. 954-983.
Buckley, G. R., ms, 1973, The
Illinois at Urbana-Champ
Buening, D. K., and Buseck,
phys. Research, v. 78, p. e
Burt, D. M., 1972, The influe
Inst. Washington Year Be
1974a, Alternative
[abs.]: Am. Geophys. Uni.
1974b, Concepts o
approach: Geol. Soc. Am
Carlaw, H. S., and Jaeger, J
Univ. Press, 386 p.
Cooper, A. R., 1968, The use
sion coefficient for multie
A. D., eds., Mass transpo
Natl. Bur. Standards Spec
1974, Vector spac
W., Giletti, B. J., Yoder,
and kinetics: Washington
Cooper, A. R., and Varshuc
effective binary diffusion
Fujita, H., and Gosting, L. J.
in three-component syste
diffusion coefficients: Am
Gibbs, J. W., 1928, The coll.
Yale Univ. Press, 431 p.
Greenwood, H. J., 1975, Th
lationships: Am. Mineral
de Groot, S. R., and Mazur
North Holland Publishin
Gupta, P. K., and Cooper, A.
sion: Physica, v. 54, p. 39
Hooyman, G. J., 1956, TF
Physica, v. 22, p. 751-759
Hooyman, G. J., Holtan, H.,
of irreversible processes.
Jost, W., 1950, Bemerkung
probleme: Zeitschr. Phy
1952, Diffusion
558 p.
Kirkaldy, J. S., 1959, Diff
theorem for constructio
diffusion equation: Can

ACKNOWLEDGMENTS

Special thanks belong to Professor James B. Thompson, Jr. whose lectures and comments have provided the background for this paper. Early drafts were improved by the suggestions of Alan Bruce Thompson, John M. Ferry, George W. Fisher, D. M. Burt, and many other patient friends. This work is published under the auspices of the Committee on Experimental Geology and Geophysics at Harvard University.

REFERENCES

- Anderson, D. E., and Buckley, G. R., 1973, Zoning in garnets—diffusion models: *Contr. Mineralogy and Petrology*, v. 40, p. 87-104.
- 1974, Modeling of diffusion controlled properties of silicates, in Hofmann, A. W., Gilotti, B. J., Yoder, H. S., Jr., and Yund, R. A., eds., *Geochemical transport and kinetics*: Washington, D.C., Carnegie Inst. Washington, p. 31-52.
- Appel, M., 1968, Solution for Fick's 2nd law with variable diffusivity in a multi-phase system: *Scripta Metallurgica*, v. 2, p. 217-222.
- Brady, J. B., 1975, Reference frames and diffusion coefficients: *Am. Jour. Sci.*, v. 275, p. 954-983.
- Buckley, G. R., ms, 1973, *The effect of diffusion on garnet zoning*: Ph.D. thesis, Univ. Illinois at Urbana-Champaign, 112 p.
- Buening, D. K., and Buseck, P. R., 1973, Fe-Mg lattice diffusion in olivine: *Jour. Geophys. Research*, v. 78, p. 6852-6862.
- Burt, D. M., 1972, The influence of fluorine on the facies of Ca-Fe-Si skarns: *Carnegie Inst. Washington Year Book* 71, p. 443-450.
- 1974a, Alternative choices of components for modeling geochemical systems [abs.]: *Am. Geophys. Union Trans.*, v. 55, p. 452.
- 1974b, Concepts of acidity and basicity in petrology—The exchange operator approach: *Geol. Soc. America Abs.*, v. 6, p. 674-676.
- Carlsaw, H. S., and Jaeger, J. C., 1947, *Conduction of heat in solids*: Oxford, Oxford Univ. Press, 386 p.
- Cooper, A. R., 1968, The use and limitations of the concept of an effective binary diffusion coefficient for multicomponent diffusion, in Wachtman, J. B., Jr., and Franklin, A. D., eds., *Mass transport in oxides*: Washington, D.C., U.S. Govt. Printing Office, Natl. Bur. Standards Spec. Pub. 296, p. 79-84.
- 1974, Vector space treatment of multicomponent diffusion, in Hofmann, A. W., Gilotti, B. J., Yoder, H. S., Jr., and Yund, R. A., eds., *Geochemical transport and kinetics*: Washington, D.C., Carnegie Inst. Washington, p. 15-30.
- Cooper, A. R., and Varshneya, A. K., 1968, Diffusion in the system $K_2O-SrO-SiO_2$: I, effective binary diffusion coefficients: *Am. Ceramic Soc. Jour.*, v. 51, p. 103-106.
- Fujita, H., and Gosting, L. J., 1956, An exact solution of the equations for free diffusion in three-component systems with interacting flows, and its use in evaluation of the diffusion coefficients: *Am. Chem. Soc. Jour.*, v. 78, p. 1099-1106.
- Gibbs, J. W., 1928, *The collected works of J. Willard Gibbs*, v. 1: New Haven, Conn., Yale Univ. Press, 434 p.
- Greenwood, H. J., 1975, Thermodynamically valid projections of extensive phase relationships: *Am. Mineralogist*, v. 60, p. 1-8.
- de Groot, S. R., and Mazur, P., 1962, *Nonequilibrium thermodynamics*: Amsterdam, North Holland Publishing Co., 510 p.
- Gupta, P. K., and Cooper, A. R., Jr., 1971, The [D] matrix for multicomponent diffusion: *Physica*, v. 54, p. 39-59.
- Hooyman, G. J., 1956, Thermodynamics of diffusion in multicomponent systems: *Physica*, v. 22, p. 751-759.
- Hooyman, G. J., Holtan, H., Jr., Mazur, P., and de Groot, S. R., 1953, Thermodynamics of irreversible processes in rotating systems: *Physica*, v. 19, p. 1095-1108.
- Jost, W., 1950, Bemerkung zur mathematischen Behandlung komplizierter Diffusionsprobleme: *Zeitschr. Physik*, v. 127, p. 163-167.
- 1952, *Diffusion in solids, liquids, gases*: New York, Academic Press, Inc., 558 p.
- Kirkaldy, J. S., 1959, Diffusion in multicomponent metallic systems IV. A general theorem for construction of multicomponent solutions from solutions of the binary diffusion equation: *Canadian Jour. Physics*, v. 37, p. 30-34.

$e_4 (SiO_4)_3$ must also be com-
n (32) have definite values 21
rms give the chemical poten-
stant depending on the num-
osen components). Therefore
e olivine compositions would
he diffusion is constrained to

desired conditions would en-
in iron oxide present. If the
ilibrated separately at the μ_{O_2}
[Fe⁺³ exchange is as rapid as
diffusion may be treated as bi-
ideal). Buening and Buseck
olivines under conditions simi-
significant μ_{O_2} dependence of
s. I suggest that what they
coefficients for interdiffusion be-
different ferric-ferrous ratios
A similar approach might be
-Mg solid solutions.

s available for use in describ-
ultimate set of (actual) com-
m number of equations of
mber of components need be
able quantities are avoided.
imate set of components may
erms of another ultimate set
ised, however, when the ref-
components. The description
fied if one is willing to use
ative amounts of atoms. Par-
ents" like KNa_{-1} , as demon-
cal exchange between alkali
small quantities of additional
s may significantly affect dif-
d. However, solutions to the
stem may be used if (1) the
binary, (2) the system is con-
n is constrained to be binary
ntials, or (4) only one set of

- Kirkwood, J. G., Baldwin, R. L., Dunlop, P. J., Gosting, L. J., and Kegeles, G., 1960, Flow equations and frames of reference for isothermal diffusion in liquids: *Jour. Chem. Physics*, v. 33, p. 1505-1513.
- Korzhinskii, D. S., 1959, *Physio-chemical basis of the analysis of the paragenesis of minerals*: New York, Consultants Bur., 142 p.
- Landau, L. D., and Lifshitz, E. M., 1959, *Fluid mechanics, Course on theoretical physics*, v. 6: Reading, Mass., Addison Wesley, 536 p.
- Oishi, I., 1965, Analysis of ternary diffusion: solutions of diffusion equations and calculated concentration distribution: *Jour. Chem. Physics*, v. 43, p. 1611-1620.
- Onsager, L., 1931a, Reciprocal relations in irreversible processes, I: *Phys. Rev.*, v. 37, p. 405-426.
- 1931b, Reciprocal relations in irreversible processes, II: *Phys. Rev.*, v. 38, p. 2265-2279.
- 1945, Theories and problems of liquid diffusion: *New York Acad. Sci. Anal.*, v. 46, p. 241-265.
- Schönert, H., 1960, Diffusion and sedimentation of electrolytes and non-electrolytes in multicomponent systems: *Jour. Phys. Chemistry*, v. 64, p. 733-737.
- Shewmon, P. G., 1963, *Diffusion in solids*: New York, McGraw-Hill Book Co., 203 p.
- Thompson, A. B., 1974, Calculations of muscovite-paragonite-alkali feldspar phase relations: *Contr. Mineralogy Petrology*, v. 44, p. 173-194.
- Thompson, J. B., Jr., 1959, Local equilibrium in metasomatic processes, in Abelson, P. H., ed., *Researches in geochemistry*: New York, John Wiley & Sons, p. 427-457.
- 1967, Thermodynamic properties of simple solutions: in P. H. Abelson, ed., *Researches in geochemistry II*: New York, John Wiley & Sons, p. 340-361.
- 1972, Oxides and sulfides in regional metamorphism of pelitic schists: *Internat. Geol. Cong.*, 24th, Montreal 1972, Sec. 10, p. 27-35.
- Thompson, J. B., Jr., and Waldbaum, D. R., 1968, Mixing properties of sanidine crystalline solutions: I. calculations based on ion-exchange data: *Am. Mineralogist*, v. 53, p. 1965-1999.
- Varshneya, A. K., and Cooper, A. R., 1972a, Diffusion in the system $K_2O-SrO-SiO_2$: II, cation self-diffusion coefficients: *Am. Ceramic Soc. Jour.*, v. 55, p. 220-223.
- 1972b, Diffusion in the system $K_2O-SrO-SiO_2$: III, interdiffusion coefficients: *Am. Ceramic Soc. Jour.*, v. 55, p. 312-317.
- 1972c, Diffusion in the system $K_2O-SrO-SiO_2$: IV, mobility model, electrostatic effects, and multicomponent diffusion: *Am. Ceramic Soc. Jour.*, v. 55, p. 418-421.
- Waldbaum, D. R., and Thompson, J. B., Jr., 1969, Mixing properties of sanidine crystalline solutions: IV. phase diagrams from equations of state: *Am. Mineralogist*, v. 54, p. 1274-1298.

SUBJ
GCHM
CCCMA Comparison of Computerized Chemical Models for
Equilibrium Calculations in Aqueous Systems¹D. K. NORDSTROM¹, L. N. PLUMMER¹, T. M. L. WIGLEY¹, T. J. WOLERY¹,
J. W. BALL¹, E. A. JENNE¹, R. L. BASSETT¹, D. A. CRERAR¹, T. M. FLORENCE¹,
B. FRITZ², M. HOFFMAN², G. R. HOLDREN, JR.², G. M. LAFON²,
S. V. MATTIGOD², R. E. McDUFF², F. MOREL², M. M. REDDY², G. SPOSITO²,
and J. THRAILKILL²

The interpretation of chemical processes in aqueous systems requires the use of modern electronic computers, particularly in the calculation of multicomponent, multiphase equilibria. Commonly, the first concern of solution chemists and aqueous geochemists is to calculate the distribution and activities of species on the assumption that equilibrium exists throughout the aqueous phase. Species distribution can then be used in several areas of analytical and applied chemistry, e.g. to examine the availability of free and reactive ions, to test solubility hypotheses, and to determine the potential bioavailability of nutrients or toxic substances. Species distribution also forms the basis for more complex computations involving solutions which change composition by reaction with other solutions and with gases and solids. Equilibrium calculations of this type are particularly helpful in solving interpretive problems encountered in such fields as chemical and environmental engineering, geochemistry, biochemistry and aquatic ecology.

This symposium demonstrates quite clearly that we depend heavily on chemical models, especially computerized models, to interpret aqueous chemical processes. Several computer programs which solve problems of simultaneous chemical equilibria are being used by a rapidly increasing number of investigators and it is necessary to review the inherent assumptions and limitations of these aqueous models. There is a temptation to use these models as ready-made interpretations

¹ Current addresses for authors can be found on page 892.UNIVERSITY OF UTAH
RESEARCH INSTITUTE
EARTH SCIENCE LAB.

42. Weaver, R.M., Jackson, M.L., and Syers, J.K. Clay mineral stability as related to activities of aluminum, silicon and magnesium in matrix solution of montmorillonite-containing soils. Clay and Clay Min. **24**, 246-252 (1976).
43. Huang, W.H., and Keller, W.D. Gibbs free energies of formation calculated from dissolution data using specific mineral analysis. III. Clay minerals. Amer. Mineral. **58**, 1023-1028 (1973).
44. Sposito, G., and Mattigod, S.V. On the chemical foundation of the sodium adsorption ratio. Soil Sci. Soc. Amer. J. **41**, 323-329 (1977).
45. Gaines, G.L., Jr., and Thomas, H.C. Adsorption studies on clay minerals. II. A formulation of the thermodynamics of exchange adsorption. J. Chem. Phys. **21**, 714-718 (1953).
46. Foscolos, A.E., and Barshad, I. Equilibrium constants between both freshly prepared and aged H montmorillonites and chloride salt solutions. Soil Sci. Soc. Amer. Proc. **33**, 242-247 (1969).
47. Peigneur, P., Maes, A., and Cremers, A. Heterogeneity of charge density distribution in montmorillonite as inferred from cobalt adsorption. Clays and Clay Min. **23**, 71-75 (1975).
48. Gast, R.G. Alkali metal cation exchange on Chambers montmorillonite. Soil Sci. Soc. Amer. Proc. **36**, 14-19 (1972).
49. Sposito, G., and Mattigod, S.V. Ideal behavior in Na - trace metal cation exchange on Camp Berteau montmorillonite. Clays and Clay Min. (In press).
50. Helgeson, H.C. Thermodynamics of hydrothermal systems at elevated temperatures and pressures. Amer. J. Sci. **267**, 729-804 (1969).
51. Page, A.L. Fate and effects of trace elements in sewage sludge when applied to agricultural lands. A literature review study. Rept. Office Res. Dev. U.S. Environ. Protection Agency, Cincinnati, Ohio, 97 p., 1974.
52. Sposito, G., Holtzclaw, K.M., and Baham, J. Analytical properties of the soluble, metal-complexing fractions in sludge-soil mixtures: II. Comparative structural chemistry of fulvic acid. Soil Sci. Soc. Amer. J. **40**, 691-697 (1976).

RECEIVED November 16, 1978.

of reality without a clear understanding of their weaknesses. These programs and models are usually developed for specific purposes and taken together they represent a wide range of capabilities and features. This paper reviews the state-of-the-art of equilibrium computations by providing a compilation and description of aqueous models in current use and by examining their consistency through a comparison of species distributions and saturation indices for two hypothetical test cases: a river water sample and a seawater sample. This review will also serve to complement the review on machine computation efficiency by Leggett (1) and the review by Perrin (2) on the applications of digital computers to analytical chemistry.

The Chemical Equilibrium Problem and Its Thermodynamic Basis

An "aqueous chemical model" needs to be defined separately from the computer program which executes calculations based on the model. Such a model can be defined as a theoretical construction which allows us to predict the thermodynamic properties of electrolyte solutions. There are several ways of constructing an aqueous model, e.g. from the Bjerrum ion association theory (3), or the Fuoss ion association theory (4,5) or the Reilly, Wood and Robinson mixed electrolyte theory (6). The choice of model must be made on the basis of the problem to be solved and each model carries with it its own set of assumptions and restrictions. Nearly all computerized models are based on the ion association theory and within this framework the species distribution problem can be formulated in two distinct but thermodynamically related ways: the equilibrium constant approach and the Gibbs free energy approach. Both approaches are subject to the conditions of 1) mass balance and of 2) chemical equilibrium. The mass balance condition requires that the computed sum of the free and derived (complexes) species be equal to the given total concentration. Chemical equilibrium requires that the most stable arrangement for a given system be found, as defined by the equilibrium constants for all mass action expressions of the system, or through the use of Gibbs free energies for all of the components and derived species. In the equilibrium constant approach the mass action expressions are substituted into the mass balance conditions resulting in a set of nonlinear equations which must be solved simultaneously. The Gibbs free energy approach is simply a transformation of variables through the thermodynamic relation:

$$\Delta G_r = \Delta G_r^\circ + RT \ln K = 0$$

which allows a different numerical approach. The total Gibbs

free energy-function is then minimized for a given set of species and their mole numbers subject to the mass balance requirement. In the former approach equilibrium constants are needed for the data base whereas in the latter approach free energy values are needed. This difference in the data base can often be an important limitation. At the present time there are more reliable and available equilibrium constants than free energy values.

By either thermodynamic approach the problem can be stated numerically as one of finding a solution to a set of nonlinear equations. It is usually not feasible to simultaneously solve these equations in exact form for a multicomponent, multiphase system and therefore an iteration procedure must be utilized. The standard method of solving the problem by the equilibrium constant approach is to use linearized matrix inversion. Convergence assumes, of course, that the solution not only exists but that it is unique. If a system can have several thermodynamically metastable states (local minima in the Gibbs function) then several nonunique solutions are possible. Recent papers by Othmer (7) and Caram and Scriven (8) have pointed out that uniqueness is characteristic of ideal systems whereas for non-ideal systems a solution may occur at the global minimum (most stable equilibrium point) but it also may occur at a nonunique local minimum. For applications in aquatic chemistry the problem of nonuniqueness is particularly important in the interpretation of solid precipitation and dissolution processes.

The choice of the thermodynamic approach dictates the general category of numerical techniques to be used. Optimization techniques such as pattern search, linear programming, steepest descent and gradient methods are all appropriate to the Gibbs function approach whereas Newton-Raphson, successive approximations and nested iterations are best suited to the equilibrium constant approach. These techniques and several other mathematical methods have been documented along with the thermodynamic formalism in the excellent reviews by Zeleznik and Gordon (9) and Van Zeggeren and Storey (10). In this report we prefer to describe the main features and capabilities of current models rather than digress on the mathematical details of each since "... any method of calculation that can be made reliable is a good method when equilibrium compositions are the only concern" (9).

Chemical models can be further characterized by their application. The intended utilization of a model usually directs the developmental stages of choosing the type of model and the mathematical method. We have grouped current computerized models into "major schools" according to their point of origin and their application. Since the second generation models frequently used the same basic numerical approach as their predecessors, the classification into schools also tends to separate different mathematical formulations.

Major Schools of Computerized Models

Generalized Method of the Equilibrium Constant Approach.

The basic mathematics of the equilibrium constant approach was derived in general form by Brinkley (11,12) and Kandiner and Brinkley (13). The development of the equations was well suited for adaptation to digital computers and Feldman, et al. (14) utilized the approach to calculate the equilibrium composition of high temperature gaseous mixtures. This approach has been strongly favored by geochemists. For example, Crerar (15) has revised this method so that arbitrary independent equilibrium constants can be used. He employed Newton-Raphson iteration with curve-crawler techniques (16) for rapid convergence and applied his routine to problems of hydrothermal chemistry. It should be pointed out that these methods are completely general, in the mathematical sense, so that only the reactions taking place in the system under investigation need be coded for computation. This routine can be useful for laboratory and experimental systems where most of the species and associated data base of non-general programs are unnecessary.

Generalized Method of the Gibbs Free Energy Minimization.

The mathematical formulation of the free energy approach was pioneered by White et al. (17) who pointed out the advantages of using alternative numerical techniques such as steepest descent and linear programming. Dayhoff et al. (18) computed equilibrium compositions for prebiological and planetary atmospheres with this approach and showed how these compositions changed at different temperatures and pressures for systems containing C, H, O, N, P, S and Cl. Holloway and Reese (19) have solved the equilibrium composition of the system C-O-H-N at high temperatures by a computerized free energy minimization model and Karpov and Kaz'min (20) have computed the distribution of species in seawater using a dual algorithm technique. For relatively simple systems where the free energies are available and reliable, the Gibbs minimization approach is convenient and dependable. For large complex systems, however, the equilibrium constant approach is preferred. If and when an accurate and internally consistent set of thermodynamic data becomes available, the Gibbs minimization will likely find greater use. We now present a brief review of non-general computerized models which uses the equilibrium constant approach and incorporates individual reactions as part of the program.

Specific Programs in Analytical Chemistry. Following the lead of Brinkley and others, several programs were independently developed to solve problems involving aqueous equilibria in analytical and physical chemistry. One of the earliest programs, HALTAFALL, came from the work of Sillen and his

colleagues (21,22). This program was designed to calculate species distribution in an aqueous phase from a knowledge of the appropriate stability constants and total concentrations. The program is general enough to handle mixing problems such as titrations involving separation of gaseous or solid phases and organic solvent extractions. The computations are carried out at constant ionic strength and constant temperature although these restrictions can be modified by the programmer. When apparent stability constants at different ionic strengths than the equilibrium problem are used, corrections are made by the Davies equation (80). The general method of calculation is by successive approximation. A companion program, LETAGROP VRID, was written to calculate stability constants for aqueous complexes from various measurements (23). Both programs are written in ALGOL. Perrin (24) and Perrin and Sayce (25) developed the COMICS program for the calculation of the equilibrium distribution of species using a type of "brute force" successive approximation (see below). COMICS has gone through several stages of modification which have been discussed by Leggett (1) and will not be further elaborated on here, except to mention a more recent version called SIAS (26). A similar program named EQBRAT is described by Detar (27) and it complements other programs (all in FORTRAN) which can handle a wide range of chemical problems. Bos and Meershoek (28) introduced Newton's method to titration calculations with the program EQUIL, written in PL/1, which increased the computation efficiency and was protected against non-convergence problems.

Successive Approximation Programs For Natural Water

Equilibria. Garrels and Thompson (29) were the first to use the method of successive approximation in a hand calculation to solve an equilibrium problem in aqueous geochemistry. Their analysis of the species distribution in seawater in terms of ion association influenced the development of several models. Barnes and Clarke (30) found this approach useful in the investigation of the corrosion properties of wells and developed the WATCHEM program to interpret iron corrosion processes. This approach was also used to initialize PATHI (31) by a subroutine called SOLSAT which existed as a separate program. A recent version of this program, called EQUIL, has evolved from the work of Fritz (32) and Droubi (33) and it is used with the programs DISSOL and EVAPOR mentioned below. The most general first-generation programs of this type are WATEQ (34,35), SOLMNEQ (36), and EQ3 (37). All three programs have been designed to accept water analyses with on site values for pH, Eh and temperature. There is no proton mass balance condition, only mass balances on cations and anions are carried out. SOLMNEQ carries a data base in the form of a table of equilibrium constants for the range 0-350°C and EQ3 contains a similar data base for 0-300°C whereas WATEQ uses the Vant

Hoff equation or analytical expressions for equilibrium constants as a function of temperature and is considered reliable for the range 0-100°C. SOLMNEQ has additional features such as the silica and Na-K-Ca geothermometers for evaluating geothermal reservoir temperatures and includes several more trace element species than WATEQ. SOLMNEQ has been expanded to include organic complexes and ion exchange equilibria and uses the pressure dependence of the equilibrium constants. EQ3 also uses pressure dependent equilibrium constants. WATEQ was originally written in PL/1 and has been revised and translated into FORTRAN by Plummer *et al.* (38) in a program called WATEQF. Manganese speciation has been added to WATEQF and the successive approximation procedure was revised to give much faster convergence. 21 aqueous species and 17 minerals of uranium have been added to WATEQF in a recent modification (39). The advantages of using PL/1 optimizing code with reorganization into several subprogram blocks along with the expansion of the data base to include several trace elements and the rapid convergence of WATEQF have been incorporated into WATEQ2 (40). A shorter version, called WATSPEC, which is preferable for handling routine water analyses has been published by Wigley (41).

The method of successive approximations has been conveniently described by Wigley (41) where either a "brute force" method or a "continued fraction" method can be used. The brute force method is the classical approach where mass balance expressions are substituted directly into the mass balance conditions and solved for total concentrations which are then compared to the analytical values. In the continued fraction method, the non-linear equations are rearranged to solve for free ion concentrations which are initially assumed to be equal to the total concentrations, as detailed by Wigley (42). These two methods are best illustrated by a simple example. Assume a solution which contains free Ca^{2+} ions, free CO_3^{2-} ions, and only one ion pair: CaCO_3 . The mass balance conditions are given by

$$m\text{Ca}(\text{total}) = m\text{Ca}^{2+} + m\text{CaCO}_3 \quad (1)$$

$$m\text{CO}_3(\text{total}) = m\text{CO}_3^{2-} + m\text{CaCO}_3 \quad (2)$$

with the restriction that (assuming an ideal solution)

$$K = \frac{m\text{CaCO}_3}{(m\text{Ca}^{2+})(m\text{CO}_3^{2-})} \quad \text{or} \quad m\text{CaCO}_3 = K(m\text{Ca}^{2+})(m\text{CO}_3^{2-}) \quad (3)$$

Substituting equation 3 into equations 1 and 2 gives

$$m\text{Ca}(\text{total}) = m\text{Ca}^{2+} + K(m\text{Ca}^{2+})(m\text{CO}_3^{2-}) \quad (4)$$

$$\text{and } m\text{CO}_3(\text{total}) = m\text{CO}_3^{2-} + K(m\text{Ca}^{2+})(m\text{CO}_3^{2-}) \quad (5)$$

Using the brute force method,

$$m\text{Ca}^{2+} = m\text{Ca}(\text{total}) - K(m\text{Ca}^{2+})(m\text{CO}_3^{2-}) \quad (6)$$

$$m\text{CO}_3^{2-} = m\text{CO}_3(\text{total}) - K(m\text{Ca}^{2+})(m\text{CO}_3^{2-}) \quad (7)$$

where $m\text{Ca}^{2+}$ and $m\text{CO}_3^{2-}$ are assumed equal to $m\text{Ca}(\text{total})$ and $m\text{CO}_3(\text{total})$ for the first estimate. Equations 6 and 7 give new values for the free ion concentrations which are then used in the next iteration. Using the continued fraction method equations 4 and 5 are rearranged to

$$m\text{Ca}^{2+} = \frac{m\text{Ca}(\text{total})}{1 + Km\text{CO}_3^{2-}} \quad (8)$$

$$m\text{CO}_3^{2-} = \frac{m\text{CO}_3(\text{total})}{1 + Km\text{Ca}^{2+}} \quad (9)$$

As before, the first estimate is made by assuming that free ion concentrations are equal to total concentrations but the second estimate comes from equations 8 and 9 which vary less than equations 6 and 7 because of the form of the equation.

This alternate form of the equations produces a faster convergence as shown in an example given by Wigley (41) and also converges more rapidly than Newton-Raphson. EQ3 employs an additional control on the continued fraction method which generates monotone sequences (43,44). Its chief virtues are strict error bounds and increased stability with respect to a wide range of analyses of aqueous solutions used as input.

Other programs of this general type include SEAWAT (45) which was specifically designed for seawater calculations, MIRE (46) which was specifically designed for anoxic marine pore waters, IONPAIR and NOPAIR (47) and CALCITE (48) which were designed for freshwaters in carbonate terrains and KATKLE 1 (49) which has been used for soil water geochemistry.

(50)
 Newton-Raphson Programs for Experimental and Natural Water Equilibria. Morel and Morgan (49) developed the FORTRAN program REDEQL for the calculation of multicomponent metal-ligand equilibria with considerable flexibility and includes a large number of metal-ligand complexes. The program is based on the equilibrium constant approach and uses Newton-Raphson iteration to find the solution to a function which compares the difference between the total calculated component concentration and the total analytical component concentration. REDEQL has the capability of imposing mineral saturation to allow dissolution and/or precipitation of various solids. Another option is

the calculation of interaction intensities and capacities (50,51,52). This program and its subsequent modifications have led to several "second generation" programs which are widely used by environmental engineers: REDEQL2, MINEQL and GEOCHEM. This family of programs can simulate adsorption behavior using the James-Healy approach, the Schindler-Stumm complexation approach or a combination of surface complexation and electric double layer (53-59). These programs also contain a data base for a constant temperature of 25°C, other temperatures cannot be calculated without changing all the equilibrium constants to those temperatures. MINEQL (60) has greater clarity and flexibility in a more compact program which utilizes Gaussian elimination to solve the matrix equation. GEOCHEM (61, unpublished data) has a greatly expanded data base covering over 800 organic species and more than 2000 inorganic species and it includes ion exchange reactions for simulating soil water reactions. Convergence problems are occasionally encountered with Newton-Raphson methods which are commonly caused by poor estimates of initial concentrations supplied by the programmer. However, several numerical techniques including under-relaxation, curve-crawling and pre-iteration optimization of starting estimates can greatly increase the reliability of the Newton-Raphson method (15,37,62). A good example is provided by the program EQUIL (62) which utilizes matrix scaling, eigen vector analysis, matrix modifications and a convergence forcer to achieve rapid and reliable convergence.

Reaction Path Simulation. The first application of computer techniques to problems of mass transfer in geochemistry began with the work of Helgeson and colleagues (63,64). The general approach of the program PATHI (31) is to describe a partial equilibrium reaction path (e.g. mineral dissolution and rock weathering) in terms of ordinary differential equations which are linear and can be solved by matrix algebra. The initial condition, which consists of an aqueous fluid, must be calculated by a species distribution iteration scheme such as the successive approximation method. Progressive reaction states can be computed by incrementing the progress variable, ξ (65), iteratively and checking the aqueous phase for saturation at each step and then dissolving or precipitating the required mass(es) of the appropriate mineral phase(s) to retain equilibrium. Thus, by integrating a set of differential equations a reaction path can be followed progressively until overall chemical equilibrium is reached by the specified system. This method has been applied to the study of weathering reactions, diagenesis, metamorphism and hydrothermal metasomatism (64), in the formation of ore deposits (66) and scaling of conduits caused by precipitation from geothermal brines (67). PATHI has been revised and modified to simulate granite weathering (32) and evaporation of closed basin lakes

(36) with the programs DISSOL and EVAPOR which use a related program, EQUIL, to calculate species distribution. These programs have been applied to the prediction of soil salinity and optimal irrigation doses as well as the general evolution of soil water during evaporation (68,69).

Several difficulties with PATHI led to very long execution times and occasional abnormal program termination. Claude Herrick and others (67) greatly improved the efficiency by adopting high-order Gear integration techniques (70,71). However, drift error incurred in the integration remains an annoyance, and the differential equation approach cannot be applied if the starting solution is supersaturated with any solids.

Wolery (37) has written a PATHI-like program, EQ6, which uses the Newton-Raphson method to solve the system of algebraic equations instead of their differential counterparts at each stage of reaction progress. The drift problem is thereby avoided. Taylor's series expressions, based on finite differences, are utilized to follow the course of the simulation and to predict starting estimates at each new point of reaction progress. EQ6 has some affinities in its numerical approach to the REDEQL school and Crerar's (15) program and it can precipitate an equilibrium assemblage of precipitates from an initially supersaturated solution.

Another program well suited for reaction path simulation is MIX2 (72) which uses a regression technique on the charge balance condition for the aqueous phase in computing pH after a reaction step. MIX2 can solve problems in mixing and titration of aqueous solutions (73,74), evaporation, heterogeneous equilibrium, and non-equilibrium heterogeneous reactions (75). Although MIX2 avoids the drift problems associated with PATHI, the aqueous model is limited to the major species in the system $\text{CaO-MgO-Na}_2\text{O-K}_2\text{O-H}_2\text{SO}_4\text{-H}_2\text{CO}_3\text{-HCl-H}_2\text{O}$ and considers only one phase boundary at a time. More advanced mass transfer programs using a log linearization technique for simultaneous solution of mass action, mass balance and charge balance equation are in preparation (76) which have broad applications to mass transfer problems.

Test Case Results

Collectively, the programs mentioned above represent the "state of the art" in the calculation of the equilibrium distribution of species in aqueous systems. As a means of examining the consistency of these programs, two test cases (a dilute river water and an average seawater analysis) were compiled and mailed to more than fifty researchers who have been active in the field of chemical modeling. These test cases may overlook many of the features of specific programs, but they provide a common basis by which most of the programs can be

compared. One approach to the comparison of aqueous models is to tabulate and examine the thermodynamic data, activity coefficients, choice of complexes, etc. Alternatively the approach taken in this survey has been to examine the results predicted by the aqueous models, an approach that integrates all the aspects of each model. In this manner the differences between models can be seen in terms of the actual results which are of value in applications to specific problems. Differences will always be apparent between the thermodynamic data base used in different models but it is difficult to ascertain whether a certain difference has any effect on the final result unless the results are all compared. It should be emphasized, however, that any type of comparison will always be inadequate because any criterion that is chosen as a basis for comparison is usually not given the same priority by another model. For example, models that are developed for reaction path simulation may sacrifice computation efficiency on a species distribution calculation if more efficiency is gained in the reaction progress calculation. In this instance, as in many others, the computerized model is developed for a specific purpose and design priorities are assigned accordingly.

Each researcher was asked to complete a questionnaire describing the details of their program and to return the computed results on the two test cases. The responses received include representatives of most of the major aqueous models known. Table I identifies the programs and researchers who supplied the information for the particular program and includes general information on types of computers used, number of cards in the source deck, primary and secondary references and availability.

Table II gives a general description of the program features such as total number of elements, aqueous species, gases, organic species, redox species, solid species, pressure and temperature ranges over which calculations can be made, an indication of the types of equations used for computing activity coefficients, numerical method used for calculating distribution of species and the total number of iterations required by these models for each of the two test cases. The chemical analyses for the two test cases are summarized in Table III. The seawater compilation was prepared in several units to assure consistency between concentrations for proper entry into the aqueous models.

The results of the river water and seawater test cases computed by the aqueous models listed in Table I are summarized in Tables IV-X. Tables IV and V compare selected major and minor species computed for the river water test case, and Tables VI and VII make a similar comparison for the seawater test case. Table VIII compares activity coefficients computed for the major species in seawater and Table IX and X tabulate saturation indices for selected minerals in the river water and seawater test

cases. The saturation index, SI, is defined as $\log IAP/K_{sp}$ where IAP is the ion activity product for the mineral and K_{sp} is the thermodynamic solubility product constant.

Discussion

The remainder of this paper is a plea for caution and restraint in interpreting the results of the test cases shown here, and in the use of computerized chemical models in general. Tables IV-X show both remarkable agreement and disagreement. In general, there is better agreement between the major species concentrations than the minors and the results for the river water tend to agree better than those for seawater. We would expect better agreement in the river water test case because of the smaller amount of complexing in the more dilute solution and the more consistent and reliable activity coefficients which can be obtained at low ionic strength.

There are several limitations which lead to the discrepancies in Tables IV-X. First of all, no model will be better than the assumptions upon which it is based. The models compiled in this survey are based on the ion association approach whose general reliability rests on several non-thermodynamic assumptions. For example, the use of activity coefficients to describe the non-ideal behavior of aqueous electrolytes reflects our uncertain knowledge of ionic interactions and as a consequence we must approximate activity coefficients with semi-empirical equations. In addition, the assumption of ion association may be a naive representation of the true interactions of "ions" in aqueous solutions. If a consistent and comprehensive theory of electrolyte solutions were available along with a consistent set of thermodynamic data then our aqueous models should be in excellent agreement for most systems. Until such a theory is provided we should expect the type of results shown in Tables IV-X. No degree of computational or numerical sophistication can improve upon the basic chemical model which is utilized.

The second limitation, almost a corollary of the first, is the reliability of the equilibrium constants (or free energies) used in the model. It is quite common for solubility product constants and complex stability constants to vary by 1 to 3 orders of magnitude and have been observed to vary by that much in these models. Quite clearly this amount of uncertainty can cause large differences in the computed results and probably contributes the largest single source of error. The thermodynamic properties of substances are currently in a state of refinement by many researchers and continual updating of the aqueous models is needed. This situation is quite frustrating for investigators who are involved in solute transport modeling since they need a general chemical model with a fixed data base. An internally consistent data base can be obtained

Table I
General Information

Program Name	EQUIL	EQ3	GEOCHEM	IONPAIR	MINEQL2	MIRE	MINEQL/REDEQL2	REDEQL2	SEAWAT	SOLMNEQ	WATEQF	WATEQ2	WATSPEC	SIAS/COMICS
Language	FORTRAN	FORTRAN	FORTRAN	FORTRAN	FORTRAN	FORTRAN	FORTRAN	FORTRAN	FORTRAN	PL/1	FORTRAN	PL/1 (optimizing)	FORTRAN	FORTRAN
Computers	UNIVAC 1110	CDC 6400/6600 7600	IBM 360/50	IBM 370/16511	CDC CYBER 74	IBM 360	IBM 370	CDC CYBER 74	CDC 6400 IBM 360 IBM 370 IBM 7094 DEC 10	IBM 370	IBM 370 ¹	IBM 370 Honeywell 60/68/80	ICL 1903 IBM 370	IBM 360
Number of Cards	3300	3048	3630	606	1500	420	1500	4000	184	2000	1857	3000	423	253
Primary Reference(s)	(32)	(37)	(50)	(47)	(60)	(46)	(50)	(50)	(45)	(36)	(34,35)	(34,35)	(41)	(25)
Secondary Reference(s)	(33)	(43,44)	(85)	(87,88)	(85)	(86)	(85)	(85)			(38)	(40)	(42)	(26)
Available ² From	B. Fritz*	T.J. Wolery*	S.V. Mattigod* G. Sposito*	J. Thral-kill*	M.R. Hoffmann*	G.R. Holdren Jr.*	F.M.M. Morel R.E. McDuff*	M.R. Hoffmann*	G.M. Lafon*	R.L. Bassett* Y.K. Kharaka ³	L. M. Plummer*	J.W. Ball* E.A. Jenne*	Geo Abstracts ⁴	T. M. Florence*

¹WATEQF is also available for use on an UNIVAC 1110 computer by contacting M.M. Reddy. ²Coauthors who contributed data given in this and subsequent tables are identified by an asterisk,*. ³U.S. Geological Survey, 345 Middlefield Road, Menlo Park, CA 94025. ⁴Geo Abstracts Limited, University of East Anglia, Norwich NR4 7TJ, England; price \$1.70. WATSPEC calculations on subsequent tables were contributed by T.M.L. Wigley.

Table II
Descriptive Program Features

Program Name	EQUIL	EQ3	GEOCHEM	IONPAIR	MINEQL2	MIRE	MINEQL/REDEQL2	REDEQL2	SEAWAT	SOLMNEQ	WATEQF	WATEQ2	WATSPEC	SIAS/COMICS
Elements ¹	20	18	44	8	38	11	*	44	7	24	19	29	16	*
Aqueous Sp.	93	140	2000	26	*	49	*	266	23	181	105	220	69	*
Gases	3	8	2	1	*	0	*	2	1	3	3	3	2	*
Organics	0	0	889	0	*	1	*	35	0	10	0	12	0	*
Redox Sp.	9	14	20	0	*	0	*	24	0	12	8	12	6	*
Minerals	120	130	185	5	*	variable	*	154	variable	158	101	309	40	*
Activity Coefficients ²	B-dot	B-dot	Davies or B-dot	EDH	Davies	EDH	Davies	Davies	B-dot	B-dot	B-dot or Davies	B-dot or Davies	B-dot or Davies	**
Temperature Range °C	0-300	0-300	25	0-25	25	25	25	25	0-100	0-350	0-100	0-100	0-100	25
Pressure range bars	1	to steam saturation or 500 bars	1	1	1	1	1	1	1-1000	1-1000	1	1	1	1
Iteration and convergence method	explicit equations	Monotone sequences and secant method	Newton-Raphson	Free ion molalities by difference	Newton-Raphson	continued fraction	Newton-Raphson	Newton-Raphson	continued fraction	continued fraction	continued fraction	continued fraction	continued fraction	brute force
Fresh Water ³	<10	5	-	7	†	3	†	32 [†]	-	7	1	2	1	†
Seawater ³	<30	6	156	-	†	5	†	57 [†]	4	11	4	4	5	29

¹excluding those of water. ²EDH - extended Debye Huckel, B-dot - extended Debye Huckel with added B¹I term, Davies - Davies equation. ³Number of iterations where one iteration is defined as one pass through the mass action equations of the aqueous model. *depends on data base. **Constant ionic medium. †depends on initial guess by user.

Table III
Test Case Data

River Water		Seawater*					
Species	mg/l	species	mg/kg soln	mmol/kg H ₂ O	mmol/l	mg/l	GFV
Na	12.	Ca	412.3	10.6617	10.5272	421.931	40.08
K	1.4	Mg	1291.8	55.08565	54.39113	1321.976	24.305
Ca	12.2	Na	10768.	485.4435	479.3230	11019.54	22.9898
Mg	7.5	K	399.1	10.5794	10.4461	408.423	39.0983
Si	8.52	Cl	19353.	565.7625	558.6293	19805.09	35.453
HCO ₃ **	75.2	SO ₄	2712.	29.2615	28.8926	2775.35	96.0576
Cl	9.9	Alkal.†	141.682	2.40659	2.37625	144.992	61.0171
SO ₄	7.7	Br	67.3	0.87294	0.86194	68.872	79.904
B	0.050	Sr	8.14	0.096285	0.095071	8.3302	87.62
Br	0.006	B	4.45	0.42665	0.42127	4.5540	10.81
I	0.0018	SiO ₂	4.28	0.073828	0.072897	4.3800	60.0843
F	0.10	F	1.39	0.075829	0.074873	1.4225	18.9984
PO ₄	0.210	Ba	0.02	0.000151	0.000149	0.0205	137.33
NO ₃	0.898	I	0.062	0.0005064	0.0005000	0.06345	126.9045
NO ₂	0.019	PO ₄	0.06	0.000655	0.000647	0.0614	94.9714
NH ₄	0.144	NO ₃	0.29	0.004847	0.004786	0.2968	62.0049
Fe(II)	0.015	NO ₂	0.02	0.000451	0.000445	0.0205	46.0055
Fe(III)	0.0007	NH ₄	0.03	0.00172	0.00170	0.0307	18.0383
Mn	0.0044	Fe	0.002	0.0000371	0.0000366	0.00205	55.847
Al	0.005	Mn	0.0002	0.00000377	0.00000373	0.000205	54.9380
Zn	0.00049	Al	0.002	0.0000768	0.0000759	0.00205	26.9815
Cd	0.0001	Zn	0.0049	0.00007768	0.00007670	0.005014	65.38
Hg	0.00001	Cd	0.0001	0.000000922	0.000000910	0.000102	112.41
Pb	0.00003	Hg	0.00003	0.000000155	0.000000153	0.0000307	200.59
Cu	0.0005	Pb	0.00005	0.000000250	0.000000247	0.0000512	207.2
Co	0.0005	Cu	0.0007	0.0000114	0.0000112	0.000716	63.546
Ni	0.0018	Co	0.00005	0.000000879	0.000000868	0.0000512	58.9332
Cr	0.0005	Ni	0.0017	0.00002056	0.00002030	0.001740	58.71
Ag	0.00004	Cr	0.0003	0.00000598	0.00000590	0.000307	51.996
Mo	0.0005	Ag	0.00004	0.000000384	0.000000379	0.0000409	107.868
As	0.002	Sb	0.00033	0.000002809	0.000002774	0.0003377	121.75
H ₂ S	0.002	Mo	0.005	0.0000540	0.0000533	0.00512	95.94
DO	10.94	As	0.004	0.0000553	0.0000546	0.000409	74.9216
Eh (V)	0.440	Li	0.181	0.027027	0.026686	0.18523	6.941
DOC	2.5	Rb	0.117	0.0014188	0.0014009	0.11973	85.4678
T°C	9.5	Cs	0.0004	0.00000312	0.00000318	0.00409	132.9054
pH	8.01	DO				6.6	
Density	1.00	Eh (V)	0.500				
		T°C	25.0				
		pH	8.22				
		Density	1.02336				

*Original data are in ppm, except total titration alkalinity which is 2,322 meq/kg soln. All other units have been derived from these values using: density = g/cc, salinity = 35.0‰, kg soln/kg H₂O = 1.03642731, and the values of Gram Formula Weight given. The derived units are given to two additional significant figures. **Titration alkalinity as HCO₃⁻; † Total titration alkalinity is 2,322 meq/kg soln, expressed here as HCO₃⁻. The total titration alkalinity includes carbonate as well as non-carbonate alkalinity. Instead of total alkalinity, the input may be expressed as total inorganic carbon which is 2,022 mmol/kg soln, or 123.377 ppm, 126.259 mg/l, 2.06924 mmol/l, 2.09566 mmol/kg H₂O, as HCO₃⁻. Alternatively total inorganic carbon may be expressed as H₂CO₃* (H₂CO₃* + H₂CO₃* + CO₃²⁻) + HCO₃⁻(total) + CO₃²⁻(total). In this case, H₂CO₃* is 0.742030 ppm, 0.759364 mg/l, 0.0122429 mmol/l; CO₃²⁻ is 0.0123992 mmol/kg H₂O; HCO₃⁻(total) is 109.469 ppm, 112.026 mg/l, 1.83598 mmol/l, 1.85942 mmol/kg H₂O; and CO₃²⁻(total) is 12.9598 ppm, 13.2625 mg/l, 0.221228 mmol/l, 0.223831 mmol/kg H₂O.

Table IV. p(m), -Log Molality, of Selected Major Species in River Water Test Case

PROGRAM	EQUIL	EQ3	IONPAIR	MINEQL2*	MIRE	MINEQL/REDEQL2	REDEQL2	SOLMNEQ	MATEQF	MATEQ2	WATERQ	MATEQ2	WATERQ
Ca ²⁺	3.532	3.529	3.522	3.541	3.530	3.541	3.539	3.527	3.525	3.525	3.525	3.525	3.525
CaSO ₄	5.537	5.578	5.6	5.58†	5.533	5.55†	5.58	5.545	5.578	5.577	5.577	5.577	5.545
CaHCO ₃	5.288	5.343	-	5.17†	5.409	5.22†	5.27	5.518	5.722	5.723	5.723	5.723	5.714
CaCO ₃	5.681	5.933	6.	5.76†	5.732	5.82†	5.27	5.959	6.000	6.001	6.001	6.001	5.992
Mg ²⁺	3.523	3.519	3.518	3.53	3.521	3.54	3.53	3.519	3.519	3.519	3.519	3.519	3.520
MgSO ₄	5.586	5.750	5.7	5.47	5.593	5.45	5.47	5.726	5.767	5.756	5.756	5.756	5.600
MgHCO ₃	5.636	5.491	5.6	5.16	5.568	5.21	5.25	6.027	5.495	5.496	5.496	5.496	5.486
MgCO ₃	5.470	6.133	6.	5.55	5.988	5.61	5.65	5.622	6.156	6.157	6.157	6.157	6.147
Mn ²⁺	3.283	3.282	3.283	3.28	3.284	3.28	3.28	3.283	3.283	3.283	3.283	3.283	3.283
MnSO ₄	6.447	6.819	7.	6.82	7.280	6.81	6.82	6.617	6.819	6.820	6.820	6.820	6.793
MnHCO ₃	6.505	-	-	-	6.500	-	-	6.496	6.495	6.496	6.496	6.496	6.494
K ⁺	4.446	4.446	4.45	4.45	4.444	4.45	4.45	4.446	4.446	4.446	4.446	4.446	4.446
KSO ₄	7.830	7.896	-	7.59	7.819	7.58	7.60	7.942	7.935	7.936	7.936	7.936	7.910
SO ₄ ²⁻	4.129	4.122	4.12	4.14	4.128	4.15	4.14	4.122	4.121	4.121	4.121	4.121	4.164
Cl ⁻	3.401	3.554	3.554	3.55	3.556	3.55	3.55	3.558	3.554	3.554	3.554	3.554	3.554
HCO ₃ ⁻	2.924	2.920	2.915	2.93	2.919	2.91	2.93	2.918	2.917	2.917	2.917	2.917	2.917
CO ₃ ²⁻	5.164	5.346	5.3	5.01	5.168	5.11	5.12	5.328	5.334	5.333	5.333	5.333	5.333
B(OH) ₃	5.361	-	-	5.37	-	-	-	5.379	5.354	5.355	5.355	5.355	5.355
B(OH) ₄ ⁻	6.570	-	-	6.41	-	-	6.42	6.726	6.690	6.711	6.711	6.711	6.686
Br ⁻	-	-	-	7.12	-	-	7.12	-	7.124	7.124	7.124	7.124	7.120
F ⁻	5.281	-	-	5.29	-	-	5.29	5.282	5.284	5.284	5.284	5.284	-
H ₄ SiO ₄	3.528	-	-	3.53†	-	-	3.53†	3.523	3.851	3.520	3.520	3.520	3.520
K ⁺	7.988	7.989	-	-	-	8.01	-	7.990	7.987	7.987	7.987	7.987	7.987
OH ⁻	5.966	6.518	6.	5.94	5.967	-	5.95	6.525	6.502	6.501	6.501	6.502	6.502
Ionic Strength	.00238	.00239	.00240	.00300	.0024	-	.00300	.00240	.00240	.00241	.00241	.00241	.00239

Table V
p(m), - Log Molality, of Selected Minor Species in River Water Test Case

PROGRAM	EQUIL	EQ3	IONPAIR	MINEQL2*	MIRE	REDEQL2	SOLMNEQ	WATEQF	WATEQ2	WATSPEC
Cr ³⁺	-	-	-	20.02	-	16.15	-	-	-	-
Mn ²⁺	7.100	8.205	-	7.14	7.138	7.13	7.099	7.119	7.119	-
MnOH ⁺	-	11.403	-	9.28	9.804	9.28	-	10.264	10.347	-
MnSO ₄ ^o	9.166	10.383	-	9.18	9.213	9.18	9.289	9.864	9.864	-
Fe ²⁺	6.711	6.639	-	15.18†	6.896	15.18†	8.389	12.167	6.579	11.953
FeOH ⁺	7.075	7.428	-	15.82†	6.855	15.83†	26.711	14.257	8.669	13.860
Fe ³⁺	19.04	16.212	-	20.88†	-	20.640†	25.811	17.635	18.596	17.408
Fe(OH) ₄ ⁻	-	8.072	-	10.44†	-	10.35†	18.172	6.989	8.340	7.028
Ni ²⁺	-	-	-	7.59	-	7.93	-	-	8.892	-
NiCO ₃ ^o	-	-	-	-	-	7.76	-	-	7.539	-
Cu ²⁺	10.15	8.763	-	9.67	-	10.42	14.772	-	11.293	-
Cu(OH) ₂ ^o	-	-	-	13.68	-	13.22	-	-	9.045	-
Ag ⁺	-	9.660	-	-	-	15.51	9.651	-	15.891	-
AgHS ^o	-	-	-	-	-	-	-	-	9.432	-
Zn ²⁺	8.131	8.129	-	8.15	-	8.48	7.129	-	8.504	-
ZnCO ₃ ^o	-	-	-	-	-	8.51	-	-	8.720	-
Zn(HS) ₂ ^o	-	-	-	-	-	-	-	-	8.790	-
Cd ²⁺	-	-	-	9.10	-	9.41	-	-	11.612	-
CdOH ⁺	-	-	-	10.15	-	11.46	-	-	12.651	-

CHEMICAL MODELING IN AQUEOUS SYSTEMS

CdHS ⁺	-	-	-	-	-	-	-	-	9.078	-
Hg ²⁺	-	16.875	-	21.07	-	20.15	41.872	-	-	-
Al ³⁺	15.69	13.697	-	17.49†	-	17.164†	13.598	13.908	15.565	14.778
Al(OH) ₄ ⁻	7.090	6.732	-	8.66	-	8.37†	6.765	6.741	8.406	6.733
Pb ²⁺	9.845	14.380	-	12.07	-	11.93	9.843	-	11.749	-
PbOH ⁺	-	-	-	11.21	-	11.68	-	-	10.378	-
PbCO ₃ ^o	-	9.839	-	9.89	-	9.86	-	-	10.025	-
NO ₃ ⁻	4.839	-	4.84	-	-	-	4.839	4.839	4.839	4.839
NH ⁺	5.098	-	-	5.14	-	5.13	5.105	5.106	5.106	10.392
PO ₄ ³⁻	10.03	-	-	11.41†	-	11.40†	10.189	10.156	10.156	-
HPO ₄ ²⁻	5.818	-	-	7.07†	5.773	7.16†	5.813	5.793	5.793	-
H ₂ PO ₄ ⁻	6.694	-	-	7.78†	6.654	8.06†	6.622	6.625	6.625	-
HAsO ₄ ²⁻	-	-	-	-	-	-	13.990	-	7.595	-
H ₂ AsO ₄ ⁻	-	-	-	-	-	-	15.046	-	8.885	-
S ²⁻	-	17.140	-	-	-	-	16.489	12.613	12.870	12.615
HS ⁻	-	7.268	-	-	-	-	7.299	7.288	7.544	7.288
H ₂ S ^o	-	8.076	-	-	-	-	8.071	8.146	8.403	8.146
I ⁻	-	-	-	7.785	-	7.86	-	-	-	-

*Calculated at 25°C. †MINEQL2 and REDEQL2 results were calculated in such a way that the solution was equilibrated with supersaturated phases. P, Ca, Fe, Al and Si species are not exactly comparable to the same species from the other programs because of this equilibration process, and, of course, all species have been affected to some degree.

38. NONDSTROM ET AL.

Comparison of Computerized Chemical Models

Table VI
p(m), -Log Molality, of Selected Major Species in Sea Water Test Case

PROGRAM	MINEQL/														
	EQUIL	EQ3	GEOCHEM	K+K ⁺	MINEQL2	MIRE	REDEQL2	REDEQL2	SEAWAT	SIAS	SOLMNEQ	WATEQF	WATEQ2	WATSPEC	
Ca ²⁺	2.013	2.027	2.21	2.024	2.12†	2.074	2.03	2.11†	2.053	2.058	2.013	2.024	2.025	2.023	
CaSO ₄ ⁰	3.062	2.928	3.12	3.046	3.00†	2.744	2.97	3.00†	2.764	2.781	3.056	2.940	2.938	2.947	
CaHCO ₃ ⁺	4.261	4.234	4.48	4.504	4.92†	4.366	4.26	4.84†	4.242	4.285	4.261	4.481	4.449	4.465	
CaCO ₃ ⁰	4.636	4.540	4.59	4.755	5.30†	4.734	4.63	5.30†	4.715	4.365	4.635	4.649	4.616	4.665	
CaCl ⁺	-	-	2.46	-	-	-	-	-	-	-	-	-	-	-	
Mg ²⁺	1.304	1.319	1.46	1.328	1.34	1.322	1.33	1.34	1.347	1.357	1.299	1.311	1.312	1.310	
MgSO ₄ ⁰	2.305	2.175	2.47	2.190	2.11	2.299	2.17	2.13	2.008	2.080	2.360	2.235	2.222	2.241	
MgHCO ₃ ⁺	3.777	3.554	3.83	3.405	4.14	3.676	3.60	4.06	3.588	2.684	3.834	2.655	3.624	3.597	
MgCO ₃ ⁰	3.619	3.940	4.14	3.745	4.32	3.684	3.67	4.32	4.121	4.664	3.689	4.045	4.014	4.062	
MgCl ⁺	-	-	1.79	-	-	-	-	-	-	-	-	-	-	-	
Na ⁺	0.336	0.320	0.41	0.328	0.34	0.335	0.33	0.34	0.321	0.314	0.336	0.320	0.320	0.323	
NaSO ₄ ⁰	1.964	2.208	1.94	2.286	2.18	2.716	2.20	2.19	2.107	-	1.965	2.178	2.195	2.146	
NaHCO ₃ ⁰	3.873	-	3.40	3.466	-	3.851	3.84	-	-	-	3.860	3.785	3.752	3.807	
K ⁺	1.982	1.983	2.04	2.007	2.01	2.000	1.99	2.01	1.981	1.976	1.982	1.983	1.983	1.985	
KSO ₄ ⁰	3.839	3.748	3.76	3.802	3.45	3.789	3.67	3.46	3.916	-	3.871	3.768	3.766	3.736	
Cl ⁻	0.257	0.247	0.33	0.25	0.25	0.265	0.25	0.25	0.247	0.253	0.256	0.247	0.247	0.249	
SO ₄ ²⁻	1.906	1.823	2.11	1.804	1.91†	1.836	1.84	1.89†	2.009	1.723	1.881	1.811	1.808	1.822	
HCO ₃ ⁻	2.884	2.816	2.87	2.792	3.56	2.815	2.90	3.39	2.808	-	2.885	2.825	2.836	2.845	
CO ₃ ²⁻	4.419	4.371	4.48	4.622	4.91	4.415	4.46	4.89	4.369	5.507	4.484	4.422	4.566	4.443	
B(OH) ₃ ⁰	3.435	-	3.51	-	3.49	-	3.45	3.48	-	-	3.506	3.430	3.431	3.481	
B(OH) ₄ ⁻	4.226	-	4.23	-	4.06	-	4.20	4.10	-	-	4.234	4.257	4.255	4.015	
Br ⁻	-	-	3.06	-	3.07	-	-	3.07	3.059	3.065	-	3.059	3.059	3.059	

CHEMICAL MODELING IN AQUEOUS SYSTEMS

F ⁻	4.228	-	4.36	-	4.39	-	-	4.38	-	4.411	4.379	4.410	4.410	-
MgF ⁺	4.792	-	4.53	-	4.56	-	-	4.58	-	-	4.464	4.442	4.443	-
Sr ²⁺	4.016	-	4.28	-	4.13†	-	-	4.119†	-	-	4.045	4.016	4.016	4.016
H ₄ SiO ₄ ⁰	4.155	4.159	4.16	-	4.19†	-	-	4.17†	-	-	4.161	4.145	4.145	4.147
H ⁺	8.125	8.126	8.15	7.966	-	-	-	-	8.095	-	8.125	8.093	8.093	8.098
OH ⁻	5.603	5.606	5.65	6.038	5.46	5.552	-	5.54	5.613	-	5.601	5.660	5.660	5.571
Ionic Strength	0.663	0.6772	0.5298	-	0.65	0.655	-	0.65	0.6595	-	0.6662	0.6801	0.6799	0.6770

*Karpov and Kaz'min (1972) using Gibbs free energy minimization on a similar seawater. †MINEQL2 and REDEQL2 results were calculated in such a way that the solution was equilibrated with supersaturated phases. Si, Al, Fe, Ca, Sr, Ba, Zn SO₄, and PO₄ species are not exactly comparable to the same species from the other programs because of this process, and, of course, all species have been affected to some degree.

38. NORDSTROM ET AL.

Comparison of Computerized Chemical Models 875

Table VII
p(m), -Log Molality, of Selected Minor Species in Seawater Test Case

PROGRAM	EQUIL	EQ3	GEOCHEM	MINEQL2	MIRE	REDEQL2	SIAS	SOLMHEQ	WATEQF	WATEQ2	WATSPEC
Li ⁺	4.572	-	4.66	-	-	-	-	4.568	4.573	4.573	4.573
Rb ⁺	-	-	5.87	-	-	-	-	-	-	5.848	-
Cs ⁺	-	-	8.56	-	-	-	-	-	-	8.506	-
Ba ²⁺	-	-	6.93	8.03†	-	8.01†	-	6.857	6.821	6.821	6.821
Cr ³⁺	-	-	25.63	28.34	-	24.55	-	-	-	-	-
Mn ²⁺	8.456	9.287	9.33	8.96	8.592	8.94	-	8.478	8.654	8.654	-
MnCl ⁺	-	-	10.26	8.74	9.067	8.75	-	29.376	8.880	8.881	-
Fe ³⁺	18.740	17.466	22.94	20.71†	-	20.26†	-	-	17.897	17.897	17.714
Fe(OH) ₃ ⁰	-	-	11.28	17.10†	-	24.14†	-	-	8.071	8.071	7.805
Fe(OH) ₄ ⁻	-	7.439	12.41	9.96†	-	9.94†	-	-	7.664	7.664	7.678
Ni ²⁺	-	-	9.23	7.77	-	7.92	7.834	-	-	8.813	-
NiCl ₂ ⁰	-	-	9.74	-	-	8.10	-	-	-	9.335	-
NiCO ₃ ⁰	-	-	7.91	5.75	-	8.61	-	-	-	7.590	-
Cu ²⁺	13.152	9.056	11.21	11.35	-	11.32	9.579	-	-	10.153	-
Cu(OH) ₃ ⁰	-	-	12.40	3.22	-	9.06	-	-	-	7.985	-
CuCO ₃ ⁰	-	-	10.01	10.82	-	10.80	-	-	-	9.070	-
Ag ⁺	-	14.797	16.79	16.82	-	16.79	-	14.477	-	14.394	-
AgCl ₄ ³⁻	-	9.517	12.48	12.08	-	12.05	-	9.617	-	9.684	-
Zn ²⁺	7.323	7.346	8.35	7.74†	-	8.06†	7.690	7.321	-	7.547	-
ZnCO ₃ ⁰	-	-	7.33	-	-	8.95†	-	-	-	7.894	-
Cd ²⁺	-	-	11.11	10.59	-	10.70	10.606	-	-	11.257	-
CdCl ⁺	-	-	9.99	9.47	-	9.41	-	-	-	9.371	-

CHEMICAL MODELING IN AQUEOUS SYSTEMS

CdCl ₂ ⁰	-	-	9.94	9.34	-	9.48	-	-	-	9.369	-
Hg ²⁺	-	23.310	-	-	-	-	-	23.426	-	-	-
HgCl ₃ ⁻	-	9.816	-	-	-	-	-	9.965	-	-	-
Al ³⁺	15.963	16.076	16.37	16.67†	-	16.15†	-	19.277	15.956	16.091	16.996
Al(OH) ₃ ⁰	7.600	-	7.72	-	-	7.58†	-	-	-	7.665	-
Al(OH) ₄ ⁻	7.287	7.114	7.25	7.53†	-	7.32†	-	10.611	7.115	7.259	7.114
Pb ²⁺	10.446	13.746	11.68	-	-	-	-	10.442	-	11.335	-
PbCl ₂ ⁰	10.380	13.591	11.41	-	-	-	-	0.372	-	11.017	-
PbCO ₃ ⁰	-	9.602	10.09	-	-	-	-	9.743	-	9.743	-
NO ₃ ⁻	5.315	-	5.30	-	-	-	-	-	5.315	5.314	5.315
PO ₄ ³⁻	9.979	-	10.48	11.81†	-	11.76†	-	10.126	10.482	10.480	-
HPO ₄ ²⁻	6.858	-	7.02	8.48†	6.673	8.43†	-	6.857	6.989	6.988	-
H ₂ PO ₄ ⁻	8.474	-	8.49	9.93†	8.295	10.06†	-	8.443	8.382	8.381	-
AsO ₄ ³⁻	-	-	11.01	-	-	-	-	-	-	10.007	-
HAsO ₄ ³⁻	-	-	8.45	-	-	-	-	-	-	7.264	-
I ⁻	-	-	6.30	6.30	-	6.21	-	-	-	6.296	-

†MINEQL2 and REDEQL2 results were calculated in such a way that the solution was equilibrated with supersaturated phases. Si, Al, Fe, Ca, Sr, Ba, Zn, SO₄, and PO₄ species are not exactly comparable to the same species from the other programs because of this process, and of course, all species have been affected to some degree.

38. NORDSTROM ET AL.

Comparison of Computerized Chemical Models

Table VIII
Activity Coefficients of Selected Major Species in Sea Water

PROGRAM	EQUIL	EQ3	MIRE	SEAWAT	SOLMNEQ	WATEQF	WATEQ2
Ca ²⁺	0.245	0.245	0.231	0.245	0.244	0.249	0.249
CaSO ₄	1.172	1.000	0.507	1.150	1.180	1.170	1.170
CaHCO ₃ ⁺	0.714	0.714	0.589	0.669	0.737	0.747	0.747
CaCO ₃	1.172	1.000	1.123	1.150	1.180	1.170	1.170
Mg ²⁺	0.315	0.315	0.296	0.314	0.263	0.288	0.288
MgSO ₄	1.172	1.000	1.323	1.150	1.180	1.170	1.170
MgHCO ₃ ⁺	0.671	0.670	0.589	0.669	0.670	0.747	0.747
MgCO ₃	1.172	1.000	0.387	1.150	1.180	1.170	1.170
Na ⁺	0.671	0.670	0.631	0.688	0.670	0.706	0.706
NaSO ₄	0.683	0.682	0.589	0.669	0.720	0.747	0.747
NaHCO ₃	1.172	-	1.123	1.150	1.180	1.170	1.170
K ⁺	0.626	0.626	0.589	0.625	0.626	0.622	0.622
KSO ₄	0.650	0.647	0.589	0.669	0.720	0.747	0.747
Cl ⁻	0.627	0.626	0.589	0.625	0.626	0.622	0.622
SO ₄ ²⁻	0.618	0.167	0.158	0.167	0.167	0.181	0.181
HCO ₃ ⁻	0.690	0.690	0.631	0.669	0.720	0.675	0.747
CO ₃ ²⁻	0.188	0.187	0.195	0.190	0.222	0.207	0.311
B(OH) ₃ ⁰	1.172	-	-	-	1.180	1.170	1.170
B(OH) ₄ ⁻	0.671	-	-	-	0.605	0.747	0.747
Br ⁻	-	-	-	0.625	-	0.747	0.747
F ⁻	0.650	-	-	-	0.649	0.747	0.747
MgF ⁺	-	-	-	-	0.689	0.747	0.747
Sr ²⁺	0.207	-	-	-	0.207	0.311	0.311
H ₄ SiO ₄ ⁰	1.000	-	1.123	-	1.180	1.170	1.170
H ⁺	0.804	0.805	-	0.750	0.804	0.747	0.747
OH ⁻	0.650	0.649	0.589	0.685	0.649	0.747	0.747
Ionic Strength	0.663	0.677	0.655	0.660	0.666	0.680	0.680

Table IX
Saturation Index for Selected Minerals in River Water Test Case

MINERAL	FORMULA	EQUIL	EQ3	IONPAIR	MIRE	SOLMNEQ	WATEQF	WATEQ2	WATSPEC
Calcite	CaCO ₃	-0.51	-0.585	-0.673	-0.461	-0.765	-0.634	-0.634	-0.63
Dolomite	CaMg(CO ₃) ₂	-0.73	-0.248	-1.340	-0.730	-1.329	-1.384	-1.386	-1.38
Siderite	FeCO ₃	-1.37	+0.456	-	-2.329	-3.377	-7.347	-1.760	-7.13
Rhodochrosite	MnCO ₃	-1.81	-3.225	-	-2.097	-2.136	-2.180	-2.180	-
Gypsum	CaSO ₄ ·2H ₂ O	-3.00	-2.962	-	-3.081	-2.942	-3.057	-2.969	-3.25
Celestite	SrSO ₄	-	-	-	-	-	-	-	-
Hydroxyapatite	Ca ₅ (PO ₄) ₃ OH	+2.82	-	-	+5.891	+5.046	-1.784	-1.722	-
Fluorite	CaF ₂	-4.39	-	-	-	-3.338	-3.079	-3.074	-
Ferric Hydrox. (Am)Fe(OH) ₃		-	-	-	-	-7.584	+1.304	-	-
Goethite	Fe(OH) ₃	+5.59	-	-	-	-1.484	+7.810	+6.843	+5.06
Hematite	Fe ₂ O ₃	+8.11	+18.332	-	-	-3.252	+15.144	+13.223	+13.52
Gibbsite (crypt.) Al(OH) ₃		-0.08	+1.948	-	-	-0.058	-0.336	-1.989	-1.19
Birnessite	MnO ₂	-	-	-	-	-	-4.114	-4.114	-
Chalcedony	SiO ₂	-	+0.490	-	-	+0.217	-0.142	+0.189	-
Quartz	SiO ₂	+0.47	+0.776	-	-	+0.697	+0.405	+0.736	+0.74
Kaolinite	Al ₂ Si ₂ O ₅ (OH) ₄	+1.83	+5.826	-	-	-	+1.638	-1.021	+2.32
Sepiolite	Mg ₃ Si ₇ O ₁₇ ·5(OH)·3H ₂ O	-4.55	-	-	-	-5.734	-3.699	-	-
FeS Amorphous	FeS	-	-	-	-	-	-7.644	-2.313	-
Mackinawite	FeS	-	-	-	-	-	-6.928	-1.560	-

Table X
Saturation Index for Selected Minerals in Seawater Test Case

MINERAL	FORMULA	EQUIL	EQ3	GEOCHEM	MIRE	SEAMAT	SOLMNEQ	WATEQF	WATEQ2	WATSPEC	ACH1	RMR2
Calcite	CaCO ₃	+0.60	+0.806	+0.67	+0.621	+0.631	+0.597	+0.742	+0.774	+0.72	+0.568 to +0.674	-
Dolomite	CaMg(CO ₃) ₂	+2.30	+3.439	+1.79	+2.277	+2.305	+2.219	+2.330	+2.394	+2.30	-	-
Siderite	FeCO ₃	-2.65	-10.276	-12.42	-	-	-6.691	-9.006	-8.973	-8.83	-	-
Rhodochrosite	MnCO ₃	-3.57	-4.444	-4.45	-4.077	-	-3.709	-3.727	-3.695	-	-	-
Gypsum	CaSO ₄ ·2H ₂ O	-0.47	-0.399	-0.76	-0.487	-0.840	-0.441	-0.439	-0.348	-0.60	-	-0.582
Celestite	SrSO ₄	-	-	-0.13	-	-	-0.988	-0.610	-0.609	-1.32	-	-
Barite	BaSO ₄	-	-	+1.12	-	-	-0.501	+0.097	+0.097	-0.34	-	-
Hydroxapatite	Ca ₅ (PO ₄) ₃ OH	+4.16	-	+3.53	+7.642	-	+7.140	+0.605	+0.670	-	-	-
Fluorite	CaF ₂	-1.61	-	-2.93	-	-	-1.048	-0.742	-0.751	-	-	-
Ferric Hydr. (Am)	Fe(OH) ₃	-	-	-2.93	-	-	-	+0.712	+0.706	-	-	-
Goethite	FeO(OH)	+5.64	-	+2.58	-	-	-	+7.809	+7.803	+5.04	-	-
Hematite	Fe ₂ O ₃	+8.21	+16.518	+5.65	-	-	-	+15.228	+15.229	+13.54	-	-
Gibbsite Crypt.	Al(OH) ₃	-0.63	+0.216	-0.57	-	-	-4.954	-1.685	-1.817	-2.69	-	-
Birnessite	MnO ₂	-	-	-1.01	-	-	-	-2.993	-2.993	-	-	-
Manganite	MnO(OH)	-	-	-2.03	-	-	-	-1.335	-1.336	-	-	-
Chalcedony	SiO ₂	-	-0.415	-1.41	-	-	-0.522	-0.537	-0.537	-0.54	-	-
Quartz	SiO ₂	-0.14	-0.143	-0.04	-	-	-0.092	-0.055	-0.054	-0.06	-	-
Kaolinite	Al ₂ Si ₂ O ₅ (OH) ₄	-0.47	+0.645	-0.67	-	-	-2.108	-2.108	-2.384	-2.24	-	-
Sepiolite Cryst.	Mg ₂ Si ₃ O ₇ ·5(OH)·3H ₂ O	-1.96	-	+1.09	-	-	-1.908	+1.059	+1.034	-	-	-

¹ Apparent constant method (see text for explanation). ² Calculated from the equations of Reilly, Wood and Robinson (6) by M. Lafon.

through the approach offered by Haas and Fisher (77) but it will take some time to compile and evaluate the appropriate data. In the meantime the lack of carefully evaluated thermodynamic data will continue to be the most serious limitation for any type of chemical modeling.

Thirdly, another corollary of the first limitation, is the inconsistency and inadequacy of activity coefficient equations. Some models use the extended Debye-Huckel equation (EDH), others the extended Debye-Huckel with an additional linear term (B-dot, 78, 79) and others the Davies equation (some with the constant 0.2 and some with 0.3, 80). The activity coefficients given in Table VIII for seawater show fair agreement because seawater ionic strength is not far from the range of applicability of the equations. However, the accumulation of errors from the consideration of several ions and complexes could lead to serious discrepancies. Another related problem is the calculation of activity coefficients for neutral complexes. Very little reliable information is available on the activity of neutral ion pairs and since these often comprise the dominant species in aqueous systems their activity coefficients can be an important source of uncertainty.

The fourth limitation is the assumption made about the redox state of aqueous systems. The distribution of redox species depends on what redox potential is assumed to dominate the chemical equilibrium. The possible alternatives include the Fe²⁺/Fe³⁺ couple, the S²⁻/SO₄²⁻ couple, the O₂/H₂O couple, the O₂/H₂O₂ couple, the NO₃⁻/NH₄⁺ couple and the redox potential measured with a platinum electrode. The wide range of values for iron, manganese, chromium and arsenic species is partly due to the inherent redox assumptions. To examine how different redox controls affect the distribution of species while other factors are kept constant, several redox options were computed on WATEQ2 for both test cases. These results are shown in Table XI. The redox elements, iron and arsenic, can be distributed according to several imposed redox potentials given total concentrations of iron and arsenic. Ferrous and ferric ions along with the two dominant forms of oxidized and reduced arsenic were computed by all the possible redox options. The range of concentrations of these species is several orders of magnitude and includes most of the values listed in Tables V and VII. If the application of a chemical model is to interpret natural water chemistry, including redox reactions, then individual redox elements such as total ferrous and total ferric should be analyzed separately when possible rather than assuming that they can be distributed according to some other equilibrium. Homogeneous redox equilibrium may not be often obtained in real systems (81) and imposed redox equilibria may not represent a realistic distribution of species.

A fifth factor is the total number of complexes considered by an aqueous model. If one model has 2 or 3 times as

Table XI

Variations in the distribution of selected redox species (in μm) caused by changing the imposed redox potential.

River Water Test Case

Imposed Redox Potential	Implied Eh (volts)	Fe ²⁺	Fe ³⁺	H ₂ AsO ₃ ⁰	HA ₂ O ₄ ²⁻
Pt Eh	0.440	11.78	17.25	25.80	7.60
O ₂ /H ₂ O	0.783	17.89	17.25	38.03	7.60
O ₂ /H ₂ O ₂	0.141	6.81	17.61	15.14	7.60
NO ₃ ⁻ /NO ₂ ⁻	0.445	11.87	17.25	25.98	7.60
NO ₃ ⁻ /NH ₄ ⁺	0.328	9.78	17.25	21.81	7.60
S ²⁻ /SO ₄ ²⁻	-0.532	6.56	29.36	7.59	24.04
Fe ²⁺ /Fe ³⁺	0.073	6.58	18.50	12.72	7.60

Seawater Test Case

Imposed Redox Potential	Implied Eh (volts)	Fe ²⁺	Fe ³⁺	H ₂ AsO ₃ ⁰	HA ₂ O ₄ ²⁻
Pt Eh	0.550	13.94	17.90	29.17	7.26
O ₂ /H ₂ O	0.731	17.85	17.90	36.98	7.26
O ₂ /H ₂ O ₂	0.133	7.94	18.09	16.76	7.26
NO ₃ ⁻ /NO ₂ ⁻	0.390	12.08	17.90	25.45	7.26
NO ₃ ⁻ /NH ₄ ⁺	0.269	10.04	17.90	21.36	7.26

many metal-ligand complexes as another model then it will have a lower concentration of free ligand, assuming negligible differences in the data base. For example, the inclusion of the calcium and magnesium chloride complexes by GEOCHEM tends to lower the free calcium, magnesium and chloride ion concentrations below those of the other models.

A sixth source of difference, which was unavoidable in preparation of the test cases, is the various ways each program handles the carbonate system. From a practical standpoint, the inorganic carbon system of natural waters is usually determined from the titration alkalinity. Because the titration alkalinity includes both carbonate and non-carbonate alkalinity, the titration alkalinity must be corrected for non-carbonate alkalinity. Most models correct for the presence of H₂BO₃ and H₃SiO₄ but many other minor species should be considered and there is no general agreement as to the precise correction for non-carbonate alkalinity. In devising the correction used originally in WATEQ, Truesdell and Jones also

considered the possibility that some non-carbonate alkalinity species were kinetically slow to react in the titration and thus were not included in the titration alkalinity. Even if we could agree on which species to subtract from the titration alkalinity, the computed carbonate system is still dependent on the equilibrium constants and activity coefficients used by the model to compute the actual concentrations of non-carbonate alkalinity species.

Some aqueous models accept only total inorganic carbon rather than titration alkalinity or carbonate alkalinity. For this reason, the sea water analysis of Table III includes total inorganic carbon which was calculated from pH, total alkalinity and salinity using the apparent sea water constants of Mehrbach et al. (82) for the dissociation of carbonic acid and the boric acid dissociation constant of Lyman (83), as expressed by Li et al. (84).

Certainly, there are differences in aqueous models in current use and the carbonate calculations will depend in part on whether the source of carbon data was total alkalinity or total inorganic carbon from Table III. For example, using the program WATEQF and data in ppm from Table III, Table XII compares some computed parameters of the carbonate system of seawater using total alkalinity and total inorganic carbon from Table III.

Table XII

Comparison of carbonate parameters computed by WATEQF in Seawater Test Case

Inorganic Carbon Data Source

Computed Parameter (= 141.682 ppm as HCO ₃ ⁻)	Total Alkalinity	Total Inorganic Carbon (= 2.09566 x 10 ⁻³ m)
Total carbon (m)	2.1421 x 10 ⁻³	2.0957 x 10 ⁻³
mHCO ₃ ⁻	1.4961 x 10 ⁻³	1.4636 x 10 ⁻³
mCO ₃ ²⁻	3.7880 x 10 ⁻⁵	3.7057 x 10 ⁻⁵
log ³ P _{CO₂}	-3.399	-3.409
SI calcite	0.7418	0.7323

The differences shown in Table XII are really quite small and well within the uncertainties of the thermodynamic data of the aqueous model. The close agreement shown in Table XII indicates that the carbonate system of WATEQF is reasonably compatible with the apparent constants of Mehrbach et al. (82) and Lyman (83). However, in comparing results in the carbonate system computed by other aqueous models, there is a

potential for differences depending on the compatibility of the equilibrium constants and activity coefficients used with the apparent constant approach for seawater.

A seventh limitation is the fact that not all of the aqueous models compute temperature corrections. The programs of the REDEQL school and those used in analytical chemistry contain a data base of equilibrium constants at 25°C and are not as reliable at other temperatures. Since the river water test case was given a temperature of 9.5°C there will be some differences between programs that correct for temperature and those that do not. The temperature correction can cause substantial changes in computed results when interpreting the chemistry of natural waters because these systems commonly vary both diurnally and seasonally over a large range in temperature and because many equilibrium constants are strongly temperature dependent.

If all of these limitations were overcome, the aqueous models described here should give consistent results. To reemphasize, the largest single source of discrepancy is the thermodynamic data base used by each model. This limitation is not apparent among the major species in a dilute solution but as the ionic strength increases and/or the concentration of the constituent decreases, the discrepancies markedly increase. This problem becomes particularly acute for trace elements where apparently small changes in equilibrium constants or pH or redox potential or temperature may produce very large changes in trace element speciation.

The effect of the thermodynamic data is particularly striking from a comparison of saturation indices in Tables IX and X. The mineral showing the best agreement in both test cases is calcite which would be expected since its properties have been extensively studied, especially in the marine environment. Using the apparent constant method the SI of calcite in seawater varies from 0.568 to 0.674 depending on the choice of data. The low value is that of Berner (90) which is compatible with the apparent dissociation constants for carbonic acid in seawater of Lyman (83). The high value is from Ingle et al. (88) which is compatible with the dissociation constants of Mehrbach et al. (82). In the river water test case gypsum SI values show very good agreement but for many other minerals there is considerable disagreement of one order of magnitude or more. SI values for several minerals show both supersaturation and undersaturation and these conditions are particularly striking for hydroxyapatite, goethite, hematite and kaolinite. In the seawater test case gypsum does not show as good agreement as in river water with values ranging from -0.35 to -0.84. Many minerals again show more than an order of magnitude difference in SI values. From an examination of these tables it should be clear that any interpretation of mineral saturation states in an aquatic environment depends

greatly on the chosen chemical model which, in turn, depends upon the reliability of the thermodynamic data base and any inherent assumptions of the behavior of electrolyte solutions.

Summary

In this review over 30 computerized chemical models have been described which can calculate the distribution of species in an aqueous system at equilibrium. Every computerized model was developed for somewhat different purposes and there is no general purpose model which can be used for all of the applications described in this report. However, an attempt has been made to point out the major differences between models as a guide to researchers interested in chemical modeling. The applications include titration simulation, solubility testing, adsorption modeling, ion exchange modeling, and progressive mass transfer reactions in heterogeneous systems. Two hypothetical test cases: a dilute river water analysis and a seawater analysis were run on a total of 13 different programs to determine the distribution of species and the saturation indices for several minerals. A comparison of these results demonstrate generally good agreement for the major species and rather poor agreement for the minor species. The major source of discrepancy is the thermodynamic data base used by the various models. Other important limitations include the number of complexes in each model, the form of the activity coefficient equation, the redox assumptions, the form of the alkalinity input and the non-carbonate alkalinity correction, and temperature and pressure corrections. The discrepancies in the test case results indicate that a great deal of caution must be exercised when interpreting aqueous chemical equilibria by a chemical modeling approach. More attention should be paid to the assumptions of a model and a great deal more work is needed on the evaluation of thermodynamic data in order to provide a consistent set of values.

Abstract

A survey of computer programs which are currently being used to calculate the distribution of species in aqueous solutions, especially natural waters, has been made in order to 1) provide an inventory of available programs with a short description of their uses, 2) compare the consistency of their output for two given test solutions and 3) identify major weaknesses or problems encountered from their use. More than a dozen active programs which can be used for distribution of species and activity calculations for homogeneous equilibria among the major anions and cations of natural waters have been inventoried. Half of these programs can also accept several trace elements including Fe, Al, Mn, Cu, Ni, Zn, Cd, Pb, Ag, Hg, As,

Ba, Sr, and B. Consistency between programs was evaluated by comparing the log of the molal concentrations of free ions and complexes for two test solutions: a hypothetical seawater analysis and a hypothetical river water analysis. Comparison of the free major ion concentrations in the river water test case shows excellent agreement for the major species. In the seawater test case there is less agreement and for both test cases the minor species commonly show orders of magnitude differences in concentrations. These differences primarily reflect differences in the thermodynamic data base of each chemical model although other factors such as activity coefficient calculations, redox assumptions, temperature corrections, alkalinity corrections and the number of complexes used all have an affect on the output.

Literature Cited

1. Leggett, D. J. Machine computation of equilibrium concentrations - some practical considerations, Talanta **24**, 535-542 (1977).
2. Perrin, D.D. Recent applications of digital computers in analytical chemistry, Talanta **24**, 339-345 (1977).
3. Bjerrum, N. Ionic association I. Influence of ionic association on the activity of ions at moderate degrees of association, Kgl. Danske Videnskab. Selskab. Math-fys. Medd. **7**, 1-48 (1926).
4. Fuoss, R. M. Properties of electrolyte solutions, Chem. Rev. **17**, 27-42 (1935).
5. Bockris, J. O'M. and Reddy, A. K. N. "Modern Electrochemistry," 622 p. Plenum Press, New York, 1970.
6. Reilly, P. J., Wood, R. H. and Robinson, R. A. Prediction of osmotic and activity coefficients in mixed-electrolyte solutions, J. Phys. Chem. **75**, 1305-1315 (1971).
7. Othmer, H. G. Nonuniqueness of equilibria in closed reacting systems, Chem. Eng. Sci. **31**, 993-1003 (1976).
8. Caram, H. S. and Scriven, L. E. Nonunique reaction equilibria in non-ideal systems, Chem. Eng. Sci. **31**, 163-168 (1976).
9. Zeleznik, F. J. and Gordon, S. Calculation of complex chemical equilibria, Ind. Eng. Chem. **60**, 27-57 (1968).
10. Van Zeggeren, F. and Storey, S. H. "The Computation of Chemical Equilibria," 176 p. Cambridge University Press, London, England, 1970.
11. Brinkley, S. R. Notes on the condition of equilibrium for systems of many constituents, J. Chem. Phys. **14**, 563-564 (1946).
12. Brinkley, S. R., Calculation of the equilibrium composition of systems of many constituents, J. Chem. Phys. **15**, 107-110 (1947).

13. Kandiner, H. J. and Brinkley, S. R. Calculation of complex equilibrium relations, Ind. Eng. Chem. **42**, 850-855 (1950).
14. Feldman, H. F., Simons, W. H. and Bienstock, D. Calculating equilibrium compositions of multicomponent, multiphase, chemical reacting systems, U.S. Bur. Mines Rep. Invest. **7257**, 22 p. (1969).
15. Crear, D. A method for computing multicomponent chemical equilibria based on equilibrium constants, Geochim. Cosmochim. Acta **39**, 1375-1384 (1975).
16. Acton, F. S. "Numerical Methods that Work," 541 p. Harper and Row, New York, 1970.
17. White, W. B., Johnson, S. M. and Dantzig, G. B. Chemical equilibrium in complex mixtures, J. Chem. Phys. **28**, 751-755 (1958).
18. Dayhoff, M.O., Lippincott, E. R., Eck, R. V. and Nagarajan, G. Thermodynamic equilibrium in prebiological atmospheres of C, H, O, N, P, S and Cl, NASA SP-3040, Washington, D.C., 260 p. 1967.
19. Holloway, J. R. and Reese, F. O. The generation of N_2 - CO_2 - H_2O fluids for use in hydrothermal experimentation I. Experimental method and equilibrium calculations in the C-O-H-N system, Amer. Mineral. **59**, 587-597 (1974).
20. Karpov, I. K. and Kaz'min, L. A. Calculation of geochemical equilibria in heterogeneous multicomponent systems, Geochem. Int. **9**, 252-265 (1972).
21. Ingri, N., Kakolowicz, W., Sillen, L. G. and Warnquist, B. High-speed computers as a supplement of graphical methods - V. HALTAFALL, a general program for calculating the composition of equilibrium mixtures, Talanta **14**, 1261-1286 (1967).
22. Dyrssen, D., Jagner, D. and Wengelin, F. "Computer Calculation of Ionic Equilibria and Titration Procedures," 250 p. John Wiley, New York, 1968.
23. Ingri, N. and Sillen, L. G. High-speed computers as a supplement of graphical methods IV. An ALGOL version of LETAGROP VRID, Arkiv. Kemi **23**, 97-121 (1965).
24. Perrin, D. D. Multiple equilibria in assemblages of metal ions and complexing species: a model for biological systems, Nature **206**, 170-171 (1965).
25. Perrin, D. D. and Sayce, I. G. Computer calculation of equilibrium concentrations in mixtures of metal ions and complexing species, Talanta **14**, 833-842 (1967).
26. Fardy, J. J. and Sylva, R. N. SIAS, a computer program for the generalized calculation of speciation in mixed metal-ligand aqueous systems, AAEC/E445, Lucas Heights, Australia, 20 p. (1978).
27. Detar, D. F. "Computer Programs for Chemistry," Vol. II, 260 p. W. A. Benjamin, New York, 1969.

28. Bos, M. and Meershoek, H. Q. J. A computer program for the calculation of equilibrium concentrations in complex systems, Anal. Chim. Acta 61, 185-194 (1972).
29. Garrels, R. M. and Thompson, M. E., A chemical model for seawater at 25°C and one atmosphere total pressure, Amer. J. Sci. 260, 57-66 (1962).
30. Barnes, I. and Clarke, F. E., Chemical properties of ground water and their encrustation effects on wells, U.S. Geol. Survey Prof. Paper 498-D, 58 p. (1969).
31. Helgeson, H. C., Brown, T. H., Nigrini, A. and Jones, T. A.; Calculation of mass transfer in geochemical processes involving aqueous solutions, Geochim. Cosmochim. Acta. 34, 569-592 (1970).
32. Fritz, B. "Etude thermodynamique et simulation des reactions entre mineraux et solutions application a la geochemie des alterations et des eaux continentales." PhD. Thesis, Univ. Louis Pasteur, Strasbourg, France, 152 p., 1975.
33. Droubi, A. Geochimie des sels et des solutions concentrees par evaporation. Modele thermodynamique de simulation. Application aux sols sales du Tchad. Ph.D. Thesis, Univ. Louis Pasteur, Strasbourg, France, 177 p., 1976.
34. Truesdell, A. H. and Jones, B. F. WATEQ, a computer program for calculating chemical equilibria of natural waters, NTIS Tech. Rept. PB2-20464 Springfield, VA 77 p. (1973).
35. Truesdell, A. H. and Jones, B. F. WATEQ, a computer program for calculating chemical equilibria of natural waters, J. Res. U. S. Geol. Survey 2, 233-274 (1974).
36. Kharaka, Y. K. and Barnes, I., SOLMNEQ: Solution-mineral equilibrium computations, NTIS Tech. Rept. PB214-899, Springfield, VA 82 p. (1973).
37. Wolery, T. J., Some chemical aspects of hydrothermal processes at mid-oceanic ridges - a theoretical study. I. Basalt - sea water reaction and chemical cycling between the oceanic crust and the oceans. II. Calculation of chemical equilibrium between aqueous solutions and minerals, Ph.D. Thesis, Northwestern Univ., Evanston, IL, 1978.
38. Plummer, L. N., Jones, B. F. and Truesdell, A. H., WATEQF - a FORTRAN IV version of WATEQ, a computer program for calculating chemical equilibrium of natural waters, U.S. Geol. Survey Water Resour. Invest. 76-13, 61 p. (1976).
39. Lueck, S. L., Runnells, D. D. and Markos, G., Computer modelling of uranium species in natural waters: applications to exploration, Geol. Soc. Amer. Ann. Mtg. Abstracts, 1978.
40. Ball, J. W., Jenne, E. A. and Nordstrom, D. K., WATEQ2 - a computerized chemical model for trace and major element speciation and mineral equilibria of natural waters, in

- Jenne, E. A., ed., "Chemical Modeling in Aqueous Systems. Speciation, Sorption, Solubility, and Kinetics," Amer. Chem. Soc., 1978 (This volume).
41. Wigley, T.M.L. WATSPEC: a computer program for determining the equilibrium speciation of aqueous solutions, Brit. Geomorph. Res. Group Tech. Bull. 20, 48 p. (1977).
42. Wigley, T. M. L., Ion pairing and water quality measurements, Can. J. Earth Sci. 8, 468-476 (1971).
43. Wolery, T. J. and Walters, L. J., Jr., Calculation of equilibrium distributions of chemical species in aqueous solutions by means of monotone sequences, Math. Geol. 7, 99-115 (1975). *J. Ind. Assoc. Math. Geol.*
44. Walters, L. J., Jr. and Wolery, T. J., A monotone-sequences algorithm and FORTRAN IV program for calculation of equilibrium distributions of chemical species, Comp. Geosci. 1, 57-63 (1975). *Older 111*
45. Lafon, G. M., Some quantitative aspects of the chemical evolution of the oceans, Ph.D. Thesis, Northwestern Univ., Evanston, IL., 136 p., 1969.
46. Holdren, G. R., Jr., Distribution and behavior of manganese in the interstitial waters of Chesapeake Bay sediments during early diagenesis, Ph.D. Thesis, The Johns Hopkins Univ., Baltimore, MD, 191 p., 1977.
47. Thrailkill, J., Solution geochemistry of the water of limestone terrains, Univ. Kentucky Water Resour. Inst. Res. Rept. 19, 125 p (1970).
48. Van Beek, C. G. E. M., personal communication.
49. Van Breeman, N. Calculation of ionic activities in natural waters, Geochim. Cosmochim. Acta 37, 101-107 (1973).
50. Morel, F. and Morgan, J. J. A numerical method for computing equilibria in aqueous chemical systems, Env. Sci. Tech. 6, 58-67 (1972). *111*
51. Morel, F., McDuff, R. E. and Morgan, J. J. Interactions and chemostasis in aquatic chemical systems: Role of pH, pE, solubility and complexation, p. 157-200, in Singer, P.C., ed., "Trace Metals and Metal-Organic Interactions in Natural Waters," Ann Arbor Science Publishers, Ann Arbor, Michigan, 1973.
- (52) Morel, F., McDuff, R. E. and Morgan, J. J. Theory of interaction intensities, buffer capacities, and pH stability in aqueous systems, with application to the pH of seawater and a heterogeneous model ocean system, Mar. Chem. 4, 1001-1028 (1976). *advised 111 MARINE CHEMISTRY*
53. James, R. O. and Healy, T. W. Adsorption of hydrolyzable metal ions at the oxide-water interface. I. Cobalt (II) adsorption on silicon dioxide and titanium dioxide as model systems II. Charge reversal of silicon dioxide and titanium dioxide colloids by adsorbed cobalt (II), lanthanum (III) and thorium (IV) as model systems III.

- Thermodynamic model of adsorption, J. Colloid Interface Sci. 40, 42-81 (1972).
54. Schindler, P. W. and Gamsjaeger, H. Acid-base reactions of the titanium dioxide (anatase) - water interface and the point of zero charge of titanium dioxide suspension, Kolloid - Z. Z. Polym. 250, 759-763 (1972).
55. Schindler, P. W., Fuerst, B., Dick, R., Wolfe, P. U. Ligand properties of surface silanol groups. I. Surface complex formation with iron (3+), copper (2+), cadmium (2+) and lead (2+), J. Colloid Interface Sci. 55, 469-475 (1976).
56. Schindler, P. W., Waelti, E. and Fuerst, B. The role of surface hydroxyl groups in the surface chemistry of metal oxides, Chimia 30, 107-109 (1976).
57. Hohl, H. and Stumm, W. Interaction of lead (2+) with hydrous-alumina, J. Colloid Interface Sci. 55, 281-288 (1976).
58. Westall, J. and Hohl, H. A general method for the computation of equilibria and determination of equilibrium constants for adsorption at hydrous oxide surfaces, in "Abstracts of Papers," Amer. Chem. Soc. Meeting, Miami Beach, FL., 1978.
59. Davis, J. A., III and Leckie, J.O. Surface ionization and complexation at the oxide/water interface, in Jenne, E. A., ed. "Chemical Modeling in Aqueous Systems. Speciation, Sorption, Solubility, and Kinetics." Amer. Chem. Soc., 1978 (This volume).
60. Westall, J. C., Zachary, J. L. and Morel F. M. M. MINEQL, a computer program for the calculation of chemical equilibrium composition of aqueous system, Tech. Note 18, Dept. Civil Eng. Mass. Inst. Tech., Cambridge, MA., 91 p., (1976).
61. Mattigod, S. V. and Sposito, G. Chemical modeling of trace metal equilibria in contaminated soil solutions using the computer program GEOCHEM; in Jenne, E.A., ed., "Chemical Modeling in Aqueous Systems. Speciation, Sorption, Solubility, and Kinetics." Amer. Chem. Soc., 1978 (This volume).
62. I, T.-P. and Nancollas, G.H. EQUIL - a computational method for the calculation of solution equilibria, Anal. Chem. 44, 1940-1950 (1972).
63. Helgeson, H. C. Evaluation of irreversible reactions in geochemical processes involving minerals and aqueous solutions - I. Thermodynamic relations, Geochim. Cosmochim. Acta 32, 853-877 (1968).
64. Helgeson, H. C., Garrels, R. M. and Mackenzie, F. T. Evaluation of irreversible reactions in geochemical processes involving minerals and aqueous solutions - II. Applications, Geochim. Cosmochim. Acta 33, 455-481 (1969).
65. DeDonder, Th. and Van Rysselberghe, P. "The Thermodynamic Theory of Affinity," Stanford University Press, Stanford, California, 1936.

66. Helgeson, H. C. A chemical and thermodynamic model of ore deposition in hydrothermal systems, Mineral Soc. Amer. Spec. Paper 3, 155-186 (1970).
67. Miller, D. G., Piwinski, A. J. and Yamauchi, R. The use of geochemical-equilibrium computer calculations to estimate precipitation from geothermal brines, UCRL-52197 Livermore, Calif., 34 p., (1977).
68. Droubi, A., Cheverry, C., Fritz, B. and Tardy, Y. Geochimie des eaux et des sels dans les sols des polders du Lac Tchad: Application d'un modele thermodynamique de simulation de l'evaporation, Chem. Geol. 17, 165-177 (1976).
69. Droubi, A., Fritz, B. and Tardy, Y. Equilibres entre mineraux et solutions; Programmes de calcul appliques a la prediction de la sahire des sols et des doses optimales d'irrigation, Cah. ORSTOM, ser. Pedol XIV, 13-38 (1976).
70. Gear, C. W. The automatic integration of ordinary differential equations, Communications of the ACM 14, 176-179 (1971). *Association for Computing Machinery*
71. Gear, C. W. Algorithm 407-DIFSUB for solution of ordinary differential equations, Communications of the ACM 14, 185-190 (1971).
72. Plummer, L. N., Parkhurst, D. L. and Kosior, D. R. MIX2: A computer program for modeling chemical reactions in natural waters, U.S. Geol. Survey Water Resour. Inv. Rept. 75-61, 73 p. (1975).
73. Plummer, L. N. Mixing of sea water and calcium carbonate ground water, Geol. Soc. Amer. Mem. 142, 219-236 (1975).
74. Wigley, T. M. L. and Plummer, L. N. Mixing of carbonate waters, Geochim. Cosmochim. Acta 40, 989-995 (1976).
75. Plummer, L. N. Defining reactions and mass transfer in part of the Floridan aquifer, Water Resour. Res. 13, 801-812 (1977).
76. Parkhurst, D. L. Plummer, L. N. and Thorstenson, D. C. Chemical models in ground-water systems, Geol. Soc. Amer. Ann. Mtg. Abstracts 1978.
77. Haas, J. L., Jr. and Fisher, J. R. Simultaneous evaluation and correlation of thermodynamic data, Amer. J. Sci. 276, 525-545 (1976).
78. Helgeson, H. C. Thermodynamics of hydrothermal systems at elevated temperatures and pressures, Amer. J. Sci. 267, 729-804 (1969).
79. Helgeson, H. C. and Kirkham, D. H. Theoretical prediction of the thermodynamic behavior of aqueous electrolytes at high pressures and temperatures II. Debye-Huckel parameters for activity coefficients and relative partial molal properties, Amer. J. Sci. 274, 1199-1261 (1974).
80. Davies, C. W. "Ion Association," 190 p. Butterworths, Washington, D.C., 1962.

81. Morris, J. C. and Stumm, W. Redox equilibria and measurements of potentials in the aquatic environment, p.270-285, in Gould, R. F., ed., "Equilibrium Concepts in Natural Water Systems," Adv. Chem. Ser. 67, 1967.
82. Mehrbach, C., Culberson, C. H., Hawley, J. E. and Pytkowicz, R. M. Measurement of the apparent dissociation constants of carbonic acid in seawater at atmospheric pressure, Limnol. Oceanogr. 18, 897-907 (1973).
83. Lyman, J. Buffer mechanism of seawater, Ph.D. Thesis, Univ. Calif., Los Angeles, CA., 196 p., 1956.
84. Li, Y. H., Takahashi, T. and Broecker, W. S., Degree of saturation of CaCO_3 in the oceans, J. Geophys. Res. 74, 5507-5525 (1969).
85. McDuff, R. E. and Morel, F. M., Description and use of the chemical equilibrium program REDEQL2, Keck Lab. Tech. Rept. EQ-73-02, Calif. Inst. Tech., Pasadena, CA, 75., (1973).
86. Holdren, G. R., Jr. and Bricker, O.P., Distribution and control of dissolved iron and manganese in the interstitial waters of the Chesapeake Bay, p. 178-196, in Drucker, H. and Wildung, R. E., ed., "Biological Implications of Metals in the Environment," ERDA Symposium Series 42, 1977.
87. Thraillkill, J., Carbonate chemistry of aquifer and stream water in Kentucky, J. Hydrol. 16, 93-104 (1972).
88. Thraillkill, J., Carbonate equilibria in karst waters, p. 745-771, in Yevjevich, V., ed., "Karst Hydrology and Water Resources," Vol. 2, Water Resources Pub., Ft. Collins, CO., 1976.
89. Wigley, T. M. L., Plummer, L. N., and Pearson, F. J., Jr., Mass transfer and carbon isotope evolution in natural water system, Geochim. Cosmochim. Acta 42, 1117-1139 (1978).
90. Berner, R. A., The solubility of calcite and aragonite in seawater at atmospheric pressure and 34.50/oo salinity, Amer. J. Sci. 276, 713-730 (1976).

INDEX

RECEIVED November 16, 1978.

¹Department of Environmental Sciences, University of Virginia, Charlottesville, VA 22903.

²U.S. Geological Survey, National Center, MS 432, Reston, VA 22092.

³Climatic Research Unit, University of East Anglia, Norwich, NR4 7TJ, England.

⁴Lawrence Livermore Laboratory, University of California, P.O. Box 808, Livermore, CA 94550.

⁵U.S. Geological Survey, WRD, 345 Middlefield Rd., MS 21, Menlo Park, CA 94025.

⁶U.S. Geological Survey, Denver Federal Center, MS 416, Box 25048, Lakewood, CO 80225.

⁷Department of Geological & Geophysical Sciences, Princeton University, Princeton, NJ 08540.

⁸Australian Atomic Energy Commission Research Establishment, Lucas Heights, N.S.W., Australia.

⁹Institut de Geologie, 1, rue Blessig, 67084 Strasbourg, France.

¹⁰Department of Civil and Mineral Engineering, University of Minnesota, Minneapolis, MN 55455.

¹¹Department of Geological Sciences, University of Rochester, Rochester, NY 14627.

¹²Department of Earth & Planetary Sciences, The Johns Hopkins University, Baltimore, MD 21218.

¹³Department of Soil & Environmental Sciences, University of California, Riverside, CA 92521.

¹⁴Department Civil Engineering, Massachusetts Institute of Technology, Cambridge, MA 02139.

¹⁵State of New York Dept. of Health, New Scotland Avenue, Albany, NY 12201.

¹⁶Department of Geology, University of Kentucky, Lexington, KY 40506.

SUBJ
GCHM
CDG

Calcite-Dolomite Geothermometry for Iron-Bearing Carbonates

The Glockner Area of the Tauern Window, Austria

M.J. Bickle and R. Powell

Department of Earth Sciences, University of Leeds, Leeds LS2 9JT, England

Abstract. The effect of the addition of iron on the calcite-dolomite solvus in the system $\text{CaCO}_3\text{-MgCO}_3$ is predicted from an approximate thermodynamic description of the systems $\text{CaCO}_3\text{-MgCO}_3$ and $\text{CaCO}_3\text{-FeCO}_3$. Coexisting calcites and dolomites in 15 samples from the Glockner area of the Tauern Window have been analysed to estimate metamorphic temperatures. These range from about 410° C at the top of the Matrei Zone, on the southern margin of the Tauern Window, to about 490° C at Hochtor in the centre of the Glockner Depression, implying a geothermal gradient of about 25° C/km during metamorphism.

Introduction

The calcite-dolomite solvus in the system $\text{CaCO}_3\text{-MgCO}_3$ was first investigated in 1955 by Harker and Tuttle (1955) and Graf and Goldsmith (1955), and they recognised that the temperature dependence of the amount of MgCO_3 in calcite in equilibrium with dolomite is potentially a precise method of estimating metamorphic temperatures. However, natural carbonates frequently contain significant amounts of other elements, particularly iron. Although there have been some experiments performed in the ternary system $\text{CaCO}_3\text{-MgCO}_3\text{-FeCO}_3$, these are insufficient to delineate the tie lines between calcite and dolomite¹, although the approximate positions of the phase boundaries are known.

In this paper, the effect of the addition of Fe on the calcite-dolomite solvus in the system $\text{CaCO}_3\text{-MgCO}_3$ is estimated, and a new geothermometer developed. This is then applied to coexisting carbonates from a 3 km structural section south of Hochtor in the Tauern Window, Austria. This allows estimates of metamorphic conditions and the geothermal gradient during metamorphism.

¹ Dolomite is used here for ordered carbonates in $\text{CaCO}_3\text{-MgCO}_3\text{-FeCO}_3$ on or near the join $\text{CaMg}(\text{CO}_3)_2\text{-CaFe}(\text{CO}_3)_2$

where $x_{\text{Mg,cc}}$ is the mole fraction of Mg in calcite (in equilibrium with dolomite)

T in K and P in bars.

The experimental data lie within ± 0.35 mole % of these curves, giving an uncertainty of better than $\pm 20^\circ \text{C}$ on the geothermometer.

The addition of FeCO_3 to this simple endmember system results in the distribution of the iron between the calcite and the dolomite. Further addition of iron eventually leads to the instability of dolomite and coexisting calcite and siderite is the stable assemblage (Goldsmith et al., 1962). If this distribution of iron can be predicted by a thermodynamic description of the calcite-dolomite solvus (in the system $\text{CaCO}_3\text{-MgCO}_3$) and the calcite-siderite solvus (in the system $\text{CaCO}_3\text{-FeCO}_3$), then an iron correction can be made to the calcite-dolomite geothermometer of Goldsmith and Newton (1969). At least for the addition of small amounts of iron to the carbonates, an iron correction is likely to be linear. There are two ways of expressing this

$$x_{\text{Mg,cc}}^* = x_{\text{Mg,cc}} + Y_1 x_{\text{Fe,cc}} \quad (2)$$

$$x_{\text{Mg,cc}}^* = x_{\text{Mg,cc}} + Y_2 x_{\text{Fe,dol}}$$

where $x_{\text{Fe,cc}}$ and $x_{\text{Mg,cc}}$ refer to the actual composition of the calcite, while $x_{\text{Mg,cc}}^*$ is the hypothetical mole fraction of magnesium in the calcite in the iron-free system, which is given by (1). Y_1 and Y_2 are temperature and pressure dependent constants, being the rate of change of magnesium in calcite with the addition of iron to the calcite and to the dolomite respectively. The thermodynamic analysis below attempts to find Y_1 and Y_2 to calibrate these geothermometer Equations (2).

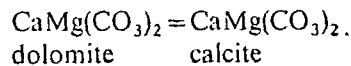
For at least some thermodynamic models of solid solutions it is possible to predict ternary phase relations from a knowledge of the constituent binary phase relations. A detailed thermodynamic description of $\text{CaCO}_3\text{-MgCO}_3\text{-FeCO}_3$ is hampered by the complexity of the equilibria involving dolomite. A model involving at least nearest and next nearest neighbour interactions in dolomite is required to describe the second order order-disorder transformation at about 1200° C in $\text{CaMg}(\text{CO}_3)_2$ and the first order transformations reflected in the calcite-dolomite and dolomite-magnesite solvi. Further, the dolomite solid solutions depart progressively from the $\text{CaMg}(\text{CO}_3)_2\text{-CaFe}(\text{CO}_3)_2$ join with the addition of iron (Rosenberg, 1967).

However, a complicated analysis is impossible because the ternary phase diagram is insufficiently well known.

² Strictly a miscibility gap as the structures of calcite and dolomite are different

$\text{CaCO}_3\text{-MgCO}_3$

The $\text{CaCO}_3\text{-MgCO}_3$ diagram can be



Using an ordered standard state for b

$$-\Delta G^0 = 0 = RT \ln \frac{x_{\text{Ca,cc}} \cdot x_{\text{Mg,cc}}}{x_{\text{Ca,M2}} \cdot x_{\text{Mg,M1}}}$$

where w_{CaMg} is the regular solution n. The M1 and M2 subscripts refer to in dolomite.

With the above assumptions, this

$$w_{\text{CaMg}} = \frac{-RT \ln x_{\text{Ca}}(1-x_{\text{Ca}})}{(1-x_{\text{Ca}})^2 + x_{\text{Ca}}^2}$$

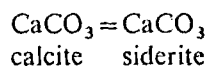
where x_{Ca} refers to calcite. This equa solvus data of Goldsmith and Newt

$$w_{\text{CaMg}} = 5360 - 0.032P \text{ cal/mole}$$

with a probable uncertainty of about

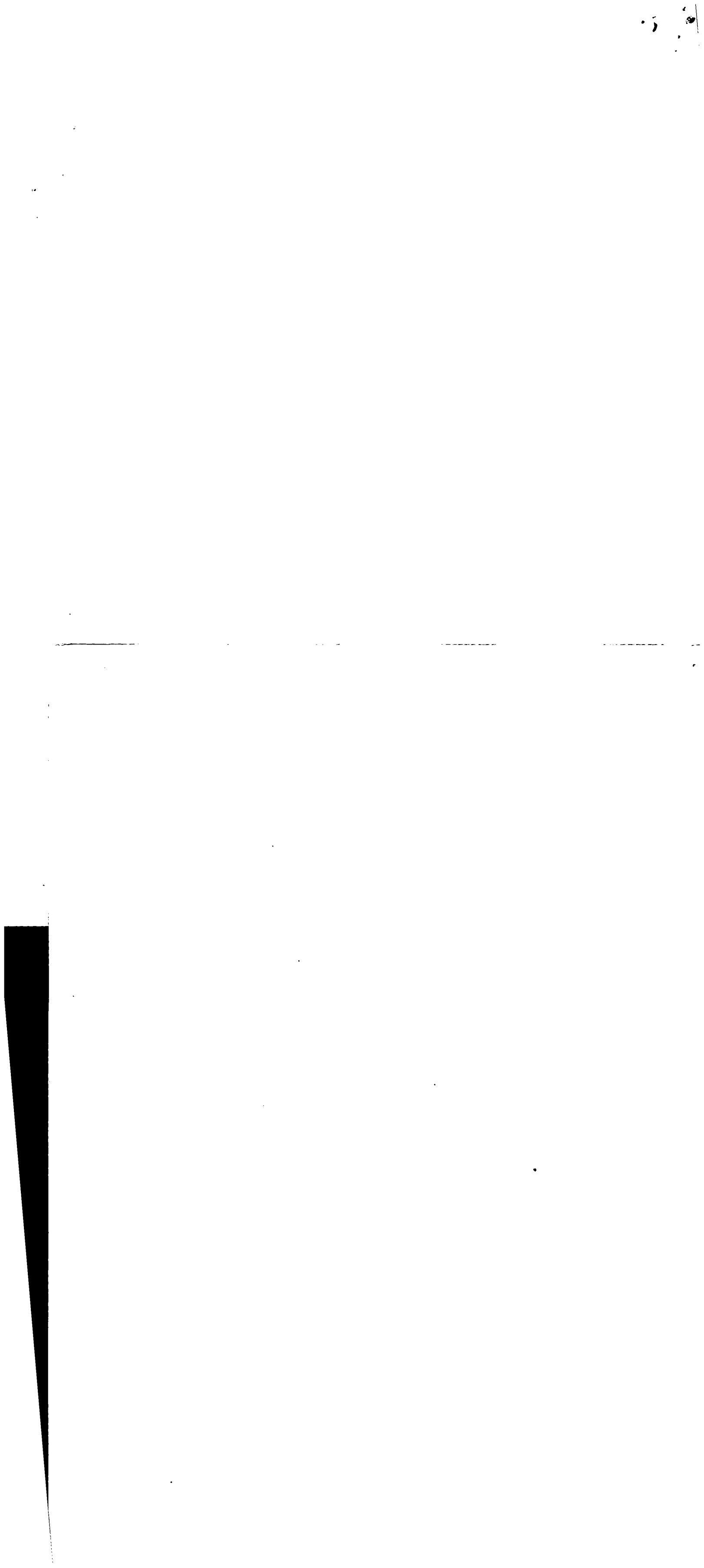
$\text{CaCO}_3\text{-FeCO}_3$

The calcite-siderite solvus is asymm dynamics of the calcite, little error is tric and using the calcite limb of th



for which the equilibrium relatio

$$-\Delta G^0 = 0 = RT \ln \frac{x_{\text{Ca,sid}} + w}{x_{\text{Ca,cc}}}$$





se calibration of the temperature
 CO_3 in calcite in equilibrium with
 400° to 900° C and up to 24 kb.
 $\ln K$ can be expressed as

$$\ln K = -0.33 \times 10^{-6} T \quad (1)$$

(in equilibrium with dolomite)

of these curves, giving an uncer-
 tainty.

ember system results in the distri-
 bution of dolomite. Further addition of iron
 and coexisting calcite and siderite
 . If this distribution of iron can be
 the calcite-dolomite solvus (in the
 system $\text{CaCO}_3 - \text{MgCO}_3$)
 the calcite-dolomite geothermo-
 for the addition of small amounts
 likely to be linear. There are two

(2)

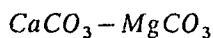
position of the calcite, while $x_{\text{Mg,cc}}^*$
 in the calcite in the iron-free
 temperature and pressure dependent
 in calcite with the addition of
 siderite. The thermodynamic analysis
 these geothermometer Equations

of solid solutions it is possible to
 use the constituent binary phase
 diagram of $\text{CaCO}_3 - \text{MgCO}_3 - \text{FeCO}_3$
 involving dolomite. A model
 for neighbour interactions in dolomite
 disorder transformation at about
 400°C is reflected in the calcite-
 siderite solvus, the dolomite solid solutions
 and the $\text{CaFe}(\text{CO}_3)_2$ join with the addition

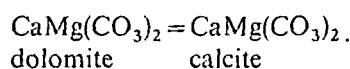
possible because the ternary phase

of dolomite are different

A simplistic approach is taken using the regular solution model and certain approximations concerning site distributions in the phases and the geometry of the ternary phase diagram. We assume that calcite is effectively disordered, while dolomite is effectively ordered at the temperatures of interest here (greenschist/amphibolite facies) (Goldsmith et al., 1962). Dolomite is therefore taken to have two sites, M1 filled with Ca and M2 filled with Mg and Fe; this further implies that dolomite does not depart significantly from the join $\text{CaMg}(\text{CO}_3)_2 - \text{CaFe}(\text{CO}_3)_2$.



The $\text{CaCO}_3 - \text{MgCO}_3$ diagram can be considered with the reaction



Using an ordered standard state for both components, the equilibrium relation is

$$-\Delta G^0 = 0 = RT \ln \frac{x_{\text{Ca,cc}} x_{\text{Mg,cc}}}{x_{\text{Ca,M2}} x_{\text{Mg,M1}}} + w_{\text{CaMg}} ((1 - x_{\text{Ca}})^2 + x_{\text{Ca}}^2)_{\text{cc}}$$

where w_{CaMg} is the regular solution model interaction parameter for Ca and Mg. The M1 and M2 subscripts refer to the mole fractions on the M1 and M2 sites in dolomite.

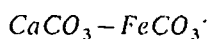
With the above assumptions, this reduces to

$$w_{\text{CaMg}} = \frac{-RT \ln x_{\text{Ca}} (1 - x_{\text{Ca}})}{(1 - x_{\text{Ca}})^2 + x_{\text{Ca}}^2}$$

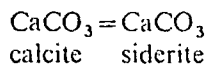
where x_{Ca} refers to calcite. This equation allows the calculation of w_{CaMg} from the solvus data of Goldsmith and Newton (1969) in the region 400° C to 600° C as

$$w_{\text{CaMg}} = 5360 - 0.032 P \text{ cal/mole} \quad \text{with } P \text{ in bars}$$

with a probable uncertainty of about ± 100 cal.



The calcite-siderite solvus is asymmetric, but if we are only interested in the thermodynamics of the calcite, little error is introduced by considering the solvus symmetric and using the calcite limb of the solvus in the calculation. Thence, for



for which the equilibrium relation is

$$-\Delta G^0 = 0 = RT \ln \frac{x_{\text{Ca,sid}}}{x_{\text{Ca,cc}}} + w_{\text{CaFe}} (x_{\text{Fe,sid}}^2 - x_{\text{Fe,cc}}^2)$$

which reduces to

$$w_{\text{CaFe}} = \frac{RT \ln \frac{1-x_{\text{Fe}}}{x_{\text{Fe}}}}{1-2x_{\text{Fe}}} \quad \text{where } x_{\text{Fe}} = x_{\text{Fe,cc}} = x_{\text{Ca,sid}}$$

Given the concordance of the high pressure data of Goldsmith et al. (1962) and the lower pressure data of Rosenberg (1963), the solvus, and thus w_{CaFe} appears to be independent of pressure. In the temperature range 400° C to 600° C

$$w_{\text{CaFe}} = 3800 \text{ cal/mole}$$

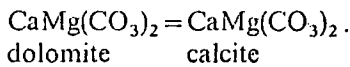
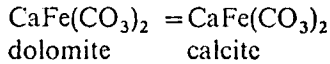
with a probable uncertainty of about ± 100 cal.

$\text{MgCO}_3 - \text{FeCO}_3$

Complete miscibility characterises the $\text{MgCO}_3 - \text{FeCO}_3$ join to the lowest experimentally achieved temperatures (295° C, Rosenberg, 1967). No Mg-Fe solvus has been reported in any mineral group, and so the assumption of ideal mixing of Mg and Fe, or $w_{\text{MgFe}} = 0$, seems reasonable.

$\text{MgCO}_3 - \text{FeCO}_3 - \text{CaCO}_3$

Two reactions are considered for dolomite-calcite equilibria in the ternary system



Applying the ternary regular solution equations, and noting that $w_{\text{MgFe}} = 0$, the equilibrium equations are

$$-\Delta G^0 = 0 = RT \ln \frac{x_{\text{Ca,cc}} x_{\text{Mg,cc}}}{x_{\text{Ca,M2}} x_{\text{Mg,M1}}} + w_{\text{CaMg}}(1-x_{\text{Fe}}-2x_{\text{Mg}}x_{\text{Ca}})_{\text{cc}} + w_{\text{CaFe}} x_{\text{Fe}}(1-2x_{\text{Ca}})_{\text{cc}} \quad (3)$$

$$-\Delta G^0 = 0 = RT \ln \frac{x_{\text{Ca,cc}} x_{\text{Fe,cc}}}{x_{\text{Ca,M2}} x_{\text{Fe,M1}}} + w_{\text{CaMg}} x_{\text{Mg}}(1-2x_{\text{Ca}}) + w_{\text{CaFe}}(1-x_{\text{Mg}}-2x_{\text{Mg}}x_{\text{Ca}}) \quad (4)$$

As we are only interested in these equations at low temperatures (below 600° C) where $x_{\text{Fe,cc}}$ and $x_{\text{Mg,cc}}$ are small (below 0.04), these equations can be drastically simplified

$$\frac{x_{\text{Fe,cc}}}{x_{\text{Fe,M1,dol}}} = \exp(-w_{\text{CaFe}}/RT) \quad (5)$$

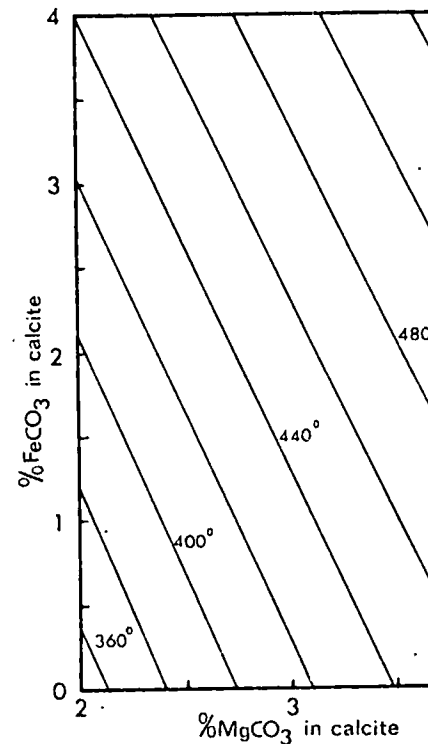


Fig. 1. %FeCO₃ in calcite plotted against % MgCO₃ in calcite, contoured for temperature in °C, at 5 kb

$$\frac{x_{\text{Mg,cc}}}{x_{\text{Mg,M1,dol}}} = \exp(-w_{\text{CaMg}}/RT)$$

combining (5) and (6) and combinin

$$x_{\text{Mg,cc}}^* = x_{\text{Mg,cc}} + x_{\text{Fe,cc}} \exp((w_{\text{CaFe}}/RT))$$

and thus the effect of iron on the sc the endmember binary systems. Al

$$x_{\text{Mg,cc}}^* = x_{\text{Mg,cc}} + x_{\text{Fe,M1,dol}} \exp(-w_{\text{CaFe}}/RT)$$

The two geothermometers (7) ar within the model, yet they will only dolomite were in equilibrium and i tions are necessary but not sufficient in diagram form, Figures 1, 2, relief carbonate pair.

The probable uncertainty in th about $\pm 20^\circ$ C. The main uncertain validity of the assumptions used i the values of w_{CaMg} and w_{CaFe} con

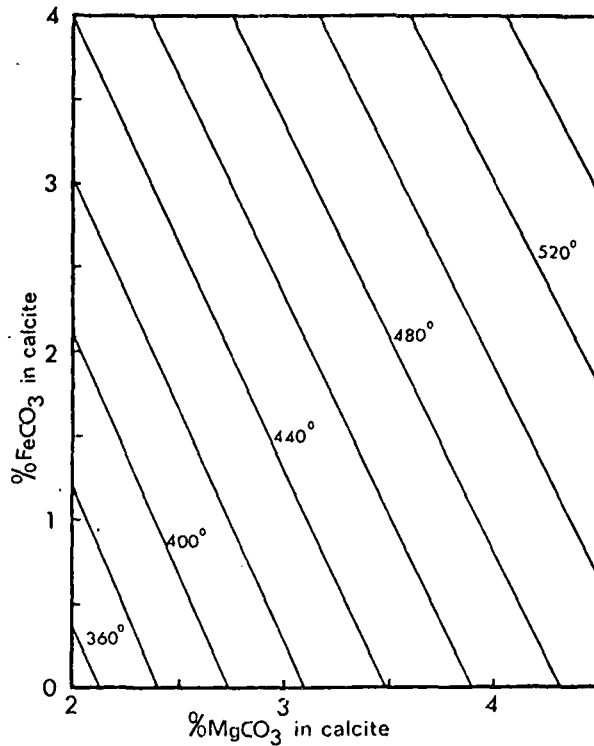


Fig. 1. %FeCO₃ in calcite plotted against %MgCO₃ in calcite for the assemblage calcite + dolomite contoured for temperature in °C, at 5 kb

$$\frac{x_{Mg,cc}}{x_{Mg,M1,dol}} = \exp(-w_{CaMg}/RT) \tag{6}$$

combining (5) and (6) and combining with (2)

$$x_{Mg,cc}^* = x_{Mg,cc} + x_{Fe,cc} \exp((w_{CaFe} - w_{CaMg})/RT) \tag{7}$$

and thus the effect of iron on the solvus is predicted from the phase diagrams of the endmember binary systems. Alternatively, from (6) and (2)

$$x_{Mg,cc}^* = x_{Mg,cc} + x_{Fe,M1,dol} \exp(-w_{CaMg}/RT). \tag{8}$$

The two geothermometers (7) and (8) are not thermodynamically independent within the model, yet they will only give the same temperature if the calcite and dolomite were in equilibrium and if the model works. However both these assertions are necessary but not sufficient. The two geothermometers can be represented in diagram form, Figures 1, 2, relieving the necessity of solving (7) and (8) for each carbonate pair.

The probable uncertainty in the Fe-free calcite-dolomite geothermometer is about ±20° C. The main uncertainty in these new geothermometers comes in the validity of the assumptions used in the thermodynamics as the uncertainties in the values of w_{CaMg} and w_{CaFe} contribute temperature uncertainties of less than

$x_{Ca,sid}$
data of Goldsmith et al. (1962) and the solvus, and thus w_{CaFe} appears ature range 400° C to 600° C

als.
CO₃ - FeCO₃ join to the lowest C, Rosenberg, 1967). No Mg-Fe up, and so the assumption of ideal sonable.

calcite equilibria in the ternary system

ations, and noting that $w_{MgFe} = 0$,
 $-x_{Fe} - 2x_{Mg}x_{Ca}$
(3)

$(1 - 2x_{Ca})$
(4)

at low temperatures (below 600° C), these equations can be drastically
(5)

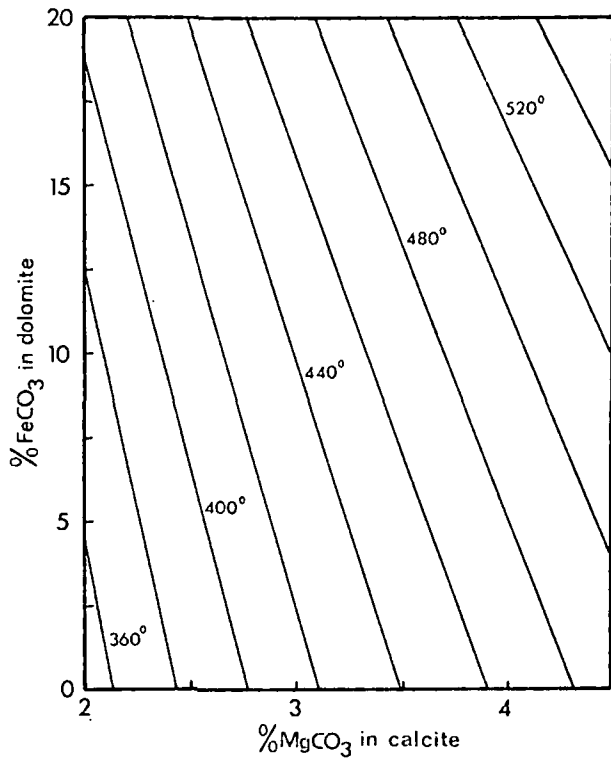


Fig. 2. %FeCO₃ in dolomite plotted against %MgCO₃ in calcite for the assemblage calcite + dolomite contoured for temperature in °C, at 5 kb

±5° C. Clearly the uncertainties increase as the iron correction gets larger, although it is impossible to say by how much. We hope they are no larger than ±30° C for the carbonates in this study.

Geology of the Glockner Area

The geology of the Glockner Depression in the Tauern Window has been described by Cornelius and Clar (1939) and Frasl and Frank (1966). The nomenclature of Oxburgh (1968) and Cliff et al. (1971) is used here. The Peripheral Schieferhülle and the Matriei Zone (Fig. 3) consist of mainly Mesozoic metasediments and metavolcanics deformed beneath the overthrust amphibolite facies metamorphics of the Altkristallin Sheet.

It is likely that a thrust unit as large as the Altkristallin Sheet would be emplaced along a near horizontal plane (e.g. Hsü, 1969) so that the prominent foliation in the underlying highly deformed units, which is parallel to the base of the Sheet, probably records the horizontal at the time of the overthrusting (see Norris et al., 1971, for further discussion). Foliation attitudes reveal that subsequent uplift has arched the thrust units exposing deeper levels in the centre of the Tauern

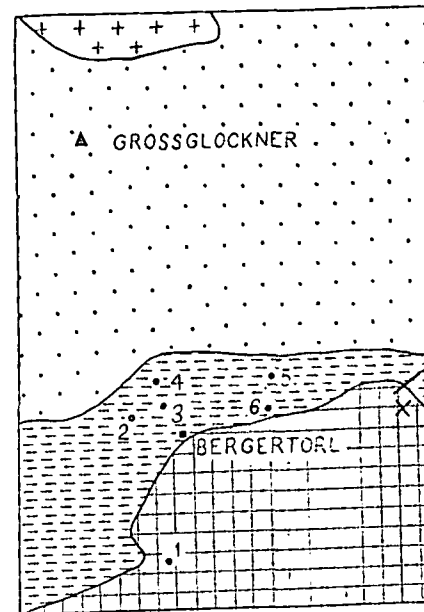


Fig. 3. Map of the central Tauern Window, A (1973). Rock units are: A) Riffle decke. B) Tr Facies, E) Matriei Zone. F) Altkristallin Sheet defined by Cliff et al. (1971). Sample localities SP816, SP827; Berger Torl (1) SP637, SP6 (6) SP 754. The line X-Ho, marks the line of

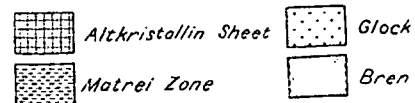
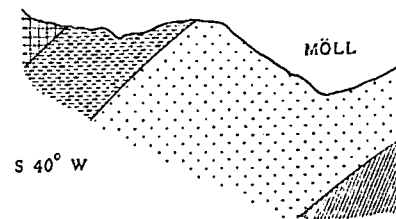


Fig. 4. Cross section across the southern margin from the map of Cornelius and Clar (1939)

Window. Using these foliation attitudes of the window allows relative structure estimated (Fig. 4).

This structural profile can be if uplift of the Central Tauern bet

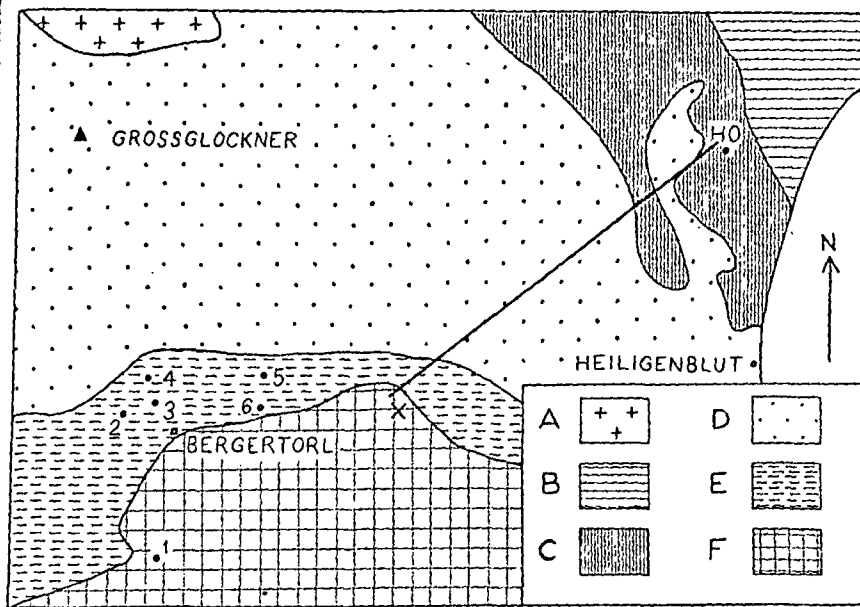


Fig. 3. Map of the central Tauern Window, Austria, compiled from Frasl and Franck (1966) and Bickle (1973). Rock units are: A) Riffle decke, B) Trias Carbonate Series, C) Brennkogel Facies, D) Glockner Facies, E) Matrei Zone, F) Alt-kristallin Sheet. Units B-D are part of the Peripheral Schieferhülle as defined by Cliff et al. (1971). Sample localities: Hochtör (Ho) SW 56, SW 77, SW 81, SW 100, SP 812, SP 816, SP 827; Berger Torl (1) SP 637, SP 639; (2) SP 783; (3) SP 466, SP 468; (4) SP 367; (5) SP 61; (6) SP 754. The line X-Ho marks the line of the section in Figure 4

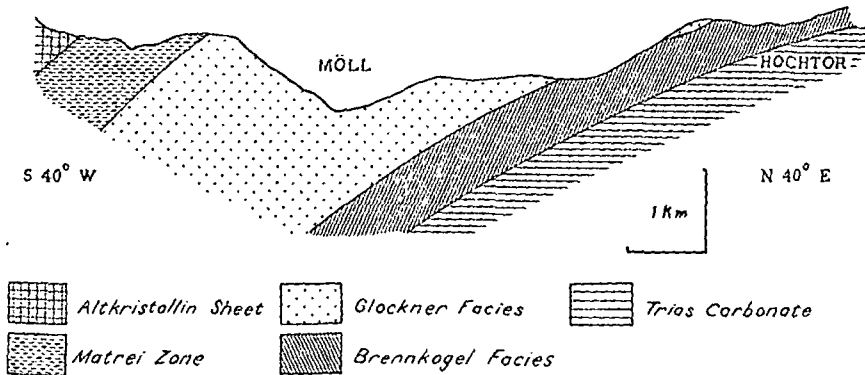


Fig. 4. Cross section across the southern margin of the Tauern Window, line X-Ho on Figure 3, drawn from the map of Cornelius and Clar (1939)

Window. Using these foliation attitudes and sections from the margin to the centre of the window allows relative structural depths at the time of overthrusting to be estimated (Fig. 4).

This structural profile can be used as a depth profile during metamorphism if uplift of the Central Tauern between overthrusting (c. 65 my) and the peak of

calcite for the assemblage calcite + dolomite

the iron correction gets larger, We hope they are no larger than

the Tauern Window has been described and Frank (1966). The nomenclature (Cliff et al., 1971) is used here. The Peripheral Schieferhülle consists of mainly Mesozoic metasedimentary overthrust amphibolite facies

Altkristallin Sheet would be emplaced (Cliff et al., 1971) so that the prominent foliation is parallel to the base of the Sheet. This overthrusting (see Norris et al., 1971) reveals that subsequent uplift levels in the centre of the Tauern

Table 1. Carbonate compositions and calculated temperatures for the Glockner area of the Tauern Window

Sample No.	Calcite			Dolomite			Structural* height metres	Temperature uncorrected for FeCO ₃ °C	Temperature corrected for FeCO ₃				
	No. analyses	MgCO ₃ mole %	3 × St error	No. analyses	FeCO ₃ mole %	3 × St error			in cc °C	in dc °C			
SW 58	12	3.31	0.20	20	2.26	0.21	5	15.1	1.8	-3066	422	474	479
SW 77	20	3.55	0.10	27	1.26	0.18	5	7.0	1.1	-3300	435	456	464
SW 81	19	3.60	0.09	19	3.09	0.10	9	14.9	0.6	-3300	438	503	495
SW100	15	3.66	0.10	15	0.83	0.06	6	5.7	1.2	-3300	441	464	466
SP812	18	3.26	0.12	18	3.11	0.13	7	16.3	1.3	-3300	420	488	481
SP816	11	3.70	0.12	16	2.49	0.13	10	12.5	1.0	-3300	443	496	491
SP827	16	3.49	0.10	16	2.05	0.10	10	15.3	2.0	-3300	432	478	490
SP 61	7	2.48	0.23	7	1.52	0.18	6	10.05	0.4	- 700	380	416	411
SP367	17	3.49	0.13	15	0.58	0.07	16	4.8	1.0	- 600	438	451	454
SP466	16	2.34	0.14	18	1.60	0.14	8	10.8	0.24	- 200	370	409	405
SP468	18	2.59	0.13	18	1.08	0.06	9	7.7	0.38	- 200	387	412	411
SP637	16	2.72	0.19	17	0.51	0.06	-	3.5 ^b	-	+ 360	395	409	408
SP639	10	3.09	0.09	10	0.1	-	2	0.1	-	+ 360	416	420	419
SP754	15	2.34	0.11	19	0.42	0.07	4	2.7	0.58	0	371	384	382
SP783	12	3.42	0.20	15	0.87	0.08	16	0.98 ^c	0.9	- 400	434	452	467

* Structural height relative to the base of the Altkristallin Sheet

^b Insufficient dolomite analyses. Value inferred from FeCO₃ content of calcite

^c Total range of FeCO₃ in dolomites from this rock ranges from 0.5 to 5 mole %. This sample is a breccia with dolomite fragments in a calcite-dolomite matrix. Measurements low in FeCO₃ may be on clast material not in equilibrium with the matrix

metamorphism (c. 35 my) is not significant. The rocks of the Peripheral Schieferhülle and the Matrei Zone as well as the basal kilometre of the Altkristallin Sheet have been metamorphosed to greenschist facies after overthrusting and this heating can be related to burial under a thick overburden (Oxburgh et al., 1971; Oxburgh and Turcotte, 1974; and Bickle et al., 1975). The geothermal gradient during this metamorphism can be estimated using carbonate thermometry on the calcite-dolomite bearing metasediments and the relative structural depths.

The compositions of calcites and dolomites from rocks in the Glockner Depression (sample localities, Fig. 3) which show little variation of within sample calcite compositions are presented in Table 1. Details of carbonate analysis by electron probe are given in Appendix 1. Manganese contents of the carbonates are ignored because there is less than 0.7 mole % MnCO₃ in the calcites and less than 1.4 mole % in the dolomites. The magnesium contents of the calcites are presented as histograms in Figure 5. The scatter of compositions to low MgCO₃ values is probably due to reequilibration of some of the calcites during cooling of the metamorphic complex. The rejected samples show these reequilibration effects without a well defined maximum in MgCO₃ content in a histogram. A problem with sample SP783 is that dolomite occurs in clasts whereas calcite occurs in the matrix, and there is the possibility that the calcite never equilibrated with the dolomite. A few anomalously high values may have resulted from small

Calcite-Dolomite Geothermometry

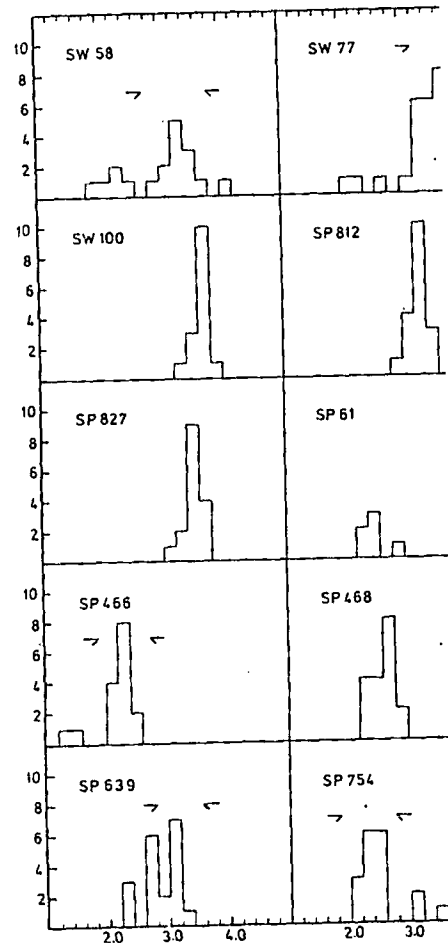


Fig. 5. Histograms of MgCO₃ contents of calcite to calculate means and standard deviations for each sample except SW 77 for which two sections

dolomite inclusions within calcite or are excluded from the calculations of

Temperatures calculated from (1), and from (7) and (8), utilising the iron given in Table 1. Temperatures are calculated at 4.25 kb at the Berger Torl locality and the uncertainty in choosing the carbonate composition is less than the temperature uncertainty than is inherent in the

The uncorrected temperatures for the samples certainly seem too low for the presence of the assemblages (Höck, 1974), while the corrected temperatures seem more reasonable, if still on the

Parameters for the Glockner area of the Tauern Window

Sample	FeCO ₃ 3 × St error	Structural ^a height metres	Temperature uncorrected for FeCO ₃ °C	Temperature corrected for FeCO ₃ in cc °C	Temperature corrected for FeCO ₃ in d. °C
15.1	1.8	-3066	422	474	479
7.0	1.1	-3300	435	456	464
14.9	0.6	-3300	438	503	495
5.7	1.2	-3300	441	464	466
16.3	1.3	-3300	420	488	481
12.5	1.0	-3300	443	496	491
15.3	2.0	-3300	432	478	490
10.05	0.4	-700	380	416	411
4.8	1.0	-600	438	451	454
10.8	0.24	-200	370	409	405
7.7	0.38	-200	387	412	411
3.5 ^b	-	+360	395	409	408
0.1	-	+360	416	420	419
2.7	0.58	0	371	384	382
0.98 ^c	0.9	-400	434	452	467

^a FeCO₃ content of calcite from 0.5 to 5 mole %. This sample is a breccia with low FeCO₃ may be on clast material not in matrix.

The rocks of the Peripheral Schieferung are about 1 kilometre of the Altkristallin Sheet facies after overthrusting and this is overlain by Oxburgh et al., 1971; and (2) the geothermal gradient is low in the peripheral schieferung. The relative structural depths.

Calcite from rocks in the Glockner area show little variation of within sample. Details of carbonate analysis by X-ray fluorescence. Manganese contents of the carbonates are low, MnCO₃ in the calcites and less than 1% in the dolomites. Barium contents of the calcites are low. The scatter of compositions to low MgCO₃ in some of the calcites during cooling. Some samples show these re-equilibration features. MgCO₃ content in a histogram. A feature occurs in clasts whereas calcite in the matrix that the calcite never equilibrated. These values may have resulted from small

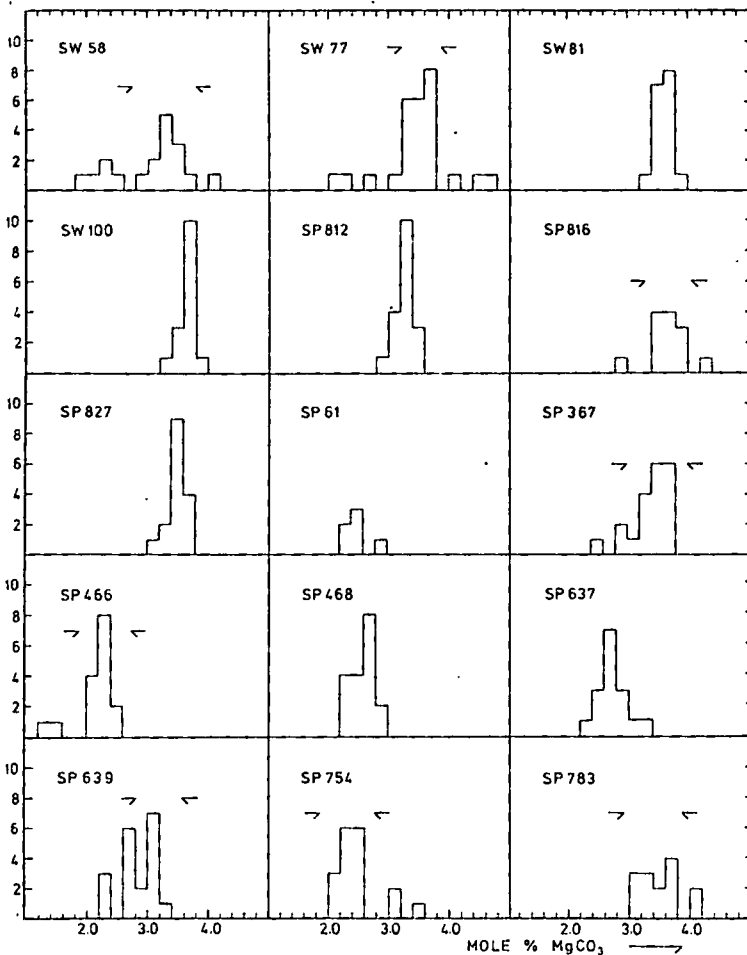


Fig. 5. Histograms of MgCO₃ contents of calcites. Arrows delineate range of MgCO₃ contents used to calculate means and standard deviations quoted in Table 1. All analyses on one probe section from each sample except SW 77 for which two sections were used.

dolomite inclusions within calcite crystals. These apparently anomalous values are excluded from the calculations of means.

Temperatures calculated from (1), ignoring the iron in the natural carbonates, and from (7) and (8), utilising the iron content of the calcite and dolomite are given in Table 1. Temperatures are calculated assuming a lithostatic pressure of 4.25 kb at the Berger Torf locality and 5 kb at the Hochtorn locality. The uncertainty in choosing the carbonate compositions for a sample contributes a smaller temperature uncertainty than is inherent in the geothermometer.

The uncorrected temperatures for the Hochtorn locality of about 425°C certainly seem too low for the presence of oligoclase and garnet in basic and pelitic assemblages (Höck, 1974), while the corrected temperatures of about 490°C seem more reasonable, if still on the low side. The scatter of temperatures from

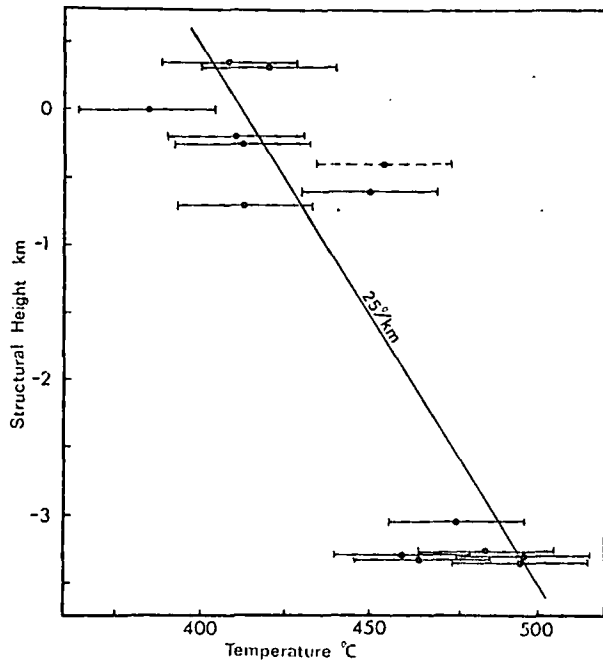


Fig. 6. Calcite-dolomite temperatures plotted against structural height inferred from Figure 4. Temperature uncertainties of $\pm 20^\circ$ are included for reference

samples which should have formed at more or less the same temperature may reflect that at least some of the samples show some reequilibration effects, and so a more realistic metamorphic maximum temperature may be about 500°C . However as the uncertainty on the geothermometers is probably at least $\pm 30^\circ$, this temperature is within the uncertainty limits of the temperatures for many of the Hochtort samples.

The corrected temperatures for the Berger Torf area, in the Matrei Zone and at the base of the Altkristallin show scatter, suggesting again that reequilibration effects are important. In these areas, the basic assemblage is albite-epidote-actinolite-chlorite-calcite-sphene, supporting the conclusion of a lower metamorphic temperature here than at Hochtort.

The temperatures for samples listed in Table 1 are plotted against structural height in Figure 6. Although there is scatter in the temperatures from the two areas, the geothermal gradient of about $20^\circ\text{C}/\text{km}$ predicted by thermal modelling (Bickle et al., 1975) is consistent with the carbonate thermometry.

Acknowledgements. The authors thank Dr. S.W. Richardson for critically reading an earlier version of the manuscript and for valuable discussions. Dr. J.V.P. Long and the Department of Mineralogy and Petrology, Cambridge are thanked for providing electron probe facilities, and for giving instruction and assistance with this analytical method. Most of this work was undertaken during research for our respective D. Phil's under the supervision of Dr. E.R. Oxburgh and Dr. S.W. Richardson at the Dept. of Geology and Mineralogy, University of Oxford during tenure of NERC Studentships.

Appendix

Microprobe Analysis of Carbonates

Operating conditions for carbonate analysis by electron microprobe: carbonates are unstable under the electron beam.

1. 120 s counts (no change in cps over 400 s)
 2. 25 nanoamp specimen current
 3. 20 kv accelerating potential
 4. 12 to 15 micron electron beam diameter
 5. mylar window between sample and spectrometer
 6. Ca standard-wollastonite. Fe and Mg (using the ZAF correction procedure of Sweatman)
- Totals both for calcites and dolomites were calculated. The reason for this is unknown.

References

- Bickle, M.J., Hawkesworth, C.J.: Regional metamorphism in the Eastern Alps. *J. Geophys. Res.* 77, 3057-3067 (1972)
- Bowen, N.L., Tuttle, O.F.: The system $\text{MgO}-\text{CaCO}_3$. *J. Geophys. Res.* 77, 3057-3067 (1972)
- Clayton, R.N., O'Neil, J.R., Mayeda, T.K.: *J. Geophys. Res.* 77, 3057-3067 (1972)
- Cliff, R.A., Norris, R.J., Oxburgh, E.R.: Metachronological studies in the Reisseck area. *E.R. Oxburgh. Jahrb. Geol. Bundesanstalt (Geol. Jahrb.)* 100, 1-10 (1975)
- Cornelius, H.P., Clar, E.: *Geologie des Grossen Rannochs*. *Zw. Geol. Anst. Wien* 25(1), 1-305 (1939)
- Frasl, G., Frank, W.: Einführung in die Geologie. *Pub. Vereinigung der Freunde der Geologie* 1971
- Friedrichsen, H.: Oxygen isotope fractionation. *Neues Jahrb. Mineral.* p. 26-33 (1971)
- Ganguly, J., Newton, R.C.: Thermal stability of calcite. *J. Petrol.* 9(3), 444-446 (1968)
- Goldsmith, J.R., Heard, H.C.: Subsolvus phase relations. *Am. J. Sci.* 267-A, 160-166 (1961)
- Goldsmith, J.R., Newton, R.C.: $P-T-X$ relations and pressures. *Am. J. Sci.* 267-A, 160-166 (1961)
- Graf, D.L., Goldsmith, J.R.: Dolomite-magnetite equilibria. *Geochim. Cosmochim. Acta* 22, 103-110 (1958)
- Graf, D.L., Goldsmith, J.R.: The solid solubility of dolomite. *Geochim. Cosmochim. Acta* 13, 218-219 (1958)
- Harker, R.I., Tuttle, O.F.: Studies in the system $\text{CaCO}_3-\text{MgCO}_3$. *Am. J. Sci.* 267-A, 160-166 (1961)
- Höck, V.: Zur Metamorphose mesozoischer Kalkalpen. *Schweiz. Mineral. Petrol. Mitt.* 54, 1-10 (1974)
- Hsü, K.J.: Role of Cohesive strength in the evolution of the Himalayas. *Geol. Soc. Am. Bull.* 80, 927-952 (1969)
- Kitahara, S., Takenouchi, S., Kennedy, G.C.: High temperatures and pressures. *Am. J. Sci.* 267-A, 160-166 (1961)
- Norris, R.J., Oxburgh, E.R., Cliff, R.A.: Structural geology in the Reisseck area. *E.R. Oxburgh. Jahrb. Geol. Bundesanstalt (Geol. Jahrb.)* 100, 1-10 (1975)

Appendix

Microprobe Analysis of Carbonates

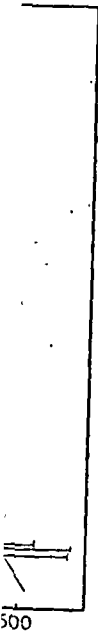
Operating conditions for carbonate analysis by electron probe have to be carefully chosen because carbonates are unstable under the electron beam. The following operating conditions were employed:

1. 120 s counts (no change in cps over 400 s)
2. 25 nanoamp specimen current
3. 20 kv accelerating potential
4. 12 to 15 micron electron beam diameter
5. mylar window between sample and spectrometer (with the absence of an electron trap on the spectrometer)
6. Ca standard-wollastonite, Fe and Mg standard-St. Johns olivine, Mn standard-Mn metal (using the ZAF correction procedure of Sweatman and Long (1969))

Totals both for calcites and dolomites were consistently low, $97.25 \pm 1.5\%$ and $98.0 \pm 1.0\%$ respectively; the reason for this is unknown.

References

- Bickle, M.J., Hawkesworth, C.J., England, P.C., Athey, D.R.: A preliminary thermal model for regional metamorphism in the Eastern Alps. *Earth Planet. Sci. Lett.* 26, 13-28 (1975)
- Bowen, N.L., Tuttle, O.F.: The system $MgO-SiO_2-H_2O$. *Geol. Soc. Am. Bull.* 60, 439-460 (1949)
- Clayton, R.N., O'Neil, J.R., Mayeda, T.K.: Oxygen isotope exchange between quartz and water. *J. Geophys. Res.* 77, 3057-3067 (1972)
- Cliff, R.A., Norris, R.J., Oxburgh, E.R.: Metamorphism, chapter 3 in: Structural, metamorphic and geochronological studies in the Reisseck and Southern Ankogel groups, the Eastern Alps; Editor E.R. Oxburgh. *Jahrb. Geol. Bundesanstalt (Austria)* 114(2) (1971)
- Cornelius, H.P., Clar, E.: Geologie des Grossglocknergebietes. *Abhandl. Reichsstelle Bodenforsch. Zweigst. Wien* 25(1), 1-305 (1939)
- Frasl, G., Frank, W.: Einführung in die Geologie und Petrographie des Penninikums im Tauernfenster. *Pub. Vereinigung der Freunde der Mineralogie and Geologie (VFMG)*, e.v. 58 p. (1966)
- Friedrichsen, H.: Oxygen isotope fractionation between coexisting minerals of the Grimstead Granite. *Neues Jahrb. Mineral.* p. 26-33 (1971)
- Ganguly, J., Newton, R.C.: Thermal stability of chloritoid at high pressure and relatively high oxygen fugacity. *J. Petrol.* 9(3), 444-446 (1968)
- Goldsmith, J.R., Heard, H.C.: Subsolidus phase relations in the system $CaCO_3-MgCO_3$. *J. Geol.* 69, 43-61 (1961)
- Goldsmith, J.R., Newton, R.C.: $P-T-X$ relations in the system $CaCO_3-MgCO_3$ at high temperatures and pressures. *Am. J. Sci.* 267-A, 160-190 (1969)
- Graf, D.L., Goldsmith, J.R.: Dolomite-magnesian calcite relations at elevated temperatures and CO_2 pressures. *Geochim. Cosmochim. Acta* B, 109-118 (1955)
- Graf, D.L., Goldsmith, J.R.: The solid solubility of $MgCO_3$ in $CaCO_3$: a revision. *Geochim. Cosmochim. Acta* 13, 218-219 (1958)
- Harker, R.L., Tuttle, O.F.: Studies in the system $CaO-MgO-CO_2$. Part 2. Limits of the solid solution along the binary join $CaCO_3-MgCO_3$. *Am. J. Sci.* 253, 274-282 (1955)
- Höck, V.: Zur Metamorphose mesozoischer Metasedimente in den mittleren Hohen Tauern (Österreich). *Schweiz. Mineral. Petrol. Mitt.* 54, (2/3) 567 (1974)
- Hsü, K.J.: Role of Cohesive strength in the mechanics of overthrust faulting and of landsliding. *Geol. Soc. Am. Bull.* 80, 927-952 (1969)
- Kitahara, S., Takenouchi, S., Kennedy, G.C.: Phase relations in the system $MgO-SiO_2-H_2O$ at high temperatures and pressures. *Am. J. Sci.* 264, 223-233 (1966)
- Norris, R.J., Oxburgh, E.R., Cliff, R.A.: Structure, Chapter IV in: Structural, metamorphic and geochronological studies in the Reisseck and Southern Ankogel groups, the Eastern Alps; Editor E.R. Oxburgh. *Jahrb. Geol. Bundesanstalt (Austria)* 114(2) (1971)



structural height inferred from Figure 4. Tem-

or less the same temperature may
some reequilibration effects, and so
perature may be about 500°C. How-
eters is probably at least $\pm 30^\circ$, this
of the temperatures for many of the

er Torl area, in the Matrei Zone and
suggesting again that reequilibration
basic assemblage is albite-epidote-
g the conclusion of a lower meta-

Table 1 are plotted against structural
er in the temperatures from the two
C/km predicted by thermal modelling
onate thermometry.

son for critically reading an earlier version
P. Long and the Department of Mineralogy
ron probe facilities; and for giving instruction
work was undertaken during research for our
burgh and Dr. S.W. Richardson at the Dept
g tenure of NERC Studentships.

- O'Neil, J.R., Clayton, R.N.: Oxygen isotope geothermometry. In: Isotopic and cosmic chemistry, pp. 157-168. Amsterdam: North Holland (1964)
- Oxburgh, E.R.: An outline of the geology of the Central Eastern Alps. *Proc. Geol. Assoc.* **76**(1), 1-46 (1968)
- Oxburgh, E.R., Cliff, R.A., Norris, R.J.: Conclusions, Chapter VI in: Structural, metamorphic and geochronological studies in the Reisseck and Southern Ankogel groups, the Eastern Alps, Editor E.R. Oxburgh. *Jahrb. Geol. Bundesanstalt (Austria)* **114**(2) (1971)
- Oxburgh, E.R., Turcotte, D.L.: Thermal gradients and regional metamorphism in overthrust terrains with special reference to the Eastern Alps. *Schweiz. Mineral. Petrog. Mitt.* **54**, (2/3), 641-662 (1974)
- Rosenberg, P.E.: Subsolidus relations in the system $\text{CaCO}_3\text{-MgCO}_3\text{-FeCO}_3$ between 350°C and 550°C. *Am. Mineralogist* **52**, 787-796 (1967)
- Sheppard, S.M.F., Schwarcz, H.P.: Fractionation of carbon and oxygen isotopes and magnesium between coexisting metamorphic calcites and dolomites. *Contrib. Mineral. Petrol.* **26**, 161-168 (1970)
- Sweatman, J.R., Long, J.V.P.: Quantitative electron probe microanalysis of rock forming minerals. *J. Petrol.* **10**(2), 332-379 (1969)
- Wasastjerna, J.A.: The crystal structure of dolomite. *Soc. Sci. Fennica, Commentationes Phys.-Math.* **II**, **14**, 14p (1924)
- Wyckoff, R.W.G., Merwin, H.E.: The crystal structure of dolomite. *Am. J. Sci.* **8**, 447-461 (1924)
- Yoder, H.S.: Spilites and serpentinites. *Carnegie Inst. Wash. Year Book* **65**, 269-283 (1966)

Received August 27, 1976/Accepted October 13, 1976

The Dislocation Structure of Experimentally Deformed

C. Goetze¹ and D.L. Kohlstedt²

¹ Department of Earth and Planetary Sciences, Cambridge, MA. 02139, U.S.A.

² Department of Materials Science and Engine

Abstract. Five specimens deformed at 980 bar were selected for a transmission electron microscopy study. Micrographs show twinning, dislocation loops, and small angle boundaries. Boundaries contain dislocations with Burgers vectors $\frac{1}{2}\langle 1\bar{1}02 \rangle$ and $\frac{1}{12}\langle 11\bar{2}0 \rangle$. Dislocation densities of specimens deformed at 980 bar are higher than the starting density and fit the theoretical dislocation densities of specimens deformed only partially with respect to the theoretical densities of the experiments and thus are larger than

Introduction

Under a range of conditions of great interest, the deformation of minerals proceeds by dislocation structures of specimens deformed under conditions which provide transmission electron microscopy views of quartz and olivine aggregates deformed under conditions (McLaren et al., 1967; Mott and Ashby, 1972; Ardell et al., 1973; Bačeta and Averbach, 1972; Phakey et al., 1972; and others). We are aware of only one such paper (Phakey et al., 1973). Barber and Wenk published transmission electron microscopy (TEM) views of Solnhofen limestone deformed in a medium apparatus over a range of usually high dislocation densities of specimens deformed at relatively low differential stresses below.

SUBJ
GCHM
CEB

RESEARCH
EARTH SCIENCE LAB.

EARTH AND PLANETARY SCIENCE LETTERS 9 (1970) 269-279. NORTH-HOLLAND PUBLISHING COMP.

CHEMICAL EXCHANGE BETWEEN SEA WATER AND DEEP OCEAN BASALTS

Roger HART

*U.S. Naval Oceanographic Office
Project GOFAR, Washington D.C., U.S.A.*

Received 29 June 1970

Analysis of 112 deep ocean basalts reported in the literature show systematic chemical trends in major elements with distance from ridge spreading centers. These same trends are observed in the weathering of single pillows and produce a chemical composition similar to volcanic alkali basalts. Upon hydration by sea water, tholeiitic ridge basalts give off silica, calcium, magnesium, and gain potassium, iron, titanium, manganese, sodium and phosphorus. Aluminum shows no apparent change. The yearly contribution to sea water in 10^{-9} grams of the major elements per cm^3 of basalt is estimated at $\text{Si}=+7.4$, $\text{Ti}=-1.6$, $\text{Fe}=-3.3$, $\text{Mn}=0.06$, $\text{Mg}=+2.3$, $\text{Na}=-0.21$, $\text{Ca}=+2.1$, $\text{K}=-0.9$, and $\text{P}=-0.14$.

1. Introduction

The concept that the major element chemistry of basalt rocks varies systematically with distance from the major oceanic ridge was first documented by McBirney and Gass [1] who showed that basalts from volcanic oceanic islands decrease in silica saturation with distance from the ridges. They correlated the decreasing silica content with diminishing heat flow away from the ridge.

Engel and Engel [2] noted that basalts dredged from the ridge axis are uniformly tholeiitic in nature while samples taken on seamounts at a distance from the ridge are more likely to be alkali basalts. They attributed the phenomenon to a process of crystal differentiation in the magma chambers of sea floor volcanoes; however, since the work of Yoder and Tilley [3], crystal differentiation is no longer considered a viable mechanism for producing an alkali basalt from a tholeiitic magma. In order to explain chemical variation of basalt samples from the Confederation Peak region of the Mid-Atlantic Ridge, Aumento [4] suggested a process of progressive degrees of partial melting of a pyrolitic melt following from the work of Green and Ringwood [5]. The concept of decreasing partial melting was correlated to progressively greater depths with distance from the

ridges by Kay, Hubbard, and Gast [6] and generalized to apply to all major ridge systems.

With the general acceptance of the sea floor spreading theory of Hess [7] and Dietz [8] and the magnetic stratigraphy theory of Vine and Mathews [9], it is now possible to suggest that systematic chemical trends correlatable with distance from ridge axis are also related to increasing age of the sea floor that has moved out from the ridge spreading centers.

Simultaneously with observations of variations in magma types across the oceanic ridges, various authors have noted the effects of sea water weathering on basalts extruded on the sea floor. One of the most important and consistent observations made is that as alteration proceeds the water content of the sample increases due to the formation of hydrated alteration minerals. Engel et al. [10] reported that alteration of ridge basalts causes an increase in H_2O , and Fe_2O_3 contents of basalts and a loss in MgO and total iron. Nichols [11] found a decrease in the percentage of calcium, magnesium and sodium and attributed the losses to leaching by sea water. Moore [12] showed that palagonization of basalt glass resulted in a loss of CaO , a lesser loss of Na , and enrichment in K and Fe . Hart and Nawalk [13] reported that the CaO and SiO_2 contents of basalts from the Puerto Rico trench decrease with increasing water content. Hart [14]

showed that K, Rb and Cs are enriched in altered portions of ridge basalts by factors of 2, 5, and 20 respectively. Myashiro et al. [15] showed that the Fe_2O_3 content of basalts increased with the H_2O content. There seems to be some agreement among the authors that the Fe_2O_3 and K contents of basalt are enriched while the CaO content is depleted upon weathering. There is disagreement among the authors as to whether total iron goes up or down. The loss of Na, Mg, and SiO_2 has been suggested but has not yet been confirmed or contested by the above mentioned authors.

A more recent approach to the problem of sea water weathering of ocean floor basalts has been to study the concentric zones of alteration visible within single boulders and pillows. There is still some disagreement as to whether the zones are produced by sea water weathering after the magma has cooled or produced by deuteritic alteration during the magmatic stage.

Myashiro et al. [15] reported three zones of visible weathering in a single basalt boulder. The outside rim is weathered to a yellow brown zone that grades into a transitional grey-brown zone surrounding the unaltered dark grey core. They show that the outer weathered rim is enriched in MnO, TiO_2 , Fe_2O_3 , P_2O_5 and total iron while depleted in SiO_2 , FeO, MgO and CaO relative to the core. Myashiro's analysis shows no conclusive trends for Al_2O_3 , Na_2O , or K. Paster [16] recognized three distinct zones of alteration within individual basalt pillows dredged from the South Pacific: 1) an outer zone of hydration depleted in magnesium and calcium and enriched in total iron and potassium; 2) a zone of serpentinization adjacent to joints and fractures attributed to deuteritic alteration between sea water and the cooling lava body; 3) a zone of chloritization in the core of the sample with depletion of magnesium and total iron attributed to high temperature deuteritic alteration. Paster [16] suggested that chemical alteration of basalt might have a major impact on the geochemical budget of the major elements in sea-water. He particularly emphasized the enrichment of sea water in iron and manganese in an effort to provide a source for manganese nodules. His results also show alteration of basalts enriches sea water in silica, calcium, and magnesium. Paster's [16] emphasis on deuteritic alteration is in opposition to the interpretations of Myashiro et al.

[15] and Hart [14] who show that the alteration is most intense in the outer zones rather than the inner zones and therefore most likely due to sea water weathering as opposed to deuteritic alteration. The importance of deuteritic alteration cannot be dismissed, particularly in thick lava bodies, but in small pillows the weathering effects of Miyashiro et al. [14] and Hart [13] are probably superimposed over the deuteritic effects particularly in samples that have been in contact with sea water for some time.

Very little work has been done in the petrology of the weathering processing. In addition to Paster's [16] observations of chloritization and serpentinization, Nawalk [17] reported the replacement of plagioclase by smectite and sericite. Nawalk [17] feels that at least part of the alteration he observed is deuteritic in nature. Engel and Engel [18] reported olivine altered to iddingsite and limonite and reported the presence of chlorite and iron oxides.

2. Results

Fig. 1 shows a plot of the percent potassium content versus age for 112 analyses of ridge basalt. The sample location and literature source are indicated for each analysis. The magnetic reversal ages were determined by plotting sample locations on maps of ocean floor residual magnetic field reversals of Vogt et al. [32], Hiertzler et al. [33] and Hays and Pitman [34]. Potassium argon ages were assigned to the reversals back to 4 mybp by Cox et al. [35] and extended to 80 mybp by paleontological dating of the oldest sediment in JOIDES cores by Maxwell [36]. Some samples could not be assigned ages because of lack of magnetic data and were not included in this study. The estimated age uncertainty for most samples is ± 1 my.

Samples with a large number of plagioclase or olivine phenocrysts were not included in order to exclude crystal differentiation effects. In an effort to avoid confusing true alkali basalts with weathering effects, alkalic samples with less than 1% H_2O were judged to be fresh alkali basalts, and not included in this study.

The most striking feature of fig. 1 is the systematic increase in the scatter of potassium values with age. Another important feature is that the median potas-

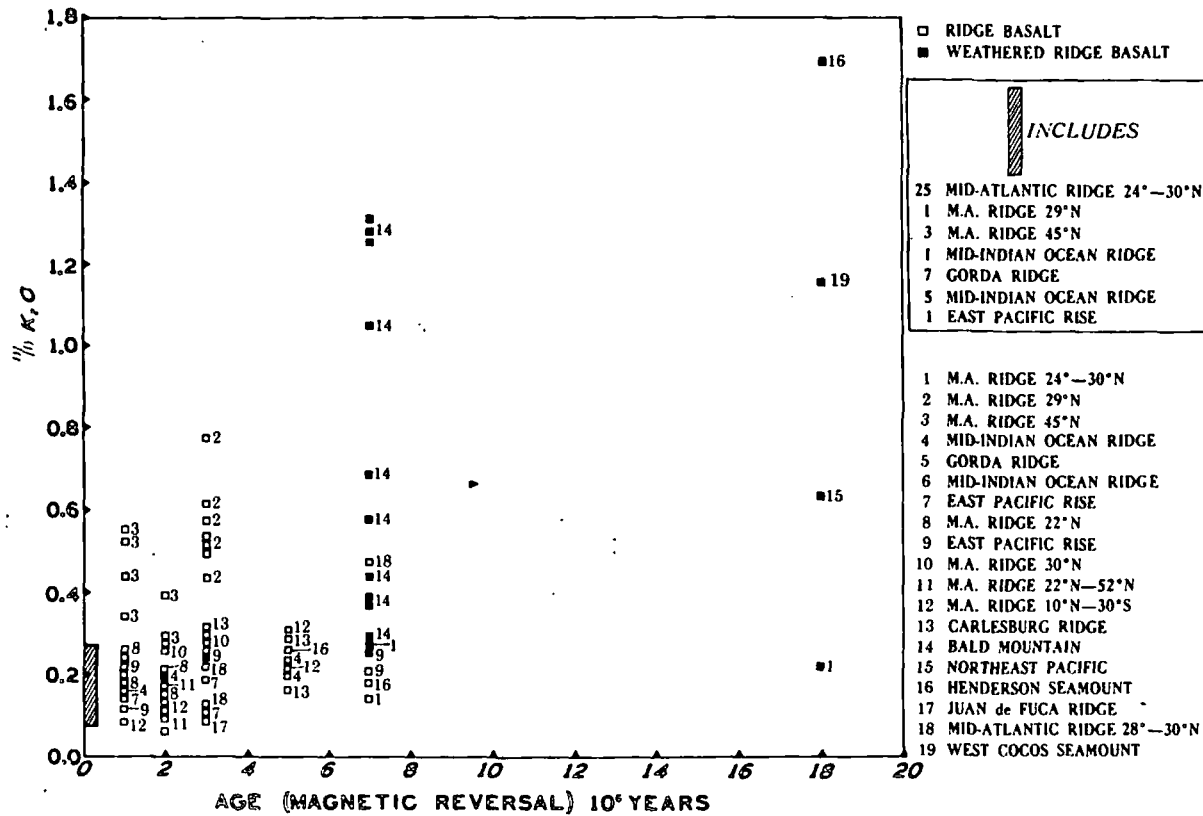


Fig. 1. A plot of percent potassium versus residual magnetic field reversal age for 112 analyses of ridge basalts. The ages of the samples were determined by plotting the sample locations on residual magnetic field reversal maps of Vogt et al. [32] for Northern Atlantic, Hiertzler et al. [33] for Indian Ocean and Southern Pacific, and Hays and Pitman [34] for Northern Pacific. The general sample locations for each analysis are indicated and taken from the following literature sources: 1) Miyashiro, Shido and Ewing [15]; 2) Muir and Tilley [19]; 3) Aumento [20]; 4) Engel, Fisher and Engel [10]; 5) Kay, Hubbard and Gast [6]; 6) Engel and Fisher [31]; 7) Bonatti [22]; 8) Melson, Thompson and Van Andel [23]; 9) Engel and Engel [24]; 10) Muir and Tilley [25]; 11) Nichols, Nawalk and Hays [26]; 12) Engel and Engel [27]; 13) Cann and Vine [27]; 14) Aumento and Loncaveric [29]; 15) Engel and Engel [18]; 16) Poldervaart and Green [30]; 17) Kay, Hubbard and Gast [6]; 18) Kay, Hubbard and Gast [6]; 19) Engel and Chase [31].

sium value of ridge basalts appears to increase with age.

Two interpretations of this plot immediately come to mind. The first interpretation follows from the suggestions of McBirney and Gass [1], Aumento [4], and Hubbard, Kay and Gast [6] that basalt magma changes its chemical composition with distance from the ridges and that a plot such as fig. 1 indicates additions from a single progressively changing magma source, or from numerous sources of a different nature. The other interpretation is that fig. 1 is the result of

samples progressively altered with time and that the high potassium values represent samples with a higher percent of altered material, while the low potassium values come from samples or sections of samples such as the center portions which are relatively fresh. In order to emphasize the importance of weathering in producing the plot shown in fig. 1, samples that were identified as altered by the authors are shaded.

The means and standard deviation for all twelve major elements, plus total iron are shown in fig. 2. The plots come out remarkably close to straight lines for

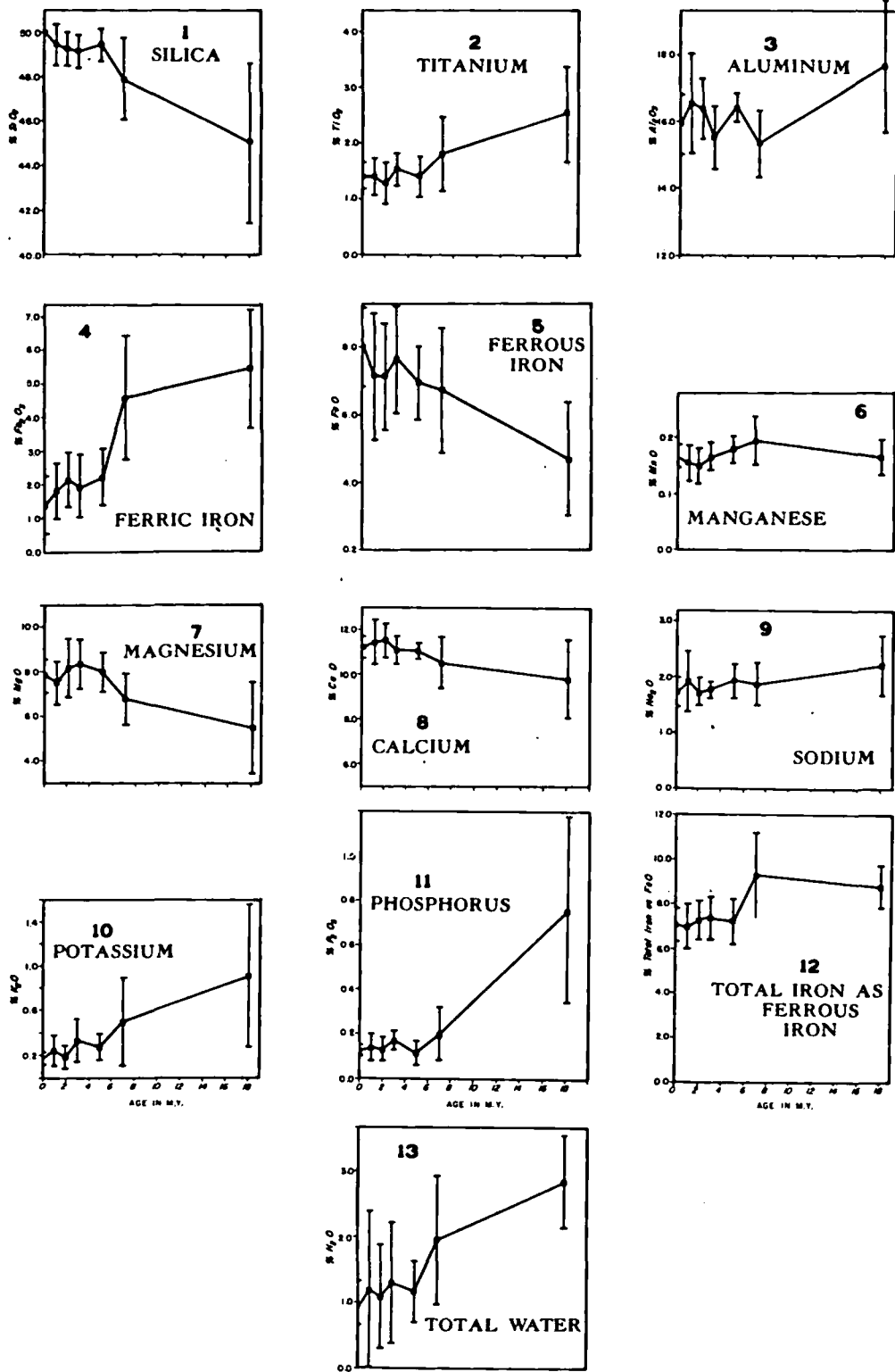


Fig. 2. Mean and standard deviation plots of oxides of the twelve major elements versus residual magnetic field reversal age.

Fig. 3. A

most m
magnes
with ag
strate a
for pot
steep co
of titan
as FeO
standar
signific
sodium
case car
sodium
expecte
in H₂O
All t
weather
fresh ric
table 1.

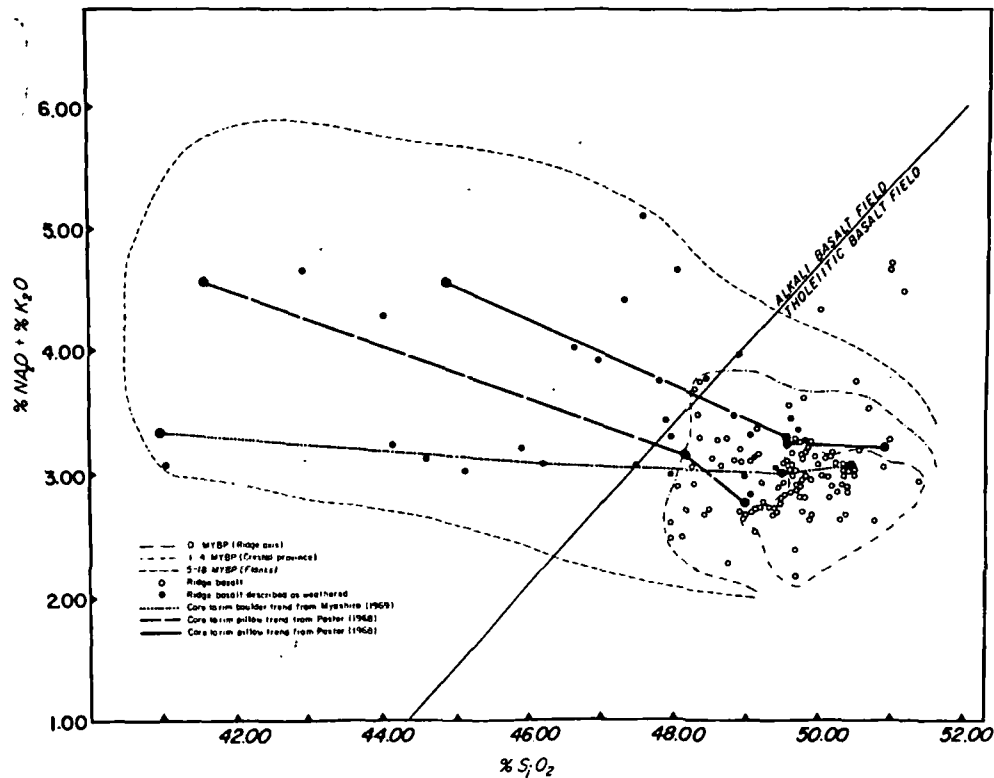


Fig. 3. A plot of the total alkalis versus silica for ridge basalts and core-to-rim weathering trends. The ridge basalts are contoured according to age to show how progressive weathering of a tholeiitic basalt produces a basalt of alkali nature.

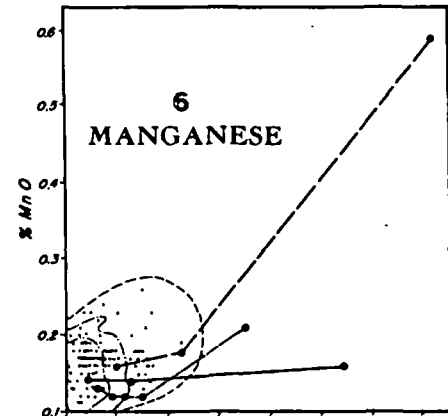
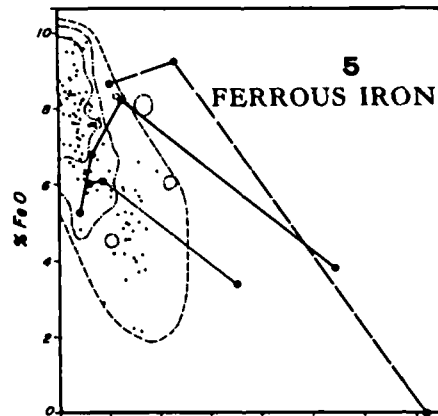
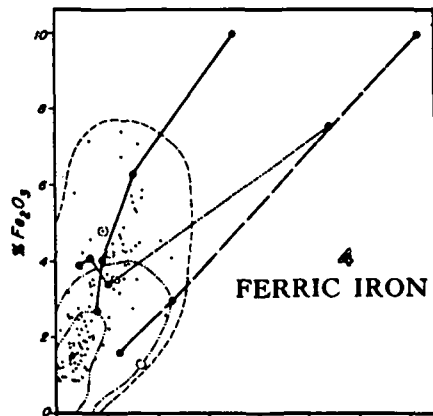
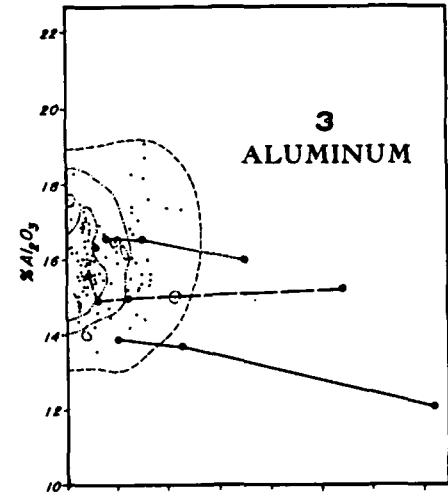
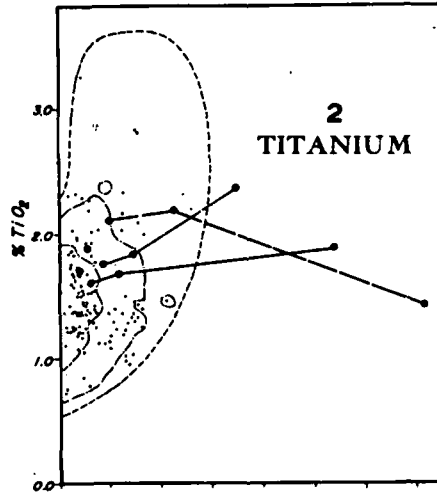
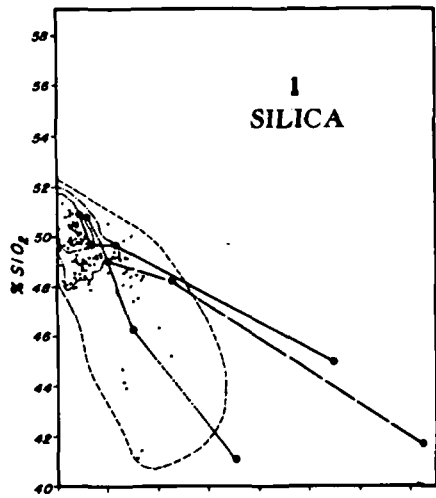
most major elements for 18 my. The oxides of silicon, magnesium, and calcium, show good trends decreasing with age; the increase in standard deviations demonstrate a similar increase in scatter as shown in fig. 1 for potassium. The slopes of the lines are relatively steep compared to the standard deviation. The oxides of titanium, potassium and phosphorus, plus total iron as FeO and water all increase with an expanding standard deviation fields and mean slopes that are significant. The oxides of aluminum, manganese and sodium do not show significant trends, although a case can be made for small increases in manganese and sodium. Ferric iron replaces ferrous iron as would be expected during the weathering process. The increase in H_2O is also indicative of weathering.

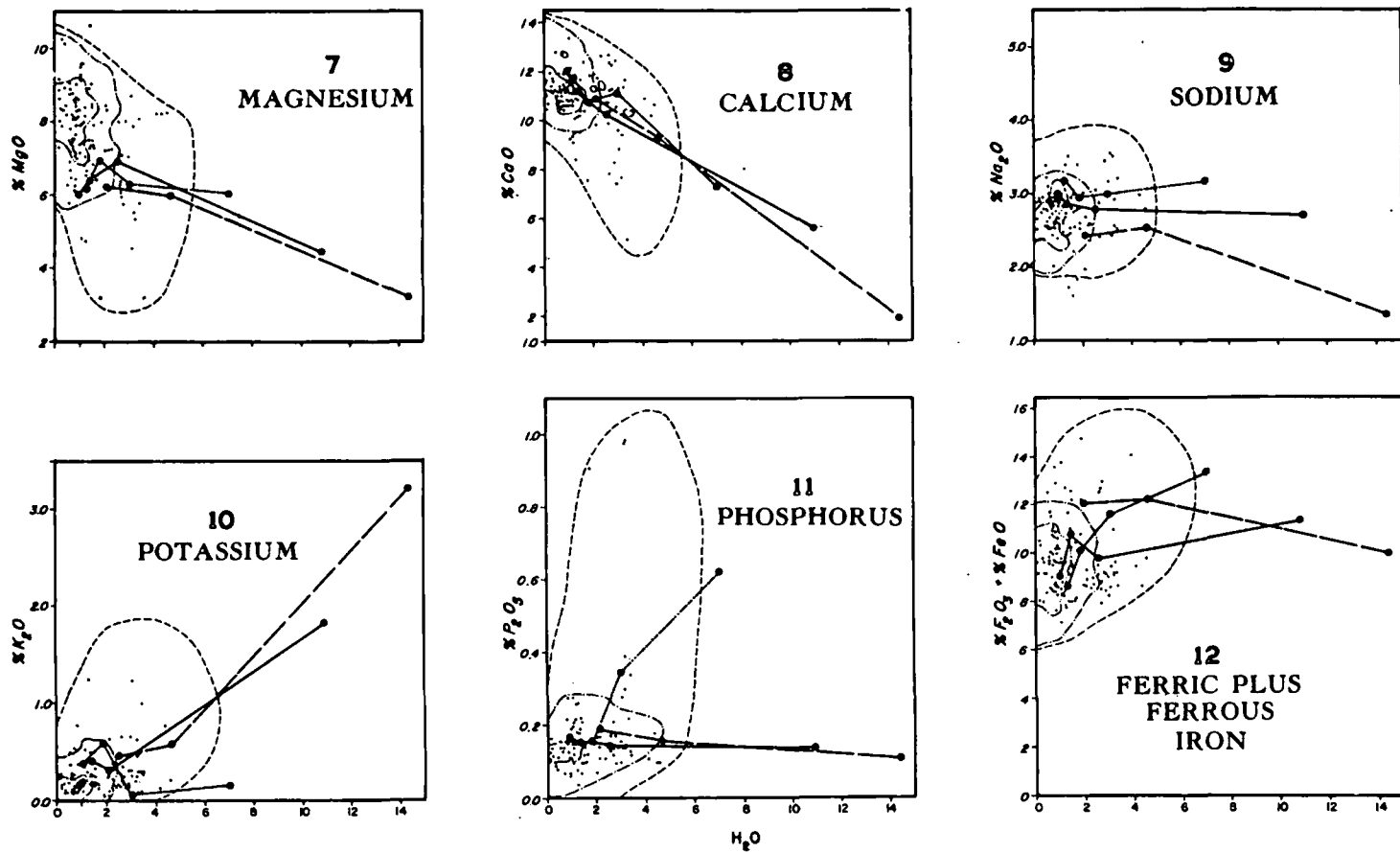
All the trends shown in fig. 2 can be interpreted as weathering trends when one makes a comparison of fresh ridge basalts with weathered ridge basalts as in table 1. The weathered ridge basalts in table 1 are

typified by concentric zones of brown discoloration, and alteration minerals such as chlorite, iddingsite and smectite replacing primary olivine, clinopyroxene and plagioclase. An average alkali basalt composition is given in table 1 to emphasize that a weathered ridge basalt can be confused with an alkali basalt with the exception of the low water and oxidized iron contents found in fresh alkali basalt.

The single sample core to rim weathering trends of Miyashiro et al. [15] and Paster [16] can be correlated with the ridge basalt age trends of fig. 2. This is done, first of all, in a plot of total alkalis versus silica in fig. 3. The single sample trends of Miyashiro et al. [15] and Paster [16] are plotted along with all the analysis of ridge basalts used previously to plot fig. 1. The ridge basalts are contoured according to age and follow the core to rim weathering trends. The dividing line between alkali and tholeiitic basalts first used by McDonald and Katsura [35] but now of questionable

- 0 MYBP (Ridge axis)
- 1-4 MYBP (Crestal province)
- 5-18 MYBP (Flanks)
- Core to rim basaltic trend from Myashiro (1969)
- Core to rim pillow trend from Paster (1968)
- Core to rim pillow trend from Paster (1968)





CHEMICAL EXCHANGE BETWEEN SEA WATER AND DEEP OCEAN BASALTS

Fig. 4. Plots of the oxides of eleven major elements and ferric plus ferrous iron versus water content for ridge basalts and core-to-rim weathering trends. The ridge basalts are contoured according to age and show that the changes in percent chemical compositions are related to water content and known weathering trends.

Table 1
Comparison of fresh ridge basalt with ridge basalt identified as altered by the authors.

Chemical constituent	Average of 45 fresh ridge basalt	Average of 24 weathered ridge basalts	Average of 178 alkalic basalts*
SiO ₂	49.92	47.92	46.9
TiO ₂	1.53	1.84	3.0
Al ₂ O ₃	15.63	15.95	15.5
Fe ₂ O ₃	1.65	4.58	3.1
FeO	8.19	6.05	8.6
MnO	0.17	0.19	0.16
MgO	7.65	6.38	6.9
CaO	11.17	10.73	10.4
Na ₂ O	2.75	2.91	3.0
K ₂ O	0.16	0.53	1.3
H ₂ O	0.95	2.19	0.8
P ₂ O ₅	0.13	0.25	0.39

* From Manson [40].

usefulness, is included only as a reference to point out that a basalt of apparent alkali nature can be produced from a tholeiitic basalt by interaction with sea water.

The core to rim weathering trends of Miyashiro [15] and Paster [16] are compared to ridge basalts in a plot of eleven major elements plus total iron versus water in fig. 4. In the core to rim trends, the water content is always greatest on the outside emphasizing

interchange with sea water as opposed to deuteric alteration. The ridge samples are contoured to age and it can clearly be seen that they pick up water and exchange elements as they get progressively older. The ridge basalts trends generally show good correlation to the core-rim trends.

Since the chemical changes reported here are all in percentages it is virtually impossible to estimate absolute gains and losses in the exchange between sea water and basalts. The percentage change of one element may only be an apparent change brought about by the change of a different element. An attempt to discuss the real chemical changes going on between sea water and basalts can be made by assuming that aluminum is constant, and that all changes relative to it are real. This assumption is supported by the common observation that aluminum is the most immobile cation during subaerial weathering of silicate rocks as discussed by Loughnan [36]. By fitting straight lines to the age plot in fig. 1, an estimate of weight change can be made for each element assuming a specific gravity of 2.60 g/cm³ for ocean floor basalt. Fig. 2 shows the net gains and losses estimated for a period of 7 X 10⁶ years. The net loss is 2.67 X 10⁻² g/cm³ greater than the net gain suggesting that either the density of the rock decreases, the

Table 2
Basalt weathering exchange with sea water in 7 X 10⁶ years*.
Units = 10⁻² g/cm³.

Constant	Lost to sea water	Gained from sea water
Al = 0	SiO ₂ = 5.2	TiO ₂ = 1.1
	MgO = 2.9	FeO = 2.6
	CaO = 2.1	MnO = 0.05
	-	NaO ₂ = 0.2
	-	K ₂ O = 0.9
	-	P ₂ O ₅ = 0.08
	-	H ₂ O = 2.6
	Total lost 10.2	Total gained 7.53

* Assuming constant aluminum composition and a constant specific gravity of 2.60 for ridge basalt.

curves
constan

The
the alte
and clay
the alte
convert
water. T
oxide d
Titanium
Potassium
mangan
small an
alteratio
added to
minerals

The r
one of t
need for
cularly i
Further
effects o
Further
between
range ba
likely ad
between
basalt of
reasons
one mag
similar c

3. Geoch

The ir
sea water
of the m
to which
floor. Pre
program
sect. Con
4000 m c
mineral r
weatherin
In ord
mg on th
the annu

curves of fig. 1 are inaccurate, or the assumption of constant aluminum is incorrect.

The loss of silica and magnesium may be a result of the alteration of olivine and clinopyroxene to chlorite and clay minerals. The loss of calcite may come from the alteration of anorthite to smectite which is then converted to illite extracting potassium from sea water. The increase in iron may be a result of iron oxide deposition as oxide coatings and cavity fillings. Titanium may go into the formation of ilmenite. Potassium probably goes into illite. Phosphorus, manganese and sodium are probably picked up in small amounts but it is difficult to predict which alteration minerals they would favor. Water is probably added to the rock both in the formation of clay minerals and as absorbed interstitial material.

The number of available analyses is inadequate and one of the purposes of this paper is to point out the need for more analysis of the deep ocean floor, particularly in regions removed from the spreading centers. Furthermore, in future studies of oceanic rocks, the effects of weathering must be taken into account. Further studies should also clarify the relationship between deuteric alteration and weathering. In the long range balance of ocean chemistry, the effects are most likely additive. Efforts should be made to distinguish between true alkali basalt and a weathered ridge basalt of alkali composition; and the underlying reasons explaining two apparently different processes, one magmatic and one weathering, producing rocks of similar composition need to be further studied.

3. Geochemical implications

The importance of the chemical exchange between sea water and basalts in the overall geochemical budget of the major elements depends largely on the depth to which sea water weathering penetrates the ocean floor. Preliminary results in the JOIDES coring program have revealed altered basalt at a depth of ten feet. Considering the hydrostatic head provided by 4000 m of sea water and fluxing ability of water in mineral reactions, it seems likely that sea floor basalt weathering will extend to significant depths.

In order to judge the importance of basalt weathering on the geochemical budget of the major elements, the annual contribution per cm^2 of ocean floor of a 1

cm deep layer of basalt is compared to annual dissolved stream supply in table 3. The basalt weathering values were derived from the age curves in fig. 2. Column 3 gives the depth of basalt weathering necessary to equate the weathering contribution to stream supply.

The effects of sediment cover in preventing the chemical exchange between sea water and ocean basalts must be further studied. In the long term balance of the oceans, sea water may only be an intermediate reservoir for cations exchanging between basalts and sediments; the net end effect would be the same whether cation exchanged directly between sediments and basalt or entered active oceanic circulation. For the present time, since we know one third of the ocean floor is virtually free of sediments, the figures for basalt weathering contribution to sea water in table 3 can be cut by one third in order to get an idea of the maximum effect of sediment cover.

Titanium is the element most likely to be controlled by the basalt weathering process, in fact, given the present estimates of stream supply, it is difficult to provide a source for the amount of titanium apparently enriched in basalts during the weathering process. The iron balance of the oceans is certainly strongly influenced by sea water action on basalts and a source of iron must be looked for. Manganese and phosphorus require greater weathering depths than do either titanium or iron; but they too may be strongly governed by weathering of basalt. Silica, magnesium and potassium all would apparently require still greater depths of basalt weathering and our present lack of knowledge of the ocean floor prohibits us from making further elaborations on these elements. The calcium and sodium concentration of sea water seem the least likely to be affected by basalt weathering.

4. Conclusions

Deep ocean basalts act as sources for silica, magnesium and calcium and act as sinks for titanium, potassium, phosphorus, manganese, total iron and sodium relative to sea water. Aluminum shows no conclusive exchange with sea water. Ferric iron replaces ferrous iron.

The chemical exchange between sea water and basalts should be considered in petrologic theories for

Table 3
Comparison of basalt weathering and stream supply.

Chemical constituent	Annual weathering contribution from 1 cm layer of basalt	Annual stream* contribution	Weathering depth in cm
SiO ₂	+ 7.4	+1.3 × 10 ⁵	17 600
TiO ₂	-1.6	+0.3 × 10 ²	18
(Fe)	-3.3	+(0.6 × 10 ³)	182
Mn	-0.06	+0.7 × 10 ²	1 166
Mg	+ 2.3	+0.4 × 10 ⁵	17 400
Na	-0.21	+6.3 × 10 ⁴	300 000
Ca	+ 2.1	+1.5 × 10 ⁵	71 500
K	-0.9	+2.3 × 10 ⁴	25 500
P	-0.14	+0.2 × 10 ³	1 430

Plus (+) indicates addition to sea water, minus (-) indicates extraction from sea water. Units 10⁻⁹ g/cm² of sea floor. Fourth column indicates depth of weathering required to equate stream supply and weathering contribution.

* From Turekian [39].

the origin of oceanic rocks and in theories concerning the geochemical mass balance of the oceans.

Acknowledgements

Bert Tanner and Troy Holcombe very helpfully wrote the computer programs. Ellyn Johnson and Gloria Shull worked on the manuscript. Peter Vogt, Leonard Johnson, Stanley Hart, Eric Schneider and Bill Moore all offered helpful discussions during the course of the work and many useful criticisms of the manuscript.

References

- [1] A.R.McBirney and I.G.Gass, Relations of Oceanic Volcanic Rocks to Mid-Oceanic Rises and Heat Flow, *Earth Planet. Sci. Letters* 2 (1967) 265.
- [2] A.E.J.Engel, C.G.Engel and R.G.Havens, Chemical Characteristics of Oceanic Basalts and the Upper Mantle, *Bull. Geol. Soc. Am.*, 76 (1965) 719.
- [3] H.S.Yoder and C.E.Tilley, Origin of Basalt Magmas, An Experimental Study of Natural Synthetic Rock Systems, *J. Petrology* 3 (1962) 342.
- [4] F.Aumento, Magmatic Evolution on the Mid-Atlantic Ridge, *Earth Planet. Sci. Letters* 2 (1967).
- [5] D.H.Green and A.E.Ringwood, Mineral Assemblages in a Model Mantle Composition, *J. Geophys. Res.* 68 (1963) 937.
- [6] R.Kay, N.J.Hubbard and P.W.Gast, Chemical Characteristics and Origin of Oceanic Ridge Volcanic Rocks, *J. Geophys. Res.* 73 (1970) 5925.
- [7] H.H.Hess, *History of Ocean Basins*, Geol. Soc. Am., *Buddington Volume* (1962) 599.
- [8] R.S.Dietz, Continent and Ocean Basin Evolution by Spreading of the Sea Floor, *Nature* 190 (1961) 854.
- [9] F.J.Vine and D.H.Matthews, Magnetic Anomalies over Oceanic Ridges, *Nature* 199 (1963) 947.
- [10] C.G.Engel, R.L.Fisher and A.E.J.Engel, Igneous Rocks of the Indian Ocean Floor, *Science* 150 (1965) 605.
- [11] G.D.Nicholls, Environmental Studies in Sedimentary Geochemistry, *Sci. Prog.* 51 (1963) 12.
- [12] J.G.Moore, Rate of Palagonitization of Submarine Basalt Adjacent to Hawaii, U.S. Geol. Survey Prof. Paper 550-D (1966) D163-D171.
- [13] S.R.Hart and A.J.Nawalk, K, Rb, Cs, and Sr. Relationships in Submarine Basalts from the Puerto Rico Trench, *Geochim. Cosmochim. Acta*, in press.
- [14] S.H.Hart, K, Rb, Cs Contents and K/Rb, K/Cs Ratios of Fresh and Altered Submarine Basalts, *Earth Planet. Sci. Letters* 6 (1969) 295.
- [15] A.F.Miyashiro, F.Shido and M.Ewing, Diversity and Origin of Abyssal Theolite from the Mid-Atlantic Ridge Near 24° and 30° North Latitude, *Cont. Mineral and Petrol.* 23 (1969) 38. *rept. on weathering*
- [16] T.P.Paster, Petrologic Variations Within Submarine Basalt Pillows of the South Pacific-Antarctic Ocean, Ph. D. Thesis, Florida State University, 1968.
- [17] A.J.Nawalk, Geology of the North Wall of the Puerto Rico Trench, Ph. D. Thesis, University of Pittsburg, 1967.
- [18] A.E.J.Engel and C.G.Engel, Basalts Dredged from the North-Eastern Pacific Ocean, *Science* 140 (1963) 1321.

- [19] I.D.Muir and C.E.Tilley, Basalts from the Northern Part of the Rift Zone of the Mid-Atlantic Ridge, *J. Petrol.* 5 (1964) 409.
- [20] F.Aumento, The Mid-Atlantic Ridge near 45° North. II. From the Area of Confederation Peak, *Canad. J. Earth Sci.* 5 (1968) 1.
- [21] C.G.Engel and R.L.Fisher, Lherzolite, Anorthosite, Gabbro and Basalt Dredged from the Mid-Indian Oceanic Ridge, *Science* 166 (1969) 1130.
- [22] E.Bonatti, Mechanisms of Deep-Sea Volcanism in the South Pacific, *Researches in Geochemistry*, 2 J.Wiley and Sons, New York, N.Y., 663, in Abdson 453.
- [23] H.G.Melson, G.Thompson and T.H.van Andel, Volcanism and Metamorphism in the Mid-Atlantic Ridge, 22° North Latitude, *J. Geophys. Res.* 73 (1968) 5925.
- [24] A.E.J.Engel and C.G.Engel, Igneous Rocks of the East Pacific Rise, *Science* 146 (1964) 477.
- [25] F.D.Muir and C.E.Tilley, Basalts from the Northern Part of the Mid-Atlantic Ridge *J. Petrol.* 7 (1964) 193.
- [26] G.D.Nichols, A.J.Nawalk and E.E.Hays, The Nature and Composition of Rock Sample Dredged from the Mid-Atlantic Ridge Between 22° N and 52° N, *Marine Geol.* 1 (1964) 333.
- [27] A.E.S.Engel and C.G.Engel, Composition of Basalts from the Mid-Atlantic Ridge, *Science* 144 (1964) 1330.
- [28] J.R.Cann and F.J.Vine, An Area on the Crest of the Carlberg Ridge, *Petrology Magnetic Survey, Phil. Trans. Roy. Soc. A.* 258 (1965) 198.
- [29] F.Aumento and B.D.Loncarevic, The Mid-Atlantic Ridge Near 45° N. III. Bald Mountain, *Canad. J. Earth Sci.* 6 1 (1962) 11.
- [30] A.Poldervaart and J.Green, Chemical Analysis of Submarine Basalts, *Am. Miner.* 50 (1965) 1723.
- [31] C.G.Engel and T.E.Chase, Composition of Basalts Dredged from Seamounts off the West Coast of Central America, V.S.G.S. Prof. Paper 525-C, C161-C163, 1965.
- [32] P.Vogt, E.D.Schneider, O.Anderson and O.Avery, Discontinuities in Sea Floor Spreading, *Tectonophysics*, in press.
- [33] J.P.Heirtzler, G.O.Dickson, E.M.Herron, W.C.Pittman, III, and X. LePichon, Marine Magnetic Anomalies, Geomagnetic Field Reversals, and Motions of the Ocean Floor and Continents, *J. Geophys. Res.* 73 (1968) 2119.
- [34] P.E.Hayes and W.C.Pitmann, III, Magnetic Lineations in the North Pacific, *North Pacific Vol. GSA*, in press.
- [35] A.Cox, R.R.Doell, G.B.Palrymple, Time Scale for Geomagnetic Reversal, in *The History of the Earth's Crust*, R.A.Rinney, ed. (Princeton University Press, Princeton, 1968).
- [36] A.F.Maxwell, Recent Deep Sea Drilling Results from the South Atlantic, AGU abstract, April, 1969.
- [37] G.A.MacDonald and T.Katsuma, Chemical Composition of Hawaiian Lavas, *J. Petrology* 5 (1964) 82.
- [38] F.C.Loughman, *Chemical Weathering of the Silicates* (Elsevier Publishing Co., New York, 1969).
- [39] K.K.Turekiam, *The Oceans, Streams and Atmosphere*, in *Handbook of Geochemistry*, Wedepohl, ed. (Springer-Verlag Publ. Co., New York, 1969).
- [40] V.Manson, *Geochemistry of Basaltic Rocks: Major Elements, in Basalts. The Poldervaart Treatise on Rocks of Basaltic Composition*, Vol. 1, H.H.Hess and A.Poldervaart, eds. (Interscience, New York, 1967).

fourth

Characteristic
rocks, J.

Am.,

tion by
1) 854.
alies overeous Rocks
5) 605.
mentarymarine Basalt
Paper 550-DRelation-
tico Trench.Cs Ratios of
Planet. Sci.sity and
lantic
it. Mineral.marine
Ocean,he Puerto
tsburg,from the
963) 1321.

Calculation of mass transfer in geochemical processes involving aqueous solutions

UNIVERSITY OF UTAH
RESEARCH INSTITUTE
EARTH SCIENCE LAB.

HAROLD C. HELGESON, THOMAS H. BROWN, ANDREW NIGRINI*
and THOMAS A. JONES†

Department of Geological Sciences, Northwestern University, Evanston,
Illinois 60201

(Received 14 November 1969; accepted in revised form 22 December 1969)

Abstract—Differential equations providing for simultaneous dissolution of multiple reactant minerals, precipitation of mineral assemblages, variable activity of H_2O , oxidation-reduction reactions, binary solid solution, and changes in activity coefficients in both open and closed systems are incorporated in a grand matrix equation describing mass transfer in geochemical processes. Computer evaluation of this equation affords quantitative prediction of the extent to which minerals are produced and/or destroyed as well as changes in the composition of phases and distribution of species in geologic systems in which an irreversible reaction takes place between a given mineral or mineral assemblage and an aqueous solution at constant temperature and pressure. Computers and thermodynamic data currently available permit mass transfer calculations to be carried out for systems involving more than 60 components, phases, and chemical species at temperatures up to 300°C.

INTRODUCTION

Most geochemical processes involve the transfer of material from one set of phases to another as a result of chemical reactions caused by changes in temperature and/or pressure, or by introduction of an aqueous phase into a mineralogic environment with which it is not in equilibrium. Weathering, diagenesis, metamorphism, and hydrothermal metasomatism are familiar examples of such processes. It has already been demonstrated that matrix equations (HELGESON, 1968), thermodynamic data (ROBIE and WALDBAUM, 1968; WAGMAN *et al.*, 1968, 1969; HELGESON, 1969), and modern computers permit theoretical prediction of equilibrium states (HELGESON, BROWN and LEEPER, 1969) and mass transfer among phases in geochemical processes involving large numbers of components, phases, and chemical species at temperatures from 0° to 300°C (HELGESON, GARRELS and MACKENZIE, 1969; HELGESON, 1970c). The purpose of the present communication is to amplify, extend, and supplement the theoretical approach employed in these calculations, particularly with respect to geochemical processes involving minerals of variable composition and those in which the activity of H_2O and/or activity coefficients change significantly. Only isothermal-isobaric processes are considered below; mass transfer as a function of temperature and/or pressure will be the subject of a later communication.

THEORETICAL CONCEPTS

A geochemical process can be represented by an array of chemical reactions describing the transfer of mass from reactant minerals to other phases in the system. These phases include the aqueous solution as well as minerals precipitated as reaction products. Geologic systems are commonly in a state of partial equilibrium during

* Present address: Canadian Geological Survey, 601 Booth Street, Ottawa, Ontario, Canada.

† Present address: Esso Production Company, P.O. Box 2189, Houston, Texas 77001

GEOCHIM ET COSMOCHEM ACTA, 1970 v. 34 p. 569-592
(591?)

SUBJ
GCHM
CMTG

with the following

geochemical processes; i.e. the systems are in equilibrium with respect to at least one chemical reaction or process, but out of equilibrium with respect to others (BARTON *et al.*, 1963; HELGESON, 1968). The equilibrium states in the system may include homogeneous equilibrium (e.g. equilibrium among species in the aqueous solution) as well as equilibrium among product minerals and the aqueous phase. A geochemical process thus involves both reversible and irreversible chemical reactions.

The theoretical approach to mass transfer calculations summarized below is based in part on the assumption that homogeneous equilibrium prevails in the system and that equilibrium is maintained among the aqueous phase and the minerals precipitated as reaction products in geochemical processes. This assumption has a kinetic corollary in that the rates of reversible reactions representing these equilibria are assumed to be at least as fast as those of the irreversible reactions involved in the process. The dissolution of reactant minerals in the aqueous phase is thus regarded as the rate-limiting step. Both kinetic considerations (HELGESON, 1970a) and comparison of theoretical predictions with the characteristics of geologic systems (HELGESON, GARRELS and MACKENZIE, 1969; HELGESON, 1970c) support this assumption.

Resumé of thermodynamic relations

Changes in the distribution of components in a system resulting from reaction of a mineral or minerals with an aqueous phase can be described in terms of reaction coefficients in an irreversible chemical reaction describing the process. These reaction coefficients, which are negative for reactants and positive for products, are defined by

$$\bar{n}_s = \frac{dm_s}{d\xi} \quad (1)$$

or

$$\bar{n}_\phi = \frac{d\bar{x}_\phi}{d\xi} \quad (2)$$

where \bar{n}_s and \bar{n}_ϕ are the reaction coefficients for the s th aqueous species, ($s = 1, 2, \dots, S$) and the ϕ th mineral ($\phi = 1, 2, \dots, \Phi$) relative to one kgm of H_2O , \bar{x}_ϕ represents the number of moles per kgm of H_2O of the ϕ th mineral in the system, m_s refers to the molality of the subscripted species in the aqueous phase, and ξ is the progress variable for the irreversible reaction (DEDONDER, 1920; PRIGOGINE and DEFAY, 1954; HELGESON, 1968).

If an aqueous phase is involved in a geochemical process, all equilibrium states in the system can be represented by a set of independent reversible reactions (reactions that cannot be derived by summing other reactions in the set) involving a mineral and/or aqueous species. For each such reaction a statement of the Law of Mass Action can be written; i.e.

$$\prod_i a_{i,j}^{\nu_{i,j}} = K_j \quad (3)$$

where $a_{i,j}$ refers to the activity of the i th species (which may be an aqueous species or a mineral; $i = 1, 2, \dots, f$) involved in the j th reversible reaction ($j = 1, 2, \dots, J$), $\nu_{i,j}$ represents the coefficient of the subscripted species in the reversible reaction, and K_j is the equilibrium constant for the j th reaction. The coefficient \bar{n}_i , in equation

(3), which is a constant value for products

The activities of (depending on the assigned a constant error in mass transfer) chemical processes (1967b, 1968, 1970 approximation of t ; ξ ; provision for so below:

where the subscriptation in equation for H_2O . Let us now by equation (1) and The activity of

where γ_s is the activity of equation (5)

Taking account of

which can be combined

Combining equation

which can be differentiated

$$\bar{n}_s' = \frac{d^2}{d\xi^2}$$

Accordingly, the differential

(3), which is a constant, is assigned a negative value for reactants and a positive value for products in the reversible reaction.

The activities of minerals that exhibit less than five or ten per cent solid solution (depending on the departure from ideality of the solid solution) can usually be assigned a constant value of unity in equation (3) without introducing significant error in mass transfer calculations. Similarly, the activity of H₂O in many geochemical processes can be regarded as a constant with a value of one (HELGESON, 1967b, 1968, 1970b). These observations permit us to write the following close approximation of the derivative of equation (3) with respect to the progress variable, ξ ; provision for solid solution and variable activity of H₂O are discussed in detail below:

$$\sum_{s=2} \hat{n}_{s,j} (d \ln a_s / d\xi) = 0 \quad (4)$$

where the subscript s again refers to the aqueous species in the system. The summation in equation (4) is taken from $s = 2$ to provide for $s = 1$ as the designation for H₂O. Let us now recast equation (4) in terms of the reaction coefficients defined by equation (1) and take its derivative with respect to the progress variable.

The activity of the s th aqueous species is related to its molality by

$$a_s = \gamma_s m_s \quad (5)$$

where γ_s is the activity coefficient of the subscripted species. The logarithmic derivative of equation (5) appears as

$$\frac{d \ln a_s}{d\xi} = \frac{d \ln m_s}{d\xi} + \frac{d \ln \gamma_s}{d\xi} \quad (6)$$

Taking account of equation (6), we can write equation (4) as

$$\sum_{s=2} \hat{n}_{s,j} (d \ln m_s / d\xi) + \sum_{s=2} \hat{n}_{s,j} (d \ln \gamma_s / d\xi) = 0, \quad (7)$$

which can be combined with equation (1) to give

$$\sum_{s=2} \hat{n}_{s,j} \bar{n}_s / m_s + \sum_{s=2} \hat{n}_{s,j} (d \ln \gamma_s / d\xi) = 0. \quad (8)$$

Combining equations (1) and (6) leads to

$$\bar{n}_s = \frac{d m_s}{d\xi} = m_s \left(\frac{d \ln a_s}{d\xi} - \frac{d \ln \gamma_s}{d\xi} \right), \quad (9)$$

which can be differentiated to

$$\bar{n}_s' = \frac{d^2 m_s}{d\xi^2} = m_s \left(\frac{d^2 \ln a_s}{d\xi^2} - \frac{d^2 \ln \gamma_s}{d\xi^2} \right) + \bar{n}_s \left(\frac{d \ln a_s}{d\xi} - \frac{d \ln \gamma_s}{d\xi} \right). \quad (10)$$

Accordingly, the derivative of equation (8) can be written as

$$\sum_{s=2} \hat{n}_{s,j} \bar{n}_s' + \sum_{s=2} \hat{n}_{s,j} \frac{d^2 \ln \gamma_s}{d\xi^2} = \sum_{s=2} \frac{\hat{n}_{s,j} \bar{n}_s^2}{m_s^2}. \quad (11)$$

Before discussing the application of these equations in a geologic context, let us first consider conservation in geochemical processes.

Conservation of mass can be expressed as

$$\sum_{\epsilon} \nu_{\epsilon,s} \bar{n}_s + \sum_{\phi} \nu_{\epsilon,\phi} \bar{n}_{\phi} = 0, \quad (12)$$

where $\nu_{\epsilon,s}$ and $\nu_{\epsilon,\phi}$ correspond to the number of moles of the ϵ th chemical element ($\epsilon = 1, 2, \dots, \bar{E}$) in one mole of the s th aqueous species and one mole of the ϕ th mineral, respectively. Because electrical neutrality is maintained in the aqueous phase, we can write

$$\sum_{s} Z_s \bar{n}_s = 0, \quad (13)$$

where Z_s represents the charge on the s th aqueous species. The derivative of equation (13) can be combined with equation (1) to give

$$\sum_{s} Z_s \bar{n}_s' = 0. \quad (14)$$

Note that the derivatives of equations (12) and (14) can be written as

$$\sum_{\epsilon} \nu_{\epsilon,s} \bar{n}_s' + \sum_{\phi} \nu_{\epsilon,\phi} \bar{n}_{\phi}' = 0 \quad (15)$$

and

$$\sum_{s} Z_s \bar{n}_s' = 0. \quad (16)$$

where \bar{n}_s' and \bar{n}_{ϕ}' are defined by equation (10) and the derivative of equation (2), respectively.

If equilibrium is maintained among aqueous species and the minerals produced in a geochemical process, the number of unknown reaction coefficients in an irreversible reaction representing the process at a given time is always equal to or less than one plus the sum of the number of chemical elements involved in the reaction and the number of independent reversible reactions that can be written to describe the equilibrium states in the system, i.e.

$$s + \Phi \leq \bar{E} + j + 1. \quad (17)$$

The number of specific statements of equations (8), (12), and (14) is thus always equal to or greater than the number of unknown reaction coefficients, and the number of derivatives of these equations (equations 11, 15, and 16) is equal to or greater than the number of derivatives of the unknown reaction coefficients. All variables and constants other than the reaction coefficients in these equations are known or can be calculated (see below), which permits the unknown reaction coefficients and their derivatives to be computed for any stage of reaction progress by simultaneous solution of sets of these equations. Because the equations are all linear in the derivatives of n_s , this can be done expediently by employing matrix algebra and computer techniques (HELGESSON, 1968), which are discussed further in the pages that follow. Note that the number 1 in equation (17) refers to the conservation of charge expressed by equation (14), which must be included in the matrix only when oxidation-reduction equilibria are considered.

Mass transfer calculations for geochemical processes can be carried out with the

Calcul

aid of the r
discussed a
aqueous spe
destroyed a
chemical re
a Taylor's e

and

where $\Delta\xi$ ref
of the s th aq
with respect
after the qua
uation of th
new solution
(and their de
coefficients a
used to evalu
 10^{-5} or less i

The theor
geochemical p
must take ir
activity of H
this end let
coefficients of

The total
chemical pro
strength of t
1969). Many
concentration
ionic strength
strength of
constants, an
zero (HELGE
the mole tra
magnitude of
transfer calc
coefficients.

The solu
NaCl, CaCl₂,
supporting el

aid of the reaction coefficients and their derivatives computed from the equations discussed above. These calculations define the changes in the molalities of all aqueous species, and the number of moles (per kg of H₂O) of each mineral produced or destroyed as a result of successive increments of progress in an overall irreversible chemical reaction representing a given process. Difference equations of the form of a Taylor's expansion are suitable for this purpose; i.e.

$$\Delta n_s = \bar{n}_s \Delta \xi + \bar{n}_s' \frac{(\Delta \xi)^2}{2!} + \bar{n}_s'' \frac{(\Delta \xi)^3}{3!} + \dots \quad (18)$$

and

$$\Delta \bar{x}_s = \bar{n}_s \Delta \xi + \bar{n}_s' \frac{(\Delta \xi)^2}{2!} + \bar{n}_s'' \frac{(\Delta \xi)^3}{3!} + \dots \quad (19)$$

where $\Delta \xi$ refers to a small increment of reaction progress, \bar{n}_s is the reaction coefficient of the *s*th aqueous species, and \bar{n}_s' and \bar{n}_s'' are the first and second derivatives of \bar{n}_s with respect to ξ . Note that in most cases equations (18) and (19) can be truncated after the quadratic terms without causing significant error in the calculations. Evaluation of the equations for a given small increment of reaction progress defines a new solution composition, which is then used to compute new reaction coefficients (and their derivatives) from the equations summarized above. Because the reaction coefficients are rarely constant during reaction progress, small values of $\Delta \xi$ are used to evaluate equations (18) and (19). In practice, increments of ξ of the order of 10⁻⁵ or less insure accuracy in the calculations.

The theoretical equations summarized above are applicable to many, but not all geochemical processes involving an aqueous phase. To generalize these relations we must take into account factors such as changing activity coefficients, variable activity of H₂O, and solid solution among reactant and product minerals. Toward this end let us first derive explicit expressions for the derivatives of the activity coefficients of aqueous species in equations (8) and (11).

ACTIVITY COEFFICIENTS

The total mole transfer of ionic species to or from the aqueous phase in a geochemical process is commonly several orders of magnitude smaller than the ionic strength of the solution (HELGESON, 1968; HELGESON, GARRELS and MACKENZIE, 1969). Many aqueous solutions involved in these processes contain relatively high concentrations (>0.5*m*) of alkali and alkaline earth chlorides; consequently, their ionic strengths remain essentially constant during reaction progress. When the ionic strength of a solution is constant the activity coefficients of aqueous species are constants, and therefore $d \ln \gamma_s / d \xi$ and $d^2 \ln \gamma_s / d \xi^2$ in equations (8) and (11) reduce to zero (HELGESON, 1968). In contrast, where significant evaporation takes place, or the mole transfer of ionic species to or from the aqueous phase is of the order of magnitude of the ionic strength of the solution, provision should be included in mass transfer calculations for the effect of changing activity coefficients on reaction coefficients.

The solute in many natural electrolyte solutions consists predominantly of NaCl, CaCl₂, NaHCO₃, or a similar simple binary salt, which we shall refer to as the supporting electrolyte; i.e. the salt present in relatively large concentrations compared

to the concentrations of other dissolved solids. Activity coefficients of both charged and neutral species in such solutions can be approximated closely for a given temperature by (HELGESON and JAMES, 1968; HELGESON, 1969)

$$\log \gamma_s = \frac{-AZ_s^2 \bar{I}^{1/2}}{1 + a_s B \bar{I}^{1/2}} + \omega_s \bar{I} \quad (20)$$

where Z_s refers to the charge on the s th species, A and B are the molal Debye-Hückel parameters, a_s is the ion size parameter for the subscripted species, ω_s stands for one of two constants (explained below) characteristic of the supporting electrolyte, and \bar{I} is the true ionic strength of the solution defined by

$$\bar{I} = \frac{1}{2} \sum_s Z_s^2 m_s \quad (21)$$

True ionic strength (\bar{I}) differs from stoichiometric ionic strength (I) in that it depends on the distribution of species among complexes in the aqueous phase.

When an activity coefficient is computed from equation (20) for a charged species, ω_s in the equation is equal to the deviation function for the supporting electrolyte (HELGESON and JAMES, 1968; HELGESON, 1969); when the species is neutral, the first term on the right side of the equation reduces to zero and ω_s is either regarded as zero or assigned a value consistent with the activity coefficient of $\text{CO}_{2(aq)}$ in the supporting electrolyte, depending on the nature of the neutral species (HELGESON, 1969).

The derivative of equation (20) with respect to the progress variable, ξ , can be written as

$$\frac{d \ln \gamma_s}{d\xi} = 2.303 (\omega_s - C_s) \bar{I}', \quad (22)$$

where

$$C_s = \frac{AZ_s^2}{2\bar{I}^{1/2}(1 + a_s B \bar{I}^{1/2})^2} \quad (23)$$

and \bar{I}' is defined by the derivative of equation (21); i.e.

$$\bar{I}' = \frac{d\bar{I}}{d\xi} = \frac{1}{2} \sum_s Z_s^2 \frac{dm_s}{d\xi} = \frac{1}{2} \sum_s Z_s^2 \bar{n}_s \quad (24)$$

The derivative of equation (22) can be written as

$$\frac{d^2 \ln \gamma_s}{d\xi^2} = 2.303 ((\omega_s - C_s) \bar{I}'' - C_s' \bar{I}'), \quad (25)$$

where C_s' and \bar{I}'' are defined by the derivatives of equations (23) and (24), respectively; i.e.

$$C_s' = -AZ_s^2 \bar{I}' \left(\frac{1 + 3a_s B \bar{I}^{1/2}}{4\bar{I}^{3/2}(1 + a_s B \bar{I}^{1/2})^3} \right) \quad (26)$$

and

$$\bar{I}'' = \frac{d^2 \bar{I}}{d\xi^2} = \frac{1}{2} \sum_s Z_s^2 \frac{d^2 m_s}{d\xi^2} = \frac{1}{2} \sum_s Z_s^2 \bar{n}_s' \quad (27)$$

Calculat

It can be \bar{n}_s and \bar{n}_s' re
efficients and
puted direct
equations (8),
can be comb
matrix equat
reaction prog

and

$$\sum_{s=2} \bar{n}_s' \left(\frac{\bar{n}_{s,1}}{m_s} \right)$$

The summatic
for designation
is discussed be

The activi
chemical proce
can be regarde
where evapora
for the effects
modification of

The activit
electrolyte solu
solute. For ex
 H_2O , but the c
this reason, an
predominantly
solutions can b
the supporting

The activit
pressuro is rela

where 0.018 is
grams of H_2O ,
of the s th elect
the salt; e.g.,
efficient of the
perature and p

It can be seen by inspection that equations (22) and (25) are linear functions of \bar{n}_s and \bar{n}_s' respectively. All variables and constants other than the reaction coefficients and their derivatives in these equations are either known or can be computed directly from thermodynamic data (HELGESON, 1969). Consequently, equations (8), (22), (23), and (24), and equations (11), (25), (26), and (27), respectively, can be combined to permit explicit calculation of \bar{n}_s and (subsequently) \bar{n}_s' from matrix equations for cases in which activity coefficients vary significantly during reaction progress. The equations in the matrices can be represented by

$$\sum_{s=2} \bar{n}_s \left(\frac{\hat{n}_{s,j}}{m_s} + \frac{2 \cdot 303 Z_s^2}{2} \sum_{i=2} \hat{n}_{s,i} (\omega_s - C_{s,i}) \right) = 0 \quad (28)$$

and

$$\sum_{s=2} \bar{n}_s' \left(\frac{\hat{n}_{s,j}}{m_s} + \frac{2 \cdot 303 Z_s^2}{2} \sum_{i=2} \hat{n}_{s,i} (\omega_s - C_{s,i}) \right) = \sum_{s=2} \bar{n}_s \left(\frac{\hat{n}_{s,j} \bar{n}_s}{m_s^2} + \frac{2 \cdot 303 Z_s^2}{2} \sum_{i=2} \hat{n}_{s,i} C'_{s,i} \right) \quad (29)$$

The summations in equations (28) and (29) are again taken from $s = 2$ to provide for designation of $s = 1$ as H₂O. Simultaneous evaluation of sets of these equations is discussed below.

ACTIVITY OF H₂O

The activity of H₂O changes insignificantly in most isothermal-isobaric geochemical processes. As indicated above, the activity of H₂O in such processes often can be regarded as a constant equal to one (HELGESON, 1967b, 1968, 1970b). However, where evaporation is involved, mass transfer calculations should include provision for the effects of changing activity of H₂O on reaction coefficients. This requires modification of some of the preceding differential equations.

The activity of H₂O rarely decreases below 0.7 during evaporation of natural electrolyte solutions, and it is relatively insensitive to compositional variation of the solute. For example, addition of CaCl₂ to an NaCl solution lowers the activity of H₂O, but the change is of the order of a tenth of the molality of CaCl₂ added. For this reason, and because the solute in many natural electrolyte solutions consists predominantly of a simple binary salt such as NaCl, the activity of H₂O in such solutions can be approximated closely by the activity of H₂O in a pure solution of the supporting electrolyte.

The activity of H₂O in a binary electrolyte solution at a given temperature and pressure is related to the total molality of the solute (m_s) by

$$\ln a_{H_2O} = -0.018 \nu_{\pm,s} m_s \hat{\phi}_s \quad (30)$$

where 0.018 is equal to the molecular weight of H₂O (in grams) divided by 10³ grams of H₂O, $\nu_{\pm,s}$ refers to the stoichiometric number of moles of ions in one mole of the s th electrolyte (i.e. the number of moles of ions appearing in the formula for the salt; e.g., $\nu_{\pm,s} = 2$ for NaCl and 3 for CaCl₂), and $\hat{\phi}_s$ is the molal osmotic coefficient of the electrolyte. The osmotic coefficient of an electrolyte at a given temperature and pressure can be computed from an extended Debye-Hückel power

function of the stoichiometric ionic strength (I) of the solution (LIETZKE and STOUGHTON, 1961; HELGESON, 1967b, 1969); i.e.

$$\hat{\phi}_e = 1 - D_e J_e + \frac{b_2 I_e}{2} + \frac{2b_3 I_e^2}{3} + \frac{3b_4 I_e^3}{4}, \quad (31)$$

where D_e and J_e are defined, respectively, by

$$D_e = \frac{2 \cdot 303 A |Z_{+,e} Z_{-,e}|}{b_1^3 I_e} \quad (32)$$

and

$$J_e = 1 + b_1 I_e^{1/2} - 2 \ln(1 + b_1 I_e^{1/2}) - \frac{1}{1 + b_1 I_e^{1/2}} \quad (33)$$

The symbols b_1 , b_2 , b_3 , and b_4 in equations (31) through (33) refer to constants (fit parameters) in the power function, and $Z_{+,e}$ and $Z_{-,e}$ stand for the stoichiometric charges on the cation and anion in the e th electrolyte.

The stoichiometric ionic strength of an electrolyte solution in which the solute consists of a binary salt is defined by

$$I_e = \frac{m_e}{2} (\nu_{+,e} Z_{+,e}^2 + \nu_{-,e} Z_{-,e}^2), \quad (34)$$

where $\nu_{+,e}$ and $\nu_{-,e}$ refer to the stoichiometric number of moles of the cation and anion, respectively, in one mole of the solute. The molality of the solute can be expressed as

$$m_e = \frac{1}{\nu_{+,e}} \sum_s \nu_{+,e,s} m_s \quad (35)$$

where $\nu_{+,e,s}$ refers to the number of moles of the cation in the formula of the e th supporting electrolyte in one mole of the s th aqueous species. Combining equations (34) and (35) leads to

$$I_e = \left(\frac{\nu_{+,e} Z_{+,e}^2 + \nu_{-,e} Z_{-,e}^2}{2\nu_{+,e}} \right) \sum_s \nu_{+,e,s} m_s \quad (36)$$

The first and second derivatives of equation (30) with respect to the progress variable, ξ , are given by

$$\frac{d \ln a_{H_2O}}{d\xi} = -0.018 \nu_{\pm,e} (\hat{\phi}_e m_e' + m_e \hat{\phi}_e') \quad (37)$$

and

$$\frac{d^2 \ln a_{H_2O}}{d\xi^2} = -0.018 \nu_{\pm,e} (\hat{\phi}_e m_e'' + 2m_e' \hat{\phi}_e' + m_e \hat{\phi}_e''), \quad (38)$$

where $\hat{\phi}_e'$, $\hat{\phi}_e''$, m_e' and m_e'' are defined by the derivatives of equations (31) and (35). The first two derivatives of equations (31) can be written, respectively, as

$$\hat{\phi}_e' = \frac{d\hat{\phi}_e}{d\xi} = -D_e J_e' - J_e D_e' + I_e' \left(\frac{b_2}{2} + \frac{4b_3 I_e}{3} + \frac{9b_4 I_e^2}{4} \right) \quad (39)$$

and

$$\hat{\phi}_e'' = \frac{d^2 \hat{\phi}_e}{d\xi^2} = -D_e J_e'' - 2J_e' D_e' - J_e D_e'' + I_e'' \left(\frac{b_2}{2} + \frac{4b_3 I_e}{3} + \frac{9b_4 I_e^2}{4} \right) + (I_e')^2 \left(\frac{4b_3}{3} + \frac{9b_4 I_e}{2} \right) \quad (40)$$

where the coefficients D_e' , J_e' , D_e'' , and J_e'' are given by the derivatives of equations (32) and (33); i.e.

$$D_e' = -\frac{2 \cdot 303 A |Z_{+,e} Z_{-,e}| I_e'}{b_1^3 I_e^2} = -\frac{D_e I_e'}{I_e} \quad (41)$$

$$D_e'' = -2 \cdot 303 A |Z_{+,e} Z_{-,e}| \left(\frac{I_e''}{b_1^3 I_e^2} - \frac{2(I_e')^2}{b_1^3 I_e^3} \right) = -\frac{D_e I_e''}{I_e} + \frac{2D_e (I_e')^2}{I_e^2} \quad (42)$$

$$J_e' = \frac{b_1^3 I_e' I_e^{1/2}}{2(1 + b_1 I_e^{1/2})^2} \quad (43)$$

and

$$J_e'' = J_e' \left(\frac{I_e''}{I_e} + \frac{I_e' (1 - b_1 I_e^{1/2})}{2I_e (1 + b_1 I_e^{1/2})} \right) \quad (44)$$

Taking account of equations (9) and (10), the first and second derivatives of equations (35) and (36) can be written as

$$m_e' = \frac{dm_e}{d\xi} = \frac{1}{v_{+,e}} \sum_i v_{+,e,i} \bar{n}_i \quad (45)$$

$$m_e'' = \frac{d^2 m_e}{d\xi^2} = \frac{1}{v_{+,e}} \sum_i v_{+,e,i} \bar{n}_i' \quad (46)$$

$$I_e' = \frac{dI_e}{d\xi} = \frac{v_{+,e} Z_{+,e}^2 + v_{-,e} Z_{-,e}^2}{2v_{+,e}} \sum_i v_{+,e,i} \bar{n}_i \quad (47)$$

and

$$I_e'' = \frac{d^2 I_e}{d\xi^2} = \frac{v_{+,e} Z_{+,e}^2 + v_{-,e} Z_{-,e}^2}{2v_{+,e}} \sum_i v_{+,e,i} \bar{n}_i' \quad (48)$$

It can be seen by inspection that equations (39) and (41), and equations (40) and (42) are linear functions of I_e' and I_e'' , respectively. Accordingly, we can write equations (39) and (40) as

$$\hat{\phi}_e' = \frac{d\hat{\phi}_e}{d\xi} = I_e' \left(\frac{J_e D_e}{I_e} - D_e I_e^{1/2} \hat{W}_e + L_e \right) \quad (49)$$

and

$$\hat{\phi}_e'' = \frac{d^2 \hat{\phi}_e}{d\xi^2} = I_e'' \left(\frac{J_e D_e}{I_e} - D_e I_e^{1/2} \hat{W}_e + L_e \right) + (I_e')^2 \left(D_e \left(\hat{W}_e \left(\frac{3}{2I_e^{1/2}} + Y_e \right) - \frac{2J_e}{I_e^2} \right) + Q_e \right) \quad (50)$$

where

$$\hat{W}_s = \frac{b_1^3}{2(1 + b_1 I_s^{1/2})^2} = \frac{J_s'}{I_s' I_s'^2} \quad (51)$$

$$Y_s = \frac{b_1}{1 + b_1 I_s^{1/2}} \quad (52)$$

$$L_s = \frac{b_2}{2} + \frac{4b_3 I_s}{3} + \frac{9b_4 I_s^2}{4} \quad (53)$$

and

$$Q_s = \frac{4b_3}{3} + \frac{9b_4 I_s}{2} \quad (54)$$

Because I_s' and I_s'' are linear functions of \bar{n}_s and \bar{n}_s' , respectively, equations (37) and (38) can be combined with equations (45), (47), and (49), and (46), (48) and (50) to give linear expressions in which all variables and constants other than the reaction coefficients and their derivatives are known or can be computed; i.e.

$$\frac{d \ln a_{H_2O}}{d\xi} = \hat{F}_s \sum \nu_{+,s} \bar{n}_s \quad (55)$$

and

$$\frac{d^2 \ln a_{H_2O}}{d\xi^2} = \hat{F}_s \sum \nu_{+,s} \bar{n}_s' - \hat{H}_s \left(\sum \nu_{+,s} \bar{n}_s \right)^2 \quad (56)$$

where

$$\hat{F}_s = -0.018 \nu_{\pm,s} \left(\frac{\hat{\phi}_s}{\nu_{+,s}} + m_s \frac{(\nu_{+,s} Z_{+,s}^2 + \nu_{-,s} Z_{-,s}^2)}{2\nu_{+,s}} \left(\frac{J_s D_s}{I_s} - I_s^{1/2} \hat{W}_s D_s + L_s \right) \right) \quad (57)$$

and

$$\hat{H}_s = 0.018 \nu_{\pm,s} \left[m_s \left(\frac{\nu_{+,s} Z_{+,s}^2 + \nu_{-,s} Z_{-,s}^2}{2\nu_{+,s}} \right)^2 \times \left(D_s \left(\hat{W}_s \left(\frac{3}{2I_s^{1/2}} + Y_s \right) - \frac{2J_s}{I_s^2} \right) + Q_s \right) + \frac{1}{\nu_{+,s}} \left(\frac{\nu_{+,s} Z_{+,s}^2 + \nu_{-,s} Z_{-,s}^2}{\nu_{+,s}} \right) \left(\frac{J_s D_s}{I_s} - \hat{W}_s D_s I_s^{1/2} + L_s \right) \right] \quad (58)$$

Equations (55) and (56) can now be combined with equations (28) and (29), respectively, to give differential equations for reversible reactions in geochemical processes in which both activity coefficients and the activity of H_2O vary; i.e.

$$\sum_{s=2} \bar{n}_s \left(\frac{\hat{n}_{s,j}}{m_s} + \frac{2 \cdot 303 Z_s^2}{2} \sum_{i=2} (\hat{n}_{s,i} (\omega_s - C_{s,i})) + \hat{n}_{s-1,j} \hat{F}_s \nu_{+,s} \right) = 0 \quad (59)$$

and

$$\sum_{s=2} \bar{n}_s' \left(\frac{\hat{n}_{s,j}}{m_s} + \frac{2 \cdot 303 Z_s^2}{2} \sum_{i=2} \hat{n}_{s,i} (\omega_s - C_{s,i}) + \hat{n}_{s-1,j} \hat{F}_s \nu_{+,s} \right) = \sum_{s=2} \bar{n}_s \left(\frac{\hat{n}_{s,j} \bar{n}_s}{m_s^2} + \frac{2 \cdot 303 Z_s^2}{2} \sum_{i=2} (\hat{n}_{s,i} C'_{s,i}) \right) + \hat{n}_{s-1,j} \hat{H}_s \left(\sum \nu_{+,s} \bar{n}_s \right)^2 \quad (60)$$

Calcul

Equatio
fixed comp
processes.
consequenc
solution on

Evaporation

As a gen
out without
reaction pro
from the aq
system. Acc
fication of tl

Material
 H_2O is chan

where $n_{i,s}^0$ re
 $\bar{n}_{i,s}^0$ refers to
of solvent H_2
stage of reac
divided by
written for
initially.

If we nov
by reaction a
changes) and
constant for
variable, ξ , c

where $\bar{n}_{i,s}$ rep
kilogram of
(i.e. $dn_{H_2O}/d\xi$)
changing, eq
per kilogram

The num
evaporation
equations (1)

Equations (59) and (60) represent reversible reactions involving minerals of fixed composition and/or aqueous species in matrix equations describing geochemical processes. Before setting up the matrix equations, let us first consider briefly the consequences of removing H₂O from the system, and examine the effects of solid solution on mass transfer in geochemical processes.

Evaporation and conservation of mass

As a general rule, calculation of mass transfer per kilogram of H₂O can be carried out without making explicit provision for changes in the mass of solvent accompanying reaction progress. This is true as long as the mass of H₂O contributed to or removed from the aqueous phase by reaction is small compared to the mass of H₂O in the system. Accordingly, few processes other than dilution or evaporation require modification of the mass transfer equations summarized above.

Material balance per kilogram of H₂O in a system in which the mass of solvent H₂O is changing can be expressed by

$$\bar{n}_{i,e} = \frac{55.5 n_{i,e}^0}{n_{H_2O}} \quad (61)$$

where $n_{i,e}^0$ represents the total number of moles of the ϵ th element in the system, $\bar{n}_{i,e}^0$ refers to the total number of moles of the ϵ th element in the system per kilogram of solvent H₂O, n_{H_2O} is the number of moles of solvent H₂O in the system at a given stage of reaction or evaporation progress, and 55.5 is equal to 1000 grams of H₂O divided by the molecular weight of H₂O in grams. Note that equation (61) is written for a system in which the aqueous phase contains one kilogram of H₂O initially.

If we now regard all evaporated H₂O as well as all H₂O produced or consumed by reaction as a part of the system (i.e. total H₂O remains constant as solvent H₂O changes) and specify a constant mass for all other components in the system, $n_{i,e}^0$ is a constant for all elements. The derivative of equation (61) with respect to the progress variable, ξ , can then be written as

$$\bar{n}_{i,e} = \frac{d\bar{n}_{i,e}}{d\xi} = - \frac{55.5 n_{i,e}^0 \bar{n}_{H_2O}}{n_{H_2O}^2} \quad (62)$$

where $\bar{n}_{i,e}$ represents the change in the total number of moles of the ϵ th element per kilogram of solvent H₂O, and \bar{n}_{H_2O} refers to the reaction coefficient of solvent H₂O (i.e. $dn_{H_2O}/d\xi$). It follows from equation (62) that where the mass of the solvent is changing, equation (12) is no longer equal to zero. In contrast, conservation of mass per kilogram of solvent H₂O in the system is now expressed by

$$\sum_{\epsilon} \nu_{\epsilon} \bar{n}_{\epsilon} + \sum_{\phi} \nu_{\phi} \bar{n}_{\phi} = \bar{n}_{i,e} = - \frac{55.5 n_{i,e}^0 \bar{n}_{H_2O}}{n_{H_2O}^2} \quad (63)$$

The number of moles of solvent H₂O in the system at any given stage of reaction or evaporation progress can be computed from a Taylor's expansion analogous to equations (18) and (19); i.e.

$$n_{H_2O} = n_{H_2O}^0 + \bar{n}_{H_2O} \Delta\xi + \frac{\bar{n}'_{H_2O} (\Delta\xi)^2}{2!} + \dots \quad (64)$$

where $n_{H_2O}^0$ is the number of moles of solvent H_2O at the end of the preceding increment of reaction or evaporation progress, and \bar{n}_{H_2O} stands for $dn_{H_2O}/d\xi$.

SOLID SOLUTION

Solid solution minerals reacting irreversibly with an aqueous phase are treated in mass transfer calculations as minerals with fixed compositions. In contrast, when a solid solution mineral is a product of the reaction, provision must be included in the calculations for changes in its composition. Compositional variation in a product mineral can be taken into account by writing reversible reactions between the mineral and the aqueous phase in terms of the activities of aqueous species and a given end member in the solid solution series. For the purpose of deriving differential equations corresponding to such reactions, let us consider a binary solid solution of end members represented by the subscripts h and l , respectively. Equilibrium between the solid solution mineral and the aqueous phase can then be represented by a statement of equation (3) written as

$$a_h^{-1} \prod a_s^{n_{s,h}} = K_j \quad (65)$$

The activity of the end member designated as h in the solid solution is related to its mole fraction (X_h) by

$$a_h = \lambda_h X_h \quad (66)$$

where λ_h is the activity coefficient of the subscripted end member in the solid solution. The first and second logarithmic derivatives of equation (66) appear as

$$\frac{d \ln a_h}{d\xi} = \frac{d \ln \lambda_h}{d\xi} + \frac{d \ln X_h}{d\xi} \quad (67)$$

and

$$\frac{d^2 \ln a_h}{d\xi^2} = \frac{d^2 \ln \lambda_h}{d\xi^2} + \frac{d^2 \ln X_h}{d\xi^2} \quad (68)$$

For the moment let us omit provision for changing activity of H_2O and retain the designation of $s = 1$ for this species. Taking account of equations (1), (5), and (67) we can then write the first and second derivatives of equation (65) as

$$-\frac{d \ln X_h}{d\xi} - \frac{d \ln \lambda_h}{d\xi} + \sum_{s=2} \frac{\hat{n}_{s,h} \bar{n}_s}{m_s} + \sum_{s=2} \hat{n}_{s,l} \frac{d \ln \gamma_s}{d\xi} = 0 \quad (69)$$

and

$$-\frac{d^2 \ln X_h}{d\xi^2} - \frac{d^2 \ln \lambda_h}{d\xi^2} + \sum_{s=2} \frac{\hat{n}_{s,h} \bar{n}_s'}{m_s} + \sum_{s=2} \hat{n}_{s,l} \frac{d^2 \ln \gamma_s}{d\xi^2} = \sum_{s=2} \frac{\hat{n}_{s,h} \bar{n}_s^2}{m_s^2} \quad (70)$$

Note that equations (69) and (70) are analogous to equations (8) and (11).

Prediction of the extent to which a mineral of variable composition is produced during a geochemical process requires equations relating the change in the mole fractions and activity coefficients of the end members in the solid solution to the change in the mass of the solid solution in the system.

Calcul

Mole fractio

The mol
related to e

and

where \bar{x}_h an
the solid so

Note that t
 ξ , can be w

If we ne

from which

Taking acc

For a binar

and thus

Equation (
give

It then als

It can be s
and \bar{n}_l . Co

Mole fraction

The mole fractions of the end members in a binary solid solution mineral are related to each other and to the mass of the end members by

$$X_h = 1 - X_i = \frac{\bar{x}_h}{\bar{x}_h + \bar{x}_i} \quad (71)$$

and

$$X_i = 1 - X_h = \frac{\bar{x}_i}{\bar{x}_h + \bar{x}_i}, \quad (72)$$

where \bar{x}_h and \bar{x}_i refer to the total number of moles of the subscripted end members in the solid solution (kg of H₂O)⁻¹. Equations (71) and (72) can be combined to give

$$\frac{\bar{x}_h}{\bar{x}_i} = \frac{X_h}{X_i} \quad (73)$$

Note that the first derivative of equation (73) with respect to the progress variable, ξ , can be written as

$$\frac{1}{\bar{x}_h} \left(\frac{d\bar{x}_h}{d\xi} \right) - \frac{1}{\bar{x}_i} \left(\frac{d\bar{x}_i}{d\xi} \right) = \frac{d \ln X_h}{d\xi} - \frac{d \ln X_i}{d\xi} \quad (74)$$

If we now let the subscript *h* designate the solid solution, we can write

$$\bar{x}_h + \bar{x}_i = \bar{x}_h \quad (75)$$

from which it follows that

$$\frac{d\bar{x}_h}{d\xi} + \frac{d\bar{x}_i}{d\xi} = \frac{d\bar{x}_h}{d\xi} \quad (76)$$

Taking account of equation (2) we can also express equation (76) as

$$\bar{n}_h + \bar{n}_i = \bar{n}_h \quad (77)$$

For a binary solid solution we can write

$$- \frac{dX_h}{d\xi} = \frac{dX_i}{d\xi} \quad (78)$$

and thus

$$- \frac{X_h}{X_i} \left(\frac{d \ln X_h}{d\xi} \right) = \frac{d \ln X_i}{d\xi} = - \frac{1 - X_i}{X_i} \left(\frac{d \ln X_h}{d\xi} \right) \quad (79)$$

Equation (74) can now be rearranged and combined with equations (73) and (79) to give

$$\frac{d \ln X_i}{d\xi} = \frac{X_h \bar{n}_i - X_i \bar{n}_h}{\bar{x}_i} \quad (80)$$

It then also follows that

$$\frac{d \ln X_h}{d\xi} = \frac{X_i \bar{n}_h - X_h \bar{n}_i}{\bar{x}_h} \quad (81)$$

It can be seen by inspection that equations (80) and (81) are linear functions of \bar{n}_h and \bar{n}_i . Consequently, these equations are well suited for mass transfer calculations,

but to use them for this purpose we must first derive explicit differential equations for the activity coefficients of the end members in the solid solution mineral.

Activity coefficients

The activity coefficient of an end member in a solid solution series can be described by

$$\ln \lambda_h = \frac{\mu_{\text{excess},h}}{RT} \quad (82)$$

where R is the gas constant, T is the absolute temperature, and $\mu_{\text{excess},h}$ refers to the excess chemical potential of the h th end member; i.e.

$$\mu_{\text{excess},h} = \mu_h - \mu_{\text{ideal},h} \quad (83)$$

where μ_h is the chemical potential of the subscripted end member in the solid solution and $\mu_{\text{ideal},h}$ is its ideal counterpart. The excess Gibbs free energy per mole of the solid solution ($\bar{G}_{\text{excess},hl}$) can be expressed in the form of the integrated Gibbs-Duhem equation as

$$\bar{G}_{\text{excess},hl} = X_h \mu_{\text{excess},h} + X_l \mu_{\text{excess},l} \quad (84)$$

Note that we can also write

$$\frac{d\bar{G}_{\text{excess},hl}}{d\xi} = \mu_{\text{excess},h} \left(\frac{dX_h}{d\xi} \right) + \mu_{\text{excess},l} \left(\frac{dX_l}{d\xi} \right) \quad (85)$$

Equations (72), (78), (84), and (85) can now be combined to give a differential equation relating the excess Gibbs free energy (of the solid solution) to its derivatives. Combining this expression with equation (82) leads to

$$\ln \lambda_h = \frac{\bar{G}_{\text{excess},hl}}{RT} + \frac{X_l}{RT} \left(\frac{d\bar{G}_{\text{excess},hl}}{dX_h} \right) \quad (86)$$

The excess Gibbs function for a binary solid solution can be represented by a Maclaurin expansion (e.g. see THOMPSON, 1967); i.e.

$$\bar{G}_{\text{excess},hl} = W_h + W_h' X_l + \frac{W_h'' X_l^2}{2!} + \frac{W_h''' X_l^3}{3!} + \dots \quad (87)$$

where W_h is the intercept and W_h' , W_h'' , and W_h''' are equal to the first, second, and third derivatives of $\bar{G}_{\text{excess},hl}$ with respect to X_l at $X_l = 0$. Note, however, that when $X_l = 0$, $\bar{G}_{\text{excess},hl} = W_h = 0$. Taking account of this identity and the fact that W_h' , W_h'' , W_h''' , etc. are constants, the derivative of equation (87) with respect to X_h can be combined with equation (78) to give

$$\frac{d\bar{G}_{\text{excess},hl}}{dX_h} = -W_h' - \frac{2W_h'' X_l}{2!} - \frac{3W_h''' X_l^2}{3!} - \dots \quad (88)$$

Equations (87) and (88) can now be combined with equation (86) to give

$$\ln \lambda_h = -\frac{1}{RT} \left(\frac{W_h'' X_l^2}{2!} + \frac{2W_h''' X_l^3}{3!} + \dots \right) \quad (89)$$

Calcu

The Gil
and pressu

or

Note that i

with equat

$$\frac{d\mu_h}{d\mu_l} =$$

Equatic
end membe
coefficients
to one. A s
coefficientsThe fir
can be writ

where

If we now

The deriva

$$\frac{d^2 \ln a_h}{d\xi^2}$$

+

where σ_h is

The Gibbs-Duhem equation for a binary solid solution at a given temperature and pressure can be written as

$$\bar{x}_h d\mu_h = -\bar{x}_i d\mu_i \tag{90}$$

or

$$X_h d\mu_h = -X_i d\mu_i \tag{91}$$

Note that if we now combine appropriate statements of the derivative of

$$\mu_i = \mu_i^0 + RT \ln a_i \tag{92}$$

with equations (67), (79), (90) and (91), we can write

$$\frac{d\mu_h}{d\mu_i} = \frac{d \ln a_h}{d \ln a_i} = \frac{d \ln X_h + d \ln \lambda_h}{d \ln X_i + d \ln \lambda_i} = \frac{d \ln X_h}{d \ln X_i} = \frac{d \ln \lambda_h}{d \ln \lambda_i} = -\frac{\bar{x}_i}{\bar{x}_h} = -\frac{X_i}{X_h} \tag{93}$$

Equation (89) represents a general power function for activity coefficients of end members in a binary solid solution series. When such solutions are ideal, all coefficients (W_h^n , W_h^m , etc.) in the expression are equal to zero, and λ_h is then equal to one. A symmetrical (regular) solid solution is represented by equation (89) when all coefficients other than W_h^n are zero.

The first derivative of equation (89) with respect to the progress variable, ξ , can be written as

$$\frac{d \ln \lambda_h}{d\xi} = \sigma_h \left(\frac{d \ln X_i}{d\xi} \right) \tag{94}$$

where

$$\sigma_h = -\frac{1}{RT} (W_h^n X_i^2 + W_h^m X_i^3 + \dots) \tag{95}$$

If we now combine equations (67), (80), (81) and (94), we can write

$$\frac{d \ln a_h}{d\xi} = \frac{\bar{n}_h (X_i - \sigma_h X_h)}{\bar{x}_h} + \frac{\bar{n}_i (\sigma_h X_h - X_i)}{\bar{x}_i} \tag{96}$$

The derivative of equation (96) with respect to the progress variable, ξ , appears as

$$\begin{aligned} \frac{d^2 \ln a_h}{d\xi^2} = & \frac{\bar{n}_h' (X_i - \sigma_h X_h)}{\bar{x}_h} + \frac{\bar{n}_h}{\bar{x}_h} \left(\frac{dX_i}{d\xi} - \sigma_h \frac{dX_h}{d\xi} - \sigma_h' X_h \right) - \frac{\bar{n}_h^2 (X_i - \sigma_h X_h)}{\bar{x}_h^2} \\ & + \frac{\bar{n}_i' (\sigma_h X_h - X_i)}{\bar{x}_i} + \frac{\bar{n}_i}{\bar{x}_i} \left(\sigma_h \frac{dX_h}{d\xi} - \frac{dX_i}{d\xi} + X_h \sigma_h' \right) - \frac{\bar{n}_i^2 (\sigma_h X_h - X_i)}{\bar{x}_i^2} \end{aligned} \tag{97}$$

where σ_h is defined by equation (95) and

$$\sigma_h' = \frac{d\sigma_h}{d\xi} = -\frac{1}{RT} \left(2X_i W_h^n \frac{dX_i}{d\xi} + 3W_h^m X_i^2 \frac{dX_i}{d\xi} + \dots \right) \tag{98}$$

Combining equations (80), (81) and (97) leads to

$$\begin{aligned} \frac{d^2 \ln a_h}{d\xi^2} = & \bar{n}_h' \frac{(X_i - \sigma_h X_h)}{\bar{x}_h} + \bar{n}_i' \frac{(\sigma_h X_h - X_i)}{\bar{x}_i} + (\sigma_h X_h - X_i) \left(\frac{\bar{n}_h^2}{\bar{x}_h^2} - \frac{\bar{n}_i^2}{\bar{x}_i^2} \right) \\ & + \bar{n}_h \left[X_i \left(\frac{X_h \bar{n}_i - X_i \bar{n}_h}{\bar{x}_h \bar{x}_i} \right) - \sigma_h' \left(\frac{X_h}{\bar{x}_h} \right) - \sigma_h X_h \left(\frac{X_i \bar{n}_h - X_h \bar{n}_i}{\bar{x}_h^2} \right) \right] \\ & + \bar{n}_i \left[\sigma_h' \left(\frac{X_h}{\bar{x}_i} \right) + \sigma_h X_h \left(\frac{X_i \bar{n}_h - X_h \bar{n}_i}{\bar{x}_h \bar{x}_i} \right) - X_i \left(\frac{X_h \bar{n}_i - X_i \bar{n}_h}{\bar{x}_i^2} \right) \right] \quad (99) \end{aligned}$$

Equations (59), (67), (69), and (96), and (60), (68), (70), and (99), respectively, can now be combined to give differential equations representing reversible reactions involving minerals of variable composition (in binary solid solutions) and aqueous species in which provision is included for variable activity coefficients and changing activity of H₂O. These equations appear as

$$\sum_{s=2} \bar{n}_s \left(\frac{\hat{n}_{s,j}}{m_s} + \left(\frac{2 \cdot 303 Z_s^2}{2} \sum_{s=2} \hat{n}_{s,j} (\omega_s - C_{s,j}) + \hat{n}_{s-1,j} \hat{F}_s \nu_{+...s} \right) \right) - \frac{\bar{n}_h (X_i - \sigma_h X_h)}{\bar{x}_h} - \frac{\bar{n}_i (\sigma_h X_h - X_i)}{\bar{x}_i} = 0 \quad (100)$$

and

$$\begin{aligned} \sum_{s=2} \bar{n}_s' \left[\frac{\hat{n}_{s,j}}{m_s} + \left(\frac{2 \cdot 303 Z_s^2}{2} \sum_{s=2} \hat{n}_{s,j} (\omega_s - C_{s,j}) + \hat{n}_{s-1,j} \hat{F}_s \nu_{+...s} \right) \right] \\ - \bar{n}_h' \left(\frac{X_i - \sigma_h X_h}{\bar{x}_h} \right) - \bar{n}_i' \left(\frac{\sigma_h X_h - X_i}{\bar{x}_i} \right) \\ = \sum_{s=2} \bar{n}_s \left[\frac{\hat{n}_{s,j} \bar{n}_s}{m_s^2} + \left(\frac{2 \cdot 303 Z_s^2}{2} \sum_{s=2} \hat{n}_{s,j} C'_{s,j} \right) \right] + \hat{n}_{s-1,j} \Omega_s (\sum \nu_{+...s} \bar{n}_s)^2 \\ + \bar{n}_h \left[X_i \left(\frac{X_h \bar{n}_i - X_i \bar{n}_h}{\bar{x}_h \bar{x}_i} \right) - \sigma_h' \left(\frac{X_h}{\bar{x}_h} \right) - \sigma_h X_h \left(\frac{X_i \bar{n}_h - X_h \bar{n}_i}{\bar{x}_h^2} \right) \right] \\ + \bar{n}_i \left[\sigma_h' \left(\frac{X_h}{\bar{x}_i} \right) + \sigma_h X_h \left(\frac{X_i \bar{n}_h - X_h \bar{n}_i}{\bar{x}_h \bar{x}_i} \right) - X_i \left(\frac{X_h \bar{n}_i - X_i \bar{n}_h}{\bar{x}_i^2} \right) \right] \\ - \bar{n}_h^2 \left(\frac{X_i - \sigma_h X_h}{\bar{x}_h^2} \right) - \bar{n}_i^2 \left(\frac{\sigma_h X_h - X_i}{\bar{x}_i^2} \right) \quad (101) \end{aligned}$$

It can be seen by inspection that equations (100) and (101), respectively, are linear functions of the reaction coefficients (of the species) and their derivatives. These expressions are thus suitable representations of reversible reactions involving solid solution minerals in the grand matrix equations derived below. However, to render the equations applicable to the general case of mass transfer in geochemical processes, we must first determine the stage of reaction progress at which a given solid solution mineral appears, and define the equilibrium composition of the phase at saturation.

Prediction of saturation compositions

Before solid solution minerals appear as reaction products, hypothetical activities of the end members designated by *h* in all possible solid solutions can be calculated

Calcula

at each stage hypothetical X_h from con

Iterative cor values of X functions ha correspondin calculation o expression a junction with equilibrium equation (65) can be com] values of the dynamic dat if one of the solution min lations. App the grand ma derivatives f

The gene] equilibria in dissolution equilibria, bi of the solven open or clos constructed (100), and (equations ca minerals and designation i elements in t during the pr by g ($g = 1$, given solid so $f_{h,s,i} = 1$ if i $f_{l,s,i} = 1$ wh are zero. Sim reaction invo these constan refers to a m an integer eq

at each stage of reaction progress from expressions of equation (65). The computed hypothetical activities of the end members (a_h) can then be used to predict values of X_h from combined expressions of equations (66), (72), and (89), i.e.

$$a_h = X_h \exp \left(- \frac{W_h''(1 - X_h)^2}{2! RT} - \frac{2W_h'''(1 - X_h)^3}{3! RT} - \dots \right). \quad (102)$$

Iterative computer techniques can be used to solve equation (102) for hypothetical values of X_h in all solid solutions for which explicit activity coefficient power functions have been defined. After computing the hypothetical values of X_h , the corresponding values of X_i can be computed from equation (71), which permits calculation of λ_i from an expression analogous to equation (89), and thus a_i from an expression analogous to equation (66). These values of a_i can then be used in conjunction with the activities of aqueous species to compute hypothetical values of the equilibrium constant (K_j) for reversible reactions corresponding to statements of equation (65) written in terms of a_i . The actual values of the equilibrium constants can be computed independently from thermodynamic data. If the hypothetical values of the equilibrium constants fail to exceed the values computed from thermodynamic data, the solution is undersaturated with respect to the solid solution phases; if one of them is equal, the solution is saturated and the composition of the solid solution mineral is specified by the corresponding value of X_h defined by the calculations. Appropriate statements of equations (100) and (101) can then be entered in the grand matrix equations (derived below) to compute reaction coefficients and their derivatives for all species involved in the precipitation of the solid solution phase.

GRAND MATRIX EQUATION FOR THE GENERAL CASE

The general case includes provision in mass transfer calculations for dissociational equilibria in the aqueous phase, congruent and incongruent reactions, simultaneous dissolution and/or precipitation of more than one mineral, oxidation-reduction equilibria, binary solid solution minerals, varying activity coefficients, evaporation of the solvent, changing activity of H₂O, and multiple reactant minerals in either open or closed systems. Grand matrix equations for the general case can be constructed with the aid of appropriate statements of equations (14), (63) and (100), and (16), (101), and the derivative of equation (63), respectively. These equations can be written in terms of the index i , which refers to both product minerals and aqueous species ($i = 1, 2, \dots, i; i = s + \Phi_p$). Let us again reserve the designation $i = 1$ for H₂O and retain the indices ϵ and j , which refer to the chemical elements in the system ($\epsilon = 1, 2, \dots, \hat{E}$) and the reversible reactions taking place during the process ($j = 1, 2, \dots, j$), respectively. Binary solid solutions are indexed by g ($g = 1, 2, \dots, g$), and h and l again refer to the respective end members in a given solid solution mineral. The symbols $f_{h,g,i}$ and $f_{l,g,i}$ represent switch constants; $f_{h,g,i} = 1$ if i refers to an end member designated by h in the g th solid solution, and $f_{l,g,i} = 1$ when i refers to an end member designated by l ; otherwise both constants are zero. Similarly, $k_{h,g,j}$ or $k_{l,g,j}$ is assigned a value of unity when the j th reversible reaction involves the subscripted end member in the g th solid solution; otherwise these constants are zero. The symbol k_i is also a switch constant; $k_i = 0$ when i refers to a mineral and $k_i = 1$ when i denotes an aqueous species. The symbol b_i is an integer equal to one if $i = 1$, otherwise $b_i = 0$. Reactant minerals are designated

$$\left[\frac{X_h \bar{n}_i}{\bar{x}_i^2} - \frac{\bar{n}_i^2}{\bar{x}_i^2} \right] \quad (99)$$

99), respectively, reversible reactions (ns) and aqueous (nts) and changing

$$\frac{X_i}{\bar{x}_i} = 0 \quad (100)$$

$$\left[\frac{X_h \bar{n}_i}{\bar{x}_i^2} - \frac{\bar{n}_i^2}{\bar{x}_i^2} \right] \quad (101)$$

ctively, are linear derivatives. These is involving solid owever, to render in geochemical at which a given tion of the phase

hetical activities can be calculated

by the subscript r ($r = 1, 2, \dots, \hat{r}$), and $\psi_{r/\hat{r}}$ refers to the relative reaction rate of the r th reactant mineral with respect to the \hat{r} th (HELGESON, 1968; HELGESON, GARRELS and MACKENZIE, 1969). With this notation we can now represent the grand matrix equations by a single expression; i.e.

$$\left[\begin{array}{c} i = 1 \longrightarrow i \\ \left\{ \begin{array}{l} e = 1 \longrightarrow e \\ j = 1 \longrightarrow j \end{array} \right. \end{array} \right] \begin{array}{ccc} \alpha_{1,e,i} & & \alpha_{5,e} \\ \alpha_{2,e+1,i} & \alpha_{4,i} & \alpha_{6,\hat{E}+1} \\ \alpha_{3,i,i} & & \alpha_{7,i} \end{array} = \quad (103)$$

A matrix equation of this form can be constructed for the reaction coefficients as well as for each of their successive derivatives. However, only two such matrices are normally required for accurate mass transfer calculations. The following definitions apply to all of the matrix equations:

$$\alpha_{1,\hat{E},i} = v_{e,i} + \frac{\delta_i n_{i,e}^0}{n_{ii,0}^2} \quad (104)$$

$$\alpha_{2,\hat{E}+1,i} = Z_i \quad (105)$$

$$\begin{aligned}
 \alpha_{3,i,i} = & k_i \left[\frac{\hat{n}_{1,i}}{m_i} + \left(\frac{2 \cdot 303 Z_i^2}{2} \sum_{i=2}^{\hat{r}} \hat{n}_{1,i} k_i (\omega_e - C_{j,i}) \right) + \hat{n}_{1,i-1} \hat{F}_e v_{+e,i} \right] \\
 & - k_{h,\sigma,j} \left(\frac{f_{h,\sigma,i} (1 - X_{i,\sigma} - \sigma_{h,\sigma} X_{i,\sigma})}{\bar{x}_{i,\sigma}} - \frac{f_{i,\sigma,i} (X_{i,\sigma} - \sigma_{h,\sigma} (1 - X_{i,\sigma}))}{\bar{x}_{i,\sigma}} \right) \\
 & - k_{1,\sigma,j} \left(\frac{f_{1,\sigma,i} (1 - X_{i,\sigma} - \sigma_{1,\sigma} X_{i,\sigma})}{\bar{x}_{i,\sigma}} - \frac{f_{h,\sigma,i} (1 - X_{i,\sigma} - \sigma_{1,\sigma} (1 - X_{i,\sigma}))}{\bar{x}_{i,\sigma}} \right) \quad (106)
 \end{aligned}$$

and

$$\alpha_{6,\hat{E}+1} = 0 \quad (107)$$

The remaining elements of the first matrix equation are defined by

$$\alpha_{1,i} = \bar{n}_i \quad (108)$$

$$\alpha_{5,e} = \sum_r \psi_{r/\hat{r}} v_{e,r} \quad (109)$$

and

$$\alpha_{7,i} = 0 \quad (110)$$

The remaining elements of the second matrix equation are given by

$$\alpha_{4,i} = \bar{n}_i' \quad (111)$$

$$\alpha_{3,e} = \frac{2\delta_i n_{i,e}^0 \bar{n}_{ii,0}^2}{n_{ii,0}^3} \quad (112)$$

Calculati

and

$$\begin{aligned}
 \alpha_{7,i} = & \sum_{i=2}^{\hat{r}} k_i \\
 & + \hat{n}_i \\
 & - \sigma_i' \\
 & + \sigma_i \\
 & - \bar{n}_i^2 \\
 & + k_i \\
 & - \sigma_i \\
 & + \sigma_i \\
 & - \bar{n}_i^2
 \end{aligned}$$

Each gran

where the Γ coefficients, a Equation (11 the changes i destroyed in

For evap as -1 , $\psi_{r/\hat{r}}$ is vector, $\alpha_{5,e}$ matrix = 0.

The proc case can be:

1. Define molali may b
2. Compl by sir equati 1969).

and

$$\begin{aligned}
 \alpha_{7,j} = & \sum_{i=2} k_i \bar{n}_i \left(\frac{\hat{n}_{1,i} \bar{n}_i}{m_i^2} + \left(\frac{2 \cdot 303 Z_i^2}{2} \sum_{i=2} \hat{n}_i C'_{j,i} \right) \right) \\
 & + \hat{n}_{s-1,j} \hat{H}_s \left(\sum_i k_i v_{+s,s} \bar{n}_s \right)^2 + k_{h,s,j} \left[\bar{n}_{h,s} \left(X_{1,s} \left(\frac{X_{h,s} \bar{n}_{1,s} - X_{1,s} \bar{n}_{h,s}}{\bar{x}_{h,s} \bar{x}_{1,s}} \right) \right. \right. \\
 & - \frac{\sigma'_{h,s} X_{h,s}}{\bar{x}_{h,s}} - \sigma_{h,s} X_{h,s} \left. \left(\frac{X_{1,s} \bar{n}_{h,s} - X_{h,s} \bar{n}_{1,s}}{\bar{x}_{h,s}^2} \right) \right) + \bar{n}_{1,s} \left(\frac{\sigma'_{h,s} X_{h,s}}{\bar{x}_{1,s}} \right. \\
 & + \sigma_{h,s} X_{h,s} \left. \left(\frac{X_{1,s} \bar{n}_{h,s} - X_{h,s} \bar{n}_{1,s}}{\bar{x}_{h,s} \bar{x}_{1,s}} \right) - X_{1,s} \left(\frac{X_{h,s} \bar{n}_{1,s} - X_{1,s} \bar{n}_{h,s}}{\bar{x}_{1,s}^2} \right) \right) \\
 & - \bar{n}_{h,s}^2 \left(\frac{X_{1,s} - \sigma_{h,s} X_{h,s}}{\bar{x}_{h,s}^2} \right) - \bar{n}_{1,s}^2 \left(\frac{\sigma_{h,s} X_{h,s} - X_{1,s}^2}{\bar{x}_{1,s}^2} \right) \left. \right] \\
 & + k_{l,s,j} \left[\bar{n}_{1,s} \left(X_{h,s} \left(\frac{X_{1,s} \bar{n}_{h,s} - X_{h,s} \bar{n}_{1,s}}{\bar{x}_{1,s} \bar{x}_{h,s}} \right) - \frac{\sigma'_{l,s} X_{1,s}}{\bar{x}_{1,s}} \right. \right. \\
 & - \sigma_{l,s} X_{1,s} \left. \left(\frac{X_{h,s} \bar{n}_{1,s} - X_{1,s} \bar{n}_{h,s}}{\bar{x}_{1,s}^2} \right) \right) + \bar{n}_{h,s} \left(\frac{\sigma'_{l,s} X_{1,s}}{\bar{x}_{h,s}} \right. \\
 & + \sigma_{l,s} X_{1,s} \left. \left(\frac{X_{h,s} \bar{n}_{1,s} - X_{1,s} \bar{n}_{h,s}}{\bar{x}_{1,s} \bar{x}_{h,s}} \right) - x_{h,s} \left(\frac{X_{1,s} \bar{n}_{h,s} - X_{h,s} \bar{n}_{1,s}}{\bar{x}_{h,s}^2} \right) \right) \\
 & - \bar{n}_{1,s}^2 \left(\frac{X_{h,s} - \sigma_{l,s} X_{1,s}}{\bar{x}_{1,s}^2} \right) - \bar{n}_{h,s}^2 \left(\frac{\sigma_{l,s} X_{1,s} - X_{h,s}}{\bar{x}_{h,s}^2} \right) \left. \right] \quad (113)
 \end{aligned}$$

Each grand matrix equation derived above can be solved by evaluating

$$\beta = \Gamma^{-1} \lambda, \quad (114)$$

where the Γ denotes the matrix, β refers to the column vector of unknown reaction coefficients, and λ stands for the reactant mineral (or known coefficient) column vector. Equation (114) can be used in conjunction with equations (18) and (19) to compute the changes in molalities of species and the number of moles of minerals produced or destroyed in geochemical processes.

For evaporative processes, the reactant is designated as H_2O with \bar{n}_{H_2O} specified as -1 , $\psi_{1,i}$ is set to zero, and the $i = 1$ column becomes the known coefficient column vector, $\alpha_{s,i}$. Note that for evaporation $\bar{n}_{H_2O} = 0$ so that $\alpha_{s,i}$ in the second derivative matrix = 0.

MASS TRANSFER CALCULATIONS

The procedure used in carrying out mass transfer calculations for the general case can be summarized as follows:

1. Define the initial composition of the aqueous phase by specifying the total molalities of components in solution. Analyses of natural aqueous solutions may be used for this purpose.
2. Compute molalities, activity coefficients, and activities of all species in solution by simultaneous solution of mass action, mass balance, and activity coefficient equations (e.g., see HELGESON, 1964; GARRELS and CHRIST, 1965; HELGESON, 1969).

3. Specify the identity, composition, and relative reaction rates of the reactant minerals; for evaporative processes, specify the reactant as H_2O with a negative reaction coefficient.
4. Set up and evaluate the grand matrix equations.
5. Increment ξ and solve for new molalities and activities of species in solution.
6. Test to determine if the solution has become saturated with respect to any mineral in the system. If not, repeat the above calculations.
7. If saturation occurs, add to the matrix equations appropriate differential equations representing reversible reactions between the product minerals and the aqueous phase, and repeat the above calculations until overall equilibrium is established.

The matrix in equation (103) will be square and nonsingular as long as the total number of species (minerals, complexes, molecules, and ions) is equal to the number of independent differential equations in the matrix. If oxidation-reduction equilibria are *not* involved in a geochemical process, conservation of charge is implicitly maintained by conservation of mass (HELGESON, 1968). For such processes, $\alpha_{2,\hat{E}+1,i}$ and $\alpha_{6,\hat{E}+1}$ are omitted from the matrix, which should then include provision for only one oxidation state of each element. At least two differential equations (one for each end member) are entered in the matrix for each binary solid solution reaction product. Either one or two such dual entries are made in each matrix for the solid solution mineral, depending on the process being investigated. If a "zoned" crystal is to be produced, the mass of the solid solution produced in previous increments of reaction progress is not permitted to react with the aqueous phase at later stages; this requires only one dual entry. Two dual entries provide for continuous equilibrium between the solid solution and the aqueous phase by allowing the earlier-formed solid solution to change its composition in response to the change in composition of the aqueous phase.

Reactant minerals may or may not be considered to be present in excess. If calculations are carried out for systems in which the aqueous phase is moving through a reactive rock, minerals produced at early stages of reaction progress may not be permitted to react with the aqueous phase later in the reaction process. For example, gibbsite precipitated as a reaction product during the hydrolysis of K-feldspar in a closed system should react at a later stage with K-feldspar to produce kaolinite (HELGESON, GARRELS and MACKENZIE, 1969). In contrast, if the increment of solution under consideration passes out of the locale in which gibbsite precipitated, the earlier-formed gibbsite will not be destroyed, and a zonal distribution of reaction products (gibbsite and kaolinite) will result. Such options can be exercised conveniently with the aid of a computer.

Computer techniques

High speed digital computers with memory storage capacities of the order of 65,000 decimal word locations (at 60 binary bits/word) or more are required for rapid and accurate evaluation of mass transfer in geochemical processes involving multi-component systems. With the exception of evaporative processes and provision for changing activity of H_2O , the theoretical equations and procedures outlined above have been programmed (in Fortran IV notation) for machine computation by a

Calc

CDC 6400
array of
and an ex
Informati
grams, w
calculatio
ment No
this mate
\$3.00 for
Service,
York 100

Program 1
Title:
Object:

Program
Title
Object

Program
Title
Object

Program
Title
Object

Program
Title
Object

Program
Title
Object

rates of the reactant
stant as H_2O with a

of species in solution.
d with respect to any
ations.

ppropriate differential
product minerals and
ntil overall equilibrium

lar as long as the total
is equal to the number
ion-reduction equilibria
arge is implicitly main-
h processes, $\alpha_2 \hat{E}_{+1}$, and
e provision for only one
equations (one for each
lution reaction product.
ix for the solid solution
"zoned" crystal is to be
s increments of reaction
ter stages; this requires
equilibrium between the
formed solid solution to
osition of the aqueous

be present in excess. If
phase is moving through
progress may not be per-
a process. For example,
olysis of K-feldspar in a
ar to produce kaolinite
st, if the increment of
ch gibbsite precipitated,
d distribution of reaction
is can be exercised con-

capacities of the order of
ore are required for rapid
rocesses involving multi-
ocesses and provision for
ocedures outlined above
chine computation by a

CDC 6400 computer. Copies of this program (Program No. 1000) along with a master array of chemical and thermodynamic data for geologic systems (HELGESON, 1969) and an explanatory summary have been deposited with the American Society for Information Science (ASIS; NAPS Document No. 00774). Ten other computer programs, which are employed to calculate thermodynamic values used in mass transfer calculations (HELGESON, 1969), have also been deposited with ASIS (NAPS Document No. 00775). Program descriptions accompany all of the programs. Copies of this material may be obtained from ASIS at a cost of \$1.00 for microfiche copies, or \$3.00 for photocopies. Orders should be sent to ASIS National Auxiliary Publication Service, c/o CCM Information Services, Inc., 22 West 34th Street, New York, New York 10001.

ABSTRACTS OF PROGRAMS

Program No. 1000

Title: PATHI

Object: Compute the number of moles of minerals produced and/or destroyed and the changes in the molalities and activities of species in multicomponent solutions of electrolytes as they react with a given mineral assemblage at a specified temperature and pressure. The method and approach used in the calculations is that presented above—see also, HELGESON (1968, 1970c) and HELGESON, GARRELS and MACKENZIE (1969).

Program No. 0802A

Title: KELLEYCOB

Object: Compute equilibrium constants and standard entropies, enthalpies, and free energies of reactions at specified temperatures using heat capacity power functions of the form $a + bT + c/T^2$ (KELLEY, 1960) and/or average heat capacities (CRISS and COBBLE, 1964) for the reactants and products (HELGESON, 1969).

Program No. 0405AR

Title: DQUANT

Object: Compute values of dissociation constants for a given aqueous species and standard entropies, enthalpies, free energies, and heat capacities of dissociation at specified temperatures using an electrostatic-nonelectrostatic model (HELGESON, 1967a—equations (14), (17), (18), and (19); HELGESON, 1969).

Program No. 0407A

Title: CURVFIT

Object: Compute least squares fits of dissociation constants for a given aqueous species at different temperatures using the theoretical equations employed in Program No. 0405AR to define the fit coefficients required to compute dissociation constants at other temperatures.

Program No. 0405R

Title: DQUANT

Object: Compute values of dissociation constants for a given aqueous species, and standard entropies, enthalpies, free energies, and heat capacities of dissociation at specified temperatures from a modified electrostatic-nonelectrostatic model (HELGESON, 1967—equation 21; HELGESON, 1969).

Program No. 0407R

Title: CURVFIT

Object: Compute least squares fits of dissociation constants for a given aqueous species at

different temperatures using the theoretical equations employed in Program No. 0405R to define the standard enthalpy and entropy of dissociation at the reference temperature, and (from Program No. 0405R) dissociation constants at other temperatures.

Program No. 0404

Title: LOGCALC

Object: Compute equilibrium constants at specified temperatures assuming the standard heat capacity of reaction to be constant and/or zero (HELGESON, 1969).

Program No. 0805

Title: COCPKFIT

Object: Compute least squares fits of equilibrium constants for a given reaction at different temperatures assuming a constant heat capacity of reaction to define the enthalpy of reaction at the reference temperature (HELGESON, 1969).

Program No. 0417

Title: HTOFIT

Object: Compute least squares fits of standard heat capacities of dissociation for a given aqueous species at different temperatures using an electrostatic-nonelectrostatic model (HELGESON, 1967a—equation 19) to define coefficients for program 0405AR.

Program No. 0701

Title: GAMMA

Object: Compute activity coefficients of aqueous ions at three concentrations of a specified supporting electrolyte. Calculations are carried out for a sequence of charges, α values, and temperatures using a deviation function for the supporting electrolyte to extend Debye-Hückel calculations for individual ions (HELGESON and JAMES, 1968; HELGESON, 1969).

Program No. 0702

Title: DISTRIB

Object: Compute stoichiometric individual ion activity coefficients for ions in a 1:1 supporting electrolyte. Provision is included for the effects of complexing, ionic interaction, and hydration (HELGESON and JAMES, 1968; HELGESON, 1969).

CONCLUDING REMARKS

The amount of pertinent thermodynamic data available, and the size and degree of sophistication of modern computers are the only limiting factors in the theoretical approach to mass transfer calculations discussed in the preceding pages. Current capabilities permit evaluation of geochemical processes involving more than 60 components, phases, and chemical species. Such calculations can be carried out at present only for idealized hypothetical models of geologic systems and geochemical processes, but continued progress in this area should ultimately enable evaluation of their actual counterparts. Work is now in progress in this laboratory to increase the versatility of the PATHI computer program and to further generalize the approach discussed above to include provision in the grand matrix equation for changing temperature and pressure, and to incorporate differential equations describing flow rates, reaction kinetics, and diffusional flux constraints in geologic systems.

Acknowledgments and thanks to the National Science Foundation for assisting with the funds obtained under Grant No. GU 2190, and Grant No. 11285, and to the University of Utah Computing Facility.

B. THOMPSON

BARTON P. B.

Soc. Amer. Chem.

CRISS C. M. a

ous solution

capacities of

DE DONDER P.

GARRELS R. L.

Row.

HELGESON H.

HELGESON H.

ated temp

HELGESON H.

(editor P. L.

HELGESON H.

minerals at

32, 352-87

HELGESON H.

pressures.

HELGESON H.

Cosmochim.

HELGESON H.

processes in

HELGESON H.

mal system

Soc. Amer. Chem.

HELGESON H.

Diagrams

One Atm. c

HELGESON H.

in geochem

Cosmochim.

HELGESON H.

tions at of

Amer. Chem.

KELLEY K. L.

ature heat

pounds. (

LIETZKE M.

motie cool

PURCONE J.

Everett.

ROBE R. A.

substance

temperat

Acknowledgments—We are indebted to R. M. GARRELS and F. T. MACKENZIE for helpful suggestions and to R. H. LEEPER, G. M. LAFON, W. R. JAMES, T. G. MUNDT and D. C. THORSTENSON for assisting with the computer programs. The work reported here was supported in part by funds obtained from the Research Committee at Northwestern University (Grants GU 1700, GU 2190, and SIDC 17), the National Science Foundation (NSF Grants GE 9758, GA 828, and GA 11285), and the Petroleum Research Fund of the American Chemical Society. Additional computing funds were made available by Northwestern University. We are also grateful to J. B. THOMPSON, JR., P. B. BARTON, and MILTON BLANDER for reviewing the manuscript.

REFERENCES

BARTON P. B., BETHKE P. M. and TOULMIN P., 3rd (1963) Equilibrium in ore deposits. *Mineral. Soc. Amer. Spec. Paper* 1, 171-185.

CRISS C. M. and COBBLE J. W. (1964) The thermodynamic properties of high temperature aqueous solutions. V. The calculation of ionic heat capacities up to 200°: Entropies and heat capacities above 200°. *J. Amer. Chem. Soc.* 86, 5391-5403.

DE DONDER Th. (1920) *Leçons de Thermodynamique et de Chimie-Physique*. Gauthier-Villars.

GARRELS R. M. and CHRIST C. L. (1965) *Solutions, Minerals, and Equilibria*, 450 pp. Harper & Row.

HELGESON H. C. (1964) *Complexing and Hydrothermal Ore Deposition*, 128 pp. Pergamon.

HELGESON H. C. (1967a) Thermodynamics of complex dissociation in aqueous solution at elevated temperatures. *J. Phys. Chem.* 71, 3121-3136.

HELGESON H. C. (1967b) Solution chemistry and metamorphism. In *Researches in Geochemistry*, (editor P. H. Abelson), Vol. II, pp. 382-404. John Wiley.

HELGESON H. C. (1968) Evaluation of irreversible reactions in geochemical processes involving minerals and aqueous solutions. I. Thermodynamic relations. *Geochim. Cosmochim. Acta* 32, 853-877.

HELGESON H. C. (1969) Thermodynamics of hydrothermal systems at elevated temperatures and pressures. *Amer. J. Sci.* 267, 729-804.

HELGESON H. C. (1970a) Interpretation of the kinetic behavior of feldspar hydrolysis. *Geochim. Cosmochim. Acta* to be published.

HELGESON H. C. (1970b) Description and interpretation of phase relations in geochemical processes involving aqueous solutions. *Amer. J. Sci.* in press.

HELGESON H. C. (1970c) A chemical and thermodynamic model of ore deposition in hydrothermal systems. In *Fiftieth Anniversary Symposium Volume*, (editor B. A. Morgan). *Mineral. Soc. Amer. Spec. Paper* 3, in press.

HELGESON H. C., BROWN T. H. and LEEPER R. H. (1969) *Handbook of Theoretical Activity Diagrams Depicting Chemical Equilibria in Geologic Systems Involving an Aqueous Phase at One Atm. and 0-300°C*, 253 pp. Freeman, Cooper.

HELGESON H. C., GARRELS R. M. and MACKENZIE F. T. (1969) Evaluation of irreversible reactions in geochemical processes involving minerals and aqueous solutions. II. Applications. *Geochim. Cosmochim. Acta* 33, 455-481.

HELGESON H. C. and JAMES W. R. (1968) Activity coefficients in concentrated electrolyte solutions at elevated temperatures (an abstract). *Abstracts of Papers, 155th National Meeting, Amer. Chem. Soc.*, April, 1968, San Francisco, California, S-130.

KELLEY K. K. (1960) Contributions to the data on theoretical metallurgy. XIII. High temperature heat content, heat capacity, and entropy data for the elements and inorganic compounds. *U.S. Bur. Mines Bull.* 584, 232 pp.

LIETZKE M. H. and STOUGHTON R. W. (1961) The calculation of activity coefficients from osmotic coefficient data. *J. Phys. Chem.* 65, 508-509.

PRIGOGINE I. and DEFAY R. (1954) *Chemical Thermodynamics*, 543 pp., translated by D. H. Everett. Longmans Green.

ROBIE R. A. and WALDBAUM D. R. (1968) Thermodynamic properties of minerals and related substances at 298.15°K (25.0°C) and one atmosphere (1.013 Bars) pressure and at higher temperatures. *U.S. Geol. Surv. Bull.* 1259, 256 pp.

SUBJ
GCHM
CND

The Character of Ni²⁺ as Demonstrated by Solid Solutions in the Ni-Fe-Zn-S System *

GERALD K. CZAMANSKE AND FRASER E. GOFF

Abstract

At 755 ± 5° C, the maximum solubility of NiS in ZnS (sphalerite) is 1.16 ± 0.2 mole percent NiS. Unit-cell edge values, *a*₀, for these Ni-bearing sphalerites differ little, and unsystematically, from those for pure sphalerite. Addition of FeS to ZnS diminishes the solubility of NiS in ZnS. Compositions of coexisting Ni-S and Fe-Ni-S phases do not precisely agree with those determined in previous studies of those systems; negligible ZnS is soluble in these phases.

The results are interpreted in terms of crystal-field theory. The number of electrons in the 3*d* orbitals of Ni²⁺ is such that tetrahedral coordination is virtually precluded for Ni²⁺. This accounts for the fact that the solubility of NiS in ZnS is markedly lower than the solubilities, in ZnS, of MnS, FeS, and CoS.

Experimental and Analytical Procedures

ZnS, FeS, NiS, NiS₂, and Ni₃S₂ were prepared from high-purity elements by reaction at elevated temperature in evacuated silica glass tubes. Materials of 99.999+ purity were used as follows: Zn and S, American Smelting and Refining Co.; Fe and Ni sheet, Johnson and Matthey and Co. The synthesized sulfides were confirmed by X-ray diffraction and served among the homogeneous electron microprobe standards used for the analytical part of our study.

Charges were weighed into silica tubes (3 mm ID and 5 mm OD), sealed, and twice held at 755° ± 5° C for a two-week period. At the end of each period, the tubes were removed from the furnaces, quenched in ice water, and opened; the contents were ground in an agate mortar, returned to their respective tubes, and the tubes were resealed. After this procedure for assisting development of homogeneous reaction products, the charges were held at 755° ± 5° C for 4 months, then quenched in ice water prior to X-ray and microprobe analysis.

Bulk compositions were chosen to explore thoroughly the limits of NiS solubility in ZnS, in both the Fe-free and Fe-bearing systems. Runs containing excess S as NiS₂ and excess Ni as Ni₃S₂ were included to preclude any difficulties stemming from uncontrolled *f*_{S₂} such as those that plagued early workers in the ZnS-FeS system (e.g., Barton and Toulmin, 1966).

All X-ray data were obtained using Ni-filtered, Cu K_{α1} radiation (λ = 1.54050 Å). Preliminary identification of run products was accomplished by scanning smear mounts on glass slides from 26° to

* Publication authorized by the Director, U. S. Geological Survey.

70° 2θ at a speed of 1° 2θ/min. Unit-cell edges were determined by mixing in CaF₂ (*a*₀ = 5.4633 Å) as an internal standard and oscillating across the sphalerite and fluorite (422) peaks at a scanning speed of 1/4° 2θ/min. Two oscillations across pure ZnS on each of three separate occasions resulted in a unit-cell edge of 5.40907 ± 0.0003 Å, slightly lower than the generally accepted value of 5.4093 ± .0002 Å (Skinner, 1961; Barton and Toulmin, 1966).

All reaction products were analyzed with an ARL EMX-SM electron microprobe, using an accelerating potential of 15 KV and a sample current of 0.02 micro amperes on brass. Synthetic sulfides used as standards included: ZnS, NiS₂, Ni₃S₂, Fe_{01.0}S_{30.0}, Ni_{0.98}Fe_{00.02}S_{39.00}, Ni_{1.88}Fe_{59.20}S_{38.91}, Ni_{0.89}Fe_{51.87}S_{38.24}, Fe_{5.79}Zn_{60.98}S_{33.23}, and Fe_{23.80}Zn_{41.80}S_{34.25}, where decimal subscripts denote weight percentages. Typically, 10 separate grains of each standard and unknown phase were occupied, and counts accumulated for approximately 10 seconds while using the instrument in the mode for fixed beam current termination. However, all product ZnS phases were reanalyzed according to a scheme in which 20 areas were analyzed and the 10 lowest Ni values used to provide the values of Tables 1 and 2. This procedure was arbitrarily chosen to minimize the possible influence of subjacent Ni-rich phases on these values. Raw count data for standards and unknowns were reduced using the U. S. Geological Survey BS90 Curve Calibration (Linear) Computer Program. Background corrections were made, drift was negligible, and matrix corrections were not attempted because of previous satisfactory experience using standards carefully matched in composition to unknowns. In this study, for example, the Ni content of NiS, run twice as an unknown, was deter-

Run
No.

N4

N5

N5A

N5B

N8A

N8B

N11

minec
value

Ele
are li

Run
No.

F5

F10

F14

F17

F19

F19A

F19B

TABLE 1. Chemical Data for Runs in the Ni-Zn-S system at 755 ± 5° C

Run No.	Starting Assemblage (mg)				NiS content of "ZnS" phases (weight percent)	Ni content of Ni-sulfide phases (weight percent)
	ZnS	NiS	NiS ₂	Ni ₃ S ₂		
N4	149.62	12.12	--	--	1.07 ± 0.13	63.8 ± 0.5
N5	189.08	24.02	--	--	1.05 ± 0.07	63.6 ± 0.5
N5A	188.44	23.94	--	10.08	1.23 ± 0.12	64.2 ± 0.5 (N5A ₁) 70.3 ± 0.3 (N5A ₂)
N5B	189.22	24.04	9.84	--	0.93 ± 0.07	46.7 ± 0.4 (N5B ₁) 61.3 ± 0.5 (N5B ₂)
N8A	40.56	11.93	--	9.91	0.92 ± 0.09	64.3 ± 0.5 (N8A ₁) 70.3 ± 0.3 (N8A ₂)
N8B	40.87	12.02	9.84	--	1.30 ± 0.23	47.2 ± 0.3 (N8B ₁) 60.6 ± 0.7 (N8B ₂)
N11	34.38	18.02	--	--	1.06 ± 0.12	64.0 ± 0.4

mined as 64.69 and 64.85, compared to the ideal value, 64.68 weight percent.

Results

Electron-microprobe analyses of all reaction phases are listed in Tables 1 and 2; reported error values

were calculated by the B890 program and correspond to one standard deviation. Indication of the validity of these values is provided in Table 2 for sample F14 in which results are presented for duplicate analyses of the "ZnS" phase.

Consideration of Table 1 shows that for the Ni-

TABLE 2. Chemical Data for Runs in the Ni-Fe-Zn-S System at 755 ± 5° C

Run No.	Starting Assemblage (mg)					Composition of "ZnS" phases (weight percent)		Composition of Ni-sulfide phases (weight percent)	
	ZnS	FeS	NiS	NiS ₂	Ni ₃ S ₂	FeS	NiS	Fe	Ni
	F5	160.78	51.81	10.70	--	--	21.3 ± 0.4	0.67 ± 0.04	32.2 ± 0.6
F10	78.29	20.18	10.42	--	--	15.8 ± 0.4	0.87 ± 0.06	24.3 ± 0.3	39.5 ± 0.5
F14	77.79	15.04	15.53	--	--	10.75 ± 0.29	0.96 ± 0.05	17.6 ± 0.5	46.3 ± 0.4
						10.82 ± 0.23	1.01 ± 0.05		
F17	38.02	4.90	10.12	--	--	7.1 ± 0.3	1.00 ± 0.09	12.1 ± 0.2	49.9 ± 0.4
F19	38.47	2.48	12.80	--	--	3.7 ± 0.2	1.15 ± 0.13	6.1 ± 0.2	58.3 ± 0.6 (F19 ₁) 4.4 ± 0.4 64.6 ± 0.9 (F19 ₂)
F19A	37.75	2.43	12.56	--	9.81	3.2 ± 0.02	1.24 ± 0.08	5.5 ± 0.2	59.1 ± 0.3 (F19A ₁) 3.7 ± 0.3 65.3 ± 1.3 (F19A ₂)
F19B	37.69	2.43	12.54	10.10	--	1.9 ± 0.07	1.18 ± 0.23	0.63 ± 0.04	46.4 ± 0.4 (F19B ₁) 5.3 ± 0.2 56.5 ± 0.4 (F19B ₂)

TABLE 3. Unit-cell edges, a., for Ni- and Ni + Fe-Sphalerites (A)

Sample	Mole Percent		a., based on (427) ^{1/2}
	NiS	FeS	
ZnS	--	--	5.4091
N4	1.15 ± 0.14	--	5.4085
N5	1.13 ± 0.08	--	5.4079
N5A	1.32 ± 0.13	--	5.4081
N5B	1.00 ± 0.08	--	5.4075
N6A	1.00 ± 0.10	--	5.4077
N6B	1.39 ± 0.25	--	5.4081
N11	1.14 ± 0.13	--	5.4080
F5	0.70 ± 0.04	23.1 ± 0.4	5.4187
F10	0.92 ± 0.06	17.2 ± 0.4	5.4165
F14	1.05 ± 0.05	11.8 ± 0.3	5.4145
F17	1.06 ± 0.10	7.6 ± 0.3	5.4127
F19	1.23 ± 0.14	4.1 ± 0.2	5.4104
F19A	1.33 ± 0.09	3.5 ± 0.03	5.4100
F19B	1.26 ± 0.25	2.1 ± 0.06	5.4090

^{1/2} values represent four measurements each from oscillations on two of three separate occasions.

Average error for all data is estimated at ± 0.0004

Zn-S system (N-series) the solubility of NiS in ZnS at 755° C may be estimated at 1.16 ± 0.2 weight percent. There are no significant differences among this overall average, the value 1.08 representing the average of the two Ni₃S₂-bearing runs, and the value 1.12 representing the average of the two NiS₂-bearing runs. Table 3 shows that the effect of the small and apparently variable NiS content on the unit-cell edges of the N-series sphalerites is also small, and irregular with respect to composition. The average value, 5.4084 Å, is 0.0007 Å smaller than the value we report for ZnS and is thus compatible with the slightly smaller radius of Ni²⁺ (Table 4).

The monosulfide solid solution (mss) in the Fe-S system is known to show a very sharp drop in the activity of FeS as pyrrhotite becomes more deficient in iron (Toulmin and Barton, 1964). This change in activity completely explains the wide range in FeS content of sphalerite (at 755°, from 54 mole percent to 13 percent) capable of being in equilibrium with pyrrhotite (Barton and Toulmin, 1966). One might ask whether such a relative change might also occur in the Ni-Zn-S system. Rosenqvist (1954) gives data for 600° C for the H₂/H₂S ratio in equilibrium with various compositions of the nickel monosulfide solid solution; these permit the computation of the activity of NiS across the solid solution and show that it drops to only about 0.87 for the most sulfur-rich compositions. Thus, to a first approximation, sphalerite in equilibrium with the sulfur-rich mss should contain about 0.87 times as much NiS as that

in equilibrium with the metal-rich mss. A temperature change of 150° will probably not change this result drastically. The 0.87 term is close enough to unity, and the experimental uncertainties sufficiently large that the present results do not appear to disagree with the thermodynamic data for Ni-S system.

Analyses for runs in the Fe-Ni-Zn-S system (F-series) are presented in Table 2. They show that the NiS content of ZnS diminishes as the FeS content of ZnS increases (Fig. 1). Because the analyses of these phases were done twice and because the error estimates appear realistic (e.g., see duplicate analysis of F14), this trend is not in doubt. As was true for the N-series runs, the presence of the ternary assemblages involving NiS₂ and Ni₃S₂ has no detectable effect on the solubility of NiS in ZnS. As a group, the unit-cell edges for the iron-bearing sphalerites obey a relation (Fig. 2) much like that reported by Barton and Toulmin (1966, Fig. 2), but show the effect of NiS content.

Analyses of reaction products in the systems Ni-S and Fe-Ni-S are presented in Tables 1 and 2 and plotted on a Fe-Ni-S ternary diagram as Figure 3. Zn contents of the Ni-sulfide and Fe-Ni-sulfide

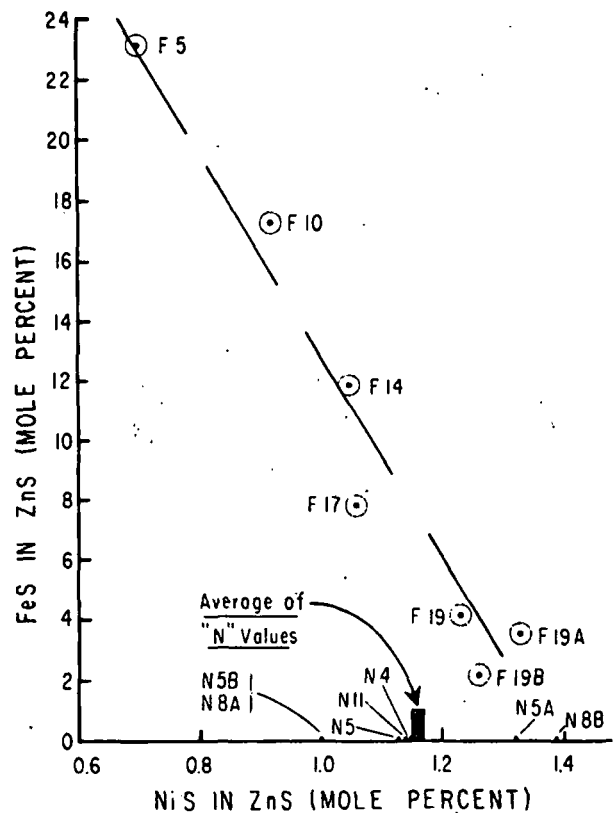


FIG. 1. The effect of FeS content upon the NiS content of sphalerite.

phases are essentially nil, although a real solubility of 0.015–0.03 percent Zn may occur. Values measured for reaction products were permissibly that much above the 0.003 percent measured for our NiS standard as an unknown. Our compositions on the Ni-S binary (in-Ni-Zn-S) and those of Yund and Kullerud (1962) do not agree. Our values for weight percent S of 29.7 for the S-rich limit of Ni_{3-2x}S₂, 35.75 for the Ni-rich limit of Ni_{1-x}S, and 39.05 for the S-rich limit of Ni_{1-x}S compare with their respective values (as read from their Figure 2) of 30.6, 35.3, and 37.95. It is puzzling that compositions N5B₁, NSB₁, and F19B₁ (see Fig. 3) appear to be slightly more S-rich than our NiS₂ standard, but we have no explanation or concern here for this fact.

Comparison is good between published reports by Kullerud (1963) and Kullerud et al. (1969) and the data of Table 2 and Fig. 3 for products of runs in the system Fe-Ni-Zn-S. The Fe-Ni-S phases produced in runs F5 through F17 lie within the field of the monosulfide solid solution (mss) that spans the ternary from about 300° to 992° C (see also Craig, 1971). Run F19B shows the expected tie-line between the S-rich limit of the mss and a (Ni,Fe)S₂ phase with minor Fe. Some (Ni,Fe)_{3-2x}S₂ has developed in run F19, so that F19₁ and F19₂, as well as F19A₁ and F19A₂, provide tie lines between the (Ni,Fe)_{3-2x}S₂ field and the Ni-rich limit of the mss. The indicated shape of the upper part of the (Ni,Fe)_{3-2x}S₂ field, with compositions F19₂ and F19A₂ more S-rich than N5A₂ and NSA₃, cannot readily be compared to the studies by Kullerud or Kullerud, Yund, and Moh, which provide diagrams for temperatures about 100° C below and above that of this study. Because an (Ni,Fe)_{3-2x}S₂ phase initially develops within the ternary at 862° C and at lower temperatures must widen in the direction of increasing metal-to-sulfur ratio and simultaneously approach the Ni-S boundary, our configuration at 755° C seems reasonable.

The distribution of Ni and Fe between the ZnS phase of the F-series runs and the coexisting Ni-Fe sulfide phases is presented in Figure 4. Data have been plotted in terms of weight percent metals to allow both the plotting of the disulfide phases and the nonstoichiometric mss phases. From data in Table 2, values may be calculated for mole percent FeS in the coexisting phases. For the two phase runs, the ratio

$$\frac{\text{Mole percent FeS in Ni-Fe sulfide}}{\text{Mole percent FeS in ZnS}}$$

is F5–2.25; F10–2.33; F14–2.54; and F17–2.70. The preference of Fe for the Ni-Fe sulfide phase is a

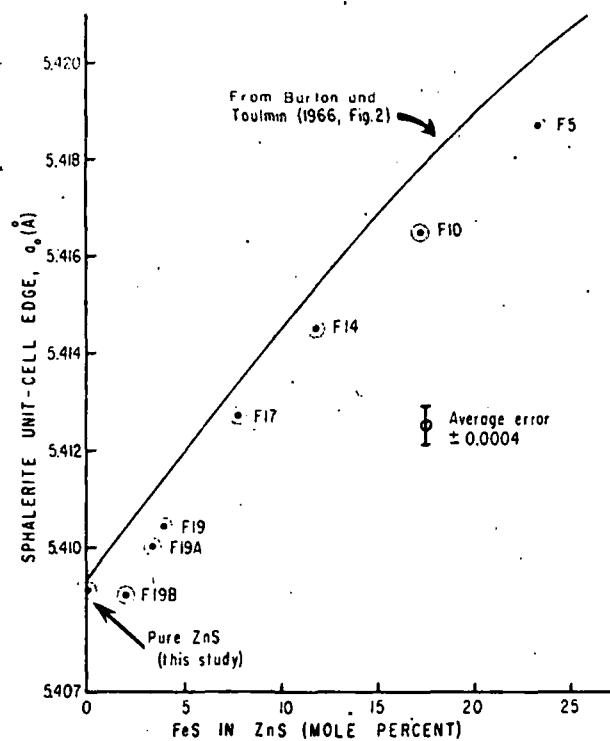


FIG. 2. Sphalerite unit cell edges, a_0 , as a function of mole percent FeS in ZnS. Note that the plotted F-series sphalerites contain NiS as well as the indicated amount of FeS.

reflection of the octahedral-site preference energy of Fe²⁺, as discussed later.

Discussion

Numerous studies have been published concerning the solubilities in ZnS of the five transition metals just preceding Zn in the periodic table of the elements (see Table 4). The solubility of MnS in ZnS is about 52 mole percent at 1,180° C and 46 mole percent at 900° C as reported by Kroger (1938, 1939). Kullerud (1953) attempted to quantify the extensive solubility of FeS in ZnS as a geothermometer, but unforeseen experimental problems intervened, and it remained for Barton and Toulmin (1966) to determine satisfactorily that the maximum solubility of FeS in ZnS ranges from 52 mole percent at 580° to 56 mole percent at 850° C. The solubility of CoS in ZnS has been determined as 33 mole percent at 850° C by Hall (1961). These writers and others, e.g., Skinner (1961) and Skinner and Bethke (1961), have established that substitution of these other transition metals for Zn in the ZnS structure causes regular changes in the ZnS unit-cell edge and that in ternary substitutional schemes the effects of the substitutional ions are additive. The Cu-Fe-Zn-S system has been studied by Toulmin

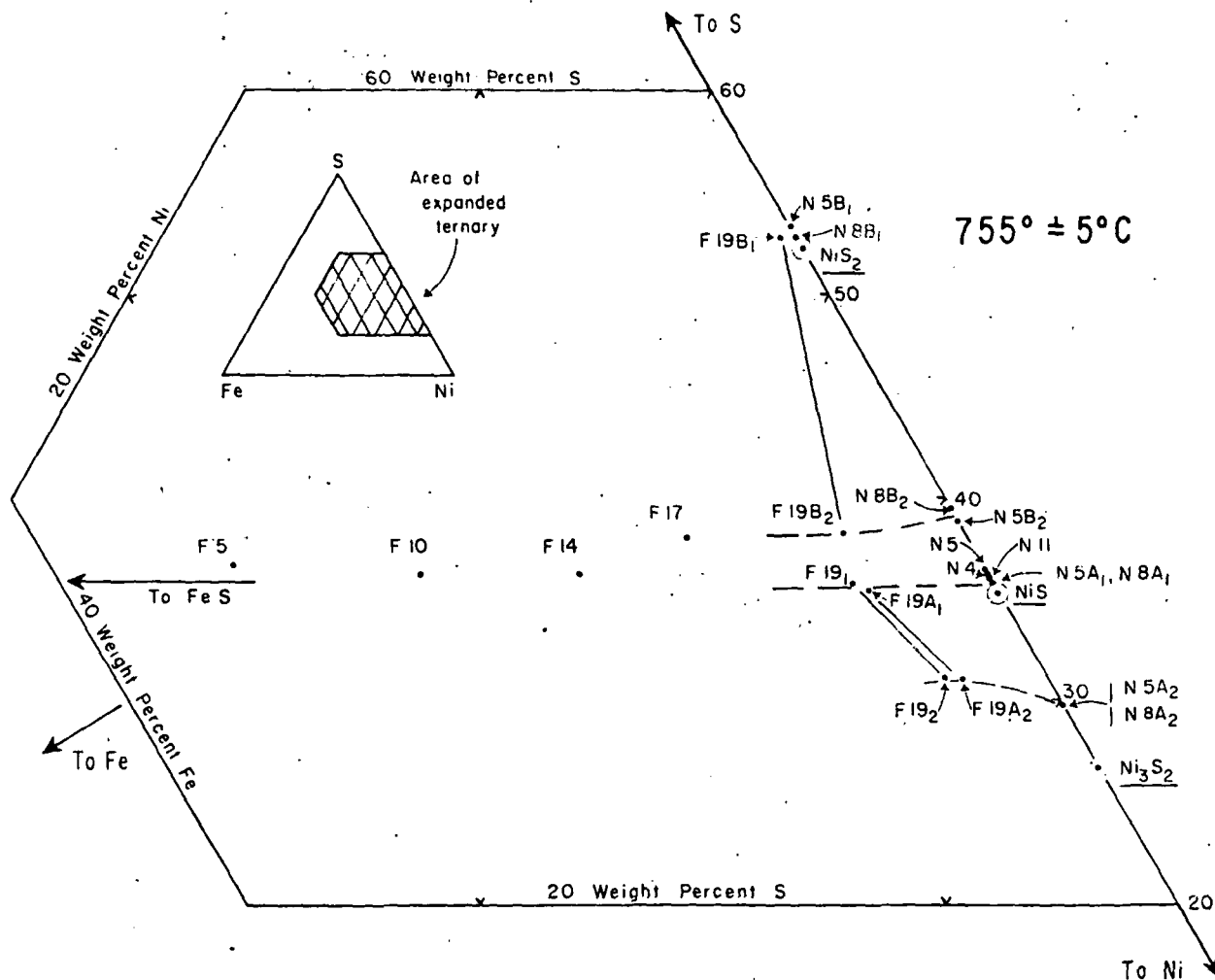


FIG. 3. Representation of reaction phase compositions in the ternary Fe-Ni-S.

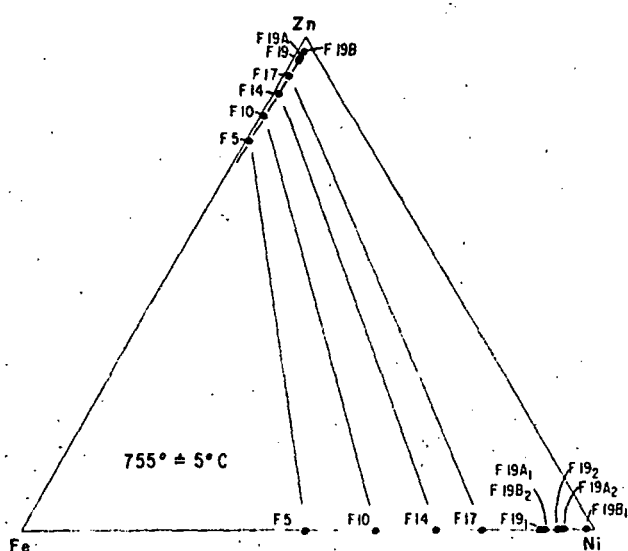


Fig. 4. Representation of the partitioning of Ni and Fe between ZnS and Fe-Ni-S phases in the ternary Fe-Ni-Zn.

(1960), whose report in abstract is necessarily brief. He indicates that the solubility of CuS in ZnS is "very small (<0.5 percent)" at temperatures up to 600° C. At 666° C, sphalerite in equilibrium with pyrite-pyrrhotite and chalcopyrite has an approximate composition $Zn_{0.815}Fe_{0.17}Cu_{0.015}S$. Thus, the solubility of NiS in ZnS reported in this study places NiS and CuS in sharp contrast to MnS, FeS, and CoS with respect to their solubilities in ZnS. An explanation of these phenomena, based on consideration of crystal-field theory, is offered in the following section of this report.

At this point it is pertinent to consider the possible sites for foreign ions, and specifically Ni, within the ZnS structures. Traditionally, the ions here discussed, as well as others such as Cd^{2+} and Hg^{2+} , which have an extensive solubility in ZnS, have logically been considered to substitute for Zn^{2+} in the tetrahedral metal ion sites in the ZnS structures. However, there are also octahedral holes in the

TABLE 4. Ionic Radii, Covalent Radii, and Electronegativity Values for Selected Transition Metal Ions (Coordination indicated parenthetically)

Ion	Ionic Radius ^{1/}	Covalent Radius ^{2/}	Mean Atomic Distance, Me-S ^{3/}	Electronegativity ^{2/}
Mn ⁺⁺	0.91	--	--	1.4
Fe ⁺⁺	0.86	1.23 (Oct.)	--	1.65
Co ⁺⁺	0.83	1.32 (Oct.)	2.31 (Oct.)	1.7
Ni ⁺⁺	0.77	1.39 (Oct.)	2.34 (Oct.)	1.7
Cu ⁺⁺	0.81	1.35 (Tet.)	2.34 (Tet.)	2.0
Zn ⁺⁺	0.83	1.31 (Tet.)	2.33 (Tet.)	1.5

^{1/} High-spin values for octahedral coordination from Whittaker and Muntus (1970).

^{2/} From Fyfe (1964, Tables 5-2 and 6-2).

^{3/} From Nowacki (1971).

structures that are normally unoccupied. Occupancy of these sites by "interstitial" metal ions is somewhat unfavorable in terms of energy because they are surrounded by a tetrahedron (sphalerite) or an octahedron (wurtzite) of near-neighbor metal ions, which lead to repulsive forces.

Manning (1966, 1967a) has made spectrophotometric studies of sphalerites doped with Cu and Fe and has interpreted the absorption-band spectra to indicate the presence of Cu²⁺ and Fe³⁺ in octahedral coordination, i.e., in interstitial rather than substitutional sites. However, Cabri (1969) does not confirm the occurrence of significant interstitial Fe³⁺ in sphalerite. From spectrophotometric studies of CdS and ZnS (wurtzite) doped with minor Ni (0.005 to 0.018 percent), Pappalardo and Dietz (1961) and Weakliem (1962) concluded that the Ni²⁺ is dominantly in tetrahedral sites. Weakliem notes that if some of the cation sites bordering the octahedral holes were unoccupied the octahedral-site preference energy of Ni²⁺ would help to make occupancy of the octahedral sites more favorable. He concludes that, for his crystals, undetectably small amounts of Ni²⁺ may in fact occupy these octahedral sites.

In an attempt to determine if the slightly different wurtzite structure would accept more NiS in solid solution than the sphalerite structure and to grow crystals suitable for spectrophotometric study, we

have made two runs at $1,120 \pm 5^\circ$ C and obtained chemically homogeneous single crystals of wurtzite containing 1.90 and 2.32 weight percent NiS. We interpret the greater solubility to be due predominantly to the 360° C temperature interval and cannot evaluate possible differences between the solubility of NiS in the two ZnS polymorphs. The crystals obtained have been sent to P. G. Manning for study. Manning (oral commun., 1971) has in progress a spectrophotometric study of Ni-doped ZnS.

Study of the wurtzite crystals produced during this work should be particularly interesting because the concentration levels are much higher than those typical for spectrophotometric studies of doped semiconductors. In fact, the concentration levels are such that, until spectra are obtained and interpreted, it may be assumed that Ni²⁺ dominantly substitutes unwillingly in tetrahedral sites, with minor substitution in octahedral sites favored by crystal-field stabilization but restricted by the fact that the octahedron near-neighbors are metal ions. The probability of placing more than 1 weight percent Ni²⁺ in interstitial sites is low (P. G. Manning, oral. commun., 1971).

Comment on the Character of Ni²⁺

It is not difficult to understand that NiS has a solubility in ZnS much smaller than that of MnS, FeS, or CoS if the problem is considered in terms of

TABLE 5. Crystal-field Theory Data for Selected Transition Metal Ions

Ion	Number of 3d electrons	Representation of 3d, high-spin, orbital occupancy	Stabilization, kcal/mole ^{1/}		Octahedral-site preference energy, kcal/mole
			Octahedral	Tetrahedral	
Mn ⁺⁺	5	↑ ↑ ↑ ↑ ↑	0.0	0.0	0.0
Fe ⁺⁺	6	↑↑ ↑ ↑ ↑	11.9(11.4)	7.9(7.5)	4.0(3.9)
Co ⁺⁺	7	↑↑ ↑↑ ↑ ↑	22.2(17.1)	14.8(15.0)	7.4(2.1)
Ni ⁺⁺	8	↑↑ ↑↑ ↑↑ ↑	29.2(29.3)	8.6(6.5)	20.6(22.8)
Cu ⁺⁺	9	↑↑ ↑↑ ↑↑ ↑↑ ↑	21.6(22.2)	6.4(6.6)	15.2(15.6)
Zn ⁺⁺	10	↑↑ ↑↑ ↑↑ ↑↑ ↑↑	0.0	0.0	0.0

^{1/} Values for transition metal oxides from Dunitz and Orgel (1957); figures in parentheses from McClure (1957).

crystal-field theory, or the more comprehensive molecular orbital theory. The problem cannot readily be interpreted in terms of a simple model involving ionic or covalent radii, radius ratios, or electronegativity (see Table 4). On the other hand, whereas molecular orbital theory permits a more elegant portrayal of sulfide bonding (e.g. Burns, 1970), it is not essential to understanding the present problem and is not here invoked. The importance of crystal-field concepts in understanding the structural chemistry, stability, and solid solution limits among the transition metal disulfides has been demonstrated by Nickel (1968, 1970). By focusing on Ni²⁺ and considering ZnS along with the more metallic, transition metal mono-sulfides, an unusually striking reflection of the importance of an orbital approach to crystal structure evolves.

The pertinent transition metal ions and characteristics of them important to this discussion are listed in Table 5. The values for site stabilization energies, based on hydrates and generally applied to oxides, must be considered relatively, though not absolutely, correct for sulfide structures. Because S²⁻ has a large radius but the same charge and bonding electron configuration as O²⁻, crystal-field splitting and absolute stabilization energies are expected to be smaller according to crystal-field theory. However, Burns (1970, Table 7.1) estimates that these values are larger for the sulfides of transition metals than for their oxides, an indication of the importance of covalence in the stabilization and the ultimate importance of considering molecular orbital theory for fuller understanding of sulfide bonding. The similarity in size and electronegativity of the transition metal ions may be clearly visualized when one con-

siders that to become divalent ions the transition metals simply donate 4s electrons (Cu²⁺ excepted) leaving partially filled 3d electron orbitals occupying roughly equal space regardless of the degree of orbital occupancy. (The contraction produced by increased nuclear charge is a relatively less important consideration.) The indicated distribution of electrons among the 3d orbitals (Table 5) is for the high-spin situation in which Hund's rule is obeyed. That is, electrons within orbitals of the same sublevel tend to have the same spin; they thus will occupy empty orbitals if available, rather than spin-pairing.

In order to appreciate the following discussion, it is essential to visualize the three-dimensional shapes of the pertinent d orbitals as shown in Figure 5.

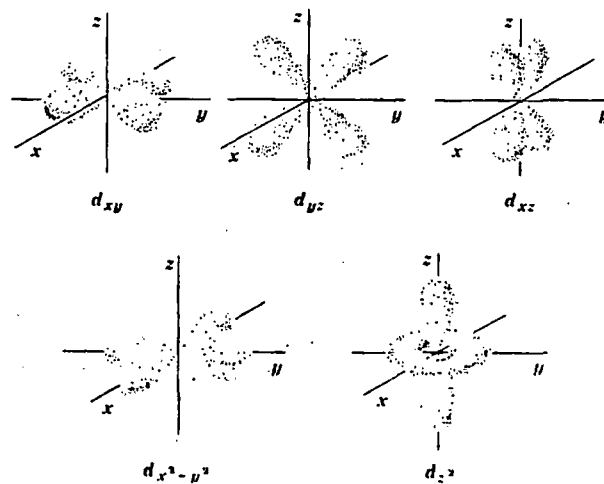


FIG. 5. Representation of the boundary surfaces of the d electron orbitals.

Each of these d orbitals, when full, contains two electrons of opposite spin. The placing of either one or two electrons in each of the five d -orbitals corresponds to a symmetrical ion which has no electrostatic preference for one or another structural coordination; this is reflected in Table 5 for the ions Mn^{2+} and Zn^{2+} . In such examples, ionic size considerations become predominant, the smaller size of Zn^{2+} dictating the tetrahedrally coordinated sphalerite and wurtzite structures, whereas Mn^{2+} has a size relative to S^{2-} , which permits it to occur in both the four-coordinated wurtzite and six-coordinated sodium chloride structures. Clearly, the fact that the valencies in chalcopyrite, a sphalerite (zinc blende) structure, and in the related bornite structure must be considered Cu^+ and Fe^{3+} (Wells, 1962, p. 883; Manning, 1967b) is related to the fact that those ions, in contrast to Cu^{2+} and Fe^{2+} , have spherically symmetric electronic configurations identical to Zn^{2+} and Mn^{2+} , respectively (Table 5).

Table 5 shows that Ni^{2+} possesses the largest octahedral-site stabilization energy and largest octahedral-site preference energy of any ion listed. In terms of crystal-field theory, Ni^{2+} is thus markedly different from ions such as Mn^{2+} and Zn^{2+} with which it is closely related by the periodic table. The significance of the fact that Ni^{2+} has eight $3d$ electrons, in terms of its octahedral-site stabilization energy, is perhaps most readily visualized in Figure 6, which shows relative orbital energy levels for various coordinations. The multiple, orbital energy levels for an ion in a particular structure reflect relative stabilization and destabilization of orbitals by the presence of anions or ligands coordinated with the ion. The levels are a representation of crystal-field splitting, the prerequisite for crystal-field stabilization. Again, it must be emphasized that the spatial geometry of the orbitals (Fig. 5) must be perceived. Furthermore, consider that with respect to the three-dimensional coordinate system, sixfold coordination of a transition metal may be visualized as placement of anions or ligands in positions along the positive and negative axes; undistorted tetrahedral coordination requires placement of anions or ligands in space between the axes; and square planar coordination may be visualized as placement of anions or ligands in the x - y plane along those axes. Finally, the most stable arrangement of anions or ligands about transition-metal orbitals is that in which repulsive interactions are minimized; in short, anions are located about cations in areas of low orbital electron density.

If Ni^{2+} is octahedrally coordinated, two spin-paired electrons are found in each of the stabilized, t_{2g} , orbitals (d_{xy} , d_{yz} , and d_{zx}), and one electron in each of the destabilized, e_g , orbitals ($d_{x^2-y^2}$ and d_{z^2}).

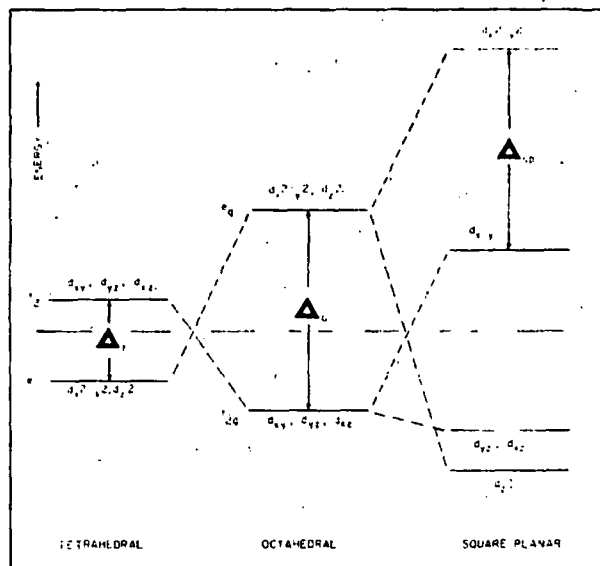


FIG. 6. Relative energy levels of d orbitals of a transition metal ion in tetrahedral, octahedral, and square-planar coordinations. NOTE: $d_{x^2-y^2}$ square planar should read d_{xy} .

This arrangement is relatively symmetrical (has no orbital angular momentum), and if the six anions are visualized to lie along the axes, they are readily perceived to be interacting with the fewest electrons possible.

If Ni^{2+} is tetrahedrally coordinated, the relative orbital stabilizations are reversed (Fig. 6). For tetrahedral coordination, only two orbitals are stabilized, $d_{x^2-y^2}$ and d_{z^2} , and only four electrons can be placed in them. Hence, the remaining four electrons must be unequally distributed among the three orbitals that lie between the coordinate axes and with which the anions or ligands most intimately interact. Several comparisons with octahedral coordination may be visualized: (1) only four of eight electrons, rather than six of eight, are in stabilized orbitals, and, given the same bond distance and ligand type, the crystal-field splitting parameter, Δ_t , is only $4/9 \Delta_o$ (Fig. 6); (2) four anions or ligands must closely interact with four electrons, rather than six anions or ligands with three electrons, resulting in considerably greater net interaction for tetrahedral coordination; (3) the d_{xy} , d_{yz} , and d_{xz} orbitals are asymmetrically filled and thus will provide an angular orbital momentum to the tetrahedral arrangement, which will effectively attempt to distort it (the Jahn-Teller effect). These three factors, whether viewed here from the standpoint of crystal-field theory or viewed from more complete molecular orbital theory, account for the large octahedral-site preference energy of Ni^{2+} .

If Ni^{2+} is to be four-coordinated, it much prefers, and is in fact particularly noted for, square planar

complexes (e.g., Wells, 1962). In terms of the preceding argument, square planar coordination may be considered to be grossly distorted tetrahedral coordination. Figure 6 shows the more complex, orbital energy configuration for square planar coordination, which allows all eight electrons to be spin-paired into only four orbitals, leaving the $d_{x^2-y^2}$ orbital empty. It is only in this complex that a low-spin Ni^{2+} ion may be formed, because only for square-planar coordination is there a crystal-field splitting energy, Δ_{sp} of Figure 6, acting to pair the unpaired electrons. With $d_{x^2-y^2}$ unoccupied, one can visualize that four anions or ligands are able to approach closely along the "x" and "y" axes with minimal electron interaction to form a structure with no asymmetry, or orbital moment. Figure 6 indicates that the stabilization energy for Ni^{2+} in this type of site would be greater than that in octahedral sites, given the same ligands.

It is relevant to extend the preceding discussion one step further to discuss these concepts specifically in terms of the ZnS polymorphs. The ZnS polymorphs must be considered to have more rigid bonding than structures of the sulfides of the associated transition metals. Although ZnS is often cited as an example of a dominantly homopolar or covalent compound, Title (1963) and Berlincourt et al. (1963) show that the bonding is more nearly 80 percent ionic and 20 percent covalent. All of the 3d electron orbitals of Zn^{2+} are filled, as are the 3p orbitals of S^{2-} . (In contrast, the partly unfilled orbitals of other divalent transition metals, and the resultant electron mobility, impart to their sulfides a component of metallic bonding and the accompanying metallic appearance.) Thus, because Ni^{2+} will accept four-coordination only if it may exert significant Jahn-Teller distortion to deform the tetrahedron and because the ZnS polymorphs are quite resistant to distortion by substitutional cations, the solubility of NiS in ZnS is markedly lower than that of MnS, FeS, or CoS.

Preceding discussion has established the fact that Mn^{2+} has no preference between octahedral and tetrahedral sites; hence the extensive solubility of MnS in ZnS is readily explicable. The appreciable stabilization energies of Fe^{2+} and Co^{2+} in octahedral and tetrahedral sites (Table 5) reflect the fact that these ions are not symmetrical in the sense of the Mn^{2+} and Zn^{2+} ions. Note, however, that Fe^{2+} and Co^{2+} have relatively small octahedral-site preference energies. This factor, in addition, of course, to their permissive ionic radii, accounts for the fact that Fe^{2+} and Co^{2+} will readily enter the tetrahedrally coordinated ZnS structures. In terms of orbital occupancy, tetrahedrally coordinated, high-spin cations with six or seven d-electrons will place single electrons in each of the d_{xy} , d_{yz} , and d_{zx} orbitals. This

arrangement is thus symmetrical for those orbitals that interact most closely with the anions or ligands and allows the anions to experience only slightly more electron repulsion than they would if they were octahedrally coordinated to the cations. Consideration of Cu^{2+} , a $3d^9$ ion, in terms of the concepts utilized here, reveals a fully adequate explanation of the low solubility of this ion in ZnS.

The effect of FeS in diminishing the solubility of NiS in ZnS (Fig. 1) demands comment. In the absence of stable ternary phases, the fact that none of the transition metals discussed form a complete solid solution series with ZnS indicates that substitution causes strain in the ZnS structure. Several characteristics of an ion may be related to its potential for inducing strain, but for the transition ions discussed here, crystal-field influences (3d electron configuration) almost certainly are more important than ionic size. In order to maintain the strain at a minimal level, one may think of the structure as preferentially accepting a less perturbing ion at the expense of a more strain-inducing ion. In this case, Fe^{2+} , an ion which has a lesser octahedral-site preference energy than Ni^{2+} (Table 5) and is thus more readily accepted in tetrahedral sites, is found to reduce the solubility of an ion which is relatively less stable in tetrahedral coordination.

Conclusion

Neither the appreciation of the peculiar geochemical behavior of Ni^{2+} in comparison with its transitional metal neighbors, nor discussion of this phenomenon in terms of crystal-field theory, is novel, but apparently the special situation of Ni^{2+} has not been so dramatically demonstrated for sulfide systems. Because the common disulfides and related minerals formed by these metals generally have the pyrite structure, or a related octahedrally coordinated structure, the studies by Nickel (1968, 1970) only slightly reflect the special character of Ni^{2+} . Similar comment applies to the observation of Burns (1970) regarding the relative distribution of Ni^{2+} and Co^{2+} between pyrite and pyrrhotite. Dunitz and Orgel's (1957) paper and the nearly simultaneous report by McClure (1957) clearly present the profound importance of crystal-field theory in understanding and predicting the distribution of the transition metals between the octahedral and tetrahedral sites of the spinel structures. Burns and Fyfe (1964) use crystal-field theory to predict phase diagrams and explain the selective uptake of transition metals from a magma, but these authors (1966) were obliged to re-emphasize that repeated attempts to explain the behavior of Ni during magmatic crystallization were inadequate because the importance of the Ni^{2+} octahedral-site preference energy and the distribution of

octahedral and tetrahedral sites in crystals and melts had not been considered.

Sulfide mineralogists are encouraged to approach problems of structure stability, solid solution, and element co-distribution from the viewpoint of the crystal-field or molecular orbital theories. The success of this approach, evidenced by this report, those just cited, and others, e.g., Rajamani and Prewitt (1972), Hulliger (1968), and Manning (1966, 1967a, 1967b) makes it clear that this is a field of importance not limited to studies of oxide and silicate mineralogy and emphasizes that more traditional approaches to these problems can sometimes fail completely. This conclusion was presaged by Fleischer (1955, p. 974) prior to the first (Burns, 1970) recognized application of crystal-field theory to geochemistry in 1959.

Nickel analyses for natural sphalerites are not plentiful. The most comprehensive published survey of trace-element data for sphalerites is that of Fleischer (1955). Of 117 references cited for sphalerite analyses, only 20 mention Ni, and many of these present no quantitative (or even numerical) data. Fleischer's summary (Table 5, p. 989) shows that Ni is the least abundant of any sphalerite trace element that he considers. For 254 reported analyses of ZnS polymorphs, 171 show no Ni, 49 show less than 50 ppm, and the maximum concentration reported is 300 ppm. Kullerud (1953) presents analyses of 54 sphalerites, of which 17 contain both Ni and Co at average concentration levels of 24 ppm Ni and 181 ppm Co. Of 213 sphalerite analyses published by Burnham (1959), 59 samples contained both Ni and Co, yielding similar average concentrations of 20 ppm Ni and 154 ppm Co. For sphalerite from Central district, New Mexico, in which both Ni and Co have been determined, the average concentrations are 9.6 and 200 ppm, respectively (Rose, 1967). Comparing these data for the two elements and considering the fact that Co concentrations are typically quite low despite a considerable solubility of CoS in ZnS, one would not readily have predicted the marked difference in the maximum solubilities of NiS and CoS in ZnS that are now established.

The most useful data would, of course, be those for sphalerites deposited in association with Ni-sulfides, for in such examples, the availability of nickel would not be in question. This situation is realized in the Upper Mississippi Valley lead-zinc district in which millerite is widespread, and more complex Ni-sulfides are being identified (A. V. Heyl, oral commun., 1971). Available analyses (Hall and Heyl, 1968) and Heyl (written commun., 1971) confirm the concentration distributions reported by Fleischer. It would clearly be of interest to compare Ni and Co concentrations in sphalerites from

higher temperature deposits containing Ni- and Co-sulfides.

Arnold et al. (1962) present one of the few opportunities to compare Ni and Co concentrations in sphalerite with those in associated pyrite and pyrrhotite. For mean values based on 8 to 23 determinations, they report: sphalerite—Ni-0.0018; Co-0.0052; pyrrhotite—Ni-0.027, Co-0.0075; and pyrite—Ni-0.035, Co-0.0732. The fifteen- to twentyfold concentration of Ni in the Fe-sulfide phases reflects the preference of Ni for octahedral coordination. The picture for Co is complicated by a high-spin, low-spin crystal-field consideration for Co²⁺ but is readily interpreted in terms of crystal-field theory.

Acknowledgments

For thoughtful review, resulting in improved presentation, we thank Paul B. Barton, Jr. and Charles L. Christ of the U. S. Geological Survey and Herbert A. Weakliem of RCA Laboratories.

U. S. GEOLOGICAL SURVEY
345 MIDDLEFIELD ROAD
MENLO PARK, CALIFORNIA 94025
May 31, September 22, 1972

REFERENCES

- Arnold, R. G., Coleman, R. G., and Fryklund, V. C., 1962, Temperature of crystallization of pyrrhotite and sphalerite from the Highland-Surprise mine, Coeur D'Alene district, Idaho: *ECON. GEOL.*, v. 57, p. 1163-1174.
- Barton, P. B., Jr., and Toulmin, P., III, 1966, Phase relations involving sphalerite in the Fe-Zn-S system: *ECON. GEOL.*, v. 61, p. 815-849.
- Berlincourt, D., Jaffe, H., and Shiozawa, L. R., 1963, Electroelastic properties of the sulfides, selenides, and tellurides of zinc and cadmium: *Phys. Rev.*, v. 129, p. 1009-1017.
- Burnham, C. W., 1959, Metallogenic provinces of the southwestern United States and northern Mexico: *New Mexico Bur. Mines Mineral Resources Bull.* 65, 76 p.
- Burns, R. G., 1970, *Mineralogical applications of crystal field theory*: Cambridge, Cambridge Univ. Press, 224 p.
- and Fyfe, W. S., 1964, Site preference energy and selective uptake of transition-metal ions during magmatic crystallization: *Science*, v. 144, p. 1001-1003.
- and Fyfe, W. S., 1966, Behavior of nickel during magmatic crystallization: *Nature*, v. 210, p. 1147-1148.
- Cabri, L. J., 1969, Density determinations: accuracy and applications to sphalerite stoichiometry: *Am. Mineralogist*, v. 54, p. 539-548.
- Craig, J. R., 1971, Violarite stability relations: *Am. Mineralogist*, v. 56, p. 1303-1311.
- Dunitz, J. D., and Orgel, L. E., 1957, Electronic properties of transition-metal oxides—II; Cation distribution amongst octahedral and tetrahedral sites: *Jour. Phys. Chem. Solids*, v. 3, p. 318-323.
- Fleischer, M., 1955, Minor elements in some sulfide minerals: *ECON. GEOL.*, 50th Ann. Vol., p. 970-1024.
- Fyfe, W. S., 1964, *Geochemistry of solids, an introduction*: New York, McGraw-Hill, 199 p.
- Hall, W. E., 1961, Unit-cell edges of cobalt- and cobalt-iron-bearing sphalerites: *U. S. Geol. Survey Prof. Paper* 424-B, p. 271-273.
- and Heyl, A. V., 1968, Distribution of minor elements in ore and host rock, Illinois-Kentucky fluorite district and Upper Mississippi Valley Zinc-lead district: *ECON. GEOL.*, v. 63, p. 655-670.

- Hulliger, F., 1968, Crystal chemistry of the chalcogenides and pnictides of the transition elements: *Structure and Bonding*, v. 4, p. 83-229.
- Kroger, F. A., 1938, Formation of solid solutions in the system zinc sulfide-manganese sulfide: *Zeitschr. Kristallographie*, v. A100, p. 543-545.
- 1939, Solid solutions in the ternary system ZnS-CdS-MnS: *Zeitschr. Kristallographie*, v. A102, p. 132-135.
- Kullerud, G., 1953, The FeS-ZnS system. A geologic thermometer: *Norsk geol. tidsskr.*, v. 32, p. 61-147.
- 1963, The Fe-Ni-S system: *Carnegie Inst. Washington Year Book* 62, p. 175-189.
- Yund, R. A., and Moh, G., 1969, Phase relations in the Fe-Ni-S, Cu-Fe-S, and Cu-Ni-S systems: *ECON. GEOL. Mon.* 4, p. 323-343.
- Manning, P. G., 1966, Cu (II) in octahedral sites in sphalerite: *Canadian Mineralogist*, v. 8, p. 567-571.
- 1967a, Absorption spectra of Fe (III) in octahedral sites in sphalerite: *Canadian Mineralogist*, v. 9, p. 57-64.
- 1967b, A study of the bonding properties of sulfur in bornite: *Canadian Mineralogist*, v. 9, p. 85-94.
- McClure, D. S., 1957, The distribution of transition metal cations in spinels: *Jour. Phys. Chem. Solids*, v. 3, p. 311-317.
- Nickel, E. H., 1968, Structural stability of minerals with the pyrite, marcasite, arsenopyrite, and löllingite structures: *Canadian Mineralogist*, v. 9, p. 311-321.
- 1970, The application of ligand-field concepts to an understanding of the structural stabilities and solid-solution limits of sulfides and related minerals: *Chem. Geology*, v. 5, p. 233-242.
- Nowacki, W., 1971, Introductory talk: *Soc. Mining Geol. Japan Spec. Issue* 2, p. 3-9.
- Pappalardo, R., and Dietz, R. E., 1961, Absorption spectra of transition ions in CdS crystals: *Phys. Rev.*, v. 123, p. 1188-1203.
- Rajamani, V., and Prewitt, C. T., 1972, Geochemistry of cobalt in sulfides: *Am. Geophys. Union Trans.*, v. 53, p. 550.
- Rose, A. W., 1967, Trace elements in sulfide minerals from the Central district, New Mexico and the Bingham district, Utah: *Geochim. et Cosmochim. Acta*, v. 41, p. 547-585.
- Rosenqvist, T., 1954, A thermodynamic study of the iron, cobalt, and nickel sulfides: *Iron Steel Inst. Jour.*, v. 176, p. 37-57.
- Skinner, B. J., 1961, Unit-cell edges of natural and synthetic sphalerites: *Am. Mineralogist*, v. 46, p. 1399-1411.
- and Bethke, P. M., 1961, The relation between unit-cell edges and composition of synthetic wurtzites: *Am. Mineralogist*, v. 46, p. 1382-1398.
- Title, R. S., 1963, Electron paramagnetic resonance spectra of Cr³⁺, Mn²⁺, and Fe³⁺ in cubic ZnS: *Phys. Rev.*, v. 131, p. 623-627.
- Toulmin, P., III, 1960, Effect of Cu on sphalerite phase equilibria—a preliminary report [abs.]: *Geol. Soc. America Bull.*, v. 71, p. 1993.
- and Barton, P. B., Jr., 1964, A thermodynamic study of pyrite and pyrrhotite: *Geochim. et Cosmochim. Acta*, v. 28, p. 641-671.
- Weakliem, H. A., 1962, Optical spectra of Ni²⁺, Co²⁺, and Cu²⁺ in tetrahedral sites in crystals: *Jour. Chem. Physics*, v. 36, p. 2117-2140.
- Wells, A. F., 1962, *Structural inorganic chemistry*: Oxford, Oxford Univ. Press, 1055 p.
- Whittaker, E. J. W., and Muntus, R., 1970, Ionic radii for use in geochemistry: *Geochim. et Cosmochim. Acta*, v. 34, p. 945-956.
- Yund, R. A., and Kullerud, G., 1962, The Ni-S system and related minerals: *Jour. Petrology*, v. 3, p. 126-175.

Geokhimiya, No. 3, 1964

Sp.

DEPENDENCE OF THE BEGINNING OF MELTING OF GRANITE
AND THE ELECTRICAL CONDUCTIVITY OF ITS MELT
ON HIGH WATER VAPOR PRESSURE

E. B. Lebedev and N. I. Khitarov
V. I. Vernadskii Institute of Geochemistry
and Analytical Chemistry
Academy of Sciences, USSR, Moscow

(ABSTRACT)

The electrical conductivity (σ) of melted El'dzurta granite was studied at H₂O vapor pressures up to 9000 atm and temperatures to 1200°C. One sample was studied dry up to 1600°C.

As the partial pressure of water increases the temperature of beginning of melting of the granite decreases, but the beginning of melting becomes almost constant above 4000 atm at 640°C. With increasing vapor pressure the electrical conductivity increases by several orders of magnitude until, at about 4000 atm and 1000°C, the pressure effect on the conductivity is diminished. In the range P_{H₂O} = 1000-8000 atm at 1200°C the value of σ varies from $6 \cdot 10^{-2}$ to $3 \cdot 10^{-1}$ ohm⁻¹ cm⁻¹.

If the considerable change in electrical conductivity of granitic rocks on melting could be detected by geophysical methods, the relations between plastic flow, metamorphism, and tectonic processes could be elucidated. —D. B. Stewart

Discussion of many geochemical and geophysical problems is difficult because of the scarcity of data on the electrical conductivity of various materials under plutonic conditions. For this reason in our experimental investigations of the effect of partial vapor pressure of water on the beginning of melting of granite, we made use of the conductance method.

Many investigations in the region of relatively low temperatures and pressures have been made by Volarovich [1, 2, 3], a pioneer in the application of the conductance method to the study of geological materials. The region of higher temperatures and normal pressures has been investigated largely by foreign scientists, but there are practically no investigations of the simultaneous effect of high temperatures and pressures on melts, and no data at all on the electrical conductivity of melts containing volatile components.

In the presence of volatiles, the electrical conductivity will depend not only on temperature and pressure but also on the contents of the volatile components and their nature. The most abundant volatile component of magma is water, and its behavior in granitic melts has been studied up to temperatures of 1200°C and pressures of 7000 atm [4, 5]. It appeared worthwhile, therefore, to investigate the effect of partial pressure of water vapor on the melting temperature of granite by the conductance method, obtaining at the same time data on the electrical conductivity of hydrous granitic melts for a broad range of temperatures and pressures.

The experiments were made in an internally heated high pressure apparatus [4]. The

measuring cell was placed in the high pressure chamber, and was calibrated by a standard 0.01 N KCl solution at 20°C and a pressure of 1 atm, and was connected to a bridge circuit. The conductance measurements were made at 100 cycles per second.

The finely powdered samples were pressed into the measuring cells under a pressure of 20,000 kg/cm². The scatter of results obtained at different pressures amounted to only 5-10% despite the parasitic capacity generated by placing the cell in the high pressure chamber and ascribable to various causes. The conductance isobars showed satisfactory reproducibility. The loss of current from the pressure chamber was controlled and did not exceed 5%.

Temperatures were measured with a Pt - PtRh (10% Rh) thermocouple pressed into the sample. Pressures up to 5000 atm were measured with a Bourdon gage (class 1), and higher pressures were measured with a man-ganin gage.

The electrical conductivity of dry granite at a pressure of 1 atm was measured for reference. The rock used in the experiments was the El'dzurta granite (Northern Caucasus), whose composition is given in Table 1, together with Noritomi's analyses of two granites [6], and Murase's analysis of obsidian [7].

Noritomi measured the electrical conductivity of granites at 1 atm pressure and temperatures up to 1050°C, while Murase obtained the values of σ for obsidian at temperatures up to 1400°C. Our data for the El'dzhura granite, Noritomi's, and Moiseyenko and Istomin's data [8] for granites, and Murase's data

Table 1
Chemical Composition of Granite Used to Determine Electrical Conductivity Dry at 1 atm

Component	El'dzhurta granite	Noritomi		Murase, obsidian
		granite 1	granite 3	
SiO ₂	72,58	67,50	76,95	74,41
TiO ₂	0,35	0,25	Trace	0,05
Al ₂ O ₃	14,11	15,77	12,59	13,33
Fe ₂ O ₃	0,57	2,61	1,31	0,08
FeO	1,53	2,25	0,12	0,86
MnO	0,04	0,10	0,02	0,05
MgO	0,65	1,82	0,22	0,43
CaO	1,72	4,49	1,08	1,90
Na ₂ O	3,17	1,99	1,02	2,99
K ₂ O	0,89	2,80	5,99	4,30
P ₂ O ₅	0,11	0,02	0,03	0,23
S	0,03	—	—	—
F	0,06	—	—	—
H ₂ O ⁻	0,08	0,06	0,06	0,29
H ₂ O ⁺	0,49	0,14	0,10	0,23
CO ₂	0,02	—	—	—
Total	99,88	99,78	99,49	99,15

Note: All commas are equivalent to decimal points.

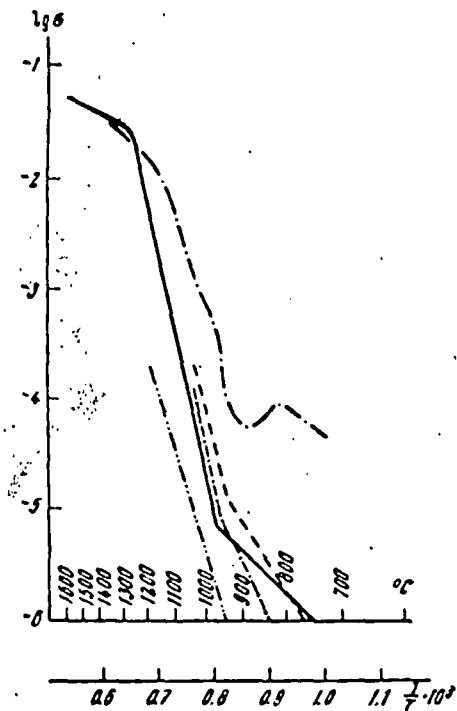


Fig. 1. Electrical conductivity of granites and obsidian
— El'dzhurta granite at 1200°C and one atm. pressure; -x-x- and - - - - Noritomi's data for granites [6]; ····· Murase's data for obsidian [7]; ····· Molsayenko and Istomin's data [8]

for obsidian are shown in Fig. 1. Our data agree well with Noritomi's. The linear dependence shown on the graph indicates that the electrical conductivity varies according to the equation $\sigma = \sigma_0 \cdot e^{-E/RT}$, where E is the activation energy, k is the Boltzmann constant, and σ_0 is a proportionality constant.

The electrical conductivity of obsidian in the interval 750-900°C differs sharply from Noritomi's and our data for granites, probably because of differences in the experimental procedure. In the interval 900-1160°C the curve for obsidian approximately parallels the curves for the granites, but passes through the corresponding values of conductivity at lower temperatures, probably because of the glassy state of the sample. The sharp change in the slope of the curve at the temperature of fusion is characteristic. At about 970°C $dG/dT = 7 \cdot 10^{-5}$ ohm⁻¹ cm⁻¹/°C, and at 1250°C the value of σ is almost ten thousand times higher than at 970°C.

Noritomi's two granites have nearly the same electrical conductivity in spite of a considerable difference in composition. It is very likely that the differences in the conductivity curves must be ascribed not only to the differences in the method of investigation but also to the mineralogy of the rocks. Unfortunately, Noritomi does not give the modes of his granites.

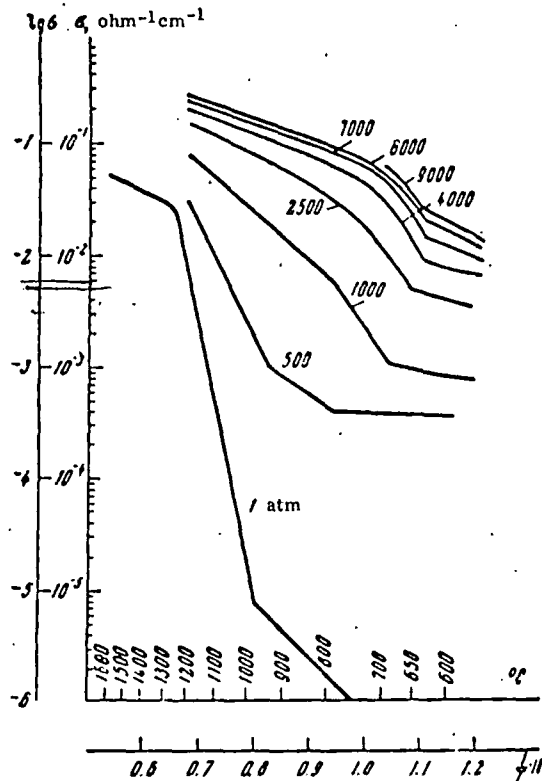


Fig. 2. Electrical conductivity of granite at 1200°C as a function of partial pressure of water vapor up to 9000 atm

The second conductivity was measured. The dependence on the partial pressure is shown. The first low temperature stages of granite, and for aluminosilicate conductivity. Accumulate and remaining granite, partial pressure 1000 atm, there is a region directed a few relic cry.

As can be seen, the conductivity isobar beginning of melting is considerably by the presence of water. The temperature of fusion is about 970°C. As pressure rises, the electrical conductivity isobar shifts together. At a temperature of 1000°C, the granite becomes molten. In the presence of water, the electrical conductivity of granite becomes several orders of magnitude higher. The greatest conductivity are observed at 1000°C. At a

As pressure rises, the electrical conductivity isobar shifts together. At a temperature of 1000°C, the granite becomes molten. In the presence of water, the electrical conductivity of granite becomes several orders of magnitude higher. The greatest conductivity are observed at 1000°C. At a

As pressure rises, the electrical conductivity isobar shifts together. At a temperature of 1000°C, the granite becomes molten. In the presence of water, the electrical conductivity of granite becomes several orders of magnitude higher. The greatest conductivity are observed at 1000°C. At a

The greatest conductivity are observed at 1000°C. At a

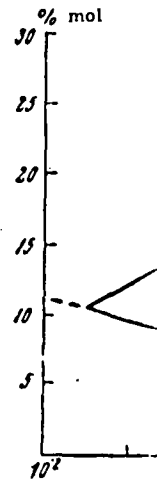


Fig. 3. Dependence of the amount of water vapor on the temperature of granite at 1200°C

ELECTRICAL CONDUCTIVITY OF GRANITIC MELTS

The second series of determinations of conductivity was made in the presence of water. The dependence of the conductivity of granites on the partial pressure of water vapor and temperature is shown in Fig. 2 together with the conductivity curve for dry granite.

The increase in electrical conductivity with pressure and temperature is not regular, for the curves have a number of inflexions. The first low temperature break corresponds to the early stages of reaction between water and granite, and formation of the first alkali-bearing aluminosilicate melts causing an increase in conductivity. As heating continues, the melts accumulate and aid in the melting of the remaining granite. In the region of relatively low partial pressures of water, not higher than 1000 atm, there is another break on the conductivity isobars corresponding to the homogenization of the melt. The quenched melts from the region directly above this break show only a few relict crystals of quartz.

As can be seen from the trend of the conductivity isobars, the temperature of the beginning of melting of granite is lowered considerably by increase in the partial vapor pressure of water. In the 500-9000 atm interval the temperature is lowered by about 155°C.

As pressure increases, its effect on the value of the electrical conductivity diminishes, and starting at 4000 atm the isobars come close together. At approximately this pressure the temperature of the beginning of melting of granite becomes stabilized.

In the presence of water the electrical conductivity of granite increases sharply as the pressure rises to 4000 atm. The values of the electrical conductivity in this pressure range are several orders higher than for dry granite.

The greatest differences in electrical conductivity are observed at temperatures up to 1000°C. At about 1200°C the conductivity

isobars form a bundle within a relatively narrow range of values of σ .

The change in electrical conductivity with partial pressure of water vapor is intimately related to the solubility of water in the granitic melt. The conductivity isobars and isotherms shown in Fig. 3 reflect the dependence of σ on the solubility of water in the melt. Increase in water content in the melt with increasing pressure promotes dissociation and lowers the total value of the activation energy of the system (Fig. 4).

As a result the conductance of the ions increases, and hence the electrical conductivity increases. The sharp decrease in the activation energy of the granitic melt with increase in $\text{P}_{\text{H}_2\text{O}}$ reflects a greater mobility of the ions which is proportional to the activation energy $\sigma = \exp \left[-\frac{E}{kT} \right]$. Judging by the values of σ in molten alkali chlorides and in granitic melts, it may be supposed that the degree of dissociation in the melt is high and that water increases the electrical conductivity of the melt.

In the absence of water, most rock-forming minerals have low electrical conductivities ($1 \cdot 10^{-8} \text{ ohm}^{-1} \text{ cm}^{-1}$ and lower) [10]. Ground waters cause an increase in the electrical conductivity of rocks, the amount of increase depending on the composition of the waters, their salinity, and their content in the rocks. The electrical conductivity of ground waters ranges broadly from $1 \text{ ohm}^{-1} \text{ cm}^{-1}$ to $0.66 \cdot 10^{-4} \text{ ohm}^{-1} \text{ cm}^{-1}$.

The experimental data on the electrical conductivity of granite in the presence of water illustrate only the simplest case of association of rock and pure water. Complications in the composition of the water have a considerable effect on the values of σ .

It is significant that beginning with 1200°C the effect of increase in the partial pressure of

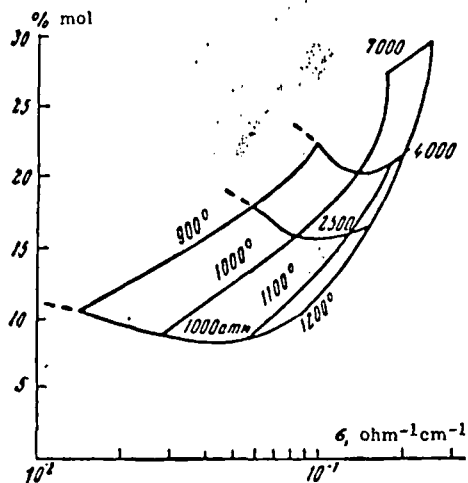


Fig. 3. Dependence of electrical conductivity on the solubility of water in granitic melt

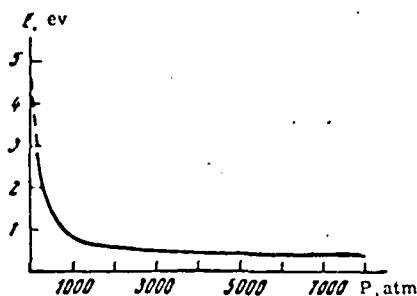


Fig. 4. Dependence of activation energy (E) on the partial pressure of water vapor in the interval 900°-1200°C

vapor on electrical conductivity decreases, and in the 1000-8000 atm interval the value of σ varies from $6 \cdot 10^{-2}$ to $3 \cdot 10^{-1} \text{ ohm}^{-1} \text{ cm}^{-1}$.

The conductivity curve of dry granite has a sharp bend at 1250°C . Judging by the investigated region, up to 1600°C the electrical conductivity curve has the same trend as the bundle of conductivity isobars for hydrous granitic melt, and all curves fall into a relatively narrow interval of conductivity values differing by no more than one order of magnitude.

Thus, the difference in the electrical conductivity of a dry granitic melt at normal pressure and a hydrous granitic melt at different partial pressures of water vapor decreases considerably with increasing temperature and pressure. The difference between an extrapolated value of σ for a melt at $T = 1350^\circ\text{C}$ and $P_{\text{H}_2\text{O}} = 1000 \text{ atm}$ with the value of σ for a dry granitic melt at the same temperature is about one half order.

It is important to bear these facts in mind in the interpretation of geophysical data on deep-seated rocks. The considerable change in the electrical conductivity at the temperature of the beginning of melting of granite might

be of considerable interest if it could be detected by geophysical methods. It would reveal the boundary of the plastic state of rocks and the zones of active metamorphism at depth, and would throw light on the connection between the plastic state of rocks and some tectonic processes.

In the experimentally investigated pressure range up to 9000 atm, the temperature of the beginning of melting of granite became almost stabilized at 4000 atm (Fig. 5). This indicates that the most favorable conditions for the metamorphism of granitic bodies in the presence of a sufficient supply of water may be expected at different depths depending on the geothermal conditions. If simple relations between temperature and depth are assumed, the beginning of melting will be determined by the position of points corresponding to different values of the geothermal gradient as shown in Fig. 5. Synchronous change in viscosity will cause structural changes in the rocks and relative increase in their mobility.

1. Volarov, fiz. kh.
2. Volarov, E. I. P. Fiziki
3. Volarov, Izvesti. geofiz.
4. Khitarov, Reng. khim.
5. Khitarov, Kadik.

Table 2

Activation Energy (E) and σ_0 of Granitic Melts at Different Values of $P_{\text{H}_2\text{O}}$

$P_{\text{H}_2\text{O}}$, atm	$\sigma_0, \text{ohm}^{-1} \text{ cm}^{-1}$	E, ev
8000	5.3	0.38
7000	4.8	0.385
4000	4.2	0.385
2500	$1.2 \cdot 10$	0.547
1000	$8.2 \cdot 10$	0.876
500	$1.4 \cdot 10^2$	1.95
Dry	$6.0 \cdot 10^{14}$	4.85

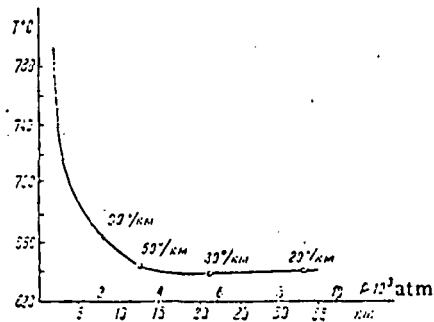


Fig. 5. Dependence of the temperature of beginning of melting of granite on $P_{\text{H}_2\text{O}}$ according to the conductance measurements

Table 3

Values of Electrical Conductivity (σ) and Activation Energy (E)

Rock	$P_{\text{H}_2\text{O}}$, atm	T, °C	$\sigma, \text{ohm}^{-1} \text{ cm}^{-1}$	E, ev	Reference
Granite	Dry	1200	$1.5 \cdot 10^{-2}$	4.85	Present authors
Granite	Dry	1000	$1.0 \cdot 10^{-2}$	3-6	Noritomi
Obsidian	Dry	1400	$3.5 \cdot 10^{-2}$	0.65	Murase
Granite	1000	1200	$9.0 \cdot 10^{-2}$	0.87	Present authors
Granite	8000	1200	$2.6 \cdot 10^{-1}$	0.38	Present authors
Molten alkali chlorides		800-900	2.4-6.6	0.1-0.4	[9]

Charges of 150 hours. (properties as shown below. D. B. Stewart)

To obtain and Mel'nik, American G.

ELECTRICAL CONDUCTIVITY OF GRANITIC MELTS

REFERENCES

1. Volarovich, M. P. and D. Tolstoi. Zh. fiz. khim. 7, 496, (1936).
2. Volarovich, M. P., A. T. Bondarenko and E. I. Parkhomenko. Tr. Instituta Fiziki zemli, No. 23 (190), (1962).
3. Volarovich, M. P. and A. T. Bondarenko. Izvestiya Akad. Nauk SSSR, seriya geofiz., No. 7, (1960).
4. Khitarov, N. I., E. B. Lebedev, E. V. Rengarten and P. V. Arsen'yeva. Geokhimiya, No. 5, (1959).
5. Khitarov, N. I., E. B. Lebedev and A. A. Kadik. Geokhimiya, No. 10, (1963).
6. Noritomi, K. J. Min. Coll. Akita University, Ser. A, 1, (1961).
7. Murase, Tsutomu. J. Fac. of Science, Hokkaido Univ., ser. VII, 1, No. 6, (1962).
8. Moiseyenko, U. I. and V. E. Istomin. Geologiya i geofizika, No. 8, (1963).
9. Yesin, O. A. and P. V. Gel'd. Fizicheskaya Khimiya Piro metallurgicheskikh Processov (Physical chemistry of pyrometallurgical processes), (1954).
10. Dakhnov, V. N. Interpretatsiya Rezul'tatov Geofizicheskikh Issledovaniy Razrezov Skvazhin (Interpretation of geophysical logs). Gostoptekhizdat (1962).

Geokhimiya No. 3, 1964
pp. 195 - 201

Received for publication, December 30, 1963
UDC 550.4:66.988

CRYSTALLIZATION IN THE SYSTEM:



B. N. Litvin and O. K. Mel'nikov
Institute of Crystallography
Academy of Sciences, USSR, Moscow

(ABSTRACT)

Charges of ZnO , SiO_2 , Na_2CO_3 , and H_2O were reacted in steel bombs at $350^\circ\text{--}500^\circ\text{C}$ and 600-2000 atm for 150 hours. Crystals of willemite, quartz, and $\text{Na}_2\text{ZnSi}_3\text{O}_8$ were recovered. Physical and optical properties and unindexed X-ray powder patterns are given. Synthesis fields of the phases are shown below; the yield of $\text{Na}_2\text{ZnSi}_3\text{O}_8$ increases as the content of Na_2CO_3 in the charge increases. — D. B. Stewart

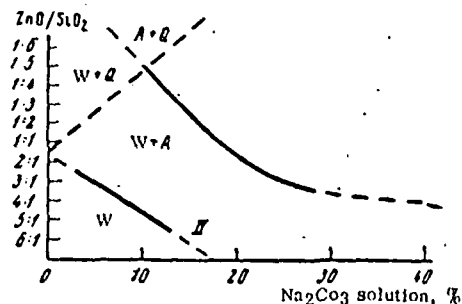


Fig. 5. Fields of crystallization of phases Q = quartz, A = $\text{Na}_2\text{ZnSi}_3\text{O}_8$, and W = willemite ($350\text{--}500^\circ\text{C}$).

To obtain a copy of the complete translation of this article, order document G12-2-64, "Litvin and Mel'nikov," 15 pp., \$2.25. Payment must accompany order. Send to Translations Office, American Geological Institute, 1444 N St. N.W., Washington, D. C., 20005.

Diffusion Flow Laws in Metamorphic Rocks

ABSTRACT

Rocks which deform by pressure solution obey a diffusion flow law with a linear viscous or Newtonian stress to strain-rate relation. Undeformed relics of original grains preserved within newly grown crystals at grain boundaries under tension and presolved surfaces, together with accumulation of inert particles at grain boundaries under compression, are diagnostic evidence of a diffusion flow law. At a given stress, strain-rate is inversely proportional to the grain size to a power of two or three. A geologically useful plot has inverse temperature versus the logarithm of grain size as coordinates. Such a graph is separated into fields by three boundaries which meet at a triple point; within each field, either lattice diffusion, grain-boundary diffusion, or a dislocation flow law is predominant. It may be possible to calibrate this graph from naturally deformed rocks. Photomicrographs of isoclinally folded greenschist-grade quartzites and rhyolitic flows from the South Mountain-Blue Ridge area in Maryland demonstrate a diffusive mass transfer deformation mechanism, but estimates of effective diffusion coefficient compared to currently available laboratory diffusion data are insufficient to identify the diffusion path with certainty. However, the comparatively low ratio of metamorphic temperature to melting temperature and the physical nature of grain boundaries in metamorphic rocks, particularly concentrations of low-density impurities at grain boundaries, suggest the grain-boundary diffusion flow law.

INTRODUCTION

A major obstacle to the understanding of the development of geological structures is our lack of knowledge of the *flow laws*—or the relations between stress and strain-rate at the time of deformation.

Regardless of the dimensions considered in a problem, ductile rocks deform as aggregates of crystalline grains, and the flow laws are decided on the scale of grains. An illustration of the importance of this problem is the controversy over the mechanisms and material properties which allow plates of lithosphere to move over the surface of planets through geological time. The question is: does a diffusion flow law hold, giving a linear stress to strain-rate relation as maintained by Gordon (1965, 1967), McKenzie (1968), and others; or is a dislocation flow law more appropriate, so that the asthenosphere is a power law material, as advocated by Orowan (1967), Weertman (1970), and others? Our lack of knowledge of the flow laws is not a special feature of the inaccessible mantle. The flow laws of crustal rocks, readily available for direct observation, are just as much of a mystery.

Have most of the grains in a thin section of naturally deformed rock changed shape by diffusive mass transfer or by dislocation motion? One point of this paper is to demonstrate that familiar "pressure solution" is equivalent to diffusion creep, and to show that direct microscopic observation can distinguish diffusion from dislocation flow. Another purpose is to clarify the theoretical relations between the different mechanisms of granular readjustment to deformation and to examine them in a geological context. Many of the ideas on these subjects are not found in the usual geological literature; a partial review will be attempted.

As we shall see, purely diffusive mass transfer is referred to in geology as "pressure solution," expressing the general idea that crystals dissolve where intensely stressed and grow where the stress is less. This idea is at least 100 yrs old, for Sorby (1863, 1879, 1908) presented convincing thin-section evidence of pressure solution and discussed its importance for

UNIVERSITY OF UTAH
RESEARCH INSTITUTE
EARTH SCIENCE LAB.

SUBJ
GCHM
DFL

diagenesis and metamorphism, while Van Hise (1896) and Becke (1903) considered pressure solution of major importance in the formation of schistosity.

More recently, the outstanding textural interpretations of Voll (1960) suggest that pressure solution combined with growth in the stretching direction is a major mechanism of deformation in the greenschist-grade rocks of the Welsh and Scottish Caledonides, the Rheinisches Schiefergebirge, the Northern Molasse basins, and the phyllite zones of the Swiss Alps. Durney (1972) illustrates nice examples from the Morcles Nappe. Many thin sections of deformed low-grade metamorphic rocks which I have seen show clear evidence of extensive pressure solution.

The theoretical understanding of pressure solution is in a much more unhappy situation. Work by Riecke (1895) was predated by Sorby, and his results are generally misinterpreted (reviewed by Turner and Verhoogen, 1960, p. 476). Clearly pressure solution should *not* be referred to as "Riecke's Principle." A theoretical treatment by Weyl (1959) was entirely concerned with pressure solution in a diagenetic context. Fundamental and often overlooked work was done, however, by Correns (1939, 1949).

In metallurgy, it was not until Nabarro (1948) that diffusive mass transfer as a possible flow law was suggested, and both Nabarro (1948) and Herring (1950) considered the bulk lattice as the diffusion path and derived a linear stress to strain-rate flow law. The possibility of the grain boundary as the diffusion path was first proposed independently by Coble (1963) and Lifshits (1963). Direct observation of metals deforming by diffusion creep was not reported until 1963 (Squires and others, 1963). At the outset, the reader is invited to compare the illustration of a metal deformed by diffusion creep (Fig. 3) with the photomicrographs of deformed metamorphic rocks (Figs. 7 and 8).

As shown later in this paper, each diffusion and dislocation flow law occupies a sector of an inverse temperature versus grain-size graph, and the sector boundaries meet at a triple point. The position of this triple point varies with certain fundamental properties of the rock, and it is possible to locate its position by observations of thin sections of naturally deformed rocks.

With a number of different processes op-

erating to produce a final result, how is it possible to find the rate-determining step? This question crops up throughout this paper; in essence, it is similar to determining the "critical path" for a whole number of different processes, where all must be finished to accomplish a given job. The various processes may be classified into two types, dependent and independent.

Two events, A and B, are dependent if A cannot proceed until B has taken place, so that the processes occur in sequence. The over-all rate is the slower of the dependent processes.

Rates of independent processes are not related to one another, and each may proceed at its own speed. The events can occur concurrently and nonsequentially. The over-all rate is the simple sum of all the independent rates, and in a sense, each process is free to compete for the largest share. The independent process with the fastest rate effectively dominates the over-all rate.

There is the matter of suitable names for the various flow laws, because they all involve some diffusion in one way or another (Orowan, 1967). In this paper, a diffusion flow law means one dominated by purely diffusion mass transfer, as opposed to dislocation flow laws in which the grains change shape by dislocation movement. The diffusion flow laws are subdivided according to the type of path—lattice or grain boundary—through which the diffusion occurs.

To discover what observations are necessary to prove diffusion flow, a brief review must be made of the assumptions underlying the derivations of the diffusion flow laws and of the available experimental evidence.

SI units are used throughout this paper.

DIFFUSION FLOW LAWS

Discussions of pressure solution in the geological literature occasionally refer to an equation worked out by Correns (1939, 1949). What is the relation between pressure solution, Correns' work, and diffusion creep? We will now draw all these different ideas together, keeping the treatment as simple as possible to emphasize the physics of the processes.

The partial molar volume v_i of a component i at temperature T and number of moles n_i can be written

$$v_i = \left(\frac{\partial \mu_i}{\partial P} \right)_{T, n_i}$$

where μ_i is the chemical potential of component i at a normal stress P . Integrating with respect to P , keeping T and n_i constant, and neglecting elastic compressibility, the chemical potential at normal stress P is

where μ_i^0 is an integration constant, the chemical potential of i at $P = 0$.

$$\therefore \mu_i^{P_1} - \mu_i^{P_2} = v_i(P_1 - P_2) \quad (1)$$

The above equation holds within the crystal proper. For material within the diffusion path, assuming ideality at a given T , P ,

$$\mu_i^P = \mu_i^0 + RT \ln c_i^P$$

where c_i is the concentration of component i , R is the gas constant, and μ_i^0 is the chemical potential at the standard state.

$$\therefore RT \ln c_i^{P_1} - RT \ln c_i^{P_2} = \mu_i^{P_1} - \mu_i^{P_2} \quad (2)$$

Now equilibrium holds between material in the crystal and in the adjacent diffusion path, so (1) and (2) may be equated

$$\begin{aligned} \therefore \mu_i^{P_1} - \mu_i^{P_2} &= v_i(P_1 - P_2) \\ &= RT \ln \left(\frac{c_i^{P_1}}{c_i^{P_2}} \right) \end{aligned}$$

This equation describes the equilibrium differences in concentration of component i under different normal stresses at opposite ends of a diffusion path. It is the modified form of van't Hoff's Law derived by Correns (1939, 1949), who correctly recognized that his equation described the driving force for "solution transfer" between crystal faces under different normal stresses.

Let the reference state be the stress free one, $P_2 = 0$, and the normal stress at a local spot on the grain be $P_1 = \sigma_n$. If we consider only a single component material with μ_0, c_0 as the chemical potential and equilibrium concentrations of the component at the reference state, then Correns' equation becomes:

$$\mu - \mu_0 = v \sigma_n = RT \ln \left(\frac{c}{c_0} \right) \quad (3)$$

But is it possible to approximate complex rock-forming minerals by a one-component material? Certain conditions must be met to permit mass transfer from one part of a dif-

fusion path to another. A Schottky defect is an anion vacancy balanced by sufficient cation vacancies to maintain charge balance. It is the only kind of point defect (1) created and destroyed entirely at the grain boundary, permitting mass transfer, (2) whose concentration is sensitive to the state of stress existing at the grain boundary, and (3) which have a self-regulating mechanism for the ionic flow so that newly deposited crystal retains stoichiometry. Consequently, Schottky defects are responsible for pressure solution and diffusion creep, and it can be shown that it is possible to consider the problem entirely in terms of the sublattice with the slowest moving vacancies, as if this component made up the entire crystal, by defining the effective atomic volume Ω as the volume of 1 Schottky defect divided by the number of slow moving vacancies in the defect (Fryer, 1972). In silicates, this is probably a vacancy in an oxygen sublattice. It is customary to discuss vacancies in terms of atomic quantities, and so Correns' equation (3) becomes, with k as Boltzman's constant,

$$\frac{\Omega \sigma_n}{kT} = \ln \left(\frac{c}{c_0} \right) = \ln \left(1 + \frac{c - c_0}{c_0} \right) \approx \frac{c - c_0}{c_0}$$

The error in this approximation is less than 10 percent when $\left(\frac{\Omega \sigma_n}{kT} \right)$ is less than 2×10^{-1} .

For typical geological conditions with a normal stress of $3.5 \times 10^8 \text{ nm}^{-2}$ (3.5 kb), temperature 625°K, and a vacancy the size of 0^{-2} we find that $\left(\frac{\Omega \sigma_n}{kT} \right)$ is 10^{-1} , so that the approximation appears to be good.

If 2 points on a grain boundary have a difference in concentration Δc as a result of a difference in normal stress $\Delta \sigma_n$,

$$\frac{\Delta c}{c_0} \approx \frac{\Omega \Delta \sigma_n}{kT} \quad (4)$$

Now we can proceed to derive the diffusion flow law more or less along the lines set out by Nabarro (1948) and Herring (1950). The flow

rate of vacancies $J = -D' \frac{\partial c}{\partial x}$ from Fick's first law at the quasi-steady state, where D' is the diffusion coefficient of vacancies. The vacancy influx is equal to the ion outflux, so $D' c_0 = -D$ in terms of the ion's diffusion coefficient D .

$$\begin{aligned} \text{Now concentration } c &= \frac{\text{number of vacancies}}{\text{number of sites}} \frac{\Omega}{\Omega} \\ &= \frac{\text{volume of vacancies}}{\text{volume of crystal}} \end{aligned}$$

As a result we are able to interpret J as the rate of volume flow of vacancies. The velocity v with which a crystal face of unit area moves out is equal to the volume rate of ions added on to the face, which is in turn equal to the volume rate of vacancies which leave this spot, so $v = J$. The strain-rate $\dot{\epsilon}$ is equal to the spatial rate of change of velocity,

$$\dot{\epsilon} = \frac{\partial v}{\partial x} = \frac{\partial J}{\partial x} = \frac{D}{c_0} \frac{\partial^2 c}{\partial x^2} \sim \frac{D \Delta c}{c_0 X^2}$$

where X is the diameter of an equant grain. Substituting in equation (4)

$$\dot{\epsilon} \sim \frac{D \Omega}{X^2 k T} \Delta \sigma_n$$

The mass flow of vacancies from one point to another within a given grain in response to the gradient in normal stress around the grain boundary changes the shape of the grain. Gradients in local normal stress around a given grain consist of components of both local mean stress and local deviatoric stress. It is necessary however to relate the strain rate to the stress on the scale of the polycrystalline aggregate rather than the local stresses around an individual grain of changing shape. Choose a volume of rock big enough to contain large numbers of grains yet small enough that the macroscopic stresses and strains on the boundaries of the volume are homogeneous. If the boundaries of the polycrystalline specimen were subjected to an entirely hydrostatic stress, the local normal stress gradients around grains would quickly relax as a result of diffusion, and the diffusion process would then cease. The local normal stress gradients are proportional to the larger scale macroscopic deviatoric stress σ acting on a polycrystalline sample. If K is a proportionality constant,

$$\sigma = K \Delta \sigma_n$$

$$\therefore \dot{\epsilon} \approx \frac{K D \Omega}{X^2 k T} \sigma$$

The purpose of the above treatment was to show that there are only a few steps from the work of Correns on the geological problem to the work by Nabarro and Herring from the metallurgical point of view.

If the diffusion path is through the bulk lattice, as originally suggested by Nabarro (1948) and Herring (1950), then

$$\dot{\epsilon} = \frac{K D_i \Omega}{X^2 k^2 T} \sigma \quad (5)$$

While if the diffusion path is along the grain boundary as Cobble (1963), Lifshits (1963); and Gifkins (1967b) suggested, then

$$\dot{\epsilon}_{gb} = \frac{K \pi D_{gb} h \Omega}{X^3 k^2 T} \sigma \quad (6)$$

In these flow laws, lattice and grain-boundary strain-rates are $\dot{\epsilon}_l, \dot{\epsilon}_{gb}$ and diffusion coefficients are D_l, D_{gb} ; r is ratio of the grain's longest to shortest dimensions, and π has its usual value. For grain ratio r up to about 3:1, K is 21, but for extremely elongate grains, K is $8r$.

What measure of strain rate and stress are we using in these equations? The intensity of the deviatoric stress acting on the polycrystalline sample may be measured by the octahedral shear stress σ . In terms of the principal values of the stress tensor $\sigma_1, \sigma_2, \sigma_3$, the octahedral shear stress is:

$$\sigma = \frac{1}{6} [(\sigma_1 - \sigma_2)^2 + (\sigma_2 - \sigma_3)^2 + (\sigma_3 - \sigma_1)^2]^{1/2}$$

Similarly, the deviatoric strain-rate can be represented in terms of the octahedral shear strain-rate

$$\dot{\epsilon} = \frac{1}{6} [(\dot{\epsilon}_1 - \dot{\epsilon}_2)^2 + (\dot{\epsilon}_2 - \dot{\epsilon}_3)^2 + (\dot{\epsilon}_3 - \dot{\epsilon}_1)^2]^{1/2}$$

The stress σ and strain-rate $\dot{\epsilon}$ are always positive.

The diffusion creep equations (5 and 6) have been rederived at least a dozen times in the past 25 yrs. We are using here results of the most complete and rigorous derivation to date, by Raj and Ashby (1971, equations 24 and 26).

It is instructive to trace the most general possible history of a vacancy from its creation to its annihilation. A vacancy can be created at a grain boundary or within the grain, with or without interference from impurities or inclusions. The vacancy then travels through the grain in a path along which the total number of vacancies may or may not be conserved at any instant. When the edge of the grain is reached, the disordered material of the grain boundaries collapses into the vacancy, eradicates it, and changes the shape of the grain. This sequence of vacancy source, diffusion path, and vacancy sink is a series of dependent processes so that the slowest must be the rate-determining step. Diffusion creep assumes that the operation of

the vacancy sources and sinks is completely unhindered and entirely located at grain boundaries, or in other words, that grain boundaries function as *ideal* sources and sinks. The rate-determining step is assumed to be the diffusion between source and sink.

The conservation of vacancies means that the divergence of the flow of vacancies is zero within the crystal, or alternatively that the Laplacian of the vacancy chemical potential μ is zero:

$$\nabla^2 \mu = 0$$

The solution of this Laplace's equation must satisfy boundary conditions of mechanical equilibrium, continuity, and chemical equilibrium. The equation of mechanical equilibrium is the same as is used in elasticity and plasticity and requires no comment, but the equations of continuity and chemical equilibrium lead to some unusual aspects which we will now discuss.

There have been two main ways of dealing with the continuity equation. Lifshits (1963), Gibbs (1965), Gifkins (1967b), and Raj and Ashby (1971) calculate the diffusional strain-rate using a space-filling aggregate of grains which are deformed in such a way that the polycrystalline continuity is always maintained. The stress field within the individual grains can be calculated (Raj and Ashby, 1971, Append. 2) and is found to be variable with large stress concentrations—what one would expect in natural polycrystalline rock. Another consequence of satisfying the continuity equation is that there is a coupled and dependent relation between diffusive mass transfer and grain-boundary sliding (Fig. 1). Diffusional creep could be called grain-boundary sliding with diffusional accommodation.

The other procedure is to avoid the problem of maintaining grain-to-grain continuity by dealing with a single grain of spherical shape (Herring, 1950; Coble, 1963; Green, 1970). In this case, a homogeneous stress field is maintained throughout the grain. The equations which result from these unrealistic abstractions are nevertheless approximately the same as those deduced from the polycrystalline model.

The equation (3) we have used for the chemical potential is

$$\mu = \mu_0 + \nu \sigma n.$$

Is this equation exact? What is its relation to the "theory of nonhydrostatically stressed solids"? The full equation for nonhydrostatically stressed solids was derived by J. W. Gibbs in 1876 and has received attention from Yang and others (1959), Kamb (1959, 1961a, 1961b), and McLellan (1970). I find the treatment by Li and others (1966) particularly clear. Green (1970) applied it to diffusion creep. This exact equation is

$$\mu = \mu_0 + \omega + \nu \sigma n.$$

Here ω is the elastic strain energy per mole, a term assumed negligible in equation (3). For typical geological conditions, this term affects the value by less than 1 percent, and so the approximation appears sound.

Changes in Grain Size and Shape

At constant stress, both lattice and grain-boundary diffusion flow laws (equations 5 and 6) have the general form:

$$\dot{\epsilon} = \frac{K'}{X^n r^m}$$

Grain size X is to a power n of 2 or 3, grain shape r to a power of 2/3 or 2, and K' is constant for the constant stress.

Green (1970) and Weertman (1970) suggested that this steady-state situation can never be the case and illustrated their interpretation with a coaxial deformation path. (Elliott, 1972). If the path is coaxial and grains do not rotate, then as the grains get more elongate, r gets larger, and the process is apparently self-exhausting. This combination of assumptions would result in the maximum possible departure from the steady state, but several processes will operate to produce a situation closer to a steady state.

1. Even in a coaxial deformation path, the grains will be continuously rotating relative to each other as a result of grain-boundary sliding. Grain-boundary sliding brings grains together and moves them apart and is constantly shuffling grains about, bringing different faces into contact. The newly precipitated part of a grain can subsequently be subjected to compressive stresses and dissolve, tending to maintain equiaxial grains.

2. A coaxial deformation path is a very special case which will only occur at local spots in the deforming rock (Elliott, 1972). With

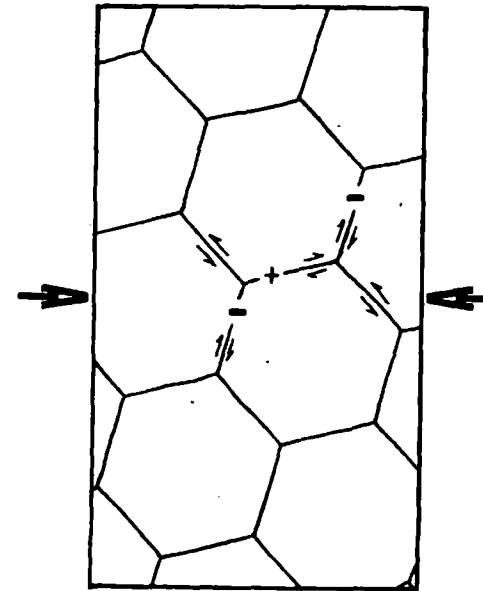


Figure 1. Space-filling array of hexagonal grains deformed by diffusion-accommodated grain-boundary sliding. For new crystal to precipitate (+) at a grain boundary under tension, the adjacent grains have to move apart. Grain-boundary sliding to give this grain separation must occur, and old crystal must be resorbed (-) at those grain boundaries under compression. Precipitation, dissolution, and grain-boundary sliding all occur simultaneously and in a certain proportion, otherwise voids will open and continuity will be destroyed.

general noncoaxial paths, the tendency to maintain equiaxial grains will be enhanced.

3. Grain size X may decrease as the grain ratio r increases. This happens if the newly precipitated crystal forms a new grain, as is often observed. Conceivably this could even produce a constant ratio $K'/X^n r^m$ and lead to a steady state.

It appears that changes with time in grain shape and size have a complex effect difficult to evaluate precisely and are clearly in need of experimental work with both coaxial and non-coaxial deformation paths. I feel that these deviations from a steady-state creep are probably a minor correction, compared for example to changes in temperature or chemical environment during the course of a typical geological deformation episode.

Experimental Evidence of Diffusion Creep

Experimental determination of the stress-strain-rate relations for a number of materials

provides unequivocal evidence of diffusion flow. Particularly convincing experiments are those of Burton and Greenwood (1970a, 1970b, 1971; see also Gifkins, 1971), who demonstrate both lattice and grain-boundary diffusion flow laws and show a linear viscous or Newtonian stress to strain-rate relation for pure copper.

Materials consisting of more than one phase can deform by diffusion creep under suitable stress levels, but the flow law may be more complex. Experimental work on magnesium alloys, polycrystalline corundum, and polycrystalline bromellite (BeO) has been reviewed by Karim (1970; see also Holt, 1970) and shown to follow a Bingham flow law for diffusion creep. Work by Burton (1971) on impure copper also suggests a Bingham flow law. Very fine grained, second-phase particles appear to inhibit the action of the grain boundaries from acting as ideal defect sources and sinks (Ashby, 1969; Greenwood, 1970; Burton, 1972). The rate of vacancy production now becomes the rate-determining step.

These second-phase particles must be extremely fine grained to have this blocking effect on grain-boundary vacancy production. Optically visible inclusions have a negligible effect on the diffusion flow law (Gibbs, 1965; Raj and Ashby, 1971). However, one important consequence of optically visible inclusions is to retard or even prevent grain-boundary migration.

For more details of experimentally determined stress to strain-rate relations, the reader is referred to the references cited above. The main concern of this paper is the possibility of demonstrating diffusion creep by direct microscopic observations in metamorphic rocks, as will be discussed next.

DIRECT OBSERVATION OF DIFFUSION CREEP

A clear idea of what precisely constitutes a grain boundary at any specific time is essential. Is the grain boundary always made up of the same material particles? What happens when part of an original grain boundary is resorbed or a part is added on?

Imagine a thin marker surface defined by inert markers, and let this surface initially coincide with the grain boundary and completely enclose a grain (Fig. 2A). When the polycrystalline aggregate is deformed, the

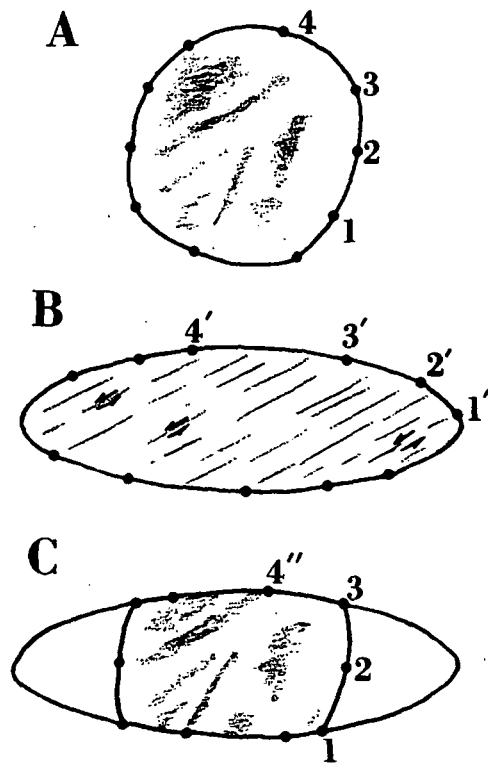


Figure 2. (A) Undeformed original grain with material points on grain boundary 1, 2, 3, 4. (B) Deformation of grain accomplished by dislocation glide. Transformed points 1', 2', 3', 4' still define the grain boundary. (C) Grain deformation by diffusion mass transfer. Relic of original grain boundary with material points 1, 2, and 3—now inside new crystal which is precipitating at each end. Solution surface cuts across top and bottom of old crystal. A material particle of some inert phase originally at 4 now accumulated at 4''. Grain boundary defined by new material particles.

grains must change shape, but there are only two geometric ways by which they can do this.

In the first method, the grain changes shape by a continuous transformation or strain. The material particles defining the grain boundary before the deformation lie on this boundary after the deformation (Fig. 2B). The mechanisms by which this grain deformation process is accomplished are dislocation processes such as slip or twinning.

In the second method (diffusion creep), material particles are removed (dissolved) from some parts of the original boundary and added elsewhere (precipitated) to the outside of the grain boundary. Inert particles accumulate at

places where the crystal is being dissolved; and in regions where new crystal is building outward, the relict grain boundary may separate new crystal from old crystal—the remnants of the grain before deformation (Fig. 2C).

Chemical bonds of the old crystal must be broken and new ones formed in the new crystal. Sites of deposition of new crystal at any instant is the grain boundary. It is impossible for the old crystal to migrate out to the position of the new grain boundary.

Diffusion creep has been widely observed in a magnesium alloy optically and by transmission electron microscope (Squires and others, 1963; Rainey and Holt, 1971 and references cited there). The original old crystals are peppered through with tiny inert particles. During deformation, grain boundaries undergoing compression accumulate inert markers as the old crystal is dissolved away, while grain boundaries under tension develop zones of new crystal which are free of the inert markers (Fig. 3).

Several authors have suggested that the zones of new crystal in the magnesium alloy could be formed by grain-boundary migration rather than diffusion creep (Vickers and Greenfield, 1967; Lee, 1969; Dunlop and Taplin, 1972). What is the difference between these two diffusive processes, and what observations could be used to distinguish them?

Grain-boundary migration is an effort to minimize the elastic strain energy stored in the crystal or to minimize surface energy, whereas the driving force for diffusion creep is a normal stress gradient. Grain-boundary migration is a short-range diffusive readjustment of local atoms, but diffusion creep involves long-range transport of material from one side of a grain to another.

Although both diffusion creep and grain-boundary migration could produce optically continuous zones of new crystal, grain-boundary migration could not produce new grains of new crystal. Dissolved parts of old crystal with inert particle accumulations at grain boundaries under compression cannot be explained by grain-boundary migration—accumulations which were observed in the magnesium alloy by Rainey and Holt (1971).

The microscopic effects of diffusion creep can be seen in thin sections from the Eocambrian Weaverton Formation of the South Mountain-Blue Ridge region in Maryland. These quartzites were deformed into tight isoclinal recumbent folds under greenschist facies at about

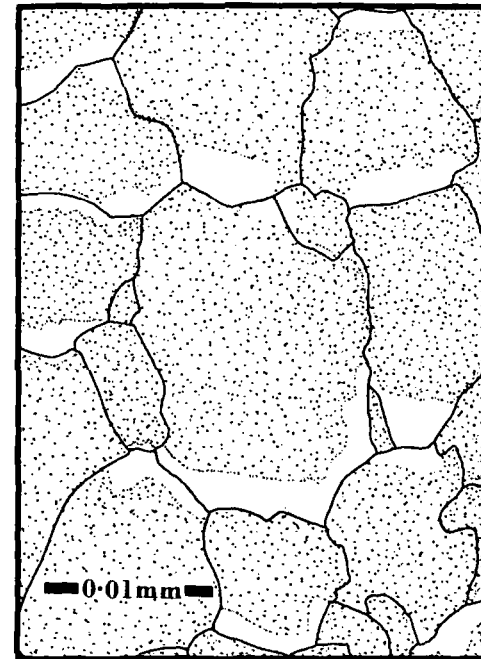


Figure 3. Original old crystal is full of finely disseminated inert particles (stippled). At grain boundaries under compression, old crystal is dissolved away leaving behind accumulations of inert particles. New crystal grows at grain boundaries under tension without inert particles (white). Vertical stretching direction, deviatoric natural strain ϵ 28 per cent in a coaxial deformation path. Drawn from microphoto (of Karim, 1970, Fig. 2) of a magnesium alloy which underwent diffusion creep.

625°K, under an overburden equivalent to a hydrostatic pressure of $3.5 \times 10^8 \text{ nm}^{-2}$ (3.5 kb).

In thin section, the dust rings which enclose the rounded detrital grains provide a recognizable marker surface enclosing the old crystals (Figs. 4, 5, 6, and 7). Where grain boundaries are under compression, the grains are presolved and the "dust" or "insoluble residue" forms zones of inert accumulations. At grain boundaries under tension, new crystal is formed outside the dust ring. This new crystal often has a diagnostic fibrous habit and frequently is full of inclusions and interleaved with minute white micas and chlorites. Occasionally, the new crystal is a new grain and not optically continuous with the old grain, so that X decreases as r increases with time.

The new quartz growing on the tensile side of opaque minerals such as magnetite and forming

"pressure shadows" is particularly spectacular. Wherever magnetite/quartz grain boundaries are under compression, the magnetite deeply penetrates into the quartz grains (Fig. 7C; Elliott, 1972, Fig. 11).

Not all grains in a thin section show pressure solution or new quartz, nor was the depth of presolving or the width of overgrowths the same in all grains. This is not unexpected due to the inhomogeneity of stress on the scale of single grains.

Stratigraphically below the Weaverton quartzites is the Catoctin Formation, a pile of Precambrian volcanic rocks which includes rhyolitic flows. These flows frequently show micropoikilitic texture—single crystals of quartz which are choked with large volumes of fine feldspar inclusions. This texture is easiest seen with a gypsum plate, when the whole field of the microscope is broken up into different patches of vivid contrasting color, each representing one micropoikilitic quartz grain.



Figure 4. Remnant of a once much larger clastic grain still preserving a short gently curved arc of dust ring D. Grain shape a result of massive removal of material from presolved surfaces P. Weaverton Formation, crossed nicols, (all photomicrographs are of thin sections cut normal to cleavage and parallel to stretching direction).



Figures 5 and 6. Sides of grains under compression show presolved surfaces outside of which are accumulations of inert grains. New quartz and some white mica



is growing in extension direction outside of dust rings *D* marking relic grain boundaries enclosing old crystal. Weaverton Formation Figure 5 (left), crossed nicols; Figure 6 (right), plane light.

Micropoikilitic texture was produced by the initial crystallization and hydration of volcanic glass at subsolidus temperatures, probably during deuteric alteration of the volcanic pile toward the end of Catoctin volcanism. The term and its significance is a result of the classic work by Florence Bascom (1893, 1896) on the Catoctin volcanic rocks from the South Mountain area (the texture is reviewed by Lofgren, 1971).

Deformed micropoikilitic texture is particularly informative. The originally subspherical quartz grains are now ellipsoidal shapes parallel to the penetrative cleavage (Fig. 8). How did the deformation of these quartz grains come about? The homogeneous extinction colors with a gypsum plate indicate few subgrains and little dislocation glide or slip. The grains have drifted apart with new fibrous quartz and white mica growing at the ends. The sides have presolved and show occasional accumulations of inert hematite, which is scattered throughout the old crystal.

In both formations, it appears that diffusion creep is the mechanism which permits the

deformation, but microscopic observations alone cannot establish whether grain boundary or lattice diffusion was dominant. It is necessary to specify the various paths along which diffusion may occur and discuss the physical nature of these paths.

DIFFUSION PATHS

What path do the vacancies travel on to accomplish pressure solution or diffusion creep? The type of path through which diffusion occurs permits a clear-cut distinction between the various diffusion processes. Four different diffusion paths can be recognized: through the bulk volume of the crystal lattice, grain boundaries ("high angle" $\geq 10^\circ$ unless otherwise designated), dislocations, and through pore fluids between the grains (Fig. 9).

Many petrologists would agree that paths must exist in deforming metamorphic rock with a diffusivity very much higher than is possible through the interior of the crystal lattice. These high diffusivity paths are implied by the term "dispersed phase" and the geological evidence suggesting the existence of



Figure 7. Hematite-cemented quartz sandstone at base of Weaverton, plane light. The dust rings indicate well-rounded, nearly circular clastic grains. Thin section is from upper limb of a recumbent isoclinal fold with local bedding/cleavage angle 14° . Straight fibers indicate an approximately coaxial deformation path.

(A) and (C) Grains show dust rings *D* cut by presolving surfaces *P*. New quartz growing outside dust rings. (B) Detail of new quartz of fibrous habit growing outside dust ring *D*. Dust ring cut off by presolved surface *P* at top. (D) Ilmenite grain impressed into and piercing *P* dust ring *D* around old quartz grain.

rapid diffusion paths has been reviewed by Gresens (1966) and Mueller (1966).

The nature of grain boundaries has been deduced both from theoretical considerations and, in metals, direct observation with the field-ion microscope. This work essentially confirms the island theory due originally to Mott (1948) and summarized below (McLean, 1965; Gibbs and Harris, 1969; Gifkins 1967a, 1969).

(1) A grain boundary encloses each crystal.
 (2) The crystal lattice is very much more ordered within the grain than at the boundary.
 (3) The grain-boundary structure consists of "islands" and "channels." The "islands" are three to five atomic spaces thick with a distorted lattice, but comparatively good fit to crystal lattices of both adjacent grains. The "channels" separate the islands from one another and are regions of very poor fit, about one or two atomic spaces thick. (4) The channels form an interconnecting network lying in the grain boundary; the major part of the grain boundary energy and rapid diffusion is associated with the channels, which have a very high density of vacancy defects. (5) The greater the atomic misfit between adjacent grains, the wider the grain boundary. Interphase grain boundaries have the highest atomic disregistry and consequently the greatest grain boundary width and greater potential for diffusive mass transport.

It is found that the zone of enhanced diffusion is not all concentrated along the channels, and two simple observations indicate a much wider effective grain boundary than one or two atomic spaces.

1. The hardness of a large lead crystal is constant within the grain interior but suddenly declines by about 10 percent at the boundary between two grains (Westbrook, 1968). The width of the zone of decreasing hardness is tens of micrometers.

2. Etched and polished specimens do not show infinitesimally thin lines at grain boundaries, but optically visible bands of the order of microns wide (Headley and others, 1970).

A major difficulty with many crystalline materials is the extreme sensitivity of diffusion coefficients to even trace impurities in the host crystal lattice—a sensitivity so great as to account for orders of magnitude discrepancies between laboratories reporting diffusion data for the same substance. These "extrinsic" effects due to impurities become particularly

important at temperatures below about 3/4 of the absolute melting point. Ionic and covalently bonded crystals are particularly sensitive to this effect. The observed enhanced diffusion along micrometer-wide grain boundaries in periclase is largely due to impurity concentrations (Wuensch and Vasilos, 1966). These impurities could be in the form of small crystals of another phase or increased impurity concentrations in solid solution near the grain boundary.

The mechanisms of diffusion processes are probably best understood in the halides. In halite, the presence of impurities such as H₂O on the grain boundary produces an enormous increase in grain boundary diffusion rates (Riggs and Wurtig, 1969). Ions of OH⁻ concentrate at grain boundaries and change either its structure or its charge distribution, or both.

In summary, it appears that grain boundaries have different diffusion properties than do grain interiors because of their different structures and their different chemistry. A sandwich model of a grain boundary appears to be most appropriate (Gibbs and Harris, 1969). The center of the sandwich has a thickness of atomic dimensions with extremely high diffusivity, and its structure is described by the island model. The two outer layers of the sandwich, of micrometer size, have a smaller enhancement of diffusion due to impurities.

Grain boundaries in metamorphic rocks are frequently peppered with concentrations of small crystals of second phases, and interphase grain boundaries are common. Micas may be especially important; for although essentially inert when in contact with quartz, they greatly increase the width of the diffusion paths (Weyl, 1959). Furthermore, it is widely held that grain boundaries in metamorphic rocks contain many substances not admitted into the crystal lattices, typically H₂O, CO₂, HCl, H₂S, and HF in various forms. These compounds all are well known to be capable of greatly disrupting the structures along crystalline surfaces. They would produce an effective grain boundary wider than normal. Metamorphic rocks appear to have the conditions favoring an enhanced diffusion along grain boundaries of the sandwich model.

Dislocations are believed to act as thin pipes of rapid diffusion through a crystal. The dislocation core is very poorly ordered and is associated with most of the diffusion. This core

is surrounded by an outer layer in which diffusion is slower than in the core, but still at a higher rate than through the bulk lattice. The dislocation can therefore be imagined as a coaxial pipe.

Low angle ($\leq 5^\circ$) grain boundaries and other semicoherent interfaces can be described by dislocation arrays and their diffusion behavior resembles coaxial pipes laid side by side in a slab. In ordinary grain boundaries, however, the dislocations lie so close together that individual dislocations lose their meaning. Dislocation pipe diffusion depends upon the dislocation density, a quantity which is very sensitive to the elastic strain energy present in the crystal lattice and the thermal and deformation history. Consequently, a dislocation pipe diffusion flow law is strongly history-dependent and difficult to treat rigorously.

Pores

I am unaware of a definition of what constitutes a "pore." In this article, I will define a pore as having a radius large enough that the bonding forces of the atoms in the surrounding crystal have negligible effects on most of the pore volume. The pores are filled with liquid or gaseous phases, materials which behave as fluids of low viscosity and density. As a result, material within a pore will have negligible stress gradients and be essentially in a hydrostatic state.

Fissures are much larger still, but the behavior of fissure and pore fluids will be similar. Pores and fissures connect with the grain lattices by means of the high diffusivity paths provided by grain boundaries and dislocation pipes.

Sedimentary rocks may have had a high pore space immediately after deposition; but by the time cementation and diagenesis is completed, usually there is little pore space remaining. It is well established that the main pore reduction process during diagenesis is pressure solution (for example, Heald, 1955). This is accomplished by diagenetic overgrowths around the clastic grains and into the pores, filling them in. Presumably under metamorphic conditions, pressure solution is also an efficient pore reduction process.

The main distinction between diagenetic and metamorphic pressure solution is the initial abundance of pore space in sedimentary rocks. However, even under conditions of diagenesis

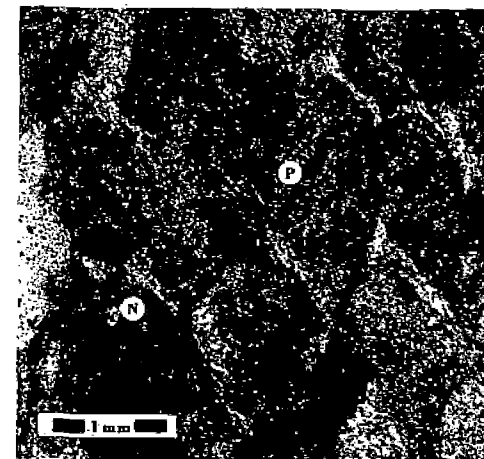


Figure 8. Dark-gray micropoikilitic quartz grains stuffed with inclusions and deformed by diffusion creep. Stretching direction is vertical. Presolved grain boundaries *P* with accumulations of inclusions at boundaries under compression; light-colored new fibrous quartz and white mica growing at grain boundaries under tension, for example above *N*. Catoñin rhyolitic flow, crossed nicols.

and deuteric alteration, pressure solution appears to proceed by diffusion other than through pore space; for example, stylolites found in dense glassy rhyolites (Bloss, 1954; Golding and Conolly, 1962) cannot have developed with the aid of an extensive pore space.

Pores and fissures (that is, veins) may be very effective in allowing mass transport into and out of a mass of rock. Progressive metamorphism is associated with intensive dehydration and decarbonation, and the large volumes which must be moved over considerable distances do so through a network of pores and fissures—but this is a larger scale than that of individual grains, with a typical dimension measured in meters.

Pores may very well be present (Brace and others, 1972), but I will now argue that for any reasonable amount of porosity in a deforming metamorphic rock, mass transfer via pores cannot be a dominant process on the scale of individual grains. Imagine a pore situated at a grain boundary (Fig. 9).

The mass transfer involves three distinct stages: (1) movement of material from that part of the grain which is under compression to the walls of the pore through the solid (via

lattice or grain boundary); (2) dissolution of the material into the pore fluid; and (3) movement of the material through the pore fluid to its site of deposition. There are two mass-transport processes involved which are dependent on one another, and the very much smaller diffusion coefficients through solids than through pore fluids mean that diffusion through the solid will be the rate-limiting step.

The effect of pores is to reduce the length of the diffusion path. This is equivalent to increasing the effective grain size at which diffusion flow laws are important.

It is a common petrological assumption that large amounts of material are transported as associated or disassociated solute species of the sort found in aqueous solutions. Silica is often considered to move in this fashion as species such as H_4SiO_4 . These types of particles are extremely large, and far too bulky to move along a grain boundary or dislocation pipe because they would jam into the crystal lattice (McLean, 1965). If transport of these large species occurs, it can do so only through pores. Possibly the species present in a pore and in a grain boundary are different because of this size control.

A monomineralic rock undergoing regional metamorphism should really be thought of as having three phases: the interior crystalline lattice phase, the phase of the grain boundaries and dislocation pipes, and the pore fluid phase. Very strong compositional gradients exist between these three phases.

Estimates of Paths

It is important to try to estimate an effective diffusion coefficient for the observed deformation of the Weaverton quartzite and Catoclin rhyolitic flows.

A general form of the diffusion flow laws (equations 5, 6) for a polycrystalline aggregate is:

$$\dot{\epsilon} = \frac{K D_e \Omega}{X^2 \tau^2 k T} \sigma$$

In general D_e , T , σ , X , and τ all vary with time. If lattice diffusion operates, then $\dot{\epsilon} = \dot{\epsilon}_l$ and $D_e = D_l$; while if grain-boundary diffusion operates, $\dot{\epsilon} = \dot{\epsilon}_{gb}$, and the effective diffusion coefficient

$$D_e = \frac{D_{gb} h \pi r^4}{X}$$

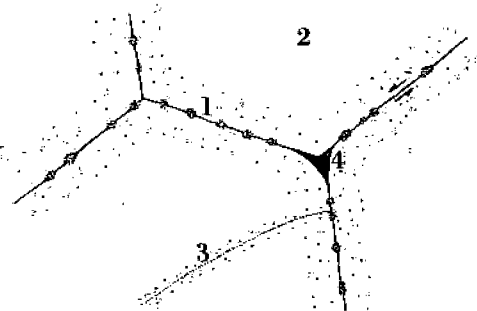


Figure 9. Possible diffusion paths in rocks. 1. Sandwich model of grain boundaries; diffusion mainly in channels (heavy stipple) but also through distorted lattice (open stipple). 2. Interior lattice of crystals. 3. Dislocation diffusion mainly through the core (dotted) but also in surrounding distorted lattice (open stipple). 4. Pore space (black). Here a pore is growing at a triple point due to grain-boundary sliding (arrows).

In a coaxial deformation path, the finite natural (or logarithmic) strain

$$\epsilon = \int_0^t \dot{\epsilon} dt$$

indicate maximum values by small m for T_m , σ_m , X_m , τ_m . Maximum diffusion D_{em} will occur at T_m . Let t_m be the time interval from start to finish of the deformation event. Define $D_e = D_{em} \bar{D}_e$, $\sigma = \sigma_m \bar{\sigma}$, $X = X_m \bar{X}$, $\tau = \tau_m \bar{\tau}$, $t = t_m \bar{t}$.

Here \bar{D}_e , $\bar{\sigma}$, \bar{X} , $\bar{\tau}$, \bar{t} , are normalized non-dimensional quantities with values between 0 and +1.

Substituting into the general diffusion flow law and removing constants from behind the integral,

$$\dot{\epsilon} = \frac{K D_{em} \Omega \sigma_m t_m}{k T_m X_m^2 \tau_m^2} \int_0^1 \frac{\bar{D}_e \bar{\sigma}}{\bar{X}^2 \bar{\tau}^2 T} \bar{d}\bar{t}$$

Now the expression behind the integral is nondimensional and within an order of magnitude of unity, so that

$$D_{em} = \frac{e k T_m X_m^2 \tau_m^2}{K \Omega \sigma_m t_m}$$

Finite natural strains ϵ with coaxial deformation paths are in the order of 20 percent, the metamorphic temperature $T_m \sim 625^\circ K$, the atomic volume of the rate-determining component Ω was probably an ion of O^{2-} , the maximum tectonic stress σ_m was probably in

the order of 10^7 nm^{-2} (100 bars), and diffusive flow is evident on grains with radii of 0.5 mm. The length of time for the deformation event responsible for these highly deformed rocks in the central Appalachians cannot be stated with any precision, but comparable deformation and syntectonic metamorphic events from the western Alps and New Zealand are no longer than 10 m.y. Using these figures, the maximum effective diffusion coefficient is $10^{-16} \text{ mm}^2 \text{ s}^{-1}$.

To date, remarkably few data are available for self-diffusion of oxygen through oxides and silicates. Some minerals which may be typical are summarized in Table 1. The large oxygen ion is usually the slowest moving and therefore the rate-determining component, and it may be reasonable to compare the self-diffusion of oxygen in different minerals at temperatures proportional to their melting points. A metamorphic temperature of $625^\circ K$ is 0.32 of the melting point of pure silica at 10^5 nm^{-2} (1 bar); comparison of diffusion coefficients at such temperatures suggests that lattice diffusion is too small by at least three orders of magnitude (Table 1).

It is probable that water has a greater effect on grain-boundary than on lattice diffusion, because of concentration of water on grain boundaries as discussed earlier. This water probably increases the diffusion coefficient of oxygen through quartz. A rough way of estimating this might be to compare the minerals at 0.46 of their melting points, which is the ratio of metamorphic temperature to the melting point of silica at $3.5 \times 10^8 \text{ nm}^{-2}$ (3.5 kb) in the presence of water (Table 1). If this comparison is correct, grain-boundary diffusion is a possible diffusion path, but the poor quality of such an estimate must be emphasized. Low temperatures also favor grain-boundary over lattice diffusion, as we shall see later.

BROKEN-GRAIN DIFFUSION FLOW

The stress within a grain may reach the level at which fractures nucleate and grow, breaking up a larger grain into a number of smaller ones. Each smaller grain has its own grain boundary which is an ideal defect source or sink. Diffusion proceeds and the strain-rate will be much enhanced by the reduction in grain size.

Larger grains are particularly liable to transgranular fracture, either because they have a greater chance of containing a flaw or else

TABLE 1. DIFFUSION THROUGH OXIDES AND SILICATES

Q diffusion in:	At = 0.32 MP	At = 0.46 MP
Albite*	$10^{-23} \times 2.0$	10^{-18}
Vitreous silica [†] , SiO ₂	$10^{-19} \times 2.1$	$10^{-13} \times 4.8$
Rutile, TiO ₂ [†]	$10^{-23} \times 4.2$	$10^{-17} \times 6.8$
Bromellite, BeO [†]	$10^{-22} \times 4.3$	$10^{-16} \times 1.5$
Cuprite, Cu ₂ O [†]	$10^{-20} \times 1.3$	10^{-15}
Bunsenite, NiO [†]	$10^{-22} \times 3.6$	10^{-15}

Note: All single-crystal data, except for silica.
 * Herigoux, 1966.
 † Review of Harrop, 1968.

because they have a greater chance of forming a microcrack from the stress concentrations around a pileup of dislocations (reviewed by Cottrell, 1964, p. 359). The result is that within a polycrystalline specimen, stress acts as an efficient grain-size reduction mill, systematically cracking all grains larger than a certain critical size.

The highly selective and systematic cracking of larger grains may be keeping all grains at a small enough size that the diffusion flow laws can dominate. Only a small percentage of grains would be cracking at any one time. Note, however, that diffusion mass transfer may cement the smaller fragments together, producing a larger elongate grain.

Grain fracturing can be seen easily if the grain and the fracture infilling are different minerals (Fig. 10). This is "microboudinage," important because of its suitability for measurement of deformation paths (Elliott, 1972). It is rare that grain fragments and fracture infilling can be distinguished if they have the same mineralogy, but a beautiful example is figured by Sander (1970, p. 363; Fig. 40). Sippel (1968) has presented very interesting evidence using cathode luminescence of widespread internal fracturing within quartz grains which is not visible with the petrographic microscope. This technique appears very promising, and broken-grain diffusion creep may be widespread.

Cataclastic rocks are generally considered to have developed in zones of particularly high stress which by itself would favor dislocation flow; but fine grain size is a distinctive feature of many of these rocks—is it possible that the grain size reduction permits such cataclastic rocks to deform by diffusion creep with a linear stress to strain-rate relation?

TRANSITION BETWEEN DISLOCATION AND DIFFUSION FLOW LAWS

In contrast to diffusion creep, dislocation-controlled creep has received considerable attention in geology (for example, Heard and Carter, 1968). Several different flow laws are possible depending upon which of the various possible dislocation mechanisms is operating. All are independent of grain size, but the stress dependence is a power function of the general form:

$$\dot{\epsilon}_d = \frac{B D_l \Omega}{kT} \sigma^n \quad (7)$$

when $\dot{\epsilon}_d$ is the strain-rate due to dislocation creep, n and B are constant for a particular dislocation mechanism, and n takes a value between 3 and 6. The dislocation creep laws appropriate for rocks have been reviewed by Weertman (1970); all are special cases of the equation (7) above.

Subgrain boundaries are arrays of disloca-

tions; and if these act as good sources and sinks of defects, then as Lifshits (1963) pointed out, the lattice diffusion creep equation must be interpreted with the subgrain radius rather than the grain radius. The subgrain size depends upon the stress to a power of 3, and so subgrain creep obeys a dislocation-type flow law (equation 7). Weertman (1970) and Green (1970) have suggested that subgrain creep may apply to rocks.

There is an important objection to the premises with which the subgrain creep law was derived. Edge dislocation components of subgrain boundaries can, in principle, emit or absorb defects, but to do this, they must increase local elastic strain energy and consequently are not ideal defect sources and sinks for defect concentrations which are near equilibrium (Gibbs and Harris, 1969). In an alloy known to undergo diffusion creep, no new crystal appears to be precipitating at subgrain boundaries; all occur at grain boundaries (Fig. 3).

Rock-forming minerals generally have fewer than the five independent slip systems which are needed to deform a polycrystalline aggregate compatibly and continuously by dislocation processes without grain-boundary sliding (the Von Mises criterion, see review of Paterson, 1969). We saw earlier that grain-boundary sliding was a necessary part of diffusion creep; consequently, grain-boundary sliding and grain deformation are dependent processes. Grain-boundary sliding is usually a faster and easier process than grain deformation (see Gibbs, 1967; Gibbs and Harris, 1969), so that grain deformation, by dislocation or diffusion creep, is the rate-determining step. This is so even though the total finite strain may be composed of about 60 percent strain due to grain-boundary sliding (Stevens, 1971)!

Grain-boundary sliding and grain deformation are treated as independent processes by Hahn and others (1967), and consequently their flow law is incorrectly derived.

How does the transition between diffusion creep and one of the dislocation creep laws occur? What is the total strain-rate affecting a specimen when the diffusion and dislocation flow laws are all operating on various grains? To answer these questions, it is necessary to briefly outline the rules to determine the appropriate flow law.

If a number of independent processes (A, B,

C, . . .) are occurring during creep, then total whole-rock strain-rate component $\dot{\epsilon}_{ij}$ is

$$\dot{\epsilon}_{ij} = f_a \dot{\epsilon}_{a ij} + f_b \dot{\epsilon}_{b ij} + f_c \dot{\epsilon}_{c ij} + \dots$$

where $\dot{\epsilon}_{a ij}$, $\dot{\epsilon}_{b ij}$, $\dot{\epsilon}_{c ij}$, are the strain-rate components corresponding to processes A, B, C, and so on. The total specimen strain-rate is the sum of the strain rates of the independent mechanisms, weighted according to the volumetric percent f_a , f_b , f_c of the grains dominated by each mechanism (Gifkins, 1970).

Process A requires both grain deformation and grain-boundary sliding; neither is sufficient on its own, so that $\dot{\epsilon}_{a ij}$ are the strain-rate components due to both the grain deformation mechanism and the grain-boundary sliding necessary for coherence.

The total strain-rate in the cases considered in this article will generally be the sum of the dislocation, grain-boundary, and lattice-diffusion creep-rates:

$$\dot{\epsilon}_{ij} = f_d \dot{\epsilon}_{d ij} + f_{db} \dot{\epsilon}_{db ij} + f_l \dot{\epsilon}_{l ij}$$

In this relation, $\dot{\epsilon}_l$, $\dot{\epsilon}_{db}$, and $\dot{\epsilon}_d$ are determined by equations (5), (6), and (7).

What is the general field within which one flow law dominates the others? How can these relations be plotted so as to be most readily usable for naturally deformed rocks? This can be answered by establishing the boundaries at which the strain-rates for any two different flow laws are equal. For cases when the contributions to the over-all specimen strain-rate $\dot{\epsilon}$ from both dislocation and grain-boundary diffusion creep are equal and lattice diffusion creep is negligible, then $\dot{\epsilon} = 2 f_d \dot{\epsilon}_d = 2 f_{db} \dot{\epsilon}_{db}$ and from equations (5) and (7)

$$\frac{D_l f_d B X^3 r^2 \sigma^{n-1}}{D_{db} f_{db} K \pi h r^{3/2}} = 1 \quad (8)$$

Similarly, when $\dot{\epsilon} = 2 f_d \dot{\epsilon}_d = 2 f_l \dot{\epsilon}_l$ and $f_{db} \dot{\epsilon}_{db}$ is negligible,

$$\frac{B X^2 r^2 f_d \sigma^{n-1}}{K f_l} = 1; \quad (9)$$

also, when $\dot{\epsilon} = 2 f_l \dot{\epsilon}_l = 2 f_{db} \dot{\epsilon}_{db}$ and $f_d \dot{\epsilon}_d$ is negligibly small,

$$\frac{D_l f_l X r}{D_{db} f_{db} \pi h r^2} = 1 \quad (10)$$

Diffusion coefficients (such as D) are strongly temperature dependent and it may be shown that

$$D = D_0 \exp(-H/RT)$$

Here D_0 and H are constants for a particular process and material but very different for different minerals and deformation processes. Because of the greater difficulty of forming and/or moving defects in the crystal than on the grain boundary, $H_l > H_{db}$.

Now,

$$\begin{aligned} \frac{D_{db}}{D_l} &= \frac{D_{db}}{D_l} \exp\left(\frac{H_l - H_{db}}{RT}\right) \\ &= \frac{D_{db}}{D_l} \exp\left[\frac{H_l}{RT}(1 - H_{db}/H_l)\right] \end{aligned}$$

by substituting the above expression into equation (8) and taking natural logarithms,

$$\begin{aligned} \frac{H_l}{RT} &= -\left(\frac{1}{1 - H_{db}/H_l}\right) \ln \left[\frac{D_{db} K \pi h r^{3/2} f_{db}}{D_l B \sigma^{n-1} f_d} \right] \\ &+ \left(\frac{3}{1 - H_{db}/H_l}\right) \ln(Xr) \quad (11) \end{aligned}$$

Similarly from equation (10)

$$\begin{aligned} \frac{H_l}{RT} &= -\left(\frac{1}{1 - H_{db}/H_l}\right) \ln \left[\frac{D_{db} \pi h r^2 f_{db}}{D_l f_l} \right] \\ &+ \left(\frac{1}{1 - H_{db}/H_l}\right) \ln(Xr) \quad (12) \end{aligned}$$

and from equation (9)

$$\ln(Xr) = \frac{1}{2} \left[\frac{K f_l}{B f_d \sigma^{n-1}} \right] \quad (13)$$

For a particular rock type and chemical environment, the variables are temperature T , grain size X , grain shape r , and stress σ . Temperature, grain size, and grain shape can be measured reasonably accurately, and the lattice-diffusion activation energy H_l of a wide variety of materials is available. It would seem that the most suitable representation is a semi-log plot with $\frac{H_l}{rT}$ for the vertical axis, versus grain size and shape $\ln(Xr)$ for the horizontal axis (Fig. 11).

On such a graph, the relation $f_d \dot{\epsilon}_d = f_{db} \dot{\epsilon}_{db}$ (equation 11) is a straight line with slope $\frac{3}{1 - H_{db}/H_l}$ and intercept with the positive horizontal axis of

$$\ln \left[\frac{D_{db} K \pi f_{db} h r^{3/2}}{D_l B f_d \sigma^{n-1}} \right]$$

The boundary along which $f_l \dot{\epsilon}_l = f_{db} \dot{\epsilon}_{db}$



Figure 10. Tension fractures in magnetite grain, fractures infilled with new quartz. Weaverton; crossed nicols.

(equation 12) is a line with slope $\frac{1}{1 - H_{gb}/H_l}$ and intercept on the horizontal axis of

$$\ln \left[\frac{D_{gb} \pi f_{gb} h r^2}{D_{ol} f_l} \right]$$

The boundary at which $f_{a\dot{e}a} = f_{i\dot{e}i}$ (equation 13) is a vertical line on the graph.

If $f_{gb\dot{e}gb} = f_{a\dot{e}a}$ and $f_{a\dot{e}a} = f_{i\dot{e}i}$, then $f_{i\dot{e}i} = f_{gb\dot{e}gb}$, and these three lines intersect at a common triple point (Fig. 4). At the triple point, the three equations (9, 10, 11) are satisfied for a particular rock type (D_{ol} , D_{gb} , H_l , H_{gb} , f_{ol} , f_d , h , X , r) and metamorphic conditions T , but the stress is a difficult variable. Equation (12) is independent of stress, and so the triple point can only migrate along the straight line of equation (12). Increasing stress moves the triple point downward and to the left along this straight line.

The calibration of this semilog plot (Fig. 11) is of key importance and could be done by laboratory experiments. For example, using radioisotope self-diffusion experiments, it is possible to measure H_{gb}/H_l , D_{ol} , D_{gb} , and h .

Another approach would be to directly calibrate positions of the triple point and slopes of the lines by varying temperature, grain size and shape, and stress in a series of creep tests. This may require faithful duplication of the chemical conditions of metamorphism, particularly trace impurities and grain-boundary concentrations of H_2O , CO_2 , and so on. Parts of the graph may be experimentally unattainable because of difficulties in deciding the proportions of grain-deformation mechanisms

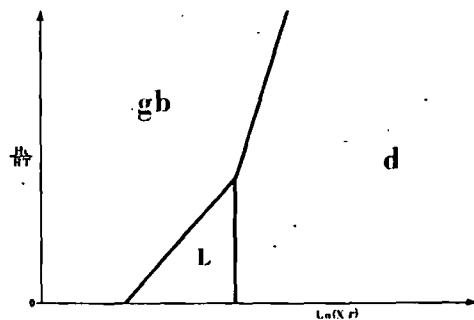


Figure 11. Semi-log plot of inverse temperature as H_l/RT versus grain size and shape as $\ln(Xr)$. Lattice diffusion l , grain-boundary diffusion gb and dislocation d flow laws are each dominant in certain fields for a particular rock type.

at the steady state, or not achieving a true secondary creep stage.

It is apparent that direct extrapolation of laboratory creep tests to the low deviatoric stress levels typical of natural deformation under conditions of regional metamorphism requires an unjustified assumption of constant deformation mechanism, for as the stress is lowered, dislocation creep is invariably replaced by a diffusion flow law.

Another alternative is to try to calibrate the graph by careful observations in naturally deformed rocks, for the approximate temperature can frequently be estimated from the petrology of the mineral assemblages, and grain size and shape are readily measurable. Such work is in progress (see Elliott, 1970).

CONCLUSIONS

Familiar pressure solution is a diffusion mass transfer process, and if the grains in a metamorphic rock have changed their shapes mainly by pressure solution, a diffusion flow law holds with a linear stress to strain-rate relation.

It was demonstrated that only a few steps relate Correns' work on pressure solution to the family of diffusion flow laws of Nabarro-Herring type.

Microscopic observations exist which permit a clear distinction between deformation dominated by dislocation processes and deformation by diffusive mass transfer.

In photomicrographs of greenschist-grade quartzites and rhyolitic flows, pressure solution is the dominant process. But there are no microscopic criteria for identifying the path along which diffusion occurred. Estimates of the effective diffusion coefficient were attempted; available data is suggestive but does not permit conclusive calculations. On physical grounds, because of the low temperatures and the effects of water, one would expect grain-boundary diffusion to dominate.

The microstructure of grain boundaries in metamorphic rocks probably resembles a sandwich, a core of channel networks one or two atomic spaces thick having very poor atomic fit and extremely high diffusivity with micron-wide zones of enhanced diffusion on both sides. Diffusion through pores is not the rate-determining step on the grain scale, but may increase the grain size at which diffusion flow is effective.

Boundaries between the lattice, grain boundary, and dislocation flow laws can be drawn on a graph of inverse temperature versus grain size. Is it possible to calibrate this graph from observations of naturally deformed rocks of varying grain size and metamorphic grade?

Grain size occurs to a power of 2 or 3 in the diffusion flow laws and is an important variable. Diffusion flow is faster with small grains, and grain-size reduction by fracturing will tend to favor diffusion flow laws. Do cataclastic rocks undergo a large part of their strain history via broken-grain diffusion creep? More specifically, can the difference in grain-size dependence be used to distinguish grain boundary from lattice diffusion flow laws in naturally deformed rocks?

Within an active mountain-building belt, it is likely that temperature, grain size and shape, and deviatoric stresses vary with time and place. No unique flow law is proposed. Pressure solution or diffusion creep might dominate in an area, then grain coarsening combined with an increase in deviatoric stress could shift the flow law to one dominated by dislocation motion. It is emphasized, however, that the triple point in naturally deformed rocks is very much farther to the right than has hitherto been suspected.

ACKNOWLEDGMENTS

Various versions of this paper have been improved by critical reading by E. Cloos, H. Eugster, R. Fletcher, G. Fisher, and H. W. Green. This work was supported by the Earth Sciences Section, National Science Foundation Grant GA-10279.

REFERENCES CITED

- Ashby, M. F., 1969, On interface-reaction control of Nabarro-Herring creep and sintering: *Scripta Metallurgica*, v. 3, p. 837-842.
- Bascom, F., 1893, Structures, origin and nomenclature of the acid volcanic rocks of South Mountain: *Jour. Geology*, v. 1, p. 813-832.
- 1896, The ancient volcanic rocks of South Mountain (Adams-Franklin Counties), Pennsylvania: *U.S. Geol. Survey Bull.* 136, 124 p.
- Becke, F., 1903, Über Mineralbestand und Struktur der kristallinen Schiefer: *Internat. Geol. Cong., Session 9*, v. 2, Vienna 1903, p. 553-570.
- Bloss, F. D., 1954, Microstylolites in a rhyolite porphyry: *Jour. Sed. Petrology*, v. 24, p. 252-254.
- Burton, B., 1971, Influence of alumina dispersions on the diffusion-creep behavior of polycrystal-

line copper: *Metal Science Jour.*, v. 5, p. 11-14.

- 1972, Interface reaction controlled diffusional creep: A consideration of grain boundary dislocation climb sources: *Materials Science and Eng.*, v. 10, p. 9-14.
- Burton, B., and Greenwood, G. W., 1970a, Contribution of grain-boundary diffusion to creep at low stress: *Metal Science Jour.*, v. 4, p. 215-218.
- 1970b, The limits of the linear relation between stress and strain rate in the creep of copper and copper zinc alloys: *Acta Metallurgica*, v. 18, p. 1237.
- 1971, Comments on the stress and temperature dependence of diffusion creep: *Scripta Metallurgica*, v. 5, p. 575-578.
- Coble, R. L., 1963, A model for boundary diffusion controlled creep in polycrystalline materials: *Jour. Applied Physics*, v. 34, p. 1679-1682.
- Cottrell, A. H., 1964, *The mechanical properties of matter*: New York, John Wiley & Sons, Inc., 430 p.
- Dunlop, G. L., and Taplin, D.M.R., 1972, A metallographic study of superplasticity in a micrograin aluminium bronze: *Jour. Materials*, v. 7, p. 316-324.
- Durney, D. W., 1972, Solution-transfer, an important geological deformation mechanism: *Nature*, v. 235, p. 315-317.
- Elliott, D., 1970, The determination of flow laws in naturally deformed quartzites: *Geol. Soc. America, Abs. with Programs (Ann. Mtg.)*, v. 2, no. 7, p. 546.
- 1972, Deformation paths in structural geology: *Geol. Soc. America Bull.*, v. 83, no. 9, p. 2621-2638.
- Fryer, G. M., 1972, Theory of stress-induced diffusion in ionic crystals: *Royal Soc. London Proc., ser. A*, v. 327, p. 81-96.
- Gibbs, G. B., 1965, Fluage par diffusion dans les solides polycristallins: *Sci. Rev. Metallurg. Mem.*, v. 62, p. 781-786.
- 1967, The role of grain boundary sliding in high temperature creep: *Materials Science and Eng.*, v. 2, p. 269-272.
- Gibbs, G. B., and Harris, J. E., 1967a, Development of the island model for grain boundaries: *Materials Science and Eng.*, v. 2, p. 181-192.
- 1967b, Superplasticity during creep: *Jour. Inst. Metals*, v. 95, p. 373-377.
- 1969a, Diffusion at solid-solid interfaces, in Gifkins, R. C., ed., *Interfaces*: Sydney, Butterworth, 384 p.
- 1969b, Grain boundary structure, in Gifkins, R. C., ed., *Interfaces*: Sydney, Butterworth, 384 p.
- Gifkins, R. C., 1970, Transitions in creep behavior: *Jour. Materials*, v. 5, p. 156-165.
- 1971, Stress and temperature dependence of diffusional creep—A reconsideration of some

- recent results: *Scripta Metallurgica*, v. 5, p. 569-573.
- Golding, H. G., and Conolly, J. R., 1962, Stylolites in volcanic rocks: *Jour. Sed. Petrology*, v. 32, p. 534-538.
- Gordon, R. B., 1965, Diffusion creep in the Earth's mantle: *Jour. Geophys. Research*, v. 70, p. 2413-2418.
- 1967, Thermally activated processes in the Earth: Creep and seismic attenuation: *Royal Astron. Soc. Geophys. Jour.*, v. 14, p. 33-43.
- Green, H. W., 1970, Diffusional flow in polycrystalline materials: *Jour. Appl. Physics*, v. 41, p. 3899-3902.
- Greenwood, G. W., 1970, Possible effects on diffusion creep of some limitation of grain boundaries as vacancy sources or sinks: *Scripta Metallurgica*, v. 4, p. 171-174.
- Gresens, R. L., 1966, The effect of structurally produced pressure gradients on diffusion in rocks: *Jour. Geology*, v. 74, p. 307-321.
- Hahn, S. J., Ree, T., and Eyring, H., 1967, Mechanism for the plastic deformation of Yule Marble: *Geol. Soc. America Bull.*, v. 78, p. 773-782.
- Harrop, P. J., 1968, Self-diffusion in simple oxides: A bibliography: *Jour. Materials*, v. 3, p. 206-222.
- Headley, T. J., Kalish, D., and Underwood, E. E., 1970, Current status of applied superplasticity, in Burke, J., and Weiss, V., eds., *Ultrafine-grain metals*: Syracuse, New York, Syracuse Univ. Press, 432 p.
- Heald, M. T., 1955, Stylolites in sandstones: *Jour. Geology*, v. 63, p. 101-114.
- Heard, H. C., and Carter, H. L., 1968, Experimentally induced "natural" intragranular flow in quartz and quartzite: *Am. Jour. Sci.*, v. 70, p. 245-278.
- Herring, C., 1950, Diffusional viscosity of a polycrystalline solid: *Jour. Appl. Physics*, v. 21, p. 437-445.
- Holt, D. L., 1970, Superplastic, fine-grain alloys in the forming of sheet metal, in Burke, J., and Weiss, V., eds., *Ultrafine-grain metals*: Syracuse, New York, Syracuse Univ. Press, 432 p.
- Kamb, W. B., 1959, Theory of preferred crystal orientation developed by crystallization under stress: *Jour. Geology*, v. 67, p. 153-170.
- 1961a, The thermodynamic theory of non-hydrostatically stressed solids: *Jour. Geophys. Research*, v. 66, p. 259-271.
- 1961b, Reply to discussions: *Jour. Geophys. Research*, v. 66, p. 3985-3988.
- Karim, A., 1970, A theory of diffusional flow with apparent non-Newtonian viscosity in fine-grained materials, in Burke, J., and Weiss, V., eds., *Ultrafine-grain metals*: Syracuse, New York, Syracuse Univ. Press, 432 p.
- Lee, D., 1969, Reply to: On the nature of superplastic deformation in the Mg-Al eutectic: *Scripta Metallurgica*, v. 3, p. 893-894.
- Li, J.C.M., Oriani, R. A., Darken, L. S., 1966, The thermodynamics of stressed solids: *Zeitschr. Phys. Chemie, N. F.*, Bd. 49, p. 271-290.
- Lifshitz, I. M., 1963, On the theory of diffusion—Viscous flow of polycrystalline bodies: *Soviet Physics, JETP*, v. 17, p. 909-920.
- Lofgren, G., 1971, Experimentally produced devitrification textures in natural rhyolitic glass: *Geol. Soc. America Bull.*, v. 82, p. 111-124.
- McKenzie, D. P., 1968, The geophysical importance of high-temperature creep, in Phinney, R. A., ed., *History of the Earth's crust*: Princeton, New Jersey, Princeton Univ. Press, 244 p.
- McLean, D., 1965, The science of metamorphism in metals, in Pitcher, W. S., and Flinn, G. W., eds., *Controls of metamorphism*: Edinburgh, Oliver and Boyd, 368 p.
- McLellan, A. G., 1970, Nonhydrostatic thermodynamics of chemical systems: *Royal Soc. London Proc.*, ser. A, v. 314, p. 443-455.
- Merigoux, H., 1966, Mesure du coefficient de diffusion de l'oxygène dans les feldspaths alcalins, *Acad. Sci. Comptes Rendus*, ser. D, v. 263, p. 1017-1018.
- Mott, N. F., 1948, Slip at grain boundaries and grain growth in metals: *Phys. Soc. [London] Proc.*, v. 60, p. 391.
- Mueller, R. F., 1966, Mobility of the elements in metamorphism: *Jour. Geology*, v. 74, p. 565-582.
- Nábarro, F.R.N., 1948, Deformation of crystals by the motion of single ions, in Report of a conference on the strength of solids: *Phys. Soc. [London] Proc.*, 75 p.
- Orowan, E., 1967, Seismic damping and creep in the mantle: *Royal Astron. Soc. Geophys. Jour.*, v. 14, p. 191-218.
- Paterson, M. S., 1969, The ductility of rocks, in Argon, A. S., *Physics of strength and plasticity*: Cambridge, MIT Press, 404 p.
- Rainey, P. E., and Holt, D. L., 1971, An observation by transmission electron microscopy of diffusional creep in a magnesium alloy: *Metallurg. Trans.*, v. 2, p. 3238-3239.
- Raj, R., and Ashby, M. F., 1971, On grain boundary sliding and diffusional creep: *Metallurg. Trans.*, v. 2, p. 1113-1127.
- Riecke, E., 1895, Über das Gleichgewicht zwischen einem festen homogenen deformierten Körper und einer flüssigen Phase: *Annalen Physic*, v. 54, p. 731-738.
- Riggs, K. R., and Wuttig, M., 1969, Cation grain boundary diffusion in NaCl: *Jour. Appl. Physics*, v. 40, p. 4682-4683.
- Sander, B., 1970, An introduction to the study of fabrics of geological bodies. [Trans. by Phillips, F. C., and Windsor, G.] London, Pergamon Press, 641 p.
- Sippel, R. F., 1968, Sandstone petrology, evidence from luminescence petrology: *Jour. Sed. Petrology*, v. 38, p. 530-554.
- Sorby, H. C., 1863, Über Kalkstein—Geschichte mit Eindrücken: *Neues Jahrb. Mineralogie*, p. 801-807.
- 1879, The anniversary address of the President: *Geol. Soc. London Quart. Jour.*, v. 35, p. 39-95.
- 1908, On the application of quantitative methods to the study of rocks: *Geol. Soc. London Quart. Jour.*, v. 61, p. 171-233.
- Squires, R. L., Weiner, R. T., and Phillips, M., 1963, Grain boundary denuded zones in a magnesium— $\frac{1}{2}$ wt% zirconium alloy: *Jour. Nuclear Materials*, v. 8, p. 77-80.
- Stevens, R. N., 1971, Grain-boundary sliding and diffusion creep in polycrystalline solids: *Philos. Mag.*, v. 23, p. 265-283.
- Turner, F. J., and Verhóogen, J., 1960, *Igneous and metamorphic petrology* (2d ed.): New York, McGraw-Hill, 694 p.
- Van Hise, C. R., 1896, Deformation of rocks: *Jour. Geology*, v. 4, p. 449-483, 593-629.
- Vickers, W., and Greenfield, P., 1967, Diffusion creep in magnesium alloys: *Jour. Nuclear Materials*, v. 24, p. 249-260.
- Voil, G., 1960, New work on petrofabrics: *Geol. Jour.*, v. 2, p. 503-567.
- Weertman, J., 1970, The creep strength of the Earth's mantle: *Rev. Geophysics*, v. 8, p. 145-168.
- Westbrook, J. H., 1968, Analysis of nature of grain boundaries in ceramics, in Fulrath, R. M., and Pask, J. A., eds., *Ceramic microstructures*: New York, John Wiley & Sons, Inc., 231 p.
- Weyl, P. K., 1959, Pressure solution and force of crystallization—A phenomenological theory: *Jour. Geophys. Research*, v. 64, p. 2001-2025.
- Wuensch, B. J., and Vasilos, T., 1966, Origin of grain boundary diffusion in MgO: *Am. Ceramic Soc. Jour.*, v. 49, p. 433-436.
- Yang, L., Horne, G. T., and Pound, G. M., 1959, Effect of elastic strain on the electrode potential of metals, in Rhodin, T. N., ed., *Physical metallurgy of stress corrosion fracture*: New York, Interscience, 394 p.

MANUSCRIPT RECEIVED BY THE SOCIETY MARCH 31, 1972

REVISED MANUSCRIPT RECEIVED SEPTEMBER 11, 1972

Erratum

Two cited references were not printed.

Correns, C. W., and Steinborn, W., 1939, "Über die Messung der sogenannten Kristallisationskraft." *Fortschr. Min. Krits. u. Petr.*, vol. 23, p. 105-108.

Correns, C. W., 1949, "Growth and Dissolution of Crystals Under Linear Pressure." *Discussions Faraday Soc.*, No. 5, p. 267-271.

ELECTROLYTE ACTIVITY COEFFICIENTS
INORGANIC PROCESSING

C. L. K.

H. P. Meissner

Calculations of activities, vapor pressures, and compositions of aqueous solutions of strong electrolytes, such as are encountered in leaching, precipitation, metal pickling, causticizing, evaporator operations, and inorganic processing, generally have been handicapped by a lack of activity coefficient data. The Debye-Hückel equation for predicting such activity coefficients unfortunately applies only in dilute solutions having concentrations far below those of common industrial interest. Activity coefficients at higher concentrations often differ greatly from salt to salt and for a given salt vary with concentration, temperature, and solution composition. Moreover, activity coefficients for an electrolyte in its pure solutions are generally not the same as those in multicomponent solutions (mixtures) of equal concentration. The object here is to review new developments in predicting these activity coefficients of strong electrolytes over normally encountered ranges of temperatures and concentrations, both in pure and in mixed solutions.

For pure solutions, the variables involved in the correlations under discussion are Γ° and I which are, respectively, the reduced activity coefficient and the ionic strength of the electrolyte. These are related to γ° , the electrolyte's mean ionic activity coefficient, and to its molality m as follows:

$$\Gamma^\circ = \gamma^\circ / Z_1 Z_2 \quad (1)$$

$$I = 0.5 m_{12} (\nu_1 Z_1^2 + \nu_2 Z_2^2) \quad (2)$$

where the stoichiometric coefficients ν_1 and ν_2 represent the number of moles of cations and anions formed per mole of electrolyte upon complete dissociation, while Z_1 and Z_2 are

Dr. C. L. Kusik is a senior staff member at Arthur D. Little, Inc., Cambridge, Massachusetts 02140. H. P. Meissner is a Professor of Chemical Engineering at the Massachusetts Institute of Technology, Cambridge, Massachusetts 02139.

0065-8812-78-8799-0173-\$00.95.

© The American Institute of Chemical Engineers, 1978.

the corresponding absolute values of the ion charges. Thus for cupric chloride, Z_1 and Z_2 are 2 and 1, while ν_1 and ν_2 are 1 and 2, respectively. In a 0.4 molal solution of cupric chloride, I is 0.5 (0.40) $(1 \times 2^2 + 2 \times 1^2)$ or 1.2. In this solution, γ° is reported as 0.425 (13); hence Γ° is $(0.425)^{1/1 \times 2}$ 0.652.

 Γ° vs. I

Relations between Γ° and I are based on the initial findings at 25°C (12) that values of Γ° for typical strong electrolytes in pure aqueous solutions vary with ionic strength I as shown graphically in Figure 1, with little curve crossover noted. Each curve may be viewed as representing the activity coefficient of a particular pure electrolyte in aqueous solution. The data for most strong electrolytes fall onto this curve family, including not only aqueous solutions derived from simple salts like sodium chloride, potassium nitrate, etc., but also hydrates like $\text{Na}_2\text{SO}_4 \cdot 10\text{H}_2\text{O}$ (12), polybasic acids and their salts like NaH_2PO_4 (11), etc. If we use these curves, it is possible that, knowing a single value of $\log \Gamma^\circ$ at some given temperature, an electrolyte's entire isotherm can be located. Thus, activity coefficients for an electrolyte can be calculated between known values or extrapolated to concentrations far exceeding that of the pure saturated

ISOTHERMAL EQUATIONS

The isotherms of Figure 1 can be well represented by equation (3). This empirical equation, developed by Meissner (3), involves the parameter q , which is a function of I for each electrolyte and each temperature.

$$\Gamma^\circ = [1 + B(1 + 0.1$$

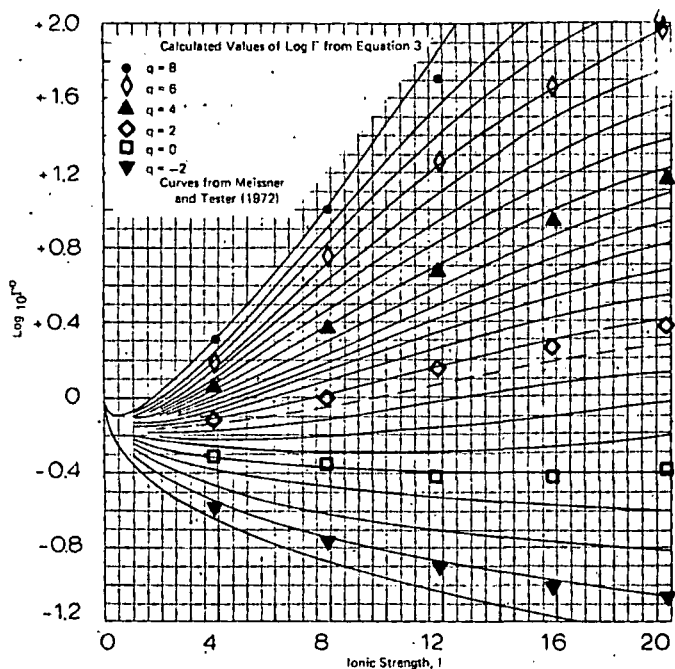


Fig. 1. Comparison of Γ values calculated from Equation (3) with earlier published results (12).

where

$$B = 0.75 - 0.065q \quad (3a)$$

$$\log_{10} \Gamma^* = \frac{-0.5107 \sqrt{I}}{1 + C\sqrt{I}} \quad (3b)$$

$$C = 1 + 0.055q \exp(-0.023 I^3) \quad (3c)$$

The values calculated from Equation (3) are plotted on log-log coordinates in Figure 2 and compared with the curves of Figure 1 for representative values of q . Data points for several electrolytes at high concentrations and 25°C are included in Figure 2 to show that these curves, within the limitations of precision discussed later, are usable to very high ionic strengths.

It is again evident that if one value of Γ° for an electrolyte is known at some concentration, preferably at an ionic strength greater than about unity, the associated value of q can be calculated for Equation (3). To illustrate, the value of q for ammonium sulfate will be calculated in an 0.5 molal solution knowing that γ° is 0.257 at 25°C for this electrolyte (13). By Equations (1) and (2), the ionic strength I is 1.5, and Γ° is $(0.257)^{1/2}$ or 0.507; hence, from Equation (3), q is found to be -0.255. Estimation of γ° at 25°C for ammonium sulfate solutions at other concentrations now involves merely further use of Equation (3). Thus, by substitution, when I is 9, γ° is calculated to be 0.134, which compares favorably with the experimental value at this concentration of 0.130 (4). Clearly, the same results could have been obtained by graphical extrapolation on Figures 1 or 2.

Much of the literature data on experimental values of Γ° is reviewed by Harned and Owen (4) and by Robinson and Stokes (13), from which the corresponding average values of q

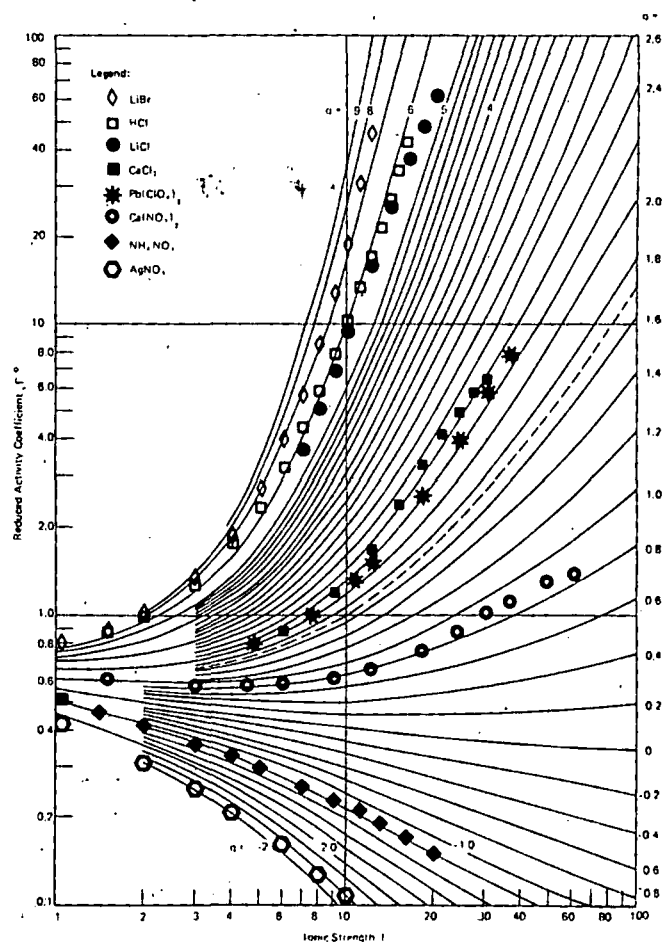


Fig. 2. Comparison of experimental activity coefficients with curves derived from Equation (3).

have been calculated in Table 1. The maximum error found in predicting Γ° by Equation (3) with q values from Table 1 is generally less than 5% over the concentrations indicated.

Lacking direct experimental values, Γ° can be estimated from data on vapor pressure lowering of aqueous solutions of the electrolyte in question (6). In the absence of all such data, predictions of Γ° can be attempted by the method of Meissner and Tester (12), or by the method of Bromley (3).

TEMPERATURE EFFECTS

Isotherms at temperatures other than 25°C are again found to fall onto the curve family of Figures 1 and 2 and therefore remain in conformity with Equation (3). It is further found that an electrolyte's isotherm at 25°C usually does not coincide with its isotherms at other temperatures. For nonsulfates, the nearer an electrolyte's isotherm lies to the dashed reference line of Figure 2, the smaller the effect of temperature. On this reference line (where $q = 1.7$), Γ° appears to be independent of temperature; $(\partial \Gamma_{ref}^\circ / \partial t)$ is zero.

Locating an electrolyte's isotherm at any temperature t involves determining $\log \Gamma_{25^\circ C}^\circ$ for the substance in question at an ionic strength of 10. The quantity $\log \Gamma_t^\circ$, again at an ionic

TABLE 1. AVERAGE VALUES OF EXPONENT q IN EQUATION (3) FOR SELECTED ELECTROLYTES

1:1 electrolyte	q/I_M^*	1:1 electrolyte	q/I_M^*	Higher electrolyte	q/I_M^*	Higher electrolyte	q/I_M^*
AgNO ₃	-2.55 <i>b</i>	LiAC	2.81 <i>a</i>	AlCl ₃	1.92 <i>d</i>	Mg(ClO ₄) ₂	4.15 <i>b</i>
CsAC	5.59 <i>a</i>	LiBr	7.27 <i>b</i>	Al ₂ (SO ₄) ₃	0.36 <i>d</i>	MgI ₂	4.04 <i>b</i>
CsBr	-0.06 <i>b</i>	LiCl	5.62 <i>b</i>	BaBr ₂	1.92 <i>b</i>	Mg(NO ₃) ₂	2.32 <i>d</i>
CsCl	0.16 <i>b</i>	LiOH	-0.08 <i>a</i>	BaCl ₂	1.48 <i>b</i>	MgSO ₄	0.15 <i>c</i>
CsI	-0.41 <i>a</i>	LiNO ₃	3.80 <i>b</i>	Ba(ClO ₄) ₂	1.90 <i>c</i>	MnSO ₄	0.14 <i>b</i>
CsOH	7.34 <i>u</i>	LiTOL	0.84 <i>b</i>	BaI ₂	2.84 <i>b</i>	MnCl ₂	1.60 <i>d</i>
CsNO ₃	-2.62 <i>u</i>	NaAC	4.20 <i>a</i>	Ba(NO ₃) ₂	-0.52 <i>c</i>	Na ₂ CrO ₄	0.41 <i>c</i>
HCl	6.69 <i>b</i>	NaBr	2.98 <i>a</i>	CaCl ₂	2.40 <i>d</i>	Na ₂ FUM	0.88 <i>b</i>
HNO ₃	3.66 <i>a</i>	NaBrO ₃	-0.68 <i>u</i>	CaI ₂	3.27 <i>b</i>	Na ₂ MAL	0.12 <i>b</i>
KAC	5.05 <i>a</i>	NaCl	2.23 <i>a</i>	Ca(NO ₃) ₂	0.93 <i>d</i>	Na ₂ S ₂ O ₃	0.18 <i>c</i>
KBr	1.15 <i>b</i>	NaClO ₃	0.41 <i>a</i>	Cd(NO ₃) ₂	1.53 <i>b</i>	Na ₂ SO ₄	-0.19 <i>c</i>
KBrO ₃	-2.00 <i>u</i>	NaClO ₄	1.30 <i>b</i>	CdSO ₄	0.016 <i>b</i>	NdCl ₃	1.42 <i>c</i>
KCl	0.92 <i>b</i>	NaCNS	2.94 <i>a</i>	CeCl ₃	1.41 <i>c</i>	(NH ₄) ₂ SO ₄	-0.25 <i>c</i>
KClO ₃	-1.70 <i>u</i>	NaF	0.37 <i>u</i>	CoBr ₂	3.08 <i>d</i>	NiCl ₂	2.33 <i>d</i>
KCNS	0.61 <i>b</i>	NaFORM	1.83 <i>a</i>	CoBr ₂	3.08 <i>d</i>	NiSO ₄	0.025 <i>c</i>
KF	2.13 <i>a</i>	NaHMAL	0.01 <i>b</i>	CoCl ₂	2.25 <i>b</i>	Pb(ClO ₄) ₂	2.25 <i>d</i>
KHMAL	-0.72 <i>b</i>	NaHSUC	0.60 <i>b</i>	CoI ₂	3.87 <i>d</i>	Pb(NO ₃) ₂	-0.97 <i>b</i>
KH ₂ PO ₄	-2.54 <i>a</i>	NaH ₂ PO ₄	-1.59 <i>a</i>	Co(NO ₃) ₂	2.08 <i>d</i>	PrCl ₃	1.40 <i>c</i>
KHSUC	0.02 <i>b</i>	NaI	4.06 <i>a</i>	CrCl ₃	1.72 <i>b</i>	Rb ₂ SO ₄	0.007 <i>b</i>
KI	1.62 <i>b</i>	NaNO ₃	-0.39 <i>b</i>	Cr(NO ₃) ₃	1.51 <i>c</i>	ScCl ₃	1.68 <i>c</i>
KNO ₃	-2.33 <i>a</i>	NaOH	3.00 <i>a</i>	Cr ₂ (SO ₄) ₃	0.43 <i>d</i>	SmCl ₃	1.47 <i>c</i>
KOH	4.77 <i>b</i>	NaPROP	5.54 <i>a</i>	Cs ₂ SO ₄	0.16 <i>b</i>	SrBr ₂	2.34 <i>b</i>
KTOL	-1.75 <i>a</i>	NaTOL	-0.80 <i>a</i>	CuCl ₂	1.40 <i>b</i>	SrCl ₂	1.95 <i>c</i>
		NH ₄ Cl	0.82 <i>b</i>	Cu(NO ₃) ₂	1.83 <i>d</i>	Sr(ClO ₄) ₂	2.84 <i>d</i>
		NH ₄ NO ₃	-1.15 <i>b</i>	CuSO ₄	0.00 <i>c</i>	SrI ₂	3.03 <i>b</i>
		RbAC	5.39 <i>a</i>	EuCl ₃	1.49 <i>c</i>	Sr(NO ₃) ₂	0.30 <i>c</i>
		RbBr	0.46 <i>b</i>	FeCl ₂	2.16 <i>b</i>	UO ₂ Cl ₂	2.40 <i>b</i>
		RbCl	0.62 <i>b</i>	K ₂ CrO ₄	0.16 <i>c</i>	UO ₂ (ClO ₄) ₂	5.64 <i>d</i>
		RbCl	0.62 <i>b</i>	K ₂ SO ₄	-0.25 <i>u</i>	UO ₂ (NO ₃) ₂	2.90 <i>b</i>
		RbI	0.45 <i>b</i>	LaCl ₃	1.41 <i>c</i>	UO ₂ SO ₄	0.066 <i>b</i>
		RbNO ₃	-2.49 <i>b</i>	Li ₂ SO ₄	0.57 <i>c</i>	YCl ₃	1.55 <i>c</i>
		TIAC	-0.73 <i>b</i>	MgAC ₂	0.83 <i>c</i>	Zn(ClO ₄) ₂	4.30 <i>a</i>
				MgBr ₂	3.50 <i>d</i>	Zn(NO ₃) ₂	2.28 <i>d</i>
				MgCl ₂	2.90 <i>d</i>	ZnSO ₄	0.05 <i>c</i>

* Calculated values of Γ compared against experimental data at 25°C up to ionic strength I_M as indicated below:
a: $I_M = 3$ to 4; *b*: $I_M = 4.5$ to 6; *c*: $I_M = 9$; *d*: $I_M = 15$; *u*: limited data, q determined usually from Γ° at highest reported concentration.

strength of 10, can now be estimated as follows (10):

$$\frac{\log(\Gamma_t^\circ/\Gamma_{25^\circ\text{C}}^\circ)_{I=10}}{t-25} = a \log(\Gamma_{25^\circ\text{C}}^\circ)_{I=10} + b \quad (4)$$

After finding $\log(\Gamma_t^\circ)_{I=10}$ and locating the desired isotherm, we can obtain Γ_t° values at any other concentration from Figure 1 or 2. Alternatively, if we recognize that $\log(\Gamma_t^\circ)_{I=10}$ is almost linear in values of q from -2 to +7, it follows that the above temperature equation can be written in terms of q with results applicable at all concentrations:

$$\frac{q_t - q_{25}}{t - 25} = a q_{25} + b^* \quad (5)$$

Here, q_{25} and q_t are the indicated solution's temperature t in degrees Centigrade. Except for sulfuric acid which does not obey the generalized correlations of Figures 1 and 2, the constants a and b^* for the sulfates are, respectively, -0.0079 and -0.0029, while for most other electrolytes (10), a is about -0.005 while $b = 0$ and $b^* = 0.0085$. To illustrate application

of Equation (5): when I is 8, Γ° for hydrochloric acid is reported by Akerlof and Teare (1) to be 5.9 at 25°C, resulting in $q = 6.23$ from Figure 3 or Equation (3). Substituting into Equation (5) and solving at 50°C with $a = -0.005$ and $b^* = 0.0085$, we find q to be 5.66. From Equation (3), $\Gamma^\circ = 4.7$ vs. Akerlof and Teare's experimental value for Γ° of 4.5 at these conditions.

VAPOR PRESSURES

Having determined the appropriate q value in Equation (3) for an electrolyte of interest, the corresponding vapor pressure of water as a function of I and $\log \Gamma^\circ$ can be determined from the Gibbs-Duhem equation (6). Values so calculated were overlaid onto Figure 2 for pure solutions of singly charged (1:1) electrolytes and are presented in Figure 3 as dotted lines in terms of the water activity (a_w°), defined in the usual manner as the ratio of the vapor pressure of water over the electrolyte solution to that of pure water at the same temperature. Thus, fixing Γ° and I determines the value of the water activ-

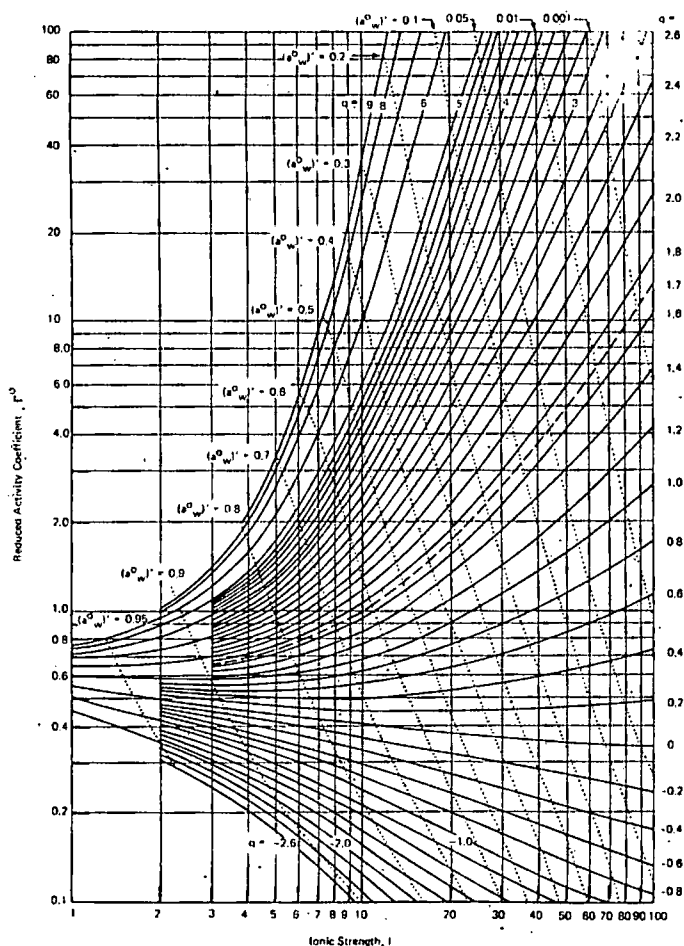


Fig. 3. Isotherms of Γ° vs. I showing lines of constant water activities for 1:1 electrolytes. For higher electrolytes, $(a_w^0)'$ values read from this figure are used in Equation (6) to determine water activities.

ity $(a_w^0)'$, regardless of the temperature. To illustrate, the activity coefficient Γ° is known to be 7.41 for a 10 molal hydrochloric acid solution at 50°C. From Figure 3*, $(a_w^0)'$ for this solution is 0.44, which compares well with the experimental value of 0.43.

At a given set of values of ionic strength I and reduced activity coefficient Γ° , water activities (and vapor pressures) of the higher electrolytes differ from those of the 1:1 electrolytes. Water activities for these higher electrolytes, namely (a_w^0) , can nevertheless be estimated at any temperature from the 1:1 water activity curves of Figure 3 by use of the following equation further derived from the Gibbs-Duhem equation (6):

$$\log (a_w^0) = (0.0156) (I) \left(1 - \frac{1}{Z_1 Z_2} \right) + \log (a_w^0)' \quad (6)$$

To illustrate at 25°C, nickel chloride is a 2:1 electrolyte for which Γ° is 1.72 when the ionic strength I is 12 (a 4.0 molal

solution). At these values of I and Γ° , $(a_w^0)'$ is 0.52 from Figure 3. If we substitute into Equation (6), $\log (a_w^0)$ for nickel chloride is -0.190 or $a_w^0 = 0.645$, which is in fair agreement with 0.635 calculated from the reported osmotic coefficient ϕ of 2.10. A further comparison of experimental water activities and values obtained from Figure 3, with Equation (6) used for higher electrolytes, is shown in Table 2. Agreement is generally seen to be within a few percent.

It is evident that knowing the vapor pressure of a solution at a given ionic strength and temperature, the corresponding value of Γ° and q can be directly determined from Figure 3 for 1:1 electrolytes [with Equation (6) first required to determine $(a_w^0)'$ for higher electrolytes]. Thus, when only the vapor pressure of water is known at some value of I , Figure 3 can be used for curve identification of a given electrolyte (δ) and the appropriate value of q determined for use in Equation (3).

ACTIVITY COEFFICIENTS IN MIXTURES

At any given ionic strength, the reduced activity coefficient of electrolyte 12 in a multicomponent (mixed) aqueous solution, namely, Γ_{12} , is usually different from its pure solution value. In mixed solutions, Γ_{12} can be estimated from pure solution values of Γ° for the various cation-anion pairs that can be formed with all Γ° values determined at the temperature and total ionic strength of the mixture. Upon identifying the cations i with the odd subscripts 1, 3, 5, etc., and anions j with even subscripts 2, 4, 6, etc., calculating I_i , I_j , and V_{ij} values as defined in the notation, $\log \Gamma_{12}$ is obtained by the following equation, applicable to solutions of two, three, four, and by extension of any number of ions:

$$\log \Gamma_{12} = \frac{Z_1}{Z_1 + Z_2} (V_{12} I_2 \log \Gamma_{12}^\circ + V_{14} I_4 \log \Gamma_{14}^\circ + \dots) / I_T + \frac{Z_2}{Z_1 + Z_2} (V_{21} I_1 \log \Gamma_{21}^\circ + V_{23} I_3 \log \Gamma_{23}^\circ + \dots) / I_T \quad (7)$$

TABLE 2. CALCULATED VS. EXPERIMENTAL VALUES OF WATER ACTIVITIES AT 25°C

Electrolyte	Ionic strength I	a_w^0 (experimental)*	a_w^0 from Figure 3 and Equation (6)
AgNO ₃	12	0.855	0.86
NH ₄ NO ₃	20	0.678	0.67
NaOH	20	0.136	0.15
	27.5	0.07	0.06
HCl	16	0.174	0.17
CaCl ₂	30	0.180	0.17
Pb(ClO ₄)	30	0.178	0.17
"	36	0.113	0.13
NH ₄ NO ₃	27.5	0.62	0.60
MgCl ₂	17.4	0.33	0.38
LiCl	19.6	0.11	0.10

*Largely calculated from the osmotic coefficient ϕ (13).

*With a stamped self-addressed envelope, requests for a full scale version of Figure 3 can be accommodated by addressing either one of the authors.

or in general, for any specific electrolyte identified by cation numbered i and anion j :

$$\log \Gamma_{ij} = \frac{Z_i}{Z_i + Z_j} (V_{i2} I_2 \log \Gamma_{i2}^\circ + V_{i4} I_4 \log \Gamma_{i4}^\circ + \dots) / I_T \\ + \frac{Z_j}{Z_i + Z_j} (V_{j1} I_1 \log \Gamma_{j1}^\circ + V_{j3} I_3 \log \Gamma_{j3}^\circ + \dots) / I_T \quad (8)$$

If only ions 1, 2, and 3 are present, then the second term contained in the first parenthesis of Equation (7) disappears, since I_4 is now zero. Similarly, if ions 5 and 6 are added to the system, then the term $V_{16} I_6 \log \Gamma_{16}^\circ$ is added in the first parenthesis of Equation (7), and $V_{25} I_5 \log \Gamma_{25}^\circ$ is added in the second parenthesis. Equation (7) is an extended version of that originally presented (7) and is applicable to all mixtures, regardless of the magnitude of Z_1, Z_2 , etc. As expected when all cations carry the same charge and all anions the same charge (for example, in mixtures of nickel chloride, copper chloride, ferrous chloride), Equation (7) simplifies to the following equation previously published (8):

$$\log \Gamma_{12} = 0.5 (Y_2 \log \Gamma_{12}^\circ + Y_4 \log \Gamma_{32}^\circ + X_1 \log \Gamma_{12}^\circ \\ + X_3 \log \Gamma_{32}^\circ) \quad (9)$$

In practice, simplified Equation (9) predicts activity coefficients in three ion solutions of singly and doubly charged ions with apparently no greater error, and in some cases less error than the more complex Equations (7) and (8). However, Equations (7) and (8) appear superior in predicting activity coefficients for solutions containing either more than three ions or having ions carrying more than a double charge. To illustrate the applicability of Equation (7) to a three-ion system, consider a mixed solution saturated at 25°C with sodium nitrate, which is 5.30 molal in Na^+ , 15.84 molal in NO_3^- , and 5.27 molal in Ca^{++} . It follows by definition that the total ionic strength I_T for this solution is $0.5(5.30)(1^2) + 0.5(15.84)(1^2) + 0.5(5.27)(2^2) = 21.1$. Designating Na^+ , NO_3^- , and Ca^{++} as ions 1, 2, and 3, then V_{12} and V_{23} are, respectively, 2.0 and 2.25, while $\log \Gamma_{12}^\circ$ and $\log \Gamma_{32}^\circ$ are, respectively, -0.60 (7) and -0.08 (4). If we substitute into Equation (7), Γ_{12} for sodium nitrate in this mixed solution is 0.45 vs. a value calculated from the solubility product of 0.38 (7).

VAPOR PRESSURES OVER MULTICOMPONENT SOLUTIONS

Corresponding to the above activity coefficient equations, the water activity for the mixed solution just discussed can be calculated from the pure solution activities of water, $(a_w^\circ)_{12}$, $(a_w^\circ)_{14}$, $(a_w^\circ)_{32}$, etc., at the total ionic strength and temperature of the mixed solution. For a four-ion system, $\log (a_w)_{\text{mix}}$ becomes

$$\log (a_w)_{\text{mix}} = W_{12} \log (a_w^\circ)_{12} + W_{14} \log (a_w^\circ)_{14} \\ + W_{32} \log (a_w^\circ)_{32} + W_{34} \log (a_w^\circ)_{34} + r \quad (10)$$

For similarly charged electrolytes such as magnesium chloride in calcium bromide, the residue term is zero and $W_{ij} = X_i Y_j$,

which yields the following previously published equation for a four-ion system (8):

$$\log (a_w)_{\text{mix}} = X_1 Y_2 \log (a_w^\circ)_{12} + X_1 Y_4 \log (a_w^\circ)_{14} \\ + X_3 Y_2 \log (a_w^\circ)_{32} + X_3 Y_4 \log (a_w^\circ)_{34} \quad (11)$$

When the electrolytes are dissimilarly charged, we have generally found the residue term r to be small, and it can usually be neglected in Equation (10).

To illustrate an application, a solution saturated at 30°C with both sodium chloride and potassium chloride is 5.09 and 2.3 molal in these two salts, respectively. Since (a_w°) values for sodium chloride and potassium chloride, namely, salts 12 and 32, are, respectively, 0.71 and 0.78 at this solution temperature and total ionic strength, then the water activity over the mixed solution $(a_w)_{\text{mix}}$ is 0.73 by Equation (10) or (11) vs. an experimental value of 0.72 (2).

Equations (10) and (11) are again readily extended to systems of more than four ions in which case the general expression for $\log (a_w)_{\text{mix}}$ can be written $\log (a_w)_{\text{mix}} = \sum_j \sum_i W_{ij} \log (a_w^\circ)_{ij} + r$, where i takes on odd values 1, 3, 5, 7, etc., representing the cations, and j takes on even values 2, 4, 6, etc., representing the anions.

CALCULATION OF SALT SOLUBILITY

Solubilities of an electrolyte in its pure and mixed solutions are related by the so-called thermodynamic solubility product $(K_t)_{sp}$ which is constant for a specific electrolyte at a given temperature in all its saturated solutions, whether pure or mixed. Thus, for pure and mixed saturated solutions of an electrolyte containing n_o waters of crystallization per mole electrolyte, the solubility products are related as follows (8):

$$(m_1)^{\nu_1} (m_2)^{\nu_2} (\gamma_{12})^{\nu_1 \nu_2} (a_w)_{\text{mix}}^{n_o} = (m_1^\circ)^{\nu_1} (m_2^\circ)^{\nu_2} (\gamma_{12}^\circ)^{\nu_1 \nu_2} (a_w^\circ)^{n_o} \quad (12)$$

For saturated solutions containing electrolytes carrying no waters of crystallization like sodium chloride, n_o is of course zero, while for salts of low solubility, like calcium carbonate, activity coefficients are close to unity. In either pure or mixed saturated solutions of low ionic strength, Equation (12) reduces to the more familiar form of the solubility product, namely

$$(m_1)^{\nu_1} (m_2)^{\nu_2} = (m_1^\circ)^{\nu_1} (m_2^\circ)^{\nu_2} \quad (13)$$

As an example of the application of Equation (12), consider two solutions A and B, each saturated with $\text{FeCl}_2 \cdot 4\text{H}_2\text{O}$, with solution A containing no other electrolyte while solution B carries some dissolved hydrochloric acid. Using appropriate values of γ_{12} and a_w , the solubility of $\text{FeCl}_2 \cdot 4\text{H}_2\text{O}$ in this case is (8)

$$[(m_1)(m_2)^2 (\gamma_{12})^3 (a_w)^4]_B = (K_t)_{sp} \\ = [(m_1^\circ)(m_2^\circ)^2 (\gamma_{12}^\circ)^3 (a_w^\circ)^4]_A \quad (14)$$

For this ferrous chloride-hydrochloric acid solution, success in using the approximate form of the activity coefficient and wa-

ter activity equation [Equations (9) and (11)] has been discussed earlier (8). In addition, the relevant solubility product equation for systems in which the number of waters of hydration n is not the same in pure and mixed solutions is given by

$$(m_1)^{\nu_1} (m_2)^{\nu_2} (\gamma_{12})^{\nu_{12}} (a_w)_{\text{mix}}^n = (m_1^0)^{\nu_1} (m_2^0)^{\nu_2} (\gamma_{12}^0)^{\nu_{12}} (a_w^0)^n k_c \quad (15)$$

The free energy change between crystals with n and n_0 waters of hydration is accounted for by the term k_c with examples of the use of the above equation given in reference 8.

The above solubility product equations have been further extended (9) to double salts containing three or more ions such as glaserite $[\text{K}_3\text{Na}(\text{SO}_4)_2]$.

PRECISION

Errors in estimating activity coefficients for various mixed electrolytes in aqueous solutions have been found to be generally within 20%. Further errors can be introduced when Γ^0 values are predicted from vapor pressure lowering, extrapolated over large ranges of ionic strength in Figure 3, or large temperature ranges by Equations (4) or (5). In addition, significant deviations from these curves can be found (12) for some electrolytes such as zinc and cadmium chlorides, bromides, and iodides, sulfuric acid, and thorium nitrate. Thus, the relations shown here should be used only when direct experimental evidence is not available.

NOTATION

a_w = activity of water, $(a_w^0)_{12}$ being for a pure solution of an electrolyte identified by subscript, $(a_w)_{\text{mix}}$ being for mixed solution. $(a_w^0)^n$ is derived from the Gibbs-Duhem expression and is equal to the activity of water for 1:1 electrolytes

$$\exp(x) = e^x$$

F = molal free energy of formation from the elements F_{n_0} referring to crystals carrying n_0 moles water of hydration per mole electrolyte, F_n referring to crystals carrying n moles water of hydration per mole electrolyte, and F_w being the free energy of liquid water, namely, -56.69 Kcal/g-mole at 25°C

I = ionic strengths indicated by the subscript. The ionic strengths I_1, I_2, \dots , of the individual ions are $0.5 m_1 Z_1^2, 0.5 m_2 Z_2^2$, and so forth. The total ionic strength I_T equals $0.5 (m_1 Z_1^2 + m_2 Z_2^2 + m_3 Z_3^2 + \dots)$. For a pure system, I_T equals $0.5 m_{12} \nu_{12} Z_1 Z_2$. The cationic strength I_c of a solution is $(I_1 + I_3 + \dots)$, the anionic strength I_a is $(I_2 + I_4 + \dots)$

$$k_c = \exp(-\Delta F_c/RT)$$

log, ln = logarithm to base 10 and base e, respectively

m = molality, in g-mole/1 000 g water. The ions or electrolyte referred to are indicated by subscript

n = number of moles of water of hydration per mole of electrolyte in its crystalline phase, n_0 and n

being used to distinguish between crystals in equilibrium with saturated pure and mixed solutions, respectively

$$r = \text{residue term} = 0.0156 I_T (W_{12} X_1 Y_2 / Z_1 Z_2 + W_{23} X_3 Y_2 / Z_2 Z_3 + \dots) - 0.0156 [I_1 / Z_1^2 + I_2 / Z_2^2 + I_3 / Z_3^2 + I_4 / Z_4^2 + \dots]$$

$$R = 1.987 \text{ cal/(g-mole} \cdot ^\circ\text{K)}$$

$$V_{ij} = \text{weighting factor } 0.5 (Z_i + Z_j)^2 / (Z_i Z_j)$$

$$W_{ij} = X_i X_j [(Z_i + Z_j)^2 / Z_i Z_j] (I_c / I_T) (I_a / I_T)$$

X = cationic fraction, as indicated by subscript i , for example, I_1 / I_c or I_3 / I_c

Y = anionic fraction, as indicated by subscript j , for example, I_2 / I_a or I_4 / I_a

Z = absolute number of unit charges on the ion, indicated by the subscript. Thus Z is unity for Na^+ , also for NO_3^- , but is 3 for Al^{3+} , also for PO_4^{3-} .

Similarly charged electrolytes are those with similar charges on cations and anions such as magnesium chloride in calcium bromide or sodium chloride in potassium chloride. Dissimilarly charged electrolytes are those where either a) all cations do not have the same charge or b) all anions do not have the same charge; examples include a mixture of sodium sulfate in magnesium chloride or sodium chloride in magnesium chloride

γ = mean ionic activity coefficient for the electrolyte indicated by the subscript, γ_{12}^0 being for the pure solution and γ_{12} for the mixed solution

Γ = reduced activity coefficient, namely, $\gamma_{12}^{1/Z_1 Z_2}$ for the electrolyte indicated by the subscript. The term Γ_{12}^0 refers to pure solutions, Γ_{12} to mixed solutions

$$\Delta F_c = \text{free energy change of crystal hydration} = F_{n_0} - F_n (n_0 - n) F_w$$

ν = moles of ions formed upon complete dissociation of 1 mole of electrolyte. Thus, ν_1 is for the indicated cation, ν_2 is for the indicated anion, while ν_{12} is the total number of ions namely $(\nu_1 + \nu_2)$. To illustrate, ν_{12} is 2 for sodium chloride and 5 for aluminum sulfate.

$$\phi = \text{osmotic coefficient } (6, 13) = -(63.9 Z_1 Z_2 \log a_w) / I$$

SUBSCRIPTS

1, 3, 5, ... = odd numbers refer to cations

2, 4, 6, ... = even numbers refer to anions

w = water

mix = values for a multicomponent solution

SUPERSCRIPTS

0 = pure electrolyte solution (that is, binary solution)
= for 1:1 electrolyte—see a_w

OTHER SYMBOLS

1:1 = electrolytes with singly charged ions where $Z_1 = 1$ and $Z_2 = 1$

$M:N$ = electrolytes having ion charges given by $Z_1 = M$, $Z_2 = N$

LITERATURE CITED

1. Akerlöf, G., and J. W. Teare, "Thermodynamics of Concentrated Aqueous Solutions of Hydrochloric Acid," *J. Am. Chem. Soc.*, **59**, 1855 (1937).
2. Adams, J. R., and A. Mertz, *Ind. Eng. Chem.*, **21**, 305 (1929).
3. Bromley, L. A., "Thermodynamic Properties of Strong Electrolytes in Aqueous Solutions," *AIChE J.*, **19**, No. 2, 313 (1973).
4. Harned, H. S., and B. B. Owen, *Physical Chemistry of Electrolyte Solutions*, 3 ed., App. A, Reinhold, New York (1958).
5. *International Critical Tables*, Vol. IV, p. 301, McGraw-Hill, New York (1928).
6. Kusik, C. L., and H. P. Meissner, "Vapor Pressures of Water over Aqueous Solutions of Strong Electrolytes," *Ind. Eng. Chem. Process Design Develop.*, **12**, 112 (1973).
7. Meissner, H. P., and C. L. Kusik, "Activity Coefficients of Strong Electrolytes in Multicomponent Aqueous Solutions," *AIChE J.*, **18**, 2294 (1972).
8. —, "Aqueous Solutions of Two or More Strong Electrolytes," *Ind. Eng. Chem. Process Design Develop.*, **12**, 205 (1973).
9. —, to be submitted to IEC (1978).
10. Meissner, H. P., et al., "Activity Coefficients of Strong Electrolytes in Aqueous Solutions—Effect of Temperature," *AIChE J.*, **18**, 3661 (1972).
11. Meissner, H. P., and N. A. Peppas, "Activity Coefficients—Aqueous Solutions of Polybasic Acids and Their Salts," *ibid.*, **19**, 4806 (1973).
12. Meissner, H. P., and J. W. Tester, "Activity Coefficients of Strong Electrolytes in Aqueous Solutions," *Ind. Eng. Chem. Process Design Develop.*, **11**, 1128 (1972).
13. Robinson, R. A., and R. H. Stokes, *Electrolyte Solutions*, 2 ed., Academic Press, New York (1959).
14. Rossini, F. D., "Selected Values of Thermodynamic Properties," *Circular 500*, National Bureau of Standards (1952).